frontiers | Research Topics

Structure-function metrology of proteins

Edited by
Alex Jones, Milena Quaglia and Isabel Moraes

Published in
Frontiers in Molecular Biosciences

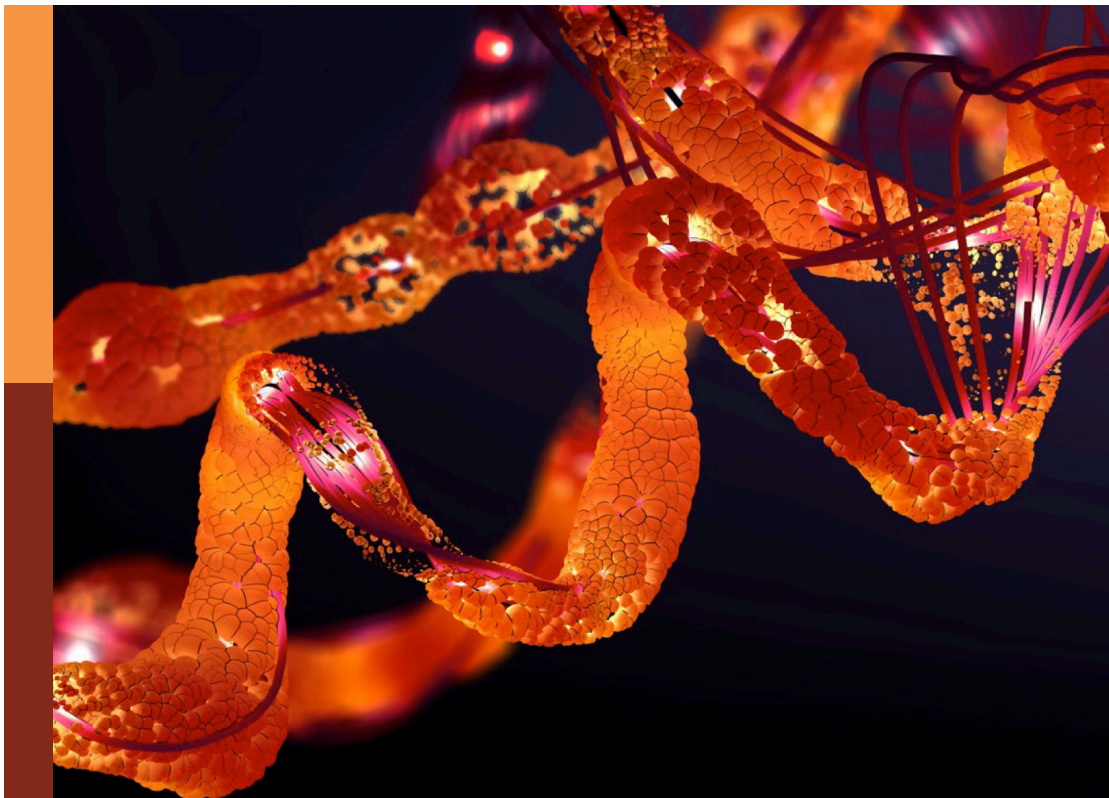

ISSN 1664-8714
ISBN 978-2-83251-895-3
DOI 10.3389/978-2-83251-895-3

About Frontiers

Frontiers is more than just an open access publisher of scholarly articles: it is a pioneering approach to the world of academia, radically improving the way scholarly research is managed. The grand vision of Frontiers is a world where all people have an equal opportunity to seek, share and generate knowledge. Frontiers provides immediate and permanent online open access to all its publications, but this alone is not enough to realize our grand goals.

Frontiers journal series

The Frontiers journal series is a multi-tier and interdisciplinary set of open-access, online journals, promising a paradigm shift from the current review, selection and dissemination processes in academic publishing. All Frontiers journals are driven by researchers for researchers; therefore, they constitute a service to the scholarly community. At the same time, the *Frontiers journal series* operates on a revolutionary invention, the tiered publishing system, initially addressing specific communities of scholars, and gradually climbing up to broader public understanding, thus serving the interests of the lay society, too.

Dedication to quality

Each Frontiers article is a landmark of the highest quality, thanks to genuinely collaborative interactions between authors and review editors, who include some of the world's best academicians. Research must be certified by peers before entering a stream of knowledge that may eventually reach the public - and shape society; therefore, Frontiers only applies the most rigorous and unbiased reviews. Frontiers revolutionizes research publishing by freely delivering the most outstanding research, evaluated with no bias from both the academic and social point of view. By applying the most advanced information technologies, Frontiers is catapulting scholarly publishing into a new generation.

What are Frontiers Research Topics?

Frontiers Research Topics are very popular trademarks of the *Frontiers journals series*: they are collections of at least ten articles, all centered on a particular subject. With their unique mix of varied contributions from Original Research to Review Articles, Frontiers Research Topics unify the most influential researchers, the latest key findings and historical advances in a hot research area.

Find out more on how to host your own Frontiers Research Topic or contribute to one as an author by contacting the Frontiers editorial office: frontiersin.org/about/contact

Structure-function metrology of proteins

Topic editors

Alex Jones — National Physical Laboratory, United Kingdom

Milena Quaglia — National Measurement Laboratory at LGC, United Kingdom

Isabel Moraes — DeepMind Technologies Limited, United Kingdom

Citation

Jones, A., Quaglia, M., Moraes, I., eds. (2023). *Structure-function metrology of proteins*. Lausanne: Frontiers Media SA. doi: 10.3389/978-2-83251-895-3

Table of contents

frontiers | Frontiers in Molecular Biosciences

TYPE Editorial
PUBLISHED 17 January 2023
DOI 10.3389/fmolb.2023.1125791

OPEN ACCESS

EDITED AND REVIEWED BY
Annalisa Pastore,
King's College London, United Kingdom

*CORRESPONDENCE
Alex R. Jones,
alex.jones@npl.co.uk

†PRESENT ADDRESS
DeepMind, London, United Kingdom

SPECIALTY SECTION
This article was submitted to Structural Biology,
a section of the journal
Frontiers in Molecular Biosciences

RECEIVED 16 December 2022
ACCEPTED 06 January 2023
PUBLISHED 17 January 2023

CITATION
Jones AR, Moraes I and Quaglia M (2023), Editorial: Structure-function metrology of proteins.
Front. Mol. Biosci. 10:1125791.
doi: 10.3389/fmolb.2023.1125791

Editorial: Structure-function metrology of proteins

Alex R. Jones[1]*, Isabel Moraes[1†] and Milena Quaglia[2]

[1]Biometrology, Chemical and Biological Sciences Department, National Physical Laboratory, Teddington, United Kingdom, [2]NML at LGC Ltd., Teddington, United Kingdom

KEYWORDS

protein metrology, biologics, higher order structure, protein function, protein engineering

Editorial on the Research Topic
Structure-function metrology of proteins

The importance of a protein's structure to its function is beyond doubt. The Protein Databank (PDB) (Berman et al., 2003) and the AlphaFold Protein Structure Database (https://aplhafold.ebi.ac.uk), based on the AlphaFold algorithm (Jumper et al., 2021), make freely available vast numbers of experimentally-determined and predicted 3D protein structures that underpin much impactful science. What is becoming increasingly clear, however, is that the structure-function paradigm of proteins is more nuanced than a collection of fixed, static 3D structures. Data from a wide range of measures have revealed varying degrees of conformational flexibility and disorder (e.g., van der Lee et al., 2014), that are not only critical to function, but that can also change during a functional cycle. This picture serves to illustrate the importance to protein metrology of using a range of different measurements, but it also reflects a complex measurement landscape. The increased use of proteins in the Life Sciences, Health, and Food industries complicates the picture further. Which measurements, or combination thereof, are required to demonstrate regulatory compliance (e.g., EU, 2011; EU, 2017) for a given application? One size is unlikely to fit all.

These factors pose important challenges for the metrology community, which seeks to standardise measurement practice, develop reference materials (RMs) and methods, and achieve traceability to the International System of Units (SI). Recent progress has seen new strategies to achieve SI traceability for peptide/protein measurement (e.g., Josephs et al., 2017; Josephs et al., 2019; Cobbaert et al., 2021; Briones et al., 2022), and increased standardisation activities such as the Joint Committee of Traceability in Laboratory Medicine, the International Federation of Clinical Chemistry, and the CCQM (Consultative Committee for Amount of Substance: Metrology in Chemistry and Biology) Working Group on Protein Analysis at the BIPM (International Bureau of Weights and Measures). Much of the activity to date, however, has focussed on traceable measurement of protein quantification and purity. In this Research Topic of 12 papers—6 *Original Research* contributions and 6 *Reviews/Perspectives*—we present a snapshot of the current state of the art in protein metrology for structural analysis. Although inevitably not comprehensive, with 67 authors contributing from National Metrology Institutes, industry, and academia from across the globe we hope it is to some degree representative. In many ways, the intention is to be forward-looking; for the Research Topic not only to summarise where we are but where we might need to go to develop a metrology fit for the life sciences.

A common theme of the Research Topic concerns the metrology of protein-based biopharmaceuticals, in particular monoclonal antibody (mAb) therapeutics. Kinumi et al, from the National Metrology Institute of Japan, National Institute of Advanced Industrial Science and Technology (NMIJ/AIST) have developed a new IgG1κ mAb RM, RM6208-a,

(AIST-MAB), for the validation and comparison of methods and instrumentation used in the analysis of biopharmaceuticals. They establish the solution concentration of AIST-MAB via amino acid analysis using isotope dilution mass spectrometry (MS) and analyse its physicochemical properties using a range of techniques (e.g., electrophoresis, chromatography methods, peptide/glycan mapping). In Yandrofski et al, the National Institute of Standards and Technology (NIST) in the United States and Agilent Technologies Ltd. review several interlaboratory studies that use another IgG1κ mAb RM, RM8671 (NISTmAb). These studies focus on measurements of both primary and higher-order structure (HOS) of NISTmAb and any post-translational modifications (PMTs) that might have occurred. From the outcomes of each study, they discuss future perspectives, with an emphasis on identifying gaps in the measurement infrastructure used in biopharmaceutical development.

In an original study from NIST, Giddens and Schiel publish a site-specific method to characterise PMTs in NISTmAb. Using a ligand that masks specific sites, they assay oxidation of the unmasked methionine residues in NISTmAb using a range of biophysical approaches (MS, surface plasmon resonance, fluorescence spectroscopy). Their intention is to adapt the method for more general use in the characterisation of PMTs that can change the biological activity of protein-based drugs. Metcalfe from the National Institute for Biological Standards and Control (NIBSC) reviews modern analytical methods for the detection and quantification of free-cysteine residues, which can impact both the stability and efficacy of therapeutic mAbs. He compares spectroscopic (e.g., optical absorption and fluorescence), MS [e.g., isotope labelling and liquid chromatography-MS (LC-MS)], and hybrid methods, again illustrating the range of complementary information provided by using different measures to elucidate a given sample.

mAbs are also used in immunoassays to detect antigens, in clinical diagnostics for example. They are often immobilised by covalent conjugation, but their antigen affinity and specificity can be altered by concomitant changes in HOS. Luckau et al. from the National Measurement Laboratory at LGC and Fleet Bioprocessing Ltd. demonstrate the power of MS methods (LC-MS and hydrogen-deuterium exchange MS) to identify correlations between changes to HOS of mAbs as a result of conjugation and immunoassay performance. Antigen RMs exist to calibrate immunoassays and for cell-based potency testing of mAbs. Because RMs might be stored for long periods before use, they are often lyophilised for stability (the same is true for many biopharmaceuticals). Matejtschuk et al. from NIBSC have investigated the importance of formulation on the preservation of activity of an interleukin-6 RM following the freeze-drying process. The lyophilised material was characterised for several formulations using thermal analysis and scanning electron microscopy, and bioactivity data were compared using a cell-based secreted embryonic alkaline phosphatase (SEAP) assay.

Stability assessment is a central consideration of protein metrology. Properly folded proteins are vital for the safety and efficacy of biopharmaceuticals. A good understanding of protein stability during measurement is also vital to inform experimental design and ensure meaningful and reproducible R&D data. Kwan et al, from the National Physical Laboratory (NPL) in the UK publish a *Perspective* with Douglas Instruments Ltd. summarising methods for the high-throughput screening of conditions that promote stability and reduce aggregation or proteolysis. Instrumentation is now available that enables rapid analysis of low volume samples in multi-well plates to assess properties like hydrodynamic radius (dynamic light scattering), thermal stability (differential scanning fluorimetry), and secondary structure (circular dichroism). Kwok et al. from BLOC Laboratories Ltd., NPL, UCB Pharm Ltd., and the Universities of Bath, Bristol and Waikato report a new thermodynamic model for the quantification of protein conformational flexibility from fluorescence spectroscopy data. Based on the red edge excitation shift (REES) effect of the intrinsic fluorophore, tryptophan, the authors test their new model against several exemplar proteins, including a therapeutic mAb and a *de novo* designed enzyme. This analysis is not only useful for stability screening, but also can help elucidate conformational dynamics that are functional.

Electron paramagnetic resonance (EPR) spectroscopy has proven to be a powerful technique with which to analyse protein conformational dynamics by measuring distance distributions between paramagnetic centres on the nanometre scale. Said et al. from the University of Freiburg evaluate the accuracy of distance measurements made between pairs of spin-correlated radicals in photo-active proteins using out-of-phase electron spin echo envelope modulation (OOP-ESEEM). In doing so, they illustrate the utility of spectral simulation in validating experimentally-derived structural parameters. Continuing with this theme, Russell et al. from the University of St. Andrews provide a comparative review of six different open access simulation/analysis packages with which to extract distance distributions from double electron resonance (DEER) EPR data. In a way that is analogous to making correlated measurements of the same sample using different modalities, the authors reveal how complementary insights can be gained from different methods of analysing the same data.

Proteins and peptides are re-engineered and *de novo* designed for functional properties that are difficult to attain from the synthesis of other organic molecules. Enzymes, for example, achieve challenging chemical transformations with remarkable specificity and selectivity and are therefore desirable targets for use as industrial biocatalysts. Ding et al. from King's College London review how a combination of structural investigation and computational modelling has aided the rational modification of enzymes. They summarise future perspectives for the field and emphasise the importance of a dynamic picture of protein structure in helping realise the potential of enzyme engineering. *De novo* designed peptides can be active species or can self-assemble into larger structures to serve as biopharmaceuticals or RMs with well-controlled and traceable properties. De Sá Magalhães et al, from University College London, NPL, and Viranova AB, report a method for using an accessible transmission electron microscopy (TEM) approach for determining critical quality attributes of virus-like particles (VLPs). VLPs have been developed as vaccines and drugs, and the authors benchmark their method against VLP model systems.

In summary, this Research Topic illustrates the importance of sound protein metrology to healthcare, industry, measurement science, and fundamental research. It also reflects some of the challenges faced, not only in the context of protein measurement, but also in life sciences metrology more broadly. Looking forward, we acknowledge that HOS is the primary distinction between biological

and chemical metrology and must formalise a metrological approach with multimodal, correlated measurement at its heart.

Author contributions

AJ wrote the manuscript with contributions from IM and MQ.

Acknowledgments

MQ, IM, and AJ acknowledge the National Measurement System of the Department for Business, Energy and Industrial Strategy for funding and thank Inês Camacho and Mike Shaw (both NPL) for valuable feedback on the manuscript.

Conflict of interest

Author MQ was employed by the company NML at LGC Ltd.

The remaining authors declare that the research was conducted in the absence of any commercial or financial relationships that could be construed as a potential conflict of interest.

Publisher's note

All claims expressed in this article are solely those of the authors and do not necessarily represent those of their affiliated organizations, or those of the publisher, the editors and the reviewers. Any product that may be evaluated in this article, or claim that may be made by its manufacturer, is not guaranteed or endorsed by the publisher.

References

Berman, H., Henrick, K., and Nakamura, H. (2003). Announcing the worldwide protein data bank. *Nat. Struct. Biol.* 10 (12), 980. doi:10.1038/nsb1203-980

Briones, A., Martos, G., Bedu, M., Choteau, T., Josephs, R. D., Wielgosz, R. I., et al. (2022). An SI-traceable reference material for virus-like particles. *iScience* 25 (5), 104294. doi:10.1016/j.isci.2022.104294

Cobbaert, C. M., Althaus, H., Begcevic Brkovic, I., Ceglarek, U., Coassin, S., Delatour, V., et al. (2021). Towards an SI-traceable reference measurement system for seven serum apolipoproteins using bottom-up quantitative proteomics: Conceptual approach enabled by cross-disciplinary/cross-sector collaboration. *Clin. Chem.* 67 (3), 478–489. doi:10.1093/clinchem/hvaa239

Eu, T. (2011). Official Journal of the European Union. *REGULATION (EU) No 1169/2011 OF THE EUROPEAN PARLIAMENT AND OF THE COUNCIL on the provision of food information to consumers, amending Regulations (EC) No 1924/2006 and (EC) No 1925/2006 of the European Parliament and of the Council, and repealing Commission Directive 87/250/EEC, Council Directive 90/496/EEC, Commission Directive 1999/10/EC, Directive 2000/13/EC of the European Parliament and of the Council, Commission Directives 2002/67/EC and 2008/5/EC and Commission Regulation (EC) No 608/2004*.Brussels and Luxembourg.

Eu, T. (2017). Official Journal of the European Union. *REGULATION (EU) 2017/746 OF THE EUROPEAN PARLIAMENT AND OF THE COUNCIL on* in vitro *diagnostic medical devices and repealing Directive 98/79/EC and Commission Decision 2010/227/EU*.Brussels and Luxembourg

Josephs, R. D., Martos, G., Li, M., Wu, L., Melanson, J. E., Quaglia, M., et al. (2019). Establishment of measurement traceability for peptide and protein quantification through rigorous purity assessment—A review. *Metrologia* 56 (4), 044006. doi:10.1088/1681-7575/ab27e5

Josephs, R. D., Stoppacher, N., Westwood, S., Wielgosz, R. I., Li, M., Quaglia, M., et al. (2017). Concept paper on SI value assignment of purity - model for the classification of peptide/protein purity determinations. *J. Chem. Metrol.* 11 (1), 1–8. doi:10.25135/jcm.1.17.02.030

Jumper, J., Evans, R., Pritzel, A., Green, T., Figurnov, M., Ronneberger, O., et al. (2021). Highly accurate protein structure prediction with AlphaFold. *Nature* 596 (7873), 583–589. doi:10.1038/s41586-021-03819-2

van der Lee, R., Buljan, M., Lang, B., Weatheritt, R. J., Daughdrill, G. W., Dunker, A. K., et al. (2014). Classification of intrinsically disordered regions and proteins. *Chem. Rev.* 114 (13), 6589–6631. doi:10.1021/cr400525m

frontiers in Molecular Biosciences

ORIGINAL RESEARCH
published: 03 December 2021
doi: 10.3389/fmolb.2021.778244

A Thermodynamic Model for Interpreting Tryptophan Excitation-Energy-Dependent Fluorescence Spectra Provides Insight Into Protein Conformational Sampling and Stability

A Kwok[1†], IS Camacho[2†], S Winter[1], M Knight[3], RM Meade[1], MW Van der Kamp[4], A Turner[3], J O'Hara[3], JM Mason[1], AR Jones[2], VL Arcus[5]* and CR Pudney[1,6]**

[1]Department of Biology and Biochemistry, University of Bath, Bath, United Kingdom, [2]Biometrology, Chemical and Biological Sciences Department, National Physical Laboratory, London, United Kingdom, [3]UCB, Slough, United Kingdom, [4]School of Biochemistry, University of Bristol, Bristol, United Kingdom, [5]School of Science, Faculty of Science and Engineering, University of Waikato, Hamilton, New Zealand, [6]BLOC Laboratories Limited, Bath, United Kingdom

It is now over 30 years since Demchenko and Ladokhin first posited the potential of the tryptophan red edge excitation shift (REES) effect to capture information on protein molecular dynamics. While there have been many key efforts in the intervening years, a biophysical thermodynamic model to quantify the relationship between the REES effect and protein flexibility has been lacking. Without such a model the full potential of the REES effect cannot be realized. Here, we present a thermodynamic model of the tryptophan REES effect that captures information on protein conformational flexibility, even with proteins containing multiple tryptophan residues. Our study incorporates exemplars at every scale, from tryptophan in solution, single tryptophan peptides, to multitryptophan proteins, with examples including a structurally disordered peptide, *de novo* designed enzyme, human regulatory protein, therapeutic monoclonal antibodies in active commercial development, and a mesophilic and hyperthermophilic enzyme. Combined, our model and data suggest a route forward for the experimental measurement of the protein REES effect and point to the potential for integrating biomolecular simulation with experimental data to yield novel insights.

Keywords: protein stability, red edge excitation shift, fluorescence, tryptophan, conformational sampling

OPEN ACCESS

Edited by:
Robert Stephen Phillips, University of Georgia, United States

Reviewed by:
Vladimir N. Uversky, University of South Florida, United States
Andrew Harry Albert Clayton, Swinburne University of Technology, Australia
Kate Stafford, Atomwise Inc., United States

****Correspondence:***
AR Jones
alex.jones@npl.co.uk
VL Arcus
varcus@waikato.ac.nz
CR Pudney
c.r.pudney@bath.ac.uk

[†]These authors have contributed equally to this work

Specialty section:
This article was submitted to Structural Biology, a section of the journal Frontiers in Molecular Biosciences

Received: *16 September 2021*
Accepted: *27 October 2021*
Published: *03 December 2021*

Citation:
Kwok A, Camacho IS, Winter S, Knight M, Meade RM, Van der Kamp MW, Turner A, O'Hara J, Mason JM, Jones AR, Arcus VL and Pudney CR (2021) A Thermodynamic Model for Interpreting Tryptophan Excitation-Energy-Dependent Fluorescence Spectra Provides Insight Into Protein Conformational Sampling and Stability. Front. Mol. Biosci. 8:778244. doi: 10.3389/fmolb.2021.778244

INTRODUCTION

Tracking protein conformational change and, even more subtly, changes in the equilibrium of available conformational states is central to molecular biosciences. Protein stability is intimately linked with the distribution of conformational states (Karshikoff et al., 2015) and, as a good generalization, increased stability tracks with a decrease in the distribution of conformational states (increasing rigidity, decreasing conformational entropy). (Vihinen, 1987). While engineering protein stability has advanced enormously, the tools to sensitively and quantitatively track these changes are lacking. There are a broad range of potential analytical tools, but only a few that can be applied

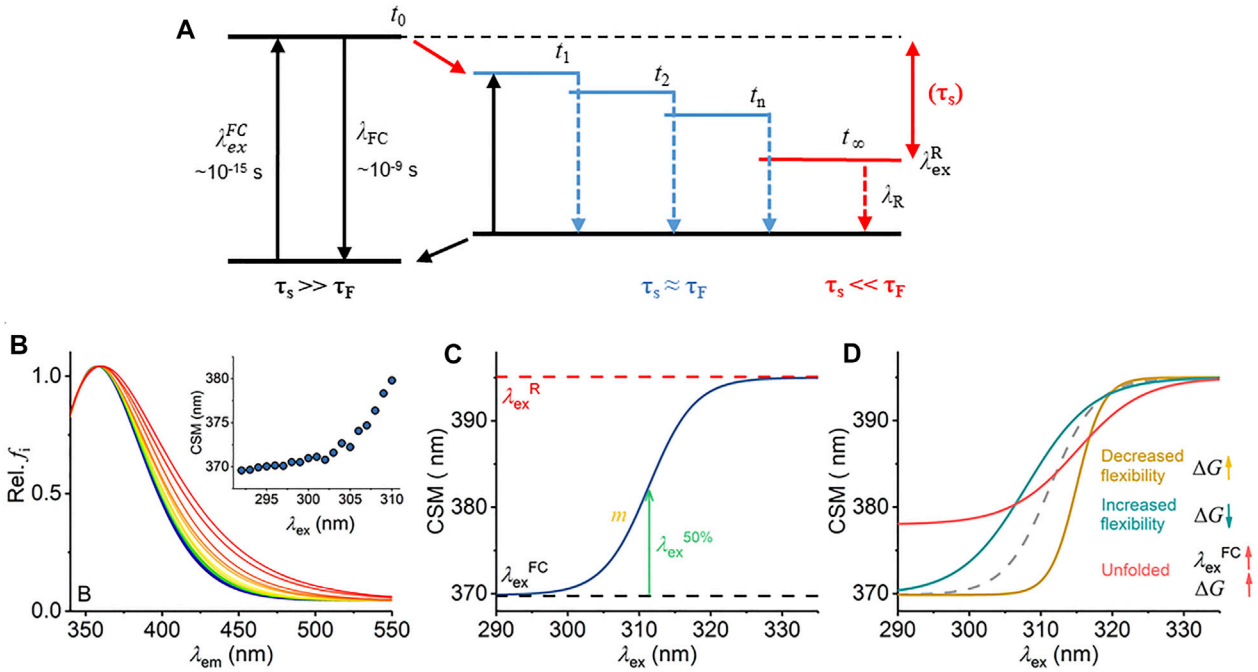

FIGURE 1 | Mechanism of the REES effect, predicted experimental observables, and graphical description of **Eq. (7)**. **(A)** Jablonski diagram illustrating the REES effect. **(B)** Example model Trp REES data showing the normalized emission spectrum with increasing excitation wavelength and inset as the change in CSM versus excitation wavelength. **(C)** Graphical depiction of **Eq. (7)**. **(D)** Predicted spectral changes resulting from variations in **Eq. (7)** from shifts in protein flexibility and conformational state (folding).

routinely to the vast majority of proteins without unreasonable requirements regarding solvent, protein concentrations, and thermal stability, or without the requirement of surface attachment or labeling. (Magliery et al., 2011). Moreover, the vast majority of protein conformational changes are subtle, described as "breathing" motions, where most structural orders (primary to quaternary) of the protein are not altered, but it is the equilibrium of conformational states (protein flexibility) that changes (Kossiakoff, 1986).

The red edge excitation shift (REES) phenomenon is a sensitive reporter of a fluorophore's environment, and the mechanism is shown in **Figure 1A**. (Azumi and Itoh, 1973; Itoh and Azumi, 1975; Azumi et al., 1976; Demchenko, 2002). Briefly, the REES effect is sensitive to shifts in the distribution of environments a fluorophore can sample. As this distribution of environments gets smaller, the REES effect becomes "smaller" (we discuss this in depth below) and vice versa. In proteins, such shifts in the distribution of states are how we conceptualize protein motions. Potentially then, the REES effect could be a powerful tool, both to study protein flexibility/motion but also (as above) stability.

Radiative fluorescence takes place after light absorption alongside non-radiative processes, which include vibrational relaxation and solvent relaxation (dipolar re-organization). Vibrational relaxation is typically fast (~10^{-12} s) relative to the lifetime of fluorescence emission (τ_F ~ 10^{-10}–10^{-9} s) and so causes a complete relaxation of the system to its lowest energy level prior to emission. This gives rise to the familiar red shift of fluorescence emission compared to absorption (Stokes shift). The Lippert–Mataga equation [**Eq. (1)**] illustrates that the greater the polarity of solvent, the larger the anticipated Stokes shift (Mataga et al., 1956; Lippert Von, 1957).

$$\bar{\nu}_A - \bar{\nu}_E = \frac{2}{hc}\left(\frac{\varepsilon - 1}{2\varepsilon + 1} - \frac{n^2 - 1}{2n^2 + 1}\right)\frac{(\mu_E - \mu_G)^2}{a^3} + L \qquad (1)$$

where the Stokes shift (difference between wavenumber of absorption and emission), $\bar{\nu}_A - \bar{\nu}_E$, is governed by the dielectric constant of the solvent, ε, specifically the reorientation of solvent dipoles; the refractive index, n; the dipole moment of the ground and excited states, μ_G and μ_E, respectively; the radius of the fluorophore cavity, a; and a constant, L.

Equation (1) assumes that the solvent relaxation is complete prior to emission. However, solvent relaxation is not necessarily always fast relative to fluorescence emission and under a range of solvent or environmental conditions can approach τ_F [~10^{-10} –10^{-9} s]. The longer solvent relaxation lifetime (τ_S) can therefore affect the level from which emission occurs and so the emission wavelength, in which case it also contributes to the Stokes shift (Azumi and Itoh, 1973; Itoh and Azumi, 1975; Azumi et al., 1976; Demchenko, 2002). Specifically, one expects that an ensemble of energetic substates is formed related to the distribution of solvent relaxation lifetimes, i.e., the available distribution of solvent–fluorophore interaction energies. The additive contribution of these states to the steady-state emission

spectrum gives rise to broad-band emission, which is observed as inhomogeneous broadening of the spectra. This broadening is then dependent on the excitation energy used, since as one decreases the excitation energy, there is an increasing photoselection of states (**Figure 1A**). Experimentally, one then observes a red shift in the emission spectra with respect to increasing excitation wavelength, i.e., decreasing excitation energy (**Figure 1B**). The inhomogeneous broadening will be dependent on a range of physical conditions that affect τ_S, including temperature, viscosity, and solvent dipole moment (and therefore the solvent dielectric constant) (Azumi and Itoh, 1973; Itoh and Azumi, 1975; Azumi et al., 1976; Demchenko, 2002).

The sensitivity of the REES effect to changes in the equilibrium of solvent–fluorophore interaction energies suggests potential for using the approach to track changes in protein conformational state using the intrinsic fluorescence of the aromatic amino acids (Demchenko, 2002; Chattopadhyay and Haldar, 2014). Indeed, tryptophan (Trp) has been shown to give a large REES effect in numerous proteins, and we point to excellent reviews that illustrate key examples (Demchenko and Ladokhin, 1988; Raghuraman et al., 2005; Chattopadhyay and Haldar, 2014; Brahama and Raghuraman, 2021). Demchenko and Ladokhin (1988) suggest that the selection between ^1L_a and ^1L_b electronic excited states of Trp acts to increase the magnitude of the red edge excitation shift. Trp has the advantage that its emission can be separated from tyrosine (Tyr) and phenylalanine (Phe) by excitation at wavelengths >~292 nm (Adman and Jensen, 1981). Trp REES is therefore a potentially excellent probe of protein conformational change, intrinsic disorder, and possibly even of changes in the equilibrium of conformational states.

We have previously applied and validated an empirical model for describing protein REES data as a function of the equilibrium of conformational states, which we call QUBES (quantitative understanding of biomolecular edge shift) (Catici et al., 2016; Jones et al., 2017; Knight et al., 2020). Herein, we refer to changes in the equilibrium of conformational states as changes in flexibility, with a more flexible protein having a broader equilibrium of conformational states. We track the changes in inhomogeneous broadening as the change in the center of spectral mass (CSM; **Eq. (2)**) of steady-state emission spectra (example shown in **Figure 1B**).

$$CSM = \frac{\sum (f_i \times \lambda_{Em})}{\sum (f_i)} \tag{2}$$

where f_i is fluorescence intensity, and λ_{Em} is the emission wavelength. The resulting data are then fit to the QUBES model [**Eq. (3)**].

$$CSM = CSM_0 + Ae^{R\Delta\lambda_{Ex}} \tag{3}$$

where CSM_0 is the CSM value independent of λ_{Em}, and λ_{Ex} is the excitation wavelength. The amplitude relative to CSM_0 and curvature of the exponential are described by A and R, respectively. We have previously found that the parameters from this empirical model could be used to track changes in protein stability (Jones et al., 2017; Knight et al., 2020; Hindson et al., 2021). That this simple model appears to provide useful insight suggests that it is approximating the protein REES effect to a level of accuracy.

While **Eq. (3)** performs well at tracking shifts in protein rigidity/flexibility (also for multi-Trp containing proteins) (Catici et al., 2016; Jones et al., 2017; Knight et al., 2020; Hindson et al., 2021), it does not relate to a specific thermodynamic parameter and neglects the fact that protein Trp emission will have a finite maximum observable spectral red shift at λ_{ex}^R. Moreover, the data from our QUBES model cannot be cross-compared to proteins with different Trp content and location in structure. Developing our QUBES model towards an accurate *a priori* thermodynamic model would therefore enhance both the accuracy and utility of the approach for studying protein dynamics/stability.

Herein, we describe a thermodynamic model for interpreting protein REES data, which builds on our early work. Using a range of model systems from Trp/solvent studies, single Trp-containing proteins and multi-Trp proteins, we find that the new model accurately tracks with independent metrics of changes in the equilibrium of protein conformational states and more gross metrics of protein folding. Moreover, our model points to the need for new experimental approaches to monitor the protein REES effect.

RESULTS AND DISCUSSION

As described by Demchenko and Ladokhin (1988), we posit a two-state model and assume $[FC] \rightleftharpoons [R]$ and $\tau_F \ll \tau_S$; then, the fractional concentration of R is given by:

$$\frac{[R]}{[FC] + [R]} = \frac{e^{\frac{-\Delta G}{RT}}}{1 + e^{\frac{-\Delta G}{RT}}} \tag{4}$$

where ΔG is the difference in free energy between the $[FC]$ (Frank–Condon) and $[R]$ (relaxed) states, noting that the RT term is gas constant temperature. We then assume that ΔG will change linearly with excitation wavelength:

$$\Delta G = \Delta G_{\lambda_{ex}^{FC}} - m\Delta\lambda_{ex} \tag{5}$$

with a gradient, m. Thus, we anticipate a two-state transition between FC and R states due to photoselection by excitation wavelength with baselines $CSM(\lambda_{ex}^{FC})$ and $CSM(\lambda_{ex}^{R})$, respectively. The gradient of the transition is given by $|\Delta G|$ at any particular λ_{Ex}.

$$CSM(\lambda_{ex}) = \frac{CSM\left(\lambda_{ex}^{FC}\right) + CSM\left(\lambda_{ex}^{R}\right)e^{\frac{-\Delta G}{RT}}}{1 + e^{\frac{-\Delta G}{RT}}} \tag{6}$$

$$CSM(\lambda_{ex}) = \frac{CSM\left(\lambda_{ex}^{FC}\right) + CSM\left(\lambda_{ex}^{R}\right)e^{m\left(\lambda_{ex} - \lambda_{ex}^{50\%}\right)/RT}}{1 + e^{m\left(\lambda_{ex} - \lambda_{ex}^{50\%}\right)/RT}} \tag{7}$$

Equations (6) and **(7)** establish three key parameters, $CSM(\lambda_{ex}^{FC})$, $CSM(\lambda_{ex}^{R})$, and ΔG, which we describe below. **Figure 1C** shows **Eq. (7)** plotted in a similar manner to the experimental data as in **Figure 1B** inset but now showing the full

range of the function. **Equation (7)** is a more complete description of the REES effect [c.f. **Eq. (3)**] since it predicts a maximum magnitude of the CSM, corresponding to the fully relaxed state, λ_{ex}^{R} (**Figure 1C**). Clearly, the emission spectra cannot become infinitely inhomogeneously broadened, and so the REES effect must saturate. Indeed, we and others have observed saturation of the REES effect with non-Trp fluorophores used as molecular probes (Gulácsy et al., 2019) or ligands (Kabir et al., 2021), and so **Eq. (7)** is logical for the REES effect in proteins. $CSM\,(\lambda_{ex}^{FC})$ is the CSM corresponding to λ_{ex}^{FC} shown in **Figure 1A**. We anticipate that $CSM\,(\lambda_{ex}^{FC})$ will be responsive to changes in solvation environment in a similar way to the spectral shift of Trp on solvent/exposure/occlusion. That is, as the Burstein classification (Reshetnyak et al., 2001) and **Eq. (1)**, increasing solvent exposure will cause $CSM\,(\lambda_{ex}^{FC})$ to red shift and a decrease in solvent exposure will cause $CSM\,(\lambda_{ex}^{FC})$ to blue shift (Reshetnyak et al., 2001).

$CSM\,(\lambda_{ex}^{R})$ is the CSM corresponding to λ_{ex}^{R} in **Figure 1A**, i.e., the completely relaxed state of the solvent. Note that this value should be fixed for a given system, unlike $CSM\,(\lambda_{ex}^{FC})$, which will be responsive to variation in the solvent environment. This parameter, therefore, represents entirely novel information over previous models of the REES effect. Specifically, $CSM\,(\lambda_{ex}^{R})$ reports on an extreme of the solvent–fluorophore interaction energy. It can therefore be considered a unique identifying parameter related to both protein structure and physiochemical environment.

The combination of $CSM\,(\lambda_{ex}^{FC})$ and $CSM\,(\lambda_{ex}^{R})$ will therefore be a unique measurement of the accessible equilibrium of protein conformational states and will be specific to a specific protein structure, molecular flexibility, and Trp content and location.

ΔG arises from **Eq. (4)**, calculated from the extracted $\lambda_{ex}^{50\%}$ and m terms in **Eq. (7)**, where $\lambda_{ex}^{50\%}$ is the λ_{Ex} at half the maximal CSM and m reflects information on the slope of the plot shown in **Figure 1C**. This gives ΔG ($\mathrm{J\,mol^{-1}}$) at a specific wavelength, which has a linear relationship to λ_{Ex} [**Eq. (5)**]. For consistency, we report the gradient of the plot of ΔG versus λ_{Ex}, giving ΔG expressed in $\mathrm{J\,mol^{-1}\,nm^{-1}}$, as the value of m. ΔG reports on the energy gap between adjacent emissive states, for example, in the most extreme case, the gap between the *FC* and *R* states as shown in **Figure 1A**. As the number of intermediate state increases, reflecting an increased distribution of solvent–fluorophore interaction energies, so the magnitude of ΔG will increase, representing a broader distribution of intermediate states.

Inspection of **Figure 1A** yields two ready predictions for the information content of the parameters in **Eq. (7)**, and we show how these are predicted to affect the resulting experimental data in **Figure 1D**:

i) A decrease in the gap between $CSM\,(\lambda_{ex}^{FC})$ and $CSM\,(\lambda_{ex}^{R})$ [i.e., an increase in $CSM\,(\lambda_{ex}^{FC})$] would reflect a narrower distribution—but unchanged number—of solvent–fluorophore interaction energies. That is, based on Hammond's postulate (Hammond, 1955), the environments of the *FC* and *R* states become more similar. Experimentally, this would manifest as an increase in the extracted magnitude of $CSM\,(\lambda_{ex}^{FC})$ since $CSM\,(\lambda_{ex}^{R})$ will be a fixed value for a given solvent–fluorophore environment.

ii) In a more rigid molecule, we expect to observe fewer intermediate states. Fewer energetically discrete solvent–fluorophore environments would reflect a larger energy gap between adjacent states (t_1, t_2, etc., **Figure 1A**). A smaller distribution of solvent–solute interaction energies would manifest as reduced inhomogeneous broadening of the emission spectra (**Figure 1C**). Experimentally, one then expects a steeper transition between $CSM\,(\lambda_{ex}^{FC})$ and $CSM\,(\lambda_{ex}^{R})$, giving rise to an increased ΔG.

Changes in both $CSM\,(\lambda_{ex}^{FC})$ and ΔG are possible and indeed likely when studying proteins. As a specific case, for a completely unfolded versus folded protein, we anticipate an increase in $CSM\,(\lambda_{ex}^{FC})$ and an increase in ΔG. That is, $CSM\,(\lambda_{ex}^{FC})$ increases due to the increase in solvent exposure of the available Trp residues and ΔG increases as the number of intermediate (discrete) solvent–fluorophore interaction energies decreases, tending towards the homogeneous single state where all Trps are completely solvent exposed, i.e., as in (i) where the environments of the *FC* and *R* states become more similar. Clearly "folded" and "unfolded" protein are two extremes of a continuum of states, for example including simple shifts in protein dynamics, molten globule-like states, and partially unfolded states. **Figure 1D** is not an exhaustive list of anticipated changes but serves to illustrate key examples.

We acknowledge that it is not possible to experimentally reach saturation of the Trp REES effect ($CSM\,(\lambda_{ex}^{R})$) using conventional spectrometers owing to the technical limitations of the intensity of UV light (using halogen lamps) and convolution of the emission spectra with the relatively broad-band excitation achieved from monochromation at the large slit widths necessary to increase illumination. In practice, we find that the signal to noise ratio becomes intractable beyond $\lambda_{Ex} \approx 310$ nm for the same concentration of protein. We discuss this in more detail below.

Tryptophan in Solution

Given that **Eq. (7)** is a new thermodynamic model for the REES effect, we first explore the sensitivity of the Trp REES effect to variation in the physical properties of the solvent. Solvent studies have been used to probe the sensitivity of the REES effect using viscous matrices such as ethylene glycol and glycerol and temperature variation, by monitoring Trp or indole emission. (Azumi et al., 1976; Demchenko and Ladokhin, 1988). One expects the REES effect to be sensitive to changes in the dielectric constant and viscosity of the solvent and the temperature owing to the effect on the lifetime of solvent relaxation as described above. We are not aware of a method to independently vary dielectric constant, viscosity, and temperature, so we have employed a matrix effect experiment, where we monitor the Trp REES effect as a function of methanol (MeOH) concentration (0%–70% v/v with buffered Tris–HCl, pH 8.0 as in **Figure 2**) and temperature (20°–50°C). **Supplementary Figure S1** shows the variation in viscosity and dielectric constant for the conditions we used. Using this approach, we are able to explore the REES effect, which is quantified using **Eq. (6)** across a range of conditions. **Figures 2A–D** show the REES data as a

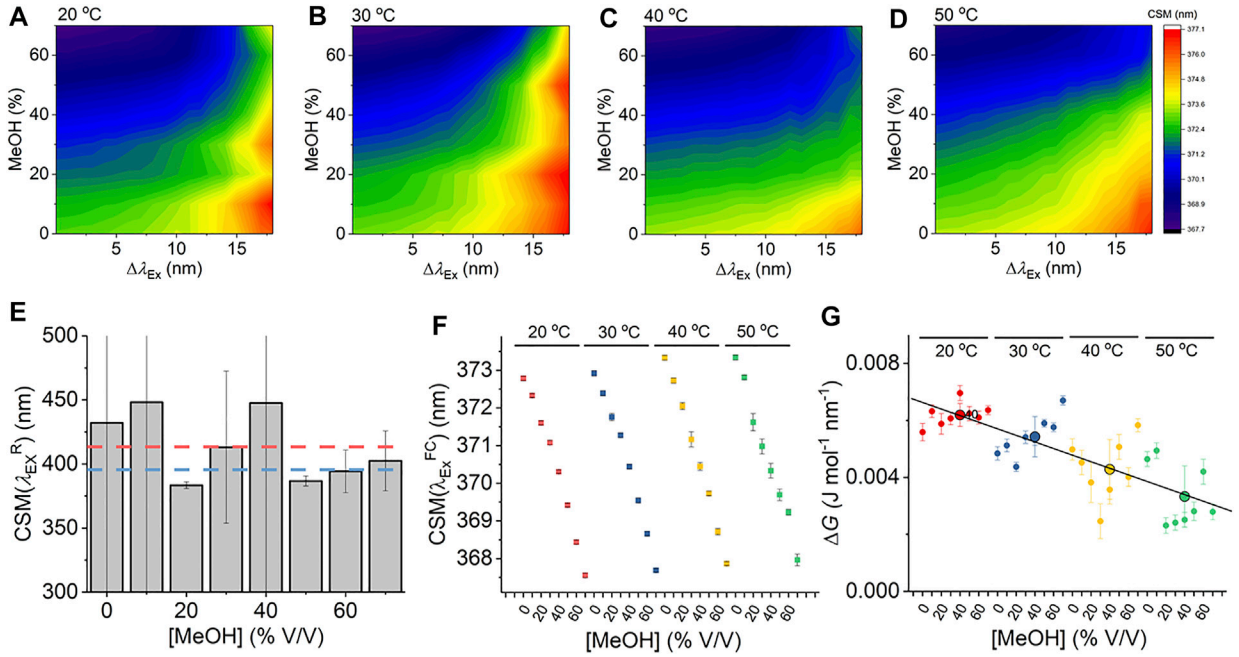

FIGURE 2 | Solvent and temperature studies of the Trp REES effect. **(A–D)** Variation in CSM for L-Trp with varying percentages of MeOH and versus temperature. **(E)** Variation in the $CSM\,(\lambda_{ex}^{R})$ value for each [MeOH] studied, where the fitted $CSM\,(\lambda_{ex}^{R})$ value is a shared parameter for each temperature at a given [MeOH]. The dashed red line shows the average $CSM\,(\lambda_{ex}^{R})$ value, and the blue dashed line shows the $CSM\,(\lambda_{ex}^{R})$ value extracted where all data are fit to **Eq. (7)** with $CSM\,(\lambda_{ex}^{R})$ as a shared parameter. **(F)** Variation in the $CSM\,(\lambda_{ex}^{FC})$ value for each condition studied. **(G)** Variation in the ΔG at fixed λ_{Ex} value for each condition studied. Large colored dots represent the average of [MeOH] at each temperature, and the error bars are the standard deviation. Conditions, 1 μM L-Trp, 50 mM Tris–HCl, pH 8.0.

function of the variation in MeOH concentration at each temperature studied. These data are then fit to **Eq. (7)**, and the resulting parameters are shown in **Figures 2E–G**.

As we describe above, accessing the limiting value of $CSM\,(\lambda_{ex}^{R})$ experimentally is challenging, and thus, the extracted value of $CSM\,(\lambda_{ex}^{R})$ from fits to **Eq. (7)** will necessarily have a large error, and in some cases, the extracted values are unrealistically large (>1,000 nm). As an alternative, one can share the value of $CSM\,(\lambda_{ex}^{R})$ during fitting, which provides much greater restraint and improved accuracy on the extracted magnitude of $CSM\,(\lambda_{ex}^{R})$. Fitting with $CSM\,(\lambda_{ex}^{R})$ as a shared parameter for all the data sets gives an average and standard deviation of $CSM\,(\lambda_{ex}^{R})$ = 398 ± 8.0 nm, respectively (**Figure 2E**). However, we are aware that this likely masks much of the real variation in the magnitude of $CSM\,(\lambda_{ex}^{R})$, not least because we expect variation in this parameter with changes in dielectric constant. Alternatively, fitting the data with shared values of $CSM\,(\lambda_{ex}^{R})$ for the same [MeOH] but at varying temperatures (**Figure 2E**) gives $CSM\,(\lambda_{ex}^{R})$ = 413.5 ± 26.2 nm. These data suggest a practical range of $CSM\,(\lambda_{ex}^{R})$ (at least across the range of the conditions explored in **Figure 2**) from ~387 to ~440 nm. **Supplementary Figure S2** shows modeled data showing the effect of varying $CSM\,(\lambda_{ex}^{R})$ on the extracted magnitude of ΔG [there is no effect on $CSM\,(\lambda_{ex}^{FC})$]. These data show a ~10% variance in ΔG across the range of $CSM\,(\lambda_{ex}^{R})$ values tested, and so the effect of using a fixed value of $CSM\,(\lambda_{ex}^{R})$ is not large. We note that the range of dielectric constant and viscosity values that this represents is far broader than for a protein in aqueous solvent. Therefore, while not ideal, until it is experimentally possible to extract data at very low excitation energies ($>\lambda_{Ex}$ = 310 nm), fixing the magnitude of $CSM\,(\lambda_{ex}^{R})$ is necessary to extract realistic values for ΔG, and our data imply that this will not cause a large effect on protein data. We therefore use $CSM\,(\lambda_{ex}^{R})$ = 398.7 (as above) to extract values of $CSM\,(\lambda_{ex}^{FC})$ and ΔG for the data shown in **Figures 2F** and **G**.

Figure 2F shows the variation in $CSM\,(\lambda_{ex}^{FC})$ for each [MeOH] at each temperature studied. At all temperatures, the magnitude of $CSM\,(\lambda_{ex}^{FC})$ decreases with increasing [MeOH]. This decrease is expected for a simple solvatochromatic shift and has been observed in numerous cases previously. This expected finding is satisfying because it validates the interpretation of $CSM\,(\lambda_{ex}^{FC})$ value as an excitation wavelength-independent metric of Trp solvation. **Supplementary Figure S3** shows the temperature dependence of $CSM\,(\lambda_{ex}^{FC})$ at each [MeOH], extracted from fitting to a simple linear function. **Supplementary Figure S3** shows a "V-shaped" temperature dependence with respect to [MeOH], with a minimum at 30% [MeOH], where there is no measurable temperature dependence of $CSM\,(\lambda_{ex}^{FC})$ within error. Therefore, our data suggest that in aqueous solvent, $CSM\,(\lambda_{ex}^{FC})$ appears to have an intrinsic temperature dependence of ~0.02 nm^{-1} K^{-1} for free Trp in aqueous solution. We consider whether this is borne out in protein samples below. **Figure 2G** shows the variation in the extracted magnitude of ΔG as a function of [MeOH] at each temperature studied. We find a general decrease in the magnitude of ΔG with increasing

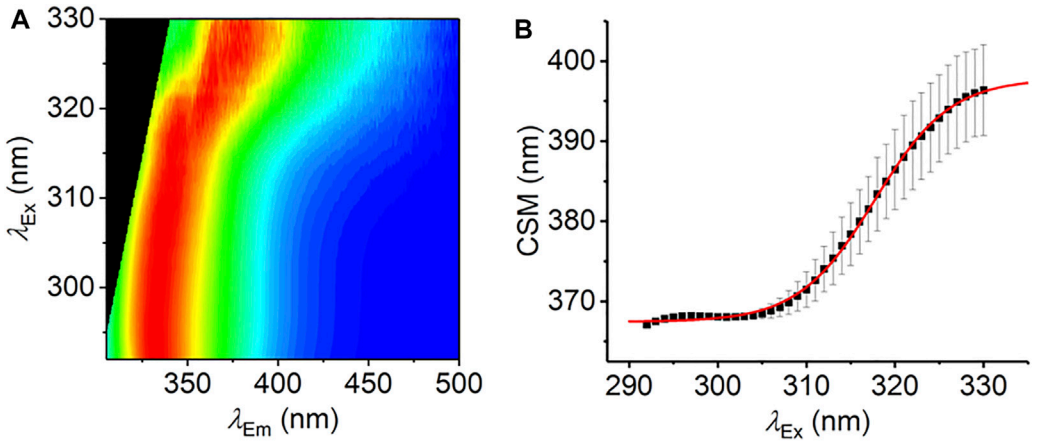

FIGURE 3 | The REES effect monitored over extended λ_{Ex} range. **(A)** Averaged, normalized raw emission spectra. **(B)** CSM data extracted from λ_{Em} = 340–500 nm. The solid red line is the fit to **Eq. (7)**. Data collected in triplicate; error bars are the standard deviation. Conditions: 1.25 mM L-Trp, MeOH, 25°C.

temperature (-0.1×10^{-3} J mol^{-1} nm^{-1} K^{-1} across the range studied). Increased temperature will increase τ_S; thus, one anticipates a smaller REES effect and, as described above, a decrease in the magnitude of ΔG as we indeed observed. Our data track with a logical and expected physical effect validates the principles used to derive **Eq. (7)**.

From **Figure 2G**, we do not observe a consistent trend in the magnitude of ΔG with respect to [MeOH]. It is not possible to independently vary viscosity, dielectric constant, and temperature, with viscosity having a strong dependence on both temperature and [MeOH]. In contrast to $CSM\,(\lambda_{ex}^{FC})$, it is evident that ΔG is acutely sensitive to such interdependencies. It is therefore not possible to assess simple trends in ΔG as a function of [MeOH]. To illustrate this point, we have plotted the magnitude of ΔG versus the calculated solvent viscosity and dielectric constant for the combination of [MeOH] and temperature used—**Supplementary Figure S1C**. From this figure, it is apparent that there is a complex trend governing the magnitude of ΔG, resembling an elliptical phase-type relationship. What these data do serve to illustrate is not only the extreme sensitivity of the REES effect to the solvent environment as predicted but also the potential sensitivity of **Eq. (7)** to track these subtle changes in the distribution of solvent–solute interaction energies. We note that the solvent conditions that we used are not particularly viscous. That we are able to observe a REES effect under these conditions (above) illustrates the sensitivity of the REES effect under less extreme conditions.

Our data using free Trp in solution provides a detailed baseline for the sensitivity of **Eq. (7)** to track the protein Trp REES effect, most notably establishing realistic ranges for the magnitude of $CSM\,(\lambda_{ex}^{R})$ and the temperature dependence of $CSM\,(\lambda_{ex}^{FC})$ and illustrating the extreme sensitivity of the magnitude of ΔG to a change in the solvent–fluorophore interaction energies. We wished to directly validate the saturation of CSM ($CSM\,(\lambda_{ex}^{R})$) as shown in **Figure 1C** and to confirm that the extracted value of $CSM\,(\lambda_{ex}^{R})$ = 398.7 from **Figure 2** is an accurate reflection of $CSM\,(\lambda_{ex}^{R})$ for Trp. As we discuss above, there are significant technical challenges in collecting a "complete" REES data set (measuring emission spectra at λ_{Ex} > 310 nm). However, using a combination of elevated L-Trp concentration (1.25 mM), a non-aqueous solvent (100% MeOH), and high excitation power (~100 μW), we have achieved this goal, as shown in **Figure 3**. **Figure 3A** shows the averaged raw spectral data. CSM is calculated in the range of 340–500 nm to be consistent across all excitation wavelengths used without being convolved of excitation peaks. From **Figure 3B**, the resulting CSM data saturate as predicted by **Eq. (6)** and fitting using **Eq. (7)** gives $CSM\,(\lambda_{ex}^{R})$ = 397.8 ± 4.0. This compares with $CSM\,(\lambda_{ex}^{R})$ = 398.7 ± 8.0 nm extracted from fitting to the Trp REES data (**Figure 2**) as described above. That these values are effectively identical is a powerful validation that $CSM\,(\lambda_{ex}^{R})$ extracted from simultaneous fitting of REES data (**Figure 2**) is accurate and that the high [Trp] used in **Figure 3** does not give rise to artifacts, e.g., from homotransfer. To our knowledge, this is the first experimental measurement of a complete REES data set. However, we note that the conditions used (very high concentration and non-aqueous solvent) are not practical for proteins, and we consider alternative routes to achieve this below. That is, the data serve to illustrate that the REES effect saturates as expected and as predicted by our model.

Single Trp Proteins

With the characterization of the REES effect for free Trp in solution in hand, we now turn to single Trp-containing proteins to establish how the REES effect (quantified with **Eq. (7)**) changes when the Trp is part of a complex polymer (protein). We have selected a large, monomeric (48 kDa; 419 aa) human regulatory protein, which natively has a single Trp [NF-κB essential modulator (NEMO)] (Barczewski et al., 2019), and a natively unstructured protein (α-synuclein, 140 aa) (Meade et al., 2019) that lacks native Trp residues but where we have engineered them into specific sites. These model systems allow us to explore a broad range of conditions and physical environments for single

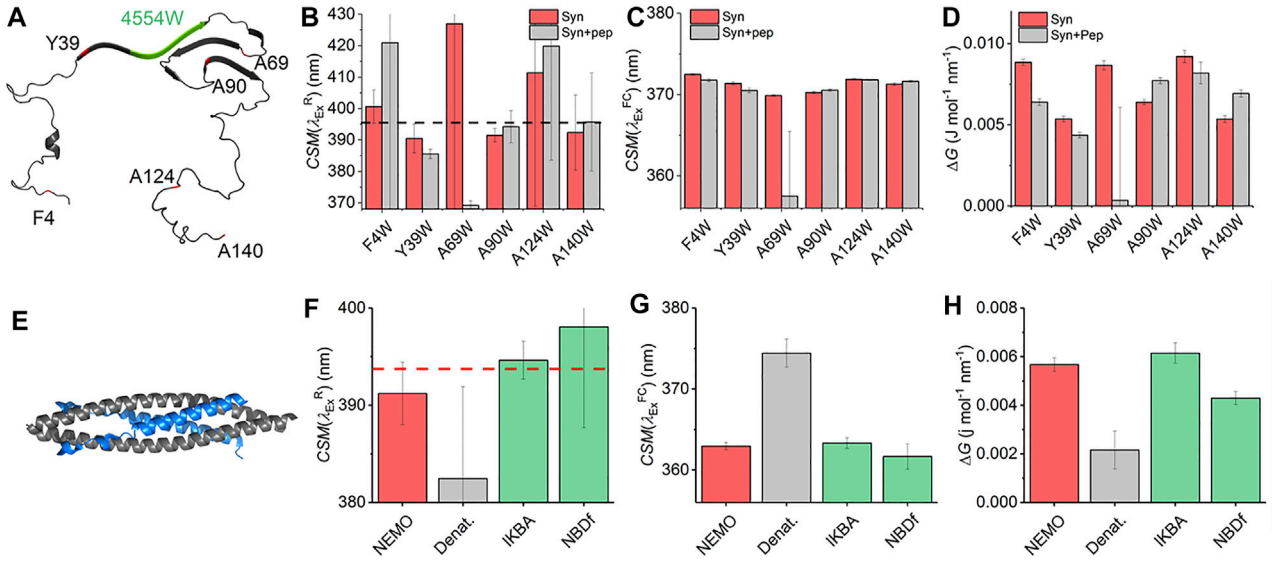

FIGURE 4 | Single Trp protein REES. **(A)** Structural model of α-synuclein (PDB 2n0A24). **(B–D)** Variation in $CSM\,(\lambda_{ex}^{R})$ **(B)**, $CSM\,(\lambda_{ex}^{FC})$ **(C)**, and ΔG **(D)** extracted from fits of raw REES data to **Eq. (7)** for α-synuclein (red bars) and in the presence of the therapeutic peptide (gray bars). The black dashed line in **(B)** shows the $CSM\,(\lambda_{ex}^{R})$ value extracted where all data are fit to **Eq. (7)** with $CSM\,(\lambda_{ex}^{R})$ as a shared parameter. **(E)** Structural model of the N-terminus of NEMO (PDB 3brv) in complex with a peptide representing IKKβ (blue). Conditions, 5 μM α-synuclein, 50 mM Tris–HCl, pH 8.0. **(F–H)** Variation in $CSM\,(\lambda_{ex}^{R})$ **(B)**, $CSM\,(\lambda_{ex}^{FC})$ **(C)**, and ΔG **(D)** extracted from fits of raw REES data to **Eq. (7)** for NEMO (red bars), under denaturing conditions (gray bars) and in the presence of ligands (green bars). The red dashed line in panel **(F)** shows the $CSM\,(\lambda_{ex}^{R})$ value extracted where all data are fit to **Eq. (7)** with $CSM\,(\lambda_{ex}^{R})$ as a shared parameter. Raw NEMO REES data as previously reported in Ref. 28.

Trp proteins. It also enables us both to explore the sensitivity of ΔG and, similar to our Trp in solution studies, define the range of $CSM\,(\lambda_{ex}^{R})$ magnitudes for protein/peptides in an aqueous environment versus the much broader range of physical conditions studied for Trp in MeOH/water mixtures as described above. **Figure 4A** shows a structural model of α-synuclein, with the location of the selected sites for Trp incorporation. α-Synuclein is thought to be a largely unstructured (lacking secondary structure) monomer, but which organizes into a β-sheet-rich fibrillar-like architecture as a repeating unit with a "Greek Key" motif (**Figure 4A**) (Meade et al., 2019). The Trp incorporation sites were selected because, in a previous work, they were found not to alter the aggregation propensity of α-synuclein but did show a measurable REES effect (Jain et al., 2013). In addition, we show data for α-synuclein in the presence and absence of a therapeutic peptide (KDGIVNGVKA), designed to prevent aggregation to the toxic species (as we have reported previously) (Jain et al., 2013). This peptide is based on residues 45–54 of the α-synuclein sequence (**Figure 4A**; green coloration), and therefore, binding will be in that location (Meade et al., 2020), and we do not expect the variants to alter this binding given they are not within this sequence. This peptide has been shown to bind to a partially aggregated form of α-synuclein (Meade et al., 2020). **Figure 4B** shows the $CSM\,(\lambda_{ex}^{R})$ value extracted from the REES data from independent fits [no shared $CSM\,(\lambda_{ex}^{R})$ value] to each of the α-synuclein variants and in the presence of the therapeutic peptide. The $CSM\,(\lambda_{ex}^{R})$ values vary between ~385 and ~425 nm (noting the very large attendant error values in **Figure 4B**) with an average and standard deviation of $CSM\,(\lambda_{ex}^{R}) = 400.4 \pm 15.4$ nm, respectively. Sharing the value of $CSM\,(\lambda_{ex}^{R})$ during the fitting to **Eq. (7)** gives $CSM\,(\lambda_{ex}^{R}) = 395.5 \pm 0.1$ nm. It is worth noting these values of $CSM\,(\lambda_{ex}^{R})$ are effectively identical to those extracted for Trp in solution (**Figures 2** and **3**). For consistency, in our data analysis, we have used $CSM\,(\lambda_{ex}^{R}) = 395.5$ to extract the magnitude of $CSM\,(\lambda_{ex}^{FC})$ and ΔG, as discussed above.

Figure 4C shows the extracted $CSM\,(\lambda_{ex}^{FC})$ values for each variant, with and without the therapeutic peptide bound. The magnitude of $CSM\,(\lambda_{ex}^{FC})$ shows variation with Trp position, likely reflecting the combination of the difference in solvent exposure and the immediate electronic environment arising from differences in amino acid composition flanking each Trp. As discussed above, this is effectively a solvatochromatic effect as is typical of Trp emission. However, in the presence of the therapeutic peptide, we find a substantial shift to a lower wavelength for A69W, suggesting a significant decrease in solvent exposure at residue 69 upon peptide binding. **Figure 4D** shows the resulting ΔG values at each site, extracted from fitting the REES data to **Eq. (7)**. We find that the magnitude of ΔG varies depending on the specific Trp location in the α-synuclein peptide, which potentially points to some non-globular local structural organization, similar to a molten globule-like protein. Alternatively, the differences might be attributable to the specific amino acid sequence immediately flanking these positions providing a different distribution of solvent–fluorophore interaction energies. Moreover, the addition of the therapeutic peptide decreases the magnitude of ΔG most significantly at a single site, residue 69, similar to our findings for $CSM\,(\lambda_{ex}^{FC})$.

The finding of a decrease in both ΔG and $CSM\,(\lambda_{ex}^{FC})$ at AA69 on peptide binding suggests that incubation with the therapeutic peptide decreases solvent exposure and increases flexibility at AA69. From **Figure 4A**, A69W is the variant that is most structurally localized with the anticipated binding site of the therapeutic peptide (green color in **Figure 4A**). Therefore, our finding of a decreased solvent exposure and shift in flexibility at AA69 is entirely consistent with the putative binding location and the disruption of the putative Greek key motif. These data are powerful evidence that the REES effect, quantified with **Eq. (7)**, could be used to track ligand binding and specifically protein–protein interactions.

NF-κB essential modulator (NEMO) is a 48 kDa human regulatory protein involved in the mediation of the NF-κB signaling pathway. A range of studies suggest that NEMO is a flexible protein and can undergo ligand-specific conformational change (Catici et al., 2015; Catici et al., 2016). NEMO has a single native Trp residue (W6), which is conveniently located close to the residues that bind to the kinase regulated by NEMO (**Figure 4E**), IκB kinase-β (IKK-β) (Barczewski et al., 2019). Moreover, there is evidence that the IKK-β substrate, IκBα, is also able to interact with NEMO (Vieille and Zeikus, 2001). We have previously reported the binding of peptide mimics of these proteins to NEMO. We note that the peptides lack Trp residues either natively (IKBα) or by design [NBD-Phe, where the native Trp of the NEMO biding domain (NBD) of IKK-β is replaced by Phe] (Catici et al., 2016). **Figures 4F–H** show the results of fitting **Eq. (7)** to NEMO REES data in native and denatured forms and in the presence of these two ligands.

From **Figure 4F** we find that the extracted magnitude of $CSM\,(\lambda_{ex}^{R})$ is similar for the different conditions that we studied (denatured in 8 M urea and with different ligands bound), although we acknowledge that the attendant error is very large. As with α-synuclein, we fit the combined data to **Eq. (7)** while sharing the $CSM\,(\lambda_{ex}^{R})$ parameter, which gives $CSM\,(\lambda_{ex}^{R}) = 394.0 \pm 1.3$. As with α-synuclein, we used this value for $CSM\,(\lambda_{ex}^{R})$ to extract the magnitude of ΔG for NEMO.

From **Figure 4G**, we find that the magnitude of $CSM\,(\lambda_{ex}^{R})$ is similar within error for NEMO with and without ligands bound. However, for the unfolded protein in 8 M urea, we found that $CSM\,(\lambda_{ex}^{R})$ increases from $CSM\,(\lambda_{ex}^{FC}) = 363 \pm 0.5$ to 374.4 ± 1.7 nm. As we discussed above, the magnitude of $CSM\,(\lambda_{ex}^{FC})$ appears to reflect the degree of solvent exposure to the aqueous environment. Therefore, the observation of an increase in $CSM\,(\lambda_{ex}^{FC})$ in the presence of denaturant is consistent with tracking an unfolded form of the protein. **Figure 4H** shows the magnitude of ΔG for denatured NEMO and with ligands bound. These data show a decrease in ΔG when NEMO is denatured ($\Delta\Delta G = 0.002 \pm 0.001$ J mol^{-1} nm^{-1}), no change outside of error in the presence of IKBα ($\Delta\Delta G = 0.006 \pm 0.0004$ J mol^{-1} nm^{-1}), and a slight decrease with NBD-Phe bound ($\Delta\Delta G = 0.004 \pm 0.0003$ J mol^{-1} nm^{-1}).

Combined, our data provide a means to interpret the physical meaning of the magnitude of ΔG. In the case of the denatured NEMO, the increase in $CSM\,(\lambda_{ex}^{FC})$ reflects the unfolding of NEMO as an increase in aqueous solvent exposure of the single native Trp residue. The observation of a decrease in the magnitude of ΔG would seem consistent with a more heterogeneous (less folded) protein. Binding of NBD-Phe similarly decreases the magnitude of ΔG but to a much lesser extent than for unfolded NEMO. Moreover, unlike in the case of the unfolded protein, the magnitude of $CSM\,(\lambda_{ex}^{FC})$ is essentially invariant within error. These data would then suggest a structurally similar protein, but with a partially restricted distribution of conformational states, arguably more "folded" than NEMO alone. This inference seems credible since binding of NEMO to IKKβ gives a well-folded α-helical dimer (**Figure 4E**), despite the binding interface being highly dynamic (Barczewski et al., 2019). Moreover, these findings track with the binding of the therapeutic peptide to α-synuclein, which shows a similar decrease in the magnitude of ΔG on ligand binding (discussed above).

NEMO and α-synuclein give similar $CSM\,(\lambda_{ex}^{R})$ values with an average and standard deviation of $CSM\,(\lambda_{ex}^{R}) = 397 \pm 15.2$ nm, respectively (**Figures 4B, F**), respectively. That is, we find a very similar $CSM\,(\lambda_{ex}^{R})$ from several different single Trp proteins, differing in size, structure, and physical environments (different location in peptide, ligand bound/free). This finding tracks well with our solution Trp studies. We note that the $CSM\,(\lambda_{ex}^{R})$ value is smaller than Trp in solution but not outside of the calculated error. Potentially, the lower $CSM\,(\lambda_{ex}^{R})$ value suggests that Trp in a peptide experiences a restricted range of solvent–solute interaction energies compared to Trp in solution, i.e., Trp in a peptide cannot access emissive states that are as low energy as those in solution. This is a logical conclusion given that Trp in a peptide will necessarily have restricted orientational freedom compared to bulk solvent. However, we stress the large error values on the $CSM\,(\lambda_{ex}^{R})$ values reflecting the anticipated range of potential $CSM\,(\lambda_{ex}^{R})$ values for Trp in peptides.

These data therefore provide a "baseline" range for $CSM\,(\lambda_{ex}^{R})$, which should reflect a limiting case for the value of $CSM\,(\lambda_{ex}^{R})$ for Trp in a peptide. Fitting all our single protein Trp and solution Trp data to a shared $CSM\,(\lambda_{ex}^{R})$ value gives $CSM\,(\lambda_{ex}^{R}) = 395.4 \pm 0.9$ nm. This value then represents a limiting value for $CSM\,(\lambda_{ex}^{R})$ drawn from a very broad range of solvent–Trp interaction energies; it is effectively an average value. Clearly, using this value of $CSM\,(\lambda_{ex}^{R})$ as a fixed standard for fitting Trp REES data has significant caveats. However, given the challenge of capturing meaningful data at elevated excitation wavelengths and that our modeled data (**Supplementary Figure S2**) showed that ΔG is highly tolerant to variation in $CSM\,(\lambda_{ex}^{R})$, we have chosen to use this value with the much more complex data sets involving multi-Trp proteins (below). For multi-Trp proteins, the extracted REES effect will be an average across all solvent–Trp environments and so the use of a well-parameterized average value of $CSM\,(\lambda_{ex}^{R})$ is logical. We discuss the potential for experimentally accessing $CSM\,(\lambda_{ex}^{R})$ below.

Multi-Trp Protein

Having established a limiting value of $CSM\,(\lambda_{ex}^{R})$, we now explore multi-Trp proteins. We have recently demonstrated that the protein REES effect can be used to predict changes in stability

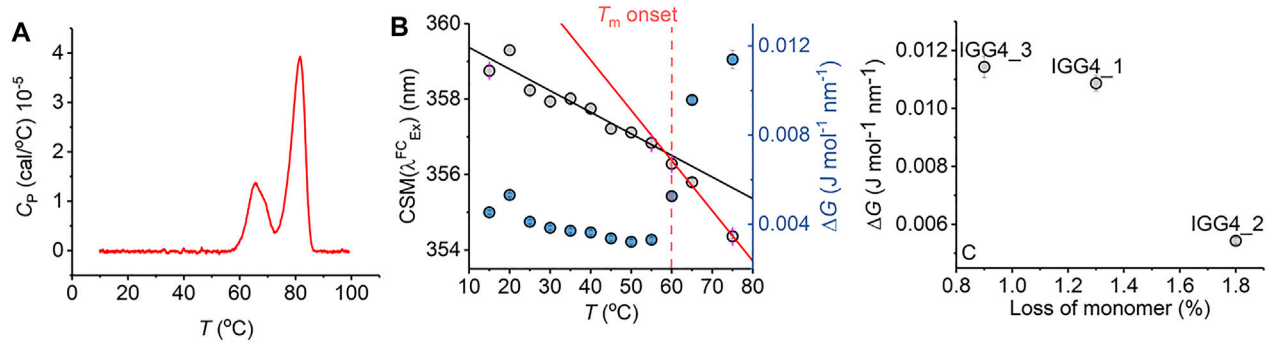

FIGURE 5 | Antibody stability prediction and the effect of temperature. **(A)** Differential scanning calorimetry data for mAb1. **(B)** Temperature dependence of parameters extracted from fitting the IgG1 REES data to **Eq. (7)**. **(C)** Percentage loss of monomer for mAb1-3 after 6 months incubation at room temperature versus ΔG extracted from fitting REEs data to **Eq. (7)** at t = 0. Raw REES data from panel **(C)** as reported previously in Ref. 14.

of multi-Trp proteins, most notably even for proteins with very large numbers of Trp residues such as monoclonal antibodies (Knight et al., 2020). Example raw spectral data are shown in **Supplementary Figure S4**. We wish to explore whether **Eq. (7)** retains this predictive power and to probe its sensitivity. **Figure 5** shows the temperature dependence of ΔG for a therapeutic mAb (IGg4-based; 150 kDa; 22 Trp residues), which is in commercial development. **Figure 5A** shows differential scanning calorimetry (DSC) data for the mAb, which shows T_m onset at 60°C, followed by two separate unfolding transitions at 67.2°C and 82.9°C. The data shown in **Figure 5B** are the result of fitting the REES data to **Eq. (7)** using $CSM\,(\lambda^{R}_{ex})$ = 395.4 as discussed above. From this figure, we find that as the temperature increases, ΔG decreases approximately linearly to ~60°C (red dashed line) and with an approximately invariant $CSM\,(\lambda^{FC}_{ex})$ within the error of the measurement. This temperature tracks with the identified T_{m} onset from the DSC data (**Figure 5A**). At >60°C, we find that $CSM\,(\lambda^{FC}_{ex})$ increases from 354.3 ± 0.1 at 55°C to 359.1 ± 0.2 at 75°C. This increase in $CSM\,(\lambda^{FC}_{ex})$ is accompanied by a larger decrease in ΔG, with $\Delta\Delta G$ = 0.0042 J mol^{-1} nm^{-1} between 55°C and 75°C, compared to $\Delta\Delta G$ = 0.0032 J mol^{-1} nm^{-1} between 15°C and 55°C. That is, we observed a breakpoint in the temperature dependence of ΔG (shown as the solid fitted lines). For the 15–55°C range, we found that the temperature dependence of ΔG is -0.1×10^{-3} J mol^{-1} nm^{-1} K^{-1}, precisely as we found for the Trp in solution (**Figure 2G**). For the 55°C –75°C range, this value becomes larger, -0.25×10^{-3} J mol^{-1} nm^{-1} K^{-1}. Thus, as the protein unfolds, we find an increase in $CSM\,(\lambda^{FC}_{ex})$ and a decrease in ΔG, exactly as with the chemically denatured NEMO (above). These data therefore demonstrate the sensitivity of the protein REES effect, fitted using **Eq. (7)**, to altered conformational states.

Notionally, changes in the equilibrium of conformational states should track with protein stability. That is, as the free energy landscape flattens, more discrete conformational states become accessible (i.e., a broader equilibrium of conformational states), including those corresponding to non-native conformations. For highly structurally similar proteins, we therefore anticipate that a decrease in the magnitude of ΔG will correlate with a less thermodynamically stable protein. **Figure 5C** shows the magnitude of ΔG for three monoclonal antibodies, in active development and all based on a common scaffold (IgG4), in relation with the fractional loss of monomer over 6 months at room temperature (reported recently; Ref. 16). From **Figure 5C**, we find that a decrease in the magnitude of ΔG correlates with a decrease in protein stability (as predicted). These data, therefore, suggest that the magnitude of ΔG is sensitive not only to the very earliest stages of protein unfolding but also to differences in thermodynamic stability.

We have explored a similar temperature relationship with the hyperthermophilic, tetrameric, glucose dehydrogenase from *Sulfolobus solfataricus* (*ss*GDH). The natural operating temperature of the *S. solfataricus* is ~77°C; *ss*GDH is extremely thermally stable even at elevated temperatures and shows very high rigidity relative to a comparable mesophilic protein. (Vieille and Zeikus, 2001). **Figure 6A** shows the far-UV circular dichroism data for *ss*GDH at a range of different temperatures. From this figure, there is some change in helical content with respect to temperature, most noticeable from the spectra at >85°C. **Figure 6B** shows the change in ellipticity at 222 nm ($\Phi_{222\mathrm{nm}}$) with respect to temperature. The solid red line in **Figure 6B** shows the fit to

$$\theta_{222nm} = \frac{b_f + a_f T + (b_u + a_u T)K_u}{1 + K_u} \tag{8}$$

where

$$K_u = exp\,(\Delta H\,(1 - T/T_m)/RT) \tag{9}$$

where a and b are the slope and intercept of the folded (f) and unfolded (u) baseline, respectively. T_{m} is the melting temperature, and ΔH is the van't Hoff enthalpy of unfolding at T_{m}. From **Figure 6B**, there is no evident complete unfolding transition, and so we have restrained the parameters in **Eq. (8)** to give a sense of where the unfolding transition would occur and an indicative T_{m}. That is, we fixed the ellipticity and gradient of the "unfolded" limb of the slope to zero, which is a reasonable approximation. Fitting the data using **Eq. (8)** gave T_{m} = 105.5 ± 5.5°C. That is, the data fits to an unfolding transition that is at an experimentally

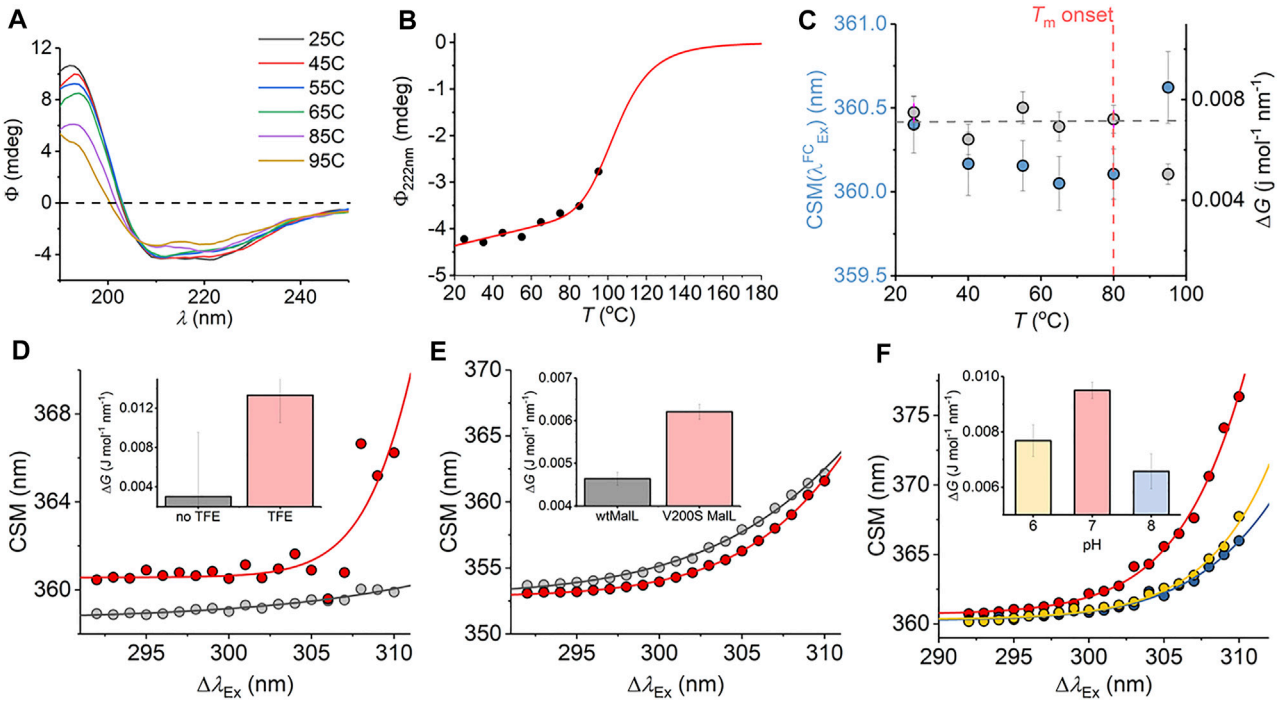

FIGURE 6 | (A–C) Temperature dependence of the *ss*GDH REES effect and correlation with unfolding. **(A)** Temperature dependence of far-UV CD spectra. **(B)** Temperature dependence of Φ_{222nm}. Solid line is the fit to **Eq. (8)** as described in the main text. **(C)** Temperature dependence of parameters extracted from fitting the *ss*GDH REES data to **Eq. (7) (D–F)** REES effect of C45 in the presence and absence of TFE, raw data as Ref. 17 **(D)**; *wt*MalL and V200S MalL, raw data as Ref. 16 **(E)**; and *ss*GDH at different pH values **(F)**. The inset bar charts **(D–F)** show the magnitude of ΔG extract from fitting to **Eq. (7)**.

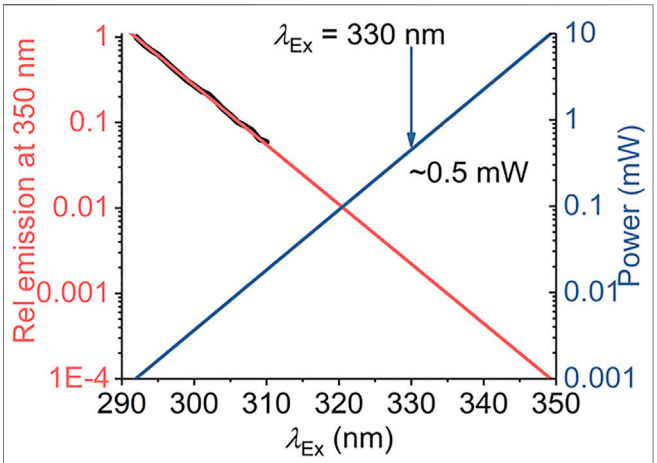

FIGURE 7 | Calculated excitation power requirements to extend protein REES measurements to λ_{Ex} > 310 nm. The black line is the experimentally extracted (natural logarithm) excitation spectrum of protein Trp (single Trp of NEMO as Ref. 15). The red line is the fit to a linear function. The blue line is the calculated power required to achieve an equivalent emission intensity at increasing values of λ_{Ex}.

inaccessible temperature. We note the significant linear slope of the "folded" limb of **Figure 6B**. This linear phase of the thermal melt does not reflect unfolding, and there is no clear consistent interpretation of the magnitude of a_f; it is essentially always removed from analysis (Fenner et al., 2010) Potentially, it reflects changes in solvent dynamics with respect to temperature or more trivial effects. The transition from this linear phase to the apparent unfolding transition is at ~ 80°C.

From **Figure 6C**, we find that the magnitude of ΔG is essentially invariant with respect to temperature (within the error of the extracted value) up to 80°C. As with mAb1, $CSM\,(\lambda_{ex}^{FC})$ shows a small decrease with respect to temperature to 80°C (<0.5 nm). As the notional unfolding transition occurs (95°C), ΔG decreases and $CSM\,(\lambda_{ex}^{FC})$ decreases. These trends are consistent with our observations with mAb1 above. However, *ss*GDH does not show the same decrease in ΔG with respect to temperature below the start of the unfolding transition as was evident with mAb1 and also from the anticipated temperature dependence of ΔG from our solution Trp studies (**Figure 2G**). This finding implies that while we anticipate that the Trp REES effect will be temperature dependent, it will be protein specific. Our data do not suggest an immediate physical model for the temperature dependence of the REES effect in different proteins. However, our data potentially point to a more rigid protein (*ss*GDH vs mAb1) having a less temperature-dependent ΔG at temperatures below any unfolding transition. The hypothesis that more rigid protein will have a less temperature-dependent REES effect seems logical given our findings of the sensitivity of the protein REES effect to even subtle changes in the equilibrium of protein conformational states.

We were able to more directly explore the trend in ΔG on changes in molecular flexibility by correlating with evidence from

NMR, simulation, and pH variation. We have recently demonstrated that a *de novo* heme peroxidase (C45; four α-helix bundle; 3 Trp residues) can be rigidified (and stabilized) in the presence of 2,2,2-trifluoroethanol (TFE) (Hindson et al., 2021). The NMR spectra (^{1}H-^{15}N TROSY-HSQC) show an increase in the number and sharpness of peaks in the presence of TFE, which is indicative of a more rigid protein (Hindson et al., 2021). This rigidification also tracks with an increase in thermal stability (Hindson et al., 2021). Fitting the REES data to **Eq. (7)** (shown in **Figure 6D**) gives a ΔG value that is measurably larger outside of error in the presence of TFE, $\Delta G = 0.003 \pm 0.001$ and 0.013 ± 0.004 J mol^{-1} nm^{-1} in the absence and presence of TFE, respectively.

For our multi-Trp examples above, we were not able to rule out conformational change convolved with changes in rigidity/flexibility. Maltose-inducible α-glucosidase (MalL) has become a paradigmatic enzyme for studying the temperature dependence of enzyme activity. (Hobbs et al., 2013). A single amino acid variant (V200S) is sufficient to increase the optimum temperature of reaction (T_{opt}) from 58°C to 75°C, having an unfolding transition at a higher temperature (Hobbs et al., 2013). Molecular dynamics simulation show that V200S is globally more rigid than the wild-type (*wt*) enzyme, despite the X-ray crystal structures being essentially identical (Hobbs et al., 2013). Therefore, by using MalL we are able to explore the effect of changes in protein rigidity alone on the REES effect. Fitting the extracted REES data to **Eq. (7)** (shown in **Figure 6E**) gives a ΔG value that is measurably larger outside of error for V200S MalL, $\Delta G = 0.006 \pm 0.0002$, than for *wt*MalL, 0.004 ± 0.0002 J mol^{-1} nm^{-1}.

Finally, we have explored pH variation with *ss*GDH. From our temperature studies (**Figures 6A–C**), we find that *ss*GDH is extremely structurally stable. In an effort to perturb the stability of *ss*GDH we have explored pH variation. **Figure 6F** shows the resulting REES data fit to **Eq. (7)** for *ss*GDH incubated at pH 6, 7, and 8. From **Figure 6F** inset, we find that the magnitude of ΔG is largest at pH 7, with a rather lower values at pH 6 and lowest at pH 8. From our data with the mAb1, C45, and MalL, we find that a larger magnitude of ΔG suggests a less flexible protein. **Supplementary Figure S5** shows the pH dependence of the dynamic light scattering (DLS) profile. From these data, we cannot identify any oligomeric change associated with pH variation. However, the DLS profiles show some variation in width, which might suggest a shift in the distribution of conformational states. These data do not obviously correlate with our REES data (**Figure 6F**), but potentially highlight the sensitivity of the REES data to capture changes in the equilibrium of conformational states, which would not otherwise be obvious.

In summary, our combined data with multi-Trp proteins (mAb1, *ss*GDH, C45, and MalL) are consistent with the finding that a decrease in the magnitude of ΔG is associated with an increase in flexibility. Moreover, and as expected, reductions in molecular flexibility are correlated with increased stability. Finally, *via* the change in the $CSM(\lambda_{ex}^{FC})$ term, we are able to use the fitting to **Eq. (7)** to separately differentiate changes in molecular flexibility with unfolding. Our data therefore suggest that the REES effect is potentially highly sensitive to changes in molecular flexibility outside of conformational change, as with our findings from MalL. These data therefore point to the sensitivity of monitoring the protein REES effect in multi-Trp proteins, quantified using **Eq. (7)**.

CONCLUSION

The REES effect is a drastically underutilized analytical tool, given its potential to sensitively track changes in protein microstates. Developing the theoretical models used to understand the effect has high potential to enable the REES effect to be used for unique applications in protein and biomolecular analysis. For example, Kabir *et al.* have recently posited a model for tracking the REES effect of a fluorescent ligand, potentially enabling the dissection of "hidden" ligand bound states of proteins (Kabir et al., 2021). Furthermore, we have demonstrated that quantifying the REES effect with **Eq. (7)** potentially allows for prediction of mAb stability, and this has potential for increasing the speed of drug development (Knight et al., 2020).

Our data suggests that the model presented here (**Eq. (7)**) represents a practically applicable, sensitive framework for quantifying the protein REES effect, based on fundamental thermodynamic theory. Specifically, we find that the magnitude of ΔG is sensitive to changes in molecular dynamics without structural change of the protein and specifically appears to be sensitive to changes in protein conformational sampling. Moreover, *via* the additional information provided by the $CSM(\lambda_{ex}^{FC})$ term, the model appears sensitive to early stage unfolding events and shows predictive power in assessing protein stability. We anticipate **Eq. (7)** could be modified to account for known numbers and locations of Trp residues (such as solvent accessible surface area and local protein molecular dynamics). Such data could be incorporated in **Eq. (7)**, e.g., as a weighting criterion to enable ΔG to be used as an independent metric of stability. Furthermore, with the advent of a large number of high-resolution protein structures, there is very high scope for the use of homology models to fulfill this purpose where specific structures are not available. We also see scope for applying this model to extrinsic fluorophore probes, and we suggest that solvent studies similar to those we report in **Figure 1** will be a valuable starting point to establish $CSM(\lambda_{ex}^{R})$.

Our model defines a maximum red shift for a given system, $CSM(\lambda_{ex}^{R})$, which is determined by the fluorophore and its environment. Practically, there is challenge in monitoring a low signal to noise emission spectrum at the elevated excitation wavelengths required to approach $CSM(\lambda_{ex}^{R})$ (>~310 nm), based on the range identified from our experiments. **Figure 7** shows modeled power requirements to achieve an equivalent intensity emission signal. From **Figure 7**, the power requirement is effectively an exponential increase. That is, to accurately characterize $CSM(\lambda_{ex}^{R})$ would require ~0.5 mW at λ_{Ex} = 330 nm. We note that the typical output of commonly used monochromated flash lamps is ~μW. However, with the rapid development and commercial availability of high-power,

stable UV LEDs, high-intensity two/three-photon laser excitation, and laser-driven UV light sources, we anticipate that this should be practically possible.

METHODS

Red Edge Excitation Shift Data Collection

All fluorescence measurements were performed using a Perkin Elmer LS50B Luminescence Spectrometer (Perkin Elmer, Waltham, MA, United States), an Agilent Cary Eclipse fluorescence spectrometer (Agilent, Santa Clara, CA, United States), or an Edinburgh Instruments FS5 fluorescence spectrometer (data in **Figure 3**; Edinburgh Instrument, Livingstone, United Kingdom) connected to a circulating water bath for temperature regulation (1°C). Samples were thermally equilibrated by incubation for 5 min at the given conditions prior to recording measurements. Emission spectra were collected for increasing increments of excitation wavelength from 292 nm upwards with increments of 1 nm. The emission spectra were typically collected and analyzed across the range of 325–500 nm to prevent first- and second-order artifacts. Typical slit widths were 5 nm in each case (1.5 nm in the case of the data in **Figure 3**). For all samples, the corresponding buffer control was subtracted from the spectra for each experimental condition. REES data were collected as described previously (Knight et al., 2020). Data were processed as described in the text by first extracting the CSM values (**Eq. (2)**) and then fitting with **Eq. (6)**. Data were composed of three to five replicates.

CD and Dynamic Light Scattering Data Collection

CD data were collected on an Applied Photophysics circular dichroism spectrometer. Corresponding buffer baselines were subtracted for each measurement. DLS data were collected on a Malvern Panalytical Zetasizer using a 50 µl quartz cuvette, thermostated to 25°C.

Protein Preparation

α-Synuclein, *ss*GDH, and mAb1 were expressed and purified as described previously in Refs. 28, 18, and 16, respectively.

DATA AVAILABILITY STATEMENT

The original contributions presented in the study are included in the article/**Supplementary Material**. Further inquiries can be directed to the corresponding authors.

AUTHOR CONTRIBUTIONS

All authors listed have made a substantial, direct, and intellectual contribution to the work and approved it for publication.

FUNDING

ARJ thanks the National Measurement System of the Department for Business, Energy and Industrial Strategy for funding. CRP acknowledges the Engineering and Physical Sciences Research Council (EPSRC) for funding (EP/V026917/1).

SUPPLEMENTARY MATERIAL

The Supplementary Material for this article can be found online at: https://www.frontiersin.org/articles/10.3389/fmolb.2021.778244/full#supplementary-material

REFERENCES

Adman, E. T., and Jensen, L. H. (1981). Structural Features of Azurin at 2.7 Å Resolution. *Isr. J. Chem.* 21, 8–12. doi:10.1002/ijch.198100003

Azumi, T., and Itoh, K-i. (1973). Shift of Emission Band upon Excitation at the Long Wavelength Absorption Edge. 1. A Preliminary Survey for Quinine and Related Compounds. *Chem. Phys. Lett.* 22, 395–399.

Azumi, T., Itoh, K. i., and Shiraishi, H. (1976). Shift of Emission Band upon the Excitation at the Long Wavelength Absorption Edge. III. Temperature Dependence of the Shift and Correlation with the Time Dependent Spectral Shift. *J. Chem. Phys.* 65, 2550–2555. doi:10.1063/1.433440

Barczewski, A. H., Ragusa, M. J., Mierke, D. F., and Pellegrini, M. (2019). The IKK-Binding Domain of NEMO Is an Irregular Coiled Coil with a Dynamic Binding Interface. *Sci. Rep.* 9, 2950. doi:10.1038/s41598-019-39588-2

Brahama, R., and Raghuraman, H. (2021). Novel Insights in Linking Solvent Relaxation Dynamics and Protein Conformations Utilizing Red Edge Excitation Shift Approach. *Emerg. Top. Life Sci.* 5, 89–101.

Catici, D. A. M., Amos, H. E., Yang, Y., van den Elsen, J. M. H., and Christopher, Roland Pudney (2016). The Red Edge Excitation Shift Phenomenon Can Be Used to Unmask Protein Structural Ensembles: Implications for NEMO-Ubiquitin Interactions. *FEBS J.* 283, 2272–2284. doi:10.1111/febs.13724

Catici, D. A. M., Horne, J. E., Cooper, G. E., and Pudney, C. R. (2015). Polyubiquitin Drives the Molecular Interactions of the NF-Kb Essential Modulator (NEMO) by Allosteric Regulation. *J. Biol. Chem.* 290, 14130–14139. doi:10.1074/jbc.m115.640417

Chattopadhyay, A., and Haldar, S. (2014). Dynamic Insight into Protein Structure Utilizing Red Edge Excitation Shift. *Acc. Chem. Res.* 47, 12–19. doi:10.1021/ar400006z

Demchenko, A. P., and Ladokhin, A. S. (1988). Red-edge-excitation Fluorescence Spectroscopy of Indole and Tryptophan. *Eur. Biophys. J.* 15, 369–379. doi:10.1007/BF00254724

Demchenko, A. P. (2002). The Red-Edge Effects: 30 Years of Exploration. *Luminescence* 17, 19–42. doi:10.1002/bio.671

Fenner, B. J., Scannell, M., and Prehn, J. H. M. (2010). Expanding the Substantial Interactome of NEMO Using Protein Microarrays. *PLoS One* 5, e8799. doi:10.1371/journal.pone.0008799

Greenfield, N. J. (2006). Using Circular Dichroism Collected as a Function of Temperature to Determine the Thermodynamics of Protein Unfolding and Binding Interactions. *Nat. Protoc.* 1, 2527–2535. doi:10.1038/nprot.2006.204

Gulácsy, C. E., Meade, R., Catici, D. A. M., Soeller, C., Pantos, G. D., Jones, D. D., et al. (2019). Excitation-Energy-Dependent Molecular Beacon Detects Early Stage Neurotoxic Aβ Aggregates in the Presence of Cortical Neurons. *ACS Chem. Neurosci.* 10, 1240–1250. doi:10.1021/acschemneuro.8b00322

Hammond, G. S. (1955). A Correlation of Reaction Rates. *J. Am. Chem. Soc.* 77, 334–338. doi:10.1021/ja01607a027

Hindson, S. A., Bunzel, H. A., Frank, B., Svistunenko, D. A., Williams, C., van der Kamp, M. W., et al. (2021). Rigidifying a De Novo Enzyme Increases Activity

and Induces a Negative Activation Heat Capacity. *ACS Catal.* 11, 11532–11541. doi:10.1021/acscatal.1c01776

Hobbs, J. K., Jiao, W., Easter, A. D., Parker, E. J., Schipper, L. A., and Arcus, V. L. (2013). Change in Heat Capacity for Enzyme Catalysis Determines Temperature Dependence of Enzyme Catalyzed Rates. *ACS Chem. Biol.* 8, 2388–2393. doi:10.1021/cb4005029

Itoh, K.-i., and Azumi, T. (1975). Shift of the Emission Band upon Excitation at the Long Wavelength Absorption Edge. II. Importance of the Solute-Solvent Interaction and the Solvent Reorientation Relaxation Process. *J. Chem. Phys.* 62, 3431. doi:10.1063/1.430977

Jain, N., Bhasne, K., Hemaswasthi, M., and Mukhopadhyay, S. (2013). Structural and Dynamical Insights into the Membrane-Bound α-Synuclein. *PLOS One* 8, e83752. doi:10.1371/journal.pone.0083752

Jones, H. B. L., Wells, S. A., Prentice, E. J., Kwok, A., Liang, L. L., Arcus, V. L., et al. (2017). A Complete Thermodynamic Analysis of Enzyme Turnover Links the Free Energy Landscape to Enzyme Catalysis. *FEBS J.* 284, 2829–2842. doi:10.1111/febs.14152

Kabir, M. L., Wang, F., and Clayton, A. H. A. (2021). Red-Edge Excitation Shift Spectroscopy (REES): Application to Hidden Bound States of Ligands in Protein-Ligand Complexes. *Ijms* 22, 2582. doi:10.3390/ijms22052582

Karshikoff, A., Nilsson, L., and Ladenstein, R. (2015). Rigidity versus Flexibility: the Dilemma of Understanding Protein thermal Stability. *FEBS. J.* 282, 3899–3917. doi:10.1111/febs.13343

Knight, M. J., Woolley, R. E., Kwok, A., Parsons, S., Jones, H. B. L., Gulácsy, C. E., et al. (2020). Monoclonal Antibody Stability Can Be Usefully Monitored Using the Excitation-energy-dependent Fluorescence Edge-Shift. *Biochem. J.* 477, 3599–3612. doi:10.1042/bcj20200580

Kossiakoff, A. A. (1986). [20]Protein Dynamics Investigated by Neutron Diffraction. *Methods Enzymol.* 131, 433–447. doi:10.1016/0076-6879(86)31051-6

Lippert Von, E. (1957). Spektroskopische bistimmung des dipolmomentes aromatischer verbindungen im ersten angeregten singulettzustand. *Z. Electrochem.* 61, 962–975.

Magliery, T. J. M., Lavinder, J. J. L., and Sullivan, B. J. S. (2011). Protein Stability by Number: High-Throughput and Statistical Approaches to One of Protein Science's Most Difficult Problems. *Curr. Opin. Chem. Biol.* 15, 443–451. doi:10.1016/j.cbpa.2011.03.015

Mataga, N., Kaifu, Y., and Koizumi, M. (1956). Solvent Effects upon Fluorescence Spectra and the Dipolemoments of Excited Molecules. *Bcsj* 29, 465–470. doi:10.1246/bcsj.29.465

Meade, R. M., Fairlie, D. P., and Mason, J. M. (2019). Alpha-synuclein Structure and Parkinson's Disease - Lessons and Emerging Principles. *Mol. Neurodegeneration* 14, 29. doi:10.1186/s13024-019-0329-1

Meade, R. M., Morris, K. J., Watt, K. J. C., Williams, R. J., and Mason, J. M. (2020). The Library Derived 4554W Peptide Inhibits Primary Nucleation of α-Synuclein. *J. Mol. Biol.* 432, 166706. doi:10.1016/j.jmb.2020.11.005

Raghuraman, H., Kelkar, D. A., and Chattopadhyay, A. (2005). Novel Insights into Protein Structure and Dynamics Utilizing the Red Edge Excitation Shift Approach. *Rev. Fluorescence*, 199–214.

Reshetnyak, Y. K., Koshevnik, Y., and Burstein, E. A. (2001). Decomposition of Protein Tryptophan Fluorescence Spectra into Log-Normal Components. III. Correlation between Fluorescence and Microenvironment Parameters of Individual Tryptophan Residues. *Biophysical J.* 81, 1735–1758. doi:10.1016/s0006-3495(01)75825-0

Tuttle, M. D., Comellas, G., Nieuwkoop, A. J., Covell, D. J., Berthold, D. A., Kloepper, K. D., et al. (2016). Solid-state NMR Structure of a Pathogenic Fibril of Full-Length Human α-synuclein. *Nat. Struct. Mol. Biol.* 23, 409–415. doi:10.1038/nsmb.3194

Vieille, C., and Zeikus, G. J. (2001). Hyperthermophilic Enzymes: Sources, Uses, and Molecular Mechanisms for Thermostability. *Microbiol. Mol. Biol. Rev.* 65, 1–43. doi:10.1128/mmbr.65.1.1-43.2001

Vihinen, M. (1987). Relationship of Protein Flexibility to Thermostability. *Protein Eng. Des. Sel* 1, 477–480. doi:10.1093/protein/1.6.477

Conflict of Interest: The authors declare that the research was conducted in the absence of any commercial or financial relationships that could be construed as a potential conflict of interest.

Publisher's Note: All claims expressed in this article are solely those of the authors and do not necessarily represent those of their affiliated organizations, or those of the publisher, the editors, and the reviewers. Any product that may be evaluated in this article, or claim that may be made by its manufacturer, is not guaranteed or endorsed by the publisher.

frontiers | Frontiers in Molecular Biosciences

ORIGINAL RESEARCH
published: 11 April 2022
doi: 10.3389/fmolb.2022.789973

Ligand-Bound Forced Degradation as a Strategy to Generate Functionally Relevant Analytical Challenge Materials for Assessment of CQAs

John P. Giddens and John E. Schiel*

[1]*National Institute of Standards and Technology, Institute for Bioscience and Biotechnology Research, Rockville, MD, United States*

Therapeutic monoclonal antibodies (mAbs) contain a variety of amino acids that are susceptible to enzymatic, chemical, and physical modifications. These modifications can happen throughout production, purification, formulation, and storage and many are known to affect the biological activity of a mAb. Methods that are able to characterize and evaluate these attributes are critical in order to understand how they might alter biological activity. Methods capable of site-specific monitoring of these critical quality attributes are extremely valuable to biopharmaceutical research but also require well-defined materials with site-specific attribute modifications. Here, we describe the development and application of a strategy to generate functionally relevant analytical challenge materials that have unique site-specific attributes. This method involves the use of a ligand that is bound to the mAb during oxidative stress resulting in unique oxidation patterns with some methionine residues protected while others are exposed to oxidation. These unique materials were used to develop a rapid surface plasmon resonance (SPR) assay that could detect methionine oxidation in both the Fab and Fc regions using specific molecular probes. The addition of uniquely oxidized materials to our data set enabled us to determine specific methionine residues vital to binding. Further analysis showed that antibody oxidation could also be rapidly detected in multiple domains from qualitative thermal melting using intrinsic tryptophan fluorescence. Methionine oxidation of an antibody was explored in this study, but we envision this method could be useful to explore structure function relationships of a variety of antibody modifications and modifications to other biologically relevant protein drugs.

Keywords: methionine oxidation, NISTmAb, mass spectrometry, surface plasmon resonance, analytical materials

OPEN ACCESS

Edited by:
Isabel Moraes,
National Physical Laboratory,
United Kingdom

Reviewed by:
James E. Noble,
National Physical Laboratory,
United Kingdom
Andrew Quigley,
Diamond Light Source,
United Kingdom

****Correspondence:***
John P. Giddens
john.giddens@nist.gov

Specialty section:
This article was submitted to Structural Biology, a section of the journal Frontiers in Molecular Biosciences

Received: *05 October 2021*
Accepted: *03 March 2022*
Published: *11 April 2022*

Citation:
Giddens JP and Schiel JE (2022) Ligand-Bound Forced Degradation as a Strategy to Generate Functionally Relevant Analytical Challenge Materials for Assessment of CQAs. Front. Mol. Biosci. 9:789973. doi: 10.3389/fmolb.2022.789973

INTRODUCTION

Therapeutic monoclonal antibodies (mAbs) are an important class of biological therapeutics widely used for the treatment of cancer, autoimmune diseases, and various infectious diseases. mAbs are susceptible to a variety of enzymatic, chemical, and physical modifications throughout production, purification, formulation, and storage that are known to alter their biological properties. The result is a complicated mixture of product variants that can pose a challenge to current analytical measurements and complicates interpretation of a modification's impact on stability and/or

function. The potential impact of product variants are evaluated during mAb development by imparting intentional stressors in excess to induce artificial changes in product quality, a process called forced degradation. Later in development, stability testing is performed on the formulated drug substance or drug product, wherein stressors model more real-world intrusions (Li et al., 2015).

Post-translational modifications (PTMs) are changes in the polypeptide occurring after translation due to enzymatic processing, although chemically induced and/or exacerbated changes are typically also included in a broader definition (Li et al., 2015). One of the most common and pervasive PTMs that affects mAbs is oxidation, which can be caused by peroxides, metal ions, and light. Methionine is the amino acid most susceptible to oxidation in mAbs, while oxidation of several other amino acids like tryptophan, cysteine, lysine, and histidine have also been reported (Chen et al., 2019). Methionine oxidation in the Fc region has been widely studied and shown to cause reduced Fc mediated activity by decreasing interactions with the neonatal Fc receptor (FcRn) and other Fc receptors (Bertolotti-Ciarlet et al., 2009; Pan et al., 2009; Gao et al., 2015; Cymer et al., 2017). Specifically, oxidation of Met 255 and Met 431 (actual sequence number varies owing to differing complementarity-determining region (CDR) lengths and often is referred to as Met 252 and Met 428) have been demonstrated to cause a decrease in binding of FcRn. Oxidation of amino acids in the CDR has also been implicated in decreased antigen binding (Dashivets et al., 2016). Others have shown that Met oxidation can interfere with immunoglobulin G (IgG) oligomerization, which is needed for C1q binding and complement dependent cytotoxicity (Mo et al., 2016). Investigation of the biological impact of antibody methionine oxidation is important for many aspects of antibody function, and higher resolution information on the effects of a specific oxidized methionines are of great interest.

Because of the global nature of stress protocols, all susceptible methionine residues are oxidized, albeit at varying rates. The rate of oxidation depends on a variety of factors, with solvent accessible surface area being the major contributing factor (Pan et al., 2009; Sokolowska et al., 2017). Although many studies have demonstrated correlations between the biological impact of IgG and methionine oxidation, direct assessment of a specific methionine residue can be difficult to evaluate because it is challenging to generate materials with oxidation at a specific methionine residue. Genetic manipulation of specific methionine residues has been used; methionine to leucine to block oxidation at a site or methionine to glutamine to mimic an oxidized methionine. These genetic modifications allowed for the expression of mAbs with site selective oxidation mimics useful in deciphering structure-function relationships of IgG binding to FcRn (Gao et al., 2015). However these sequence-engineered materials have altered primary amino acid sequence and do not directly represent the same product. Another approach attempted to enrich Met-oxidized species using affinity chromatography with ligands that can distinguish methionine oxidation at certain residues (Stracke et al., 2014). This approach can enrich a certain population of Met-oxidized antibodies, but is rather cost prohibitive at scale and still cannot provide sufficiently pure material.

As an alternative, we envisioned a method that allows for a binding partner known to interact with specific methionine residues to mask oxidation at that site when chemical oxidation was performed in the presence of that ligand. By decreasing the solvent exposure, the kinetic rate of oxidation should decrease drastically. The publicly available IgG1κ monoclonal antibody Reference Material 8671, NISTmAb, was chosen as an example material due to its usefulness in evaluation and development of emerging analytical measurement technologies (Schiel et al., 2015). Here we present a method to generate functionally relevant, selectively oxidized materials that are useful as analytical challenge materials. We chose to generate a library of these selectively oxidized mAbs in combination with traditionally oxidized samples and characterized each sample with mass spectrometry to access the quantity of residue-specific modifications. Furthermore, we use these unique challenge materials to demonstrate how a rapid surface plasmon resonance-based assay and a thermal unfolding assay can differentiate the impact of oxidation at different regions of the mAb, providing highly valuable information that could be useful in the assessment of critical quality attributes of antibody therapeutics.

MATERIALS AND METHODS

Preparation of the Stressed Samples

NISTmAb Alone vs. NISTmAb With Protein A in Solution

Two sets of oxidized samples were generated, one with NISTmAb alone (Nox 1, Nox 3, and Nox 6) and the other with a mixture of NISTmAb and protein A (PAox 1, PAox 3, PAox 6). Nox samples were generated as follows: 100 µL of NISTmAb at 10 mg/ml was added to each vial followed by the addition of 22.6 µL of phosphate-buffered saline (137 mmol/L NaCl, 2.7 mmol/L KCl, 10 mmol/L Na_2HPO_4) (PBS) pH 7.4 and 4.2 µL of 30% (w/w) H_2O_2 to give a final concentration of H_2O_2 of 1% and a final concentration of NISTmAb of 7.88 mg/ml. Samples were incubated at 25°C, protected from light. Samples were centrifuged for 5 min at 10,000 rpm and reactions were stopped by buffer exchanging back into formulation buffer (pH 6.0, 25 mmol/L L-Histidine) using zeba spin desalting columns 7K MWCO (Thermo Scientific) at the following time points: 1, 3, and 6 h to generate $^{1\%}Nox_{1hr}$, $^{1\%}Nox_{3hr}$, and $^{1\%}Nox_{6hr}$. PAox samples were generated as follows: 100 µL of NISTmAb at 10 mg/ml was added to each vial followed by the addition of 22.6 µL of protein A at 25 mg/ml in PBS and 4.2 µL of 30% (w/w) H_2O_2 to give a final concentration of H_2O_2 of 1% and a final concentration of NISTmAb of 7.88 mg/ml. Samples were incubated at 25°C, protected from light. Samples were centrifuged for 5 min at 10,000 rpm and reactions were stopped by buffer exchanging back into formulation buffer (pH 6.0, 25 mmol/L L-Histidine) using zeba spin desalting columns 7K MWCO (Thermo Scientific) at the following time points: 1, 3, and 6 h to generate $^{1\%}PAox_{1hr}$, $^{1\%}PAox_{3hr}$, and $^{1\%}PAox_{6hr}$.

Standard in Solution Oxidation Time Course

To achieve forced oxidation, 8.01 µL of 30% (w/w) H_2O_2 was added directly to a 800 µL vial (8 mg at 10 mg/ml) of NISTmAb RM 8671 samples to obtain a final concentration of 0.3% H_2O_2 and 9.9 mg/ml of NISTmAb. Samples were incubated at 25°C, protected from light. Samples were centrifuged for 5 min at 10,000 rpm and reactions were stopped by buffer exchanging back into formulation buffer (pH 6.0, 25 mmol/L L-Histidine) using zeba spin desalting columns 7K MWCO (Thermo Scientific) at the following time points: 30 min, 1, 2, 4, 6, 8, 16, 32 h. A NISTmAb Bex sample was generated by buffer exchanging a NISTmAb RM 8671 vial into formulation buffer using the same method as oxidized samples. A NISTmAb control sample was also generated by incubating a NISTmAb vial without the addition of H_2O_2, at 25°C and protected from light for 32 h and then buffer exchanged into formulation buffer using the same method as oxidized samples. All buffer exchanged samples were measured for a concentration (all samples were between 7 mg/ml to 8 mg/ml) using a NanoDrop 1000C, aliquoted to 50 µL, and stored at −80°C.

Oxidation While Bound to Protein A Column

NISTmAb (8 mg) was loaded onto a 1 ml MabSelect SuRe protein A column (GE Lifesciences) and the column was washed with PBS pH 7.4 for 5 column volumes. To achieve forced oxidation a solution of H_2O_2 in PBS was run over the column at a flow rate of 0.5 ml/min for a specific amount of time. Five CPA samples were generated using a different amount of H_2O_2 and different exposure times: $^{0.3\%}CPA_{2hr}$, $^{0.3\%}CPA_{4hr}$, $^{0.3\%}CPA_{6hr}$, $^{0.0375\%}CPA_{16hr}$, and $^{3\%}CPA_{1hr}$ (Where the superscript denoted H_2O_2% and subscript denotes time exposed to H_2O_2 on the protein A column). After the oxidation, the column was washed with PBS pH 7.4 for 5 column volumes to get rid of any excess H_2O_2. Bound IgG was eluted using a citric acid solution (100 mmol/L pH 3.0) and quickly neutralized with 1.5 mol/L tris buffer pH 8.8. Fractions containing eluted NISTmAb were combined and concentrated using amicon ultra centrifugal filter unit 10 KDa (Millipore). Samples were then centrifuged for 5 min at 10,000 rpm and buffered exchanged back into formulation buffer (pH 6.0, 25 mmol/L L-Histidine) using zebra spin desalting columns 7K MWCO (Thermo Scientific) and aliquots were stored at −80°C. The concentrations of all samples were measured using a Nanodrop 2000 C system and ranged from 7 mg/ml to 8 mg/ml.

LC-MS Analysis

IdeS Subunit Analysis

The antibody samples were diluted to 3 mg/ml into 0.25 mol/L Tris-HCl, pH 7.5 and one unit of IdeS protease was added for every 1 µg of antibody. The samples were digested by incubating the solution at 37°C for 30 min. The digested samples were then diluted 1:10 into a denaturing buffer comprised of 6 mol/L guanidine HCl in 0.25 mol/L Tris-HCl, pH 7.5. The mAbs were then reduced by adding dithiothreitol (DTT) to a final concentration of 25 mmol/L for 60 min at 45°C. The samples were then buffer exchanged into 0.1% formic acid (FA) and 10% acetonitrile in LC-MS grade water using a zebra spin filter column. 2.5 µg of each peptide digest was injected onto a Waters UPLC Protein Ethylene Bridged Hybrid C4 column (150 × 2.1 mm i.d. 1.7 µm BEH particles, 300 Å) set to 60°C and analyzed by liquid chromatography-electrospray ionization-mass spectrometry (LC-ESI-MS/MS) using an Agilent 1200 Infinity II series LC system coupled to an Agilent 6545XT AdvanceBio LC/Q-TOF. The chromatographic method was initiated with 80% Mobile Phase A (0.1% FA in water) and 20% Mobile Phase B (0.1% FA in acetonitrile) with a flow rate of 0.4 ml/min. The separation was achieved over 20 min starting with a 5 min isocractic hold at 20% B followed by a gradient to 45% B in 15 min. The column was then washed by ramping up to 95% B in 1 min followed by a 4 min hold at 95% B. The column was equilibrated by returning the flow to 20% B followed by a 2 min hold at 20% B. The MS instrument was operating in positive ion mode with the following source settings: gas temp 350°C, drying gas 8 L/min, nebulizer 2.4×10^5 Pa, sheath gas temp 275°C, sheath gas flow 11 L/min, VCap 5000 V, nozzle voltage 1000 V, fragmentor 250 V, skimmer 65 V, Oct 1 RF Vpp 750 V. The mass range for MS1 was 300–3,200 m/z and data was acquired at 1 spectra/s.

Peptide Mapping Analysis

The antibody samples were prepared and digested following a previous publication (Mouchahoir and Schiel, 2018). Briefly, the samples were denatured in a buffer comprised of 6 mol/L guanidine HCl, 1 mmol/L ethylenediaminetetraacetic acid (EDTA) in 0.1 mol/L Tris-HCl, pH 7.8. The mAbs were then reduced with a final concentration of 5 mmol/L dithiothreitol (DTT) for 60 min at 4°C and alkylated with a final concentration of 10 mmol/L of iodoacetamide (IAM) for 60 min at 4°C. The samples were then buffer exchanged into 1 mol/L urea in 0.1 mol/L Tris, pH 7.8 and trypsin was added at a 1:18 (enzyme: sample) mass ratio. The digestion was incubated for 4 h at room temperature. The reaction was stopped by adding 0.1% formic acid (FA) in LC-MS grade water was added at a 1:1 volume ratio and the digests were stored at -80°C until analysis. 2.5 µg of each peptide digest was injected onto a Agilent Zorbax RRHD StableBond C18 column (150 mm × 2.1 mm i.d. 1.8 µm BEH particles, 300 Å) set to 40°C and analyzed by LC-ESI-MS/MS using an Agilent 1200 Infinity II series LC system coupled to an Agilent 6545XT AdvanceBio LC/Q-Tof. The chromatographic method was initiated with 99% Mobile Phase A (0.1% FA in water) and 1% Mobile Phase B (0.1% FA in acetonitrile) with a flow rate of 0.25 ml/min. The separation was achieved over 72 min starting with a 5 min isocractic hold at 1% B followed by a steep gradient to 10% B in 1 min ending with a gradient to 35% B in 64 min. The column was then washed by ramping up to 90% B in 2 min followed by a 5 min hold at 90% B and then back down to 1% B in 2 min followed by an isocratic at 1% B for 2 min. The gradient was then raised to 10% B over 2.5 min, then to 45% B in 8 min, and lastly to 90% B in 1.5 min. A final isocratic hold at 90% for 6 min was performed and the column was equilibrated by returning to 1% B for 14 min before the next sample. The MS instrument was operating in positive ion mode with the following source settings: gas temp 325°C, drying gas 13 L/min, nebulizer 2.4×10^5 Pa, sheath gas temp 275°C, sheath gas flow 12 L/min, VCap

4000 V, nozzle voltage 500 V, fragmentor 175 V, skimmer 65 V, Oct 1 RF Vpp 750 V. The mass range for MS1 was 100 m/z to 2,400 m/z and 50 m/z to 2,400 m/z in MS2. Ions were selected for MS/MS with a narrow 1.3 m/z window then fragmented by collision induced dissociation using the formula, collision energy = 3.6*(m/z)/100 + 4.8. The MS2 conditions were as follows: Top 10, 3,000 counts abs threshold/0.001% rel threshold, active exclusion enabled with exclusion after 3 spectra and released after 0.2 min. The MS data was analyzed using Genedata Expressionist software. Briefly, raw data was imported into Genedata Expressionist and a workflow was run that includes background subtraction followed by retention time alignment, MS peak detection, charge assignment, MS/MS consolidation and peak detection. The MS1 mass tolerance was set at 10 ppm and MS2 mass tolerance was 50 ppm for peptide identification. The oxidation percentage of each Met residue was calculated by dividing the peak area of the oxidized peptide by the sum of the peak areas of both oxidized and nonoxidized peptide.

Size Exclusion Chromatography Analysis

SEC analysis was performed according to a previously developed method (Turner et al., 2018). Briefly, all samples were analyzed on an Agilent high pressure liquid chromatography system using isocratic elution (100 mmol/L sodium phosphate supplemented with 250 mmol/L sodium chloride, pH 6.8) at 0.30 ml/min and monitored at 280 nm. 60 µg of antibody sample was injected onto a Waters Acquity UPLC Protein BEH SEC column (1.7 µm particle size, 200 Å pore size, 4.6 × 150 mm length).

SPR Analysis

SPR experiments were performed using a Biacore T200 system (GE Healthcare) with analysis temperature set to 25°C and sample compartment temperature set to 15°C. Series S Sensor Chip CAP, PBS-P + Buffer 10x [0.2 mol/L phosphate buffer with 27 mmol/L KCl, 1.37 mol/L NaCl and 0.5% v/v Surfactant P20 (Tween 20)], and Biotin CAPture Kit were all obtained from GE Healthcare. A peptidic epitope of the NISTmAb with the sequence NSELLSLINDMPITNDQKKLMSNN and N-terminal acetylation, C-terminal amidation, and a C-terminal biotinylated lysine residue was synthesized by Genscipt. Recombinant biotinylated protein A (29989) and protein L (21189) were purchased from Thermo Fisher.

Measurements were conducted using a double-capture method *via* the oligonucleotide-immobilized CAP sensor chip, Biotin CAPture reagent (streptavidin bound to an oligonucleotide complementary to the strand on the CAP chip), and the various biotinylated ligands (protein A, F peptide, and protein L). Biotin capture reagent was injected for 300 s at a flow rate of 2 µL/min to capture approximately 3,000 response units (RU) followed by a 60 s injection at 5 µL/min into Fc2 of biotinylated protein A (0.02 µg/µL) to give a capture level of 275 RU to 305 RU, another 60 s injection at 5 µL/min into Fc3 of biotinylated F peptide (5 µg/µL) to give a capture level of 295 RU to 305 RU, and a final 60 s injection at 5 µL/min into Fc4 of biotinylated protein L (0.02 µg/µL) to give a capture level of 220 RU to 230 RU. Samples were diluted in running buffer (PBS-P+ pH 7.4) to a concentration of 200 nmol/L and flowed over each flow channel at a flow rate of 50 µL/min. Each complex was allowed to associate and dissociate for 100 and 300 s, respectively. Following the association and dissociation phases of the experiment, the chip was regenerated with an injection of regeneration buffer 1 for 120 s (6 mol/L guanidine-HCL, 0.25 mol/L NaOH) and injection of regeneration buffer 2 for 120 s (30% acetonitrile in 0.25 mol/L NaOH).

A binding affinity response point was taken at the maximum binding level at the end of the association phase for each sample. The RU value was normalized for each ligand by dividing each data point by the maximum value of NISTmAb Bex for that ligand in each experiment. The relative binding level for each sample to each ligand was calculated by averaging sample replicates over three independent experiments and the standard deviation along with %CV were also calculated.

Thermal Unfolding Analysis

Thermal unfolding experiments were performed using a Tycho NT 6.0 system (NanoTemper). All samples were diluted to 1 mg/ml in formulation buffer (pH 6.0, 25 mmol/L L-Histidine) before analysis. Samples were heated from 35°C to 95°C over 3 min, and intrinsic fluorescence at 350 and 300 nm were monitored, providing a relative thermal stability for each sample. Unfolding profiles were generated by plotting the fluorescence ratio of 350 nm/330 nm. NanoTemper software then calculated the inflection temperatures by taking the first derivative of this ratio where max and min peaks correlate to inflection temperatures. The average value and standard deviation of inflection temperatures and initial ratio was calculated using three sample replicates.

Statistical Analysis

Graphpad Prism version 9.1.2 was used for all statistical analysis. The unpaired *t*-test was performed with the following settings: Assume Gaussian distribution and two-tailed *p* value calculation. The nonlinear regression analysis was performed using either a straight line model for linear data or One phase decay model for nonlinear data using standard settings. The standard error of regression (Sy.x) was calculated and the 90% prediction bands (the area that 90% of future data points are expected) were also plotted. Replicates were accounted for by using the number of samples (N) and the standard deviation.

RESULTS AND DISCUSSION

Method to Change Methionine Oxidation Kinetics at a Specific Site: Solution Phase Protein A Protection Proof of Principle

Oxidative stress of NISTmAb in the presence of protein A in solution was used to initially assess the ability of protein A to mask, and thereby protect, Fc methionine residues from oxidation. The levels of oxidation of NISTmAb alone and NISTmAb with protein A in solution (1:2 molar ratio) were compared after exposure to a strong accelerated oxidative stress condition, 1% hydrogen peroxide (H_2O_2) solution, for 1, 3, and 6 h. The global oxidation levels of both sets of oxidized samples,

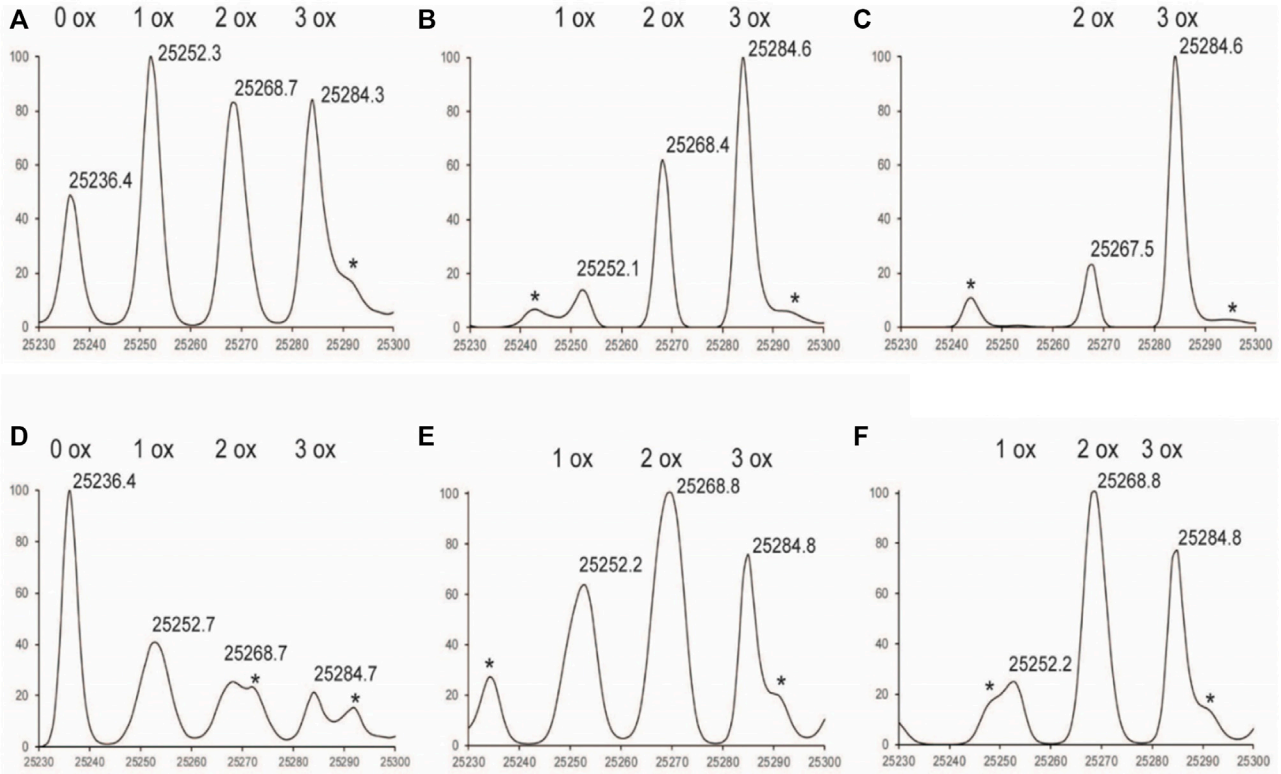

FIGURE 1 | Deconvoluted LC-MS Spectrum of Fc subunit zoomed in to G0F **(A)** $^{1\%}Nox_{1hr}$**(B)** $^{1\%}Nox_{3hr}$ **(C)** $^{1\%}Nox_{6hr}$ **(D)** $^{1\%}PAox_{1hr}$ **(E)** $^{1\%}PAox_{3hr}$ **(F)** $^{1\%}PAox_{6hr}$
*Denotes adduct peaks that do not correspond to actual oxidized antibody peaks.

NISTmAb alone ($^{1\%}Nox_{1hr,}$ $^{1\%}Nox_{3hr,}$ $^{1\%}Nox_{6hr}$) and NISTmAb with protein A ($^{1\%}PAox_{1hr}$, $^{1\%}PAox_{3hr}$, $^{1\%}PAox_{6hr}$) were monitored by liquid chromatography mass spectrometry (LC-MS) and compared to the unstressed NISTmAb RM 8671. A rapid subunit mass analysis was employed which entailed enzymatic digestion with IdeS to specifically cleave IgG in the hinge region, resulting in three subunits after reduction of disulfide bonds: Fc/2, Fd', and LC. A representative spectrum of all three subunits of NISTmAb RM 8671 is shown in **Supplementary Figure S1**. The analytical method was capable of identifying all previously reported proteoforms of the NISTmAb and deemed suitable for preliminary oxidation screening. A full list of identified masses, including observed and theoretical masses for all proteoforms, can be found in **Supplementary Table S1**.

Exposure to H_2O_2 resulted in up to six methionine oxidation events observed on the NISTmAb: three events in the Fc region, one in the LC, and two in the Fd subunit (**Figures 1–3**). Each glycoform of the Fc was observed to oxidize at the same rate, therefore the mass range was zoomed in to focus on the G0F glycoform for easier visualization in **Figure 1**. As the Fc methionine residues oxidize over time in the Nox samples, four distinct species can be detected corresponding to 0, 1, 2, and 3 oxidized methionine residues with each oxidation event adding +16 da (**Figures 1A–C**). Longer time courses resulted in a larger relative abundance of scFc containing more oxidation events. The oxidation profile of the scFc of PAox samples showed substantially less oxidation than Nox at all time points (**Figures 1D–F**).

The oxidation profiles of the LC and Fd subunits of Nox and PAox samples, however, were quite similar and showed nearly the same oxidation levels at each timepoint (**Figure 2**, **Figures 3A–C** vs. **Figures 3D–F**). The LC subunit shows two distinct species corresponding to 0 and 1 oxidized methionine while the Fd subunit shows three distinct species corresponding to 0, 1, and 2 oxidized methionine residues (**Figure 2**, **Figures 3A–C**). The IdeS subunit analysis of these samples indicate that methionine oxidation kinetics of the Fc region of NISTmAb due to H_2O_2 exposure can be significantly slowed when protein A is added to the solution. Presumably the protein A remains bound to NISTmAb Fc to a sufficient degree, blocking putative oxidation sites, while the oxidation rates in the Fab region remain relatively unchanged.

While our in solution oxidation results were promising, the solution phase protection method had a few limitations leading to a final product that was not ideal for further downstream studies: 1) protein A was still in solution and while bound to NISTmAb cannot easily be removed 2) protein A is a multidomain protein that has five different domains that all bind IgG Fc with varying degrees (Ljungberg et al., 1993) and 3) some protein A domains have also been shown to bind to the Fab region. To address these issues, another strategy was developed that takes advantage of a

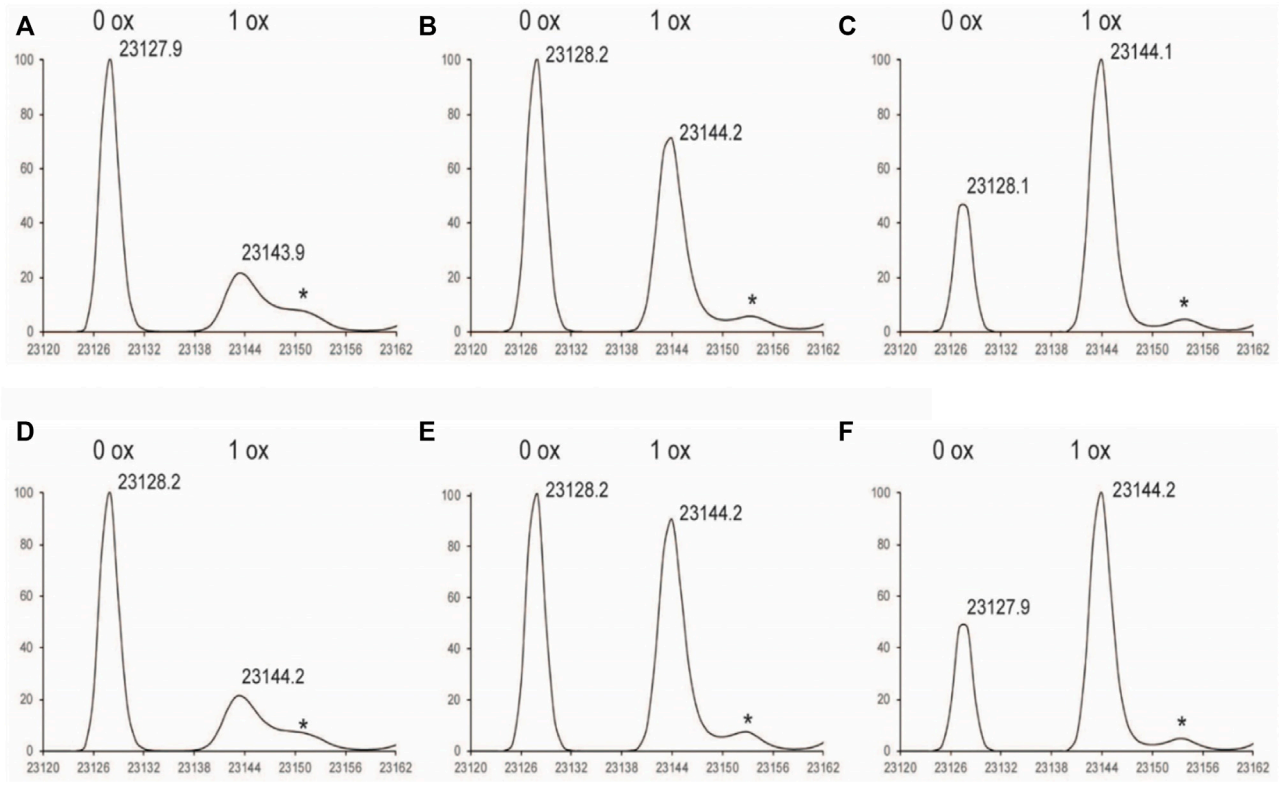

FIGURE 2 | Deconvoluted LC-MS Spectrum of LC subunit **(A)** $^{1\%}Nox_{1hr}$ **(B)** $^{1\%}Nox_{3hr}$ **(C)** $^{1\%}Nox_{6hr}$ **(D)** $^{1\%}PAox_{1hr}$ **(E)** $^{1\%}PAox_{3hr}$ **(F)** $^{1\%}PAox_{6hr}$ *Denotes adduct peaks that do not correspond to actual oxidized antibody peaks.

commercially available resin, MabSelect SuRe, which contains an engineered protein A covalently conjugated to agarose matrix. The MabSelect SuRe resin contains a tetramer of a Z domain, an alkali tolerant mutant of the B domain of protein A, which has multiple properties that address previously mentioned drawbacks of the free in solution oxidation method: 1) the protein A is attached covalently to the resin and has low ligand leaching (GE Healthcare, 2005) 2) the use of only the Z domain has less affinity and selectivity variation vs. the multi-domain protein A and 3) the Z domain has been shown to have little to no Fab binding (Jansson et al., 1998). On column oxidation was therefore pursued for the generation of samples with unique oxidation profiles when compared to traditional solution phase oxidation without protein A.

Generation of Selectively Oxidized NISTmAb Samples and Comparison to Standard Forced Oxidized Time Course Samples Using LC-MS/MS Analysis

After the in solution proof of principle studies and the rationale for a more optimized approach, a larger scale study was performed to generate both standard forced oxidized samples along with a set of uniquely oxidized samples generated by oxidation on a protein A column for comparison purposes. Traditional accelerated forced oxidized samples (no protein A) with a wide range of total oxidation were generated using conditions known to produce materials with low levels of oxidation all the way to near complete oxidation of all susceptible methionine residues. A lower H_2O_2% was used, 0.3%, so that functionally relevant materials with very low levels of oxidation could be generated. Samples were stressed for a range of time points from 30 min to 32 h at 25°C focusing on early time points in the linear oxidation range and named according to the H_2O_2% and amount of time oxidized ($^{0.3\%}Nox_{0.5hr}$, $^{0.3\%}Nox_{1hr}$, etc). A NISTmAb buffer exchange reference (NISTmAb Bex) was made without the addition of H_2O_2 but following a similar buffer exchange workup and NISTmAb control (NISTmAb Ctrl) was made without the addition of H_2O_2 but a 32 h incubation at 25°C to control for any changes that might occur over time. The exact conditions are detailed in the materials and methods. Another set of selectively oxidized samples was also generated by performing the forced oxidation while NISTmAb was bound to a protein A column. Specifically, three samples were generated using the same 0.3% H_2O_2 to allow for a direct comparison to time course stressed samples: 2, 4, and 6 h and named accordingly $^{0.3\%}CPA_{2hr}$, $^{0.3\%}CPA_{4hr}$, $^{0.3\%}CPA_{6hr}$. Two other selectively oxidized samples were generated to evaluate on/off equilibrium effects: one with gentle stress over a long time period (0.0375% H_2O_2 for 16 h), $^{0.0375\%}CPA_{16hr}$ and another with heavy stress for a short time period (3% H_2O_2) for 1 h, $^{3\%}CPA_{1hr}$. The exact conditions of all on

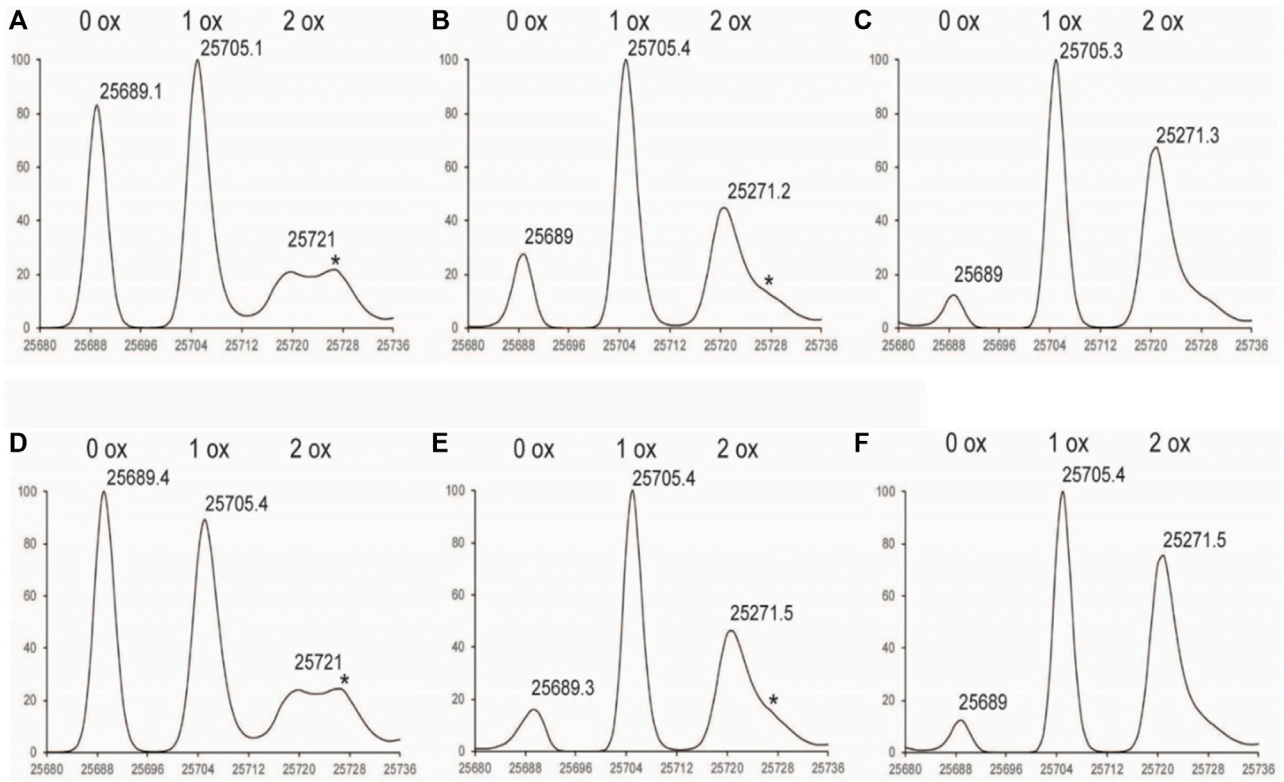

FIGURE 3 | Deconvoluted LC-MS Spectrum of Fd subunit **(A)** $^{1\%}Nox_{1hr}$ **(B)** $^{1\%}Nox_{3hr}$ **(C)** $^{1\%}Nox_{6hr}$ **(D)** $^{1\%}PAox_{1hr}$ **(E)** $^{1\%}PAox_{3hr}$ **(F)** $^{1\%}PAox_{6hr}$ *Denotes adduct peaks that do not correspond to actual oxidized antibody peaks.

column oxidized samples are detailed in the materials and methods.

To demonstrate site specific changes in the oxidation profile of on column stressed material, tryptic peptide mapping combined with liquid chromatography mass spectrometry (LC-MS) was performed. Following peptide identification by tandem mass spectrometry, the extent of quantifiable methionine oxidation was determined by quantitative evaluation of the modified tryptic peptides relative to their respective unmodified parent peptides as described in methods section. All peptides containing a given Met residue were collated to provide the residue-specific quantification results. Among the eight methionine residues, only six changed significantly under our $^{0.3\%}$Nox accelerated stress conditions: HC M34, M101, M255, M361, M431 and LC M4 as summarized in **Figure 4A**. The levels of other typical modifications (deamidation, isomerization, glycation) were monitored and found that no other significant modifications occurred in any of the $^{0.3\%}$Nox samples. The $^{0.3\%}$Nox samples showed an increase in oxidation over time (**Figure 4A**). Typically, methionine residues in the Fc are known to be the most susceptible to oxidation while methionine residues in the variable regions of the Fab vary in their susceptibility to oxidize depending on a variety of factors including solvent-accessibility of the methionine residue, expression host, and process conditions (Yang et al., 2017). Specifically, the oxidation rates of susceptible methionine residues in NISTmAb ordered as the following: M255 > M101 > M431 > M361 > LC M4>M34. The oxidation profile of $^{0.3\%}$Nox samples can be generalized with three tiers of oxidation with the first and most susceptible being M255 and M101, followed by M431 and M361 s, and third and least susceptible being M34 and LC M4.

M255 was oxidized at much lower rate in the $^{0.3\%}$CPA samples when identical timepoints were considered (indicated by black dashes in **Figure 4B**), implying that when NISTmAb is bound to protein A, M255 is protected from oxidation. In addition to the dramatic protection observed for M255 oxidation, a slight decrease (and hence minor protection) in oxidation at M431 was also shown in the $^{0.3\%}CPA_{2hr}$ sample but not seen in the 4 and 6 h samples. While a direct comparison in the $^{0.3\%}CPA_{4hr}$ and $^{0.3\%}CPA_{6hr}$ samples did not show lower oxidation at M431 it was clear that oxidation was lower at M431 than M361 in CPA samples but in Nox samples the opposite was true so oxidation in the presence of protein A did seem to have a slight protective effect on M431 as well. This phenomenon is in agreement with the known relative solvent exposure of protein A-bound IgG1; protein A is known to be in close contact with M255 while M431 is also nearby (Deis et al., 2015). Interestingly, a higher rate of oxidation at M101 (and to a lesser degree M361 and LC M4) was observed when compared to other residues. This could indicate a conformational change of the Fab when IgG is bound to protein A that makes M101 more accessible and/or an orientational effect while ligand-bound. Specifically, the

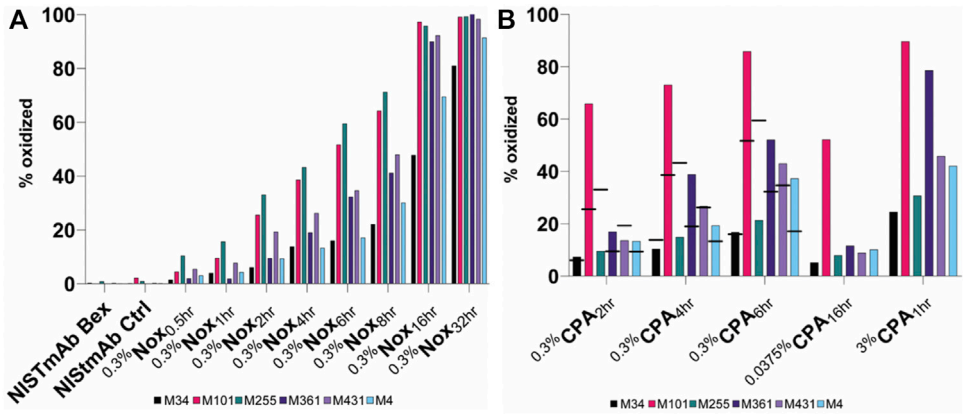

FIGURE 4 | Relative abundance of oxidized methionine residues in NISTmAb samples **(A)** NISTmAb Bex and Ctrl with Nox Samples **(B)** CPA samples. Black dashes (–) are used in the 0.3% CPA samples to denote the relative abundance of each methionine residue from equaivlanet Nox sample for comparison purposes.

oxidation rates of susceptible methionine residues in CPA samples ordered as the following: M101 > M361 > M431 > LC M4>M255 > M34. The oxidation profile of CPA samples can be generalized with three tiers of oxidation with the first and most susceptible being M101, followed by M361, M431, and LC M4 second, and third and least susceptible being M34 and M255.

A similar phenomenon was seen in the $^{0.0375\%}CPA_{16hr}$ and $^{3\%}CPA_{1hr}$ samples with M255 showing a much slower oxidation rate relative to the other methionine residues when compared to standard forced oxidized $^{0.3\%}$Nox samples; M255 displayed the fastest oxidation rate in Nox samples but in CPA samples it was much slower, second to last. $^{0.0375\%}CPA_{16hr}$ was shown to be a very interesting material with a high level of M101 oxidation (52%) while having only small amounts (<15%) of oxidation at all other sites. This material could be of interest to elucidate specific effects M101 oxidation might have on NISTmAb while minimizing the influence of other oxidation effects. $^{3\%}CPA_{1hr}$ was shown to be the most oxidized CPA sample, and the strategy of heavy stress for a short period did not seem to provide the same level of protection at M255 when compared to the milder conditions. Taken together, these measurements indeed confirm the ability of a ligand to mask a specific epitope from oxidation and the ability to generate uniquely oxidized challenge materials.

Surface Plasmon Resonance: Assessment of NISTmAb Using Domain Specific Molecular Probes

Previous studies have shown that oxidation in both the Fab and Fc regions can affect binding to both antigen and Fc receptor targets. In order to characterize both domains and therefore potentially unique bioactivity of the novel challenge materials created herein, a surface plasmon resonance (SPR) assay was designed that could assess binding at distinct and separate locations using a set of NISTmAb binding proteins as molecular probes. Specifically, ligands were selected that are known to bind in both the Fab and Fc regions so functionality

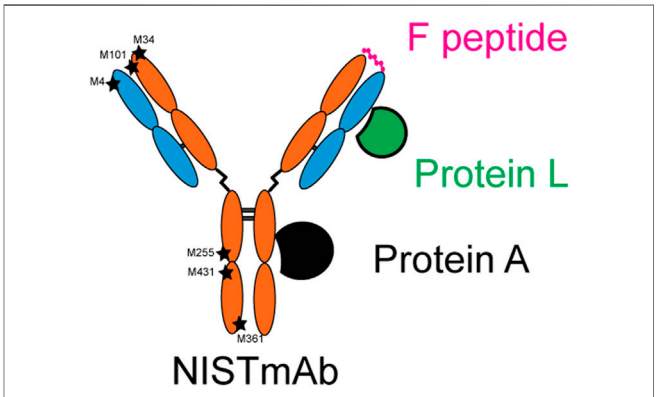

FIGURE 5 | Diagram of molecular probes used in SPR assay and the relative location they bind.

of both domains could be assessed. Two common bacterial proteins were selected that are known to have a high affinity for NISTmAb and have known binding sites: protein A which binds to the Fc and protein L which binds to the variable region of the LC Fab without interfering with antigen binding site. A peptidic epitope, F peptide, known to bind with high affinity to the NISTmAb CDR of the Fab was also included. A schematic diagram showing the three molecular probes and the relative location they bind to NISTmAb is shown in **Figure 5**. A reversible biotin capture system was used for each of the ligands that has been shown to be an efficient SPR assay platform that allows for a generic regeneration condition and repeatable capture (Karlsson et al., 2018). The assay depends on a special sensor chip CAP which has a pre-immobilized oligonucleotide on the surface. Sequential steps of the assay include: 1) A biotin capture reagent (streptavidin modified with the complementary oligonucleotide) is hybridized to the CAP chip, 2) The biotinylated ligand (protein A, protein L, or F peptide) is captured by streptavidin, 3) the adsorption/desorption of the analyte is observed, and 4) finally the sensor chip surface is

completely regenerated back to the bare oligonucleotide (**Supplementary Figure S2**).

A unique target of the current assay was to demonstrate that reliable and quantitative differentiation of the binding could be achieved with a single replicate of material and sole observation of the maximum response level as opposed to detailed concentration-dependent equilibrium and/or kinetic fitting models. Repeatability of this platform (additional details in materials and methods) was demonstrated using 20 consecutive cycles of ligand capture and NISTmAb Bex as the analyte. Response levels for each of the biotinylated ligands were repeatable with coefficient of variations (CV) of less than 3.4% (**Supplementary Table S2**). Very repeatable ligand capture levels are vital for assay performance and were achieved by the addition of 0.1% bovine serum albumin to both protein A and protein L solutions but not needed in the F peptide solution. The binding response for each NISTmAb Bex replicate was also confirmed to be repeatable with CVs of less than 3.3% (**Supplementary Table S3**). These results indeed confirmed that the assay was repeatable and that this assay could provide reliable data on our oxidized sample set. The final experimental design for future use therefore consisted of 20 cycles with 3 startup cycles to prep the surface, 3 NISTmAb Bex samples run at the beginning, middle, and end, and 14 samples run once in a randomized order. Samples were all diluted to 200 nmol/L concentration and run over once per experiment. Each experiment was repeated 3 times providing 3 measurements for each oxidized sample and nine measurements of NISTmAb Bex. After analysis of all samples, the repeatability and reproducibility of the assay was also confirmed by measuring the response level in response units (RU) for each of the biotinylated ligands after each cycle. All three ligands also showed intra assay CV less than 2% and inter assay CV of less than 5% (**Supplementary Table S4–6**). All oxidized samples were characterized by size exclusion chromatography (SEC) to ensure that samples did not have any substantial changes in high molecular weight (HMW) or low molecular weight (LMW) species that would have interfered with SPR and thermal unfolding studies. The HMW, monomer, and LMW species were determined for each sample and summarized in **Supplementary Table S7**. Overall, all the oxidized samples except $^{0.0375\%}$CPAox$_{16hr}$ showed only minor differences when compared to NISTmAb Bex and the small difference in that one sample was noted but was not considered an issue for further biophysical studies.

Surface Plasmon Resonance: Effects of Methionine Oxidation on NISTmAb Binding to Domain Specific Molecular Probes

General Trends of Nox Samples

The relative binding affinity of oxidized NISTmAb samples binding to protein A can be seen in **Figure 6A** and the representative sensorgrams in **Supplementary Figures S3A,B**. A significant decrease in relative binding affinity correlating to increasing oxidation levels can be quickly identified when looking at $^{0.3\%}$Nox time course samples. The least oxidized sample, $^{0.3\%}$Nox$_{0.5hr}$, showed relatively small changes (94.7%) in binding to protein A relative to NISTmAb Bex, whereas the $^{0.3\%}$Nox$_{32hr}$ sample, which is the most oxidized sample with near complete oxidation of the six methionine residues shown to oxidize under our conditions, showed a drastic decrease in the relative binding affinity to protein A (38.5%). The F peptide binding results showed a similar trend of decreasing relative binding affinity with increasing global oxidation as shown in **Figure 6B** and the representative sensorgrams in **Supplementary Figures S3C,D**. The least oxidized sample, $^{0.3\%}$Nox$_{0.5hr}$, showed relatively small changes (94.6%) in binding to F peptide relative to NISTmAb Bex. On the other side of the time course scale, the $^{0.3\%}$Nox$_{32hr}$ sample, which is the most oxidized sample with near complete global oxidation, showed large changes to the relative binding to F peptide (53.7%). While the protein A and F peptide binding data showed major changes due to oxidation, the protein L binding data showed very little changes as oxidation increased (**Figure 6C**) (**Supplementary Figures S3E, F**). The least oxidized sample, $^{0.3\%}$Nox$_{0.5hr}$, showed no real changes (99.3%) in binding to protein L relative to NISTmAb Bex. Even the near completely oxidized $^{0.3\%}$Nox$_{32hr}$ sample showed only a small change in relative binding to protein L (92.6%).

General Trends of CPA Samples

The relative binding affinity of $^{0.3\%}$CPA samples binding to protein A, F peptide, and protein L can also be seen in **Figures 6A–C**, respectively. The binding level of identical time points of $^{0.3\%}$Nox samples is shown with a solid line in each figure. The relative binding affinity of $^{0.3\%}$CPA samples to protein A was higher when compared to identical time points of $^{0.3\%}$Nox samples, implying that protection from oxidation due to the protein A masking did indeed help maintain rebinding to a protein A ligand. This phenomenon, while interesting, was expected as M255 has been shown to be vital for high affinity protein A binding and was shown to be protected from oxidation in the 0.3 %CPA samples.

Protein A masking had little to no effect on protein L binding as indicated in **Figure 6C**. This may be the expected result considering protein A and protein L binding regions are spatially distributed as demonstrated in **Figure 5**, and no methionine residues of IgG are known to be involved in protein L binding, a supposition supported by our observation of little to no change in Nox sample binding to protein L. Protein A masking did, however, have an effect on F peptide binding (**Figure 6B**). The relative binding affinity of $^{0.3\%}$CPA samples to F peptide was lower when compared to identical time points of $^{0.3\ \%}$Nox samples, implying that the changes in oxidation rates due to the protein A masking did affect F peptide binding. Qualitative comparison of **Figure 4B** reveals that M101 had the largest increase in oxidation vs. the equivalent Nox time points. A correlation would make sense considering M101 is located in the CDR and therefore probable to have some effect on antigen binding. On the other hand, M361 and LC M4 are also consistently more oxidized in the 0.3 %CPA samples, making a conclusive correlation subjective at best

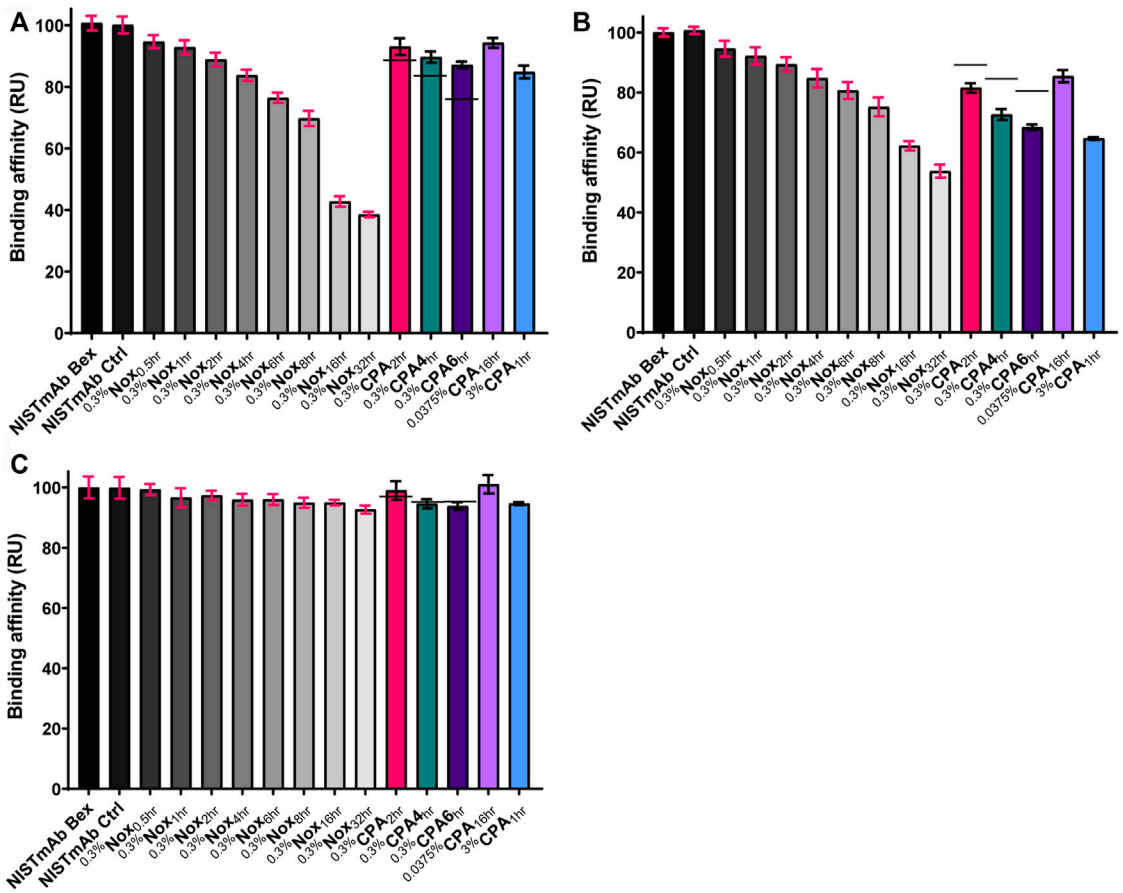

FIGURE 6 | Relative binding affinity of NISTmAb samples: **(A)** Protein A binding affinity (RU) **(B)** F peptide binding affinity (RU) **(C)** Protein L binding affinity (RU). The standard deviation of each measurement is noted with error bars. Black dashes (–) are used in the 0.3% CPA samples to denote the relative binding affinity from equivlent timed Nox sample for comparison purposes.

without epitope mapping and of course neglecting the possibility of allosteric effects.

Site-Specific Correlation: % Met Oxidized vs. Relative Binding

Peptide mapping analysis was used to evaluate oxidation at specific methionine residues and combined with relative binding affinity by SPR to further explore site-specific structure/function correlations. **Figure 7** A through D shows a consistent trend for Met residues in the $^{0.3\%}$Nox samples (in black), an increase in oxidation at each site appears to correlate with a decrease in protein A relative binding. Based on these samples alone, however, no confident site-specific correlations can be made because oxidation at all methionine residues is increasing and roughly correlating with a decrease in protein A binding. Inclusion of the CPA samples (in pink), however, allow for a more selective and confident site-specific relationship because oxidation rates at some residues remain unaltered, while others change as a result of ligand protection. CPA samples for M101 and M361, for example, show a higher relative binding at the same % oxidation (**Figures 7A,C**) and these data stay widely from the $^{0.3\ \%}$Nox regression line and fall completely out of 90% prediction bands. These data indicate oxidation at these sites is not the dominant driver of protein A binding reduction. However, CPA samples for M255 and M431 trend more closely to the $^{0.3\ \%}$Nox regression line (**Figures 7B,D**), indicating decreased protein A binding is more closely associated with oxidation at these sites. Previous reports have indeed demonstrated that oxidation in the Fc region disrupts protein A binding as it binds to a region where M255 and M431 are located and where the C_H2 and C_H3 domains interact (Deis et al., 2015; Gallagher et al., 2018). In the above example, it is our position that if a specific residue is a causal factor in reducing binding, then alteration of the kinetics of that oxidation (e.g., slowed *via* ligand-bound protection) will not alter the trend of relative binding vs. site-specific %Met oxidation. Specifically, CPA data points will deviate farther from the Nox regression model when residues are not involved in binding while CPA data points will trend closer to the Nox regression model when they are involved in binding. To quantitate this distance, the standard error of regression (Sy.x) of CPA data points was calculated from the Nox regression model. The Sy.x values are shown in

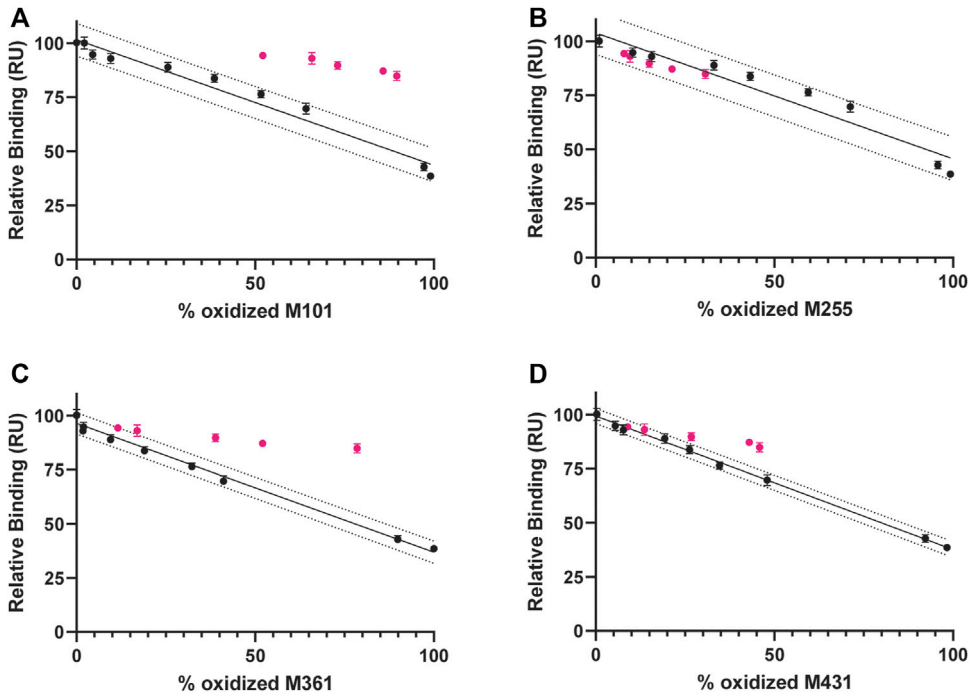

FIGURE 7 | Correlation between protein A binding and Met ox ($^{0.3\%}$Nox samples in black and CPA samples in pink) and linear regression analysis of Nox samples (solid black line) with 90% prediction bands (dotted black line) **(A)** M101 **(B)** M255 **(C)** M361 **(D)** M431.

Supplementary Table S8 and show significantly larger values for M101 and M361, more intermediate value for M431, and lowest for M255. In summary, oxidation at M255 correlates strongly to decreased protein A binding while oxidation at M431 might have a minor secondary effect and oxidation at M101 and M361 seem to play no direct role in decreased protein A binding.

A similar trend can be seen in **Supplementary Figures S4 A–D** for Met residues in the $^{0.3\%}$Nox samples, an increase in oxidation at each site appears to correlate with a decrease in F peptide relative binding. More selective and confident correlations are achieved when the CPA samples are added to these plots. CPA samples for M34 and M255 show a lower relative binding to F peptide at the same % oxidation and these data stay widely from the $^{0.3\ \%}$Nox regression line and fall completely out of 90% prediction bands (**Supplementary Figures. S4 C,D**). CPA samples for LC M4 and M101, on the other hand, trend more closely to the Nox regression line (**Supplementary Figures S4 A,B**). Again the Sy.x was calculated and values are shown in **Supplementary Table S9**. The values are significantly higher for M34 and M255, more intermediate for LC M4, and lowest for M101. In summary, oxidation at M101 correlates strongly to decreased F peptide binding while oxidation at LC M4 might have a minor secondary effect and oxidation at M34 and M255 seem to play no direct role in decreased F peptide binding. Previous reports have shown that the oxidation of a residue in the CDR of an antibody can disrupt antigen binding (Haberger et al., 2014), and the current F peptide binding data indicates that methionine oxidation can indeed cause a significant decrease in the ability of NISTmAb to bind to a peptide antigen.

Surface Plasmon Resonance: Sensitivity to Detect Changes in Oxidation

To determine what samples had statistical differences in the binding affinity when compared to the unstressed NISTmAb Bex sample, an unpaired *t*-test was used to calculate the differences between the $^{0.3\%}$Nox samples and the NISTmAb Bex sample (**Supplementary Table S10**). First, any differences due to storage at room temperature for an extended period of time were ruled out by demonstrating that the binding of NISTmAb Bex and NISTmAb Ctrl were not statistically different. Looking next at the least oxidized sample, $^{0.3\%}$Nox$_{0.5hr}$, it did indeed show significant differences in binding to protein A when compared to NISTmAb Bex with a corresponding *p* value of 0.0028. All other samples were also statistically different than NISTmAb Bex with *p*-values of less than 0.0001. An unpaired *t*-test was again used to determine the statistical difference in relative binding affinity to F peptide. The binding of NISTmAb Bex and NISTmAb Ctrl were not statistically different when binding to F peptide which confirms that no modifications due to storage at 25°C for 32 h led to any detectable changes. Again the least oxidized Nox sample, $^{0.3\%}$Nox$_{0.5hr}$, could be differentiated from NISTmAb Bex with F peptide binding as the relative binding affinity was

statistically different with a p value of 0.0008. All other samples were also statistically different than NISTmAb Bex with p-values of less than 0.0001. A summary of p values for all samples can be found in **Supplementary Table S8**. Taken together both protein A and F peptide binding are good indicator of oxidation and even small amounts of oxidation could be detected using this approach.

The sensitivity of detection of specific oxidized methionine residues in NISTmAb could be estimated by using the experimental data from our least oxidized sample, $^{0.3\%}Nox_{0.5hr}$. protein A binding was indicative of methionine oxidation at M255 and the sensitivity of detection was estimated to be 10% of M255 oxidation from experimental data of sample $^{0.3\%}Nox_{0.5hr}$. F peptide binding was indicative of methionine oxidation at M101 and the sensitivity of detection was estimated to be 5% of M101 oxidation from experimental data of sample $^{0.3\ \%}Nox_{0.5hr}$.

Overall the trends for the traditional Nox samples were as expected—higher global oxidation, indicated increase in oxidation at all susceptible Met residues (**Figure 4A**), resulted in decreased binding for oxidation-affected interactions. In general, oxidation affects NISTmAb binding to protein A > F peptide and only the smallest amount for protein L. The general trend also held for the CPA samples, oxidized samples demonstrated lower binding affinity compared to NISTmAb Bex. Both protein A and F peptide make excellent molecular probes to distinguish methionine oxidation in NISTmAb as they can detect only minor changes in oxidation but protein L was unable to detect these minor changes. This SPR assay has been demonstrated to be a rapid method to detect oxidation at both the Fc and Fab regions in the same analytical run.

Assessment of NISTmAb Stability With Thermal Unfolding Assay

In the discussion above we utilized the uniquely oxidized CPA samples to demonstrate that localized changes in oxidation would inevitably affect ligand binding in that region. The SPR assay developed was therefore inferred to be sensitive to oxidation of specific Met residues. A logical question to then ask is whether other biophysical assays indicative of stability may also be localized using similar techniques. Qualitative thermal melting studies with intrinsic tryptophan fluorescence were therefore performed to identify correlations between methionine oxidation and domain stability. Oxidation of IgG is known to destabilize the Fc domain of IgG resulting in changes in the melting temperature (Chumsae et al., 2007; Gao et al., 2015). Previous differential scanning calorimetry (DSC) measurements of NISTmAb have determined that there are three distinct melting temperatures, 69.2°C, 83.1°C, and 93.4°C, corresponding to C_H2, C_H3, and Fab domains (Gokarn et al., 2015). To examine the thermal stability of stressed samples in the current study, a thermal unfolding assay was performed that measures the intrinsic fluorescence from aromatic amino acid residues. Changes in the fluorescence ratio 350 nm/330 nm were measured with increasing temperature, and the midpoint unfolding inflection temperatures (Ti) were calculated along with the initial 350 nm/330 nm ratio.

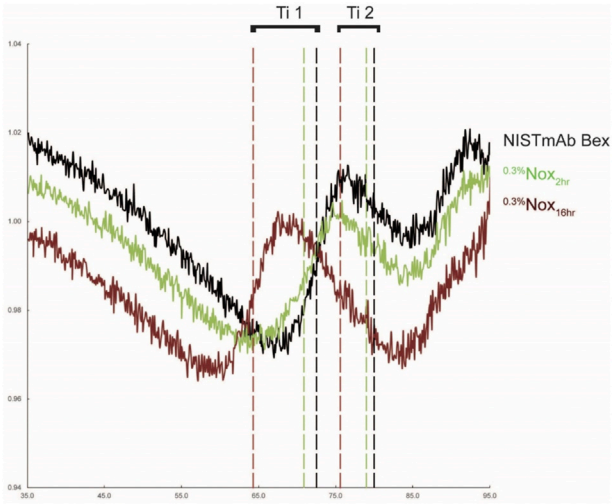

FIGURE 8 | Unfolding profiles of NISTmAb Bex, a lightly oxidized sample ($^{0.3\%}Nox_{2hr}$), and a heavily oxdized sample ($^{0.3\%}Nox_{16hr}$) with calculated inflection temperatures for the C_H2 (Ti_1) and C_H3 (Ti_2) domains (.

Representative unfolding profiles of NISTmAb Bex, a lightly oxidized sample ($^{0.3\%}Nox_{2hr}$), and a heavily oxidized sample ($^{0.3\%}Nox16_{hr}$) are shown in **Figure 8**. These unfolding profiles showed two clear changes that relate to the level of oxidation. First, the initial ratio of detected fluorescence signal decreases while oxidation increases indicated by the downward shift of the profile at 35°C (the beginning of the assay measurement). This decrease signifies a change in the amount of solvent exposed tryptophan or tyrosine residues. Second, the thermal stability of oxidized samples decreased as methionine oxidation increased indicated by the leftward shift (decreasing value) in both Ti_1 and Ti_2. Three distinct Ti's could be determined for NISTmAb Bex: 72.5°C (Ti_1), 80.0°C (Ti_2), and 89.1°C (Ti_3). The software was unable to determine Ti_3 for all samples, however manual inspection of the first derivative of the raw data shows Ti_3 was similar for all oxidized samples. The complete results of the unfolding measurements including the initial ratio and unfolding temperatures for all samples can be found in **Figure 9**.

General Trends of Nox Samples

When looking over the thermal unfolding data it is evident that as oxidation increases the initial ratio and both unfolding temperatures decrease significantly. A small decrease in the initial ratio can be seen in **Figure 9A** correlating to increasing oxidation levels when looking at $^{0.3\%}$Nox time course samples. The decrease of the initial ratio is small in value, 0.003, for the least oxidized sample, $^{0.3\%}Nox_{0.5hr}$, and 0.021 for the most oxidized sample. While these values are indeed small, the measurement of the initial ratio was shown to be extremely precise with the average coefficient of variation of 0.09% indicating that even small differences could be reliably measured.

A large decrease in the Ti_1 can be seen in **Figure 9B** correlating to increasing oxidation levels when looking at $^{0.3\%}$Nox time course samples. The least oxidized sample, $^{0.3\%}Nox_{0.5hr}$,

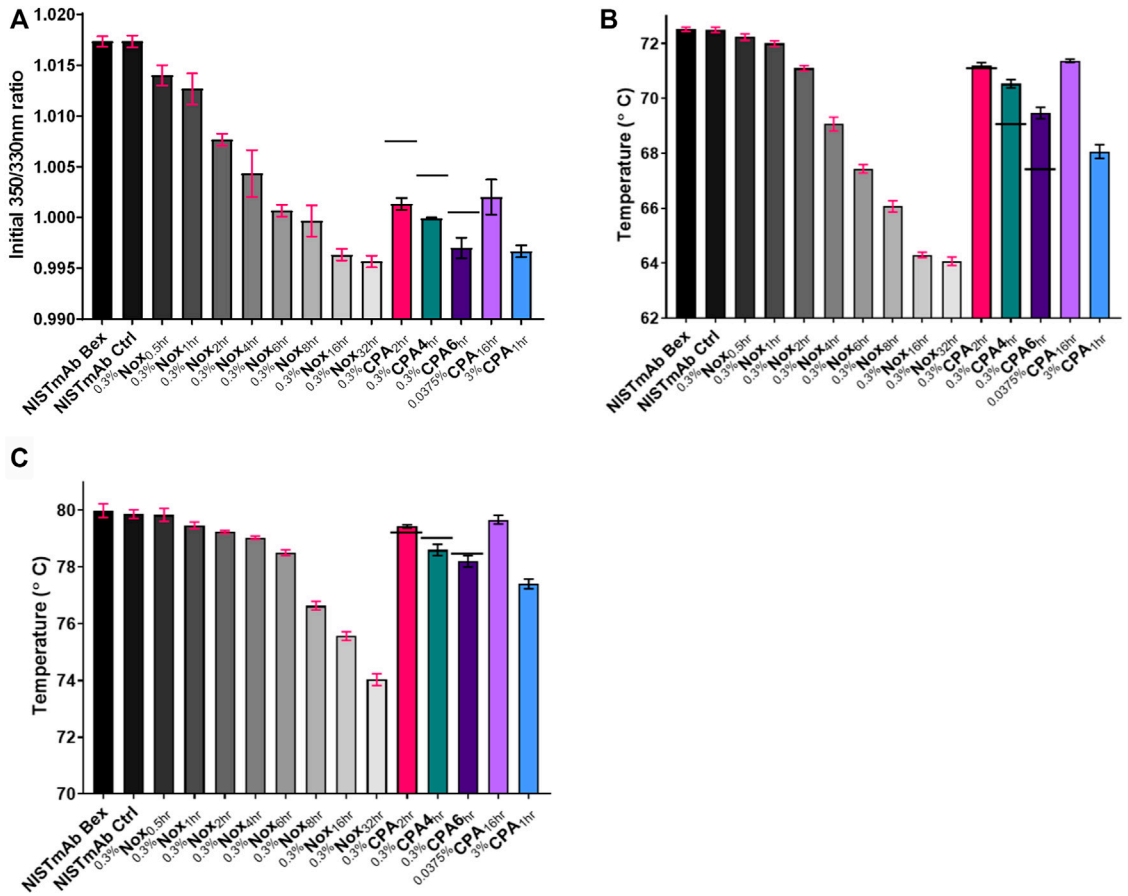

FIGURE 9 | Thermal unfolding analysis using Tycho NT 6.0 **(A)** Initial 350 nm/330 nm ratio **(B)** Inflection Temperature 1 **(C)** Inflection Temperature 2. The standard deviation of each measurement is noted with error bars. Black dashes (–) are used in the 0.3% CPA samples to denote the relative binding affinity from equivlent timed Nox sample for comparison purposes.

showed a small decrease in Ti_1 of 0.3°C relative to NISTmAb Bex. Whereas, the $^{0.3\%}Nox_{32hr}$ sample, the most oxidized sample, showed a drastic decrease in Ti_1 of 8.45°C. Similarly, a large decrease in the measured Ti_2 can be seen in **Figure 9C** correlating to increasing oxidation levels when looking at $^{0.3\%}$Nox time course samples. The least oxidized sample, $^{0.3\%}Nox_{0.5hr}$, showed a small decrease in Ti_2 of 0.15°C relative to NISTmAb Bex. Whereas, the $^{0.3\ \%}Nox_{32hr}$ sample, the most oxidized sample, showed a substantial decrease in Ti_1 of 5.95°C.

General Trends of CPA Samples

The initial ratio and thermal unfolding temperatures of $^{0.3\ \%}$CPA samples can also be seen in **Figures 9A–C**, respectively. The measured initial ratio/unfolding temperature of identical time points of $^{0.3\%}$Nox samples is shown with a solid line in each figure for comparison purposes. The initial ratio of $^{0.3\%}$CPA samples was much lower when compared to identical time points of $^{0.3\%}$ Nox samples, implying that changes in the methionine oxidation pattern due to the protein A masking did decrease the initial ratio. This significant decrease in initial ratio was seen in heavily oxidized Nox samples suggesting that oxidation of M101 is likely to be the cause of the change as it is heavily oxidized in all CPA samples. This phenomenon is confirmed when comparing the other CPA samples especially $^{0.0375\%}CPA_{16hr}$ which has very low levels of oxidation at all sites except M101. $^{0.0375\%}CPA_{16hr}$ has a similar amount of oxidation at M101 as $^{0.3\%}Nox_{6hr}$ and these samples indeed have similar initial ratio values, 1.002 and 1.001 respectively. Taken together oxidation at M101 seems to have a strong effect on the initial ratio and oxidation at this site seems to induce a structural change that exposes a tyrosine or tryptophan residue likely in the Fab region.

Protein A masking also had an effect on the measured Ti_1 (**Figure 9B**). The Ti_1 of $^{0.3\%}$CPA samples was much higher at time points 4 h and 6 h but essentially the same at 2 h when compared to identical time points of $^{0.3\%}$Nox samples. This implies that changes in the oxidation rates due to protein A masking did increase the stability of the C_H2 domain by blocking oxidation. Presumably, this effect is mostly due to the much lower amount of oxidation at M255 in CPA as it is the most protected residue and also is located in the C_H2 domain. While the initial ratio and Ti1 values were significantly affected by protein A masking oxidation, the value of Ti_2 of $^{0.3\%}$CPA samples was slightly higher at 2 h and

slightly lower at 4 and 6 h compared to $^{0.3\%}$Nox samples (**Figure 9C**). The changes in oxidation rates due to the protein A masking had a smaller effect on the stability of the C_H3 domain of NISTmAb. This effect is most likely due to the higher amounts of oxidation at M361 and M431 in the CPA samples both of which are located in the C_H3 domain of NISTmAb.

Site-Specific Correlation: % Met Oxidized vs. Initial Ratio/Unfolding Temperatures

Peptide mapping analysis was used to evaluate oxidation at specific methionine residues and combined with thermal unfolding analysis to further explore site-specific structure/function correlations. Plots of the initial ratio of the $^{0.3\%}$Nox samples against the % oxidized of methionine at all sites were generated and nonlinear regression analysis was used to model Nox data sets (**Supplementary Figures S5A–F**). A consistent trend can be seen for all Met residues in the Nox data, an increase in oxidation at each site correlates with a decrease in the value of the initial ratio. More selective and confident correlations are achieved when the CPA samples are added to these plots. CPA samples for M34, M255, and M431 stay widely from the $^{0.3\%}$Nox regression model and fall completely out of 90% prediction bands (**Supplementary Figures S5B, D, F**). On the other hand, CPA samples for LC M4, M101, and M361 trend more closely to the Nox regression model (**Supplementary Figures S5A,C,E**). The Sy.x of CPA data was calculated and the values are shown in **Supplementary Table S11**. The Sy.x was significantly higher for M34, M255, and M431, more intermediate for LC M4 and M361, and lowest for M101. In summary, oxidation at M101 correlates strongly with the decrease in initial ratio, while oxidation at LC M4 and M361 could play a more secondary role. Methionine oxidation at these sites seem to induce structural change that causes a tyrosine or tryptophan residue to be less exposed, resulting in a shift of the fluorescence toward lower wavelengths.

Strong correlating trends can be seen when Ti_1 is plotted vs. % of methionine oxidation in the Nox samples (**Supplementary Figures S6A–F**). Again, CPA samples were added to these plots to get a more precise idea of which oxidized methionine residues play a stronger role in the decrease of thermal stability of NISTmAb. CPA samples for LC M4, M101, and M361 stay widely from the $^{0.3\%}$Nox regression model and fall completely out of 90% prediction bands (**Supplementary Figures S6A,C,E**). On the other hand, CPA samples for M34, M255, and M431 trend more closely to the Nox regression model (**Supplementary Figures S6B,D,F**). The Sy.x of the CPA data was calculated and the values are shown in **Supplementary Table S12**. The Sy.x was significantly higher for LC M4, M101, and M361, more intermediate for M34 and M431, and lowest for M255. These data indicate that oxidation at M255 correlates strongly with the decrease in thermal stability of the CH2 domain, while oxidation at M34 and M431 could play more secondary roles.

Similar strong correlations are observed after plotting Ti_2 vs. % of methionine oxidation in the Nox samples (**Supplementary Figures S7A–F**). CPA samples for M101 stay widely from the Nox regression model whereas all others trend closely to their respective model. The Sy.x of the CPA data was calculated and the values are shown in **Supplementary Table S13**. The Sy.x was higher for M101 while all other methionine residues show relatively low values. These data indicate that global methionine oxidation at multiple residues contribute to the decrease in thermal stability of the CH3 domain.

PERSPECTIVES

In order to evaluate methods that are capable of attribute specific monitoring, well-defined materials with site specific attribute modifications are needed. We explored a strategy that could generate selectively oxidized antibody materials with specific attribute changes that differ from global chemical oxidation. This ligand masking method takes advantage of the ability of a specific binding partner to bind and mask its binding region on an antibody. Once bound, an accelerated stress procedure was performed to generate a product with a unique methionine oxidation pattern. This approach generated materials that showed protection from oxidative stress at a specific methionine residue, M255, while other methionine residues were exposed to varying levels of oxidation. While this method still cannot provide perfect control over oxidation, unique materials with specific attribute modifications were generated that could not be made using a traditional approach. Other strategies can achieve similar unique materials; however, this method has some distinct advantages that make it an interesting approach. First, no genetic manipulations are needed that can mimic or block oxidation which can be arduous and require the expression and purification of new mAbs. Also these oxidation mimicking mutants (e.g., glutamine to mimic oxidized methionine) do share similarities in chemical structure and hydrophobicity. They are indeed different in structure, and the exact contribution still must be demonstrated. Another typical method relies on tedious chromatographic separations in combination with fractionation that can be difficult on a larger scale. In some cases oxidation variants can be almost impossible to separate without a very specialized affinity column.

Assigning criticality to a specific amino acid residue can be a challenging task due to the global nature of typical stress studies. While certain residues are typically modified at higher rates than others, multiple residues are most often modified, making correlations between a site-specific modification and biological activity difficult. Often multiple residues in both the Fab and Fc regions are susceptible to modifications, but the effect of each are difficult to differentiate. The ligand masking approach allowed generation of materials with unique modification patterns. The effect of this oxidation was explored by measuring changes in relative binding affinity and the thermal stability of these modified materials when compared to NISTmAb Bex. With the help of these uniquely stressed materials, specific attribute changes could be correlated to specific changes in these analytical assays; a pre-requisite to assigning attribute criticality with heightened specificity.

In this study, we explored the effect methionine oxidation has on the ability of NISTmAb to bind to three IgG binding proteins including protein A, an antigen mimic F peptide, and protein L. A SPR assay was developed that demonstrated the ability of these proteins to serve as molecular probes to rapidly reveal stress induced oxidation in NISTmAb samples. High throughput analytical screening technologies are important to quickly identify critical process parameters and to monitor critical product quality attributes. Both protein A and F peptide could easily distinguish samples with low levels of oxidation whereas protein L was not a good ligand for detecting oxidation. Peptide mapping analysis combined with relative binding affinity by SPR analysis allowed for correlations to be made between increases in oxidation at specific methionine residues and decreases in binding to a specific molecular probe. The SPR assay in this study serves as an interesting approach to rapid analysis of oxidation at multiple sites that uses very little material and can be run without any sample prep. One could envision an SPR readout that can accurately estimate the % oxidation at a variety of specific sites if the right molecular probes were used. In addition, other targeted assays could be developed using different molecular probes that are able to detect other stress induced modifications such as deamidation or aggregation. This sort of label-free binding assay could provide rapid results about the integrity of antibody samples and detect a variety of higher order structural changes.

In addition to usefulness in assessing attribute criticality, such selectively oxidized samples also serve as useful and interesting materials for various analytical challenges. Analytical challenge materials are a vital part of demonstrating and determining method capability. Traditional accelerated degradation studies can indeed produce useful materials that can contain a variety of induced amino acid modifications that can challenge various analytical methods. In some cases, the ability of a method to detect and to quantitate a site specific modification might be required, so a more selectively modified challenge material would be of great advantage. These materials with selective modifications can serve as important resources to determine if a method can distinguish site specific modifications versus global changes. For example, the ability of the different LC-MS methods used to characterize oxidized materials in this study is clearly distinguished when comparing IdeS subunit monitoring versus peptide mapping. IdeS subunits can monitor oxidation levels of each subunit (i.e. scFc, Fd, and LC), but peptide mapping is able to determine oxidation at the peptide levels giving us residue specific information. A similar phenomenon can be seen when comparing the SPR and thermal unfolding analysis as the SPR method can give us information about the oxidation levels at specific epitopes while the thermal unfolding studies provide a correlation between oxidation and domain stability. The selectively oxidized CPA samples provided useful and interesting challenge materials for these assays and helped push the limits of each method to detect domain and residue specific oxidation.

CONCLUSION

In summary, we developed a strategy to generate uniquely stressed antibody materials by performing the stress in the presence of a bound ligand protein A. These materials were characterized with mass spectrometry to quantitate site specific methionine oxidation. Substantial changes in the oxidation rate and level of multiple methionine residues were shown when compared to materials stressed in solution without bound protein A. With these uniquely oxidized materials in hand, we developed a rapid SPR assay that could detect methionine oxidation in both the Fab and Fc regions using specific molecular probes. The addition of our uniquely oxidized materials to our data set allowed us to hone in on specific methionine residues vital to binding. Further analysis showed that antibody oxidation could also be rapidly detected using thermal unfolding analysis as the stability decreases in multiple domains. The industry relevant stress of accelerated oxidation was used, but other industry relevant stress conditions could be chosen and a similar ligand masking approach could protect specific residues from modification. In the future more studies may reveal other proteins or peptides that can provide site specific protection and use these masking agents to elucidate specific structure function attributes related to a variety of antibody modifications. In addition to monoclonal antibodies, the use of other modalities such as other protein drugs or viral vectors could be of great interest especially when knowledge of structure function relationships is not as developed as mAbs.

DATA AVAILABILITY STATEMENT

The raw data supporting the conclusion of this article will be made available by the authors, without undue reservation.

AUTHOR CONTRIBUTIONS

JG and JS contributed to conception and design of the study. JG performed the experimental work. JG and JS wrote sections of the manuscript. JG and JS contributed to manuscript revision, read, and approved the submitted version.

FUNDING

This work was supported by the National Institute of Standards and Technology (NIST).

SUPPLEMENTARY MATERIAL

The Supplementary Material for this article can be found online at: https://www.frontiersin.org/articles/10.3389/fmolb.2022.789973/full#supplementary-material

REFERENCES

Bertolotti-Ciarlet, A., Wang, W., Lownes, R., Pristatsky, P., Fang, Y., McKelvey, T., et al. (2009). Impact of Methionine Oxidation on the Binding of Human IgG1 to FcRn and Fcγ Receptors. *Mol. Immunol.* 46, 1878–1882. doi:10.1016/j.molimm.2009.02.002

Chen, Y., Doud, E., Stone, T., Xin, L., Hong, W., and Li, Y. (2019). Rapid Global Characterization of Immunoglobulin G1 Following Oxidative Stress. *MAbs* 11, 1089–1100. doi:10.1080/19420862.2019.1625676

Chumsae, C., Gaza-Bulseco, G., Sun, J., and Liu, H. (2007). Comparison of Methionine Oxidation in thermal Stability and Chemically Stressed Samples of a Fully Human Monoclonal Antibody. *J. Chromatogr. B* 850, 285–294. doi:10.1016/j.jchromb.2006.11.050

Cymer, F., Thomann, M., Wegele, H., Avenal, C., Schlothauer, T., Gygax, D., et al. (2017). Oxidation of M252 but Not M428 in Hu-IgG1 Is Responsible for Decreased Binding to and Activation of Hu-FcγRIIa (His131). *Biologicals* 50, 125–128. doi:10.1016/j.biologicals.2017.09.006

Dashivets, T., Stracke, J., Dengl, S., Knaupp, A., Pollmann, J., Buchner, J., et al. (2016). Oxidation in the Complementarity-Determining Regions Differentially Influences the Properties of Therapeutic Antibodies. *mAbs* 8, 1525–1535. Taylor & Francis. doi:10.1080/19420862.2016.1231277

Deis, L. N., Wu, Q., Wang, Y., Qi, Y., Daniels, K. G., Zhou, P., et al. (2015). Suppression of Conformational Heterogeneity at a Protein-Protein Interface. *Proc. Natl. Acad. Sci. U.S.A.* 112, 9028–9033. doi:10.1073/pnas.1424724112

Gallagher, D. T., Galvin, C. V., and Karageorgos, I. (2018). Structure of the Fc Fragment of the NIST Reference Antibody RM8671. *Acta Cryst. Sect F* 74, 524–529. doi:10.1107/s2053230x18009834

Gao, X., Ji, J. A., Veeravalli, K., John Wang, Y., Zhang, T., Mcgreevy, W., et al. (2015). Effect of Individual Fc Methionine Oxidation on FcRn Binding: Met252 Oxidation Impairs FcRn Binding More Profoundly Than Met428 Oxidation. *J. Pharm. Sci.* 104, 368–377. doi:10.1002/jps.24136

GE Healthcare (2004). *MabSelect SuRe-studies on Ligand Toxicity, Leakage, Removal of Leached Ligand, and Sanitization; 11-0011-64 AA*. Amersham: Amersham Application Note 2004, Process-scale antibody purification.

Gokarn, Y., Agarwal, S., Arthur, K., Bepperling, A., Day, E. S., Filoti, D., et al. (2015). "Biophysical Techniques for Characterizing the Higher Order Structure and Interactions of Monoclonal Antibodies," in *State-of-the-Art and Emerging Technologies for Therapeutic Monoclonal Antibody Characterization Volume 2. Biopharmaceutical Characterization: The NISTmAb Case Study* (ACS Publications), 285–327. doi:10.1021/bk-2015-1201.ch006

Haberger, M., Bomans, K., Diepold, K., Hook, M., Gassner, J., Schlothauer, T., et al. (2014). Assessment of Chemical Modifications of Sites in the CDRs of Recombinant Antibodies: Susceptibility vs. Functionality of Critical Quality Attributes. *MAbs* 6, 327–339. doi:10.4161/mabs.27876

Jansson, B., Uhlén, M., and Nygren, P.-Å. (1998). All Individual Domains of Staphylococcal Protein A Show Fab Binding. *FEMS Immunol. Med. Microbiol.* 20, 69–78. doi:10.1016/s0928-8244(97)00108-9

Karlsson, R., Fridh, V., and Frostell, Å. (2018). Surrogate Potency Assays: Comparison of Binding Profiles Complements Dose Response Curves for Unambiguous Assessment of Relative Potencies. *J. Pharm. Anal.* 8, 138–146. doi:10.1016/j.jpha.2017.12.008

Li, W., Kerwin, J. L., Schiel, J., Formolo, T., Davis, D., Mahan, A., et al. (2015). "Structural Elucidation of post-translational Modifications in Monoclonal Antibodies," in *State-of-the-art and Emerging Technologies for Therapeutic Monoclonal Antibody Characterization Volume 2. Biopharmaceutical Characterization: The NISTmAb Case Study* (ACS Publications), 119–183. doi:10.1021/bk-2015-1201.ch003

Ljungberg, U. K., Jansson, B., Niss, U., Nilsson, R., Sandberg, B. E. B., and Nilsson, B. (1993). The Interaction between Different Domains of Staphylococcal Protein A and Human Polyclonal IgG, IgA, IgM and F(ab')2: Separation of Affinity from Specificity. *Mol. Immunol.* 30, 1279–1285. doi:10.1016/0161-5890(93)90044-c

Mo, J., Yan, Q., So, C. K., Soden, T., Lewis, M. J., and Hu, P. (2016). Understanding the Impact of Methionine Oxidation on the Biological Functions of IgG1 Antibodies Using Hydrogen/deuterium Exchange Mass Spectrometry. *Anal. Chem.* 88, 9495–9502. doi:10.1021/acs.analchem.6b01958

Mouchahoir, T., and Schiel, J. E. (2018). Development of an LC-MS/MS Peptide Mapping Protocol for the NISTmAb. *Anal. Bioanal. Chem.* 410, 2111–2126. doi:10.1007/s00216-018-0848-6

Pan, H., Chen, K., Chu, L., Kinderman, F., Apostol, I., and Huang, G. (2009). Methionine Oxidation in Human IgG2 Fc Decreases Binding Affinities to Protein A and FcRn. *Protein Sci.* 18, 424–433. doi:10.1002/pro.45

Schiel, J. E., Davis, D. L., and Borisov, O. (2015). "State-of-the-art and Emerging Technologies for Therapeutic Monoclonal Antibody Characterization Volume 3. Defining the Next Generation of Analytical and Biophysical Techniques," in *ACS Symposium Series* (ACS Publications), 455.

Sokolowska, I., Mo, J., Dong, J., Lewis, M. J., and Hu, P. (2017). Subunit Mass Analysis for Monitoring Antibody Oxidation. *mAbs* 9, 498–505. Taylor & Francis. doi:10.1080/19420862.2017.1279773

Stracke, J., Emrich, T., Rueger, P., Schlothauer, T., Kling, L., Knaupp, A., et al. (2014). A Novel Approach to Investigate the Effect of Methionine Oxidation on Pharmacokinetic Properties of Therapeutic Antibodies. *mAbs* 6, 1229–1242. Taylor & Francis. doi:10.4161/mabs.29601

Turner, A., Yandrofski, K., Telikepalli, S., King, J., Heckert, A., Filliben, J., et al. (2018). Development of Orthogonal NISTmAb Size Heterogeneity Control Methods. *Anal. Bioanal. Chem.* 410, 2095–2110. doi:10.1007/s00216-017-0819-3

Yang, R., Jain, T., Lynaugh, H., Nobrega, R. P., Lu, X., Boland, T., et al. (2017). Rapid Assessment of Oxidation via Middle-Down LCMS Correlates with Methionine Side-Chain Solvent-Accessible Surface Area for 121 Clinical Stage Monoclonal Antibodies. *MAbs* 9, 646–653. doi:10.1080/19420862.2017.1290753

Author Disclaimer: Certain commercial equipment, instruments, and materials are identified in this paper in order to specify the experimental procedure. Such identification does not imply recommendation or endorsement by the National Institute of Standards and Technology, nor does it imply that the material or equipment identified is necessarily the best available for the purpose.

Conflict of Interest: The authors declare that the research was conducted in the absence of any commercial or financial relationships that could be construed as a potential conflict of interest.

Publisher's Note: All claims expressed in this article are solely those of the authors and do not necessarily represent those of their affiliated organizations, or those of the publisher, the editors and the reviewers. Any product that may be evaluated in this article, or claim that may be made by its manufacturer, is not guaranteed or endorsed by the publisher.

frontiers | Frontiers in Molecular Biosciences

REVIEW
published: 05 May 2022
doi: 10.3389/fmolb.2022.876780

Interlaboratory Studies Using the NISTmAb to Advance Biopharmaceutical Structural Analytics

Katharina Yandrofski[1], Trina Mouchahoir[1], M. Lorna De Leoz[2], David Duewer[3], Jeffrey W. Hudgens[1], Kyle W. Anderson[1], Luke Arbogast[1], Frank Delaglio[1], Robert G. Brinson[1], John P. Marino[1], Karen Phinney[3], Michael Tarlov[3] and John E. Schiel[1]*

[1]Institute for Bioscience and Biotechnology Research, National Institute of Standards and Technology, Rockville, MD, United States, [2]Agilent Technologies, Santa Clara, CA, United States, [3]National Institute of Standards and Technology, Gaithersburg, MD, United States

Biopharmaceuticals such as monoclonal antibodies are required to be rigorously characterized using a wide range of analytical methods. Various material properties must be characterized and well controlled to assure that clinically relevant features and critical quality attributes are maintained. A thorough understanding of analytical method performance metrics, particularly emerging methods designed to address measurement gaps, is required to assure methods are appropriate for their intended use in assuring drug safety, stability, and functional activity. To this end, a series of interlaboratory studies have been conducted using NISTmAb, a biopharmaceutical-representative and publicly available monoclonal antibody test material, to report on state-of-the-art method performance, harmonize best practices, and inform on potential gaps in the analytical measurement infrastructure. Reported here is a summary of the study designs, results, and future perspectives revealed from these interlaboratory studies which focused on primary structure, post-translational modifications, and higher order structure measurements currently employed during biopharmaceutical development.

Keywords: monoclonal antibody, biopharmaceutical, nistmab, therapeutic protein, interlaboratory study

OPEN ACCESS

Edited by:
Milena Quaglia, National Measurement Laboratory at LGC, United Kingdom

Reviewed by:
Adam Barb, University of Georgia, United States
Vojtech Franc, ProQR Therapeutics, Netherlands

****Correspondence:***
Katharina Yandrofski
Katharina.yandrofski@nist.gov

Specialty section:
This article was submitted to Structural Biology, a section of the journal Frontiers in Molecular Biosciences

Received: *15 February 2022*
Accepted: *21 March 2022*
Published: *05 May 2022*

Citation:
Yandrofski K, Mouchahoir T, De Leoz ML, Duewer D, Hudgens JW, Anderson KW, Arbogast L, Delaglio F, Brinson RG, Marino JP, Phinney K, Tarlov M and Schiel JE (2022) Interlaboratory Studies Using the NISTmAb to Advance Biopharmaceutical Structural Analytics. Front. Mol. Biosci. 9:876780. doi: 10.3389/fmolb.2022.876780

INTRODUCTION

Monoclonal antibodies (mAbs) have become the most prevalent biopharmaceutical modality, used to treat indications from viral infections to cancer. Numerous other protein-based drugs continue to evolve including antibody drug conjugates (ADCs), bispecifics, coagulation factors, and cytokines, among others. In addition, new modalities such as viral vector mediated gene therapies and vaccines, mRNA vaccines, and adoptive cell therapies have more recently emerged to fill previously unmet medical needs. Common to all modalities is the need for comprehensive structural characterization, identification of relevant critical quality attributes, and quality control of these features to maintain safety and efficacy. Lessons learned regarding analytical best practices for mAbs, perhaps the most widely characterized and understood from a structure-function perspective, can be ported to other modalities.

Comprehensive evaluation of the fundamental performance metrics and analytical capability of a technology are a pivotal first step prior to adapting, translating, or evolving measurement methods to

A

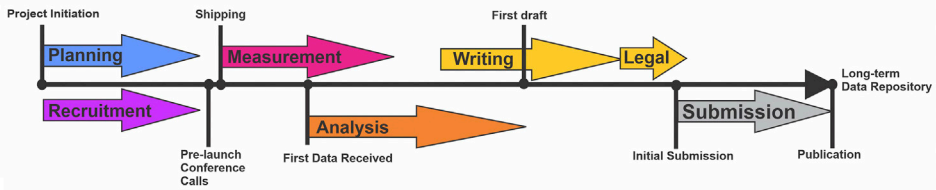

B

Study and Duration	Project Initiation	Pre-Launch Conference Calls	Shipping	First Data Received	First Draft	Initial Submission	Publication	Long-Term Data Repository
MAM	May 2016	July 2016	July 2017	September 2017	September 2018[a] February 2020[b]	March 2020[a] In Progress[b]	March 2021[a] In Progress[b]	In Progress
Glycosylation	March 2014	May 2014	June 2015	July 2015	June 2017[c] August 2017[d]	June 2017[c] July 2019[d]	August 2017[c] October 2019[d]	N/A
NMR HOS	April 2015	May 2016	June 2016	December 2016	December 2017	June 2018	December 2018[e]	December 2018
HDX-MS	June 2013	June 2014	October 2013	September 2015	May 2018	February 2019	May 2019[f]	March 2019

FIGURE 1 | Timeline of Global NISTmAb Interlaboratory Studies. **(A)** Representative timeline identifying the key milestones for an interlaboratory study. **(B)** Corresponding dates and key milestones for each NISTmAb interlaboratory study (MAM, glycosylation, NMR HOS, and HDX-MS).[a] MAM New Peak Detection Publication (Mouchahoir et al., 2021).[b] MAM Attribute Analytics Publication (In progress).[c] Glycosylation Interagency Internal Report (DeLeoz et al., 2017). [d] Glycosylation Interlaboratory Publication (De Leoz et al., 2020).[e] NMR HOS Interlaboratory Publication (Brinson et al., 2019).[f] HDX-MS Interlaboratory Publication (Hudgens et al., 2019a)

new systems. Innovative analytical technologies are often performed to enable deep characterization, elucidate mechanisms of action, or better understand the intricacies of a manufacturing process. These emerging technologies, despite their potential for profound leaps in product or process understanding, may have limited historical precedence, thus presenting a barrier to rapid adoption. Interlaboratory studies may serve to lower these barriers by providing a means of harmonizing technical approaches, reporting community-wide performance metrics (i.e. precision), defining method best practices, and/or understanding the underpinning principles and sources of uncertainty in a measurement system.

Publicly available biopharmaceutical product-representative test materials are a pre-requisite to interlaboratory evaluation of community wide performance metrics. The NIST monoclonal antibody (NISTmAb) was introduced as a tool for advancing analytical methods pertaining to monoclonal antibodies. The NISTmAb reference material (RM) 8,671 is a recombinant humanized IgG1κ expressed in murine suspension cell culture that has undergone biopharmaceutical industry standard upstream and downstream purification to remove process related impurities. This RM is intended primarily for use in evaluating the performance of methods for determining physicochemical and biophysical attributes of monoclonal antibodies. It also provides a representative test molecule for development of novel technologies for therapeutic protein characterization. (Mouchahoir and Schiel, 2018; Schiel and Turner, 2018; Schiel et al., 2018; Turner and Schiel, 2018; Turner et al., 2018). The NISTmAb first debuted in a series of small interlaboratory characterization studies in 2015. (Schiel et al., 2014; Schiel et al., 2015a; Schiel et al., 2015b). This series of reports provided a useful baseline to identify measurements for which method advancement and regulatory assimilation would benefit from additional technology development and interlaboratory studies. Highly focused interlaboratory studies have since been reported by NIST and independent communities to harmonize best practices, deepen community consensus on method performance, and document a baseline performance upon which future method evolution may be based (DeLeoz et al., 2017; Hudgens et al., 2019a; Brinson et al., 2019; Coffman et al., 2020; Srzentić et al., 2020; Mouchahoir et al., 2021). A number of those interlaboratory studies are reviewed here, with the intention to spur future partnerships to target additional assays and/or method evolution through well-planned interlaboratory studies.

The design, coordination, implementation, writing, and publishing of each of these studies is an extensive community-wide effort that spans multiple years (**Figure 1**). Planning and recruitment stages of an interlaboratory study coincide and are often synergistic. Sample sets, measurement protocols, and reporting structures can evolve based on community feedback, considering study design is exceedingly difficult to change post-launch. Sample identity and preparation is a critical step most often performed by the study organizers, but in consultation with participants. This stage may involve alteration of material properties to "challenge" the analytical method and/or prepare the sample for analysis (i.e. digestion, mixing, or vialing). Samples must be suitable with respect to material properties for the intended use in the measurement system, be non-proprietary to enable public dissemination/publication of results, and be of sufficient stability, homogeneity, and purity.

The measurement phase of an interlaboratory study is conducted at each partners' individual site. Participants are typically asked to complete a pre-defined report template and when possible, include raw data. Although reporting is templated, participation in such a study involves a significant commitment by participants and their parent organizations. The study design is intended to minimize financial and time commitment burden on the participants, but this aspect should not be overlooked as the intellectual engagement of experts in the field are critical to industry-relevant impact. Submitted datasets are most commonly anonymized via third party vendors to protect potential intellectual property, after which combined analysis of the anonymized data is conducted by the study organizers. Analysis, interpretation, and formulating the discussion around results are again a community effort involving all study participants. Numerous iterations of data analyses and participant feedback led to a first draft, initially approved by all co-authors, and then sent to partners legal for review. Use of a non-competitive material and data anonymization are critical to assure freedom to operate. Writing, submission, and acceptance can be a rather lengthy process to allow all authors and partner institutions to ultimately agree on the presentation and interpretation of results. Each of the studies reviewed herein are a consensus of 15–75 organizations. Interlaboratory studies represent broad industry commitment to achieve a high degree of unity and enable implementation of current best practices, evolve analytical methods, and expedite their uptake. A representative sampling of NISTmAb interlaboratory studies are reviewed here, specifically those that included one or more NIST organizers (multi-attribute method, glycosylation analysis, nuclear magnetic resonance, and hydrogen deuterium exchange interlaboratory studies). Each study had a slightly unique design and output, as necessitated by the intricacies of that particular method, which are reported herein to include the study Purpose and Method Description, Summary of Results, and Learnings and Future Perspectives. (Hudgens et al., 2019a; Brinson et al., 2019; De Leoz et al., 2020; Mouchahoir et al., 2021).

MULTI-ATTRIBUTE METHOD INTERLABORATORY STUDY

Purpose and Method Description

The multi-attribute method (MAM) builds upon industry experience with mass spectrometry (MS)-based peptide mapping (Formolo et al., 2015; Rogstad et al., 2017; Noor et al., 2020) and holds promise for use in the quality control (QC) space (Rogers et al., 2013; Rogers et al., 2015; Xu et al., 2017; Zhang and Guo, 2017; Rogstad et al., 2019; Millán-Martín et al., 2020; Sokolowska et al., 2020; Zhang et al., 2020; Mouchahoir et al., 2021). MAM is designed to monitor the status of pre-defined quality attributes within a therapeutic protein sample (*e.g.*, post-translational modifications (PTMs), enzymatic clips, isomerization, *etc.*) and/or detect process impurities (*e.g.,* host cell proteins) in the sample. The basic workflow of a MAM platform begins with enzymatic digestion of the therapeutic protein, followed by separation of the resulting peptides by liquid chromatography (LC) and identification of the peptides by high-resolution mass spectrometry detection. Elegant software platforms are then used to interrogate the data to monitor changes in PTM levels within the sample (*i.e.*, attribute analytics) and/or to detect impurities and unanticipated PTM changes in a non-targeted manner by comparison of the sample to a reference prepared in parallel (*i.e.*, new peak detection (NPD). NPD is performed by first aligning reference and test sample data files according to *m/z* and retention time as depicted in **Figure 2A**. The data undergo "peak picking" where ions that meet a predetermined signal threshold (the new peak detection threshold) and display typical peptide isotope distributions are designated as peaks (bounded by blue, green or brown boxes in **Figure 2A**). The peaks detected in each sample are compared to the corresponding peaks (*i.e.*, *m/z* and retention time match within a set tolerance) in the other sample. Peaks present in the test sample but not the reference sample are reported as new peaks, conversely peaks present in the reference sample but not in the test sample are missing peaks. If a peak is present in both samples and the difference in abundance between samples surpasses a set threshold (the fold-change threshold), it is reported as a changed peak. Unchanged peaks (below the fold-change threshold) are not reported. Prior knowledge of peak identity is not required; thus, NPD is an untargeted analysis that can potentially detect unexpected impurities or differences.

The potential for MAM to be implemented in the QC space as a replacement for a number of single-attribute assays has piqued the interest of the biopharmaceutical industry, and members of the industry are currently working to develop the platform for such use. Naturally, the adoption of new platforms comes with inherent risk which can slow the implementation of new technologies. The MAM interlaboratory study was therefore established to aid industry members at the beginning stages of MAM development and to provide a survey of the current performance of MAM across the industry (Mouchahoir et al., 2021). The study used the NISTmAb as a model therapeutic-like protein to evaluate the instrumentation and software processing used for MAM, and here we discuss the portion of the study that evaluated the NPD function of MAM. This was the first such industry-wide study to evaluate the performance of MAM.

Study Design and Protocols. Twenty-eight participating laboratories were recruited from members of the MAM Consortium (www.mamconsortium.org) and included representation from the industry, government, and software and instrument vendors. Each participating laboratory received a "kit" with the necessary materials for the study. The kit included four tryptic digests of the NISTmAb: one digest acted as the reference (Reference Sample) against which the other digests were compared for NPD, a second digest contained an additional set of 15 synthetic peptides spiked in to mimic impurities (Spike Sample), and a third digest was prepared from a NISTmAb sample that had first undergone high pH stress (pH Stress Sample) to test the untargeted analysis of changes in PTM levels. The fourth digest (Unknown) was the same sample as the Reference, however the identity was not revealed to the participants and served as a negative control. The kit also included a vial containing 15 synthetic peptides (Calibration Sample) to gauge instrument performance across laboratories and a vial of 0.1% formic acid in water for use as a blank injection to prepare the column.

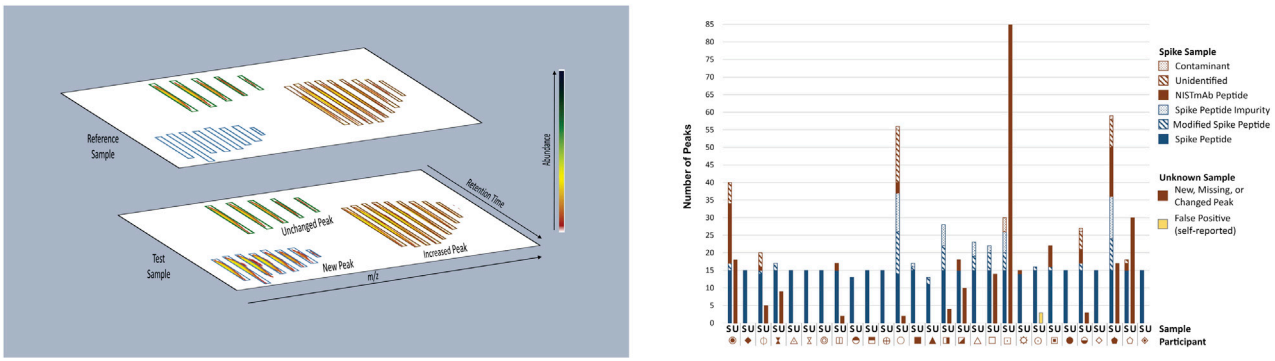

FIGURE 2 | Overview of MAM New Peak Detection Data Analysis. **(A)** A representation of new peak detection data is shown for a single charge state/isotope cluster for a new peak, changed peak, and unchanged peak **(B)** Peaks Reported as New, Missing, or Changed in Spike and Unknown Samples. New, missing, and changed peaks detected in the Spike (S) and Unknown (U) Samples were reported by each participant. For the Spike Sample, peaks that conformed to expectation are represented in blue: Spike Peptides, Modified Spike Peptides (*e.g.,* Spike Peptide with a PTM) and Spike Peptide Impurities (*e.g.,* Spike Peptide with additional residue, truncation, etc.); peaks that did not conform to expectation are represented in red: NISTmAb Peptides, Unidentified Peaks, Contaminants. Peaks detected in the Unknown Sample did not conform to expectation and are represented in red without further categorization. One participant self-reported peaks in the Unknown Sample as false positives (represented in yellow) and thus were counted as a conforming result. Each participant is represented by a unique symbol. This figure was adapted from Mouchahoir et al., 2021 (https://pubs.acs.org/doi/10.1021/jasms.0c00415), with permission from ACS Publications; further permissions related to this material should be directed to ACS.

Each participant followed the same LC-MS method and used the same column for sample analysis, but instruments and software packages for data analysis varied. The Calibration Sample was injected a total of three times, interspersed at the beginning, middle, and end of the queue. Participants were asked to report the retention time, observed mass, and summed extracted ion chromatogram (XIC) area for each Calibration Peptide. Each of the NISTmAb digests was injected twice. The first injection was acquired in MS-only mode to be used for the NPD analysis itself, and the second was acquired in MS-MS mode to be used for confident identification of peptides. Participants were asked to use their standard MAM analysis platforms on these samples and report any peaks detected as new, missing, or changed in abundance in the Spike, pH Stress, and Unknown Samples when compared to the Reference Sample.

Results

Instrument Performance: Calibration Sample. ASTM Standard E691-18 (Standard Practice for Conducting an Interlaboratory Study to Determine the Precision of a Test Method) (ASTM, 2018) was used to evaluate the interlaboratory precision metrics of the retention times, mass accuracy, and fold-change values for each Calibration Peptide. Retention time repeatability standard deviations within each participating lab fell below 0.25 min, while reproducibility standard deviations between laboratories were measured between 1.4 min and 2.0 min. The larger variation in retention times between laboratories was expected due to the use of different LC systems. The high-resolution mass spectrometers used for the study achieved mass accuracy values of less than ±5 ppm, which is within the expected performance range for these instruments and is well within typical mass accuracy tolerance windows for database searching and NPD peak picking. Quantitative performance was measured by calculating the fold-change in abundance for each of the 15 peptides (*i.e.*, ratio of a given peptide XIC from one injection to the XIC of the same peptide in another injection). Since the same volume of Calibration Sample was loaded onto the LC-MS system for each injection, the theoretical fold-change was 1 for each peptide. All but one of the absolute fold-change values for the Calibration Peptides averaged less than 1.26 with reproducibility standard deviations less than 0.35. Together, these performance metrics suggested that the instruments being used across the industry for MAM are performing within expected specifications.

New Peak Detection: Spike and Unknown Samples. Participants performed NPD on the Spike and Unknown Digests and reported any peaks that were new, missing, or changed in abundance (≥five-fold) when compared to the Reference Sample (**Figure 2B**). For the Spike Digests, fifteen of the participants conformed to expectation by detecting all 15 Spike Peptides as new peaks, with no additional new, missing or changed peaks reported (with the exception of synthetic impurities known to be inherent to the Spike Peptide mixture). Thirteen participants reported false positives (new, missing, or changed peaks that included NISTmAb peptides, unidentified peaks, and system contaminants), false negatives (fewer than fifteen Spike Peptides detected as new peaks), or both. Conformity to expectation for the Unknown Sample was met by sixteen participants who did not report any differences between the Unknown and References Samples. Peaks reported by non-conforming participants included NISTmAb peptides, unidentified peaks, keratin peptides (contaminants from the digestion process), a trypsin peptide, and one participant reporting carry-over of Spike Peptides.

The authors assigned a likely source for 92% of the non-conforming peaks for which a corresponding raw data file was

available. This data evaluation showed the false positive peaks to be the result of 1) inadequacy of the column conditioning steps prescribed in the study protocol (causing large retention time shifts for a few NISTmAb peptides between the Reference and other samples and thereby interfering with peak alignment during software processing); 2) sample degradation (clipped peptides unique to four participants seemed to have been generated some time between shipment of the kit to the participants and injection onto the column); 3) system contamination (*e.g.,* plasticizer, trifluoroacetic acid adducts); 4) instrument-induced artifacts (*e.g.*, in-source fragmentation, metal adduction); 5) peak abundance (low signal not well-distinguished from background); and 6) group-wise comparison of all four sample (rather than individual Reference to Sample comparisons; limited to one participant). False negative results (*i.e.,* Spike Peptides not reported as new peaks) were attributed to peak signal falling below the NPD threshold set during the peak picking process (*i.e.*, distinguishing signal arising from true peptide peaks from noise), a value that was set according to each participant's unique platform parameters.

New Peak Detection: pH Stress Samples. The degraded pH Stress Sample was expected to contain multiple new, missing, or changed peaks but the complexity of this sample did not lend itself to providing the authors with a definitive profile of expected differences to be found when compared to the Reference Sample. To survey the pH Stress Sample results the authors evaluated the consensus between peaks reported as new, missing, or changed by calculating the coincidence frequency (ω^c) (number of participants reporting a given peak) of each unique peak reported across laboratories and plotting the resulting values against the calculated peak coincidence population values [$M(\omega^c)$] (number of peaks with the given coincidence frequency) (Hudgens et al., 2019a). The six highest ω^c values ranged from 26 to 18 participants, each with a corresponding $M(\omega^c)$ value of 1 peak (**Supplementary Figure S1**). There were no peaks achieving the maximum possible ω^c of 28 participants (*i.e.*, no peak was reported by all participants). Processed NPD data files from one participant were available to aid our understanding of the low consensus values attained for the pH Stress Sample. These data showed incidences of new and changed peaks falling just below the participant's NPD and fold-change thresholds, and co-elution with overlapping mass-to-charge ratios as the likely culprits.

Learnings/Future Perspective

Evaluating the results of this interlaboratory study allowed the authors to gauge the performance of MAM across the industry and provide insights for improving the platform, especially for those in the beginning stages of developing their platforms.

The Calibration Sample provided a broad overview of instrument performance, with the results indicating that the instruments being used for MAM are performing within their expected ranges. Their performance, however, was not predictive of NPD performance in the other samples. The results of participants whose Spike and Unknown Sample analyses did not conform to expectation highlighted the importance of proper sample handling and instrument preparation (*i.e.,* column conditioning or washing) to ensure the integrity of the results. While in these cases the participants rightfully detected the differences between the samples as new peaks, these "nuisance positives" can cost valuable time and resources in a real-world situation as they would necessitate a follow-up investigation. The false positives generated by low abundant ions and the false negatives in the Spike Sample hint that NPD thresholds need to be carefully considered to strengthen the accuracy of the results. Investigation of the low consensus results for the pH Stress Sample also appear to have revealed FCD and NPD threshold settings as the primary source of differing results between participants. Although many participants used similar settings for their MAM evaluation they did not all achieve the same results, indicating that there is no universal threshold that may be applied across all instrument models, software platforms, or even samples.

Perhaps the key takeaway message from this study is that NPD can perform well in identifying new, changed, and missing peaks in the hands of many laboratories. MAM-specific system suitability protocols and criteria that include system performance, sample handling, and NPD/FCD thresholds may improve the success metrics. For example, a product-specific standard spiked with peptides representative of the product's known process impurities and/or degradants could be run in parallel with the reference and product test samples. Appropriate system suitability sample design would include an empirical determination of appropriate process/product-specific impurity spike peptide quantities and associated NPD and FCD thresholds, considered in conjunction with desired process- and product-specific performance criteria. For example, the thresholds may be set by first finding the threshold value that is low enough to detect all spiked peptides, then continuing to lower that value as far as possible without generating any false positives. That NPD threshold could then be challenged by comparing process/product-specific reference and "unknown" samples and confirming that no new peaks are detected. A passing system suitability result for the optimized sample would require all spiked peptides to be detected as new or changed peaks with no additional peaks reported.

Overall, the MAM NPD interlaboratory study was a valuable way to understand the status of MAM throughout the industry, to identify potential pitfalls and provide guidance to users for improving their MAM methods. By taking the items discussed here into consideration the authors of the study believe that MAM NPD will be found ready for widespread implementation across the industry.

GLYCOSYLATION INTERLABORATORY STUDY

Purpose and Method Description

Glycosylation is the enzymatically driven covalent addition of monosaccharide residues to specific amino acids. These carbohydrates, known as glycans, play a crucial role in the safety and efficacy of therapeutic glycoproteins, including immunogenicity (Yehuda and Padler-Karavani, 2020), protein

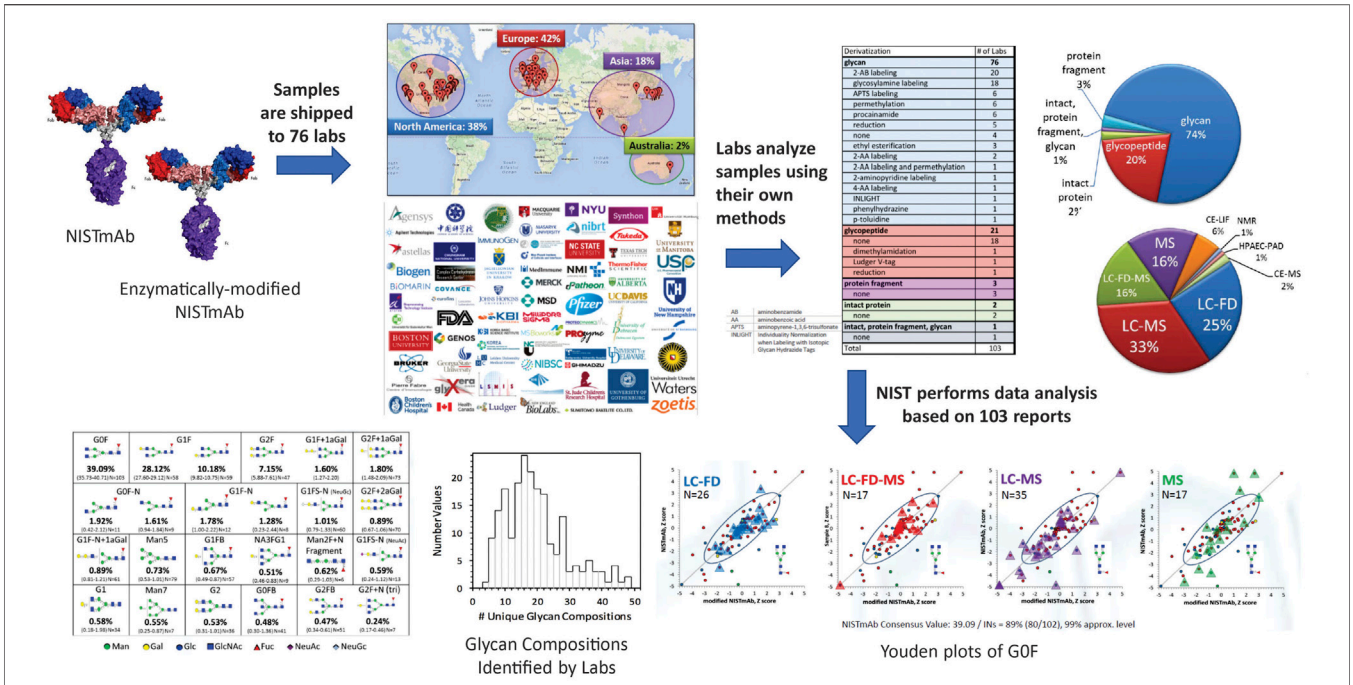

FIGURE 3 | Schematic description of the glycosylation interlaboratory study. Participating laboratories used the glycoanalytical and detection method(s) of their choice to determine relative abundance of glycans.

folding (Shental-Bechor and Levy, 2008), and thermal and protease stability (Zheng et al., 2014). Even with identical amino acid sequences, glycan alterations could arise during the manufacturing process of biologic drugs. Therefore, glycan characterization is critical.

Identification and quantitation of glycans is challenging due to their inherent heterogeneity in branching, linkage, and number of monosaccharide residues. To address this hurdle, laboratories employ a wide variety of derivatization, separation, identification, and quantification methods for glycosylation analysis.

Study Design and Protocols. The NIST glycosylation interlaboratory study (DeLeoz et al., 2017; De Leoz et al., 2020) was a broad-based interlaboratory study to determine the measurement variability of current glycosylation analysis methods. Participants included laboratories in biopharmaceutical companies, universities, research centers, government entities, and research hospitals, each of which chose their own measurement techniques. Laboratories analyzed enzymatically released N-glycans, digested glycopeptides, cleaved protein fragments or intact proteins to obtain glycan distributions (**Figure 3**).

NISTmAb has one site of N-glycosylation at the Fc region of the monoclonal antibody. Laboratories compared the glycosylation of two NISTmAb Primary Sample 8,670 samples: 1) NISTmAb and 2) 70% NISTmAb +30% NISTmAb without terminal β-1,4 gal glycans. Study participants were provided a spreadsheet to report the percent relative abundance of the glycans observed along with details associated with the method utilized for glycoanalysis. Data were analyzed without any normalization using several robust statistical analysis methods to measure variability and characterize glycan distributions. Having two similar samples enabled the formal separation of random from systematic variation using the two-sample Youden method (Youden, 1972).

Results

Overview of Methods. Results were based on 103 reports from 76 laboratories in Europe, North America, Asia, and Australia. Laboratories employed a wide variety of techniques to characterize glycosylation: released glycans, glycopeptides, protein fragment or intact protein with or without derivatization. Detection methods included mass spectrometry, liquid chromatography, fluorescence detection, capillary electrophoresis, anion exchange chromatography, pulsed amperometric detection, nuclear magnetic resonance spectrometry, or a combination of these techniques.

Analysis of enzymatically released glycans is the most common technique. Industry laboratories most commonly used fluorescent labelling for released glycans but university laboratories preferred MS-based glycopeptide analysis or non-fluorescently labeled glycan analysis. On average, biopharmaceutical laboratories reported a lower number of glycan compositions than university laboratories. Differences in methods and number of glycans identified could be attributed to the laboratory's objectives. For example, industry laboratories use validated chromatographic methods for a targeted set of glycans for QC and regulatory approval and limited their analyses to major glycans in mAbs. Alternatively, some groups in academia maximized the number of glycans they could identify for untargeted discovery.

Broadly, most laboratories used chromatography for separation followed by identification either by accurate mass or chromatographic retention times. Some laboratories combined both for identification. The number of glycan compositions reported by a single lab ranged from 4 to 48. Laboratories that employed MS only generally reported more glycan compositions. Laboratories that used MS with exoglycosidases, retention time (RT), fluorescence detection (FD) and/or MS/MS reported isomers. However, the range in the number of different reported compositions within each category was large.

Glycan Identification and Quantification. A total of 116 glycan compositions were reported by the laboratories, of which 57 compositions could be assigned community consensus abundance values. **Supplementary Figures S2A,C** summarize the percent abundances of the said 57 glycan compositions for A) NISTmAb and C) mod-NISTmAb. Only glycans reported at least six times for either NISTmAb or mod-NISTmAb are included in the plot. The glycan compositions are sorted in order of decreasing NISTmAb percent abundances.

Glycan compositions [h3n4f1], [h4n4f1] and [h5n4f1] are the most abundant compositions making up more than 85% of the total glycan abundance [see **Supplementary Figure S2** caption for nomenclature for (glycan composition)]. Measurement repeatability is generally better for more abundant glycans. Horwitz observed that the interlaboratory CV is indirectly proportional to the analyte concentration no matter the analytical method or number of laboratories (Horwitz, 1982). This trend can be observed in **Supplementary Figure S2A** where the most abundant glycans on the left have tighter boxplots.

The dashed red line in **Supplementary Figure S2B** denotes the expected 1.0 ratio of mod-NISTmAb/NISTmAb when mod-NISTmAb and NISTmAb have similar glycan % abundances. Glycan compositions with terminal β-1,4 gal as their dominant structure are shown in red font in **Supplementary Figure S2A,B,C**. In theory, glycans with terminal β-1,4 gal (red font) should fall below this red line, *i.e.*, they have lower percent abundance in mod-NISTmAb than in NISTmAb. As expected, **Supplementary Figure S2B** shows most of the reported glycans with terminal β-1,4 gal below the red line.

Each boxplot in **Supplementary Figure S2A,B,C** depicts the central 50% of the values with the horizontal middle line as the consensus median. The width of each box is proportional to the square root of the number of laboratories that identified that glycan. For example, 102 of the 103 data sets identified [h3n4f1] and [h4n4f1] and these two compositions have the widest boxes.

Variability in Methods. The boxplots of mod-NISTmAb/NISTmAb ratios in **Supplementary Figure S2B** display between-data set differences in the measurements of the two samples. Since the number and identity of the reported glycan compositions in the two samples were nearly the same within each data set, these ratios are not affected by normalization factors and could help demonstrate comparability.

Supplementary Figure S2D shows a target plot (Duewer et al., 1999) of the average variability and bias of the mod-NISTmAb/NISTmAb ratios in relation to the consensus medians. Each dot represents an aggregate score of a unique glycan composition in a result set. The *y*-axis shows the "concordance" or mean bias of the mod-NISTmAb/NISTmAb ratios calculated from $z_i = (\sum(x_{ij} - \bar{x}_j)/s_j)/n_j$, where x_{ij} is the ratio of glycan composition j in the data set i, $\bar{x}_j$ is the consensus location of glycan composition j, s_j is the consensus dispersion for glycan composition j, and n_j is the number of data sets that report values for glycan composition j in both samples. Because the ratio distributions of most compositions are heavily-tailed, $\bar{x}_j$ is estimated using the median and s_j is estimated using the scale-adjusted median absolute deviation from the median (MAD_E). the "apparent precision" of the biases or the bias estimate variability, estimated as SD, as shown in the *x*-axis:

$$s(z_i) = \sqrt{\sum_j \left(\left(x_{ij} - \bar{x}_j\right)/s_j\right)^2 \Big/ \left(n_j - 1\right)}.$$

"Comparability" distances d_i from (0,0), the ideal (z_i, s (z_i)) value, are depicted as semicircles:

$$d_i = \sqrt{z_i^2 + s^2(z_i)}.$$

The dots are colored based on their comparability distances: two comparability units are green, roughly indicating "Good" agreement with the consensus mod-NISTmAb/NISTmAb ratio estimates; between two and three units are yellow for "Moderate"; and greater than three units are red for "Questionable". No systematic trend was observed when the target plot was examined by analyte, analytical technique, laboratory type, or number of replicates.

Youden two-sample analyses of glycan compositions were performed to distinguish random errors from systematic bias (Youden, 1972; Shirono et al., 2013). For example, most laboratories that used HILIC separation are within the univariate median for [h3n4f1] and [h4n4f1] glycans. For [h3n3f1], some laboratories that used HILIC are within the consensus median and some show the same proportional bias in both NISTmAb and mod-NISTmAb, which indicates a calibration issue. For [h5n4f1], laboratories that used HILIC show significant scatter, suggesting measurement challenges for this glycan composition.

Community Consensus Medians. The community consensus medians for NISTmAb glycosylation derived from this interlaboratory study (De Leoz et al., 2020) agree well with published NISTmAb glycosylation values (Formolo et al., 2015) for glycan abundance greater than or equal to 1%. Although it is challenging to get consensus at lower percent abundance, only three of the published values are outside the study's central 50% distribution.

Learnings/Future Perspective

This NIST glycosylation interlaboratory study provided a "snap shot" of the current state of measurement methods and precision for measurement of relative glycan abundances in a monoclonal antibody. Although the methods varied widely, agreement to the community consensus medians did not depend on a specific method, analyte, or laboratory type but on the measurement precision. Thus, ensuring within-laboratory repeatability is vital

to the harmonization of glycosylation analysis methods between-laboratories. Methods used in the different laboratories could be corrected by calibration methods as appropriate standards become available. One such standard, NIST SRM 3655, was released in January of 2022 and is comprised of thirteen aqueous solutions of free reducing glycans commonly found in monoclonal antibody therapeutics. (SRM, 2021a). The certified mass fraction of each glycan was determined, thus enabling future studies to incorporate quantitative calibration and/or control materials.

The NIST glycosylation interlaboratory study provides a robust estimate of community consensus median relative values for NISTmAb glycosylation from an unmatched plethora of approaches applied to the same material. The values serve as a seminal starting point for comparing mAb glycosylation analysis methods. Further data mining studies on this large data set, such as comparing methods for identification, quantification or normalization, could help expose underlying systematic trends. Assigning degrees of confidence in identification with one, two, three, or four orthogonal values could be another area to explore.

The study warrants harmonization of glycosylation analysis methods. A thorough understanding of the sources of deviations could help harmonize methods for mAb glycosylation analyses. Less abundant glycan structures are challenging to identify especially without standards. In many cases, glycan structures are routinely assigned based on biological reasoning. The use of exoglycosidases helps narrow down potential hits but is of limited value for minor glycans or complex mixtures. The emerging field of ion mobility mass spectrometry could potentially aid in isomer separation and identification (Toraño et al., 2021).

NUCLEAR MAGNETIC RESONANCE HIGHER ORDER STRUCTURE INTERLABORATORY STUDY

Purpose and Method Description

The entirety of the structural elements from primary sequence to quaternary interactions has been termed the "higher order structure" (Almog et al., 1996) of a therapeutic protein. This critical quality attribute is essential for the safety and efficacy of these drugs, with deviation from the correct higher order structure (HOS) leading to lower product efficacy and adverse clinical outcomes (Fisher et al., 2016; Weiss et al., 2016). Currently, spectroscopic techniques (*e.g.*, Fourier transform infrared (FT-IR), differential scanning calorimetry (DSC), Raman, and circular dichroism (CD) that are predominately used to assess the HOS of a therapeutic cannot deliver high-resolution fingerprints of HOS and site-specific assignment of HOS perturbations. Development of robust, high-resolution analytical techniques that can be applied for HOS characterization throughout the lifecycle of a therapeutic protein, from development to manufacture, has therefore emerged as a major priority in the pharmaceutical industry.

To address this critical gap, two-dimensional nuclear magnetic resonance (2D NMR) methods have been developed to assess the HOS of a therapeutic at atomic level resolution (Aubin et al., 2008). While NMR methods were initially successfully implemented for small therapeutic proteins using $^{1}H,^{15}N$ heteronuclear correlations, it was unlikely that this NMR method could provide adequate sensitivity and resolution at natural isotopic abundance for mAbs (MW ~ 150,000 Da) due to technical limitations arising from the high molecular weight, where slow molecular tumbling rate drastically reduces the resolution and sensitivity of the NMR measurement. Alternatively, the methyl group affords a faster internal rotational correlation due to the free rotation around the sp^3 bond axis, so that NMR signals from methyl groups can be observed effectively even for large proteins. Accordingly, $^{1}H,^{13}C$ NMR methyl fingerprinting methods were successfully implemented and determined to be sensitive reporters of overall protein fold, since methyl bearing amino acids are distributed throughout the protein molecule (Arbogast et al., 2015). Further studies indicated that even slight deviations in the glycoform distribution can be detected by this 2D NMR method (Arbogast et al., 2017).

Despite the successful implementation of methyl fingerprinting, wide adoption of this method for industrial HOS assessment required additional harmonization and demonstration of interlaboratory precision. Indeed, the 2D $^{1}H,^{13}C$ heteronuclear correlation experiment can be considered an NMR technique with many possible approaches for experimental implementation, including pulse sequence choice, acquisition parameters, and acquisition strategy (*e.g.*, uniform sampling versus non-uniform sampling). To fully harmonize the experimental methods and the analysis components of the 2D-NMR method, a global interlaboratory study was conducted with equal representation from academia, government, and industry, involving 26 laboratories from 9 countries, using the NIST-Fab, the Fab fragment derived from papain cleavage of the NISTmAb as the model therapeutic protein for the IgG1 molecular class (Brinson et al., 2019). In addition, two subsequent studies (Brinson et al., 2020; Sheen et al., 2020) followed, which used the interlaboratory data to further develop NMR processing and analysis tools well suited for biopharmaceutical applications.

Study Design and Protocols. The coordination, design, implementation, writing, and publishing of the NMR interlaboratory study was an extensive effort spanning nearly 4 years (**Figure 1**). The recruitment phase was launched officially at the CASSS-sponsored Higher Order Structure Meeting in April 2015 and took approximately 1 year. Equal representation was sought and achieved from industry, academia, and government laboratories. Further, 39 total magnets were represented in the study, ranging from 500 to 900 MHz, with at least two magnets represented at each field strength. In late May and early June 2016 four pre-launch conference calls were conducted to discuss the experimental protocols and receive feedback from partnering laboratories.

To ensure that the 2D NMR experimental protocol could be implemented at a field as low as 500 MHz, the NIST-Fab was used due to its smaller molecular weight compared to the intact molecule. A uniformly-labeled ^{15}N, 20%-labeled ^{13}C NIST-Fab was also produced from *Pichia pastoris* to serve as the system

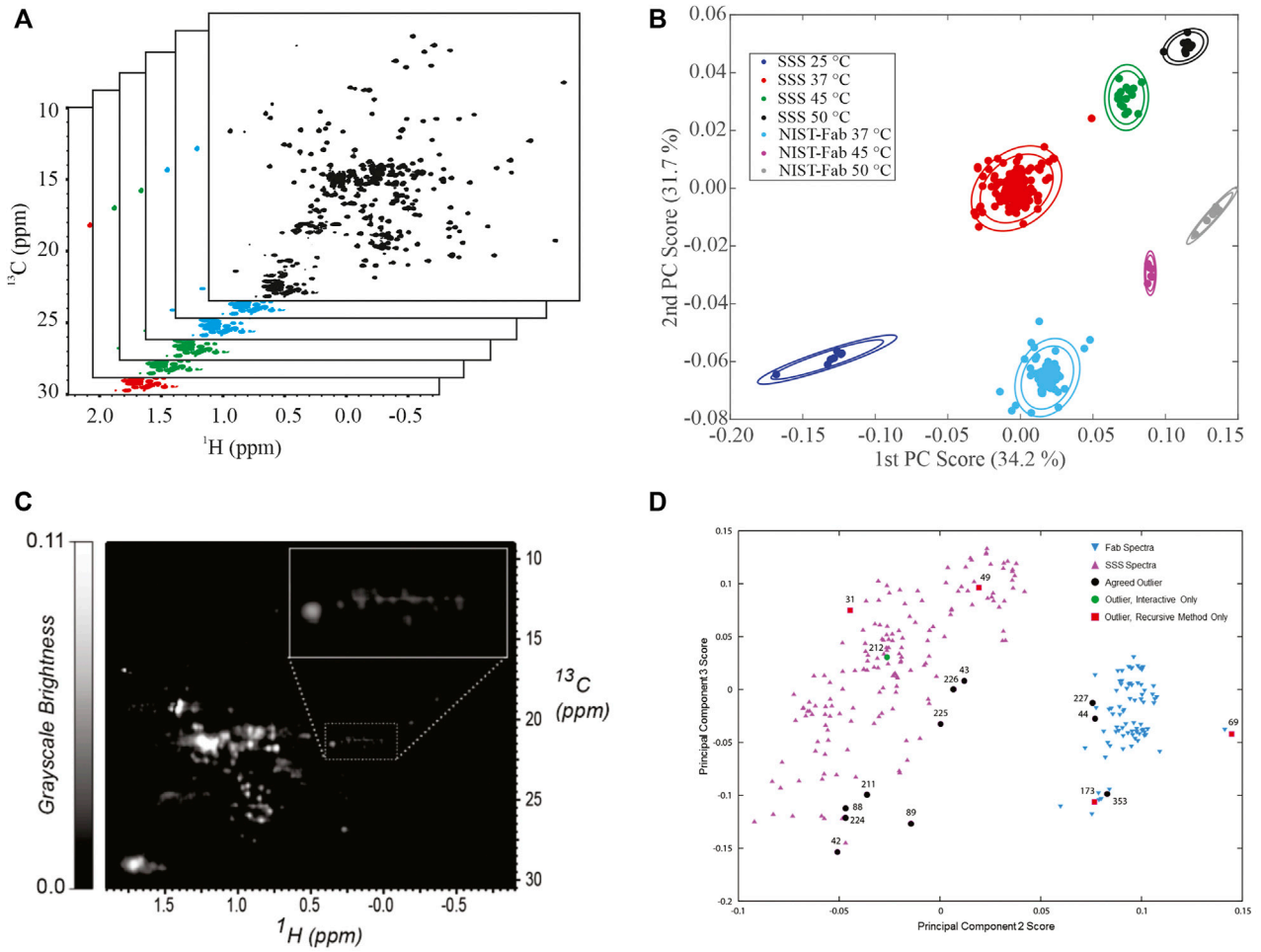

FIGURE 4 | Representative Analysis of Data from NMR interlaboratory study. **(A)** simulated data package of many 1H, 13C methyl fingerprints; **(B)** PCA score plot of the interlaboratory NMR study; **(C)** Converted grayscale image of a 1H, 13C methyl fingerprint; **(D)** PCA score plot of 252 spectra used in the automated analysis of outliers. Panel 5B was reprinted from *Brinson et al., 2019* (https://doi.org/10.1080/19420862.2018.1544454), with permission from Taylor and Francis Group, LLC. Please note the article was published under a creative commons open access license. Permission is granted subject to the terms of the License under which the work was published. Panels 5C and 5D were Reprinted from Sheen et al., 2020 (https://doi.org/10.1016/j.chemolab.2020.103973) with permission from Elsevier.

suitability sample (SSS). Each partnering laboratory was asked to perform one 2D $^{1}H,^{15}N$ gradient selected heteronuclear single quantum coherence spectroscopy (gHSQC) and six 2D $^{1}H,^{13}C$ gHSQC experiments using different acquisition strategies, including uniform sample (US) and non-uniform sampling (Magnusson and Ellison, 2008) and slightly different acquisition parameters. All partnering laboratories were also given the option to use different temperatures, pulse sequences such as the selective optimized flip angle short transient (SOFAST) heteronuclear multiple quantum coherence spectroscopy (HMQC), or their own laboratory experimental protocols. For data submission, all data packages were sent directly to a third party, National Association of Proficiency Testing (NAPT), who removed institutional identifiers from the submissions. This data anonymization was implemented to avoid bias for or against any partner.

Public Web Data Repository. The complete data package from the interlaboratory NMR study, included all blinded data, non-uniform sampling schedules, and processing scripts, was archived and is available at the following URL: https://www.ibbr.umd.edu/groups/nistmab-nmr

Results

Interlab Precision Analysis. The precision of peak positions for both $^{1}H,^{15}N$ and $^{1}H,^{13}C$ gHSQC spectra was calculated using the combined chemical shift deviation (CCSD) and determined to be within the digital resolution of the measurement, 3.3 ± 1.8 ppb and 2.3 ± 0.8 ppb respectively, averaged across all magnetic fields. The $^{1}H,^{15}N$ CCSD value was consistent with the precision determined from an earlier interlaboratory NMR study on a small therapeutic protein (Ghasriani et al., 2016). Precision only degraded slightly from experiments performed with partner-generated NUS schedules and SOFAST-HMQC experiments; however, these experiments still had a very high precision of 5.3 ± 2.7 ppb. Indeed, these metrics point to the exquisite reproducibility and robustness of the NMR measurement, even

for experiments for which deviations occurred from the established experimental protocol.

Principal Component Analysis. Application of principal component analysis (PCA) to $^{1}H,^{13}C$ weighted peak tables afforded clustering of spectra into 7 groups by sample type, SSS versus NIST-Fab, and temperature (**Figures 4A,B**). All outliers could be explained by deviations from experimental protocol, such as temperature miscalibration, a custom NUS schedule, or another experimental set-up problem. As such, the PCA on peak position confirms the reproducibility of the measurement and shows the applicability of the method even at 500 MHz. Validation of a cluster assignment for a spectrum could be evaluated using the Dunn index or silhouette values (Brinson et al., 2020).

In addition to analyses of peak position, a 2D spectrum is a matrix of frequency-indexed points with intensity. In a follow-up manuscript to the original *mAbs* publication, the spectral matrixes of the methyl fingerprint region were used as input for PCA (Brinson et al., 2020). While seven clusters could still be identified, overlap of clusters was clearly observed. Further, a field dependence within PCA space was clearly identified, in part due to the intrinsic resolution differences between the multiple field strengths employed in the interlaboratory study. It is noted that the interlaboratory study was designed for harmonization of experimental protocols and the establishment of spectral similarity rather than addressing the issue of the field dependence in PCA analysis.

Image Analysis and Automated Outlier Detection. In addition to a matrix of frequency-indexed points, a 2D NMR spectrum was converted into a grayscale image followed by spectral classification with the Kullback-Leibler metric for spectral dissimilarity (**Figure 4C**) (Sheen et al., 2020). In this study using 252 $^{1}H,^{13}C$ gHSQC measurements from the interlaboratory study, the majority of spectra were properly classified using a recursive version of the automated method, which performed in a manner similar to human visual analysis (**Figure 4D**). In addition, this method detected three outliers that were initially missed by human eye but were determined to be true outliers after detailed analysis of each individual spectrum.

Learnings/Future Perspective

The global NMR interlaboratory study benchmarked and harmonized the 2D NMR method to support its adoption for biopharmaceutical applications. While this specific case study focused on the NISTmAb, this method will also be amenable for small proteins, other mAbs, and other protein-based modalities. Indeed, the method was determined to be very robust: a highly similar answer is obtained despite slight deviations in acquisition protocol. These experimental variations include acquisition strategy (US vs NUS), pulse sequence choice, user, lab, or magnetic field. Further, this study has allowed for development of automated tools, including processing and spectral analysis. As an illustration of the acceptance of this method and utility of the benchmark data collected in the interlaboratory study, one NMR vendor has integrated the entire interlaboratory study package into its software for the basis of implementing chemometric analyses for biopharmaceutical applications. (Bruker, 2021).

When the interlaboratory study was designed, the NISTmAb was cleaved into its constituent domains, and the HOS of NIST-Fab evaluated to ensure the molecular size would be accessible at 500 MHz. Since this time, it has been established that the 2D NMR method is applicable to intact mAbs at fields as low as 600 MHz (Arbogast et al., 2017). Such a development is important, and it allows for minimal sample manipulation for many mAb-based therapeutics. Couple this with the Selective Excipient Reduction/Removal (SIERRA) filter to remove interferences from excipient signals (Arbogast et al., 2018), and the 2D NMR method allows for the assessment of this therapeutic class under many pharmaceutically relevant conditions.

Design of the NMR interlaboratory study primarily focused on experimental harmonization and creation of an NMR database for development of chemometric tools. While the initial analysis focused on peak positions, this approach requires visual analysis by an expert to define the peak lists, possibly resulting in biased evaluation. By contrast, analysis methods that use the total spectral matrix or images of the spectra can be performed automatically, although with potentially less specificity; PCA performed directly on the total spectral matrixes only showed loose separation into the expected clusters due to resolution difference from the multiple field strengths (Brinson et al., 2020). In the "real world" setting of the pharmaceutical laboratory, highly standardized HOS assessments will be performed on a single qualified magnet with validated protocols, which improves the performance of direct matrix analysis. Indeed, in two additional studies on intact NISTmAb, for which the field strength was controlled, PCA on the total spectral matrix of the methyl region detected very subtle changes resulting from alterations to the glycoform distribution as well as the concentration of formulation excipients (Arbogast et al., 2020; Brinson et al., 2020). Such an application overcomes the limitations of using the total spectral matrix of a chosen fingerprint region. The processing and analysis workflow could then be automated, making this information rich method accessible for the non-expert user.

The interlaboratory NMR study confirmed the repeatability and reproducibility of the measurement, and clearly established the technique as an effective tool to characterize HOS at all stages of therapeutic protein development and manufacturing. The data generated by the study has further helped to develop new analysis methods and to establish best practices. While this study provides a basis for defining spectral similarity, it remains an open question as to what degree of spectral perturbation is needed to affect a clinically meaningful change, and the degree of spectral response will likely be product specific.

HYDROGEN-DEUTERIUM EXCHANGE MASS SPECTROMETRY INTERLABORATORY STUDY

Purpose and Method Description

Hydrogen-deuterium exchange mass spectrometry (HDX-MS) is an established, powerful analytical tool for investigating protein-ligand interactions, protein folding, and protein dynamics (Engen et al., 2021). The great success of HDX-MS in these research areas has encouraged its development as a tool for QC of biopharmaceutical products.

Recent years have witnessed notable progress in the development of statistical methods for HDX-MS that will help realize QC applications; (Hourdel et al., 2016; Saltzberg et al., 2017; Weis et al., 2019; Hageman et al., 2021; Anderson et al., 2022); however, the effectiveness of statistical methods hinges on the quality of the HDX-MS measurements. For peptide level measurements HDX-MS measurement quality is characterized by protein sequence coverage and resolution, measurement variance, and absence of measurement bias.

The NIST interlaboratory HDX-MS project determined the reproducibility of continuous-labeling, bottom-up HDX-MS measurements (Gallagher and Hudgens, 2016; Hudgens et al., 2019a). Reproducibility is the precision of the analytical protocol after considering its application across different laboratories that have measured the same sample. Precision is just the closeness of agreement among measured values obtained by replicate measurements on the same or similar objects under specified conditions (JCGM, 2012). Precision is characterized by the components of intra-laboratory repeatability, intra-laboratory intermediate measurement precision, and inter-laboratory reproducibility (JCGM, 2012). Determinations of reproducibility allow for variations of instruments, reagents, locations, and operators.

An understanding of reproducibility is necessary for the use of HDX-MS in commerce, such as QC of biopharmaceutical production, lot qualification, and acceptance of a determination of similarity between a biosimilar candidate and its innovator therapeutic protein. Quality control of a biopharmaceutical requires that measurement criteria of its critical quality attributes (CQA) remain stable over the 20 + year lifetime of a biopharmaceutical product. During this period QC laboratory location, personnel, and instrumentation will undoubtably change.

To gain insight into the degree of variation that a biopharmaceutical QC laboratory will encounter, NIST initiated the interlaboratory HDX-MS project which recruited 15 laboratories to contribute HDX-MS measurements on a standardized sample of NIST-Fab. Information gained from a reproducibility determination can guide the selection of operation protocols and apparatus during establishment of an HDX-MS quality control laboratory.

Study Design and Protocols. During the NIST interlaboratory HDX-MS study, each laboratory received a standardized kit that contained buffered solution of Fab fragment of NISTmAb reference material (PDB: 5K8A), (Marino et al., 2015; Karageorgos et al., 2017; Gallagher et al., 2018), and vials of buffers and reagents used during the sample labeling, sample denaturing, and quenching steps (**Figure 5**). The kit harmonized solution pH, salt concentration and disulfide bond reducing power.

During the HDX-MS interlaboratory project the laboratories and investigators were permitted use of any instrumentation and software. The laboratories were not directed to report specific peptide sequences nor were they told the deuterium uptake rates of previously observed peptides. As required by the instrumentation incumbent in each laboratory, operators adjusted protein and deuterium concentrations, and each operator selected one of four D2O bath temperatures;

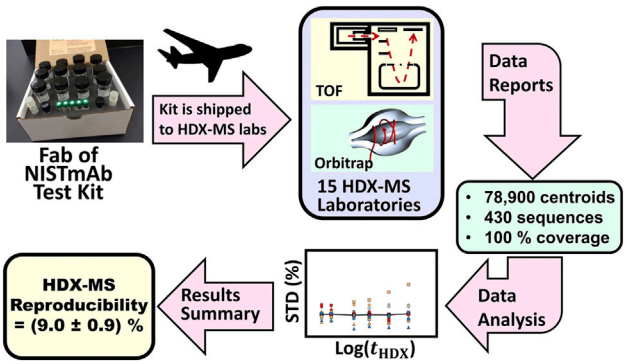

FIGURE 5 | Schematic description of the HDX-MS interlaboratory study. Fab of NISTmAb test kits containing standardized solutions were overnight shipped to participating laboratories. Laboratories measured peptic peptide centroids and reported these results to NIST. NIST evaluated the accumulated data to determine interlaboratory precision.

T_{HDX} (*Lab#*) = 25°C, 24°C, 21°C, and 3.6°C; resulting in a diverse powerset spanning a range of operating conditions.

Public Web Data Repository. A complete package of anonymized data from the interlaboratory HDX-MS study, is publicly available. (Hudgens et al., 2019b).

Results

Protein sequence coverage. Each laboratory conducted proteomics studies on the NIST-Fab sample and reported centroid measurements of peptides manifesting strong intensity and an absence of interference from co-eluting peaks. The laboratory cohort used pepsin protease to digest Fab of NISTmAb into 609 peptide ions originating from 430 sequences of the light and heavy chains. On average, laboratories reported 103 peptide sequences; however, datasets ranged between 41 and 175 peptide sequences, giving ≈60–99% sequence coverage of the Fab protein. Despite this dispersion in the number of peptide sequences reported by laboratories, an analysis determined that the six instrument-software configurations share nearly equal capacity to detect and identify peptides from NIST-Fab.

The commonality of like sequences across all datasets was characterized by coincidence frequency ω^c, the number of laboratories reporting a specific peptide sequence, and $M(\omega^c)$, the sequence coincidence population, which is the number of peptide sequences of each coincidence frequency, ω^c. For example, $M(1) = 245$ is the population of sequences found only once among all laboratory datasets. Across the laboratory cohort, $M(\omega^c)$ falls rapidly with increasing coincidence frequency, such that only two peptide sequences are reported by all laboratories, *i.e.*, $M(15) = 2$ (Figure S3). In fact, nearly 50% of all reported sequences are unique, *i.e.*, $\omega^c = 1$.

Precision. Each laboratory submitted spreadsheets listing centroids, $\langle m\ (t_{HDX})\rangle$, for each peptide at t_{HDX} = 0, 30, 60, 300, 900, 3,600 s, 14,400 s. The spreadsheet also listed reference centroids for each peptide, $\langle m\ (t_{HDX} = \infty_{pseudo})\rangle$, from a perdeuterated control sample. The 15 data sets contain

≈78,900 centroid measurements of the heavy and light chains of the Fab fragment, which differences, $\langle m\ (t_{HDX})\rangle - \langle m\ (t_{HDX} = 0)\rangle$, yield $D\ (t_{HDX})$'s. The record for each peptide comprised three "runs", each conducted on a different day. Each "run" comprised three replicant centroid measurements, termed "reps", conducted on the same day. Plots of variances of $D\ (t_{HDX})$ for all peptides showed that most laboratories (87%) achieved centroid mass laboratory repeatability precisions of $\langle s^{Lab}\rangle$ less than or equal to (0.15 ± 0.01) Da ($1\sigma_{\bar{x}}$), where $\sigma_{\bar{x}}$ is the standard error of the mean. All laboratories achieved $\langle s^{Lab}\rangle$ less than or equal to 0.4 Da. Plots of $D\ (t_{HDX})$ variance vs. t_{HDX} demonstrated that such plots can detect problems with instrumentation and procedures.

To account for the diverse solution environments of the different laboratory settings, analyses of reproducibility used $\%E^{peptide}_{corrected}(t_{HDX})$, which includes an adjustment for H for D back-exchange during the quench and analysis procedures and a correction for non-unitary deuterium fractions in the exchange solution, F^{D_2O} (≡ $\%D_2O/100\,\%$): (Zhang and Smith, 1993; Mayne, 2016):

$$\%E^{peptide}_{corrected}(t_{HDX}) = \frac{D^{peptide}(t_{HDX}) \cdot 100\,\%}{F^{D_2O}\left(\langle m(\infty)\rangle^{peptide} - \langle m(0)\rangle^{peptide}\right)}$$

where $m(\infty)^{peptide}$, approximated by $m(\infty_{pseudo})^{peptide}$, is the centroid mass of a peptide from a protein sample containing only deuterons at its amide sites.

For immersions of protein at T_{HDX} = (3.6–25) °C and for D_2O exchange times of t_{HDX} = (30 s–4 h) the reproducibility of back-exchange corrected, deuterium uptake measurements for the 15 laboratories is $\sigma^{15\ Labs}_{reproducibility}(t_{HDX})$ = (9.0 ± 0.9) % (1σ). A nine-laboratory cohort that immersed samples at T_{HDX} = 25 °C exhibited reproducibility of $\sigma^{25C\ cohort}_{reproducibility}(t_{HDX})$ = (6.5 ± 0.6) % for back-exchange corrected, deuterium uptake measurements.

Factors affecting HDX-MS measurement precision. Main effects analyses of *mean response* (mean deuterium uptake) of peptides as a function of solution and operational variables can suggest contributions leading to increased measurement variance (Filliben et al., 2003). For several variables *mean response* changed in accord with theory and design of the experiment. As examples, peptide exchange *mean response* increased from 18 to 48% between t_{HDX} = 30 s and $t_{HDX} = \infty_{pseudo}$, and *mean response* of peptides were distinct, as expected for sequences residing in different local structural environments. A procedure used by some laboratories of flash freezing protein samples immediately after the t_{HDX} period expires was shown to have no adverse effect on the *mean response*. *Mean response* for the variable, "*run#*" was essentially constant, indicating that laboratory platforms maintained stable, day-to-day solution and temperature environments.

Main effects analyses revealed non-ideal *mean responses* for variables, T_{HDX}, *Lab#*, and $\%D_2O$. Since amides undergo ≈3 × increases in exchange rates for each increment of 10 °C, (Jensen and Rand, 2016), $\%E^{peptide}_{corrected}(t_{HDX})$ should increase smoothly with increasing T_{HDX}. Contrarily, a jagged response pattern is observed for laboratories reporting T_{HDX} = 22 °C, 24 and 25°C, suggesting that the reported exchange bath temperatures may differ from the true temperatures. Although stable temperature can be maintained by ice baths or electronic temperature stabilizing equipment, verification that T_{HDX} reported by sensors is the true temperature requires regular calibration against a temperature standard traceable to a recognized standards organization (Nicholas and White, 2001; SMR, 2021b). The HDX-MS kit instructions did not require verifications of the true T_{HDX}. Hence, laboratories reporting the same T_{HDX} may have acquired data at several temperatures, leading to dispersions of $D\ (t_{HDX})$. Similarly, the *mean response* was expected to be invariant with $\%D_2O$; however, the sparse sample size for each dilution value correlated $\%D_2O$ tightly with *Lab#*. Regardless, the variance of *mean response* for $\%D_2O$ result suggests that volumetric dilution accuracy may vary among laboratories.

Mean response for the variable, "*rep#*" exhibited ≈3.5% reduction between the first and third "*rep*". Since each series of "*reps*" is executed within the same run, the steady reduction of response is evidence for increasing accumulation on columns of residual peptides from previous chromatographic analyses that have completely back-exchanged (Fang et al., 2011; Majumdar et al., 2012).

Learnings/Future Perspective

The HDX-MS interlaboratory comparison provided guidance that can be used to improve the acquisition of HDX-MS data. For short-term projects, such as mapping of protein-ligand interactions, the main effects analyses suggest a need for more precise control over the volumetric fractions that determine the exchange bath deuterium content and aggressive washing of the protease, trap, and analytical columns between chromatography runs. The study also showed that repeatability plots of average measurement deviation vs. t_{HDX} can detect procedural problems during measurement campaigns. For protein folding experiments knowledge of true T_{HDX} will improve derivations of thermodynamic properties.

Information gained from the NIST interlaboratory determination of reproducibility can guide the selection of operation protocols and apparatus during establishment of an HDX-MS quality control laboratory. The reproducibility, $\sigma^{25C\ cohort}_{reproducibility}(t_{HDX})$ = (6.5 ± 0.6) %, is likely sufficient for many QC programs, and the observation that contemporaneous instrument-software combinations can achieve this precision should embolden the use of HDX-MS for QC applications. Recommendations for hardware and protocol improvements given above will further reduce the uncertainty budget of HDX-MS.

The observation that sequence coincidence population $M(\omega^c)$ falls off rapidly with the number of reporting laboratories, where ω^c is the number of measurement instances during a product lifetime, indicates that the QC laboratory is unlikely to be successful if it relies only on a chromatography system to elute the same set of peptides over years. The potential for failure exists because datasets containing ≈ 250 peptide sequences are much smaller than the 8,100 peptide sequences containing 4 to 30 amino acids predicted by an *in silico* digestion calculation of NIST-Fab. Over the short-term, instrument and operator bias will favor observation of the same peptide sequences, but as HDX-MS system conditions change slightly, the somewhat stochastic behavior of pepsin will cause new peptides to appear and others to disappear. Although the total number of peptide sequences in each dataset may remain unchanged, not all sequences may be available for comparison with the reference peptide sequence set.

Prospective QC laboratories can select instrumentation and protein models that can sidestep the obstacle presented by comparing datasets containing few peptide sequences that are the same as observed for the HDX-MS dataset, derived for the biopharmaceutical reference material. First, mass spectrometry instrumentation provisioned with electron transfer dissociation (ETD) (Landgraf et al., 2012; Huang and Hudgens, 2013; Jensen et al., 2015; Hamuro, 2017) and/or ultraviolet photodissociation (UVPD) (Mistarz et al., 2018) can trim larger peptides into smaller peptides and allow subtraction of the deuterium content from post translational modifications. Thus, the QC laboratory can modify the mass spectrometer data acquisition procedures to subject eluting peaks to ETD and UVPD and produce an ensemble of sequences that match the reference material dataset. Secondly, the QC laboratory can construct a dynamics model of the therapeutic protein by observing many overlapping peptides, such that single-amide resolution D-uptake rates are known of the entire sequence. This dynamics model could accommodate comparisons involving nearly any ensemble of peptide sequences.

To facilitate HDX-MS measurements of improved accuracy, precision, and greater peptide coverage, NIST has developed a HDX-MS chromatography apparatus that addresses metrology problems found during the HDX-MS interlaboratory comparison (Hudgens, 2020). To expand the size and sequence coverage in HDX-MS datasets, this apparatus can automatically switch between two distinct protease columns to produce two distinct peptide sequence ensembles during a single run. To eliminate noise and chromatographic carryover from aggregates and agglomerates, quaternary pumps flush and backflush protease, trap and analytical columns with various cleaning solutions. While the chromatographic gradient elutes peptides from the trap and separates them on the analytical column, the protease column undergoes an additional backflush cleaning cycle. Idle columns are stored in place and are perpetually cleaned and conditioned. To minimize back-exchange and also maximize the number of sequences in datasets, protein proteolysis is conducted at $(0 \pm 0.06)^{o}C$, and the trap and analytical columns separate proteolytic peptides at $(-30 \pm 0.02)^{o}C$, permitting chromatography runs as long as 0.75 h. The expanded analysis gradient better separates chromatographic peaks, resulting in lower peak overlap and larger dataset coverage.

Temperatures within HDX-MS apparatus can become poorly regulated, due to elevated temperature in the site facility. However, the large thermal mass and liquid coolant system of this HDX-MS instrument maintains internal zone temperatures at their setpoints as the laboratory temperature varies from 20°C to 30°C. These improvements to HDX-MS instrumentation, stimulated by findings of the HDX-MS interlaboratory comparison project, will improve HDX-MS metrology, in general, and facilitate the development of QC facilities in the biopharmaceutical industry.

GLOBAL DISCUSSION/FUTURE PERSPECTIVES

Interlaboratory testing to evaluate similarity of results achieved by multiple laboratories performing the same analytical measurement is a fundamental concept in international metrology. A variety of documentary standards such as ISO 17025, ISO/TS 21748 and ASTM D7778-15 are available to assist in guiding design and implementation of an interlaboratory study to obtain consensus values, precision estimates, and establish if a given laboratory in a cohort has a systematic bias or is in control with community performance. Key comparisons are invaluable in interlaboratory studies, particularly in international metrology as part of the International Bureau of Weights and Measures (BIPM). As part of their mission to promote global comparability of measurements, the BIPM coordinates, in consultation with internationally representative committees, a variety of international key measurement comparisons to facilitate international trade and scientific discovery. Historically, these key comparisons involve measurements that are traceable to a fundamental unit of measurement (*i.e.*, kg, second). The Protein Analysis Working Group (PAWG) for example, coordinates studies on the ability to perform absolute concentration determination of biomolecules in complex matrices. (Josephs et al., 2019). More recently, this working group has begun to discuss physicochemical measurement properties as possible additions to key comparisons as a response to the increasingly vital nature of such measurements to industrial biotechnology (CCQM, 2021).

The NISTmAb interlaboratory studies reviewed herein include participation from a broad sampling of biopharmaceutical companies, federal stakeholders, instrumentation vendors, and academic experts. The intent of the studies has slightly orthogonal drivers in that metrological traceability and/or analytical proficiency is not the main driver; however, their impact on fostering international agreement, and thus industrial impact, should not be overlooked. The availability of the NISTmAb has spurred this series of rather unique interlaboratory studies. The NISTmAb and other biopharmaceutical products are inherently complex materials for which measurements are continuously evolving. Interlaboratory studies conducted on NISTmAb to date fall into a few broad categories based on their intended purpose: 1) Survey of analytical approaches, 2) Technical performance evaluation, 3) Harmonization and/or analytical proficiency to enable platform adoption. Of those studies conducted, the current interlaboratory studies described herein fit into the first and second categories.

Interlaboratory studies for surveying analytical approaches are designed to better understand the nature and variety of analytical approaches being applied by a community for a given measurand. For example, a battery of methods has been developed for measurement of glycans, and was a driver in the inception of the NISTmAb platform (Schiel et al., 2012). A few of these analytical methods were applied to NISTmAb in a 3-lab study as part of its initial characterization (Prien et al., 2015). The glycosylation interlaboratory study expanded the scope to a comprehensive, industry-wide example of a survey-based interlaboratory study. Study participants used a variety of sample preparation and analysis approaches ranging from intact antibody, fragments, glycopeptides, or released glycans. The full range of available sample preparation, data acquisition, and results interpretation strategies were reported. The global interlaboratory study informed the broader community of what methods were being employed where, such that a more informed decision may be made

to determine which methods are most suitable for a given laboratory's intended use (De Leoz et al., 2020).

The remaining studies reviewed herein have been geared toward technical evaluation of a given analytical method. In a typical method validation performed to meet ICH Q2 (R1) (Guideline, 2005), the between-site reproducibility is required to set appropriate specifications and it is typically performed harmonizing all equipment, operating procedures, samples, etc. The MAM, NMR, and HDX-MS studies sought to harmonize a significant number of steps that may include sample preparation, instrument settings, and/or data analysis, while other aspects such as analyst, equipment, and software were at the participants' discretion A goal of these experiments was to reduce the number of variables and hone in on specific aspects of the particular measurement system that may contribute to measurement uncertainty. Each study had a slightly unique design and output, as necessitated by the intricacies of that particular method, yet every study enabled reporting of community-wide performance metrics (i.e. precision, robustness, detection limits, etc.). It should be noted that these community performance metrics do not represent product specifications that can be utilized in a pass/fail mode, but rather they present preliminary milestones in analytical performance when using the NISTmAb as an external system suitability control and/or developing a method for an in-house proprietary material. More importantly, the common sources of uncertainty along with potential mitigation strategies were identified. Such information is valuable to assure proper procedural controls and identify opportunities for continuous method improvement.

Provided sufficient evolution and acceptance, each of these methods could 1 day become routine measurements performed on mAbs and other protein systems. In this case, the third and final category of interlaboratory harmonization study may be performed. Platform adoption would be enabled by broadly expanding measurements to numerous analytes, users, etc., wherein participants would follow all previously determined best practices. A higher order measurement system (i.e., primary calibrators, system suitability controls, etc.) would enable determination of values and associated uncertainty estimates representative of true interlaboratory variation. Interestingly, some measurements we are describe with these multifaceted approaches, such as structure and structure-function relationships, may not resolve to a single well-defined number and associated uncertainty. However, the antithesis of the preceding statement, is that novel data reduction strategies may in fact 1 day provide a single similarity scoring value, a feat in part made possible by availability of evolved analytical measurement best practices. (Arbogast et al., 2020; Brinson et al., 2020).

While the intended purpose of an interlaboratory study supporting protein structure measurements may differ, the need for a representative test material remains constant. Such a material must be well characterized, stable, and homogeneous with respect to the relevant material attributes must be utilized. Each measurand may not necessarily be well characterized and available on the certificate, in fact for technology development interlaboratory studies the intended measurand is likely not part of an assignable measurement system as are traditional metrological values. In this circular reality of measurement science, broadly available test materials support measurement innovation, while measurement innovation increases product and manufacturing process understanding. Through numerous publications, including the interlaboratory studies described herein, the NISTmAb RM 8671 has been shown to be a valuable test material for interlaboratory studies. Its properties along with use cases highlight some of these important characteristics. The test material to be utilized should also be available long term with an appropriate quality system to ensure stability and continuity of material properties. This is typically achieved using cold storage and a continuous testing strategy. The ideal material would be a Reference Material developed following ISO Guidelines. If batches or lots are necessary, as they may well be for future materials available in only small quantities, an uncertainty evaluation considering the potential for inter-lot variation and drift should be considered and accounted for by the sponsoring institution. By no means is this an exhaustive list of considerations for an appropriate interlaboratory material and associated study design, but the intent is to highlight major considerations before delving in to the specific measurement system to be evaluated.

CONCLUSION

The availability of the NISTmAb has enabled a series of interlaboratory studies that have a dual-intended purpose: 1) to allow open information sharing to discuss experiences among companies, government agencies, and academicians alike, 2) to assist scientists in making informed decisions when selecting an analytical method, as well as appropriate sample preparation, data acquisition, and data analysis settings. It is likely that interlaboratory studies like those employing NISTmAb can be similarly used to assess the state-of-the-art of analytical characterization of new and emerging modalities. Additional pre-competitive materials representative of a given product class, as well as targeted interlaboratory studies to evaluate their properties and measurement bias, will be critical as the landscape of both pharmaceutical modalities and analytical methods continues to evolve.

AUTHOR CONTRIBUTIONS

All authors listed have made a substantial, direct, and intellectual contribution to the work and approved it for publication.

ACKNOWLEDGMENTS

All authors acknowledge support of the NIST Biomanufacturing Program.

SUPPLEMENTARY MATERIAL

The Supplementary Material for this article can be found online at: https://www.frontiersin.org/articles/10.3389/fmolb.2022.876780/full#supplementary-material

REFERENCES

Almog, O., Gallagher, D. T., Tordova, M., Hoskins, J., Bryan, P., and Gilliland, G. L. (1996). Crystal Structure of Subtilisin BPN′ Folded without the Prodomain. *Acta Cryst. Sect A.* 52, C103. doi:10.1107/s0108767396095025

Anderson, K. W., Bergonzo, C., Scott, K., Karageorgos, I. L., Gallagher, E. S., Tayi, V. S., et al. (2022). HDX-MS and MD Simulations Provide Evidence for Stabilization of the IgG1-FcγRIa (CD64a) Immune Complex through Intermolecular Glycoprotein Bonds. *J. Mol. Biol.* 434 (2), 167391. doi:10.1016/j.jmb.2021.167391

Arbogast, L. W., Delaglio, F., Brinson, R. G., and Marino, J. P. (2020). Assessment of the Higher-Order Structure of Formulated Monoclonal Antibody Therapeutics by 2D Methyl Correlated NMR and Principal Component Analysis. *Curr. Protoc. Protein Sci.* 100 (1), e105. doi:10.1002/cpps.105

Arbogast, L. W., Brinson, R. G., and Marino, J. P. (2015). Mapping Monoclonal Antibody Structure by 2D 13C NMR at Natural Abundance. *Anal. Chem.* 87 (7), 3556–3561. doi:10.1021/ac504804m

Arbogast, L. W., Delaglio, F., Schiel, J. E., and Marino, J. P. (2017). Multivariate Analysis of Two-Dimensional 1H, 13C Methyl NMR Spectra of Monoclonal Antibody Therapeutics to Facilitate Assessment of Higher Order Structure. *Anal. Chem.* 89, 11839–11845. doi:10.1021/acs.analchem.7b03571

Arbogast, L. W., Delaglio, F., Tolman, J. R., and Marino, J. P. (2018). Selective Suppression of Excipient Signals in 2D 1H-13C Methyl Spectra of Biopharmaceutical Products. *J. Biomol. NMR* 72 (3-4), 149–161. doi:10.1007/s10858-018-0214-1

ASTM (2018). *Standard Practice for Conducting an Interlaboratory Study to Determine the Precision of a Test Method*. DesignationConshohocken, PA: ASTM International, 6911–E718.

Aubin, Y., Gingras, G., and Sauvé, S. (2008). Assessment of the Three-Dimensional Structure of Recombinant Protein Therapeutics by NMR Fingerprinting: Demonstration on Recombinant Human Granulocyte Macrophage-colony Stimulation Factor. *Anal. Chem.* 80 (7), 2623–2627. doi:10.1021/ac7026222

Brinson, R. G., Arbogast, L. W., Marino, J. P., and Delaglio, F. (2020). Best Practices in Utilization of 2D-NMR Spectral Data as the Input for Chemometric Analysis in Biopharmaceutical Applications. *J. Chem. Inf. Model.* 60 (4), 2339–2355. doi:10.1021/acs.jcim.0c00081

Brinson, R. G., Marino, J. P., Delaglio, F., Arbogast, L. W., Evans, R. M., Kearsley, A., et al. (2019). Enabling Adoption of 2D-NMR for the Higher Order Structure Assessment of Monoclonal Antibody Therapeutics. *MAbs* 11 (1), 94–105. doi:10.1080/19420862.2018.1544454

Bruker (2021). *Biologics HOS (Higher Order Structure)*. Rheinstetten, Germany: Bruker BioSpin.

CCQM (2021). *Consultative Committee for Amount of Substance: Metrology in Chemistry and Biology (CCQM) Strategy 2021-2030*. Cedex, France: International Bureau of Weights and Measures.

Coffman, J., Marques, B., Orozco, R., Aswath, M., Mohammad, H., Zimmermann, E., et al. (2020). Highland Games: A Benchmarking Exercise in Predicting Biophysical and Drug Properties of Monoclonal Antibodies from Amino Acid Sequences. *Biotechnol. Bioeng.* 117 (7), 2100–2115. doi:10.1002/bit.27349

De Leoz, M. L. A., Duewer, D. L., Fung, A., Liu, L., Yau, H. K., Potter, O., et al. (2020). NIST Interlaboratory Study on Glycosylation Analysis of Monoclonal Antibodies: Comparison of Results from Diverse Analytical Methods. *Mol. Cell Proteomics* 19 (1), 11–30. doi:10.1074/mcp.RA119.001677

DeLeoz, M. L. A., Duewer, D. L., and Stein, S. E. (2017). *NIST Interlaboratory Study on the Glycosylation of NISTmAb, a Monoclonal Antibody Reference Material June 2015 to February 2016, Report 8186*. Gaithersburg, MD: NIST Interagency/Internal Report NISTIR.

Duewer, D. L., Kline, M. C., Sharpless, K. E., Thomas, J. B., Gary, K. T., and Sowell, A. L. (1999). Micronutrients Measurement Quality Assurance Program: Helping Participants Use Interlaboratory Comparison Exercise Results to Improve Their Long-Term Measurement Performance. *Anal. Chem.* 71 (9), 1870–1878. doi:10.1021/ac981074k

Engen, J. R., Botzanowski, T., Peterle, D., Georgescauld, F., and Wales, T. E. (2021). Developments in Hydrogen/Deuterium Exchange Mass Spectrometry. *Anal. Chem.* 93 (1), 567–582. doi:10.1021/acs.analchem.0c04281

Fang, J., Rand, K. D., Beuning, P. J., and Engen, J. R. (2011). False EX1 Signatures Caused by Sample Carryover during HX MS Analyses. *Int. J. mass Spectrom.* 302 (1-3), 19–25. doi:10.1016/j.ijms.2010.06.039

Filliben, J. J. T., and Trutna, L. (2003). *Design of Experiments (DOE) Mean Plot [Online]*. Gaithersburg, MD: National Institute of Standards and Technology. Available at: https://www.itl.nist.gov/div898/handbook/(Accessed 1229, 2021).

Fisher, A. C., Lee, S. L., Harris, D. P., Buhse, L., Kozlowski, S., Yu, L., et al. (2016). Advancing Pharmaceutical Quality: An Overview of Science and Research in the U.S. FDA's Office of Pharmaceutical Quality. *Int. J. Pharm.* 515 (1-2), 390–402. doi:10.1016/j.ijpharm.2016.10.038

Formolo, T., Ly, M., Levy, M., Kilpatrick, L., Lute, S., Phinney, K., et al. (2015). "Determination of the NISTmAb Primary Structure," in *State-of-the-Art and Emerging Technologies for Therapeutic Monoclonal Antibody Characterization*. Editors J. Schiel, D. Davis, and O. Borisov (Washington, DC: American Chemical Society), 1–62. doi:10.1021/bk-2015-1201.ch001

Gallagher, D. T., Karageorgos, I., Hudgens, J. W., and Galvin, C. V. (2018). Data on crystal Organization in the Structure of the Fab Fragment from the NIST Reference Antibody, RM 8671. *Data in Brief* 16, 29–36. doi:10.1016/j.dib.2017.11.013

Gallagher, E. S., and Hudgens, J. W. (2016). "Mapping Protein-Ligand Interactions with Proteolytic Fragmentation, Hydrogen/Deuterium Exchange-Mass Spectrometry," in *Isotope Labeling of Biomolecules - Applications*. Editor Z. Kelman, 357–404. doi:10.1016/bs.mie.2015.08.010

Ghasriani, H., Hodgson, D. J., Brinson, R. G., McEwen, I., Buhse, L. F., Kozlowski, S., et al. (2016). Precision and Robustness of 2D-NMR for Structure Assessment of Filgrastim Biosimilars. *Nat. Biotechnol.* 34 (2), 139–141. doi:10.1038/nbt.3474

Guideline, I. H. T. (2005). Validation of Analytical Procedures: Text and Methodology. *Q2 (R1)* 1 (20), 05.

Hageman, T. S., Wrigley, M. S., and Weis, D. D. (2021). Statistical Equivalence Testing of Higher-Order Protein Structures with Differential Hydrogen Exchange-Mass Spectrometry (HX-MS). *Anal. Chem.* 93 (18), 6980–6988. doi:10.1021/acs.analchem.0c05279

Hamuro, Y. (2017). Regio-Selective Intramolecular Hydrogen/Deuterium Exchange in Gas-phase Electron Transfer Dissociation. *J. Am. Soc. Mass. Spectrom.* 28 (5), 971–977. doi:10.1007/s13361-017-1612-4

Horwitz, W. (1982). Evaluation of Analytical Methods Used for Regulation of Foods and Drugs. *Anal. Chem.* 54 (1), 67–76. doi:10.1021/ac00238a002

Hourdel, V., Volant, S., O'Brien, D. P., Chenal, A., Chamot-Rooke, J., Dillies, M.-A., et al. (2016). MEMHDX: an Interactive Tool to Expedite the Statistical Validation and Visualization of Large HDX-MS Datasets. *Bioinformatics* 32 (22), btw420–3419. doi:10.1093/bioinformatics/btw420

Huang, R. Y.-C., and Hudgens, J. W. (2013). Effects of Desialylation on Human α1-Acid Glycoprotein-Ligand Interactions. *Biochemistry* 52 (40), 7127–7136. doi:10.1021/bi4011094

Hudgens, J. W. (2020). Construction of a Dual Protease Column, Subzero (-30 oC) Chromatography System and Multi-Channel Precision Temperature Controller for Hydrogen-Deuterium Exchange Mass Spectrometry. *J. Res. Natl. Inst. Stan.* 125, 1. doi:10.6028/jres.125.025

Hudgens, J. W., Gallagher, E. S., Karageorgos, I., Anderson, K. W., Filliben, J. J., Huang, R. Y.-C., et al. (2019a). Interlaboratory Comparison of Hydrogen-Deuterium Exchange Mass Spectrometry Measurements of the Fab Fragment of NISTmAb. *Anal. Chem.* 91 (11), 7336–7345. doi:10.1021/acs.analchem.9b01100

Hudgens, J. W., Gallagher, E. S., Karageorgos, I., Anderson, K. W., Huang, R. Y.-C., Chen, G., et al. (2019b). Hydrogen-Deuterium Exchange Mass Spectrometry (HDX-MS) Centroid Data Measured between 3.6 °C and 25.4 °C for the Fab Fragment of NISTmAb. *J. Res. Natl. Inst. Stan.* 124, 124009. doi:10.6028/jres.124.009

JCGM (2012). *"JCGM 200: 2012 International Vocabulary of Metrology – Basic and General Concepts and Associated Terms (VIM) Joint Committee for Guides in Metrology 2012*. 2008 edn with minor corrections. Cedex, France: International Bureau of Weights and Measures.

Jensen, P. F., Larraillet, V., Kettenberger, H., Hilger, M., and Rand, K. D. (2015). Investigating the Interaction between the Neonatal Fc Receptor and Monoclonal Antibody Variants by Hydrogen/deuterium Exchange Mass

Spectrometry. *Mol. Cell Proteomics* 14 (1), 148–161. doi:10.1074/mcp.M114.042044

Jensen, P. F., and Rand, K. D. (2016). "Hydrogen Exchange," in *Hydrogen Exchange Mass Spectrometry of Proteins: Fundamentals, Methods, and Applications*. Editor D. D. Weis. 1st edition (Chichester, UK: John Wiley & Sons), 1–17. doi:10.1002/9781118703748.ch1

Josephs, R. D., Martos, G., Li, M., Wu, L., Melanson, J. E., Quaglia, M., et al. (2019). Establishment of Measurement Traceability for Peptide and Protein Quantification through Rigorous Purity Assessment-A Review. *Metrologia* 56 (4), 044006. doi:10.1088/1681-7575/ab27e5

Karageorgos, I., Gallagher, E. S., Galvin, C., Gallagher, D. T., and Hudgens, J. W. (2017). Biophysical Characterization and Structure of the Fab Fragment from the NIST Reference Antibody, RM 8671. *Biologicals* 50, 27–34. doi:10.1016/j.biologicals.2017.09.005

Landgraf, R. R., Chalmers, M. J., and Griffin, P. R. (2012). Automated Hydrogen/deuterium Exchange Electron Transfer Dissociation High Resolution Mass Spectrometry Measured at Single-Amide Resolution. *J. Am. Soc. Mass. Spectrom.* 23 (2), 301–309. doi:10.1007/s13361-011-0298-2

Magnusson, B., and Ellison, S. L. R. (2008). Treatment of Uncorrected Measurement Bias in Uncertainty Estimation for Chemical Measurements. *Anal. Bioanal. Chem.* 390 (1), 201–213. doi:10.1007/s00216-007-1693-1

Majumdar, R., Manikwar, P., Hickey, J. M., Arora, J., Middaugh, C. R., Volkin, D. B., et al. (2012). Minimizing Carry-Over in an Online Pepsin Digestion System Used for the H/D Exchange Mass Spectrometric Analysis of an IgG1 Monoclonal Antibody. *J. Am. Soc. Mass. Spectrom.* 23 (12), 2140–2148. doi:10.1007/s13361-012-0485-9

Marino, J. P., Brinson, R. G., Hudgens, J. W., Ladner, J. E., Gallagher, D. T., Gallagher, E. S., et al. (2015). "Emerging Technologies to Assess the Higher Order Structure of Monoclonal Antibodies," in *State-of-the-Art and Emerging Technologies for Therapeutic Monoclonal Antibody Characterization, Volume 3: Defining the Next Generation of Analytical and Biophysical Techniques*. Editors J. E. Schiel, D. L. Davis, and O. V. Borisov (Washington, DC: American Chemical Society), 17–43.

Mayne, L. (2016). "Hydrogen Exchange Mass Spectrometry," in *Methods in Enzymology*. Editor Z. Kelman (Academic Press), 335–356. doi:10.1016/bs.mie.2015.06.035

Millán-Martín, S., Jakes, C., Carillo, S., Buchanan, T., Guender, M., Kristensen, D. B., et al. (2020). Inter-laboratory Study of an Optimised Peptide Mapping Workflow Using Automated Trypsin Digestion for Monitoring Monoclonal Antibody Product Quality Attributes. *Anal. Bioanal. Chem.* 412, 6833–6848. doi:10.1007/s00216-020-02809-z

Mistarz, U. H., Bellina, B., Jensen, P. F., Brown, J. M., Barran, P. E., and Rand, K. D. (2018). UV Photodissociation Mass Spectrometry Accurately Localize Sites of Backbone Deuteration in Peptides. *Anal. Chem.* 90 (2), 1077–1080. doi:10.1021/acs.analchem.7b04683

Mouchahoir, T., Schiel, J. E., Rogers, R., Heckert, A., Place, B. J., Ammerman, A., et al. (2021). New Peak Detection Performance Metrics from the MAM Consortium Interlaboratory Study. *J. Am. Soc. Mass. Spectrom.* 32 (4), 913–928. doi:10.1021/jasms.0c00415

Mouchahoir, T., and Schiel, J. E. (2018). Development of an LC-MS/MS Peptide Mapping Protocol for the NISTmAb. *Anal. Bioanal. Chem.* 410 (8), 2111–2126. doi:10.1007/s00216-018-0848-6

Nicholas, J. V., and White, D. R. (2001). *Traceable Temperatures: An Introduction to Temperature Measurement and Calibration*. West Sussex, England: Wiley.

Noor, Z., Ahn, S. B., Baker, M. S., Ranganathan, S., and Mohamedali, A. (2020). Mass Spectrometry-Based Protein Identification in Proteomics-A Review. *Brief Bioinform* 22, 1620–1638. doi:10.1093/bib/bbz163

Prien, J. M., Stöckmann, H., Albrecht, S., Martin, S. M., Varatta, M., Furtado, M., et al. (2015). "Orthogonal Technologies for NISTmAb N-Glycan Structure Elucidation and Quantitation," in *State-of-the-art and Emerging Technologies for Therapeutic Monoclonal Antibody Characterization Volume 2. Biopharmaceutical Characterization: The NISTmAb Case Study* (ACS Publications), 185–235. doi:10.1021/bk-2015-1201.ch004

Rogers, R., Livingston, B., Kerr, J., Deng, S., Nightlinger, N., Scott, B., et al. (2013). "MS in QC: A Single Multi-Attribute Method for Quality Control and Release Testing of Biologics," in *10th Symposium on the Practical Applications of Mass Spectrometry in the Biotechnology Industry* (Boston (MA): MA).

Rogers, R. S., Nightlinger, N. S., Livingston, B., Campbell, P., Bailey, R., and Balland, A. (2015). Development of a Quantitative Mass Spectrometry Multi-Attribute Method for Characterization, Quality Control Testing and Disposition of Biologics. *mAbs* 7 (5), 881–890. doi:10.1080/19420862.2015.1069454

Rogstad, S., Faustino, A., Ruth, A., Keire, D., Boyne, M., and Park, J. (2017). A Retrospective Evaluation of the Use of Mass Spectrometry in FDA Biologics License Applications. *J. Am. Soc. Mass. Spectrom.* 28 (5), 786–794. doi:10.1007/s13361-016-1531-9

Rogstad, S., Yan, H., Wang, X., Powers, D., Brorson, K., Damdinsuren, B., et al. (2019). Multi-Attribute Method for Quality Control of Therapeutic Proteins. *Anal. Chem.* 91 (22), 14170–14177. doi:10.1021/acs.analchem.9b03808

Saltzberg, D. J., Broughton, H. B., Pellarin, R., Chalmers, M. J., Espada, A., Dodge, J. A., et al. (2017). A Residue-Resolved Bayesian Approach to Quantitative Interpretation of Hydrogen-Deuterium Exchange from Mass Spectrometry: Application to Characterizing Protein-Ligand Interactions. *J. Phys. Chem. B* 121 (15), 3493–3501. doi:10.1021/acs.jpcb.6b09358

Schiel, J. E., Au, J., He, H.-J., and Phinney, K. W. (2012). LC-MS/MS Biopharmaceutical Glycoanalysis: Identification of Desirable Reference Material Characteristics. *Anal. Bioanal. Chem.* 403 (8), 2279–2289. doi:10.1007/s00216-012-5749-5

Schiel, J. E., Davis, D. L., and Borisov, O. B. (2014). "State-of-the-Art and Emerging Technologies for Therapeutic Monoclonal Antibody Characterization Volume 1," in *Monoclonal Antibody Therapeutics: Structure, Function, and Regulatory Space* (American Chemical Society).

Schiel, J. E., Davis, D. L., and Borisov, O. B. (2015a). "State-of-the-Art and Emerging Technologies for Therapeutic Monoclonal Antibody Characterization Volume 2," in *Biopharmaceutical Characterization: The NISTmAb Case Study* (American Chemical Society).

Schiel, J. E., Davis, D. L., and Borisov, O. B. (2015b). "State-of-the-Art and Emerging Technologies for Therapeutic Monoclonal Antibody Characterization Volume 3," in *Defining the Next Generation of Analytical and Biophysical Techniques* (American Chemical Society).

Schiel, J. E., Turner, A., Mouchahoir, T., Yandrofski, K., Telikepalli, S., King, J., et al. (2018). The NISTmAb Reference Material 8671 Value Assignment, Homogeneity, and Stability. *Anal. Bioanal. Chem.* 410 (8), 2127–2139. doi:10.1007/s00216-017-0800-1

Schiel, J. E., and Turner, A. (2018). The NISTmAb Reference Material 8671 Lifecycle Management and Quality Plan. *Anal. Bioanal. Chem.* 410 (8), 2067–2078. doi:10.1007/s00216-017-0844-2

Sheen, D. A., Shen, V. K., Brinson, R. G., Arbogast, L. W., Marino, J. P., and Delaglio, F. (2020). Chemometric Outlier Classification of 2D-NMR Spectra to Enable Higher Order Structure Characterization of Protein Therapeutics. *Chemometrics Intell. Lab. Syst.* 199, 103973. doi:10.1016/j.chemolab.2020.103973

Shental-Bechor, D., and Levy, Y. (2008). Effect of Glycosylation on Protein Folding: a Close Look at Thermodynamic Stabilization. *Proc. Natl. Acad. Sci. U.S.A.* 105 (24), 8256–8261. doi:10.1073/pnas.0801340105

Shirono, K., Iwase, K., Okazaki, H., Yamazawa, M., Shikakume, K., Fukumoto, N., et al. (2013). A Study on the Utilization of the Youden Plot to Evaluate Proficiency Test Results. *Accred Qual. Assur.* 18 (3), 161–174. doi:10.1007/s00769-013-0978-7

Sokolowska, I., Mo, J., Rahimi Pirkolachahi, F., McVean, C., Meijer, L. A. T., Switzar, L., et al. (2020). Implementation of a High-Resolution Liquid Chromatography-Mass Spectrometry Method in Quality Control Laboratories for Release and Stability Testing of a Commercial Antibody Product. *Anal. Chem.* 92 (3), 2369–2373. doi:10.1021/acs.analchem.9b05036

SRM (2021a). *SRM 3655: Glycans in Solution*. Gaithersburg, MD: National Institute of Standards and Technology; U.S. Department of Commerce.

SMR (2021b). Supplementary Materials Related to NIST Policy On Metrological Traceability *[Online]*. Gaithersburg, MD: National Institute of Standards and Technology. Available at: https://www.nist.gov/traceability/supplementary-materials-related-nist-policy-metrological-traceability (Accessed AUG 30, 2021).

Srzentić, K., Fornelli, L., Tsybin, Y. O., Loo, J. A., Seckler, H., Agar, J. N., et al. (2020). Interlaboratory Study for Characterizing Monoclonal Antibodies by Top-Down and Middle-Down Mass Spectrometry. *J. Am. Soc. Mass. Spectrom.* 31 (9), 1783–1802. doi:10.1021/jasms.0c00036

Toraño, J. S., Aizpurua-Olaizola, O., Wei, N., Li, T., Unione, L., Jiménez-Osés, G., et al. (2021). Identification of Isomeric N-Glycans by Conformer Distribution

Fingerprinting Using Ion Mobility Mass Spectrometry. *Chemistry (Weinheim an der Bergstrasse, Germany)* 27 (6), 2149. doi:10.1002/chem.202004522

Turner, A., and Schiel, J. E. (2018). Qualification of NISTmAb Charge Heterogeneity Control Assays. *Anal. Bioanal. Chem.* 410 (8), 2079–2093. doi:10.1007/s00216-017-0816-6

Turner, A., Yandrofski, K., Telikepalli, S., King, J., Heckert, A., Filliben, J., et al. (2018). Development of Orthogonal NISTmAb Size Heterogeneity Control Methods. *Anal. Bioanal. Chem.* 410 (8), 2095–2110. doi:10.1007/s00216-017-0819-3

Weis, D. D. (2019). Comment on Houde, D.; Berkowitz, S. A.; Engen, J. R., the Utility of Hydrogen/Deuterium Exchange Mass Spectrometry in Biopharmaceutical Comparability Studies. J. Pharm. Sci. 2011, 100, 2071-2086. *J. Pharm. Sci.* 108 (2), 807–810. doi:10.1016/j.xphs.2018.10.010

Weiss, W. F., Gabrielson, J. P., Al-Azzam, W., Chen, G., Davis, D. L., Das, T. K., et al. (2016). Technical Decision Making with Higher Order Structure Data: Perspectives on Higher Order Structure Characterization from the Biopharmaceutical Industry. *J. Pharm. Sci.* 105 (12), 3465–3470. doi:10.1016/j.xphs.2016.09.003

Xu, W., Jimenez, R. B., Mowery, R., Luo, H., Cao, M., Agarwal, N., et al. (2017). A Quadrupole Dalton-based Multi-Attribute Method for Product Characterization, Process Development, and Quality Control of Therapeutic Proteins. *MAbs* 9 (7), 1186–1196. doi:10.1080/19420862.2017.1364326

Yehuda, S., and Padler-Karavani, V. (2020). Glycosylated Biotherapeutics: Immunological Effects of N-Glycolylneuraminic Acid. *Front. Immunol.* 11, 21. doi:10.3389/fimmu.2020.00021

Youden, W. J. (1972). Graphical Diagnosis of Interlaboratory Test Results. *J. Qual. Technology* 4 (1), 29–33. doi:10.1080/00224065.1972.11980509

Zhang, Y., and Guo, J. (2017). Characterization and QC of Biopharmaceuticals by MS-based 'multi-Attribute Method': Advantages and Challenges. *Bioanalysis* 9 (6), 499–502. doi:10.4155/bio-2017-0004

Zhang, Z., Chan, P. K., Richardson, J., and Shah, B. (2020). An Evaluation of Instrument Types for Mass Spectrometry-Based Multi-Attribute Analysis of Biotherapeutics. *MAbs* 12 (1), 1783062. doi:10.1080/19420862.2020.1783062

Zhang, Z., and Smith, D. L. (1993). Determination of Amide Hydrogen Exchange by Mass Spectrometry: A New Tool for Protein Structure Elucidation. *Protein Sci.* 2 (4), 522–531. doi:10.1002/pro.5560020404

Zheng, K., Yarmarkovich, M., Bantog, C., Bayer, R., and Patapoff, T. W. (2014). Influence of Glycosylation Pattern on the Molecular Properties of Monoclonal Antibodies. *MAbs*, 649–658. doi:10.4161/mabs.28588

Authors's Disclaimer: Certain commercial equipment, instruments, or materials are identified to adequately specify the experimental procedure. Such identification does not imply recommendation or endorsement by the National Institute of Standards and Technology, nor does it imply that the materials or equipment identified are necessarily the best available for the purpose.

Conflict of Interest: Author MLdL was employed by company Agilent Technologies.

The remaining authors declare that the research was conducted in the absence of any commercial or financial relationships that could be construed as a potential conflict of interest.

Publisher's Note: All claims expressed in this article are solely those of the authors and do not necessarily represent those of their affiliated organizations, or those of the publisher, the editors and the reviewers. Any product that may be evaluated in this article, or claim that may be made by its manufacturer, is not guaranteed or endorsed by the publisher.

frontiers | Frontiers in Molecular Biosciences

PERSPECTIVE
published: 16 May 2022
doi: 10.3389/fmolb.2022.890862

Measuring Protein Aggregation and Stability Using High-Throughput Biophysical Approaches

Tristan O. C. Kwan[1], Stefan A. Kolek[2], Amy E. Danson[1], Rosana I. Reis[1], Ines S. Camacho[1], Patrick D. Shaw Stewart[2] and Isabel Moraes[1]**

[1]National Physical Laboratory, Teddington, United Kingdom, [2]Douglas Instruments Ltd., Hungerford, United Kingdom

Structure-function relationships of biological macromolecules, in particular proteins, provide crucial insights for fundamental biochemistry, medical research and early drug discovery. However, production of recombinant proteins, either for structure determination, functional studies, or to be used as biopharmaceutical products, is often hampered by their instability and propensity to aggregate in solution *in vitro*. Protein samples of poor quality are often associated with reduced reproducibility as well as high research and production expenses. Several biophysical methods are available for measuring protein aggregation and stability. Yet, discovering and developing means to improve protein behaviour and structure-function integrity remains a demanding task. Here, we discuss workflows that are made possible by adapting established biophysical methods to high-throughput screening approaches. Rapid identification and optimisation of conditions that promote protein stability and reduce aggregation will support researchers and industry to maximise sample quality, stability and reproducibility, thereby reducing research and development time and costs.

Keywords: protein aggregation, DLS, DSF, CD, crystallography, cryo-EM, drug discovery, high-throughput

OPEN ACCESS

Edited by:
Qian Han,
Hainan University, China

Reviewed by:
Jim Warwicker,
The University of Manchester, United Kingdom
Lee Makowski,
Northeastern University, China

****Correspondence:***
Patrick D. Shaw Stewart
patrick@douglas.co.uk
Isabel Moraes
isabel.moraes@npl.co.uk

Specialty section:
This article was submitted to Structural Biology, a section of the journal Frontiers in Molecular Biosciences

Received: *06 March 2022*
Accepted: *25 April 2022*
Published: *16 May 2022*

Citation:
Kwan TOC, Kolek SA, Danson AE, Reis RI, Camacho IS, Shaw Stewart PD and Moraes I (2022) Measuring Protein Aggregation and Stability Using High-Throughput Biophysical Approaches. Front. Mol. Biosci. 9:890862. doi: 10.3389/fmolb.2022.890862

INTRODUCTION

Human health is continuously challenged not only by external toxic substances but also by microorganisms such as pathogenic bacteria and viruses. Thus, understanding biology at a cellular and molecular level is paramount to human existence. Proteins are sophisticated molecular machines essential in all cellular processes. However, because of their complex intrinsic three-dimensional (3D) molecular network of hydrogen bonds, Van der Waals forces, hydrophobic interactions and disulfide links, proteins have a natural tendency to denature (unfold) or aggregate (formation of non-physiological dimers and higher-order aggregates). The pathways and mechanisms by which proteins unfold and aggregate are not yet fully understood. However, external factors such as temperature, pH, ionic strength, different buffer systems, mechanical stress or even the presence of "foreign bodies" like dust, glass particles and microscopic oil droplets can lead to structural and behavioural changes of the protein in solution.

Currently, there are many critical reasons why scientists need to monitor aggregation and stability of proteins in solution. Firstly, pure and stable protein material is always required for structural studies for any of the three most popular methods—X-ray crystallography, NMR spectroscopy, and cryo-electron microscopy (cryo-EM) (Chari et al., 2015; Kozak et al., 2016; Kotov et al., 2019; Kwan et al., 2019). Protein purification strategies and protocols are particularly dependent on the target protein that frequently misbehaves when isolated in solution. Therefore, the ability to quickly search

chemical spaces that increase protein stability with minimal amounts of sample is critical to such biophysical applications. Over the last few decades, however, developments in gene editing tools, molecular biology, instrumentation, and light sources, along with many other multidisciplinary approaches, have enabled a *new age* in protein structure determination (Adli, 2018). Consequently, structural biologists have pursued more challenging targets such as integral membrane proteins and protein-protein complexes. Moreover, the structural biology community is also now strongly focused on time-resolved approaches to study protein dynamics and conformational changes over time (Kwan et al., 2020; Bonvin, 2021; Cohen, 2021). Secondly, critical to biopharmaceutical industry and biomedicine, protein unfolding and aggregation also poses many challenges in the development of biologics (therapeutic agents manufactured in living systems such as a bacteria, plant or animal cells) because of its impact on the final product quality in terms of safety, clinical efficacy, and immunogenicity (Ratanji et al., 2014; Roberts, 2014; Krause and Sahin, 2019). Presently, the most popular biologics in the market are monoclonal antibodies, cytokines, enzymes, and peptide hormones. Although these may offer many clinical advantages when compared with small molecule drugs, they are far more complex to develop and produce at a larger scale (Plant et al., 2014; Puetz and Wurm, 2019; Jovčevska and Muyldermans, 2020). By their intrinsic nature, protein-based drugs are extremely sensitive to physical and chemical environmental factors such as temperature, shear-forces, light, pH, glycosylation, and enzymatic action Rajan et al., 2021. Hence, probing protein aggregation during the development and manufacturing of protein-based drugs is essential to achieve a final product that is not only stable for long-term storage but also harbors fewer impurities that stimulate an anti-drug immune response (Ratanji et al., 2014; Svilenov et al., 2018; Ribeiro et al., 2019). Finally, production of high-quality protein is also important in many other industrial applications such as agriculture, food and beverage processing, production of cosmetics and biofuels, and in biotechnology applications such as biosensors and optogenetics (Zhang and Cohen, 2017).

Nevertheless, inherent to all these approaches is the protein sample quality in terms of purity and stability. Currently, a variety of biophysical techniques are available to study protein behaviour in solution. These range from simple approaches to complex methods that require both technical expertise and costly instruments. For example, Makowski et al. (2022) reviewed the use of a set of key bionanotechnologies for preparing functional and stable membrane proteins in diverse types of lipoparticles in combination with several biophysical assays, including affinity-capture self-interaction nanoparticle spectroscopy (AC-SINS). In a seminal study by Jain et al. (2017), 137 isotypematched IgG1 antibodies were evaluated with a dozen biophysical property assays to define the boundaries of drug-like behaviour for future studies. Screening multiple macromolecular constructs is distinct from the exploration of chemical space with a single target, and will not be considered further here.

In this perspective, we have summarised simple and readily available approaches protein aggregation and stability within a high-throughput (HTP) setting. These biophysical techniques are also capable of screening and probing the addition of specific ligands, additives or excipients to the protein of interest that can reduce its propensity to unfold or aggregate, as well as its susceptibility to proteolysis (Senisterra and Finerty, 2009).

HTP APPROACHES FOR MEASURING AND ANALYSING PROTEIN STABILITY

Automation and miniaturisation combined with multi-well microplates have enabled the development of HTP approaches where many samples (up to thousands) are tested in parallel under given conditions. Introduced by pharmaceutical companies in the early 1990s for the massive screening of potential "drug-like" compounds, HTP approaches are extensively used by scientists today in academic laboratories, research institutes and industry in a variety of applications (Macarron et al., 2011; Kwan et al., 2019; Kiriiri, et al., 2020).

Recently, researchers have started to use HTP approaches to explore chemical space by testing protein samples against premixed sets of buffers, excipients, additives, salts, osmolytes, and co-factors (often referred as stability screens). Suitable stability screens are commercially available in 96- and 384-well format, or they can be assembled in-house. To maximise the throughput towards evaluation of protein behaviour in the presence of such stability screens or ligands, HTP approaches were also applied to simple but robust biophysical methods such as dynamic light scattering (DLS), differential scanning fluorimetry (DSF) and circular dichroism (CD). Each of these biophysical methods provides different types of information and, whether used as a standalone or integrated, they have proven to be noteworthy screening tools when probing protein aggregation or to identify conditions that promote protein integrity and stability in solution (**Figure 1**).

HTP Dynamic Light Scattering

DLS is a common technique employed to assess the behaviour of proteins in solution. This simple yet powerful and non-invasive biophysical measurement correlates the random motion of particles in a fluid with their sizes. During a DLS experiment, particles in solution are illuminated by a visible and monochromatic laser light while a detector records the light scattered by the particles. The intensity of light fluctuates at a frequency that is determined by the particles' size. Because proteins and other macromolecules in solution are not always spherical in shape and are always solvated, the size calculated by a DLS instrument is referred to as the "hydrodynamic radius". The physical principles of light scattering and DLS have been extensively described in the literature (International Organization for Standardization, 1996; Lorber et al., 2012; Stetefeld et al., 2016; Kwan et al., 2019). For DLS experiments, the data are usually presented in terms of sample polydispersity. If the sample remains monodisperse and shows a peak at the expected size, the protein can be assumed to be stable in the chemical and physical conditions (temperature) used (Shiba et al., 2010). With the development of HTP approaches to DLS, the

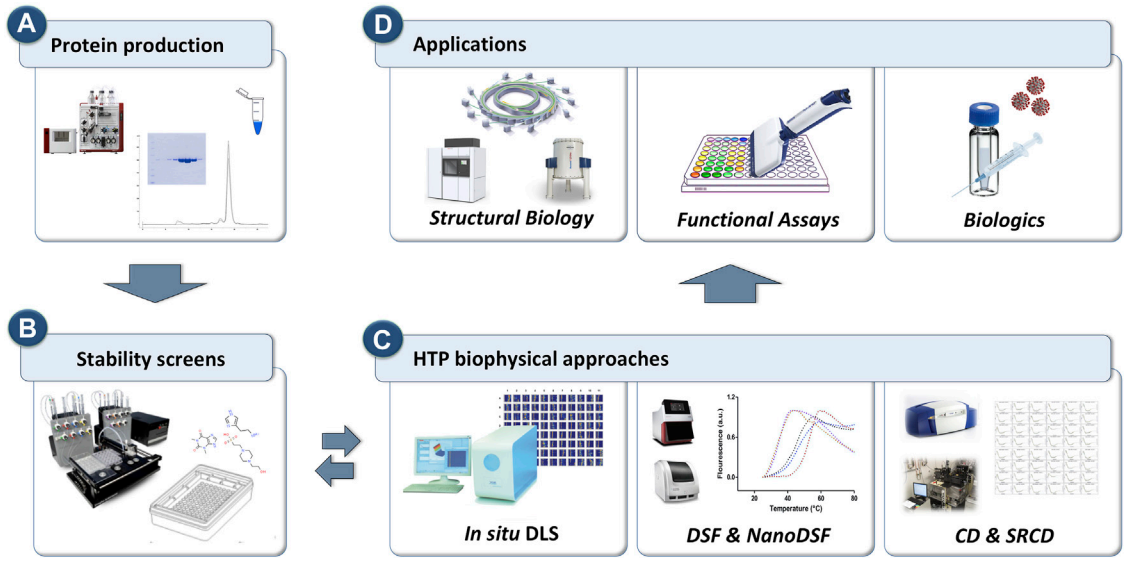

FIGURE 1 | Schematic representation of the workflow for the HTP biophysical approaches to probe protein behavior for downstream and upstream applications. **(A)** Proteins are purified using standard purification strategies. **(B)** HTP screens are prepared to explore chemical space. **(C)** *in situ* Dynamic Light Scattering (DLS), differential scanning fluorimetry (DSF) and circular dichroism (CD) that can operate in HTP mode are used as primary screening tools to probe protein stability. **(D)** Three key applications where protein monodispersity and stability is crucial.

behaviour of proteins can now be determined in the presence of ligands, substrates, additives, and buffers in parallel at microlitre volumes in plate formats (Meyer et al., 2015; Kwan et al., 2019; Dauer et al., 2021) Moreover, the DLS measurement can be run over several time points, allowing degradation or changes in aggregation to be monitored over time. For example, we found that a bacterial ABC transporter, which is a membrane protein, tended to aggregate after purification. We used a 96-component screen to monitor aggregation over 9 h. The screen contained a set of conditions that has previously increased solubility and stability of proteins. We were able to identify 12 reagents that reduced aggregation of the ABC transporter (**Supplementary Figure S1**). Note that DLS provides extra information about the degree of aggregation, including the size of aggregates and the number of peaks, whereas other methods such as DSF give only a single numerical value corresponding to the "melting point" of the protein. HTP DLS provides a practical and simple probe for stability that can be implemented easily in the protein production workflow and downstream applications in structural biology such as crystallography and/or cryoEM. Finally, for the production of biologics, HTP DLS measurements can also be used to determine sample quality and be implemented as a quality control measurement between production batches (Hulse et al., 2013; Yu et al., 2013; Bhirde et al., 2018; Dauer et al., 2021).

HTP Differential Scanning Fluorimetry

DSF, also commonly referred to as thermal-shift assay or ThermoFluor assay, is an inexpensive and highly sensitive biophysical technique that can be used to determine the thermal stability of a target protein in the presence or absence of ligands, substrates, and buffers. The DSF principle measures the protein thermal denaturation over time (typically about $1^{\circ}C\ min^{-1}$) and is based on the relationship between protein stability and its Gibbs free energy of unfolding (ΔG_u). When the amount of unfolded protein equals the amount of folded protein, the value of ΔG_u becomes zero and the system has reached what is known as the protein "melting point" temperature (T_m). Proteins with higher stability have larger ΔG_u values and therefore a higher T_m. The DSF experimental setup is very simple and typically does not require expensive equipment. The protein sample, in the presence of a highly sensitive fluorescent probe, also known as a "reporter" or extrinsic dye, is gradually heated over time (in order to trigger denaturation) from its stable baseline temperature. This eventually results in exposure of the hydrophobic regions that are usually buried within the protein's folded structure. As more of the protein's hydrophobic regions become exposed, an increasing number of dye molecules bind to the hydrophobic sites, resulting in an increase of the fluorescence signal. Once the protein reaches its maximum unfolded state, it starts to aggregate and precipitate, and consequently, the dye molecules dissociate and the fluorescence signal drops (Bai et al., 2019). In the majority of the instruments, the DSF output is displayed as a series of sigmoidal curves, also known as "melt curves", where the point of inflection gives the T_m value (**Supplementary Figure S2A**). Although there are many fluorescent dyes available on the market, the most frequently used for soluble proteins is SYPRO Orange, which is inexpensive, highly sensitive and has low interference with small molecules. Its excitation/emission wavelength (480 nm/569 nm) is usually compatible with most filters available in fluorescent plate readers and RT-PCR machines. However, because SYPRO Orange also binds to the hydrophobic regions of lipids and detergent micelles, it is

unsuitable for membrane protein studies. Instead, a reactive thiol-specific fluorochrome, N-[4-(7-diethylamino-4-methyl-3-coumarinyl)phenyl] maleimide (CPM), was introduced in 2008 (Alexadrov et al., 2008), which specifically reacts with the cysteine side chains that are usually buried in the interior of membrane proteins. Therefore, as the target membrane protein unfolds, the cysteines become exposed and the CPM fluorescence signal increases. **Supplementary Figure S2B** shows DSF results obtained for the membrane protein LacY with CPM dye in combination with five detergents that were identified from a detergent screen. Note, however, that the use of the CPM dye is associated with two limitations. One is its excitation/emission wavelength (387 nm/463 nm) that requires specific filters that usually are only available by request. The other limitation is that the protein of study must have cysteine residues in the transmembrane domains. More recently, a label-free DSF method known as nanoDSF was developed (Alexander et al., 2014; Gao et al., 2020; Real-Hohn et al., 2020). In this approach the protein's intrinsic fluorescence, based on signals mainly from the native tryptophan residues, is measured at both 330 and 350 nm in low-volume capillaries, which produces more robust data in comparison to detection at a single wavelength. NanoDSF is especially useful for studying membrane proteins (Kwan et al., 2019; Gao et al., 2020) and viral particles (Real-Hohn, et al., 2020).

Either DSF or nanoDSF approaches are also used to optimise protein buffers for long-term storage, and to determine optimal conditions for protein refolding (Biter et al., 2016; Wang et al., 2017) and protein stability in solution, greatly aiding structural studies such as crystallisation and cryo-EM (Martinez et al., 2021). Finally, the DSF approach is also extensively used in early drug discovery platforms. Many proteins can be stabilised by the binding of low molecular weight ligands, usually resulting in an increase of the T_m and therefore, DSF is regarded as a simple and inexpensive, and popular method to assess protein-ligand interactions (Huynh and Partch, 2015).

The multi-well design of thermal cycling machines and fluorescent plate readers, including instruments that make use of small volume glass capillaries, allow DSF to be used as a HTP tool requiring relatively low (microliter range) sample volumes. A downside of DSF, however, is that larger macromolecular complexes may not unfold cooperatively (thus having multiple transition states), making stabilising conditions difficult to identify (Stark and Chari, 2016). This is particularly problematic if cryo-EM is the intended downstream process, as typically this is the method of choice for the structural elucidation of large protein complexes.

HTP Circular Dichroism

CD is a biophysical technique that measures the differential absorption between left and right circularly polarised light by a chiral molecule. Polypeptide backbone information can be obtained from measurements taken in the far-UV region of 180–250 nm, due to the amide electronic transitions, and can provide estimates on the protein secondary structure content such as alpha-helices and beta-sheets (Kwan et al., 2019; Miles et al., 2021). The near-UV region of 260–300 nm is used to characterise the aromatic side chain transitions of tyrosine, tryptophan, and phenylalanine, which are often situated at binding sites, and thus measurements in this region provide valuable information regarding ligand interactions (Kwan et al., 2019).

The application of CD can be significantly broadened by the elevated photon flux of a synchrotron, which improves the signal-to-noise levels considerably, giving rise to a technique known as synchrotron radiation CD (SRCD). SRCD is capable of measuring at lower wavelengths, greatly improving the analysis of beta-sheet content and fold motifs, as well as at lower sample volumes and concentrations (Wallace et al., 2011; Hussain and Siligardi, 2016), which is a significant advantage when studying membrane proteins, for which high concentrations and volumes are difficult and costly to produce. Additionally, higher ionic solutions can be measured (up to 500 mM NaCl) due to the higher flux, which extends the buffer screening capability of conventional CD (Hussain and Siligardi, 2016). For example, beamline B23 at Diamond Light Source operates in a HTP manner (also referred to as HT-CD), with 96 or 384-well suprasil quartz plates available for data collection, in which protein samples of just 15 ul at 0.5 mg/ml can be measured allowing users to screen a wide range of buffers and/or ligands without the laborious task of changing and washing each cuvette (Hussain et al., 2016). **Supplementary Figure S3** shows results obtained with HT-CD for two membrane proteins in combination with 12 detergents. CD data analysis is also swift due to the introduction of software that enables users to remotely process results quickly and easily (Hussain et al., 2015). Recent advances have led to the development of time-resolved SRCD (TR-SRCD), which is capable of subpicosecond temporal resolutions, providing insight into biological mechanisms at a molecular level (Auvray et al., 2019).

PERSPECTIVE SUMMARY

Purified proteins are critical tools in a variety of research and industrial applications. However, these vital molecular machines are inherently unstable and prone to aggregation both *in vivo* and *in vitro*. Protein aggregates vary from small dimers to large assemblies that can be specifically formed during protein production and the storage process, including prolonged storage. Unfortunately, protein aggregates are usually irreversible and exceptionally stable. Therefore, effective strategies to quickly probe and quantify protein aggregation including protein stability *in vitro* are urgently needed. However, one of the major challenges is the absence of a single analytic approach that is able to cover the whole spectrum of protein behaviour *in vitro*, and therefore several different biophysical approaches are usually required.

Over the years, with the development of HTP technology, many traditional biophysical techniques such as DLS, DSF, and CD have evolved from standalone approaches, where samples used to be measured one at a time, to robust and sensitive methods able to analyse dozens of samples in parallel using minimal amounts of material and in standard workflows that can be applied to many targets. Each of these HTP biophysical

TABLE 1 | Summary of the strengths and limitations of the HTP biophysical methods presented in this perspective.

Method	Strengths	Limitations	Sample specification
Dynamic light scattering (DLS)	• Simple protocol and data analysis • Fast set up • High throughput • Low protein consumption • Low consumable costs • Temperature range between 10 to 40°C • Measurements can be taken over long time periods • Direct measurement of aggregation • Direct measurement of oligomerisation	• Measurements are affected by the introduction of air bubbles during sample preparation • Measurements are highly sensitive to temperature and solvent viscosity (this note is for instruments without temperature control) • Sometimes difficult to resolve polydisperse samples of similar sizes, e.g., monomers/dimers within 1–2 nm	Volume: 0.2 to 2 µl per well Concentration: 0.25 to 50 mg/ml Sample delivery: Multi-well plates
Differential scanning fluorimetry (DSF) *Fluorescence Dye-based (DSF)* and *Label Free DSF (NanoDSF)*	• Simple protocol and data analysis • Fast experiment • High throughput • Low protein consumption • Low consumable costs • Inexpensive sample preparation • Rapid assessment of buffers, ligands and mutations in protein stability	• Difficult to interpret for larger macromolecular complexes • Fluorescence dye-based DSF -Requires the use of a fluorescent dye -Ligands and detergents may interact with the dye -The use of reducing agents interfere with certain dyes (e.g., CPM and SyproOrange) -Plate readers need to have the correct filter • NanoDSF (label free DSF) -Its signal is highly dependent of the protein aromatic residues such as tryptophan	Volume: 50 µl per well or 10 µl per capillary Concentration: 0.01 to 200 mg/ml (depending on the instrument used) Sample delivery: Multi-well plate or 10 µl glass capillaries
Circular dichroism (CD) and synchrotron radiation circular dichroism (SRCD)	• Reasonably easy to set up • Relatively low amounts of sample • Fast set up • Semi-high throughput • Low consumable costs • Temperature melt range between 5 to 95°C • Accurate protein secondary structure quantification • Direct measurement of protein conformational changes/dynamics	• Requires high sample concentration if protein buffer has high salt concentration • Limited to buffers and ligands that do not strongly absorb in the far-UV region • Not applicable to cloudy or colloid samples	Volume and concentration: 1 mg/ml in a volume of ~25 µl when using a 0.1 mm cuvette Sample delivery: Quartz single cuvettes or 96/384 multi-well plates made of fused quartz

methods has its own strengths and weaknesses (see **Table 1**), thus their applicability will depend on the information required.

One of the major advances in drug discovery and development has been its synergy with a wide variety of such biophysical methods (Raynal et al., 2014; Renaud et al., 2016; Holdgate et al., 2019; Kiriiri, et al., 2020). Today, modern medicine relies heavily on the use of conventional drugs (synthetic small chemical substances) and biologics (e.g., proteins, antibodies and small peptides) as therapeutic agents. While genomic and proteomic approaches have uncovered an increasing number of potential druggable proteins, compelling Pharma businesses to adopt target-based drug discovery strategies, many challenges still remain. These include poor understanding of the mode of action of the target protein and its interaction with the therapeutic agent, as well as difficulties associated with the manufacturing of high-quality protein-based biologics in terms of purity and stability (Davis 2020; Emmerich et al., 2021). In this perspective, we sought to direct the reader's attention to the application of conventional and simple biophysical methods within automated HTP settings that are able not only to assess protein stability and integrity in solution but also to probe protein behaviour in the presence of multi-parametric screens of buffers, excipients, additives, salts, osmolytes, and co-factors. Moreover, these HTP biophysical approaches can make significant contributions to downstream applications such as X-ray crystallography, NMR and cryo-EM, as well as to the

upstream applications in drug discovery, development and formulation.

DATA AVAILABILITY STATEMENT

The original contributions presented in the study are included in the article/**Supplementary Material**, further inquiries can be directed to the corresponding authors.

AUTHOR CONTRIBUTIONS

TK, SK, AD, IC, PS, and IM conceptualised, drafted and finalized the manuscript. TK, SK, AD, and RR executed the experiments. All authors approved the submitted version.

ACKNOWLEDGMENTS

We acknowledge funding from the United Kingdom's Department of Business, Energy and Industrial Strategy (BEIS). We are grateful for support from the Membrane Protein Laboratory under Wellcome Trust grant number 20289/Z16/Z. We thank the award of experimental time (SM123352) on the B23 Beamline at Diamond Light Source (United Kingdom) and we acknowledge the support of Dr. Giuliano Siligardi and Dr. Rohanah Hussain.

SUPPLEMENTARY MATERIAL

The Supplementary Material for this article can be found online at: https://www.frontiersin.org/articles/10.3389/fmolb.2022.890862/full#supplementary-material

REFERENCES

Adli, M. (2018). The CRISPR Tool Kit for Genome Editing and beyond. *Nat. Commun.* 9, 1–13. doi:10.1038/s41467-018-04252-2

Alexander, C. G., Wanner, R., Johnson, C. M., Breitsprecher, D., Winter, G., Duhr, S., et al. (2014). Novel Microscale Approaches for Easy, Rapid Determination of Protein Stability in Academic and Commercial Settings. *Biochimica Biophysica Acta (BBA) - Proteins Proteomics* 1844, 2241–2250. doi:10.1016/j.bbapap.2014.09.016

Alexandrov, A. I., Mileni, M., Chien, E. Y. T., Hanson, M. A., and Stevens, R. C. (2008). Microscale Fluorescent Thermal Stability Assay for Membrane Proteins. *Structure* 16, 351–359. doi:10.1016/j.str.2008.02.004

Auvray, F., Dennetiere, D., Giuliani, A., Jamme, F., Wien, F., Nay, B., et al. (2019). Time Resolved Transient Circular Dichroism Spectroscopy Using Synchrotron Natural Polarization. *Struct. Dyn.* 6, 054307. doi:10.1063/1.5120346

Bai, N., Roder, H., Dickson, A., and Karanicolas, J. (2019). Isothermal Analysis of ThermoFluor Data Can Readily Provide Quantitative Binding Affinities. *Sci. Rep.* 9, 1–15. doi:10.1038/s41598-018-37072-x

Bhirde, A. A., Chiang, M.-J., Venna, R., Beaucage, S., and Brorson, K. (2018). High-Throughput In-Use and Stress Size Stability Screening of Protein Therapeutics Using Algorithm-Driven Dynamic Light Scattering. *J. Pharm. Sci.* 107, 2055–2062. doi:10.1016/j.xphs.2018.04.017

Biter, A. B., de la Peña, A. H., Thapar, R., Lin, J. Z., and Phillips, K. J. (2016). DSF Guided Refolding as a Novel Method of Protein Production. *Sci. Rep.* 6, 1–9. doi:10.1038/srep18906

Bonvin, A. M. J. J. (2021). 50 Years of PDB: a Catalyst in Structural Biology. *Nat. Methods* 18, 448–449. doi:10.1038/s41592-021-01138-y

Chari, A., Haselbach, D., Kirves, J.-M., Ohmer, J., Paknia, E., Fischer, N., et al. (2015). ProteoPlex: Stability Optimization of Macromolecular Complexes by Sparse-Matrix Screening of Chemical Space. *Nat. Methods* 12, 859–865. doi:10.1038/nmeth.3493

Cohen, A. E. (2021). A New Era of Synchrotron-Enabled Macromolecular Crystallography. *Nat. Methods* 18, 433–434. doi:10.1038/s41592-021-01146-y

Dauer, K., Pfeiffer-Marek, S., Kamm, W., and Wagner, K. G. (2021). Microwell Plate-Based Dynamic Light Scattering as a High-Throughput Characterization Tool in Biopharmaceutical Development. *Pharmaceutics* 13, 172. doi:10.3390/PHARMACEUTICS13020172

Davis, R. L. (2020). Mechanism of Action and Target Identification: a Matter of Timing in Drug Discovery. *iScience* 23, 101487. doi:10.1016/j.isci.2020.101487

Emmerich, C. H., Gamboa, L. M., Hofmann, M. C. J., Bonin-Andresen, M., Arbach, O., Schendel, P., et al. (2021). Improving Target Assessment in Biomedical Research: the GOT-IT Recommendations. *Nat. Rev. Drug Discov.* 20, 64–81. doi:10.1038/s41573-020-0087-3

Gao, K., Oerlemans, R., and Groves, M. R. (2020). Theory and Applications of Differential Scanning Fluorimetry in Early-Stage Drug Discovery. *Biophys. Rev.* 12, 85–104. doi:10.1007/s12551-020-00619-2

Holdgate, G., Embrey, K., Milbradt, A., and Davies, G. (2019). Biophysical Methods in Early Drug Discovery. *ADMET DMPK* 7, 222–241. doi:10.5599/admet.733

Hulse, W. L., Gray, J., and Forbes, R. T. (2013). Evaluating the Inter and Intra Batch Variability of Protein Aggregation Behaviour Using Taylor Dispersion Analysis and Dynamic Light Scattering. *Int. J. Pharm.* 453, 351–357. doi:10.1016/J.IJPHARM.2013.05.062

Hussain, R., Benning, K., Javorfi, T., Longo, E., Rudd, T. R., Pulford, B., et al. (2015). CDApps: Integrated Software for Experimental Planning and Data Processing at Beamline B23, Diamond Light Source. *J. Synchrotron Radiat.* 22, 465–468. doi:10.1107/S1600577514028161

Hussain, R., Jávorfi, T., Rudd, T. R., and Siligardi, G. (2016). High-Throughput SRCD Using Multi-Well Plates and its Applications. *Sci. Rep.* 6, 1–6. doi:10.1038/srep38028

Hussain, R., and Siligardi, G. (2016). Characterisation of Conformational and Ligand Binding Properties of Membrane Proteins Using Synchrotron Radiation Circular Dichroism (SRCD). *Adv. Exp. Med. Biol.* 922, 43–59. doi:10.1007/978-3-319-35072-1_4

Huynh, K., and Partch, C. L. (2015). Analysis of Protein Stability and Ligand Interactions by Thermal Shift Assay. *Curr. Protoc. Protein Sci.* 79, 28–29. doi:10.1002/0471140864.ps2809s79

International Organization for Standardization (1996). *13321 Particle Size Analysis - Photon Correlation Spectroscopy*. Available at: https://www.iso.org/obp/ui/#iso:std:iso:13321 (Accessed November 9, 2021).

Jain, T., Sun, T., Durand, S., Hall, A., Houston, N. R., Nett, J. H., et al. (2017). Biophysical Properties of the Clinical-Stage Antibody Landscape. *Proc. Natl. Acad. Sci. U.S.A.* 114, 944–949. doi:10.1073/pnas.1616408114

Jovčevska, I., and Muyldermans, S. (2020). The Therapeutic Potential of Nanobodies. *BioDrugs* 34, 11–26. doi:10.1007/s40259-019-00392-z

Kiriiri, G. K., Njogu, P. M., and Mwangi, A. N. (2020). Exploring Different Approaches to Improve the Success of Drug Discovery and Development Projects: a Review. *Futur J. Pharm. Sci.* 6, 1–12. doi:10.1186/s43094-020-00047-9

Kotov, V., Bartels, K., Veith, K., Josts, I., Subhramanyam, U. K. T., Günther, C., et al. (2019). High-throughput Stability Screening for Detergent-Solubilized Membrane Proteins. *Sci. Rep.* 9, 1–19. doi:10.1038/s41598-019-46686-8

Kozak, S., Lercher, L., Karanth, M. N., Meijers, R., Carlomagno, T., and Boivin, S. (2016). Optimization of Protein Samples for NMR Using Thermal Shift Assays. *J. Biomol. NMR* 64, 281–289. doi:10.1007/s10858-016-0027-z

Krause, M. E., and Sahin, E. (2019). Chemical and Physical Instabilities in Manufacturing and Storage of Therapeutic Proteins. *Curr. Opin. Biotechnol.* 60, 159–167. doi:10.1016/j.copbio.2019.01.014

Kwan, T. O. C., Axford, D., and Moraes, I. (2020). Membrane Protein Crystallography in the Era of Modern Structural Biology. *Biochem. Soc. Trans.* 48, 2505–2524. doi:10.1042/BST20200066

Kwan, T. O. C., Reis, R., Siligardi, G., Hussain, R., Cheruvara, H., and Moraes, I. (2019). Selection of Biophysical Methods for Characterisation of Membrane Proteins. *Ijms* 20, 2605. doi:10.3390/ijms20102605

Lorber, B., Fischer, F., Bailly, M., Roy, H., and Kern, D. (2012). Protein Analysis by Dynamic Light Scattering: Methods and Techniques for Students. *Biochem. Mol. Biol. Educ.* 40, 372–382. doi:10.1002/bmb.20644

Macarron, R., Banks, M. N., Bojanic, D., Burns, D. J., Cirovic, D. A., Garyantes, T., et al. (2011). Impact of High-Throughput Screening in Biomedical Research. *Nat. Rev. Drug Discov.* 10, 188–195. doi:10.1038/nrd3368

Makowski, E. K., Schardt, J. S., and Tessier, P. M. (2022). Improving Antibody Drug Development Using Bionanotechnology. *Curr. Opin. Biotechnol.* 74, 137–145. doi:10.1016/j.copbio.2021.10.027

Martinez, S. E., Singh, A., De Wijngaert, B., Sultana, S., Dharia, C., Vanbuel, H., et al. (2021). Assembly and Cryo-EM Structure Determination of Yeast Mitochondrial RNA Polymerase Initiation Complex Intermediates. *Star. Protoc.* 2, 100431. doi:10.1016/j.xpro.2021.100431

Meyer, A., Dierks, K., Hussein, R., Brillet, K., Brognaro, H., and Betzel, C. (2015). Systematic Analysis of Protein-Detergent Complexes Applying Dynamic Light Scattering to Optimize Solutions for Crystallization Trials. *Acta Cryst. Sect. F.* 71, 75–81. doi:10.1107/S2053230X14027149

Miles, A. J., Janes, R. W., and Wallace, B. A. (2021). Tools and Methods for Circular Dichroism Spectroscopy of Proteins: A Tutorial Review. *Chem. Soc. Rev.* 50, 8400–8413. doi:10.1039/D0CS00558D

Plant, A. L., Locascio, L. E., May, W. E., and Gallagher, P. D. (2014). Improved Reproducibility by Assuring Confidence in Measurements in Biomedical Research. *Nat. Methods* 11, 895–898. doi:10.1038/nmeth.3076

Puetz, J., and Wurm, F. M. (2019). Recombinant Proteins for Industrial versus Pharmaceutical Purposes: a Review of Process and Pricing. *Processes* 7, 476. doi:10.3390/pr7080476

Rajan, R., Ahmed, S., Sharma, N., Kumar, N., Debas, A., and Matsumura, K. (2021). Review of the Current State of Protein Aggregation Inhibition from a Materials Chemistry Perspective: Special Focus on Polymeric Materials. *Mat. Adv.* 2, 1139–1176. doi:10.1039/d0ma00760a

Ratanji, K. D., Derrick, J. P., Dearman, R. J., and Kimber, I. (2014). Immunogenicity of Therapeutic Proteins: Influence of Aggregation. *J. Immunotoxicol.* 11, 99–109. doi:10.3109/1547691X.2013.821564

Raynal, B., Lenormand, P., Baron, B., Hoos, S., and England, P. (2014). Quality Assessment and Optimization of Purified Protein Samples: Why and How? *Microb. Cell Fact.* 13, 1–10. doi:10.1186/s12934-014-0180-6

Real-Hohn, A., Groznica, M., Löffler, N., Blaas, D., and Kowalski, H. (2020). NanoDSF: *In Vitro* Label-free Method to Monitor Picornavirus Uncoating and Test Compounds Affecting Particle Stability. *Front. Microbiol.* 11, 1442. doi:10.3389/fmicb.2020.01442

Renaud, J.-P., Chung, C.-W., Danielson, U. H., Egner, U., Hennig, M., Hubbard, R. E., et al. (2016). Biophysics in Drug Discovery: Impact, Challenges and Opportunities. *Nat. Rev. Drug Discov.* 15, 679–698. doi:10.1038/nrd.2016.123

Ribeiro, R., Abreu, T. R., Silva, A. C., Gonçalves, J., and Moreira, J. N. (2019). Insights on the Formulation of Recombinant Proteins. *Curr. Pharm. Biotechnol.* 171, 23–54. doi:10.1007/10_2019_119

Roberts, C. J. (2014). Protein Aggregation and its Impact on Product Quality. *Curr. Opin. Biotechnol.* 30, 211–217. doi:10.1016/j.copbio.2014.08.001

Senisterra, G. A., and Finerty, P. J. (2009). High Throughput Methods of Assessing Protein Stability and Aggregation. *Mol. Biosyst.* 5, 217–223. doi:10.1039/B814377C

Shiba, K., Niidome, T., Katoh, E., Xiang, H., Han, L., Mori, T., et al. (2010). Polydispersity as a Parameter for Indicating the Thermal Stability of Proteins by Dynamic Light Scattering. *Anal. Sci.* 26, 659–663. doi:10.2116/ANALSCI.26.659

Stark, H., and Chari, A. (2016). Sample Preparation of Biological Macromolecular Assemblies for the Determination of High-Resolution Structures by Cryo-Electron Microscopy. *Microsc. (Tokyo)* 65, 23–34. doi:10.1093/jmicro/dfv367

Stetefeld, J., McKenna, S. A., and Patel, T. R. (2016). Dynamic Light Scattering: a Practical Guide and Applications in Biomedical Sciences. *Biophys. Rev.* 8, 409–427. doi:10.1007/S12551-016-0218-6

Svilenov, H., Markoja, U., and Winter, G. (2018). Isothermal Chemical Denaturation as a Complementary Tool to Overcome Limitations of Thermal Differential Scanning Fluorimetry in Predicting Physical Stability of Protein Formulations. *Eur. J. Pharm. Biopharm.* 125, 106–113. doi:10.1016/j.ejpb.2018.01.004

Wallace, B. A., Gekko, K., Vrønning Hoffmann, S., Lin, Y.-H., Sutherland, J. C., Tao, Y., et al. (2011). Synchrotron Radiation Circular Dichroism (SRCD) Spectroscopy: An Emerging Method in Structural Biology for Examining Protein Conformations and Protein Interactions. *Nucl. Instrum. Methods Phys. Res. Sect. A Accel. Spectrom. Detect. Assoc. Equip.* 649:177–178. doi:10.1016/j.nima.2010.10.135

Wang, Y., van Oosterwijk, N., Ali, A. M., Adawy, A., Anindya, A. L., Dömling, A. S. S., et al. (2017). A Systematic Protein Refolding Screen Method Using the DGR Approach Reveals that Time and Secondary TSA Are Essential Variables. *Sci. Rep.* 7, 9355. doi:10.1038/s41598-017-09687-z

Yu, Z., Reid, J. C., and Yang, Y.-P. (2013). Utilizing Dynamic Light Scattering as a Process Analytical Technology for Protein Folding and Aggregation Monitoring in Vaccine Manufacturing. *J. Pharm. Sci.* 102, 4284–4290. doi:10.1002/jps.23746

Zhang, H., and Cohen, A. E. (2017). Optogenetic Approaches to Drug Discovery in Neuroscience and beyond. *Trends Biotechnol.* 35, 625–639. doi:10.1016/j.tibtech.2017.04.002

Conflict of Interest: SK, PS were employed by the Douglas Instruments Ltd.

The remaining authors declare that the research was conducted in the absence of any commercial or financial relationships that could be construed as a potential conflict of interest.

Publisher's Note: All claims expressed in this article are solely those of the authors and do not necessarily represent those of their affiliated organizations, or those of the publisher, the editors and the reviewers. Any product that may be evaluated in this article, or claim that may be made by its manufacturer, is not guaranteed or endorsed by the publisher.

frontiers | Frontiers in Molecular Biosciences

ORIGINAL RESEARCH
published: 01 June 2022
doi: 10.3389/fmolb.2022.915167

DEER Data Analysis Software: A Comparative Guide

*Hannah Russell, Robyn Cura and Janet E. Lovett**

SUPA School of Physics and Astronomy and BSRC, University of St Andrews, St Andrews, United Kingdom

Pulsed dipolar electron paramagnetic resonance (PDEPR) spectroscopy experiments measure the dipolar coupling, and therefore nanometer-scale distances and distance distributions, between paramagnetic centers. Of the family of PDEPR experiments, the most commonly used pulsed sequence is four-pulse double electron resonance (DEER, also known as PELDOR). There are several ways to analyze DEER data to extract distance distributions, and this may appear overwhelming at first. This work compares and reviews six of the packages, and a brief getting started guide for each is provided.

Keywords: EPR/ESR, DEER/PELDOR, pulsed dipolar spectroscopy, DeerAnalysis, DEERNet, Tikhonov regularization, neural networks, Gaussian models

OPEN ACCESS

Edited by:
Alex Jones,
National Physical Laboratory,
United Kingdom

Reviewed by:
Gareth Eaton,
University of Denver, United States
Alistair Fielding,
Liverpool John Moores University,
United Kingdom

****Correspondence:***
Janet E. Lovett
jel20@st-andrews.ac.uk

Specialty section:
This article was submitted to Structural Biology, a section of the journal Frontiers in Molecular Biosciences

Received: *07 April 2022*
Accepted: *10 May 2022*
Published: *01 June 2022*

Citation:
Russell H, Cura R and Lovett JE (2022) DEER Data Analysis Software: A Comparative Guide. Front. Mol. Biosci. 9:915167. doi: 10.3389/fmolb.2022.915167

1 INTRODUCTION

Pulsed dipolar electron paramagnetic resonance (PDEPR) spectroscopy is a set of experiments that can be used to determine nanometer scale distances between paramagnetic centers by measuring their magnetic dipole-dipole interaction (Jeschke, 2012; Goldfarb and Stoll, 2018; Abdullin and Schiemann, 2020). This is a valuable technique in the study of biomacromolecules, as it can be used to ascertain their complexes and conformations. The most widely used PDEPR technique is double electron resonance (DEER, or PELDOR), (Milov et al., 1981; Milov et al., 1984; Martin et al., 1998; Schiemann et al., 2021). Applications of DEER in structural biology rely on pairwise coupling of spin-half centres with reasonably well-defined distance distributions, especially between nitroxide spin labels and this is the situation that will be discussed in this work (Haugland et al., 2017; Schiemann et al., 2021).

The DEER technique relies on the application of two microwave frequencies. The most commonly applied version of the experiment is the four-pulse (Martin et al., 1998). For four-pulse DEER, a three-pulse refocused echo sequence is applied at one frequency of the EPR absorption profile of the sample. The second frequency is applied elsewhere in the EPR spectrum with a non-overlapping, or only weakly overlapping, excitation band and is used to pump the spins. If the spins are coupled through the dipole-dipole interaction, then the pumped spins will affect the magnetic field experienced by the observed spins. The observer echo sequence has fixed time delays and the pump pulse is applied between the second and third pulses with a sequential increase in delay time. This means that the detected refocused echo over the course of the experiment, often called the DEER time trace, is modulated with the dipole-dipole coupling frequency.

Analysis of the time trace, assuming weak coupling so that the dipolar frequency is dependent on the inverse cube of the separation between centers, provides information on the distance between the coupled spins. The size of the DEER signal, the modulation depth, can provide information on the number of coupled spins (Bode et al., 2007). In theory the distances between pairwise interactions can be found from analysis of the Fourier transform of the DEER time trace, but in practice this is inaccurate, especially if there is a distribution of distances between the centers. There are a range of free-to-download software packages for providing the distance distributions and the mathematics of

these fall broadly into one or more of Tikhonov regularisation, model based approaches, or trained deep-neural networks (Jeschke et al., 2006; Brandon et al., 2012; Fábregas Ibáñez et al., 2020; Keeley et al., 2022).

One major source of complication in analyzing DEER data is that the time trace is actually a convolution of the pairwise interactions, often called the form factor or, alternatively, the *intra*molecular contribution, and the interactions of randomly distributed spins within the bulk of the sample, often called the background signal, or *inter*molecular contribution. This manifests as an overall signal decay. For homogeneously distributed molecules the form is a simple exponential decay. This is the 3D background function. The background may be better described by a stretched exponential depending on the exact nature of the sample and measuring conditions. The time trace will also have a random noise associated with the measurement and may contain artefacts. One common artefact is signal associated with the so-called "2 + 1" effect, caused by the overlap of the observer and pump pulses, which appears as a distortion at the end of the time trace data set, though may be reduced if Gaussian-shaped pulses are used rather than rectangular (Teucher and Bordignon, 2018).

The analysis of the DEER signal for distances must therefore account for the pairwise and the background signals, provide error estimation, and either allow truncation of the data to remove avoidable artefacts, or not be badly affected by their presence. Additionally, the software should be intuitive to use and produce user-independent output. It may be an advantage if the package can be a stand alone executable rather than run using expensive environments, though this should be a minor consideration over the scientific aspects of providing stable and reproducible results with useful error estimation.

The recent DEER-community led white paper recommended using a combination of analysis approaches to be sure of results and included the implementation of ComparativeDeerAnalyzer (Schiemann et al., 2021). This recommendation forms the motivation behind the work presented here. We hope to answer the following questions: what are the different analysis approaches from a non-expert user perspective; how can they be used; are they reliable?

Six programs will be discussed and compared for analysis of some typical data sets. The first software used in this work is DeerAnalysis, which to date has been the most commonly used software package for analyzing DEER data (Jeschke et al., 2006) and can be downloaded from (Jeschke, 2022). This program is run through the Matlab environment and works via a graphical user interface (GUI). DeerAnalysis utilises an approximate Pake transformation (APT), Tikhonov regularization and neural network analysis via DEERNet (it no longer includes model-based approaches) (Jeschke et al., 2006; Worswick et al., 2018). In this work DeerAnalysis will be used in user-defined mode with Tikhonov regularization and using "automation" which is referred to as ComparativeDeerAnalyzer (see below). DeerLab also uses Tikhonov regularization but assumes full control over fitting the background within a given parametric model (Fábregas Ibáñez et al., 2020; Fábregas-Ibáñez et al., 2022). DeerLab is a Python-based program, and installation instructions are available at (Fábregas Ibáñez et al., 2021).

LongDistances uses a GUI and is a Windows executable (Altenbach, 2021a). It offers a number of analysis approaches including Tikhonov regularization and Gaussian fitting in a single package, but here we will focus on LongDistances' "Model Free" method. It is available at (Altenbach, 2021b). DD also uses a GUI, but is Matlab based. It assumes that distributions are Gaussian or can be expanded into a series of Gaussian distributions (Stein et al., 2015). DD can be downloaded from (Hustedt, 2018). DEERNet uses deep neural networks to extract distance distributions in a single step, without the need for background fitting (Worswick et al., 2018). The latest version is available in Spinach (Hogben et al., 2011) [available from (Kuprov, 2021)] and also integrated as an option into DeerAnalysis (Jeschke et al., 2006). Both packages are Matlab-based. ComparativeDeerAnalyzer runs through a Windows-based executable and through DeerAnalysis using the "automation" option (which will be used in this work) (Schiemann et al., 2021). It combines results from DEERNet and DeerLab to give a mean distance distribution and a combined uncertainty. Though it should be noted that the versions of DEERNet and DeerLab used by ComparativeDeerAnalyzer are often not the most up-to-date or reliable versions available.

Attempting to learn to use these various software packages and extract results for onward presentations may appear a daunting prospect to the uninitiated user. This paper has the following layout: first, we hope to lay the groundwork to simply import and analyze a DEER data set, and also give insight into the output files to clarify their usability for future plotting and comparison for each software; then, the methods carried out for analysis comparisons are presented, followed by the results themselves; finally, there will be a discussion regarding the results, applicability and usability of each analysis method.

2 MATERIALS AND METHODS

2.1 Getting Started

2.1.1 DeerAnalysis

DeerAnalysis (Jeschke et al., 2006) is a Matlab-based package that exists in two modes; "automation" (ComparativeDeerAnalyzer) and user-defined. It is available for download from (Jeschke, 2022), and an accompanying manual can be found within the download folder. Here we introduce user-defined mode but using as many program-calculated values as possible. To begin, obtain the program from the web and set it in the Matlab path, then type DeerAnalysis in the command window to open the GUI. The version of DeerAnalysis discussed here is DeerAnalysis2022 which has significant differences to earlier versions, as detailed in the downloadable documentation.

The following paragraphs describe the workflow shown by **Figure 1A**. The methodology for user-defined mode is as follows; the user uploads a measured data set; the program accepts input data files in the form of Bruker Elexsys (.dta/.dsc), WIN-EPR, and ASCII. DeerAnalysis will automatically select a zero time and phase correction value. The criteria for these are described in the DeerAnalysis documentation. That being said, any value between 0 and the entire length of data can be input to the text box and

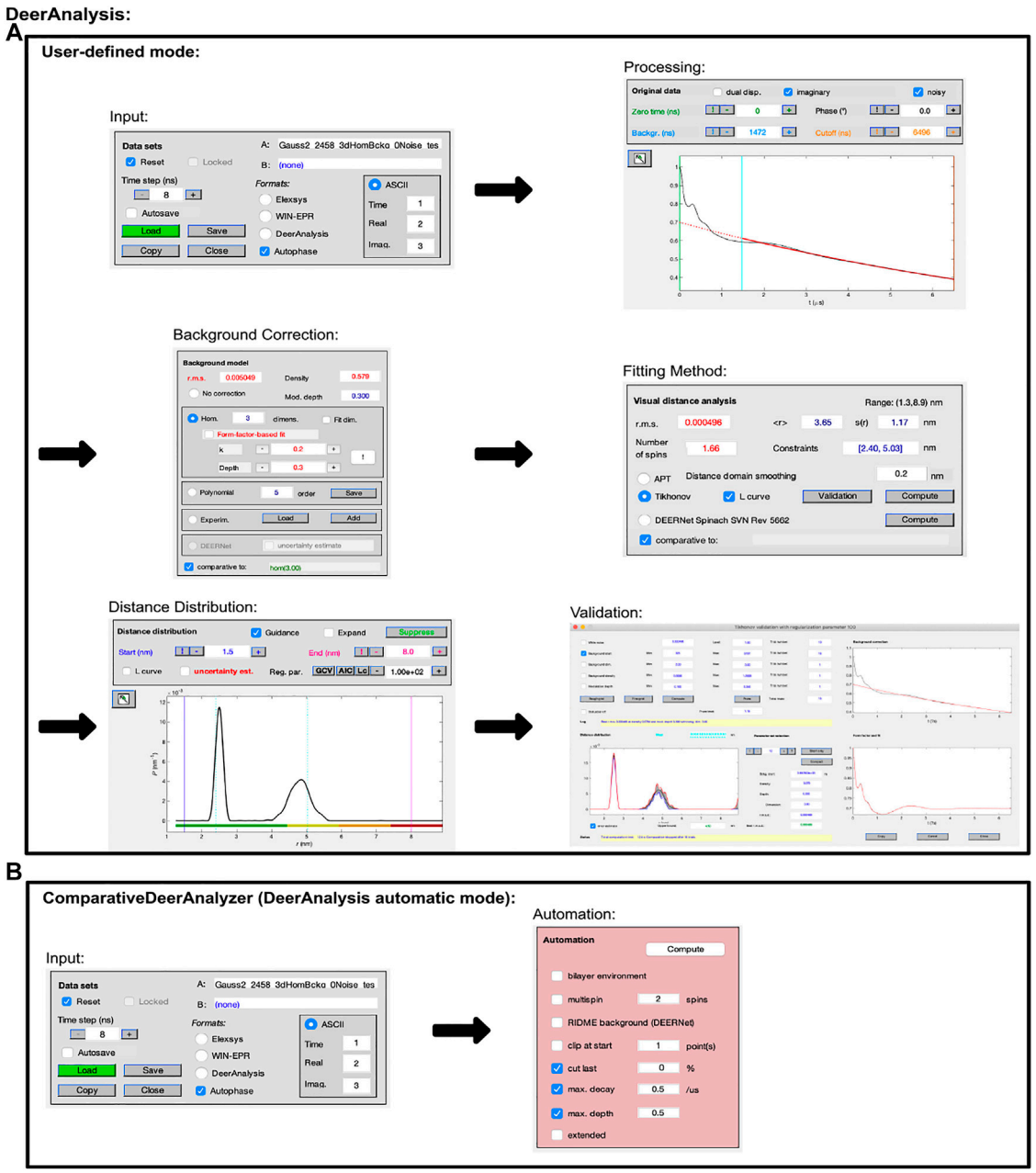

FIGURE 1 | DeerAnalysis2022 workflow. The program is Matlab-based and available on all operating systems. Data set shown is simulated noiseless, which was an ASCII file. For users using Elexsys file types, "Elexsys" should be selected in place of "ASCII"; **(A)** "user-defined" mode; **(B)** "automation" mode (otherwise known as ComparativeDeerAnalyzer, which is also available as a standalone Windows executable).

selected as the zero point. Likewise, any value can be selected as the phase correction, background start, and amount of data cut from the end. DeerAnalysis's user-defined mode includes the option of automatically determining the "optimal" value for each of these fitting parameters by pressing the "!" button present next to each. After selecting parameters, a background should be fitted. The default background is a 3D homogeneous model but other options are available, including an experimentally determined one.

At this stage the distance distribution box contains the result from the approximate Pake transformation (APT) which is fast to calculate but not very accurate (Jeschke et al., 2002). DeerAnalysis offers the user several different approaches to analyze the data, and this is selected using the panels. Probably the most common approach to analyzing DEER time traces with DeerAnalysis is to use Tikhonov regularization with the L-curve method for determining the regularization parameter (Chiang et al., 2005;

DeerLab:

Input Code:

```
import numpy as np
import deerlab as dl

# Experimental parameters
tau1 = 0       # First inter-pulse delay (µs)
tau2 = 6.896       # Second inter-pulse delay (µs)
deadtime = 0  # Acquisition deadtime (µs)

# Loading experimental data
data = np.loadtxt('data_path')
t = data[:,0]/1000 # µs
Vexp = data[:,1]

# Pre-processing
Vexp = dl.correctphase(Vexp) # Phase correction
Vexp = Vexp/np.max(Vexp)     # Normalizing
t = t + deadtime             # Accounting for deadtime

Nsamples = 20 # Number of boostrap samples

# Distance vector
r = np.arange(1.5,6,0.01) # nm

# Constructing model
Vmodel = dl.dipolarmodel(t,r, experiment = dl.ex_4pdeer(tau1,tau2, \
                                                        pathways=[1]))

# Fitting model to data
results = dl.fit(Vmodel,Vexp,bootstrap=Nsamples)

# Print results and save
print(results)
np.savetxt('Fitted_Signal.txt', np.asarray((t, Vexp, results.model, \
                                        *results.modelUncert.ci(95).T)).T)
np.savetxt('Distribution.txt', np.asarray((r, results.P, \
                                       *results.PUncert.ci(95).T)).T)
```

Output:

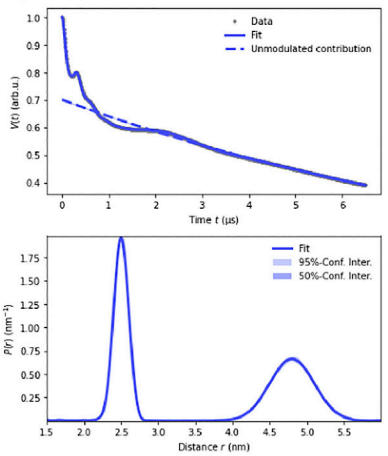

FIGURE 2 | DeerLab pre-release v0.14.0 workflow. The package is Python-based and available on all operating systems. Data set shown is simulated noiseless, which was an ASCII file. For users using Elexsys file types, the lines of code "data_path = '/. . ./data/datafile.DTA'" and "t,Vexp = dl.deerload (data_path)" should be used in place of "data = np.loadtxt ('data_path')" and the two following lines in panel one.

Edwards and Stoll, 2018). The distance distribution graph also contains colored markers along the *x*-axis which represent a measure of the confidence in the distance presented based on the length of the time trace. This is described further in the accompanying manual.

DeerAnalysis uncertainties when Tikhonov regularization is used are calculated via "Validation". Selecting this opens a new GUI and the parameters to vary are clearly set out, for example, background start value, white noise level etc. The program then runs through the calculation for each of the varied parameters and this gives a measure of uncertainty.

The figures can be saved directly, or data files of the results are saved as six text files, further described in the documentation, by pressing the "save" button. However, after validation, the best fit determined by the optimal parameters determined previously will be overwritten in favor of the validation fit. We therefore recommend saving both sets of results separately and that your results plot contains the best fit and the validation uncertainties. The final output data can then be plotted again using the Matlab *plot* function.

2.1.2 DeerLab

DeerLab is a script-based analysis package run through the Python environment, and accepts Bruker Elexsys (.dta/.dsc) and ASCII format input files. The DeerLab documentation (Fábregas Ibáñez et al., 2021) provides clear and straightforward instructions for the installation and general use of the program. The version of DeerLab described here is pre-release 0.14.0, meaning that it is not the final stable version of the program and is still under development.

The code in **Figure 2** shows how data is imported and processed. In this case the code implements a 3D background and Tikhonov regularization. It can be adapted for numerous experiments, fitting methods, and models. The functions used in **Figure 2** are: *correctphase* which minimizes the imaginary and maximizes the real components of the signal; *dipolarmodel* which requires the user to input time data (*t*), which should account for the deadtime, alongside the distance range, and an experiment model. The distance range, commonly defined as *r*, is set by the user and should be determined such that the lower limit is dependent on the pulse bandwidth and time increment. In this example the lower limit is 1.5 nm which is typical for a 12 ns rectangular pump pulse. The upper limit should consider the overall time trace length and the expected distances present in the sample, here it is set at 6 nm. A range of experimental models are available for use. In this work "ex_4pdeer" is used which assumes a 4-pulse DEER experiment. The parameters required by this function are the τ_1 and τ_2 time delays of the experiment and the number of dipolar pathways, which will be based on the experiment and the type of pulses used. For 4-pulse DEER, a single pathway will be required for data without a 2 + 1 effect component, but if this artefact is present, then a second pathway should be included by changing "pathways=[1]" to "pathways=[1,2]." Without giving the *dipolarmodel* function any additional information, it will assume a non-parametric distribution and a 3D homogeneous background, which are common analysis

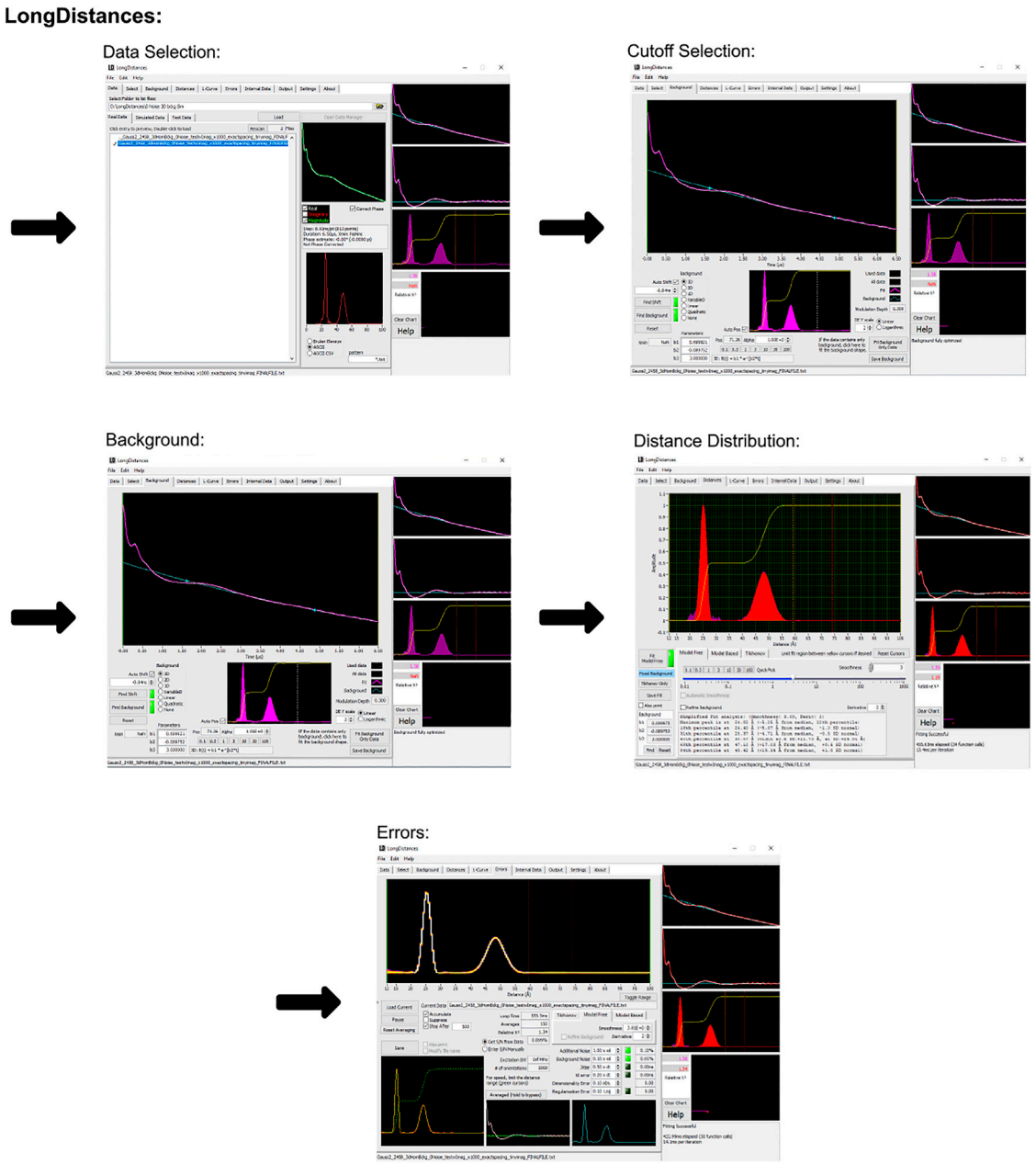

FIGURE 3 | LongDistances workflow. The package was developed in LabVIEW and is available as a Windows executable only. Data set shown is simulated noiseless, which was an ASCII file. For users using Elexsys type files, "Bruker Elexsys" should be selected in panel one in place of "ASCII".

methods for DEER data. The non-parametric method is solved using Tikhonov regularization. Rather than using the L-curve method typically implemented in DeerAnalysis, the regularization parameter is determined according to the Akaike information criterion (AIC) (Akaike, 1974) by default. Parametric model options such as Gaussian, are also available. DeerLab uses least-squares fitting to determine the optimal parameter values to fit the data for the distance distribution, background, and experiment. Finally, the model set up using *dipolarmodel* can be fit to the phase-corrected input data using the *fit* function. While these models and functions provide accurate results, the user should always check that the parameter values and general goodness-of-fit indicators make sense: implementing "print(results)" will mean that DeerLab presents these results too.

The default method for error-analysis in DeerLab is covariance-matrix uncertainty. Given its speed and ease, the calculation is included in all DeerLab fit functions, and they return covariance-based errors for all fitted parameters. For much more accurate uncertainty estimates, however, DeerLab offers

bootstrap analysis (Efron and Tibshirani, 1986). Though this is significantly more computationally expensive, it is the recommended method and is the one used in this work. Bootstrapping is easy to implement in DeerLab, and requires only "bootstrap = Nsamples" to be added as an input in the *fit* function for use.

The fitted data can be accessed using "results" where "results.model" and "results.P" return the fitted dipolar signal, and distance distribution results, respectively. To save the data to plot it elsewhere, the final two lines of code in panel one of **Figure 2** can be used to save the fitted dipolar signal and distance distribution results, with associated uncertainties, respectively. The data is saved as a .txt file.

2.1.3 LongDistances

LongDistances exists only as a Windows executable program. Its installation requires the user to visit the Hubbell lab website (Altenbach, 2021b) and download the zip file containing all their offered software. Upon download, LabVIEW 2020 Runtime "lite" should be installed, alongside the LongDistances program. Full installation instructions are available on the web (Altenbach, 2021c), and a further *readme* document is available in the zip file for extra installation instructions. The version of LongDistances described here is v1073.

The LongDistances GUI consists of a series of tabs leading to different stages of the analysis. A workflow of this process can be seen in **Figure 3**. First is the "data" tab, here, the user's data can be selected and imported to the program. The program's accepted input files are Bruker Elexsys (.dta/.dsc) and ASCII formats. The next tab is entitled "select" and is where the time range for analysis is selected. LongDistances implements a largely mouse-based control so that to cut data from the time trace, the cursor can simply be used to cut data from either side of the DEER signal. Next, a background should be fit to the data in the "background" tab. The zero time is automatically calculated and applied to the data, but can be overwritten by the user, and the "find background" button should be pressed to fit a background. There are a number of background model options available. After a background has been determined, the user can navigate to the "distances" tab. Here, several fitting options are available, including Tikhonov regularization and a sum of Gaussians model-based approach, but the recommended process for distance distribution determination is the model-free method, which is described by the author as being similar to non-negative Tikhonov regularization. This approach uses a "smoothness" parameter. To determine the ideal value for this parameter, the user should use their own intuition and choose a value "by-eye". The value should be one that smooths the resulting distribution but should not be so high a number that it causes the result to become over-broadened. The smoothness parameter can be altered by the user using the slider, text box or selecting a provided value.

LongDistances offers the user the ability to calculate uncertainties on most fit parameters. Repeated analysis with varying parameters is carried out to determine the uncertainties in the data. This feature is available within the "error" tab. Finally, for future use of the results, five main outputs are provided upon saving the analysis. These are the named "filename_" followed either by DEER, DIST, DIST_ERROR, or RSLT, depending on what data the file contains, or the fifth output which is a .png.

2.1.4 DD

DD is a Matlab-based analysis package specializing in Gaussian distributions (Brandon et al., 2012; Hustedt et al., 2021). The version of DD described here is 7C, which is available from (Hustedt, 2018) and includes an accompanying user manual.

The following procedure is illustrated as a workflow in **Figure 4**. DEER data is uploaded using the "Find" button in the "Data File" panel. It accepts input files in the form of Bruker Elexsys (.dta/.dsc) and ASCII. Automatically, DD will optimize the zero time and phase correction values, but a "process" option is also present that will re-calculate these values, which may be necessary. An example of an occasion where this may be necessary is post any truncation of the data, which can be achieved by typing values into the text boxes in the "Data File" panel. The user is then presented with a new pop-up window that shows the raw data and newly zero time and phase corrected result.

The second and largest box within the GUI lets the user select the number of Gaussians they want to fit the data with, while the third box fits the background. The pre-selected background model assumes a three-dimensional distribution of spins. DD also gives the user the option to fit the background with a calculated model that takes into consideration the spin concentration and the excluded volume of the sample. After selecting the fitting process and parameters, which can be edited by typing values directly into the text boxes, the data is fit by pressing the green "FIT" button.

To determine the optimal number of Gaussians to fit the distance distribution to, a number of statistical parameters should be referred to. DD offers any number of Gaussians from 1–8, and according to the DD user manual (Hustedt, 2018), the "best" fit should be determined by the chi-square, χ^2 (goodness of fit); the closer the value is to 1, the better the fit. The second criteria for determining the optimal fit is the Bayesian information criterion (BIC) (Schwarz, 1978), the lowest BIC indicates the best fit.

DD calculates errors by determining the uncertainty using the delta method, wherein the partial derivative of the best fit is taken at a particular distance with respect to all fit parameters (Hustedt et al., 2018).

To save data in DD, the user presses the "write" button. By default, data is set to save to a single Excel document with a number of sheets containing the various output data sets, but this can be changed by pressing the "options" button and navigating to the output tab where the data can be saved as either ASCII or .mat files.

2.1.5 DEERNet

The version of DEERNet discussed here is the full script based version which is available through Spinach 2.6.5625 and can be downloaded from (Kuprov, 2021). Installation then only requires the user to add Spinach to their Matlab path. There

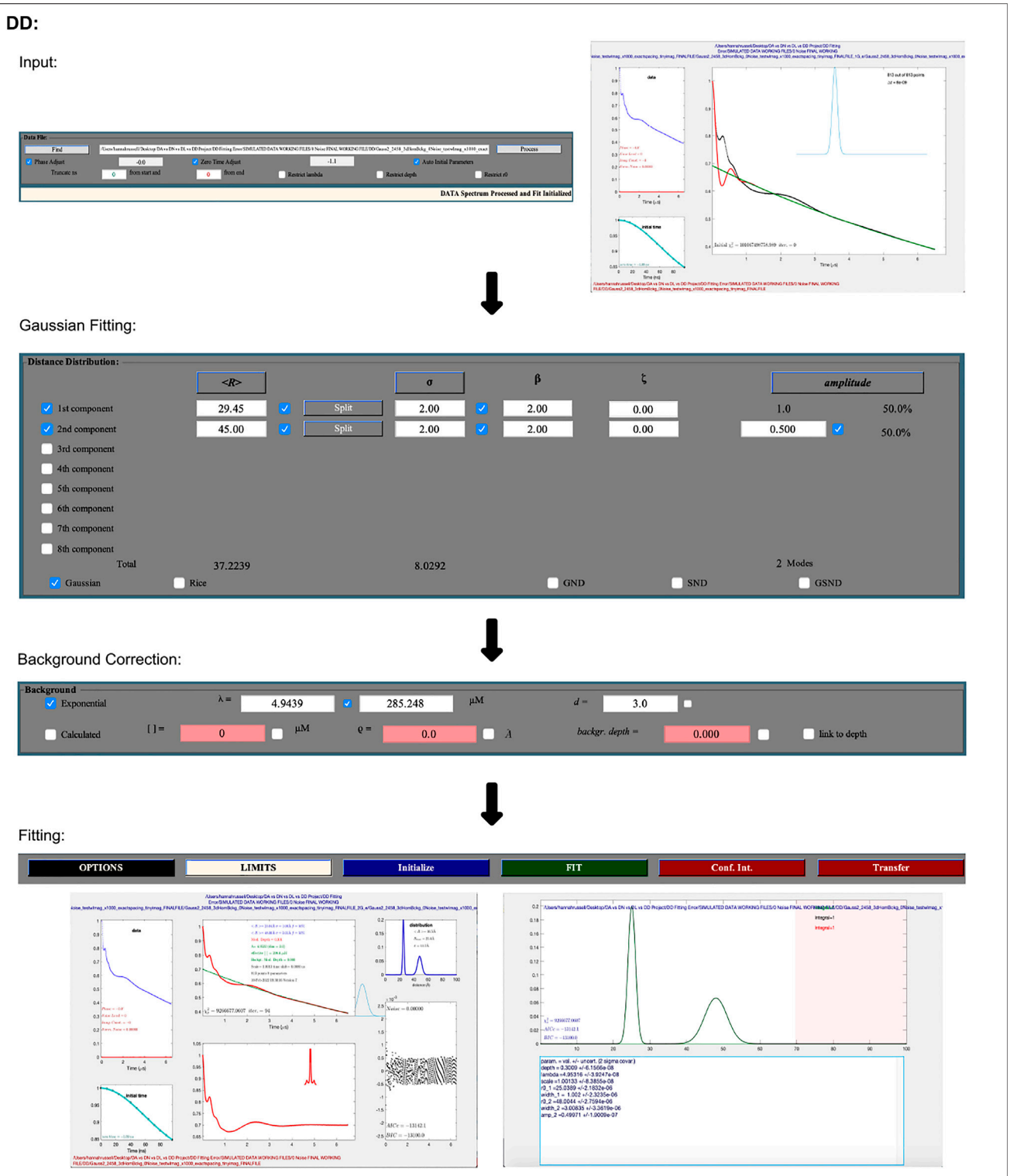

FIGURE 4 | DD workflow. The package is Matlab-based and available on all operating systems. Data set shown is simulated noiseless, which was an ASCII file. No additional steps or changes are required for importing different file types.

Spinach DeerNet:

Input Code:

```
data = load('datafile');
time_axis = data(:,1);
deer_trace = data(:,2);
deernet(deer_trace,time_axis); drawnow()
```

Output Plots:

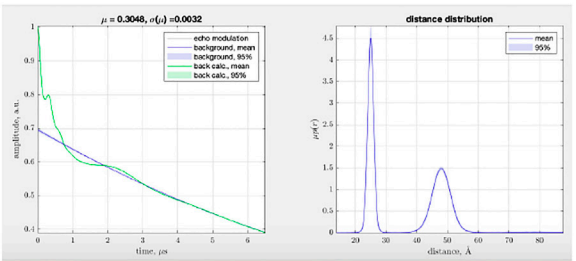

Saving (right click for menu):

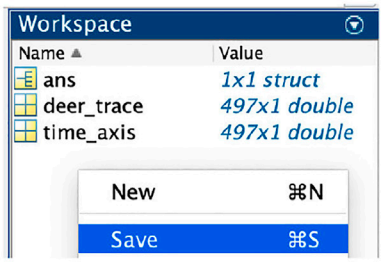

FIGURE 5 | Spinach 2.6.5625 DeerNet workflow. The package is Matlab-based and available on all operating systems. Data set shown is simulated noiseless, which was an ASCII file. For users using Elexsys type files, the first three lines of the input code should be replaced with the single line "[deer_trace, time_axis] = elexsys2deernet ('datafile')". Note that no file extensions should be added to the end of "datafile" when using this function. In the output plot panel, the numbers above the DEER trace signified by μ and $\sigma(\mu)$ represent the modulation depth, and the standard deviation in the modulation depth, respectively.

exist a series of links in the downloaded folder with further details on installation and instructions on how to get started.

In the script-based version of DEERNet, the user's only input to the process is to select the data, which can be done using the code given in **Figure 5**. The accepted input file formats are Bruker Elexsys (.dta/.dsc) and ASCII. After running this piece of code, the user will be presented with a pop-up window showing the fitted background and extracted distance distributions both with 95% uncertainty bounds (for an example, see **Figure 5**). In DEERNet, distance distribution uncertainties are calculated through the training of the neural networks on different, randomly generated, data inputs and performing statistical analysis on their output results.

Data can be saved from Matlab into a .mat file which saves the input and output data. This must be further dealt with by the user if they wish to have an ASCII-type data file.

Pre-packaged DEERNet runtime libraries are used in ComparativeDeerAnalyzer and DeerAnalysis.

2.1.6 ComparativeDeerAnalyzer

ComparativeDeerAnalyzer is available from (Jeschke, 2022), where the download includes a short explanatory document (Schiemann et al., 2021). It is available both as a Windows-based executable (version 2.0) and in DeerAnalysis2022 when run using the "automation" option. In this version of ComparativeDeerAnalyzer, DeerLab is run through version 0.9.1 and DEERNet through Spinach SVN Rev 5662. ComparativeDeerAnalyzer aims to provide a solution to the existing issue in the field of different results being obtained by different analysis packages. To combat this, the package offers a, so-called, consensus result which is determined as being the mean of DeerLab's Tikhonov regularization and DEERNet acquired distributions, where the associated uncertainty is made up of both the method's errors. The DEERNet uncertainties are calculated via training of the neural networks with simulated data sets, and the variation in their results is used to track the uncertainties, while the Tikhonov errors are determined as being twice the standard deviation of 11 different, equally spaced, backgrounds over 55 iterations. For each background, 5 trials are performed wherein the noise is varied.

The program has limited user input and this is controlled through the checkbox options that can be seen in panel two of **Figure 1B** for DeerAnalysis 2022. This includes the option for the user to cut-off a pre-determined amount of the data, but otherwise ComparativeDeerAnalyzer will determine whether to remove data points. We note that the degree of input has increased in the newest releases, since the original version allowed for none (Schiemann et al., 2021).

ComparativeDeerAnalyzer mode in DeerAnalysis is accessed by loading the data, as shown in the first panel of **Figure 1B**, and pressing "compute." A prompt will guide the user to choose a datafile to import (Bruker Elexsys (.dta/.dsc) or ASCII accepted). All parameters and calculations are carried out directly using DeerLab 0.9.1 Tikhonov regularization and DEERNet Spinach SVN Revision 5662.

The output is a PDF containing the individual fits and distributions of the data, and also plots of the consensus result based on the two. The parameters used for the analysis are also presented at the end of the document. Also shown at the

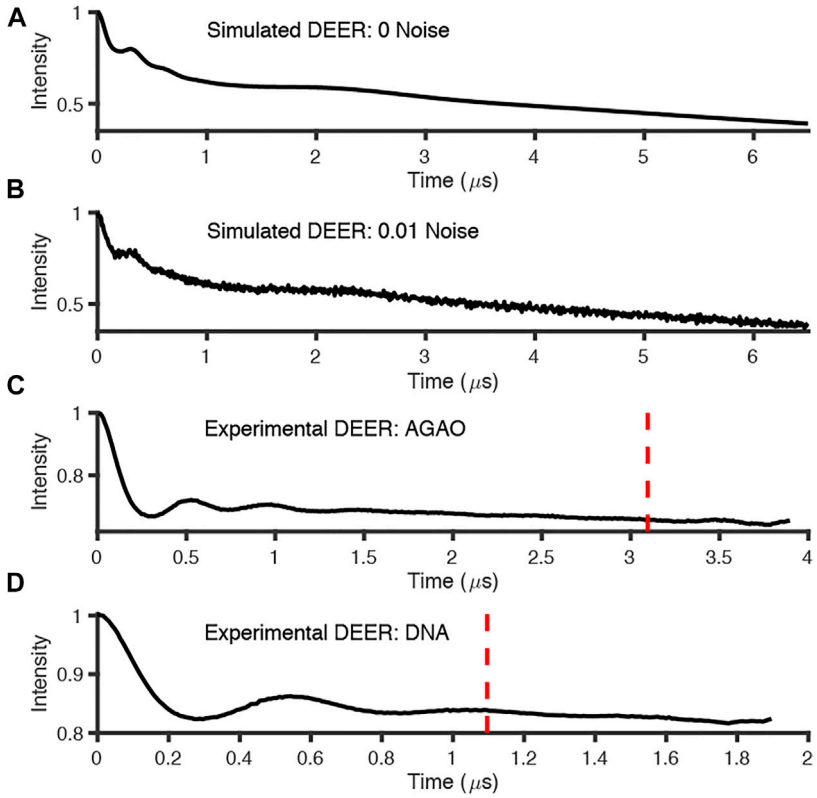

FIGURE 6 | Simulated and experimental DEER traces where red dotted line signifies 800 ns cut from end points; **(A)** simulated noiseless; **(B)** simulated noisy; **(C)** experimental AGAO; **(D)** experimental DNA measurements. Further details of the data sets in the main text.

bottom of the PDF are the save locations of the output data. A number of csv files are saved: these include the distributions from DEERNet, DeerLab, and the consensus fits and distributions. Further files include the meta-data and also the results in.mat format.

2.2 Versions

In this work the following operating systems, coding packages, and analysis packages were used; MacOS Mojave Version 10.14.6, Windows 10 (used for LongDistances only), Matlab R2021a, Python version 3.8.5 through Spyder 5.0.5 via Anaconda Navigator 2.04, DeerAnalysis2022 (which includes ComparativeDeerAnalyzer 2.0), DEERNet via Spinach version 2.6.5625, DD version 7C, DeerLab pre-release version 0.13.2 for data simulation, DeerLab pre-release version 0.14.0 for data analysis, 64 bit LabVIEW 2020 "lite" Runtime engine, and LongDistances1073.

2.3 Generating Simulated DEER Data

DeerLab v0.13.2 was used to simulate DEER data containing two distinct distance distributions. Simulations were used to produce sets of data with known distance distributions to allow comparison to the results from the analysis programs. To do this, the "dd_Gauss2" function was used with parameters (2.5, 0.1, 0.5, 4.8, 0.3, 0.5) corresponding to two Gaussians (Gaussian 1: mean distance 2.5 nm, standard deviation 0.1 nm, relative weight 0.5; Gaussian 2: mean distance 4.8 nm, standard deviation Gaussian 0.3 nm, relative weight 0.5). The modulation depth was set at 0.3 and the time axis was set between 0 and 6496 ns with 8 ns resolution. Noise could be added and was found to be necessary on the imaginary part for DD to process the data. The data called noise-free in fact has a noise level of 10^{-7} on the imaginary part. Data with noise added had a 0.01 level. The background function can be varied. 3D backgrounds were created with the "dd_hom3d" function with a spin concentration of 300. 2D backgrounds were created with the "bg_homfractal" function with a pumped spin fractal concentration of 300×10^{-7} μmol/dm^d and a fractal dimension, d, of 2. Data from these analyses are not shown in this paper though results are discussed briefly.

2.4 Experimental DEER Data

Two sets of different experimental DEER data were used for testing and demonstrating the different packages. The data were all from nitroxide Q-band 4-pulse DEER and the samples are the copper amine oxidase protein from *Arthrobacter globiformis* (AGAO) and spin-labelled DNA. Experimental details are given in the relevant publications and the data are freely available with links presented in the publications (Hardwick et al., 2020; Russell et al., 2021).

TABLE 1 | DeerAnalysis parameters.

Data set	Maximum time (ns)	Zero time (ns)	Background start (ns)	Tikhonov parameter	Modulation depth
1	6496	0	1472	100	0.300
2	6496	0	2592	1000	0.314
3	3896	331	952	7.94	0.287
	3096	331	544	25.1	0.286
4	1896	330	336	10	0.141
	1096	330	352	10	0.139

TABLE 2 | DD parameters.

Data set	Maximum time (ns)	Zero time (ns)	No. of Gaussians	Modulation depth
1	6496	0.0	2	0.301
2	6496	0.0	2	0.307
3	3896	330.7	3	0.289
	3096	330.7	3	0.289
4	1896	330.2	3	0.142
	1096	330.2	2	0.142

TABLE 3 | LongDistances parameters.

Data set	Maximum time (ns)	Zero time (ns)	Smoothness parameter	Modulation depth
1	6496	0.0	3	0.300
2	6496	0.0	3	0.304
3	3896	330.7	3	0.293
	3096	330.7	3	0.287
4	1896	330.1	3	0.149
	1096	330.1	1	0.147

2.5 Data and Fitting Parameters

The simulated data and experimental DEER time traces (**Figure 6**) were analyzed using all six packages following the procedures set out in the Getting Started section. The parameters and selected output variables are presented in **Tables 1–3** for DeerAnalysis, DD and LongDistances respectively. The key to the "Data set" column is that data set 1 is simulated with no noise; Data set 2 is simulated with 0.01 noise level; data set 3 is the experimental data from spin-labelled AGAO; data set 4 is the experimental spin-labelled DNA data.

In all the DeerLab fits, the function "ex_4pdeer" was used to assume a 4-pulse DEER experiment, and *dipolarmodel* used no input arguments so as to run with the default non-parametric (*i.e.,* Tikhonov regularization) and 3D homogeneous background fitting models. For the simulated data sets (noiseless and noisy) only a single pathway was applied, as no 2 + 1 effect artefact is present, and the experimental parameters $\tau_1 = 0\ \mu$s, $\tau_2 = 6.896\ \mu$s and deadtime = 0 μs were used for both sets of simulated data. For the experimental data sets (AGAO and DNA), two fits were conducted in each program, one with 0 ns cut from the data, and one with 800 ns cut, to remove the 2 + 1 effect. In DeerLab, a second pathway can be included in the dipolar model to account for this artefact. Therefore, the 0 ns cut data used two pathways, while the 800 ns cut data used one. The AGAO experimental parameters were $\tau_1 = 0.4\ \mu$s, $\tau_2 = 4\ \mu$s and deadtime = 0.08 μs and for DNA these were $\tau_1 = 0.4\ \mu$s, $\tau_2 = 3\ \mu$s and deadtime = 0.08 μs. In all analyses, bootstrap analysis was used to calculate the uncertainties in the results. The DeerLab documentation encourages the use of 1000 bootstrap samples to avoid non-convergence of the confidence intervals. However, due to this being computationally expensive and requiring greater lengths of time to run, only 20 bootstrap samples were used in this work as this proved to be a sufficient number to ensure convergence of the confidence intervals for our data sets.

DEERNet requires no user input or fitting parameters. Variations of the code in **Figure 5** were used, and similarly, ComparativeDeerAnalyzer was run without any user input.

3 RESULTS

3.1 Results From Simulated DEER Data

The six packages were tested on simulated DEER time traces which had been generated from two equally weighted non-overlapping Gaussian distributions with different standard deviations. The two Gaussian's were centered at 2.50 and 4.80 nm with respective full-width-at-half-maximum (FWHM) values of 0.24 and 0.71 nm. The overall mean of the input data

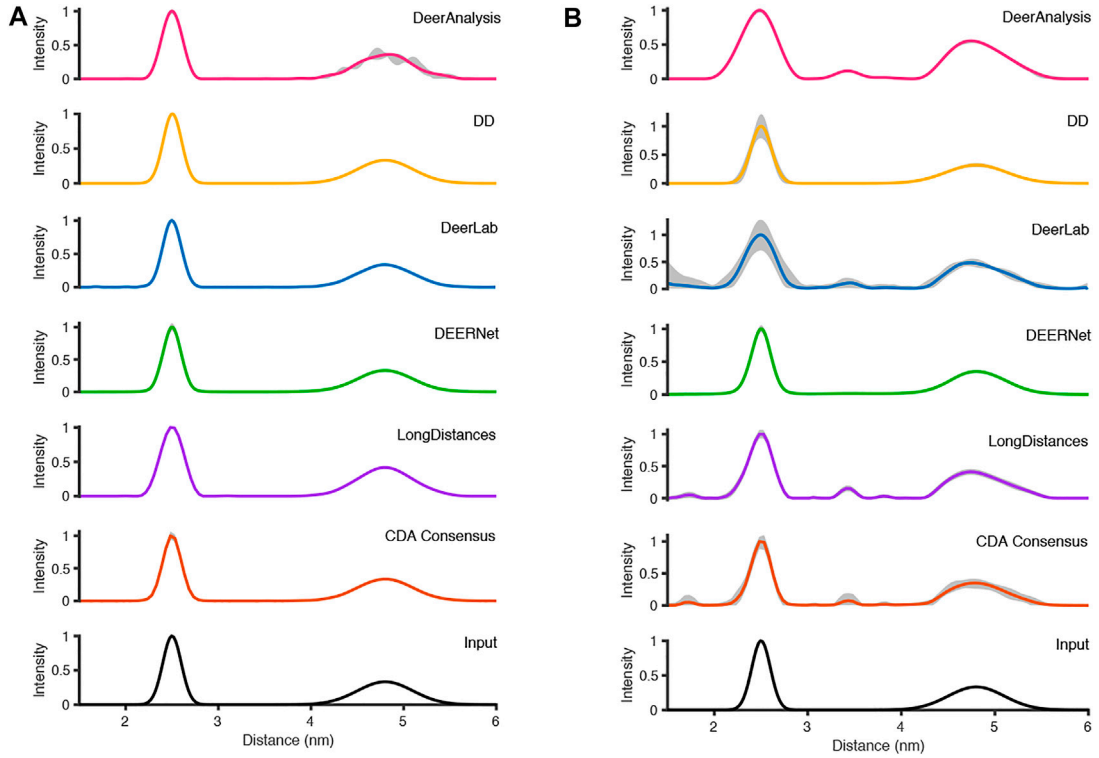

FIGURE 7 | The analysis of the simulated DEER time traces using the various analysis packages (CDA Consensus is the consensus result from ComparativeDeerAnalyzer) and the original input distance distributions are shown at the bottom: **(A)** noiseless data; **(B)** noisy data.

TABLE 4 | Results from each program for the simulated DEER-with-no-noise data set.

	Overall mean (nm)	Mean main peak 1 (nm)	FWHM main peak 1 (nm)	Mean main peak 2 (nm)	FWHM main peak 2 (nm)	Height of peak 2 compared to peak 1 (%)
DeerAnalysis	3.65	2.50	0.26	4.80	0.69	36
DD	3.65	2.50	0.24	4.80	0.71	33
DeerLab	3.64	2.50	0.24	4.80	0.70	34
DEERNet	3.69	2.50	0.23	4.80	0.70	33
LongDistances	3.65	2.50	0.30	4.80	0.70	42
CDA Consensus	3.67	2.50	0.24	4.80	0.69	34
Mean of Results	3.66	2.50	0.25	4.80	0.70	35
Standard Deviation	0.02	0.00	0.03	0.00	0.01	3.4

TABLE 5 | Results from each program for the simulated DEER-with-noise data set.

	Overall mean (nm)	Mean main peak 1 (nm)	FWHM main peak 1 (nm)	Mean main peak 2 (nm)	FWHM main peak 2 (nm)	Height of peak 2 compared to peak 1 (%)
DeerAnalysis	3.60	2.47	0.45	4.84	0.75	56
DD	3.62	2.50	0.26	4.80	0.76	32
DeerLab	3.56	2.58	0.38	4.84	0.75	48
DEERNet	3.62	2.50	0.25	4.82	0.67	35
LongDistances	3.60	2.48	0.30	4.84	0.74	41
CDA Consensus	3.59	2.49	0.26	4.83	0.72	35
Mean of Results	3.60	2.50	0.32	4.83	0.73	41
Standard Deviation	0.02	0.04	0.08	0.02	0.03	9.2

was 3.65 nm. The equal weighting of the peaks means that the second, broader peak is 33% the size of the first peak. The results of processing the simulated data are presented in **Figure 7** and statistics are given in **Tables 4** and **5**. The tables present the overall mean of the distance distributions from each of the results, and the mean and FWHM for the two most probable distance distribution peaks (which correspond to the expected input peaks in all cases). The tables also present a mean and standard deviation for results from all the packages in each of these categories.

Figure 7A shows that the output from the programs were all very similar when the input DEER time trace had effectively no noise present. The uncertainties were barely visible except for the DeerAnalysis result where the longer, broader distance had some oscillatory variation following the validation procedure. **Table 4** further highlights how well the packages reproduced the input distance distributions with the only variation coming from very small differences in the FWHM values and in the relative heights of the two peaks. The first peak from the LongDistances analysis was slightly broadened and varied by more than one standard deviation from the mean (0.30 nm compared to the input value of 0.24 nm and the mean from all results value of 0.25 nm). This also led to the % height of the second peak being a little larger than the mean or input value.

The results from the different packages varied more for the simulated data with a modest level of noise, and the results are shown in **Figure 7B**. By visual inspection, the Gaussian fitting from DD produced the input well with some uncertainty visible on the shorter, more narrow, distance. DEERNet also gave back the input very well and with almost no uncertainty. The other packages, which used Tikhonov regularization or similar, give an output with an erroneous apparent distance centered around 3.3 nm. Though only in DeerAnalysis and LongDistances was this seen as having certainty, and therefore the results have been affected by the presence of appreciable noise on the simulated data. The DeerLab result had a much larger degree of uncertainty compared to the noiseless input data result shown in **Figure 7A**. The uncertainty had also increased for ComparativeDeerAnalyzer and DD but appears reduced for the DeerAnalysis result. The shape of the longer distance peak appeared visibly asymmetric for the results from DeerAnalysis, DeerLab, LongDistances and ComparativeDeerAnalyzer.

Some statistical results from each package are shown in **Table 5**. The standard deviations were small at less than 0.1 nm, meaning that all packages produced a result in good agreement with the rest. The overall mean of the entire distribution from each package was 3.60 nm with a standard deviation of 0.02 nm, which was shorter than the overall mean of the input (3.65 nm). The mean of the first prominent peak was 2.50 nm with a standard deviation of 0.04 nm. This fit the mean for this peak from the input data well. Only the result from DeerLab varied significantly: approximately two standard deviations away. The second prominent peak was at 4.83 nm with a standard deviation of 0.02 nm: almost all the programs slightly overestimated the mean position of the peak. The widths of the main peaks were slightly broader than the input values. The height ratio of the two peaks varied much more than for the results from the input data with no noise. In particular, the DeerAnalysis result was notably far from the input value.

3.2 Results From Experimental DEER Data

The experimentally measured DEER data used in these tests were measured to good signal-to-noise levels and have both visible modulations (indicative of reasonably narrow distance distributions) and visible artefacts at the end of the time traces (**Figure 6**).

The analysis procedures were run twice for most packages: once for the full-length experimental time traces, and once for the data with 800 ns removed from the end before analysis to remove the data points that may have been distorted by measurement artefacts. The exception to this approach was for ComparativeDeerAnalyzer which was run without any user input, and determined that 11% of the AGAO and 1% of the DNA data was cut from the end of the traces. The first test system, from the spin-labelled protein AGAO, was analyzed by all packages to have an asymmetric distance distribution (**Figure 8A**). The second system, spin-labelled DNA, consistently gave a more symmetric single-distance distribution (**Figure 8B**).

For the analysis approaches that used Tikhonov regularization (DeerAnalysis and DeerLab), where the full-length and the cut data were processed, the distance distributions became more smooth upon time trace truncation. This was also true for DD processing of the DNA data. The other analysis procedure results appeared more consistent across the AGAO and DNA data whether the data were truncated or not. DEERNet probably influenced the stability of the consensus result shown from ComparativeDeerAnalyzer. Most of the results have only small error or uncertainty levels as calculated by the programs, though DeerAnalysis for the 800 ns truncated DNA data set had a little more visible uncertainty at the long distance end.

Some statistical results are presented in **Tables 6** and **7** for the AGAO and DNA results respectively. In the tables the "Overall Mean" refers to the mean of the entire distribution, where as the mean or FWHM of the main peak is the result for the most prominent distance peak in the distribution.

The standard deviation from the mean of all the AGAO and DNA results from the different programs was less than 0.1 nm for the overall mean, mean of the main peak, and FWHM of the main peak. This indicates that all the programs are performing well, or at least are in broad agreement, as they return the main aspects of the distance distribution for the AGAO and DNA, regardless of the appearance of the distributions in **Figure 8**. The main peak of the AGAO result was at a mean position of 2.88 nm with a standard deviation of 0.03 nm across all results/analysis methods tested. Only one result (from DEERNet) fell slightly outside one standard deviation of the mean. The mean for the overall distribution was larger than for the main peak since the AGAO distance distribution was asymmetric, as determined by all the programs. The FWHM of this peak was 0.21 nm with a standard deviation of 0.04 nm with LongDistances slightly overestimating the width, and one of the DeerLab datasets being a little more narrow. The overall mean and the mean of the main peak in the DNA result were very close together since the

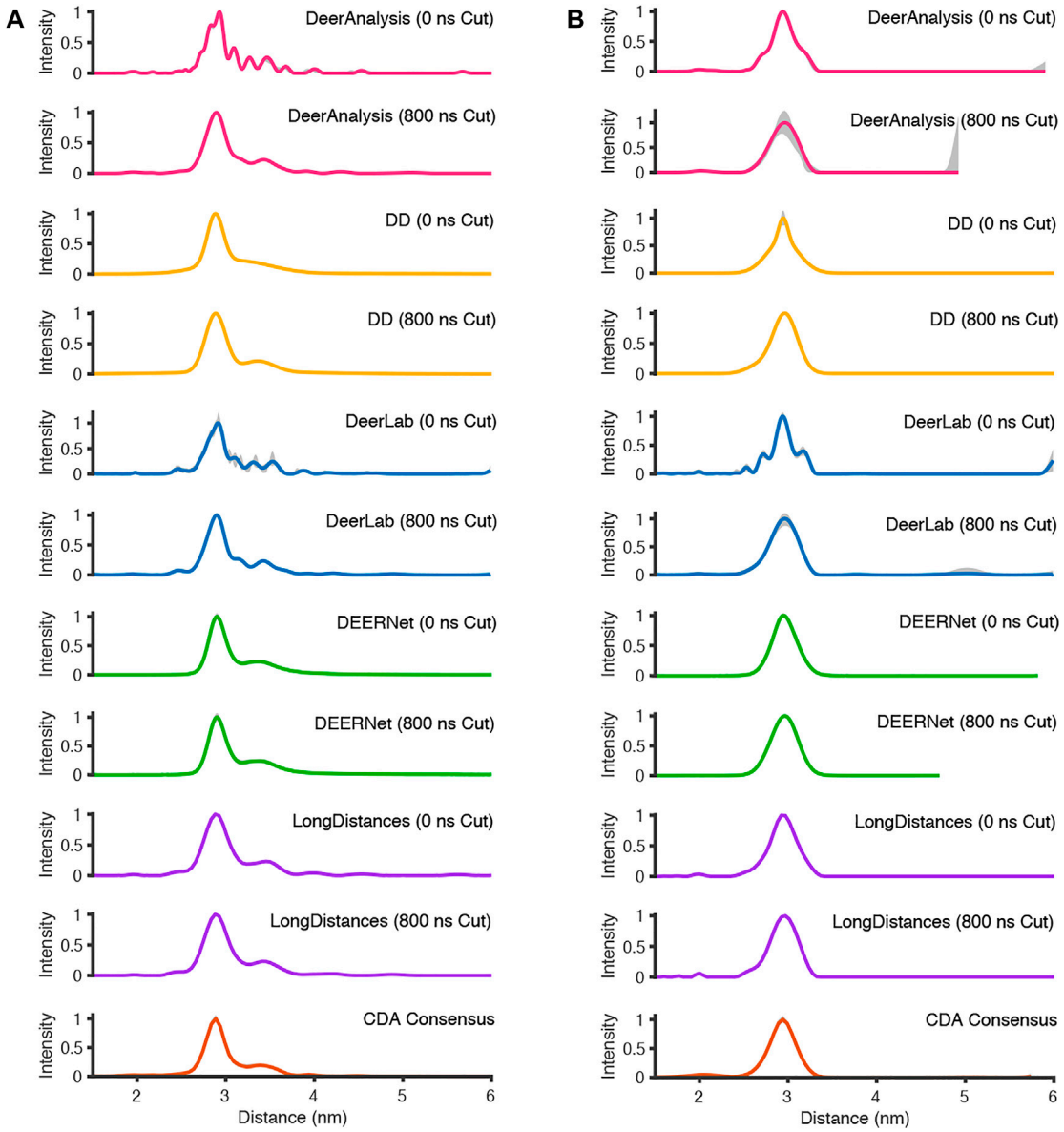

FIGURE 8 | The analysis of the experimental DEER time traces using the various analysis packages (CDA Consensus is the consensus result from ComparativeDeerAnalyzer) **(A)** AGAO; **(B)** DNA.

distribution from the DNA appeared to be more symmetric than the AGAO result. The mean of the main peak was at 2.94 nm with a standard deviation of just 0.01 nm. The FWHM for the main peak was determined to be 0.31 nm with a standard deviation of 0.07 nm. On inspection of the data in **Figure 8B** and the tabulated results, the variation chiefly came from the results from DD and DeerLab for the non-truncated data where the end artefacts were present.

4 DISCUSSION

We have demonstrated the use of six free-to-access packages for analyzing typical DEER time traces (pairwise spin-half dipolar interactions without orientation selection) to extract distance distributions. We have shown that all six are able to extract distances and provide uncertainty bounds of some kind.

Let us first consider accessibility. DeerAnalysis, DD and DEERNet require Matlab, and DEERNet requires several additional toolboxes. LongDistances and ComparativeDeerAnalyzer's Windows executable version are both standalone packages and so are free. DeerLab uses Python which is freely available. However, the wide range of uses of DeerLab, and the programming environment rather than a GUI, may also make it more intimidating for users without any prior experience of Python or DEER data analysis. DeerNet also does not have a GUI but offers almost no user input and so the

TABLE 6 | Results from each program for the AGAO data, with both 0 ns cut and 800 ns cut.

	Data truncated	Overall mean (nm)	Mean main peak (nm)	FWHM main peak (nm)
DeerAnalysis	0 ns	3.06	2.90	0.19
	800 ns	3.05	2.87	0.20
DD	0 ns	3.07	2.85	0.19
	800 ns	3.07	2.85	0.24
DeerLab	0 ns	3.08	2.86	0.15
	800 ns	3.05	2.88	0.20
DEERNet	0 ns	3.15	2.91	0.19
	800 ns	3.19	2.93	0.20
LongDistances	0 ns	3.06	2.90	0.27
	800 ns	3.05	2.90	0.27
CDA Consensus	11%	3.00	2.87	0.20
Mean of Results		3.08	2.88	0.21
Standard Deviation		0.05	0.03	0.04

TABLE 7 | Results from each program for the DNA data set, with both 0 ns cut and 800 ns cut.

	Data truncated	Overall mean (nm)	Mean main peak (nm)	FWHM main peak (nm)
DeerAnalysis	0 ns	2.93	2.95	0.27
	800 ns	2.93	2.95	0.37
DD	0 ns	2.94	2.94	0.24
	800 ns	2.93	2.93	0.34
DeerLab	0 ns	3.05	2.95	0.14
	800 ns	3.00	2.94	0.36
DEERNet	0 ns	2.97	2.96	0.32
	800 ns	2.95	2.95	0.36
LongDistances	0 ns	2.92	2.94	0.34
	800 ns	2.92	2.94	0.37
CDA Consensus	1%	2.90	2.93	0.33
Mean of Results		2.95	2.94	0.31
Standard Deviation		0.04	0.01	0.07

user only needs to follow some basic protocols. DeerAnalysis, DD, ComparativeDeerAnalyzer and LongDistances all have a graphical front end and are intuitive to use once the provided guidance has been read. We hope our guide on getting started will be a useful addition to the authors' own documentation and we feel it pertinent to emphasize that intuitive use does not necessarily mean best, or even correct, results.

To expand on the discussion of the authors' own documentation, we consider three areas: length, difficulty, and quality. DD has the shortest documentation of the packages, though it is easy to follow and clearly lays out the processes that should be undertaken by the user. DEERNet's documentation is short but clear and tells the user everything they need to know to do their own analyses. Further, the mathematics and neural network descriptions and explanations are neatly laid out in the associated publications. DeerAnalysis has an excellent manual included in its download zip file. The length is such that it could be read in full by the user with ease, and it plainly lays out every detail of the package. Likewise, the zip file contains a short and simple manual for the running of ComparativeDeerAnalyzer. DeerLab's documentation is extensive yet easy to follow and is split into digestible pages and sections. The documentation for LongDistances is split into sections for each of the GUI tabs where the functional processes are described succinctly and can additionally be accessed by pressing the "Help" button. In all cases direct communication with the authors when there are questions, is possible and even encouraged. DD, DeerAnalysis and ComparativeDeerAnalyzer documentation is provided in the download file, while the documentation for the other packages are web-based and linked to from the download pages.

While DeerAnalysis and DEERNet allow for editing of the final figure outputs of the results, the other packages do not. Therefore, for future presentation of the results, it is necessary for the results to be saved as text-type files, or similar, to facilitate this. DeerNet is the only program that does not allow for the results to be saved as text-type files for further figure preparation but the .mat saved file output can be saved as text files by the user. The saved files include meta-data such as modulation depths, with the exception of DeerLab, for which the user should note down the modulation depth. In our experience the programs all presented very similar values of the modulation depth parameter for a given data set, see **Tables 1–3**.

The next point to consider is the user input required to run the packages. All packages allow for truncation of the data set. We did

not run ComparativeDeerAnalysis in this way so as to leave that as a fully automatic process for our types of data. Truncating the artefactual experimental time traces was seen to alter the final results in our tests for the programs tested, except for DEERNet (**Figure 8**).

With the exception of DEERNet, which has no parameters to adjust, the packages offer the user the ability to define most of the variables, but following a workflow as defined by the user manuals and avoiding unnecessary variable changes should remove user-induced errors. Methods should be published with the data analysis results to aid reproducible and transparent data handling.

The programs, apart from DEERNet, allow for some variation in the background model with DeerLab, DeerAnalysis, and DD offering the most flexibility. Some preliminary checks with a simulated data set similar to the noise-free set used here but with a "2D" stretched exponential background (detailed in the Materials and Methods section) suggested that for small deviations from the homogeneous background the induced error was minor though the certainty bounds on the distance results improved when the correct background function was applied. The extent to which the packages are able to deal with different background forms has not been investigated more thoroughly in this work since there are a wide range of possible backgrounds, and the user is reminded to be cautious when analyzing non-standard DEER data in whatever form that takes. We note that the RIDME (relaxation induced dipolar modulation enhancement) experiment, which like DEER measures dipolar coupling frequency, suffers from a, to date, not well predicted background function and that DeerNet (and ComparativeDeerAnalyzer) has recently been expanded to include RIDMENets (Milikisyants et al., 2009; Keller et al., 2019; Ritsch et al., 2019; Keeley et al., 2022).

Now the discussion moves to the output results from the packages. First of all, we will consider the best fit results, not the uncertainty/error ranges. All the packages gave a good approximation of the distance distributions for the test data (simulated and experimental) used in this paper (see **Tables 4–7**). We found that by analyzing the data using multiple approaches the user is able to gain a better appreciation of the system being measured and assurance over the shape of distributions. For example, the body of results in **Figure 8** clearly indicates that the AGAO distance distribution is asymmetric and the spin-labelled DNA distribution is essentially Gaussian.

DeerAnalysis and DeerLab utilized Tikhonov regularization to stabilize the ill-posed inverse transformation of the time traces to distance distributions. They use different methods for optimizing the regularization parameter, which will ultimately affect the smoothness and broadness of the distribution. In the analysis of the simulated data (**Figure 7**), both programs are less robust when there is noise on the data though the overall distributions remain smooth. For the experimentally-collected DEER data, the approaches tend to give over-defined results until the data are truncated to remove end-artefacts, and then the smoothness of the presumed real underlying distribution is recovered. LongDistances' model-free fitting, which is similar to, but not the same as, Tikhonov regularization gives simulated data results that are smooth (as defined by the user) but are affected by the inclusion of noise in the data, much like DeerAnalysis and DeerLab. For the experimentally-collected results, the distributions remain relatively consistent, and appear largely unaffected by the 2 + 1 effect artefacts in the full-length result.

The parameterized-model approach of DD worked well for the data sets presented here with some improvement made when the spin-labelled DNA data was truncated. DEERNet gave consistent outputs for all the data sets. The results from DEERNet appear to stabilize the consensus result in ComparativeDeerAnalyzer.

While all the programs offer an approach to calculating uncertainty, we have seen in our tests that some of these are more useful than others. We found that running validation in DeerAnalysis was very prone to user input and quite slow compared to the other methods. The uncertainty in LongDistances often appeared to be underestimated with the methods we used, with all distance distributions given no, or very little, uncertainty. Meanwhile, the errors reported by DeerLab seem reasonable for the simulated and experimental data. DEERNet appears unaffected by the longer-time artefact, with its results remaining consistent (and presumably accurate) for the tests. The confidence intervals from DEERNet are negligible for the data sets used here.

The consensus result from ComparativeDeerAnalyzer is the result of using output from DEERNet to inform DeerLab. Only if DEERNet does not find a result will the default parameters for DeerLab follow those seen in the DeerLab documentation. This means that in general, the output from DeerLab in ComparativeDeerAnalyzer's report will not be the same as DeerLab calculations carried out in accordance with the documentation.

While each package has its disadvantages and downfalls, they each also have advantages and strengths. DeerAnalysis, in user-defined mode, gives the user both freedom and the ability to be constrained to automatically determined parameters, but falters due to over-complicated error analysis and the potential for user bias. The advantages of DD are that it has a simple and intuitive layout, and its focus on a single analysis method limits sources of confusion for new users. The user must decide how many Gaussians to include, which is a simple process that only requires the user to test different numbers of Gaussians to determine which achieves the lowest BIC value. For the data presented in this paper, DD worked well, though some user input to truncate data containing artefacts improved the final distance distributions. LongDistances in particular provided a friendly environment for understanding the role of the smoothness parameter on the appearance of the result with a simple slider bar and mouse-based control, possibly making it a good method for teaching students the effect of parameters on DEER data analysis. DeerLab has seemingly limitless uses and capabilities (see the documentation), but it may appear off-putting to non-coders and to those new to DEER data analysis. DEERNet, while being code-based in its Spinach-

form, is less intimidating and produced consistently accurate results with what appeared to be reasonable error estimates for our data sets. The downsides of DEERNet are that its nets are intrinsically somewhat blackbox, and in its full form it requires a number of Matlab toolboxes which may make its use prohibitive to some users. Incorporating parts of the last two packages and providing a "Consensus" result is ComparativeDeerAnalyzer. With the community-led white paper guiding users towards single-step analysis and multi-platform comparisons (Schiemann et al., 2021), future users may lean towards ComparativeDeerAnalyzer as a first port-of-call. We have however shown that the use of other packages may provide further insight into the data, and simpler approaches can lead to a better understanding of the final results. Also, the requirement to alter fitting parameters may be required in certain circumstances. It is not the purpose of this work to say any package is "better" than another, but rather to demonstrate how each package compares to the others, and how to get started in each.

DATA AVAILABILITY STATEMENT

Publicly available datasets were analyzed in this study. This data can be found here: https://doi.org/10.17630/99a46d98-c92d-439a-9462-31b660dcd952.

AUTHOR CONTRIBUTIONS

The work was conceived by RC and JEL. HR performed all the work shown in the manuscript with supervision by JEL. The manuscript was written by HR and JEL.

FUNDING

We acknowledge financial support from EPSRC (studentship to HR EP/R513337/1) and The Royal Society (URF to JEL URF150698). The UKRI block grant to St Andrews will be used to support the journal charges for open access.

ACKNOWLEDGMENTS

We would like to thank Professor Gunnar Jeschke, Luis Fábregas Ibáñez, Dr. Christian Altenbach, Dr. Ilya Kuprov and Professor Eric Hustedt for their invaluable help with their programs, and extensive comments and corrections on the original manuscript. For useful discussions we thank the St Andrews and Dundee (STAND) EPR groups. Simulated and experimental DEER time traces supporting this publication can be accessed at https://doi.org/10.17630/99a46d98-c92d-439a-9462-31b660dcd952.

REFERENCES

Abdullin, D., and Schiemann, O. (2020). Pulsed Dipolar EPR Spectroscopy and Metal Ions: Methodology and Biological Applications. *ChemPlusChem* 85, 353–372. doi:10.1002/cplu.201900705

Akaike, H. (1974). A New Look at the Statistical Model Identification. *IEEE Trans. Autom. Contr.* 19, 716–723. doi:10.1109/tac.1974.1100705

Altenbach, C. (2021). *Long Distances*. Available at: http://www.biochemistry.ucla.edu/Faculty/Hubbell/.

Altenbach, C. (2021). *Long Distances*. Available at: https://sites.google.com/site/altenbach/labview-programs/installation.

Altenbach, C. (2021). *Long Distances – A Program to Analyze DEER Data, Vol. 31*. New York: International EPR Society, EPR Newsletter, 12–13. Available at: https://ieprs.org/newsletter/vol-31-2/.

Bode, B. E., Margraf, D., Plackmeyer, J., Dürner, G., Prisner, T. F., and Schiemann, O. (2007). Counting the Monomers in Nanometer-Sized Oligomers by Pulsed Electron–Electron Double Resonance. *J. Am. Chem. Soc.* 129, 6736–6745. doi:10.1021/ja065787t

Brandon, S., Beth, A. H., and Hustedt, E. J. (2012). The Global Analysis of DEER Data. *J. Magnetic Reson.* 218, 93–104. doi:10.1016/j.jmr.2012.03.006

Chiang, Y.-W., Borbat, P. P., and Freed, J. H. (2005). The Determination of Pair Distance Distributions by Pulsed ESR Using Tikhonov Regularization. *J. Magnetic Reson.* 172, 279–295. doi:10.1016/j.jmr.2004.10.012

Edwards, T. H., and Stoll, S. (2018). Optimal Tikhonov Regularization for DEER Spectroscopy. *J. Magnetic Reson.* 288, 58–68. doi:10.1016/j.jmr.2018.01.021

Efron, B., and Tibshirani, R. (1986). Bootstrap Methods for Standard Errors, Confidence Intervals, and Other Measures of Statistical Accuracy. *Stat. Sci.* 1, 54–75. doi:10.1214/ss/1177013815

Fábregas Ibáñez, L., Jeschke, G., and Stoll, S. (2021). *Deer Lab*. Available at: https://jeschkelab.github.io/DeerLab/.

Fábregas Ibáñez, L., Jeschke, G., and Stoll, S. (2020). DeerLab: a Comprehensive Software Package for Analyzing Dipolar Electron Paramagnetic Resonance Spectroscopy Data. *Magn. Reson.* 1, 209–224.

Fábregas-Ibáñez, L., Jeschke, G., and Stoll, S. (2022). Compactness Regularization in the Analysis of Dipolar EPR Spectroscopy Data. *J. Magn. Reson.* 339, 107218.

Goldfarb, D., and Stoll, S. (2018). *EPR Spectroscopy: Fundamentals and Methods*. Hoboken, NJ, USA: Wiley.

Hardwick, J. S., Haugland, M. M., El-Sagheer, A. H., Ptchelkine, D., Beierlein, F. R., Lane, A. N., et al. (2020). 2′-Alkynyl Spin-Labelling Is a Minimally Perturbing Tool for DNA Structural Analysis. *Nucleic Acids Res.* 48, 2830–2840. doi:10.1093/nar/gkaa086

Haugland, M. M., Anderson, E. A., and Lovett, J. E. (2017). Tuning the Properties of Nitroxide Spin Labels for Use in Electron Paramagnetic Resonance Spectroscopy through Chemical Modification of the Nitroxide Framework. *Electron Paramagn. Reson.* 25, 1–34. doi:10.1039/9781782629436-00001

Hogben, H. J., Krzystyniak, M., Charnock, G. T. P., Hore, P. J., and Kuprov, I. (2011). Spinach - A Software Library for Simulation of Spin Dynamics in Large Spin Systems. *J. Magnetic Reson.* 208, 179–194. doi:10.1016/j.jmr.2010.11.008

Hustedt, E. (2018). *DD*. Available at: https://lab.vanderbilt.edu/hustedt-lab/software/dd/.

Hustedt, E. J., Stein, R. A., and Mchaourab, H. S. (2021). Protein Functional Dynamics from the Rigorous Global Analysis of DEER Data: Conditions, Components, and Conformations. *J. Gen. Physiol.* 153, E201711954. doi:10.1085/jgp.201711954

Hustedt, E. J., Marinelli, F., Stein, R. A., Faraldo-Gómez, J. D., and Mchaourab, H. S. (2018). Confidence Analysis of DEER Data and its Structural Interpretation with Ensemble-Biased Metadynamics. *Biophysical J.* 115, 1200–1216. doi:10.1016/j.bpj.2018.08.008

Jeschke, G. (2022). *Deer Analysis 2022*. Available at: https://epr.ethz.ch/software.html.

Jeschke, G., Koch, A., Jonas, U., and Godt, A. (2002). Direct Conversion of EPR Dipolar Time Evolution Data to Distance Distributions. *J. Magn. Reson.* 155, 72–82. doi:10.1006/jmre.2001.2498

Jeschke, G., Chechik, V., Ionita, P., Godt, A., Zimmermann, H., Banham, J., et al. (2006). DeerAnalysis2006-a Comprehensive Software Package for Analyzing Pulsed ELDOR Data. *Appl. Magn. Reson.* 30, 473–498. doi:10.1007/bf03166213

Jeschke, G. (2012). DEER Distance Measurements on Proteins. *Annu. Rev. Phys. Chem.* 63, 419–446. doi:10.1146/annurev-physchem-032511-143716

Keeley, J., Choudhury, T., Galazzo, L., Bordignon, E., Feintuch, A., Goldfarb, D., et al. (2022). Neural Networks in Pulsed Dipolar Spectroscopy: a Practical Guide. *J. Magn. Reson.* 338, 107186. doi:10.1016/j.jmr.2022.107186

Keller, K., Qi, M., Gmeiner, C., Ritsch, I., Godt, A., Jeschke, G., et al. (2019). Intermolecular Background Decay in RIDME Experiments. *Phys. Chem. Chem. Phys.* 21, 8228–8245. doi:10.1039/c8cp07815g

Kuprov, I. (2021). *Spinach*. Available at: http://spindynamics.org/group/?page_id=12.

Martin, R. E., Pannier, M., Diederich, F., Gramlich, V., Hubrich, M., and Spiess, H. W. (1998). Determination of End-To-End Distances in a Series of TEMPO Diradicals of up to 2.8 Nm Length with a New Four-Pulse Double Electron Electron Resonance Experiment. *Angew. Chem. Int. Ed.* 37, 2833–2837. doi:10.1002/(sici)1521-3773(19981102)37:20<2833:aid-anie2833>3.0.co;2-7

Milikisyants, S., Scarpelli, F., Finiguerra, M. G., Ubbink, M., and Huber, M. (2009). A Pulsed EPR Method to Determine Distances between Paramagnetic Centers with Strong Spectral Anisotropy and Radicals: the Dead-Time Free RIDME Sequence. *J. Magnetic Reson.* 201, 48–56. doi:10.1016/j.jmr.2009.08.008

Milov, A., Salikhov, K., and Shirov, M. (1981). Application of the Double Resonance Method to Electron Spin Echo in a Study of the Spatial Distribution of Paramagnetic Centers in Solids. *Fiz. Tverd. Tela* 23, 975–982.

Milov, A. D., Ponomarev, A. B., and Tsvetkov, Y. D. (1984). Electron-electron Double Resonance in Electron Spin Echo: Model Biradical Systems and the Sensitized Photolysis of Decalin. *Chem. Phys. Lett.* 110, 67–72. doi:10.1016/0009-2614(84)80148-7

Ritsch, I., Hintz, H., Jeschke, G., Godt, A., and Yulikov, M. (2019). Improving the Accuracy of Cu(ii)-Nitroxide RIDME in the Presence of Orientation Correlation in Water-Soluble Cu(ii)-Nitroxide Rulers. *Phys. Chem. Chem. Phys.* 21, 9810–9830. doi:10.1039/c8cp06573j

Russell, H., Stewart, R., Prior, C., Oganesyan, V. S., Gaule, T. G., and Lovett, J. E. (2021). DEER and RIDME Measurements of the Nitroxide-Spin Labelled Copper-Bound Amine Oxidase Homodimer from Arthrobacter Globiformis. *Appl. Magn. Reson.* 52, 995–1015. doi:10.1007/s00723-021-01321-6

Schiemann, O., Heubach, C. A., Abdullin, D., Ackermann, K., Azarkh, M., Bagryanskaya, E. G., et al. (2021). Benchmark Test and Guidelines for DEER/PELDOR Experiments on Nitroxide-Labeled Biomolecules. *J. Am. Chem. Soc.* 143, 17875–17890. doi:10.1021/jacs.1c07371

Schwarz, G. (1978). Estimating the Dimension of a Model. *Ann. Stat.* 6, 461–464. doi:10.1214/aos/1176344136

Stein, R. A., Beth, A. H., and Hustedt, E. J. (2015). A Straightforward Approach to the Analysis of Double Electron-Electron Resonance Data. *Meth. Enzymol.* 563, 531–567. doi:10.1016/bs.mie.2015.07.031

Teucher, M., and Bordignon, E. (2018). Improved Signal Fidelity in 4-pulse DEER with Gaussian Pulses. *J. Magnetic Reson.* 296, 103–111. doi:10.1016/j.jmr.2018.09.003

Worswick, S. G., Spencer, J. A., Jeschke, G., and Kuprov, I. (2018). Deep Neural Network Processing of DEER Data. *Sci. Adv.* 4, eaat5218. doi:10.1126/sciadv.aat5218

Conflict of Interest: The authors declare that the research was conducted in the absence of any commercial or financial relationships that could be construed as a potential conflict of interest.

Publisher's Note: All claims expressed in this article are solely those of the authors and do not necessarily represent those of their affiliated organizations, or those of the publisher, the editors and the reviewers. Any product that may be evaluated in this article, or claim that may be made by its manufacturer, is not guaranteed or endorsed by the publisher.

frontiers | Frontiers in Molecular Biosciences

ORIGINAL RESEARCH
published: 06 June 2022
doi: 10.3389/fmolb.2022.842041

Characterization and Value Assignment of a Monoclonal Antibody Reference Material, NMIJ RM 6208a, AIST-MAB

Tomoya Kinumi[1,2], Kazumi Saikusa[1], Megumi Kato[1], Reiko Kojima[2], Chieko Igarashi[2], Naohiro Noda[2,3] and Shinya Honda[2,3]*

[1]National Metrology Institute of Japan (NMIJ), National Institute of Advanced Industrial Science and Technology (AIST), Tsukuba, Japan, [2]Manufacturing Technology Association of Biologics (MAB), Kobe, Japan, [3]Biomedical Research Institute, National Institute of Advanced Industrial Science and Technology (AIST), Tsukuba, Japan

Monoclonal antibodies have been established as the largest product class of biopharmaceuticals. Since extensive characterization is required for development and quality control of monoclonal antibody, a widely available reference material (RM) is needed. Herein, a humanized IgG1κ monoclonal antibody reference material, RM 6208-a, AIST-MAB, was established by the National Metrology Institute of Japan, National Institute of Advanced Industrial Science and Technology (NMIJ/AIST). The monoclonal antibody solution was produced as a pharmaceutical grade using a Chinese hamster ovary-derived cell line. The assigned indicative value represents the concentration of the antibody with a heterotetrameric structure including oligomeric forms, determined by an amino acid analysis using isotope dilution mass spectrometry, and their homogeneity and stability were assessed. In addition to antibody concentration, various physicochemical properties, including peptide mapping data, charge variants, and aggregates, were examined. This RM is intended for use in validation of analytical procedures and instruments such as a system suitability test for quantification of antibody. It is also intended for comparing and evaluating the results of antibody analyses across analytical methods and analytical laboratories such as inter-laboratory comparison. Both the material and the set of data from our study provide a tool for an accurate and reliable characterization of product quality attributes of monoclonal antibodies in biopharmaceutical and metrology communities.

Keywords: monoclonal antibody, biopharmaceutical, reference material, amino acid analysis, physicochemical property, antibody concentration

OPEN ACCESS

Edited by:
Milena Quaglia,
National Measurement Laboratory at LGC, United Kingdom

Reviewed by:
Mark Lowenthal,
National Institute of Standards and Technology, United States
Kathleen L. Hefferon,
Cornell University, United States

****Correspondence:***
Tomoya Kinumi
t.kinumi@aist.go.jp

Specialty section:
This article was submitted to Structural Biology, a section of the journal Frontiers in Molecular Biosciences

Received: *23 December 2021*
Accepted: *21 April 2022*
Published: *06 June 2022*

Citation:
Kinumi T, Saikusa K, Kato M, Kojima R, Igarashi C, Noda N and Honda S (2022) Characterization and Value Assignment of a Monoclonal Antibody Reference Material, NMIJ RM 6208a, AIST-MAB. Front. Mol. Biosci. 9:842041. doi: 10.3389/fmolb.2022.842041

Abbreviations: CD, circular dichroism; CEX, cation exchange chromatography; CHO, Chinese hamster ovary; cIEF, capillary isoelectric focusing; CRM, certified reference material; DLS, dynamic light scattering; DTT, dithiothreitol; ELISA, enzyme-linked immunosorbent assay; FI, flow imaging; GAPDH, glyceraldehyde-3-phosphate dehydrogenase; HC, heavy chain; HCP, host cell–derived protein; ISO, International Organization for Standardization; LC, light chain; LC-FL, liquid chromatography–fluorescent detection; LC-MS, liquid chromatography–mass spectrometry; LC-MS/MS, liquid chromatography–tandem mass spectrometry; NMIJ, National Metrology Institute of Japan; NIST, National Institute of Standards and Technology; NTA, nano tracking analysis; PTM, posttranslational modification; qPCR, quantitative polymerase chain reaction; RM, reference material; SEC, size-exclusion chromatography; SEC-MALS, size exclusion chromatography–multi-angle static light scattering; TCEP, tris(2-carboxyethyl)phosphine; TSA, thermal shift assay; UV, ultraviolet.

1 INTRODUCTION

Monoclonal antibodies have dominated the biopharmaceutical market among various modalities. The number of approved antibody drugs in the US and the EU has increased nearly three-fold from 2010 to 2019 (Kaplon et al., 2020). In 2020, it is reported that 15 antibody therapeutics have been approved worldwide (Kaplon and Reichert, 2021). Because the production of antibody drug utilizes the biosynthetic process of living organisms, the design and management of the development and manufacturing process affect the quality of the final product directly. Moreover, the quality among different production lots differs considerably even if the same production cells are used, and properties of the follow-on biologics (biosimilars) made by different manufacturers differ from those of the original products.

Therefore, physicochemical properties such as structural heterogeneity and aggregation should be evaluated in detail to demonstrate product consistency and equivalence. To address this situation, the International Council for Harmonisation of Technical Requirements for Pharmaceuticals for Human Use (ICH) Q6B provides guidelines for specification on the characterization of biopharmaceuticals, and the establishment of acceptance criteria as well as analytical procedures (ICH Q6B, 1999). In terms of primary structure, structural heterogeneity includes posttranslational modifications (PTMs), such as glycosylation, disulfide bond mismatch, deamidation of asparagine residues, oxidation of methionine and tryptophan, glycosylation, and cleavage of the polypeptide chain (Liu et al., 2008; Beck et al., 2013). The variety of higher-order structures, such as denaturation, misfolding, and aggregation, should also be evaluated. The results of these quality attributes may vary depending on the measurement method, and many technologies are under development (Le Basle et al., 2020).

National metrology institutes (NMIs) have been leading to establish traceable measurement to a known reference, particularly focusing on the development of a reference material (RM) traceable to Système International d'Unités (SI). The provision of a reliable RM and calibration service by NMIs is defined by international standards, such as ISO 17025 and ISO 17034, which provide requirements to support best practices in production and maintenance of the RM and quality system (ISO 17034, 2016; ISO/IEC 17025, 2017). Although different platforms exist among biopharmaceutical and metrology communities, there is need for a well-characterized and widely available monoclonal antibody RM that validates methods and measurement results for the development of an analytical technology. Among the various properties, antibody concentration is the fundamental basis for many properties, including physicochemical properties, biological activities, and immunochemical properties, as well as any quantitative assays of protein–protein interaction and protein–ligand interaction parameters such as binding constant and enzyme activity.

The National Institute of Standards and Technology (NIST), first released an antibody RM, namely, NISTmAb (RM 8671), which is a recombinant humanized IgG1κ solution, and whose assigned antibody concentration was determined by absorption spectrometry (Schiel et al., 2018) as the reference value, and size heterogeneity (Turner et al., 2018) and charge heterogeneity (Turner and Schiel, 2018) were also assigned as its reference values. Moreover, this material provides a case study of important quality characteristics measured through collaborative measurements involving pharmaceutical companies and research institutes, in addition to the reference values determined independently by NIST (Schiel et al., 2014; 2015a; 2015b).

In antibody analysis, there is an increasing demand for a widely available and metrologically reliable monoclonal antibody RM. The National Metrology Institute of Japan/National Institute of Advanced Industrial Science and Technology (NMIJ/AIST) has developed a RM of a monoclonal antibody solution, namely, NMIJ RM 6208a, AIST-MAB. This RM is a recombinant monoclonal antibody (humanized IgG1κ) solution in 10 mmol/L potassium phosphate buffer (pH 7.0) produced from Chinese hamster ovary (CHO)–derived cell line. The assigned indicative value of this material represents the antibody concentration with a heterotetrameric structure including oligomeric forms determined by an amino acid analysis. We also characterized a wide variety of physicochemical properties of this material in addition to the antibody concentration. This RM is intended for use in validation of analytical procedures and instruments such as a system suitability test for quantification of antibody. It is also intended for comparing and evaluating the results of antibody analyses across analytical methods and analytical laboratories such as inter-laboratory comparison. Thus, the material can be used for various quality analyses rather than for a specific biopharmaceutical product.

Herein, we report the development of AIST-MAB. The assigned indicative value represents the concentration of the antibody, which was determined by two independent amino acid analyses based on isotope dilution mass spectrometry using liquid phase and gas phase hydrolyses with liquid chromatography–tandem mass spectrometry (LC/MS/MS). The amino acid analysis using isotope dilution mass spectrometry has been used as a "gold standard" for the method of traceable protein quantification (Burkitt et al., 2008; Munoz et al., 2011) and for the value assignment of various certified reference materials from NMIJ, including C-peptide (Kinumi et al., 2012), C-reactive protein (Kato et al., 2015), and human serum albumin (Kinumi et al., 2017). Along with a quantitative analysis by the amino acid analysis, homogeneity and stability tests were conducted, and values were assigned in accordance with ISO 17034. The resulting indicative value of this material has been determined to be 5.00 (± 0.19) g/L, the number following ± represents the expanded uncertainty with a coverage factor $k = 2$ giving a level of confidence of approximately 95%. Moreover, we describe the value assignment as well as the analytical results for various physicochemical properties of AIST-MAB in detail.

2 MATERIALS AND METHODS

2.1 Materials

Acetonitrile and formic acid for an LC-MS analysis (LC-MS grade) were obtained from Fujifilm Wako Pure Chemical

(Japan). The reagents used were of the highest grade obtained from Fujifilm Wako Pure Chemical (Japan), unless otherwise stated. All the aqueous solutions and solvents were prepared using ultrapure water purified with the Milli-Q purification system (Merck Millipore, USA).

2.2 Preparation of the Candidate Material

The candidate material was expressed using the CHO-derived cell line. After fermentation of the antibody-producing CHO cell line in a serum-free culture medium for 7 days using the Allegro XRS 25 Bioreactor (Pall, USA), the culture supernatant was prepared using the Millistak Pod depth filtration system (EMD Millipore, USA) to remove cells and debris. Thereafter, it was purified further by three-step chromatographic technique using protein A affinity (RTP MabSelect SuRe, Cytiva, USA), anion-exchange (RTP Capto Q, Cytiva, USA), and cation-exchange (RTP Capto S, Cytiva, USA) columns. The purified material was treated using the Planova 20 N virus removal filter (Asahi Kasei Medical, Japan), concentrated through Pellicon ultrafiltration (EMD Millipore, USA) and buffer exchange to 10 mmol/L potassium phosphate buffer (pH 7.0) in a good manufacturing practice (GMP) grade facility. The raw material (1 ml) was dispensed into polypropylene vials sterilely using a Microlab STARlet 8ch liquid handling system (Hamilton, USA) with a FluidX XSD-48Pro automated capper/decapper system (Azenta Life Sciences, USA) and stored at −80°C. These processes were performed at Manufacturing Technology Association of Biologics at Kobe, Japan.

2.3 Structural Analyses *via* Mass Spectrometry

LC-MS for structural analyses was performed using a maXis II electrospray ionization quadrupole time-of-flight mass spectrometer (Bruker, Germany) in a positive ion mode coupled with an LC-30A Nexera HPLC system (Shimadzu, Japan). The data were analyzed using Data Analysis 4.3 software (Bruker, Germany).

2.3.1 Intact Mass Spectrometry

We injected 1 µl of the candidate RM into an LC-MS system using the AQUITY UPLC Protein BEH C4 column (1.7 µm, 2.1 mm diameter × 100 mm length, Waters, USA), mobile phase A: 0.1% formic acid/H_2O, B: 0.1% formic acid/acetonitrile, flow rate: 0.2 ml/min, column temperature: 60°C, and gradient condition: 5–15 %B in 15 min. The mass spectrometer was operated under the following conditions: capillary voltage: 4500 V, nebulizer gas: 1.2 bar, dry gas: 6 L/min, isCID: 30 eV, quadrupole ion energy 4 eV, collision energy: 8 eV, mass range: *m/z* 500–3000, and spectra rate: 3 Hz. The mass spectrometer was calibrated using ESI-L Low concentration tuning mix (G1969-85000, Agilent Technologies, USA).

2.3.2 LC-MS Measurement for Light and Heavy Chains

To 5 µl of the candidate RM, 50 µl of water and 5 µl of 500 mmol/L TCEP [tris(2-carboxyethyl)phosphine] were added and incubated at 37°C for 2 h. A volume of 2 µl of material was injected into the LC-MS system. The gradient condition used was 5 %B 2 min, 5–15 %B 1 min, 15–25 %B 3 min, and 25–35 %B 15 min, and other measurement conditions were same as intact mass spectrometry.

2.3.3 LC-MS Measurement for IdeS Digestion

To 50 µl of the candidate RM, 50 µl of 50 mmol/L phosphate buffer and 4 µl of IdeS protease (IdeS FabRICATOR, 270 U, Sigma-Aldrich, USA) were added and incubated at 37°C for 1 h. The reduced form was obtained by adding an additional 5 µl of 500 mmol/L TCEP prior to IdeS digestion and incubation at 37°C for 1 h. A volume of 3 µl of the resulted solution was injected into the LC-MS system. The measurement conditions were same as those used for light and heavy chains.

2.3.4 Peptide Mapping

To 100 µl of 8 mol/L guanidine hydrochloride, 1 mmol/L ethylenediaminetetraacetic acid, 250 mmol/L Tris-HCl (pH 8.0), and 20 µl of the candidate RM were added, and then 5 µl of 500 mmol/L dithiothreitol (DTT, Sigma-Aldrich, USA) was added and incubated at 37°C for 1 h. Thereafter, the reaction mixture was incubated for 1 h in the dark at room temperature with 12 µl of 500 mmol/L iodoacetic acid, followed by 5 µl of 500 mmol/L DTT. After desalting using a NAP-5 gel filtration column (Cytiva, USA), trypsin or Lys-C (lysylendopeptidase) or Glu-C (mass spectrometry grade, FUJIFILM Wako Pure Chemical, Japan) was added to a 300 µl fraction of desalted NAP-5 elutant at 1:25 (enzyme: substrate) ratio of protein content and incubated at 37°C overnight for trypsin, Lys-C, and Glu-C, or 1 h for trypsin digestion. The reaction was terminated by adding 1 µl trifluoroacetic acid, and then 5 µl was injected into LC-MS/MS for the measurement. For peptide mapping by trypsin in a non-reduced condition, the sample was prepared using the aforementioned procedure without reduction and alkylation steps by DTT and iodoacetic acid. The measurement conditions were as follows: the chromatography column used was AQUITY UPLC Peptide BEH C18 (3.5 µm, 2.1 mm diameter × 150 mm length, Waters, USA); mobile phase A: 0.1% formic acid/H_2O; B: 0.1% formic acid/acetonitrile; flow rate: 0.2 ml/min; column temperature: 45°C; and gradient condition: 2 %B 3 min, 2–7 %B 1 min, 7–10 %B 4 min, 10–25 %B 32 min, and 25–38 %B 15 min. The mass spectrometer was operated under the following conditions: capillary voltage: 4500 V, nebulizer gas: 1.2 bar, dry gas: 6 L/min, isCID: 0 eV, quadrupole ion energy 5 eV, collision energy: 10 eV, mass range: *m/z* 100–3500, and spectra rate: 5 Hz. The LC-MS/MS data were acquired by a data-dependent MS/MS mode; precursor ions: number of precursor 2, active exclusion exclude after two spectra, release after 0.1 min, and reconsider precursor 2.0. The mass spectrometer was calibrated using 5 mmol/L ammonium formate in 50% isopropanol/water by internal calibration.

2.4 Chromatography

Cation exchange chromatography (CEX) was performed using an LC-20A Prominence HPLC system with an ultraviolet (UV) detector (Shimadzu, Japan) and a BioPro IEX SF column

(5 μm, 4.6 mm diameter × 100 mm length, YMC, Japan). A volume of 5 μl of the candidate RM was injected into the LC-UV system. The measurement conditions were as follows: mobile phase A: 20 mmol/L 2-(*N*-morpholino) ethanesulfonic acid (MES) (pH 6.0), mobile phase B: 20 mmol/L MES, 200 mM NaCl (pH 6.0), flow rate: 0.5 ml/min, column temperature: 30°C, and gradient condition: 10–80 %B 30 min. Absorbance was detected at a wavelength of 215 nm. The performance criteria were set to 5.6 (± 1.2) min for α-chymotrypsinogen A from bovine pancreas (Sigma-Aldrich, USA), and 23.2 (± 0.9) min for equine myoglobin (Serva, USA) based on two sigmas of averaged retention time.

Size-exclusion chromatography (SEC) was performed using the LC-UV system used for CEX. The chromatography column used was a TSK gel G3000SW$_{XL}$ (5 μm, 7.8 mm diameter × 300 mm length, TOSOH, Japan). A volume of 10 μl of the candidate RM was injected into the LC-UV system. The measurement conditions were as follows: 100 mmol/L sodium phosphate buffer containing 100 mmol/L Na_2SO_4 (pH6.8) in isocratic elution, flow rate: 0.4 ml/min, and column temperature: 25°C. Absorbance was detected at a wavelength of 280 nm. The system performance was evaluated using molecular weight marker proteins for SEC from Oriental Yeast (Japan) consisting of five proteins. The performance criteria based on two sigmas of averaged retention time were set to 20.0 (± 0.1) min for glutamate dehydrogenase, 23.1 (± 0.1) min for lactose dehydrogenase, 24.9 (± 0.1) min for enolase, 27.2 (± 0.1) min for myokinase, and 28.9 (± 0.1) min for cytochrome C.

2.5 Electrophoreses

Microchip electrophoresis was performed using the LabChip GXII Touch24 electrophoresis system (PerkinElmer, USA). The sample solution was prepared by using 2 μl of diluted the candidate RM at approximately 2.5 mg/g using the Protein Express Assay Reagent Kit (PerkinElmer, USA) at 70°C for 10 min, according to the manufacturer's instruction. The results of the three lanes were averaged to obtain the measurement results. Measured molecular masses were calibrated using a molecular weight marker supplied with the Protein Express Kit (PerkinElmer, USA). The standard deviation of the measured molecular masses was confirmed to be less than 5%.

Capillary isoelectric focusing was performed using an iCE3/Alcott720NV capillary isoelectric focusing system with Fc cartridge (100 μm diameter × 50 mm length, ProteinSimple, USA). The sample solution was prepared with 0.4 mg/mL as the final concentration of the candidate RM in 4% pharmalyte (pH 3–10), 0.35% methylcellulose, and 10 mmol/L arginine solution. Electrophoresis conditions were 1500 V for 1 min while prefocusing and 3 kV for 4.5 min when focusing on detection at 280 nm. The measurements were repeated thrice. Samples were measured after confirming that the isoelectric points of human hemoglobin (Sigma-Aldrich, USA) were within 7.1 ± 0.1 and 7.2 ± 0.1, and the variation in triplicate measurements of the peak height of a high pI marker (pI 9.77) supplied with High pI marker (102219, ProteinSimple, USA) was less than 10%.

2.6 Glycan Mapping

Sample preparation including hydrolysis by peptide *N*-glycosidase F (PNGaseF) and 2-aminobezamide (2-AB) derivatization of glycans from the candidate RM was performed using the EZGlyco mAb-N Kit with 2-AB (BS-X4410, Sumitomo Bakelite, Japan). A volume of 2 μl of the resulted glycan mixture solution obtained with 8 μl of candidate RM was injected into an LC-fluorescence detection (LC-FL) system for analysis. The LC-FL system used was a Nexera 30A HPLC system with a fluorescence detector (Shimadzu, Japan) with an AQUITY UPLC Protein BEH Amide column (1.7 μm, 2.1 mm diameter × 150 mm length, Waters, USA). The measurement conditions were as follows: mobile phase A: 100 mmol/L ammonium formate (pH 4.5), B: acetonitrile, flow rate: 0.2 ml/min, column temperature: 45°C, gradient condition: 75–50 %B 50 min, fluorescent detection: excitation at 330 nm, and detection at 420 nm.

2.7 Analysis of Impurities

2.7.1 Host Cell–Derived Protein Assay

Residual amount of HCP was quantified by enzyme-linked immunosorbent assay (ELISA) using a commercial ELISA kit, CHO Host Cell Proteins 3rd Generation F550 (Cygnus Technologies, USA), according to the manufacturer's instruction. In brief, 100 μl of Anti-CHO-HRP was added into each well of an anti-CHO–coated 96-well plate followed by adding 50 μL of triplicate samples (n = 3), standards, or blank controls were added in each well and incubated for 3 h at room temperature on a plate shaker. Thereafter, the plates were washed four times with 350 μl of wash solution. To each well, 100 μl of HRP substrate, 3,3′,5,5′-tetramethyl-benzidene, was added and incubated at 25°C for 30 min before adding the stop solution. The absorbance of the reactant at 450 nm in each well was recorded using an Enspire 2300 multilabel plate reader (PerkinElmer, USA).

2.7.2 Protein A Assay

Residual amount of protein A was quantified *via* the amplified luminescent proximity homogeneous assay (AlphaLISA®) using a commercial kit, Residual Protein A kit AL287 (PerkinElmer, USA), according to the manufacturer's instruction (Protocol 2). In brief, 60 μl of triplicate samples (n = 3) or standards were mixed with 120 μl of 3× dissociation buffer in a tube, heated at 98°C for 60 min, and centrifuged for 5 min at ≥ 200 *g*. Thereafter, 10 μl of supernatants were transferred to each well of a 96-well plate, and then 20 μl of 5× anti-protein A acceptor beads were added and the mixture was incubated at room temperature for 30 min. Subsequently, 20 μl of 5× biotinylated antibody anti-protein A were added into each well, followed by incubation at room temperature for 60 min, after which 50 μl of 2× SA-donor beads were added, and the mixture was incubated at room temperature for 30 min in the dark. The emission from the donor beads at 615 nm was recorded using an Enspire 2300 multilabel plate reader.

2.7.3 Host Cell–Derived DNA Assay

The residual amount of host cell–derived DNA was quantified *via* the quantitative polymerase chain reaction (qPCR) using a StepOnePlus Real-Time PCR System (Applied Biosystems, USA). First, DNA was extracted using a commercial kit, DNA Extraction and Amplification Kit D555T (Cygnus Technologies, USA), according to the manufacturer's instruction. In brief, 500 µl of duplicate samples (n = 2), samples for addition recovery tests (n = 2), standard, and control were placed in a 2 ml microfuge tubes, and then 25 µl of 1× Proteinase K was added to them. The tubes were gently vortexed for 5 s, incubated at 60°C for 30 min, and centrifuged for 1 min at 10,000 rpm. After this, 500 µl of extraction buffer was added to the tubes, which were vortexed for 10 s, and 1 ml of precipitation buffer was added to the tubes and vortexed for 10 s. The tubes were incubated for 10 min and centrifuged at 10,000 rpm for 10 min. After decanting supernatants, 1.5 ml of DNA wash buffer was introduced to each tube, followed by vortexing for 5 s, incubating at room temperature for 20 min, and centrifuging at 10,000 rpm for 5 min. After decanting supernatants again, pellets were re-suspended in 50 µl of DNA TE buffer and incubated at 50°C for 2–3 min to dissolve CHO DNA completely. Thereafter, DNA amplification was performed using TB Green Premix Ex Taq GC (TaKaRa, Japan) and custom primers for glyceraldehyde-3-phosphate dehydrogenase (GAPDH) gene as the target region. In brief, 10 µl of samples, samples for addition recovery tests, standard, and control were added to 25 µl of the PCR mixtures containing SYBR Premix Ex Taq GC, Rox reference dye, and GAPDH primers and transferred to each well of a qPCR assay plate. The PCR amplification parameters were as follows: heating stage: 95°C for 30 s, cycling stage: 45 cycles at 95°C for 10 s and 60°C for 30 s, and melting curve stage: 95°C for 15 s followed by 60°C for 60 s and 95°C for 15 s. The samples were tested in quadruplicate (n = 4) in the qPCR measurement.

2.7.4 Endotoxin Assay

Endotoxin was quantified by turbidimetry using Toxinometer ET-6000 (FUJIFILM Wako Pure Chemical, Japan) with Limulus ES-II Single Test (FUJIFILM Wako Pure Chemical, Japan), according to Japanese Pharmacopoeia (Japanese Pharmacopoeia 2016). In brief, 200 µl of duplicate samples (n = 2) or standards were mixed with the Limulus amebocyte lysate agents, incubated at 37 ± 1 °C for 60 ± 2 min in the toxinometer, and subsequently subjected to turbidimetric analysis.

2.8 Preparation of Standard Solutions and Blend Mixtures for Amino Acid Analyses

The standard solutions of natural amino acids were gravimetrically prepared by dissolving the following NMIJ CRMs in 10 mmol/L HCl: L-aspartic acid (NMIJ CRM 6027a), L-glutamic acid (NMIJ CRM 6026a), L-proline (NMIJ CRM 6016a), L-valine (NMIJ CRM 6015a), L-isoleucine (NMIJ CRM 6013a), L-leucine (NMIJ CRM 6012a), L-phenylalanine (NMIJ CRM 6014a), and L-alanine (NMIJ CRM 6011a). The standard mixture of amino acids was gravimetrically prepared by mixing the standard solution of each amino acid in the same molar ratio of as that of each amino acid composition in the monoclonal antibody molecule. The following isotopically labeled amino acids (Cambridge Isotope Laboratories, USA) were used as the internal standard: L-$^{13}C_4{}^{15}N$-Asp, L-$^{13}C_5{}^{15}N$-Glu, L-$^{13}C_5{}^{15}N$-Pro, L-$^{13}C_6{}^{15}N_2$-Lys, L-$^{13}C_5{}^{15}N$-Val, L-$^{13}C_6{}^{15}N$-Ile, L-$^{13}C_6{}^{15}N$-Leu, L-$^{13}C_9{}^{15}N$-Phe, and L-$^{13}C_3{}^{15}N$-Ala. The candidate RM (0.1 ml) and the mixture of isotopically labeled amino acids (0.1 ml) were gravimetrically dispensed into a glass vial. The dispensed solutions were dried with gentle nitrogen flow. Calibration blends were gravimetrically prepared by mixing the standard mixture of natural amino acids and mixture of isotopically labeled amino acid solutions. The calibration blends (0.2 ml) were dispensed into a glass vial and dried by gentle nitrogen flow.

2.9 Amino Acid Analyses

For liquid-phase hydrolysis, dried sample blend and calibration blend in a glass vial were dissolved by adding 0.2 ml of 6 mol/L HCl and 0.1% phenol. Samples were hydrolyzed at 150°C for 1 and 3 h, 160°C for 1 and 3 h, and 170°C for 1 and 3 h using an ETHOS One microwave digestion system (Milestone SRL, Italy) after purging with nitrogen. The hydrolysate was analyzed by pre-column derivatization with *N*-butylnicotinic acid *N*-hydroxysuccinimide ester iodide and measured *via* LC-MS/MS under the selected ion monitoring (SRM) mode.

For gas-phase hydrolysis, the dried sample in the glass vial was hydrolyzed under the gas phase by 6 mol/L HCl and 2% phenol at 130°C for 18, 24, and 48 h as well as 150°C for 18, 24, and 48 h using a Pico-tag workstation hydrolysis system (Waters, USA) after purging with nitrogen. The hydrolysate was analyzed by hydrophilic interaction chromatography (HILIC)-MS/MS under the SRM mode. The detailed measurement conditions for amino acid analyses are described in the supplementary material.

2.10 Homogeneity and Stability Tests

Homogeneity was assessed by measuring the relative area percentage of the main peak obtained by CEX in triplicate for twelve selected vials.

Stability was evaluated as acceleration (stored at 4, or 25°C), long-term (stored at −80°C), short-term (stored at −20°C), and freeze-thaw cycles (up to five times) tests. The long-term stability test was performed *via* CEX and UV absorption at 280 nm (see the below section) using a previous lot of the preceding product. The acceleration, short-term, and freeze-thaw cycles tests were performed *via* CEX, SEC, and UV absorption at 280 nm using the candidate RM.

2.11 Density Measurement

The density of the candidate RM was measured using a vibration type of the density meter (DMA5000EX, Anton Paar, Austria) in triplicate. Calibration was performed using dried air and pure water density standard (QAT182462, Kyoto Electronics, Japan).

2.12 Ultraviolet (UV) Absorbance Measurement

UV absorbance measurement was performed using a UV-2550 spectrophotometer (Shimadzu, Japan) calibrated with potassium dichromate solution and optical filter, according to the Japanese

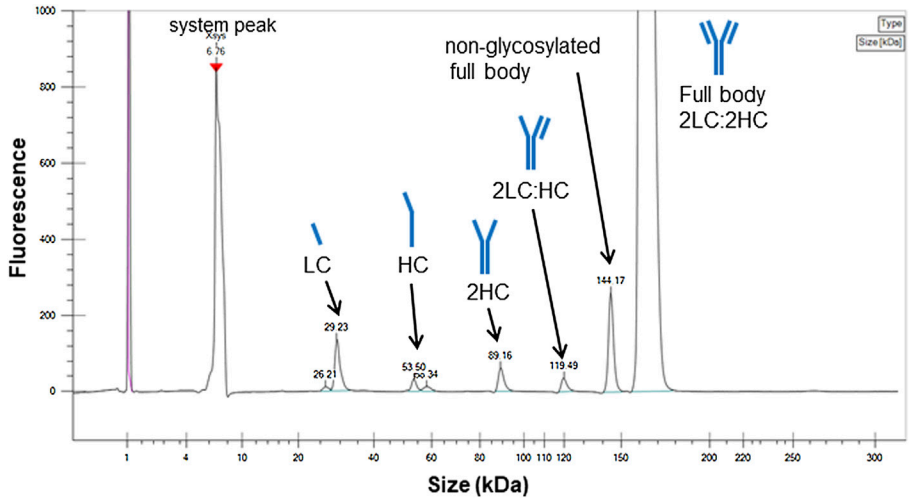

FIGURE 1 | Electropherogram of the candidate reference material (RM) analyzed by sodium dodecyl sulfate microchip electrophoresis under denatured and non-reducing condition. Peak assignments are based on the migration times. LC, light chain; HC, heavy chain.

Industrial Standards (JIS) K0115 (JIS K0115, 2004). A quartz cell with nominal 1-mm optical path length (1/Q/1, Starna Scientific, England) was used to measure the absorbance of the candidate RM at 280 nm and at 1 nm of the band path. Absorbance was measured using a double-beam spectrophotometer without a reference cell, using the same procedure as that used for a single-beam type instrument. A solvent blank sample was measured first, then the sample solution was measured using the same optical cell, and their difference was used to determine the absorption of the sample solution.

3 RESULTS AND DISCUSSION

3.1 Assessment of Size Heterogeneity and Charge Variants

The desired target structure of IgG1 is a heterotetrameric structure with two heavy chains (HC) and two light chains (LC; full body, 2LC:2HC). However, biopharmaceutical products usually contain free subunit chains, fragments of each subunit, or products with insufficient tetramer formation owing to disulfide bond scrambling as the size variants (Gaza-Bulseco and Liu, 2008; Leblanc et al., 2017; Turner and Schiel, 2018). These small size variants were analyzed *via* electrophoresis under denatured and non-reducing condition using a microchip electrophoresis system, whose result is presented in **Figure 1**.

Peaks were assigned according to the molecular size, indicating free LC, HC, partial molecules, 2HC and 2LC:HC, and non-glycosylated. The peak area ratio of the full body was estimated to be 93%, which was considered to be a minimum value. This is because the sample may dissociate into the partial molecules depending on the sample preparation conditions, and the area ratio may vary depending on the measurement conditions. In addition to the evaluation *via* electrophoresis, the size heterogeneity was assessed *via* SEC, which enabled to analyze fragmented products to aggregated macro molecule. As shown in **Figure 2**, the chromatogram obtained *via* SEC with UV detection exhibited four peaks assigned as oligomers (oligomeric form 1 and 2) and truncated products (truncated form 1 and 2) with the area percentage of (93.7 ± 0.2) % of the monomer peak. The entities regarding oligomeric forms 1 and 2 were attributed to trimer and dimer with area percentage of (0.42 ± 0.01) % and (5.72 ± 0.14) %, respectively. The entities of truncated forms 1 and 2 were (0.16 ± 0.01) %, which was negligibly small compared to the sum of the monomeric and oligomeric forms.

The heterogeneity owing to charge variants was assessed *via* CEX and capillary isoelectric focusing (cIEF). The net charge of the monoclonal antibody may depend on the PTMs including deamidation and conformational changes, resulting in the charge distribution of the molecule (Du et al., 2012; Fekete et al., 2015; Turner and Schiel, 2018). The chromatogram obtained *via* CEX is shown in **Figure 3A**. The chromatographic peaks on the chromatogram were divided into three, and the area percentages of each peak were (35.9 ± 0.1) % for the acidic peak (47.8 ± 0.2) % for the main peak, and (16.4 ± 0.1) % for the basic peaks. The electropherogram obtained *via* cIEF is shown in **Figure 3B**, and exhibited area percentages of indicated (54.3 ± 0.9) % for the acidic peak (42.1 ± 0.6) % for the main peak, and (3.6 ± 0.3) % for basic peak. The charge distribution was evaluated using two independent methods with different measurement principles, and results indicated similar main peak contents with area percentages of 47.8 and 42.1%, although not identical. The isoelectric point of the candidate RM obtained *via* cIEF was 9.03.

3.2 Structural Analyses

Confirmation of the primary structure and identification of the PTM were performed by mass spectrometry–based analyses, including intact mass spectrometry, middle-down structural characterization, and peptide mapping.

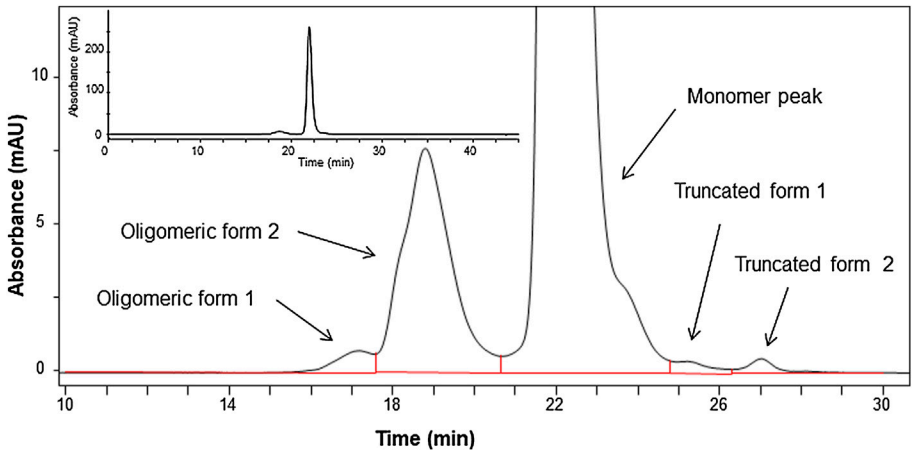

FIGURE 2 | Chromatogram of the candidate reference material (RM) analyzed by size-exclusion chromatography (SEC) monitored at 280 nm. Insert shows expanded chromatogram.

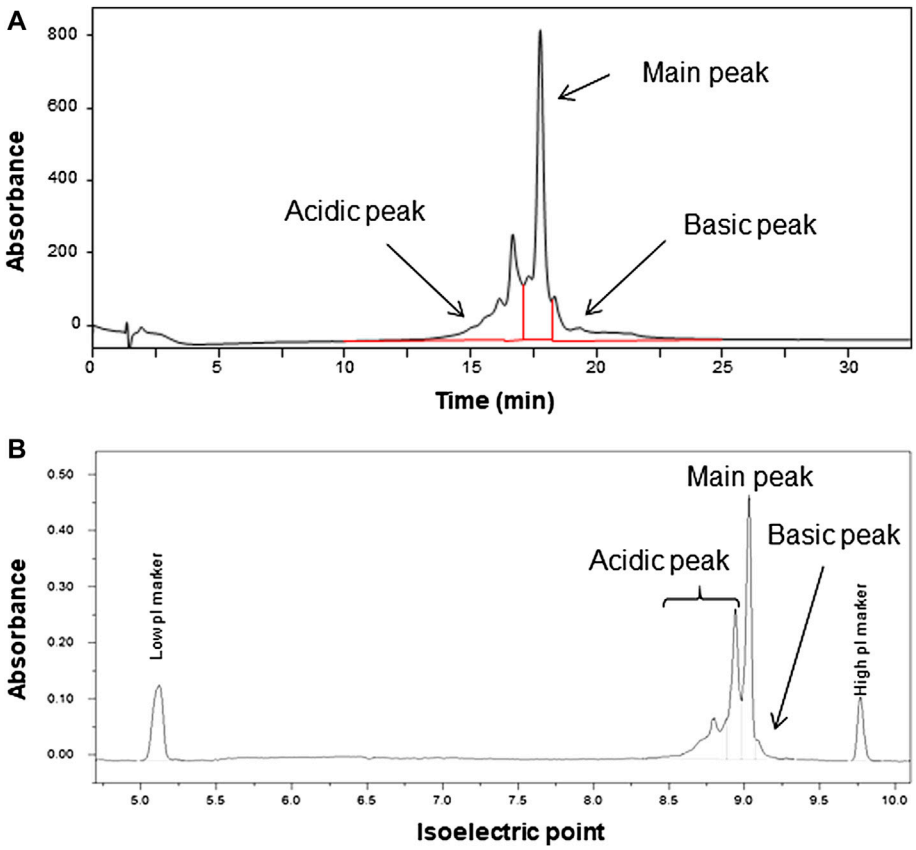

FIGURE 3 | Chromatogram analyzed by cation exchange chromatography (CEX) **(A)** and electropherogram analyzed by capillary isoelectric focusing **(B)** of the candidate reference material (RM).

3.2.1 Intact Mass Spectrometry

Intact mass spectrometry, which can measure the molecular mass of the antibody sample without any sample treatment reveals the molecular mass distribution of the entire molecule along with the major modifications (Lyubarskaya et al., 2006; Brady et al., 2007). The deconvoluted mass spectrum of an intact molecule measured through LC-MS is shown in **Figure 4** with the most abundant peak at 148,062 in molecular mass.

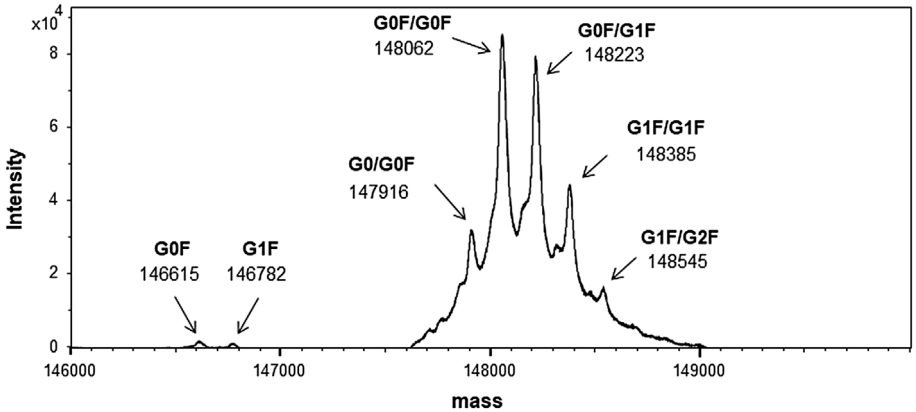

FIGURE 4 | Mass spectrum of the candidate reference material (RM) (intact mass spectrometry). Peaks are shown as averaged mass, and they are assigned based on the glycoform. The calculated and observed masses are summarized in **Supplementary Table S1**.

Owing to the broad distribution of stable isotopes demonstrated in the IUPAC atomic weight table, the molecular weight was calculated using the average of the minimum and maximum atomic weight values (Wieser and Coplen, 2011). The molecular weight of this material calculated using the atomic weights of 12.0106 (C), 1.00798 (H), 15.9994 (O), 14.0069 (N), and 32.0675 (S) was 148,056, and the molecular formula was $C_{6560}H_{10132}N_{1728}O_{2090}S_{44}$, considering a heterotetrameric structure with 16 disulfide linkages and two G0F glycan molecules. Other peaks were also assigned according to the difference in the glycosylation pattern with the calculated mass as summarized in **Supplementary Table S1**. It was confirmed that one glycan was modified to the antibody molecule in partial glycosylation.

3.2.2 Structure of Light Chain and Heavy Chain

The two main subunits, LC and HC were obtained by reduction of IgG with TCEP, and were analyzed *via* LC-MS. The deconvoluted mass spectrum of HC is shown in **Supplementary Figure S1** with the assignment of the glycan structure. The calculated masses and the observed masses of LC and HC are summarized in **Supplementary Table S2**.

3.2.3 Middle-Down Structural Characterization

For further structural analysis, middle-down structural characterization was performed by investigating the structure of IdeS protease-digested subunits *via* LC-MS (Chevreux et al., 2011; Wang et al., 2013). IdeS protease digests specifically at a single recognition site below the hinge region of the human IgG to provide two molecules, F (ab)' and scFc. F (ab)' consists of 1–239 of HC and LC *via* disulfide bond linkage, and scFc is a part of HC with 240–449 (C-terminal end). These IdeS digested products were reduced using DTT to yield Fd' with 1–239 of HC and LC from F (ab)', and scFc. The reduced pool was analyzed *via* LC-MS, and the deconvoluted mass spectrum of scFc is shown in **Figure 5**.

The scFc domain possessed *N*-glycosylation site, and the small size of fragment facilitated the observation of the detailed PTM *e.g.* glycosylation pattern. The calculated and observed masses of scFc as well as F (ab)' and Fd' are summarized in **Supplementary Table S3**. The measurement of the range of molecular masses of scFc, can be performed at a resolution that allows sufficient separation of the isotope peaks in the mass spectrum. Therefore, we identified 12 glycan structures with scFc and the non-glycosylated form and confirmed the structure of scFc.

3.3 Glycan Mapping

N-linked glycans of the candidate RM were analyzed by glycan mapping using LC-FL for the 2-AB–derivatized glycans. Various sample preparations including glycan release with PNGaseF, derivatization with 2-AB and clean-up were conducted using a commercial preparation kit. The chromatogram obtained *via* LC-FL is shown in **Figure 6**.

The area percentages of triplicate measurements are summarized in **Supplementary Table S4**. The major assigned 10 peaks were from typical hybrid and high mannose types of *N*-linked glycan of monoclonal antibody produced by CHO cells (Hossler et al., 2009). Based on the results of glycan mapping and analysis of scFc in the previous section, we identified 12 major glycoforms. However, 20 peaks with the relative area ratios greater than 0.1% were observed on the chromatogram, and almost half of the structures are currently unknown. Reliable absolute quantification of glycans has been difficult, and it is necessary to conduct more in-depth analysis in the future by accumulating data through inter-method comparisons and collaborative measurements for structural analysis of unidentified glycans and precise quantification (Wada et al., 2007; De Leoz et al., 2020). The use of recently available certified reference material for glycan analysis, NIST SRM 3655, glycans in solution (Lowenthal and Phinney, 2021) enables highly reliable and accurate analysis.

3.4 Peptide Mapping

Peptide mapping is a widely used bottom-up technique for identifying conformation of the primary structure and modifications such as PTM, N/C-terminal extension, and

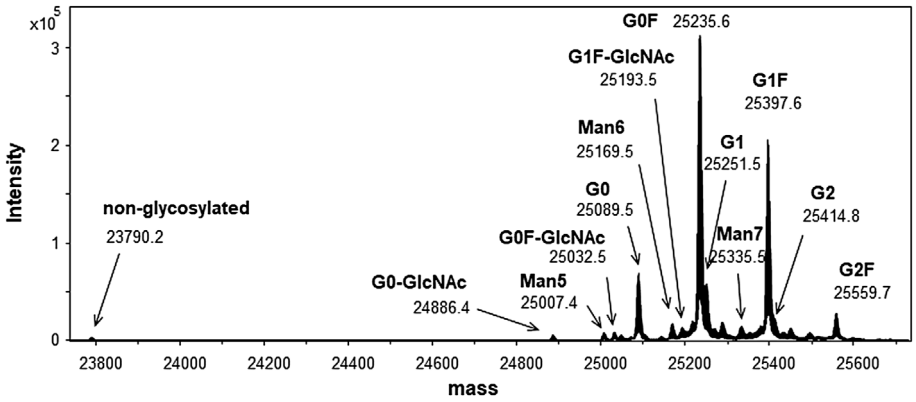

FIGURE 5 | Mass spectrum of scFc fragment obtained by IdeS digestion. Peaks are shown as averaged mass. The calculated and observed masses are summarized in **Supplementary Table S3**.

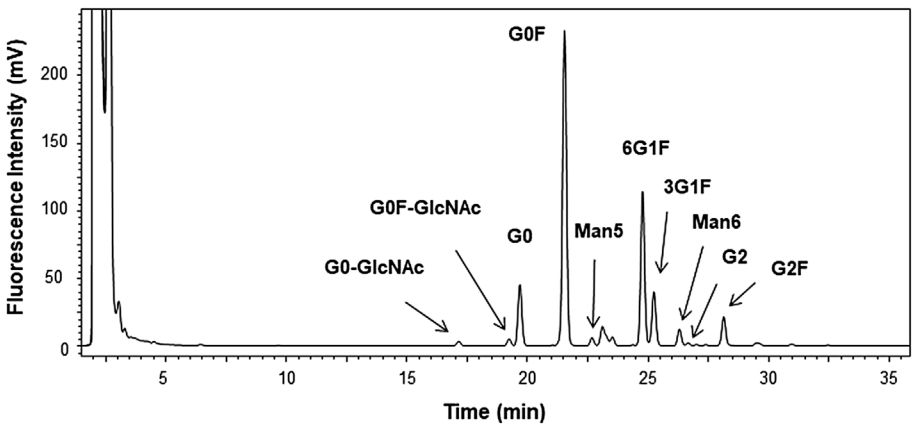

FIGURE 6 | Chromatogram of 2-aminobenzamide–derivatized glycan by liquid chromatography–fluorescent detection (LC-FL) performed as glycan mapping. Glycan was released using peptide *N*-glycosidase F from the candidate reference material (RM). Peaks are assigned for 10 of the peaks with greater than 0.1% in the relative peak area ratio. The relative area ratios are summarized in **Supplementary Table S4**.

truncation (Beck et al., 2013). Peptide mapping typically involves denaturation, reduction, and alkylation of protein prior to enzymatic digestion, followed by separation and analysis of the resulting peptide mixture by reversed phase LC-MS/MS (Ren et al., 2009; Lauber et al., 2013; Mouchahoir and Schiel, 2018). For peptide mapping of the candidate RM, enzymatic digestion was performed using trypsin, Lys-C, and Glu-C with different sequence specificities to achieve the highest possible sequence coverage. The results of peptide mapping using these three proteases under reduced condition are presented in **Figure 7A** for LC and (B) for HC, and the results with the retention times, calculated masses (monoisotopic masses), and observed masses for the identified peptides are summarized in **Supplementary Table S5A–C.**

Trypsin is the most commonly used protease because of the strict substrate specificity, high activity, and the favorable size of peptides yielded for mass spectrometry (Olsen et al., 2004). Digested peptide fragments generated using trypsin covered most of the entire sequence, but small peptides consisting of a few residues were undetectable. However, peptide mapping with Lys-C and Glu-C digestion in addition to trypsin digestion complementarily and successfully covered the entire sequence. The peptide mapping with the three proteases confirmed the amino acid sequence of the candidate RM to be exactly as designed.

Furthermore, peptide mapping by trypsin digestion revealed the modified structure including N and C terminal structure of HC, deamidation on asparagine residues, oxidation on methionine residues, as well as glycosylation site. The results of peptide mapping regarding these modifications are summarized in **Table 1**.

Peptide mapping by trypsin digestion showed partial N-terminal pyroglutamylation of the HC and addition of a lysine residue at the C-terminus of the HC. For deamidation of asparagine residues, the isotopic patterns of Asn and deamidated Asn overlapped when high-resolution mass

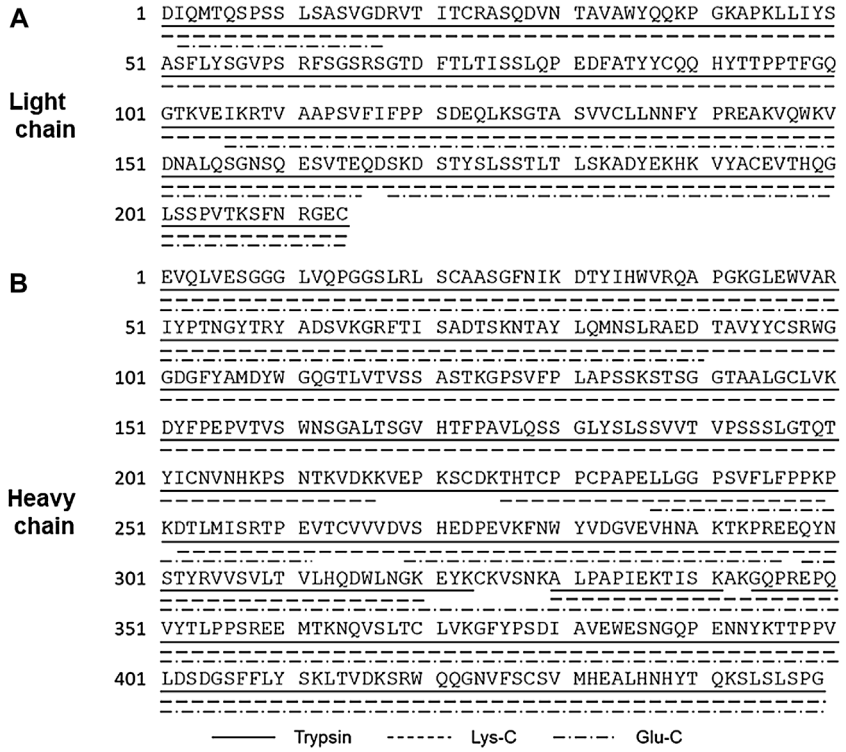

FIGURE 7 | Summary of peptide mapping of light chain **(A)** and heavy chain **(B)** using trypsin, Lys-C, and Glu-C. Peptide identification is summarized in **Supplementary Table S5**.

TABLE 1 | Summary of peptide mapping for modified structure including N and C terminal, deamidation, and oxidation *via* trypsin digestion. Calculated and observed masses represent monoisotopic masses.

Structure	Retention time, min	Calculated mass	Observed mass, *m/z*	Charges
Pyroglutamylation at N-terminal H1-19, heavy chain	48.6	932.5003	932.4995	2
Lys addition at C-terminal H443-449, heavy chain	13.5	394.7298	394.7289	2
Deamidation on N30 L25-42, light chain	23.0	664.6661	664.6650	3
Deamidation on N55 H51-59, heavy chain	11.2	543.2673	543.2664	2
Deamidation on N84 H77-87, heavy chain	25.4	656.3223	656.3214	2
Deamidation on N318 H305-320, heavy chain	60.7	603.6689	603.6686	3
Deamidation on N387 or 392 or 393 H374-395, heavy chain	19.5	660.3568	660.3557	3
Oxidation on M107 H99-124, heavy chain	54.6	934.0907	934.0899	3
Oxidation on M255 H252-258, heavy chain	48.1	426.2188	426.2179	2

spectrometry was used. Therefore, peptides with variation in both mass and retention time were determined to be deamidated. The results showed that N30 at the LC, and N55, N84, N318, N387, N392, or N393 at the HC were deamidated. A tryptic peptide, H374-395 carried three asparagine residues (N387, N392, and N393) in the peptide chain. Although we were unable to identify the deamidation site from these data, N387 was a part of the -Asn-Gly- sequence, which is known to be susceptible to deamidation, and those deamidation has been reported (Zhang et al., 2014; Huang et al.,

TABLE 2 | Summary of peptide mapping for structural analysis of disulfide bond formation **(A)**. Identified peptides with a disulfide bond **(B)** amino acid sequence of peptide shown in **(A)**. Tryptic digestion was performed under non-reducing conditions. Calculated and observed masses are shown as monoisotopic mass. L and H represent light chain and heavy chain, respectively.

(A) Identified crosslinking peptides *via* disulfide bond

Peptide	Disulfide linkage	Retention time, min	Calculated mass	Observed mass, *m/z*	Charges *z*
L19-24/L67-103	C23-C88	57.6	964.8563	964.8556	5
L127-142/L191-267	C134-C194	48.9	712.1576	712.1572	5
H20-30/H88-98	C22-C96	26.9	597.0272	597.0266	4
H137-150/H151-213	C147-203	68.3	1320.4944	1320.4938	6
H259-277/H324-325	C264-324	27.2	583.0323	583.0314	4
H364-373/H420-442	C370-428	37.6	769.9725	769.9721	5
L208-214/H222-225	C214(L)-C223(H)	4.7	421.1699	421.1692	3
H226-251/H226-251	C229(H1)-C229(H2) C232(H1)-C232(H2)	65.4	910.1384	910.1380	6

(B) Amino acid sequence of peptide forming disulfide linkage shown in **(A)**

L19-24	VTITCR
L67-103	SGTDFTLTISSLQPEDFATYYCQQHYTTPPTFGQGTK
L127-142	SGTASVVCLLNNFYPR
L191-267	VYACEVTHQGLSSPVTK
L208-214	SFNRGEC
H20-30	LSCAASGFNIK
H88-98	AEDTAVYYCSR
H137-150	STSGGTAALGCLVK
H151-213	DYFPEPVTVSWNSGALTSGVHTFPAVLQSSGLYSLSSVVTVP-SSSLGTQTYICNVNHKPSNTK
H226-251	THTCPPCPAPELLGGPSVFLFPPKPK
H259-277	TPEVTCVVVDVSHEDPEVK
H324-325	CK
H364-373	NQVSLTCLVK
H420-442	WQQGNVFSCSVMHEALHNHYTQK

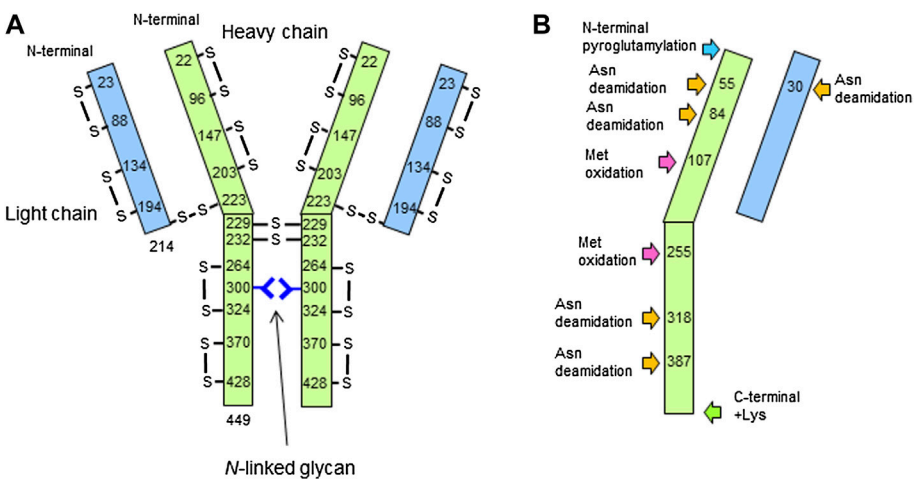

FIGURE 8 | Structure of the candidate reference material (RM) determined by this study. Size of light chain (LC) and heavy chain (LC), disulfide bond formation, and glycosylation site **(A)**, as well as N/C-terminal modifications, Asn deamidation, and Met oxidation **(B)** are described.

2016). Therefore, N387 could be deamidated among the three asparagine residues. Oxidized methionine residues were found at M107 and M255 of HC.

It is known that IgG1 forms 16 pairs of disulfide bonds to form a heterotetrameric structure with two light chains and two heavy chains (Liu and May 2012). For the analyses of disulfide bond formation, trypsin digestion was performed under non-reducing condition by skipping the reduction and alkylation steps, and the results are summarized in **Table 2**.

The peptide mapping under non-reducing condition successfully revealed disulfide bond sites within the LC and HC, between the LC and HC, as well as between the heavy

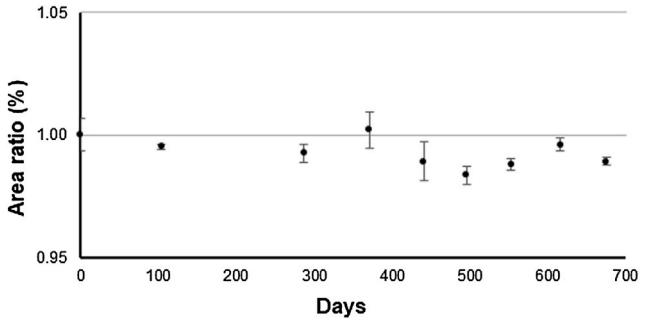

FIGURE 9 | Time course of the main peak of the antibody solution of previous production batch stored at −80°C by triplicate measurement using cation exchange chromatography. *Y*-axis represents the relative peak area ratio of the main peak. This measurement was performed as a long-term stability test.

chains. Based on the above results, the structure determined by mass spectrometry–based analyses is shown in **Figure 8**.

3.5 Homogeneity and Stability of the Candidate RM

Assigning the indicative value (antibody concentration) of candidate RM was performed according to the NMIJ quality system in accordance with ISO 17025 and 17034. Assessing the homogeneity and stability is essential to ensure consistency of the indicative value, and it is mandatory to state their conformity to the international standards.

Homogeneity was assessed through three repeat measurements of the relative area percentage of the main peak obtained by CEX. 12 vials taken by stratified random sampling from whole batch were used for this test. The homogeneity data obtained by analysis of variance (ANOVA) showed that the mean square between-vial variance could not be obtained because of larger value of the variance of within-vial. Therefore, the uncertainty associated with the inhomogeneity was estimated using **Eq. 1**, considering the measurement variability described in ISO Guide 35 (ISO Guide 35, 2017).

$$u_{bb} = \sqrt{\frac{MS_{within}}{n}} \times \sqrt[4]{\frac{2}{\nu MS_{within}}} \quad (1)$$

where MS_{within} represents the mean square within-vial variance, n represents number of measurement replicates per vial, ν represents degree of freedom of MS_{within}.

The calculated u_{bb} according to **Eq. 1** was 0.103%, and this value was used as the relative standard uncertainty.

The stability was evaluated as acceleration, long-term, short-term stabilities, and free-thaw cycle tests *via* CEX. The acceleration test was performed at 4 and 25°C by CEX, SEC, and UV absorption at 280 nm. Time course of the relative area percentage of the main peak obtained by CEX is shown in **Supplementary Figure S2A** at 4°C and (B) at 25°C. The area ratio of the main peak obtained by CEX decreased after 10 days at 4°C and 3 days at 25°C. Monomer peak ratio on SEC analysis decreased only by 0.8% in 40 days at 25°C (data not shown). No change was observed by UV absorption for 122 days at 4°C and for 40 days at 25°C (data not shown). These results indicated that CEX was the most sensitive method for monitoring the stability.

The long-term stability test was performed using an antibody solution from the previous production batch produced using same production process, and it was monitored for up to 675 days at −80°C *via* CEX. The area ratio of the main peak by CEX over the monitoring period is shown in **Figure 9**.

A trend analysis was performed according to ISO Guide 35 to determine whether a linear approximation to instability would show a trend in the data over the monitoring period. The result indicated that the significance of the linear regression was not found. By multiplying the uncertainty derived from the slope of the linear regression by 3 years, the uncertainty associated with long-term stability was determined to be 0.923%. The short-term stability was monitored for up to 304 days at −20°C *via* CEX (data not shown). The results of the trend analysis over the monitoring period according to ISO Guide 35 indicated that the significance of the linear regression was not found. The uncertainty associated with the short-term stability was determined to be 0.955% based on the uncertainty derived from the slope of the linear regression.

In addition, freeze-thaw cycle tests were examined as follows: The candidate RM stored at −80°C was moved from a freezer and placed in an incubator at 25°C for 1 h and then returned to the freezer at −80°C. The freeze-thaw cycle test was conducted by repeating this cycle up to five times using CEX, SEC, and UV absorption at 280 nm. The results of the test showed no significant difference over five-times as summarized in **Supplementary Table S6**, and it can be concluded that freeze-thaw up to five times does not affect the results of any of the methods examined, as well as the indicative value.

3.6 Value Assignment of Indicative Value *via* Amino Acid Analyses

Antibody concentration, which is as an indicative value of the RM, was determined *via* amino acid analyses. To ensure the reliability of the amino acid analysis, hydrolyses with hydrochloric acid by microwave-assisted liquid phase (liquid phase) and gas phase were performed independently, and isotope dilution mass spectrometry was used to determine the hydrolyzed amino acids. Amino acid analysis requires complete hydrolysis of the sample into its constituent amino acids. Because the optimal conditions for hydrolysis vary depending on the sample protein, we examined the optimal conditions for the candidate RM (Burkitt et al., 2008; Feng et al., 2020). The hydrolysis conditions were examined at 150, 160, and 170°C for 1 and 3 h for the liquid phase hydrolysis and 130 and 150°C for 18, 24, and 48 h for the gas phase hydrolysis. The optimum conditions were 160°C for 3 h for microwave-assisted liquid phase hydrolysis and 150°C for 48 h for gas phase hydrolysis based on the highest recovery of the eight measured amino acids and the smallest difference between the measured amino acids.

Hydrolyses of the candidate RM were performed under the optimized condition on three separate days and three repeated measurements using LC-MS/MS. The measured concentrations

TABLE 3 | Quantitative results of the candidate reference material (RM) by amino acid analyses obtained from liquid phase hydrolysis **(A)** and gas phase hydrolysis **(B)**. The detailed uncertainty budgets are summarized in **Supplementary Table S7**.

(A) Results obtained from liquid phase hydrolysis–amino acid analysis (nmol/g)

Measured amino acid	Asp	Glu	Pro	Val	Ile	Leu	Phe	Ala
Measured concentration	33.39	33.89	33.42	33.48	34.18	33.58	33.90	34.22
Standard uncertainty	0.1889	0.3454	0.3256	0.2482	0.3628	0.2207	0.5399	0.4881

(B) Results obtained from gas phase hydrolysis–amino acid analysis (nmol/g)

Measured amino acid	Asp	Glu	Pro	Val	Ile	Leu	Phe	Ala
Measured concentration	32.92	33.94	33.76	33.77	33.96	33.71	33.75	35.97
Standard uncertainty	0.7506	0.2116	0.1611	0.1452	0.2349	0.3823	0.2684	0.4297

for each amino acid were divided by the number of the amino acid residues in the candidate RM. The quantitative results of each amino acid along with the associate uncertainties are summarized in **Table 3** for the liquid phase hydrolysis and for the gas phase hydrolysis. The detailed uncertainty budget is shown in **Supplementary Table S7**.

The protein concentration was obtained by calculating the weighted mean of the quantitative results of the eight amino acids. From the calculation, the concentrations of the candidate RM obtained *via* liquid phase and gas phase hydrolyses were (33.68 ± 0.42) nmol/g and (33.94 ± 0.98) nmol/g, respectively (the number following ± represents the standard uncertainty.).

The validity of the analyses was confirmed using certified reference material of human serum albumin (NMIJ CRM 6202a) with a certified value of the concentration (74.3 ± 3.2) g/L (expanded uncertainty with coverage factor, k = 2) (Kinumi et al., 2017). The quantitative results by liquid phase and gas phase hydrolyses were (74.4 ± 0.9) g/L and (74.1 ± 0.8) g/L, respectively (the number following ± represents the standard deviation.). This indicates that the amino acid analysis was sufficiently accurate and suitable for the value assignment.

3.7 Impurity Assessment and its Influence on the Result of Amino Acid Analyses

In addition, we assessed protein, peptide, and amino acid impurities in the candidate RM which may affect the result of the amino acid analyses. The raw material was highly purified by three-step-chromatography as equivalent to that used in the production of biopharmaceutical. Possible impurities should be considered are HCP and protein A, which could be contaminated during the purification process (Hogwood et al., 2014). The quantitative results of HCP and protein A by ELISA were 3.2 ng/mg protein and 0.2 ng/mg protein respectively, which were significantly low, and did not affect the results of amino acid analyses of the material. To assess peptide and free amino acid contaminants, amino acid analysis was performed for hydrolysate by hydrochloric acid hydrolysis of filtrates with a 10 kDa ultrafiltration device (Amicon ultra, Millipore, USA) for the candidate RM and phosphate buffer (as the blank sample). The quantitative results indicated that contents of the eight measured amino acid in the filtrate of the candidate RM were equivalent or lower compared to those of the blank. These results indicate no impurities that could affect the results of amino acid analysis, and the values obtained can be corresponded to the concentration of antibody.

Furthermore, quantitative analysis was performed for host cell–derived DNA and endotoxin which are often considered process-related impurities, and their quantification results were below the lower limit of quantification (Host cell–derived DNA, 10.0 pg/mg protein; endotoxin, 0.01 EU/mg protein).

3.8 Establishing the Indicative Value

As the measurand is a heterotetrameric structure including oligomeric forms, the indicative value can be determined by using the results of amino acid analysis. The concentration of the candidate RM was calculated from the weighted mean of the results of the amino acid analyses by liquid phase and gas phase hydrolyses, which was to be 33.75 nmol/g. Finally, the indicative value of the candidate RM was determined to be 5.00 g/L by converting the unit to mass concentration using the molecular weight (148,056) and the density (1.0008 g/cm^3 at 20°C) measured by a vibration-type density meter. The molecular weight was calculated based on the amino acid sequence with 16 disulfide linkages and the most abundant glycan structure (G0F/G0F) described in previous section.

The uncertainty associated with the concentration from two amino acid analyses was calculated according **Eq. 2** (Kinumi et al., 2017):

$$u^2(x) = \sum w_i^2 u^2(x_i) + Dif^2, \quad (2)$$

where w_i represents the weight of the quantitative results by liquid phase and gas phase hydrolyses, u (x_i) represents the uncertainty of the quantitative results by the two hydrolysis methods, and *Dif* represents the difference between the two quantitative methods calculated as a rectangular distribution of the two quantitative results. From the equation, the standard uncertainty associated with amino acid analysis was calculated to be 0.19 g/L.

In conclusion, the uncertainty budget is summarized in **Table 4** according to ISO Guide 35, considering the following uncertainty components: amino acid analysis for value assignment, inhomogeneity of the material, long-term instability, and short-term instability. The uncertainty estimation of the indicative value of the candidate RM was calculated as the combined standard uncertainty by summing the squares of the uncertainty components listed in **Table 4**.

TABLE 4 | Uncertainty budget for the indicative value of NMIJ RM 6208a, AIST-MAB.

Uncertainty components (%)	
Amino acid analysis	1.30
Inhomogeneity	0.10
Instability (long-term)	0.92
Instability (short-term)	0.95
Combined standard uncertainty (Rel, %)	1.86
Expanded uncertainty (k = 2) (g/L)	0.19

Overall, the indicative value of the candidate RM was determined to be (5.00 ± 0.19) g/L, and the number following ± represents the expanded uncertainty (coverage factor k = 2).

3.9 Extinction Coefficient at 280 nm

Because the absorbance of the protein solution can be measured using a low cost instrument with high reproducibility and simple measurement principle based on the Lambert-beer's law, the absorbance at 280 nm is frequently used to determine antibody concentration (Miranda-Hernandez et al., 2016; Cole et al., 2018). Antibody concentration is essential in the quality control of an antibody drug, and the accurate determination of the extinction coefficient at 280 nm of the RM can lead to various application of the RM with high accuracy.

The extinction coefficient of the candidate RM was obtained according to the Lambert-Beer equation: the absorbance measured by a spectrophotometer at 280 nm using an optical cell with an assessed optical path length; the antibody concentration determined as the indicative value by amino acid analysis. The absorbance of the candidate RM was measured using a quartz cell with an optical path length of 1 mm. Because the absorbance at 280 nm is approximately 0.7 when measured with an optical path length of 1 mm, which is appropriate for accurate measurement. Because the only available optical cell whose optical path length was evaluated was a 10 mm cell supplied by Hitachi Ltd determined to be (10.00 ± 0.05) mm, the extinction coefficient at 280 nm of potassium hydrogen phthalate solution was determined using this 10 mm cell, and the optical path length of the 1 mm cell was obtained using the determined extinction coefficient of the potassium hydrogen phthalate solution. Finally, the optical path length of the 1 mm optical cell was determined to be (1.02 ± 0.01) mm (the number following ± represents the standard uncertainty.). To measure the absorbance of protein solutions containing aggregates, it is necessary to consider the effect of light scattering. The correction of the light scattering at 280 nm was made using the results of absorbance measurements at 320–350 nm according to literature (Maity et al., 2009). Using the indicative value (measured antibody concentration), optical path length, and absorbance at 280 nm using the 1 mm optical cell, the extinction coefficient was found to be (1.41 ± 0.03) L/(g cm) with the correction of light scattering (the number following ± represents the standard uncertainty.). The extinction coefficient of proteins at 280 nm is often predicted using the equation by Pace et al., based on the numbers of tryptophan, tyrosine, and cystine residues in the protein molecule (Pace et al., 1995). The calculated absorption coefficient of the candidate RM is 1.42 L/(g cm), which is consistent with the experimental result. We performed an inter-laboratory comparison on UV measurement at 280 nm for monoclonal antibody solution, and we found that the standard deviation of the measurement results of 34 laboratories was approximately 10%, indicating a large variation among laboratories (Kinumi et al., 2021). It has been shown that this difference in absorbance can be reduced by conducting system suitability test. The use of this material enables validation of absorbance measurement and it can realize more accurate measurement.

3.10 Other Physicochemical Properties, Analyses of Particle Size and Higher-Order Structure

The physicochemical properties of the candidate RM regarding its particle size and higher-order structure were also analyzed by SEC-MALS (**Supplementary Figure S3**), DLS (**Supplementary Figure S4**), NTA (**Supplementary Figure S5**), FI (**Supplementary Figure S6**), CD (**Supplementary Figure S7**), and TSA (**Supplementary Figure S8**). The molecular weight calculated from SEC-MALS was 1.35×10^5, indicating that the main peak corresponded to the IgG monomer. The relative UV peak area (94.6%) demonstrated that most of the candidate RM was dispersed as monomeric form. The DLS measurements presented a typical value (11.4 nm) of hydrodynamic diameter for the IgG monomer and no significant peaks for aggregates, which was consistent with the SEC-MALS results. The presence of detectable amounts of submicrometer-sized particles was clarified *via* NTA analysis. The mode diameter, mean diameter, and particle concentration were 194 nm, 206 nm, and 5.81×10^8 particles/mL, respectively. The FI measurements demonstrated that the candidate RM contained considerable number of micrometer-sized particles (e.g., ~7,000 particles/mL for a particle of ≥5 nm diameter) compared with trastuzumab-US (Hutterer et al., 2019). The CD spectrum of the candidate RM exhibited a typical shape of a globular protein rich in β-sheet structures. The thermal denaturation temperatures revealed by TSA analysis were 69.7 and 80.4°C, which were comparable to the values reported for trastuzumab-US (Hutterer et al., 2019). These results indicate that the candidate RM maintains the higher-order structure of the native IgG.

3.11 AIST-MAB and NISTmAb, the Difference and Complementary Information of the Properties

NISTmAb (RM 8671) from NIST is the humanized IgG1κ solution produced using mouse-derived NS0 cells, and assigned the antibody concentration, size heterogeneity, and charge heterogeneity as the reference values. This material also provides with the case study of various properties.

AIST-MAB was produced using CHO cell line, which is used in the production of over 70% of biopharmaceuticals of which

almost all of the monoclonal antibodies (Lalonde and Durocher, 2017). The difference in the host cells for the production, can lead to a large difference in properties, especially in the glycan structure. Even both materials are recombinant humanized IgG1κ, the amino acid sequence, buffer formulation, and method used for value assignment in addition to host cells were between them differed. The development of antibody reference material with different properties, specifically produced by the CHO cells, presents considerable advantage in antibody characterization. Conversely, to evaluate the various properties of monoclonal antibodies, orthogonal approaches of analyses using multiple reference materials can provide complementary information and improve the quality of characterization. The reference materials are not exclusive to each other, and the availability of multiple reference materials for antibody characterization could expand the scope of the utilization of each reference material.

4 CONCLUSION

The monoclonal antibody reference material presented here, NMIJ RM 6208a, AIST-MAB provides a tool that enables a wide range of analytical techniques to be extensively compared and evaluated, going beyond quality control with in-house reference materials. The indicative value represents the antibody concentration with associated uncertainty; however, the most of properties and the corresponding results are method-defined. The measurement results of various physicochemical properties with underpinning by accurate antibody concentration are more reliable and allow for promising measurement. Reference materials that can be used across analytical methods and analytical laboratories enable the development and standardization of analytical methods as well as the verification of in-house consistency in measurements. From a metrological point of view, the capability of inter-laboratory comparisons will open up the possibility of development of traceable measurements for various properties relevant to the antibody analysis. The AIST-MAB is currently available from NMIJ/AIST and contributes to the development of more advanced and reliable analytical techniques for antibody characterization.

DATA AVAILABILITY STATEMENT

The original contributions presented in the study are included in the article/**Supplementary Material**, further inquiries can be directed to the corresponding author.

AUTHOR CONTRIBUTIONS

TK wrote the first draft of the manuscript and made the figures. SH wrote section of the manuscript. TK, MK, NN, and SH conducted the procurement of raw material and developed the experimental design. TK, KS, RK, and CI conducted the experiments and analyzed the data. All authors reviewed, edited, and approved the final manuscript.

FUNDING

The authors acknowledge the financial support provided by "Discovering and Manufacturing Pharmaceutical Infrastructure for Next-Generation Treatments and Diagnoses" (JP17ae0101003, JP18ae0101056, and JP19ae0101056) of Japan Agency for Medical Research and Development (AMED).

ACKNOWLEDGMENTS

We thank Ryoko Mizuno, Sakae Eyama, Tomoko Oshikata, Kiyoko Yamagishi, and Yan Wen Feng for their technical assistance as well as Akiko Takatsu for helpful discussion. We also thank the Manufacturing Technology Association of Biologics for providing the raw material.

SUPPLEMENTARY MATERIAL

The Supplementary Material for this article can be found online at: https://www.frontiersin.org/articles/10.3389/fmolb.2022.842041/full#supplementary-material

REFERENCES

Beck, A., Wagner-Rousset, E., Ayoub, D., Van Dorsselaer, A., and Sanglier-Cianférani, S. (2013). Characterization of Therapeutic Antibodies and Related Products. *Anal. Chem.* 85, 715–736. doi:10.1021/ac3032355

Brady, L. J., Martinez, T., and Balland, A. (2007). Characterization of Nonenzymatic Glycation on a Monoclonal Antibody. *Anal. Chem.* 79, 9403–9413. doi:10.1021/ac7017469

Burkitt, W. I., Pritchard, C., Arsene, C., Henrion, A., Bunk, D., and O'Connor, G. (2008). Toward Système International d'Unité-Traceable Protein Quantification: From Amino Acids to Proteins. *Anal. Biochem.* 376, 242–251. doi:10.1016/j.ab.2008.02.010

Chevreux, G., Tilly, N., and Bihoreau, N. (2011). Fast Analysis of Recombinant Monoclonal Antibodies Using IdeS Proteolytic Digestion and Electrospray Mass Spectrometry. *Anal. Biochem.* 415, 212–214. doi:10.1016/j.ab.2011.04.030

Cole, K. D., DeRose, P., He, H. J., Stein, E. V., Lang, B., Schiel, J., et al. (2018). NIST Spectroscopic Measurement Standards. *Biopharm. Int.* 31, 22–34.

De Leoz, M. L. A., Duewer, D. L., Fung, A., Liu, L., Yau, H. K., Potter, O., et al. (2020). NIST Interlaboratory Study on Glycosylation Analysis of Monoclonal Antibodies: Comparison of Results from Diverse Analytical Methods. *Mol. Cell. Proteomics* 19, 11–30. doi:10.1074/mcp.RA119.001677

Du, Y., Walsh, A., Ehrick, R., Xu, W., May, K., and Liu, H. (2012). Chromatographic Analysis of the Acidic and Basic Species of Recombinant Monoclonal Antibodies. *MAbs* 4, 578–585. doi:10.4161/mabs.21328

Fekete, S., Beck, A., and Guillarme, D. (2015). Characterization of Cation Exchanger Stationary Phases Applied for the Separations of Therapeutic Monoclonal Antibodies. *J. Pharm. Biomed. Analysis* 111, 169–176. doi:10.1016/j.jpba.2015.03.041

Feng, L., Huo, Z., Xiong, J., and Li, H. (2020). Certification of Amyloid-Beta (Aβ) Certified Reference Materials by Amino Acid-Based Isotope Dilution High-Performance Liquid Chromatography Mass Spectrometry and Sulfur-Based High-Performance Liquid Chromatography Isotope

Dilution Inductively Coupled Plasma Mass Spectrometry. *Anal. Chem.* 92, 13229–13237. doi:10.1021/acs.analchem.0c02381

Gaza-Bulseco, G., and Liu, H. (2008). Fragmentation of a Recombinant Monoclonal Antibody at Various pH. *Pharm. Res.* 25, 1881–1890. doi:10.1007/s11095-008-9606-3

Hogwood, C. E., Bracewell, D. G., and Smales, C. M. (2014). Measurement and Control of Host Cell Proteins (HCPs) in CHO Cell Bioprocesses. *Curr. Opin. Biotechnol.* 30, 153–160. doi:10.1016/j.copbio.2014.06.017

Hossler, P., Khattak, S. F., and Li, Z. J. (2009). Optimal and Consistent Protein Glycosylation in Mammalian Cell Culture. *Glycobiology* 19, 936–949. doi:10.1093/glycob/cwp079

Huang, L.-J., Chiang, C.-W., Lee, Y.-W., Wang, T.-F., Fong, C.-C., and Chen, S.-H. (2016). Characterization and Comparability of Stress-Induced Oxidation and Deamidation on Vulnerable Sites of Etanercept Products. *J. Chromatogr. B* 1032, 189–197. doi:10.1016/j.jchromb.2016.05.007

Hutterer, K. M., Polozova, A., Kuhns, S., McBride, H. J., Cao, X., and Liu, J. (2019). Assessing Analytical and Functional Similarity of Proposed Amgen Biosimilar ABP 980 to Trastuzumab. *Biodrugs* 33, 321–333. doi:10.1007/s40259-019-00350-9

ICH Q6B (1999). ICH Harmonised Tripartite Guideline, Specifications: Test Procedures and Acceptance Criteria for Biotechnological/Biological Products– Q6B, International Council for Harmonisation of Technical Requirements for Pharmaceuticals for Human Use. Available at: https://database.ich.org/sites/default/files/Q6B%20Guideline.pdf.

ISO 17034 (2016). *General Requirements for the Competence of Reference Material Producer*. Geneva: International Organization for Standardization.

ISO Guide 35 (2017). *Reference Materials — Guidance for Characterization and Assessment of Homogeneity and Stability*. Geneva: International Organization for Standardization.

ISO/IEC 17025 (2017). *General Requirements for the Competence of Testing and Calibration Laboratories*. Geneva: International Organization for Standardization.

Japanese Pharmacopoeia (2016). *The Japanese Pharmacopoeia*. 17th Edition. Available at: https://www.mhlw.go.jp/file/06-Seisakujouhou-11120000-Iyakushokuhinkyoku/JP17_REV_1.pdf.

JIS K0115 (2004). *General Rules for Molecular Absorptiometric Analysis*. Tokyo, Japan: Japan Industrial Standards.

Kaplon, H., Muralidharan, M., Schneider, Z., and Reichert, J. M. (2020). Antibodies to Watch in 2020. *MAbs* 12, 1703531. doi:10.1080/19420862.2019.1703531

Kaplon, H., and Reichert, J. M. (2021). Antibodies to Watch in 2021. *MAbs* 13, 1860476. doi:10.1080/19420862.2020.1860476

Kato, M., Kinumi, T., Yoshioka, M., Goto, M., Fujii, S.-i., and Takatsu, A. (2015). Development of C-Reactive Protein Certified Reference Material NMIJ CRM 6201-b: Optimization of a Hydrolysis Process to Improve the Accuracy of Amino Acid Analysis. *Anal. Bioanal. Chem.* 407, 3137–3146. doi:10.1007/s00216-014-8190-0

Kinumi, T., Goto, M., Eyama, S., Kato, M., Kasama, T., and Takatsu, A. (2012). Development of SI-Traceable C-Peptide Certified Reference Material NMIJ CRM 6901-a Using Isotope-Dilution Mass Spectrometry-Based Amino Acid Analyses. *Anal. Bioanal. Chem.* 404, 13–21. doi:10.1007/s00216-012-6097-1

Kinumi, T., Noda, N., and Honda, S. (2021). Interlaboratory Comparison on Ultraviolet Absorption Measurement for Monoclonal Antibody Solution. *Seibutsu-kogaku* 99, 23–28. doi:10.34565/seibutsukogaku.99.1_23

Kinumi, T., Sakaguchi, Y., and Takatsu, A. (2017). Development of a Certified Reference Material of Human Serum Albumin: Certification and Value Assignment via Amino Acid Analyses. *Anal. Methods* 9, 4574–4580. doi:10.1039/c7ay01415e

Lalonde, M.-E., and Durocher, Y. (2017). Therapeutic Glycoprotein Production in Mammalian Cells. *J. Biotechnol.* 251, 128–140. doi:10.1016/j.jbiotec.2017.04.028

Lauber, M. A., Koza, S. M., McCall, S. A., Alden, B. A., Iraneta, P. C., and Fountain, K. J. (2013). High-Resolution Peptide Mapping Separations with MS-Friendly Mobile Phases and Charge-Surface-Modified C18. *Anal. Chem.* 85, 6936–6944. doi:10.1021/ac401481z

Le Basle, Y., Chennell, P., Tokhadze, N., Astier, A., and Sautou, V. (2020). Physicochemical Stability of Monoclonal Antibodies: A Review. *J. Pharm. Sci.* 109, 169–190. doi:10.1016/j.xphs.2019.08.009

Leblanc, Y., Ramon, C., Bihoreau, N., and Chevreux, G. (2017). Charge Variants Characterization of a Monoclonal Antibody by Ion Exchange Chromatography Coupled On-Line to Native Mass Spectrometry: Case Study After a Long-Term Storage at +5 °C. *J. Chromatogr. B* 1048, 130–139. doi:10.1016/j.jchromb.2017.02.017

Liu, H., Gaza-Bulseco, G., Faldu, D., Chumsae, C., and Sun, J. (2008). Heterogeneity of Monoclonal Antibodies. *J. Pharm. Sci.* 97, 2426–2447. doi:10.1002/jps.21180

Liu, H., and May, K. (2012). Disulfide Bond Structures of IgG Molecules. *MAbs* 4, 17–23. doi:10.4161/mabs.4.1.18347

Lowenthal, M. S., and Phinney, K. W. (2021). *Glucans in Solution*. Gaithersburg, Maryland, USA: Standard Reference Material 3655, National Institute of Standards and Technology.

Lyubarskaya, Y., Houde, D., Woodard, J., Murphy, D., and Mhatre, R. (2006). Analysis of Recombinant Monoclonal Antibody Isoforms by Electrospray Ionization Mass Spectrometry as a Strategy for Streamlining Characterization of Recombinant Monoclonal Antibody Charge Heterogeneity. *Anal. Biochem.* 348, 24–39. doi:10.1016/j.ab.2005.10.003

Maity, H., Karkaria, C., and Davagnino, J. (2009). Effects of pH and Arginine on the Solubility and Stability of a Therapeutic Protein (Fibroblast Growth Factor 20): Relationship Between Solubility and Stability. *Curr. Pharm. Biotechnol.* 10, 609–625. doi:10.2174/138920109789069297

Miranda-Hernández, M. P., Valle-González, E. R., Ferreira-Gómez, D., Pérez, N. O., Flores-Ortiz, L. F., and Medina-Rivero, E. (2016). Theoretical Approximations and Experimental Extinction Coefficients of Biopharmaceuticals. *Anal. Bioanal. Chem.* 408, 1523–1530. doi:10.1007/s00216-015-9261-6

Mouchahoir, T., and Schiel, J. E. (2018). Development of an LC-MS/MS Peptide Mapping Protocol for the NISTmAb. *Anal. Bioanal. Chem.* 410, 2111–2126. doi:10.1007/s00216-018-0848-6

Muñoz, A., Kral, R., and Schimmel, H. (2011). Quantification of Protein Calibrants by Amino Acid Analysis Using Isotope Dilution Mass Spectrometry. *Anal. Biochem.* 408, 124–131. doi:10.1016/j.ab.2010.08.037

Olsen, J. V., Ong, S.-E., and Mann, M. (2004). Trypsin Cleaves Exclusively C-Terminal to Arginine and Lysine Residues. *Mol. Cell. Proteomics* 3, 608–614. doi:10.1074/mcp.T400003-MCP200

Pace, C. N., Vajdos, F., Fee, L., Grimsley, G., and Gray, T. (1995). How to Measure and Predict the Molar Absorption Coefficient of a Protein. *Protein Sci.* 4, 2411–2423. doi:10.1002/pro.5560041120

Ren, D., Pipes, G. D., Liu, D., Shih, L.-Y., Nichols, A. C., Treuheit, M. J., et al. (2009). An Improved Trypsin Digestion Method Minimizes Digestion-Induced Modifications on Proteins. *Anal. Biochem.* 392, 12–21. doi:10.1016/j.ab.2009.05.018

Schiel, J. E., Davis, D. L., and Borisov, O. V. (2014). "State-of-the-Art and Emerging Technologies for Therapeutic Monoclonal Antibody Characterization Volume 1," in Monoclonal Antibody Therapeutics: Structure, Function, and Regulatory Space. ACS Symposium. Series. 1176, Washigton, DC. doi:10.1021/bk-2014-1176

Schiel, J. E., Davis, D. L., and Borisov, O. V. (2015a). "State-of-the-Art and Emerging Technologies for Therapeutic Monoclonal Antibody Characterization Volume 2," in Biopharmaceutical Characterization: The NISTmAb Case Study, Volume 2. Biopharmaceutical Characterization: The NISTmAb Case Study. ACS Symposium. Series. 1201, Washigton, DC. doi:10.1021/bk-2015-1201

Schiel, J. E., Davis, D. L., and Borisov, O. V. (2015b). "State-of-the-Art and Emerging Technologies for Therapeutic Monoclonal Antibody Characterization, Volume 3," in Defining the Next Generation of Analytical and Biophysical Techniques. ACS Symposium. Series. 1202, Washigton, DC. doi:10.1021/bk-2015-1201

Schiel, J. E., Turner, A., Mouchahoir, T., Yandrofski, K., Telikepalli, S., King, J., et al. (2018). The NISTmAb Reference Material 8671 Value Assignment, Homogeneity, and Stability. *Anal. Bioanal. Chem.* 410, 2127–2139. doi:10.1007/s00216-017-0800-1

Turner, A., and Schiel, J. E. (2018). Qualification of NISTmAb Charge Heterogeneity Control Assays. *Anal. Bioanal. Chem.* 410, 2079–2093. doi:10.1007/s00216-017-0816-6

Turner, A., Yandrofski, K., Telikepalli, S., King, J., Heckert, A., Filliben, J., et al. (2018). Development of Orthogonal NISTmAb Size Heterogeneity Control

Methods. *Anal. Bioanal. Chem.* 410, 2095–2110. doi:10.1007/s00216-017-0819-3

Wada, Y., Azadi, P., Costello, C. E., Dell, A., Dwek, R. A., Geyer, H., et al. (2007). Comparison of the Methods for Profiling Glycoprotein Glycans-HUPO Human Disease Glycomics/Proteome Initiative Multi-Institutional Study. *Glycobiology* 17, 411–422. doi:10.1093/glycob/cwl086

Wang, B., Gucinski, A. C., Keire, D. A., Buhse, L. F., and Boyne II, M. T. (2013). Structural Comparison of Two Anti-CD20 Monoclonal Antibody Drug Products Using Middle-Down Mass Spectrometry. *Analyst* 138, 3058–3065. doi:10.1039/c3an36524g

Wieser, M. E., and Coplen, T. B. (2010). Atomic Weights of the Elements 2009 (IUPAC Technical Report). *Pure Appl. Chem.* 83, 359–396. doi:10.1351/PacRep-10-09-14

Zhang, Y. T., Hu, J., Pace, A. L., Wong, R., Wang, Y. J., and Kao, Y.-H. (2014). Characterization of Asparagine 330 Deamidation in an Fc-Fragment of IgG1 Using Cation Exchange Chromatography and Peptide Mapping. *J. Chromatogr. B* 965, 65–71. doi:10.1016/j.jchromb.2014.06.018

Conflict of Interest: The authors declare that the research was conducted in the absence of any commercial or financial relationships that could be construed as a potential conflict of interest.

frontiers | Frontiers in Molecular Biosciences

REVIEW
published: 23 June 2022
doi: 10.3389/fmolb.2022.890826

OOP-ESEEM Spectroscopy: Accuracies of Distances of Spin-Correlated Radical Pairs in Biomolecules

*Tarek Al Said, Stefan Weber and Erik Schleicher**

Institute of Physical Chemistry, University of Freiburg, Freiburg, Germany

In addition to the commonly used electron–electron double resonance (ELDOR) technique, there are several other electron paramagnetic resonance (EPR) methods by which structure information can be obtained by exploiting the dipolar coupling between two radicals based on its characteristic r^{-3} dependence. In this contribution, we explore the potential of out-of-phase-electron-spin echo envelope modulation (OOP-ESEEM) spectroscopy to collect accurate distance information in photo-sensitive (bio) molecules. Although the method has already been applied to spin-correlated radical pairs in several classes of light-active proteins, the accuracy of the information obtained has not yet been extensively evaluated. To do this in a system-independent fashion, OOP-ESEEM time traces simulated with different values of the dipolar and exchange couplings were generated and analyzed in a best-possible way. Excellent agreement between calculated and numerically fitted values over a wide range of distances (between 15 and 45 Å) was obtained. Furthermore, the limitations of the method and the dependence on various experimental parameters could be evaluated.

Keywords: EPR spectroscopy, coupled radical pair, distance determination, dipolar coupling, OOP-ESEEM

OPEN ACCESS

Edited by:
Alex Jones,
National Physical Laboratory,
United Kingdom

Reviewed by:
Yasuhiro Kobori,
Kobe University, Japan
Sergei Dzuba,
Institute of Chemical Kinetics and Combustion (RAS), Russia
Hiroki Nagashima,
Saitama University, Japan

****Correspondence:***
Erik Schleicher
Erik.Schleicher@physchem.uni-freiburg.de

Specialty section:
This article was submitted to Structural Biology, a section of the journal Frontiers in Molecular Biosciences

Received: *06 March 2022*
Accepted: *05 May 2022*
Published: *23 June 2022*

Citation:
Al Said T, Weber S and Schleicher E (2022) OOP-ESEEM Spectroscopy: Accuracies of Distances of Spin-Correlated Radical Pairs in Biomolecules. Front. Mol. Biosci. 9:890826. doi: 10.3389/fmolb.2022.890826

INTRODUCTION

One of the most fundamental goals of protein studies is to obtain a mechanistic understanding of biological function at a molecular level. Data on protein structure, the dynamics of structure elements and reaction kinetics are typically collected for this purpose. During the last decades, robust technological developments in the fields of X-ray crystallography, NMR, and cryogenic electron microscopy (cryo-EM) have contributed to the wealth of solved protein structures in the RCSB Protein Data Bank. X-ray crystallography remains the standard for obtaining crystal structure data at atomic resolution, although conclusions on the protein dynamics on various time scales in the protein's physiological state may not directly be drawn. Cryo-EM, with its advantage of simpler sample preparation, is the currently most evolving method (Fernandez-Leiro and Scheres, 2016). Although this technique provides snapshots of a protein, dynamic properties that govern the protein's functional output are still lacking. Solution NMR is potentially the best tool to study protein dynamics and structure; however, the technique is limited to smaller proteins or protein complexes and demands expensive stable-isotope-labeling strategies. Thus, biophysical methods are desired which provide structure data on the nanometer scale and dynamic information of biomolecules without extensive sample manipulation and preparation. Fluorescence-based methods, such as fluorescence resonance energy transfer (FRET), have proven quite powerful in this respect as they are

sensitive down to the single-molecule level and provide real-time dynamics over several time scales (Loura and Prieto, 2011). However, FRET lacks precision and applicability when it comes to quantifying distances or distance changes. Therefore, other spectroscopic methods such as EPR are applied to obtain structure (and also dynamic) information on biomolecules.

The most commonly used EPR method for determining distances from dipolar couplings between radicals in biomolecules is pulsed electron–electron double-resonance (abbreviated PELDOR or DEER) (Pannier et al., 2000; Schiemann and Prisner, 2007; Jeschke, 2012), and to a lesser extent, relaxation-induced dipolar modulation enhancement (RIDME) spectroscopy (Kulik et al., 2001), or the more recently devised laser-DEER or laser-IMD techniques (Hintze et al., 2016; Dal Farra et al., 2019). By these methods, the distance between magnetic momenta is measured, which are either intrinsically present in the (bio)molecule of interest or introduced *via* selective spin labeling (Klare, 2013). Since several excellent reviews on the accuracy of the PELDOR method are available [for example, (Edwards and Stoll, 2016, Edwards and Stoll, 2018; Hustedt et al., 2018)], the focus of this study is on the applicability and accuracy of a further pulsed EPR method for distance determination: pulsed out-of-phase electron-spin-echo envelope modulation (OOP-ESEEM) EPR (Salikhov et al., 1992).

Distance Determination in Correlated Radical Pairs

If two (or more) unpaired electron spins are present in a system, their interactions are described by the spin Hamiltonian which comprises contributions from exchange interaction, zero-field splitting, and dipolar coupling. If light-induced electron transfer takes place between a donor and an acceptor moiety of the system, a spin-correlated coupled radical pair is generated, which may be observed provided the EPR detection is sufficiently fast (Weber, 2017). Such a spin pair may be singlet (spin quantum number $S = 0$) or triplet ($S = 1$) configured depending on the multiplicity of the precursor state (see below). It should be noted in this context that although a photogenerated triplet state is also paramagnetic and may be considered as a very strongly coupled pair of spins within a molecular moiety, electron transfer is not needed for its generation.

In case the spins are strongly coupled, that is, they are within a very short distance with respect to each other, the exchange interaction describing the energy difference between the singlet state and the triplet manifold becomes very large. Hence, the triplet sublevels may be treated separately from the singlet level for the purpose of detection of EPR resonances. As a result, the zero-field splitting becomes dominant, which can be described by the two so-called zero-field splitting parameters, D and E, for a review see, e.g., Richert et al. (2017). These can be extracted from an EPR spectrum by spectral simulations. D and E depend on the average distance of the unpaired electrons, the delocalization of the wave function across the molecule, and the rhombicity of the interaction (Richert et al., 2017; Weber, 2017). However, because of the strong coupling, only a distance estimation becomes possible for pure triplets.

In case the two electron spins are more distant from each other, the exchange interaction and zero-field splitting are much weaker; one may speak of a spin pair or a radical pair. If radical pairs are formed by fast light-induced electron transfer, in which at least one electronically excited moiety acts as an electron acceptor or donor, a charge-separated state with two unpaired correlated electron spins is formed because the precursor spin multiplicity is transferred to the charge-separated state due to the conservation of spin-angular momentum. In this context, the distinction between a spin-correlated radical pair and an (uncorrelated) biradical needs to be made. Spin-correlation of radical pairs manifests itself in EPR spectra as electron-spin polarization that affects the intensities of resonant transitions. In contrast to spectra of thermally equilibrated spin states, spin-correlated radical pairs exhibit enhanced absorptive and emissive resonances provided the detection system is fast enough (Weber, 2017). This is because spin correlation has a limited lifetime. Its decay may be relatively slow as long as the distance and the relative orientation of the radical pair partners remain static. This is the case, for example, in some radical pairs formed between cofactors and/or amino acid residues within a protein framework, in polymer compositions consisting of donor and acceptor materials, or in synthetically prepared molecules with donor and acceptor moieties. Spin-correlated coupled radical pairs generated by light-induced electron transfer have thus been observed in photosystems involved in photosynthesis (Harvey and Wasielewski, 2021), in cryptochromes and photolyases (Biskup et al., 2009; Schleicher and Weber, 2012), in phototropins (Kay et al., 2003), in light-active decarboxylases (Sorigué et al., 2017), in biomimetic systems of artificial photosynthesis (Hou et al., 2019), and in polymer-fullerene blends devised for organic photovoltaics (Niklas and Poluektov, 2017).

With increasing distance r, the exchange interaction falls off exponentially—more strongly than the dipolar interaction, which follows an r^{-3} dependence. The exchange interaction accounts for the quantum-mechanic indistinguishability of the two electrons and thus depends on the overlap of the respective orbitals. The dipolar interaction depend not only on the distance but also on the orientation of the radical pair with respect to the direction of the external magnetic field. Electron-spin polarization in spin-correlated coupled radical pairs may be understood with the coupled correlated radical pair (CCRP) formalism (Adrian, 1972; Closs et al., 1987; Hore et al., 1987). Such resonances can be directly detected using transient EPR spectroscopy (Weissman, 1982; Weber, 2017) and pulsed EPR methods such as OOP-ESEEM spectroscopy (Salikhov et al., 1992; Tang et al., 1994). All methods have their strengths and weaknesses in the determination of the relevant interaction parameters. Transient EPR spectroscopy is not ideal for extracting distance information as the dipolar interaction between the two radicals has little influence on the spectral shape but affects the amplitude of a radical-pair signature in cases of weaker couplings (Stehlik et al., 1989). OOP-ESEEM, on the other hand, is a method that is ideal for

TABLE 1 | Radical pair distances in various protein systems determined using OOP-ESSEM and comparison to the respective distances obtained from crystal structures or structure models.

Protein and Organism	Radical Pair	Distance from OOP-ESEEM/Å	Distance obtained by crystal structure (a) or by calculation (b)/Å	Reference
Rhodobacter sphaeroides R26 RC	$[P865^{\bullet+}\ Q_A^{\bullet-}]$	28.4	28.3 (a)	Zech et al. (1996); Bittl and Zech (1997)
Synechococcus elongatus PS I	$[P700^{\bullet+}\ A_1^{\bullet-}]$	25.4		
Spinach PS I	$[P700^{\bullet+}\ A_1^{\bullet-}]$	25.3 ± 0.3		Dzuba et al. (1997)
C. reinhardtii PS I	$[P700^{\bullet+}\ A_1^{\bullet-}]$	25.4 ± 0.03	24.5 (a)	Santabarbara et al. (2006)
Spinach PS I	$[P700^{\bullet+}\ A_1^{\bullet-}]$	25.4 ± 0.03	26.0 (a)	
Synechocystis sp. PS I	$[P700^{\bullet+}\ A_1^{\bullet-}]$	25.5 ± 0.02	24.5 (a)	
Synechocystis sp. PS I	$[P700^{\bullet+}\ A_1^{\bullet-}]$	26.1 ± 0.2	24.5 (a)	Savitsky et al. (2013)
Artificial photosynthetic systems	$[BDX^{\bullet+}\ PI^{\bullet-}]$	25.0 ± 0.1	25.4 (b)	Carmieli et al. (2009)
	$[TTF^{\bullet+}\ PI^{\bullet-}]$	28.1 ± 0.1	27.3 (b)	
	$[DMJ^{\bullet+}\ NI^{\bullet-}]$	38.0 ± 0.2	37.6 (b)	
Spinach PS II	$[P680^{\bullet+}\ Q_A^{\bullet-}]$	27.4 ± 0.3	27 (a)	Hara et al. (1997)
	$[Y_z^{\bullet+}\ Q_A^{\bullet-}]$	34 ± 1	34 (a)	Zech et al. (1997)
Drosophila cryptochrome	$[FAD^{\bullet-}\ TrpD^{\bullet+}]$	22.4 ± 0.5	21.6 (a)	Nohr et al. (2017)
E. coli photolyase	$[FAD^{\bullet-}\ TrpC^{\bullet+}]$	19.5 ± 0.5	20.5 (a)	
Pigeon cryptochrome 4	$[FAD^{\bullet-}\ TrpD^{\bullet+}]$	21.2 ± 0.2	20.9 (a)	Hochstoeger et al. (2020)
	$[FAD^{\bullet-}\ TrpC^{\bullet+}]$	17.5 ± 0.1	17.5 (a)	
European robin cryptochrome	$[FAD^{\bullet-}\ TrpD^{\bullet+}]$	21	21.3 (a)	Xu et al. (2021)
	$[FAD^{\bullet-}\ TrpC^{\bullet+}]$	18	17.6 (a)	

measuring distances between radicals; the basics of this technique will be summarized in brief in the following section.

Basics of the OOP-ESEEM Method

The pulsed OOP-ESEEM EPR experiment (Salikhov et al., 1992; Tang et al., 1997) is capable of directly measuring the strengths of exchange and dipolar interactions in short-lived radical pair states. OOP-ESEEM has been previously applied to examine spin-correlated radical pairs in a number of proteins (see **Table 1**), composite materials designed for organic photovoltaic devices (Lukina et al., 2015), and labeled DNA hairpins (Olshansky et al., 2019). In brief, this low-temperature EPR experiment comprises a canonical two-microwave-pulse echo sequence $[h\nu–t_{DAF}–(\xi_1)_x–\tau–(\xi_2)_x–\tau–\text{echo}]$ applied after a short laser pulse that initiates radical pair formation (**Figure 1**). In general, the precise flip angles ξ_i of the pulses, which can differ significantly from 90° (and 180°) (Tang et al., 1997; Krzystyniak, 2003), should be optimized during the experimental setup. The maximum OOP-ESEEM signal can be determined by adjusting the pulse length at constant microwave power or vice versa. The echo intensity in the out-of-phase channel detected as a function of the separation time between the microwave pulses thus becomes modulated by

$$\omega_{\text{mod}} = 2J - 2D\left(3\cos^2\theta - 1\right)/3 \tag{1}$$

as a result of dipolar and exchange interactions, with θ being the orientation of the dipolar axis with respect to the direction of the external magnetic field (Salikhov et al., 1992), and D and J are the dipolar and exchange interaction, respectively, both in angular frequency units. This modulation can be converted by sine Fourier transformation (SFT) into a frequency spectrum. From the resulting Pake doublets the dipolar and exchange couplings can be extracted at high precision from turning and inflection points of spectral simulations (Hoff et al., 1998; Fursman and Hore, 1999; Santabarbara et al., 2006). They correspond to the frequencies at which the dipolar axis is parallel and perpendicular to the magnetic field, respectively. These frequencies are given by

$$\nu_\perp = \pm\ (2D/3 + 2J) \text{ and } \nu_\parallel = \pm\ (-4D/3 + 2J) \tag{2}$$

Both parameters, D and J, can hence be extracted from the two frequencies. By using the point-dipole approximation (PDA), the distance r between the radicals can be calculated based on the relation (Hoff et al., 1998; Santabarbara et al., 2005)

$$D/\text{MHz} = -78.08 \times 10^3 / (r/\text{Å})^3 \text{ or } D/\text{mT} = -2786 / (r/\text{Å})^3 \tag{3}$$

Please note that there is a factor of 3/2 between **Eq. 3** and the relation commonly used in PELDOR spectroscopy to extract distance information: $\nu_\perp = -52.16 \times 10^3 \text{MHz}/(r/\text{Å})^3$ (Jeschke, 2012). The reason for this is that PELDOR is typically applied to systems containing spins at larger distances (> 20Å); hence, J is assumed zero and only one of the two frequencies ($\nu_\perp$) of the Pake pattern needs to be read out (Reginsson and Schiemann, 2011). In this case **Eq. 2** simplifies to $|D| = 3\nu_\perp/2$.

In comparison to other methods for distance determination, such as PELDOR spectroscopy (Jeschke, 2012), OOP-ESEEM is conceptually more straightforward and requires only two pulses of the same microwave frequency (instead of four or more pulses of different frequencies) (see below). Typically, the method is applied to the examination of short-lived spin pairs generated in an unmodified protein system: hence, any potentially structure-

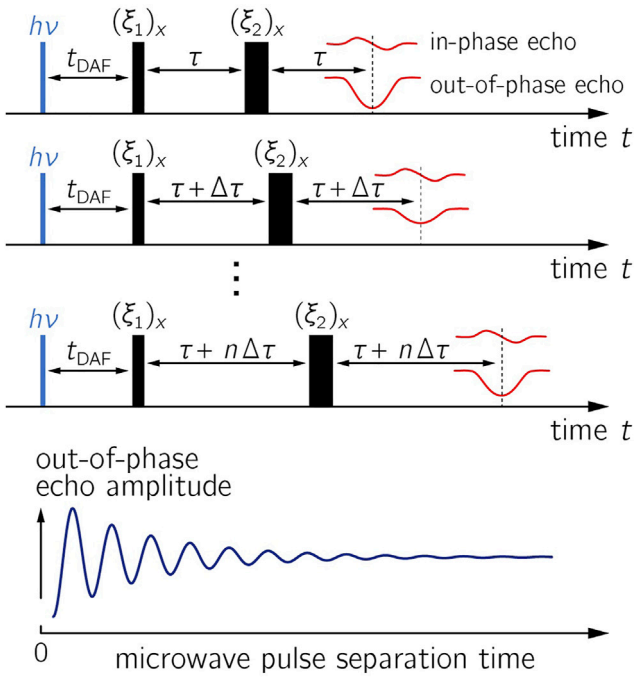

FIGURE 1 | OOP-ESEEM pulse sequence. In the upper panels, the evolution of the in-phase and out-of-phase (OOP) echo components are depicted; the resulting time trace with respect to the pulse separation time is shown in the lower panel. Parameters: t_{DAF}, time delay after the laser flash ($h\nu$); $(\xi)_x$, flip angles of microwave pulses with phase *x*; in-phase and out-of-phase (OOP) signals denote the signals in the *y*- and *x*-channels during quadrature detection. During the experiment, the time between the microwave pulses is varied stepwise while t_{DAF} is kept constant. The amplitude of the OOP signal is recorded as a function of the microwave pulse separation time.

disturbing effects, as they may occur upon site-directed spin labeling, are avoided.

The anisotropies of the Zeeman interaction and the orientation of the two radicals with respect to each other have only a minute influence on the out-of-phase echo modulation (Bittl and Zech, 2001) as long as the experiment is carried out at not too high microwave frequencies and corresponding magnetic field strengths so that orientation-selection effects (Harmer, 2016; Schnegg, 2017) can be neglected. Furthermore, hyperfine couplings and their anisotropies have only a minor effect on the shape of the OOP-ESEEM time traces despite the fact that other ESEEM techniques are particularly sensitive to these (van Doorslaer, 2017). Theoretical studies treating the case of broadband microwave excitation in OOP-ESEEM corroborate this finding (Dzuba, 1997; Timmel et al., 1998): Anisotropic hyperfine couplings contribute only as a second-order effect to the echo modulation (Tang et al., 1995). In only a few experimental studies using the OOP-ESEEM technique slight distortions of the earliest echo modulations by hyperfine couplings were observed, although the obtained distances remained unaffected (Fursman and Hore, 1999; Nohr et al., 2017).

Information on the orientation of the dipolar coupling tensor have been previously obtained by examination of single crystals that have been rotated with respect to the direction of the external magnetic field (Bittl et al., 1997). It is conceivable that such information may also be obtained using orientation selection effects at high magnetic fields (Savitsky et al., 2007; Savitsky et al., 2013; Harmer, 2016; Schnegg, 2017), oriented samples (Hasegawa et al., 2017), or by exploiting selective optical sample excitation using polarized light (Hamada et al., 2021). However, to the best of our knowledge, such techniques have not yet been applied to OOP-ESEEM.

Theory predicts that not only singlet-configured radical pairs but also triplet-configured ones exhibit an OOP ESEEM effect. The echo amplitude of the latter is expected to assume opposite polarity and its intensity to be reduced by a factor of three (Tang et al., 1997). Thus, the sign of the echo modulation could, in principle, be used to assign the precursor multiplicity, singlet or triplet, of a given radical pair. A comparison of experimental OOP-ESEEM data from $^1[P_{865}^{\bullet+}\ Q_A^{\bullet-}]$ and $^3[P_{865}^{\bullet+}\ Q_A^{\bullet-}]$, however, revealed almost identical time traces and no indication of any polarity change (Borovykh et al., 2002; Kulik et al., 2003).

In principle, the OOP-ESEEM method benefits from the initial spin-correlation in a radical-pair generation that manifests itself in strongly polarized resonances, thereby significantly increasing the signal-to-noise ratio (SNR) of detected spin echoes and consequently of their modulation. Also, information on the precursor spin multiplicity is obtained from such experiments, thereby revealing traits of the photochemistry of a system. The method thus complements the PELDOR technique, which is widely applied to measure distances and their distributions in uncorrelated but coupled biradicals. The OOP-ESEEM experiment requires only two pulses at one microwave frequency, but a laser pulse, which is required for the generation of the radical pair by photoexcitation, needs to be applied and the microwave pulse sequence tied to it. With modern EPR instrumentation, this is nowadays straightforward. Photogeneration of radical pairs could be a problem for the measurement of distances using OOP-ESSEM if a sample suffers from photodecomposition. In such a case, only a limited SNR can be reached, and the sample needs to be renewed for increasing the SNR if available in larger quantities. Here, PELDOR has a clear advantage as the experiment can be repeated without sample loss until the desired SNR is reached. The fact that typically optical sample excitation is used for the generation of spin-correlated radial pairs (although other methods for generating a spin-correlated state are conceivable) is, however, limiting the application of the OOP-ESEEM method. Intrinsically, very few proteins are eligible as long as the addition of light-active labels and/or redox-active amino acids by biochemical and molecular biology methods is still a conceptual challenge.

MATERIALS AND METHODS

We will evaluate the applicability of OOP-ESEEM in detail by comparing distances derived from this method with those obtained using other methods for structure determination, such as X-ray crystallography. In addition, the accuracy of the

method will be evaluated by analyzing artificially generated echo decay curves. Specifically, it shall be clarified how accurate the information obtained by this method is, on which length scales the method is applicable and which limitations are involved.

Calculation of OOP-ESEEM Spectra

Our calculations of OOP-ESEEM echo decay curves were performed under the assumption of weak dipolar coupling between the radicals and the validity of the point-dipole approximation (a dipolar coupling tensor of axial symmetry). We further assumed microwave pulses that are able to excite the entire range of spectral resonances. In addition, the following simplifications were made: Both parts of the radical pair have an isotopic *g*-value of 2.0023. Hyperfine couplings were disregarded; hence, it was assumed that the calculated echo trace from the OOP channel was unaffected by additional nuclear ESEEM. Furthermore, effects of zero-quantum coherence were ignored, which can be achieved experimentally by applying the microwave pulse sequence after a sufficiently long t_{DAF} (see **Figure 1**) (Hoff et al., 1998). The τ-dependent echo intensity can then be determined for a disordered ensemble by

$$S(\tau) = A \exp(-\tau/T_d) \int_0^{2\pi} \int_0^{\pi} \sin(\omega_{mod}(\theta)\tau) \sin(\theta)\, d\theta\, d\phi \quad (4)$$

Here $\omega_{mod}(\theta)$ is the observed frequency modulation (see **Eq. 1**), θ and ϕ are the angles between the external magnetic field and the axis connecting the two magnetic point dipoles, A is the amplitude of the signal, and T_d is the relaxation time (Salikhov et al., 1992). This integral can be rewritten as the sum of Fresnel integrals

$$S(\tau) = \frac{2\pi^{1.5}}{\sqrt{D\tau}} H \exp\left(\frac{-\tau}{T_d}\right)\left[\sin\left(\frac{2(D+3J)\tau}{3}\right)\mathrm{FrC}\left(2\sqrt{\frac{D\tau}{\pi}}\right) - \cos\left(\frac{2(D+3J)\tau}{3}\right)\mathrm{FrS}\left(2\sqrt{\frac{D\tau}{\pi}}\right)\right] \quad (5)$$

with the sine and cosine Fresnel functions

$$\mathrm{FrC}(z) = \int_0^z \cos(\pi u^2/2) du \text{ and} \quad (6a)$$

$$\mathrm{FrS}(z) = \int_0^z \sin(\pi u^2/2) du \quad (6b)$$

and the amplitude factor H. All calculated spectra were generated on the basis of the above-mentioned functions. Starting values used for the simulations are noted in the respective Tables. Prior to the sine Fourier transformation to calculate the frequency spectrum, the signal was first multiplied by a Hamming window and zero-filled to double its length. Error margins of all parameters were obtained using the Cramér–Rao lower bounds theorem (Fursman and Hore, 1999).

Matlab Routine and Algorithm

All calculations were performed using Matlab R2019a (The MathWorks, Natick, MA, United States). Unless otherwise noted, the used values were: $T_d = 0.35\mu s$, $H = 1$, probe pulse step width = 2–10 ns. Simulated OOP ESEEM decays and corresponding frequency spectra were scaled to similar amplitudes for comparability. Reconstruction was performed using the autoregressive (AR) model described below. To do this, the order p was increased until the reconstructed region was identified as noisy by visual inspection, and it was verified that the residuals were uncorrelated (Neumaier and Schneider, 2001). It has to be mentioned that this criterion could not be fulfilled for certain signals with high SNR; in this case, the reconstruction was optimized manually. Fitting was performed by minimizing the sum of the squares of the offsets of simulated and modeled curves using the "lsqcurvefit" routine with the trust region reflective algorithm (options: maximum iterations: 200; termination tolerance: 10^{-10}; maximum function evaluations: 10,000). The squared norm of the residuals was calculated as a performance criterion in cases where fits with different starting values were compared. Boundary conditions are given in the Results and Discussion section.

Calculation of Mass and Spin Density Centers-of-Gravity

Mass and spin density centers-of-gravity were calculated by DFT-optimized structures including all atoms of the respective molecule and by the Mulliken spin densities from the output of the respective calculation. 1-Ethyl-lumichrome and truncated tryptophan were drawn with Avogadro (Hanwell et al., 2012) (**Supplementary Figure S1**) and used in DFT calculations with the Orca program package (Neese, 2012). Geometry optimizations were carried out with the BP86 functional (Perdew, 1986; Becke, 1988) in conjunction with the def2-TZVPP basis set (Weigend and Ahlrichs, 2005) using the RI approximation. EPR property calculations were performed on the obtained geometries with the B3LYP functional (Becke, 1986; Lee et al., 1988) in conjunction with the EPR-II basis set (Barone, 1996) using the RICOSX approximation.

RESULTS AND DISCUSSION

Published OOP-ESEEM Distances

First, we analyzed the accuracy of previously published radical-pair distances in proteins. For this purpose, previously published distances obtained by the OOP-ESEEM method were collected in **Table 1** and compared with values from other structure-determination methods. To date, OOP ESEEM has been applied to only a few protein systems. Beginning in the mid-1990s, several reports were published on light-induced radical pairs in photosystems (Zech et al., 1996; Bittl and Zech, 1997; Dzuba et al., 1997; Zech et al., 1997; Santabarbara et al., 2006; Savitsky et al., 2013). Depending on the generated radical pair, distances of ≈25, ≈28 and ≈34 Å were obtained (**Table 1**). In this context, also oriented membranes (Yoshii et al., 1999) and single crystals (Bittl et al., 1997) of photosystems have been investigated, which allowed the determination of the orientation of the dipolar coupling axis with respect to the crystallographic axes from the angular dependence of the observed echo modulation.

In recent years, radical pairs generated in a further family of light-active proteins were investigated by this method: the photolyases and cryptochromes. The question addressed in these studies was which redox-active amino acid acts as the final electron donor in the photoreduction of the light-excited flavin adenine dinucleotide (FAD) cofactor (Aubert et al., 2000) along a cascade of tryptophan (Trp) residues. Depending on the organism and variant, either the third (TrpC) or fourth Trp (TrpD) of a conserved chain of four Trp residues (TrpA, TrpB, TrpC, and TrpD) could be identified as electron donor (**Table 1**) (Nohr et al., 2017; Hochstoeger et al., 2020; Xu et al., 2021). All distances yet determined by this method were found to be in very good agreement with calculated or structure data. Hence, it is evident that the method yields very good results in different systems.

It should also be noted that the distance distributions extracted from OOP-ESEEM time traces are very narrow (see the experimental time traces in the publications listed in **Table 1**), which is quite different from typical distance distributions from PELDOR studies of proteins (Schiemann et al., 2021). This result is unusual on first inspection because (nitroxide) spin labels, as commonly used in PELDOR spectroscopy, are rather small molecules with localized electron spin density, whereas the radicals involved in the OOP-ESEEM publications are often larger and thus have a more extended spin density distribution. The reason could be that all involved amino acids and cofactor radicals are embedded inside a larger protein (complex) and therefore have well-defined positions and orientations. In addition, their motional degrees of freedom are rather restricted. On the other hand, site-directed spin labeling of a protein is often restricted to its surface, where the linking cysteine residues are more readily accessible. However, spin centers at protein surfaces have typically larger conformational degrees of freedom, thus yielding broader distance distributions. An additional reason for the observed narrow distance distributions of OOP-ESEEM is that in the protein systems studied so far, electron transfer after light irradiation occurs stepwise *via* a chain of redox-active molecules, but the intermediate radical pairs formed in this process have a lifetime too short to contribute to the OOP signal. Thus, only the terminal, longest-lived radical pair is detected and analyzed.

Distance Dependence of *D* and *J*

In a coupled radical pair, both exchange and dipolar interactions depend on the distance r (**Figure 2**): While the dipolar interaction follows an r^{-3} dependence, the exchange interaction falls off more strongly with increasing distance r, following an exponential relationship: $J(r) \sim \exp(\beta r)$. The magnitude of $D(r)$ can be easily estimated using **Eq. 3**. This is not so straightforward for J as the strength of the exchange coupling does not only depend on the distance but also on the electronic structure of the radical pair partners and the medium in between. The latter is expressed by the factor β, which parametrizes the exponential decay of the exchange coupling with the distance for a given medium (De Kanter et al., 1977):

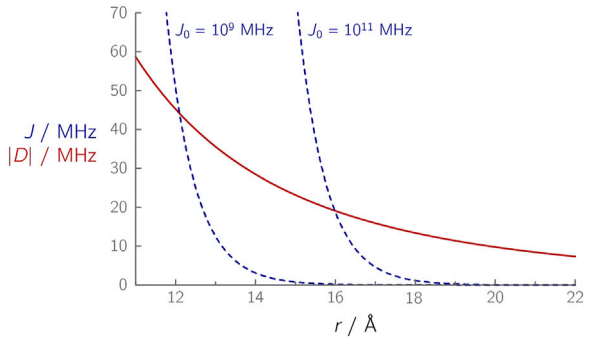

FIGURE 2 | Calculated distance dependences of $|D(r)|$ (red curve) and $J(r)$ (dashed blue curves) in a radical pair. The spin–spin couplings D and J were calculated using **Eqs. 3** and **7**, respectively, using $\beta = 1.4$ Å^{-1}, and the J_0 values indicated next to the respective curves.

$$J(r) = J_0 \exp(\beta r) \tag{7}$$

An analogous relationship applies to the electronic coupling V^2, which is proportional to the exchange coupling and also plays a role in Marcus' theory (Marcus and Sutin, 1985). For the electronic coupling, a value of $\beta = 1.4$ Å^{-1} was found for proteins (Moser et al., 1992). The magnitude of J_0 is per se unknown; however, it can be estimated using **Eq. 7** for systems in which J has been determined experimentally (**Table 1**). For the FAD–TrpC radical pairs ($J \approx 0.05$ MHz) in the photolyase/cryptochrome protein family, J_0 values of $\approx 1 \cdot 10^9$ MHz were determined, while for the FAD–TrpD radical pair ($J \approx 0.03$ MHz), J_0 values are larger ($\approx 1 \cdot 10^{11}$ MHz) (Nohr et al., 2017; Hochstoeger et al., 2020; Xu et al., 2021). Although the radical pair composition is identical in both cases, the different J_0 values (**Figure 2**) indicate that other parameters, in this case, differences in the protein environment, have an influence that should not be ignored. Furthermore, at larger distances, it becomes increasingly difficult to determine J accurately: The small J value in case of the FAD–TrpD radical pair in cryptochromes contains a larger uncertainty (Hochstoeger et al., 2020), which could alternatively explain the significant discrepancies between the abovementioned J_0 values. As a comparison, a much larger J_0 value of $\approx 1 \cdot 10^{13}$ MHz was estimated for the primary radical pair of a photosynthetic reaction center (Efimova and Hore, 2008), thus demonstrating that J_0 can differ by several orders of magnitude, depending on the radical pair composition and the environment in which it is embedded.

D and J are of similar magnitude in a distance range of ≈13–16 Å, **Figure 2** (O'Dea et al., 2005). At distances larger than ≈17 Å, D becomes the dominant parameter that essentially reflects the modulation frequency of an OOP-ESEEM time trace. In all yet published studies of weakly coupled radical pairs in proteins, distances between ≈17 Å (Nohr et al., 2017; Hochstoeger et al., 2020; Xu et al., 2021) and ≈33 Å (Zech et al., 1999; Santabarbara et al., 2005) were obtained; D was found to be at least one order of magnitude larger than J.

Applicability of the Point-Dipole Approximation

From an OOP-ESEEM experiment, the effective distance r between the two electron spins is, in general, determined *via* the D value under the assumption of the validity of the point-dipole approximation (**Eq. 3**). By comparing the calculated distance with a distance extracted from a structure model or from an experimentally determined structure, it is then possible to assign the involved amino acids that take place in radical pair formation. It is thus important that the applied approximation describes the structure of the molecule as accurately as possible, in particular, if two (or even more) amino acids with similar distances could potentially be a part of the coupled radical pair. Often, r is determined by measuring the distance between the respective atom of the highest electron spin density ("point-dipole model") in the two radicals. For instance, in an $[FAD^{\bullet-}\cdots Trp^{\bullet+}]$ radical pair, these are the center between N(5) and C(4a) of the $FAD^{\bullet-}$ and the C(3) atom of the $Trp^{\bullet+}$ (Nohr et al., 2017); in a protein with two nitroxyl radicals, this would be the center of each of the two NO bonds. Alternatively, the center of gravity of the electron spin density distributions of the respective radicals can be determined either experimentally by hyperfine spectroscopy (Harmer, 2016) or theoretically, for example, *via* calculations at the DFT level of theory, and the distance between the two centers of gravities can then be determined ("center-of-gravity model").

These two models were compared with a refined "distributed point–dipole model" (Bertrand et al., 1996), which takes the local dipoles of all pairs of atoms into account, and furthermore, with a quantum mechanical solution (Riplinger et al., 2009). Aromatic and non-aromatic nitroxides connected *via* different linker groups served as model systems; the distances between such biradical systems were determined *via* X-ray crystallography. Short distances and strongly delocalized electron spins lead to a failure of all point-dipole approximation models as J, and the quantum mechanical exchange part of D then play major roles. J depends on the orientation of the two radical moieties with respect to each other, as this strongly influences the overlap of the respective SOMOs. While the point-dipole approximation fails for unsaturated linkers between the two molecules even at larger distances, such models become more accurate with increasing distances for saturated linkers; in particular, the center-of-gravity approximation leads to very good results.

In principle, the distance between two coupled radicals also depends on their mutual orientation. Different orientations may result in an incorrect assignment, especially if no structure information on a system is available. The reason is that OOP-ESEEM measures the distance between the centers of the respective electron spin density distributions, which may not coincide with the centers of gravities of the two radical-pair halves. How large this error could be can only be estimated, as the uncertainty depends on the differences in the centers of gravity with respect to their spin density distributions. As an example, a $[Flavin^{\bullet-}\cdots Trp^{\bullet+}]$ radical pair with a distance of 20 Å was studied. Both radicals are unsymmetric, and hence, the respective centers of gravity and centers of spin density distribution do not coincide (both molecules and the corresponding electron spin density distributions are shown in **Supplementary Figure S1**). The molecules were rotated in 90°-steps with respect to each other without altering the distance of their centers of gravity. Depending on their respective orientation, the spin density distance varied by up to ±0.5 Å, that is, by up to 5%. This result shows that although there are only small differences between the center of mass and the center of spin density in both molecules, the influence of the orientation on the accuracy of the determined distance should not be neglected. This is especially relevant for molecules with very asymmetric spin density distributions.

The Influence of Dipolar and Exchange Interaction on the OOP-ESEEM Time Trace

To determine the accuracy of the OOP-ESEEM method on spin-correlated radical pairs in proteins, first, the parameter space of D and J was probed (in the subsequent Figures, time traces are always depicted on the left-hand side and the corresponding spectra obtained by SFT on the right). Calculations with altered D parameters (−2, −6, −10, and −14 MHz) and a fixed small J value of +0.01 MHz were performed (**Supplementary Figure S2**). As expected, an increase in the absolute D value leads to an increase in the modulation frequency. The corresponding frequencies $\nu_{\parallel}$ and $\nu_{\perp}$ in the SFT spectra are clearly separated from each other and can be easily read out. Two different relaxation times T_d, 0.35 and 0.1 µs, were used in each case. The corresponding SFT spectra reveal that fast relaxation only causes difficulties if it is much shorter than one oscillation period of the time traces, that is, if $T_d < 2/\omega_{eff}$. This is the case only for very small absolute D values ($|D| < 2$MHz), which correspond to large distances (>33 Å). Here the relaxation time is so short that the first maximum is shifted relative to the signal with the more inefficient relaxation. A fit and, in particular, an SFT-based analysis would lead to an incorrect result, as demonstrated by the altered frequency $\nu_{\parallel}$. Such an effect can be counteracted if a realistic T_d value can be estimated (based on data from other methods) and used as a fitting parameter. The situation improves considerably for larger absolute D values: As long as at least one full oscillation period can be analyzed, inflection points appear at identical positions in the SFT spectra but are less pronounced at shorter relaxation times due to the smaller number of detected modulations. This could, in principle, lead to larger uncertainties in experimental data with low SNRs.

The influence of the parameter J at a constant D value of −8 MHz is shown in **Supplementary Figure S3**. An increase of J from 0.01 to 0.1 MHz has hardly any effect on the time trace and on the frequency spectra. J values that are in the order of the magnitude of $|D|$ (in this case: $J = 0.5$ and 1 MHz), however, show a clear decrease in the modulation frequency, and an increasingly strong initial rise of the signal can be detected. The reason for the frequency decrease can be explained by the different signs of J and D, as the two interactions cancel each other out to some extent (Efimova and Hore, 2008).

Constraints in Experimental OOP-ESEEM Time Traces and Corresponding Spectra

A number of difficulties can complicate a straightforward spectral analysis of experimental data sets: 1) Observation of only a few modulations due to fast relaxation and/or a weak spin-echo signal can obscure a proper analysis. 2) ESEEM signals caused by nuclear spins are often superimposed, thus leading to additional frequencies in the OOP time trace. Fortunately, they typically have a much smaller amplitude than the dipolar modulations. If such additional frequencies preclude an unambiguous analysis, increasing the magnetic field and correspondingly the microwave detection frequency can be a simple solution (Savitsky et al., 2013; Nohr et al., 2017) as modulation depths of nuclear ESEEM frequencies depend on the magnetic field (van Doorslaer, 2017). 3) The adjustment of the proper microwave-detection phase is often rather difficult. This is due to the fact that in the vast majority of cases, no dark-stable EPR signal can be detected due to the lack of any paramagnetic species prior to sample irradiation. Improper phasing, however, may lead to nuclear ESEEM frequencies "leaking" from the in-phase channel into the OOP channel. This effect has been extensively studied previously (Fursman and Hore, 1999): Nuclear frequencies become visible in the SFT spectrum. These can, to some extent, "wash out" the outer regions of the SFT spectrum, thus making the read-out of $\nu_{\parallel}$ difficult. However, it has been shown that the superposition of nuclear frequencies does not lead to large errors in the determination of D (Fursman and Hore, 1999). 4) The typical deadtime of a pulsed EPR spectrometer (Stoll, 2017) precludes detection of the early response to the application of the OOP ESEEM pulse sequence (typically ≈100 ns after the last microwave pulse). Hence, one has to cope with a "truncated" time trace. In the following sections, the influence of the missing data due to the spectrometer deadtime and the reconstruction of these on the frequency spectrum obtained by SFT will be investigated.

Reconstruction of the Early Time Points of the Time Trace

Truncation of the early part of the OOP time trace can have a certain impact on the resulting SFT spectrum. Fortunately, information on D and J is still present in the echo modulation of the later parts of the time trace, but the first part should be determined by reconstruction for a proper analysis. The influence of the spectrometer deadtime and the reconstruction of the early time trace on the SFT spectrum will be analyzed in more detail below (**Figure 3**). For a reasonable reconstruction, it is helpful to have a rough estimate of the exchange interaction J, as larger values of this parameter define the initial rise of the time trace. If J is much smaller than $|D|$, the shape of the signal is analogous to that depicted in **Supplementary Figure S2**. If J is expected to be in the range of $|D|$, initial shapes, as exemplified in the upper panel of **Supplementary Figure S3**, can be assumed. The OOP-ESEEM time trace can now be reconstructed using a number of different methods: 1) A linear extrapolation can be used by plotting a straight line from the first measured point to the time point at $t = 0$, which per definition has zero intensity. This method can be extended by using a polynomial extrapolation. 2) A least-squares fitting of the truncated time trace can be performed. Here, **Eq. 5**, which contains the parameters H, T_d, D, and J, is fitted to the measured time trace, and the resulting optimal fitting function is then extrapolated back to the point at $t = 0$. 3) Some studies have used the "maximum entropy method" to reconstruct the missing time points (Bittl and Zech, 1997). 4) Precise predictions can be obtained using an autoregressive (AR) model (Neumaier and Schneider, 2001). Here, an m-dimensional AR model of order p is applied, which is composed of vectors v_ν measured at discrete time points ν according to the following equation:

$$v_\nu = w + \sum_{l=1}^{p} A_l v_{\nu-l} + \varepsilon_\nu \tag{8}$$

A_1 to A_p are the coefficient matrices, $\varepsilon_\nu = \text{noise}(C)$ are uncorrelated m-dimensional vectors with a covariance matrix C that has a mean of zero, and w is a vector of y-axis terms that is set to zero because the mean of the time signal should also be zero. The parameters (A, C, w) are assessed with a stepwise least-square fit to the (here one-dimensional) discrete time trace, with p as the optimization criterion (Neumaier and Schneider, 2001). The reconstruction of the data point $S(k)$ within the experimental deadtime then takes place backwards *via* the last k—l points according to $S(k) = \sum_{l=1}^{p} A_l(l) S(k-l)$ until the point at $t = 0$ is reached.

Figure 3 displays time traces with identical D and J values ($D = -11$ MHz and $J = 2$ MHz), including Gaussian noise (SNR = 50), which were reconstructed by different reconstruction methods. The complete time trace (without an experimental deadtime) is shown for comparison. Additional signals appear in the SFT spectra for the time traces without reconstruction and with linear reconstruction. Linear reconstruction can additionally lead to an underestimation of the reconstructed oscillation amplitude and can cause additional modulations in the SFT spectrum due to the discontinuity of the time trace. On the other hand, the time trace reconstructed by the AR model and its respective SFT spectrum shows only minor differences compared to the deadtime-free spectrum.

It is worth mentioning that in all scenarios described above, the frequency $\nu_{\perp}$ remains virtually unchanged. On the other hand, the frequency $\nu_{\parallel}$ can only be read out accurately if the signal was reconstructed by the AR method, so the latter is the only one of the methods presented here that is suitable to determine the inflection point and thus $\nu_{\parallel}$, which is crucial for an exact determination of both D and J parameters. A linear reconstruction is only justified if the earliest minimum or maximum can still be detected, that is, the signal falls or rises monotonically from the zero point to the first detected point. This is the case either if the deadtime is short enough or the oscillation period is long enough [see the reconstructed signals in (Dzuba et al., 1995)].

For a best-possible reconstruction, it is beneficial to have a rough estimate of how the signal behaves within the experimental deadtime. If structure data on the radical pair of interest is available, D can be determined *via* the point-dipole approximation, and J at least indirectly either by using the distance dependence shown in **Figure 2** or *via* electronic coupling within the framework of Marcus' theory (Marcus and

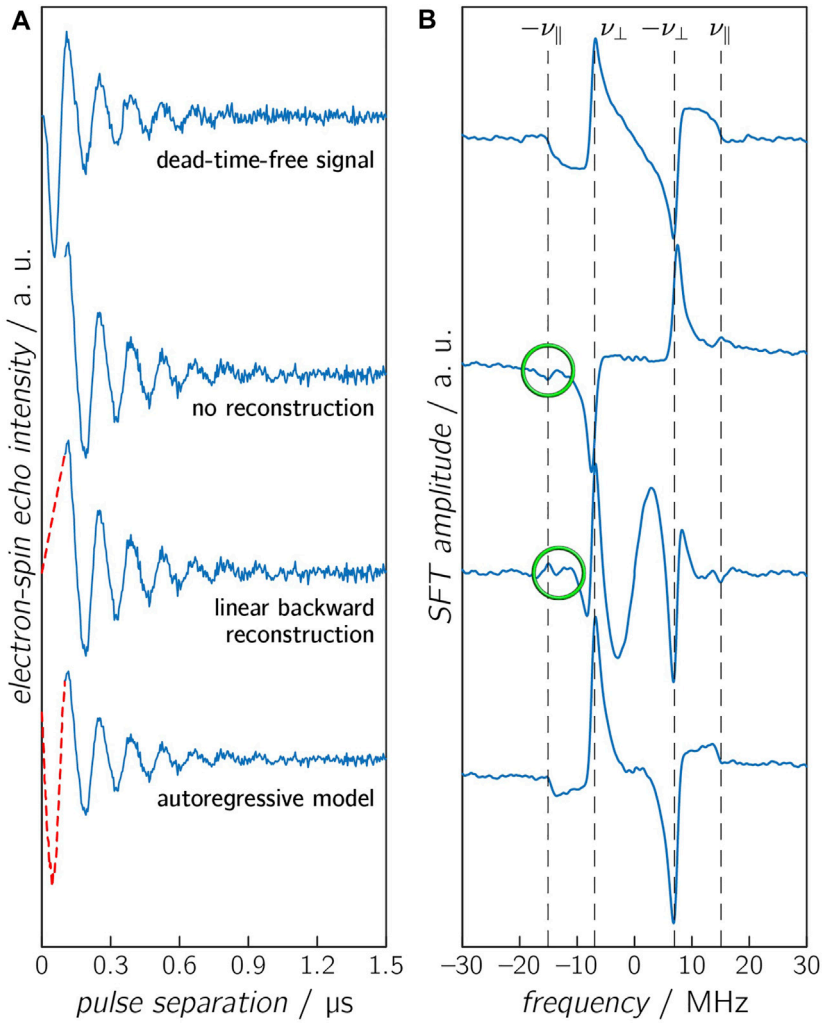

FIGURE 3 | Calculated OOP-ESEEM time traces **(A)**, including noise (SNR = 50) with a spectrometer deadtime of 100 ns, and the corresponding SFT spectra **(B)**. The missing first 100 ns were either not reconstructed (second panel), reconstructed with a linear model (third panel), or reconstructed with an AR model (lowest panel). The untruncated time trace is depicted in the upper panel. The vertical dashed lines in the SFT spectra depict the frequencies $\nu_\perp$ and $\nu_\parallel$. Differences between calculated and reconstructed values of $\nu_\parallel$ are highlighted in green.

Sutin, 1985). These estimates can then be used as initial values of D and J.

Calculated Examples of OOP-ESEEM Time Traces

To evaluate the accuracy of the distance determination at various distances, a series of time traces using different combinations of D and J values were calculated and compared with the results of numerical simulations (**Figure 4** and **Supplementary Figure S4**). To the calculated time traces, Gaussian noise of varying intensity was added to ensure that these data sets resemble those typically obtained from experiments. With an SNR of 100, the time trace differs only slightly from a noise-free data set. However, an SNR of 5 renders a time trace in which the modulation is only barely visible. Additional SNR values of 10 and 20 were chosen, which are in the range of typical experimental SNRs. The first 100 ns of each time trace were first truncated to mimic the spectrometer deadtime and then reconstructed using the AR model. The chosen D and J value pairs provide a good estimation of different distance ranges. At the short end, around 15 Å, J and $|D|$ assume comparable values. Results based on the point-dipole approximation become invalid, thus making the distance determination less accurate. At the other end, at distances larger than 45 Å, the dipolar coupling becomes very small so that modulations can only be detected in case of very long relaxation times, which was reflected by using two T_d values, 0.35 and 0.10 µs. To account for the entire distance range under investigation, distances of 16.5, 17.6, 19.2, 21.4, 34, and 43.7 Å, respectively, were used, which correspond to D values of −17.5, −4.5, −1, −8, −2, and −1 MHz. The respective J values were estimated using **Eq. 7** with $J_0 = 1{\cdot}10^{11}$ MHz, resulting in values of 10.0, 2.0, 0.2, 0.01, 0.00, and 0.00 MHz.

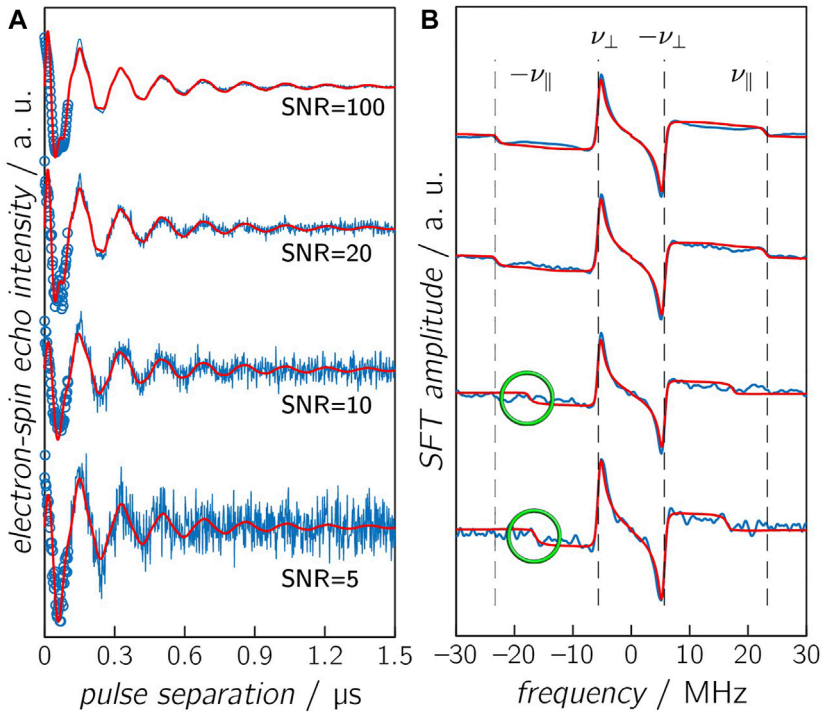

FIGURE 4 | Calculated OOP-ESEEM time traces **(A)** and corresponding SFT spectra **(B)**. Calculated time trace (D = −14.5 MHz and J = 2 MHz), including reconstruction with the AR model (circles) and various SNR levels, are depicted in blue, and results from numerical simulations are depicted in red. The vertical dashed lines in the SFT spectra are the correct frequencies $\nu_{\parallel}$ and $\nu_{\perp}$. Please note that calculated and simulated frequency $\nu_{\parallel}$ are only identical in case of an SNR ≥20, and differences are highlighted in green. Other parameters are summarized in **Table 3**.

TABLE 2 | Comparisons of calculated OOP-ESEEM time traces using different D and J value combinations with results from numerical simulations using **Eq. 5**. Starting values for least-squares fittings were T_d = 0.25 µs and H = 1. D, J, T_d, and H were allowed by the fitting routine to be varied in the intervals −20 MHz ≤ D ≤ 0, 0 ≤ J ≤ 10 MHz, 0 ≤ T_d ≤ 10 µs, and 0 ≤ H < ∞. The distance r was calculated using **Eq. 3**. Obtained distances with increased error margin (>10%) or incorrect values are highlighted in orange.

Distance and T_d	SNR	Simulation parameters/MHz		Starting values/MHz		Fit results/MHz		Distance
		D	J	D	J	D	J	r/Å
r = 34.0 Å T_d = 0.35 µs	100	−2.0	0.00	−3.5	0.1	−1.997(4)	<0.01	33.94(6)
	20					−2.00(2)	<0.01	33.9(3)
	10					−2.01(3)	<0.01	33.9(5)
	5					−1.96(6)	0.00(2)	34(1)
r = 34.0 Å T_d = 0.10 µs	100	−2.0	0.00	−3.5	0.1	−1.96(2)	<0.01	34.2(4)
	20					−1.96(5)	<0.01	34(1)
	10					−2.10(9)	<0.01	33(1)
	5					−1.3(7)	<0.01	39(22)
r = 42.7 Å T_d = 0.35 µs	100	−1.0	0.00	−2.5	0.1	−1.001(1)	<0.01	42.72(6)
	20					−1.001(7)	<0.01	42.7(3)
	10					−0.99(2)	<0.01	42.8(6)
	5					−1.02(3)	<0.01	42(12)
r = 42.7 Å T_d = 0.10 µs	100	−1.0	0.00	−2.5	0.1	−0.97(2)	<0.01	43.1(8)
	20					−0.95(9)	<0.01	44(4)
	10					−1.0(2)	<0.01	42(6)
	5					−0.2(13)	<0.01	61(229)

After deadtime reconstruction, the time traces were fitted by numerical simulation to obtain optimized values for D, J, and T_d using starting values that were ±15% off the correct values. The values of D and J were obtained by the fit, and the respective SFT spectrum was calculated from the "experimental" data and from the optimal fit results. The calculated "correct" frequencies $\nu_{\perp}$ and

TABLE 3 | Comparisons of calculated OOP-ESEEM time traces using different D and J value combinations with results from numerical simulations using **Eq. 5**. Starting values for least-squares fittings were $T_d = 0.25$ µs and $H = 1$. The starting values for D and J were 15% off the theoretical values. D, J, T_d, and H were allowed by the fitting routine to be varied in the intervals -20 MHz $\leq D \leq 0$, $0 \leq J \leq 15$ MHz, $0 \leq T_d \leq 10$ µs, and $0 \leq H < \infty$. The distance r was calculated using **Eq. 3**. Obtained distances with increased error margin (>10%) or incorrect values are highlighted in orange.

Distance	SNR	Simulation parameters/MHz		Starting values/MHz		Fit results/MHz		Distance from PDA
		D	*J*	*D*	*J*	*D*	*J*	*r*/Å
r = 21.4 Å	20	–8.0	0.01	–8.5	0.0	–8.00(5)	0.00(1)	21.41(5)
	10					–8.2(2)	0.00(4)	21.2(3)
	5					–8.2(6)	0.04(7)	21.2(5)
r = 19.2 Å	20	–11.0	0.20	–8.5	0.1	–10.5(1)	0.00(3)	19.5(2)
	10					–10.5(1)	0.00(4)	19.5(2)
	5					–10.2(3)	0.00(7)	19.6(4)
r = 17.6 Å	100	–14.5	2.00	–12.5	1.0	–14.41(6)	1.96(2)	17.56(7)
	20					–14.5(8)	2.00(2)	17.53(9)
	10					–11.6(1)	1.04(4)	18.8(2)
	5					–11.2(1)	0.89(5)	19.1(3)
r = 16.5 Å	100	–17.5	10.00	–15.5	8.0	–17.4(1)	9.98(4)	16.4(1)
	20					–17.8(1)	10.11(5)	16.4(1)
	10					–17.2(2)	9.89(7)	16.6(2)
	5					–13.9(2)	8.83(7)	17.3(3)

$\nu_\parallel$ are labeled by vertical dashed lines in the respective Figures in order to judge the accuracy of the SFT spectra of the reconstituted and fitted time-domain signals. The distance between the two radicals was then determined using the fitted D values and **Eq. 3**. The corresponding results are summarized in **Table 2** (for longer distances) and **Table 3** (for shorter distances); exemplary time traces and corresponding SFT spectra are shown in **Figure 4** for the combination $D = -14.5$ MHz and $J = 2$ MHz and in **Supplementary Figure S4** (for the combination $D = -2.0$ MHz and $J = 0$ MHz).

Several conclusions can be drawn from such numerical simulations (**Tables 2**, **3**): 1) At the rather long distance of 34 Å, correct distances with small error margins are obtained as long as SNR ≥5 and the relaxation time is sufficiently long (≥0.35 µs) (see **Table 2**). This is not surprising as J was assumed zero. Hence, the modulation of the time trace is governed solely by D, and consequently, the number of fitted parameters is reduced by one. In the SFT spectrum, one frequency is sufficient for an unambiguous assignment as $\nu_\perp$ is now ± (2/3) $|D|$ (see above). Consequently, even at lower SNRs, the distance can be determined precisely from $\nu_\perp$. Making relaxation more efficient (0.1 µs) affects the accuracy of the simulation results. In this case, the obtained distance is trustworthy only at an SNR ≥10. Increasing the distance to 42.7 Å in combination with a relaxation time of 0.1 µs leads to values being trustworthy only at an SNR ≥20 (**Supplementary Figure S4**). This clearly shows that the relaxation time is the limiting factor for the accuracy of the distance determination at longer distances. 2) For shorter distances (**Table 3**), the situation becomes more complicated as J typically assumes non-zero values, which can be of the same order as $|D|$. The time traces in **Figure 4** ($D = -14.5$ MHz and $J = 2$ MHz) show that the reconstruction at $t = 0$ does not always approach exactly zero, but the AR model is capable of reconstructing even small-amplitude oscillations with high accuracy. Therefore, good fit results were obtained for time traces with smaller J values (≤0.2 MHz) as long as the SNR ≥5. The fitting procedure of time traces with larger J values renders increasingly inaccurate distance data for low SNRs, as seen from the data of the combinations SNR ≤10 and $J = 2.0$ MHz and SNR ≤5 and $J = 10.0$ MHz (**Table 3** and **Figure 4**). 3) The threshold SNR below which the fit yields inaccurate or even wrong distance data varies for each individual experimental data set and depends, for instance, on the choice of the starting values and the algorithm used for data reconstruction. However, it becomes evident that the accuracy of the distance determination decreases as soon as J is of the order of $|D|$. Furthermore, reconstruction at poor SNRs can lead to additional oscillation artifacts that actually belong to the noise. This trend is confirmed in the frequency spectra (**Figure 4B**). While at SNRs ≥20, both frequencies $\nu_\parallel$ and $\nu_\perp$ can be determined correctly, incorrect values of $\nu_\parallel$ are extracted at lower SNRs. This finding is not unexpected for Pake patterns as the amplitude of the SFT at $\nu_\perp$ is much larger than that at $\nu_\parallel$ (Weil et al., 1994), which allows an unambiguous readout of only $\nu_\perp$ even at low SNRs.

To examine artifacts of fitting in more detail, OOP-ESEEM time traces (SNR = 20) with $D = -14.5$ MHz, $J = 2$ MHz, and truncated at 100 ns were calculated and then reconstructed using the AR model (see **Supplementary Table S4** and **Supplementary Figure S5**). Three different sets of starting values of D and J were used. Depending on those, ambiguous values for $\nu_\parallel$ were obtained in the SFT spectra that resulted in incorrect D and J values. This result raises the question of whether and if a quantitative distinction can be made between good and bad fit results. The analysis of the residual sum of squares (RSS) shows that in this example, the lowest value indeed corresponds to the best fit

(**Supplementary Table S4**). Unfortunately, this cannot be generalized as such validation parameters are strongly influenced by the SNR of the measurement. Nevertheless, there are some ways to avoid ambiguous fit results: 1) The SNR of the experimental time trace can be increased as much as economically possible. However, this strongly depends on the used sample and its parameters, such as photostability and quantum yield of electron transfer. 2) The number of parameters to be fitted can be reduced manually by reading out $\nu_\perp$ from the SFT spectrum; a procedure that is reliable even at lower SNRs (**Figure 4**, SNR = 5), and subsequently numerically fitting the SFT spectrum using this $\nu_\perp$ value. 3) A global fitting algorithm can be used for the simultaneous analysis of the OOP-ESEEM time trace and its SFT spectrum. Hence, the limiting factor for the accuracy of distance determination at shorter distances is typically the determination of $\nu_\parallel$.

SUMMARY AND OUTLOOK

In this study, we evaluated the accuracy and applicability of the OOP-ESEEM method in terms of published distance determinations and investigated the influence of different parameters on the analysis of experimental data in more detail. By numerical fitting of calculated model time traces, limitations of the method were derived as a function of the SNR and the distance of a spin-correlated radical pair. Some of the difficulties encountered in experiments, such as contributions from nuclear ESEEM, incorrect phase settings, or partial orientation selection due to the limited bandwidth of applied microwave pulses, which can lead to distortions of the time traces, were not included in the calculated time traces. Therefore, we attempted to take these effects into account by considering strongly different SNRs. By evaluating the distances and their respective uncertainties obtained by spectral simulation, information on the accuracy of the method at different distance regions was obtained.

At large distances, above ≈22 Å, the analysis of OOP-ESEEM time traces is rather straightforward, as in such cases, J approaches 0, and the modulation of the time trace is solely governed by D. Therefore, only the frequency $\nu_\perp$ needs to be determined, which can be achieved even at limited SNRs and after non-perfect deadtime reconstruction of the OOP-ESEEM time trace (**Table 2** and **Supplementary Figure S4**). The only constricting parameter is the relaxation time, which should be long enough so that at least one modulation can be detected and analyzed. At shorter radical pair distances, around 20 Å, the method still yields reliable distance data even with lower SNRs, and distances can be determined with an uncertainty of less than 0.5 Å. The reason is that J is still orders of magnitude smaller than $|D|$, and therefore the spectrum is still dominated by the D parameter. In addition, the relaxation time is, in most cases, long enough with respect to the modulation period to not limit the analysis. However, the accuracy of the method decreases when J and $|D|$ are similar in size, which could be, depending on the value of J_0, the case for distances of less than ≈18 Å. Here, unambiguous values for D and J cannot be determined without further information from independent methods. This significantly increases the uncertainty of determining distances. In principle, the method can provide excellent accuracy even in this distance range, provided good start values for the numerical simulations are available. This holds for most proteins as either crystal structure data or at least a structure model is available. Moreover, only a few amino acids are intrinsic candidates for the formation of spin-correlated radical pairs, and the number of amino acids potentially involved can usually be narrowed down, leaving only a few possibilities. Thus, realistic starting values of D (**Eq. 3**) and J, either from **Figure 2** or **Eq. 7**, can be estimated. **Figure 4** clearly demonstrates that, with good starting values, trustworthy distance data can be obtained even at low SNRs.

Because of the title of the special "research topic," we have limited this study to distance determinations in proteins; however, it should be made clear that the OOP-ESEEM method, as well as its accuracy and limitations described here, can be applied just as well to all other types of molecular systems as long as they form spin-correlated radical pairs. However, due to the typically less defined structure of such systems, broader distance distributions may be expected (Popov et al., 2017; Beletskaya et al., 2020). Accordingly, the method has great potential, which has not yet been fully exploited due to the few examples investigated so far. We hope that this will improve in the near future, especially if new labeling methods become available that can be applied to both the protein and to binding partners such as DNA (Olshansky et al., 2019). It may be even possible to generate new donor-acceptor molecules (Reece et al., 2007; Weng et al., 2020) or even *de novo* designed proteins (Keller et al., 2017; Liu et al., 2018; Zollitsch et al., 2018) that can be used to perform light-induced electron transfer.

Finally, it has been suggested recently that the effect of chiral-induced spin selectivity, which, among other things, enhances the anisotropy of the reaction yield of magnetic field effects, may be detected in the in-phase channel of an OOP-ESEEM signal if applied on oriented samples (Luo and Hore, 2021). If this could be confirmed experimentally, another exciting area of application could be added to the method.

AUTHOR CONTRIBUTIONS

ES and TA designed the study. TA performed all calculations. ES, SW, and TA wrote the manuscript.

ACKNOWLEDGMENTS

SW and ES thank the DFG (235777276/GRK1976) for financial support. ES would like to thank Hans-Fischer Gesellschaft for continuous support.

SUPPLEMENTARY MATERIAL

The Supplementary Material for this article can be found online at: https://www.frontiersin.org/articles/10.3389/fmolb.2022.890826/full#supplementary-material

REFERENCES

Adrian, F. J. (1972). Singlet-Triplet Splitting in Diffusing Radical Pairs and the Magnitude of Chemically Induced Electron Spin Polarization. *J. Chem. Phys.* 57 (12), 5107–5113. doi:10.1063/1.1678196

Aubert, C., Vos, M. H., Mathis, P., Eker, A. P. M., and Brettel, K. (2000). Intraprotein Radical Transfer during Photoactivation of DNA Photolyase. *Nature* 405, 586–590. doi:10.1038/35014644

Barone, V. (1996). "Structure, Magnetic Properties and Reactivities of Open-Shell Species from Density Functional and Self-Consistent Hybrid Methods," in *Recent Advances in Density-Functional Methods*. Editor D. P. Chong (Singapore: World Scientific Publishing), 287–334.

Becke, A. D. (1986). Density Functional Calculations of Molecular Bond Energies. *J. Chem. Phys.* 84, 4524–4529. doi:10.1063/1.450025

Becke, A. D. (1988). Density-functional Exchange-Energy Approximation with Correct Asymptotic Behavior. *Phys. Rev. A* 38, 3098–3100. doi:10.1103/physreva.38.3098

Beletskaya, E. A., Lukina, E. A., Uvarov, M. N., Popov, A. A., and Kulik, L. V. (2020). Geminate Recombination in Organic Photovoltaic Blend PCDTBT/PC71BM Studied by Out-of-phase Electron Spin Echo Spectroscopy. *J. Chem. Phys.* 152 (4), 044706. doi:10.1063/1.5131855

Bertrand, P., Camensuli, P., More, C., and Guigliarelli, B. (1996). A Local Spin Model to Describe the Magnetic Interactions in Biological Molecules Containing [4Fe–4S]+ Clusters. Application to Ni–Fe Hydrogenases. *J. Am. Chem. Soc.* 118 (6), 1426–1434. doi:10.1021/ja951981w

Biskup, T., Schleicher, E., Okafuji, A., Link, G., Hitomi, K., Getzoff, E. D., et al. (2009). Direct Observation of a Photoinduced Radical Pair in a Cryptochrome Blue-Light Photoreceptor. *Angew. Chem. Int. Ed.* 48, 404–407. doi:10.1002/anie.200803102

Bittl, R., Zech, S. G., Fromme, P., Witt, H. T., and Lubitz, W. (1997). Pulsed EPR Structure Analysis of Photosystem I Single Crystals: Localization of the Phylloquinone Acceptor. *Biochemistry* 36, 12001–12004. doi:10.1021/bi971645n

Bittl, R., and Zech, S. G. (2001). Pulsed EPR Spectroscopy on Short-Lived Intermediates in Photosystem I. *Biochimica Biophysica Acta (BBA) - Bioenergetics* 1507, 194–211. doi:10.1016/s0005-2728(01)00210-9

Bittl, R., and Zech, S. G. (1997). Pulsed EPR Study of Spin-Coupled Radical Pairs in Photosynthetic Reaction Centers: Measurement of the Distance between and in Photosystem I and between and in Bacterial Reaction Centers. *J. Phys. Chem. B* 101, 1429–1436. doi:10.1021/jp962256q

Borovykh, I. V., Kulik, L. V., Dzuba, S. A., and Hoff, A. J. (2002). Out-of-Phase Stimulated Electron Spin−Echo Appearing in the Evolution of Spin-Correlated Photosynthetic Triplet-Radical Pairs. *J. Phys. Chem. B* 106, 12066–12071. doi:10.1021/jp0213912

Carmieli, R., Mi, Q., Ricks, A. B., Giacobbe, E. M., Mickley, S. M., and Wasielewski, M. R. (2009). Direct Measurement of Photoinduced Charge Separation Distances in Donor−Acceptor Systems for Artificial Photosynthesis Using OOP-ESEEM. *J. Am. Chem. Soc.* 131, 8372–8373. doi:10.1021/ja902864h

Closs, G. L., Forbes, M. D. E., and Norris, J. R. (1987). Spin-polarized Electron Paramagnetic Resonance Spectra of Radical Pairs in Micelles: Observation of Electron Spin-Spin Interactions. *J. Phys. Chem.* 91, 3592–3599. doi:10.1021/j100297a026

Dal Farra, M. G., Richert, S., Martin, C., Larminie, C., Gobbo, M., Bergantino, E., et al. (2019). Light-induced Pulsed EPR Dipolar Spectroscopy on a Paradigmatic Hemeprotein. *ChemPhysChem* 20, 931–935. doi:10.1002/cphc.201900139

De Kanter, F. J. J., Kaptein, R., and Van Santen, R. A. (1977). Magnetic Field Dependent Biradical CIDNP as a Tool for the Study of Conformations of Polymethylene Chains. *Chem. Phys. Lett.* 45, 575–579. doi:10.1016/0009-2614(77)80093-6

Dzuba, S. A., Gast, P., and Hoff, A. J. (1995). ESEEM Study of Spin-Spin Interactions in Spin-Polarised P+QA− Pairs in the Photosynthetic Purple Bacterium Rhodobacter Sphaeroides R26. *Chem. Phys. Lett.* 236, 595–602. doi:10.1016/0009-2614(95)00259-7

Dzuba, S. A., Hara, H., Kawamori, A., Iwaki, M., Itoh, S., and Tsvetkov, Y. D. (1997). Electron Spin Echo of Spin-Polarised Radical Pairs in Intact and Quinone-Reconstituted Plant Photosystem I Reaction Centers. *Chem. Phys. Lett.* 264, 238–244. doi:10.1016/s0009-2614(96)01302-4

Dzuba, S. A. (1997). Spin-correlated Radical Pairs in Photosynthetic Reaction Centers: Role of Anisotropic Hyperfine Interaction as Revealed by Computational Modeling. *Chem. Phys. Lett.* 278, 333–340. doi:10.1016/s0009-2614(97)01044-0

Edwards, T. H., and Stoll, S. (2016). A Bayesian Approach to Quantifying Uncertainty from Experimental Noise in DEER Spectroscopy. *J. Magnetic Reson.* 270, 87–97. doi:10.1016/j.jmr.2016.06.021

Edwards, T. H., and Stoll, S. (2018). Optimal Tikhonov Regularization for DEER Spectroscopy. *J. Magnetic Reson.* 288, 58–68. doi:10.1016/j.jmr.2018.01.021

Efimova, O., and Hore, P. J. (2008). Role of Exchange and Dipolar Interactions in the Radical Pair Model of the Avian Magnetic Compass. *Biophysical J.* 94, 1565–1574. doi:10.1529/biophysj.107.119362

Fernandez-Leiro, R., and Scheres, S. H. W. (2016). Unravelling Biological Macromolecules with Cryo-Electron Microscopy. *Nature* 537, 339–346. doi:10.1038/nature19948

Fursman, C. E., and Hore, P. J. (1999). Distance Determination in Spin-Correlated Radical Pairs in Photosynthetic Reaction Centres by Electron Spin Echo Envelope Modulation. *Chem. Phys. Lett.* 303, 593–600. doi:10.1016/s0009-2614(99)00185-2

Hamada, M., Iwata, T., Fuki, M., Kandori, H., Weber, S., and Kobori, Y. (2021). Orientations and Water Dynamics of Photoinduced Secondary Charge-Separated States for Magnetoreception by Cryptochrome. *Commun. Chem.* 4, 141. doi:10.1038/s42004-021-00573-4

Hanwell, M. D., Curtis, D. E., Lonie, D. C., Vandermeersch, T., Zurek, E., and Hutchison, G. R. (2012). Avogadro: an Advanced Semantic Chemical Editor, Visualization, and Analysis Platform. *J. Cheminform* 4, 17. doi:10.1186/1758-2946-4-17

Hara, H., Dzuba, S. A., Kawamori, A., Akabori, K., Tomo, T., Satoh, K., et al. (1997). The Distance between P680 and QA in Photosystem II Determined by ESEEM Spectroscopy. *Biochimica Biophysica Acta (BBA) - Bioenergetics* 1322, 77–85. doi:10.1016/s0005-2728(97)00081-9

Harmer, J. R. (2016). Hyperfine Spectroscopy - ENDOR. *eMagRes* 5, 1493–1514. doi:10.1002/9780470034590.emrstm1515

Harvey, S. M., and Wasielewski, M. R. (2021). Photogenerated Spin-Correlated Radical Pairs: from Photosynthetic Energy Transduction to Quantum Information Science. *J. Am. Chem. Soc.* 143, 15508–15529. doi:10.1021/jacs.1c07706

Hasegawa, M., Nagashima, H., Minobe, R., Tachikawa, T., Mino, H., and Kobori, Y. (2017). Regulated Electron Tunneling of Photoinduced Primary Charge-Separated State in the Photosystem II Reaction Center. *J. Phys. Chem. Lett.* 8, 1179–1184. doi:10.1021/acs.jpclett.7b00044

Hintze, C., Bücker, D., Domingo Köhler, S., Jeschke, G., and Drescher, M. (2016). Laser-induced Magnetic Dipole Spectroscopy. *J. Phys. Chem. Lett.* 7, 2204–2209. doi:10.1021/acs.jpclett.6b00765

Hochstoeger, T., Al Said, T., Maestre, D., Walter, F., Vilceanu, A., Pedron, M., et al. (2020). The Biophysical, Molecular, and Anatomical Landscape of Pigeon CRY4: A Candidate Light-Based Quantal Magnetosensor. *Sci. Adv.* 6, eabb9110. doi:10.1126/sciadv.abb9110

Hoff, A. J., Gast, P., Dzuba, S. A., Timmel, C. R., Fursman, C. E., and Hore, P. J. (1998). The Nuts and Bolts of Distance Determination and Zero- and Double-Quantum Coherence in Photoinduced Radical Pairs. *Spectrochimica Acta Part A Mol. Biomol. Spectrosc.* 54, 2283–2293. doi:10.1016/s1386-1425(98)00211-x

Hore, P. J., Hunter, D. A., McKie, C. D., and Hoff, A. J. (1987). Electron Paramagnetic Resonance of Spin-Correlated Radical Pairs in Photosynthetic Reactions. *Chem. Phys. Lett.* 137, 495–500. doi:10.1016/0009-2614(87)80617-6

Hou, Y., Zhang, X., Chen, K., Liu, D., Wang, Z., Liu, Q., et al. (2019). Charge Separation, Charge Recombination, Long-Lived Charge Transfer State Formation and Intersystem Crossing in Organic Electron Donor/acceptor Dyads. *J. Mat. Chem. C* 7, 12048–12074. doi:10.1039/c9tc04285g

Hustedt, E. J., Marinelli, F., Stein, R. A., Faraldo-Gómez, J. D., and McHaourab, H. S. (2018). Confidence Analysis of DEER Data and its Structural Interpretation with Ensemble-Biased Metadynamics. *Biophysical J.* 115, 1200–1216. doi:10.1016/j.bpj.2018.08.008

Jeschke, G. (2012). DEER Distance Measurements on Proteins. *Annu. Rev. Phys. Chem.* 63, 419–446. doi:10.1146/annurev-physchem-032511-143716

Kay, C. W. M., Schleicher, E., Kuppig, A., Hofner, H., Rüdiger, W., Schleicher, M., et al. (2003). Blue Light Perception in Plants. *J. Biol. Chem.* 278, 10973–10982. doi:10.1074/jbc.m205509200

Keller, S. G., Pannwitz, A., Mallin, H., Wenger, O. S., and Ward, T. R. (2017). Streptavidin as a Scaffold for Light-Induced Long-Lived Charge Separation. *Chem. Eur. J.* 23, 18019–18024. doi:10.1002/chem.201703885

Klare, J. P. (2013). Site-directed Spin Labeling EPR Spectroscopy in Protein Research. *Biol. Chem.* 394, 1281–1300. doi:10.1515/hsz-2013-0155

Krzystyniak, M. (2003). Anomalous Pulse Angle Dependence of the Single and Double Quantum Echoes in a Photoinduced Spin-Correlated Coupled Radical Pair. *Appl. Magn. Reson.* 24, 447–465. doi:10.1007/bf03166948

Kulik, L. V., Borovykh, I. V., Gast, P., and Dzuba, S. A. (2003). Selective Excitation in Pulsed EPR of a Spin-Correlated Triplet-Radical Pair. *J. Magnetic Reson.* 162, 423–428. doi:10.1016/s1090-7807(03)00052-1

Kulik, L. V., Dzuba, S. A., Grigoryev, I. A., and Tsvetkov, Y. D. (2001). Electron Dipole-Dipole Interaction in ESEEM of Nitroxide Biradicals. *Chem. Phys. Lett.* 343, 315–324. doi:10.1016/s0009-2614(01)00721-7

Lee, C., Yang, W., and Parr, R. G. (1988). Development of the Colle-Salvetti Correlation-Energy Formula into a Functional of the Electron Density. *Phys. Rev. B* 37, 785–789. doi:10.1103/physrevb.37.785

Liu, X., Kang, F., Hu, C., Wang, L., Xu, Z., Zheng, D., et al. (2018). A Genetically Encoded Photosensitizer Protein Facilitates the Rational Design of a Miniature Photocatalytic CO2-reducing Enzyme. *Nat. Chem.* 10, 1201–1206. doi:10.1038/s41557-018-0150-4

Loura, L. M., and Prieto, M. (2011). FRET in Membrane Biophysics: an Overview. *Front. Physiol.* 2, 82. doi:10.3389/fphys.2011.00082

Lukina, E. A., Popov, A. A., Uvarov, M. N., and Kulik, L. V. (2015). Out-of-phase Electron Spin Echo Studies of Light-Induced Charge-Transfer States in P3HT/PCBM Composite. *J. Phys. Chem. B* 119, 13543–13548. doi:10.1021/acs.jpcb.5b02142

Luo, J., and Hore, P. J. (2021). Chiral-induced Spin Selectivity in the Formation and Recombination of Radical Pairs: Cryptochrome Magnetoreception and EPR Detection. *New J. Phys.* 23, 043032. doi:10.1088/1367-2630/abed0b

Marcus, R. A., and Sutin, N. (1985). Electron Transfers in Chemistry and Biology. *Biochimica Biophysica Acta (BBA) - Rev. Bioenergetics* 811, 265–322. doi:10.1016/0304-4173(85)90014-x

Moser, C. C., Keske, J. M., Warncke, K., Farid, R. S., and Dutton, P. L. (1992). Nature of Biological Electron Transfer. *Nature* 355, 796–802. doi:10.1038/355796a0

Neese, F. (2012). The ORCA Program System. *WIREs Comput. Mol. Sci.* 2, 73–78. doi:10.1002/wcms.81

Neumaier, A., and Schneider, T. (2001). Estimation of Parameters and Eigenmodes of Multivariate Autoregressive Models. *ACM Trans. Math. Softw.* 27, 27–57. doi:10.1145/382043.382304

Niklas, J., and Poluektov, O. G. (2017). Charge Transfer Processes in OPV Materials as Revealed by EPR Spectroscopy. *Adv. Energy Mater.*, 7. Art. No. 1602226. doi:10.1002/aenm.201602226

Nohr, D., Paulus, B., Rodriguez, R., Okafuji, A., Bittl, R., Schleicher, E., et al. (2017). Determination of Radical-Radical Distances in Light-Active Proteins and Their Implication for Biological Magnetoreception. *Angew. Chem. Int. Ed.* 56, 8550–8554. doi:10.1002/anie.201700389

O'Dea, A. R., Curtis, A. F., Green, N. J. B., Timmel, C. R., and Hore, P. J. (2005). Influence of Dipolar Interactions on Radical Pair Recombination Reactions Subject to Weak Magnetic Fields. *J. Phys. Chem. A* 109, 869–873. doi:10.1021/jp0456943

Olshansky, J. H., Krzyaniak, M. D., Young, R. M., and Wasielewski, M. R. (2019). Photogenerated Spin-Entangled Qubit (Radical) Pairs in DNA Hairpins: Observation of Spin Delocalization and Coherence. *J. Am. Chem. Soc.* 141, 2152–2160. doi:10.1021/jacs.8b13155

Pannier, M., Veit, S., Godt, A., Jeschke, G., and Spiess, H. W. (2000). Dead-Time Free Measurement of Dipole-Dipole Interactions between Electron Spins. *J. Magnetic Reson.* 142, 331–340. doi:10.1006/jmre.1999.1944

Perdew, J. P. (1986). Density-functional Approximation for the Correlation Energy of the Inhomogeneous Electron Gas. *Phys. Rev. B* 33, 8822–8824. doi:10.1103/physrevb.33.8822

Popov, A. A., Lukina, E. A., Rapatskiy, L., and Kulik, L. V. (2017). Time-domain Shape of Electron Spin Echo Signal of Spin-Correlated Radical Pairs in Polymer/fullerene Blends. *J. Magnetic Reson.* 276, 86–94. doi:10.1016/j.jmr.2017.01.016

Reece, S. Y., Seyedsayamdost, M. R., Stubbe, J., and Nocera, D. G. (2007). Direct Observation of a Transient Tyrosine Radical Competent for Initiating Turnover in a Photochemical Ribonucleotide Reductase. *J. Am. Chem. Soc.* 129, 13828–13830. doi:10.1021/ja074452o

Reginsson, G. W., and Schiemann, O. (2011). Pulsed Electron-Electron Double Resonance: beyond Nanometre Distance Measurements on Biomacromolecules. *Biochem. J.* 434, 353–363. doi:10.1042/bj20101871

Richert, S., Tait, C. E., and Timmel, C. R. (2017). Delocalisation of Photoexcited Triplet States Probed by Transient EPR and Hyperfine Spectroscopy. *J. Magnetic Reson.* 280, 103–116. doi:10.1016/j.jmr.2017.01.005

Riplinger, C., Kao, J. P. Y., Rosen, G. M., Kathirvelu, V., Eaton, G. R., Eaton, S. S., et al. (2009). Interaction of Radical Pairs Through-Bond and Through-Space: Scope and Limitations of the Point−Dipole Approximation in Electron Paramagnetic Resonance Spectroscopy. *J. Am. Chem. Soc.* 131, 10092–10106. doi:10.1021/ja901150j

Salikhov, K. M., Kandrashkin, Y. E., and Salikhov, A. K. (1992). Peculiarities of Free Induction and Primary Spin Echo Signals for Spin-Correlated Radical Pairs. *Appl. Magn. Reson.* 3, 199–216. doi:10.1007/bf03166790

Santabarbara, S., Kuprov, I., Fairclough, W. V., Purton, S., Hore, P. J., Heathcote, P., et al. (2005). Bidirectional Electron Transfer in Photosystem I: Determination of Two Distances between P700+ and A1- in Spin-Correlated Radical Pairs. *Biochemistry* 44, 2119–2128. doi:10.1021/bi048445d

Santabarbara, S., Kuprov, I., Hore, P. J., Casal, A., Heathcote, P., and Evans, M. C. W. (2006). Analysis of the Spin-Polarized Electron Spin Echo of the [P700+A1-] Radical Pair of Photosystem I Indicates that Both Reaction Center Subunits Are Competent in Electron Transfer in Cyanobacteria, Green Algae, and Higher Plants. *Biochemistry* 45, 7389–7403. doi:10.1021/bi060330h

Savitsky, A., Dubinskii, A. A., Flores, M., Lubitz, W., and Möbius, K. (2007). Orientation-resolving Pulsed Electron Dipolar High-Field EPR Spectroscopy on Disordered Solids: I. Structure of Spin-Correlated Radical Pairs in Bacterial Photosynthetic Reaction Centers. *J. Phys. Chem. B* 111, 6245–6262. doi:10.1021/jp070016c

Savitsky, A., Niklas, J., Golbeck, J. H., Möbius, K., and Lubitz, W. (2013). Orientation Resolving Dipolar High-Field EPR Spectroscopy on Disordered Solids: II. Structure of Spin-Correlated Radical Pairs in Photosystem I. *J. Phys. Chem. B* 117, 11184–11199. doi:10.1021/jp401573z

Schiemann, O., Heubach, C. A., Abdullin, D., Ackermann, K., Azarkh, M., Bagryanskaya, E. G., et al. (2021). Benchmark Test and Guidelines for DEER/PELDOR Experiments on Nitroxide-Labeled Biomolecules. *J. Am. Chem. Soc.* 143, 17875–17890. doi:10.1021/jacs.1c07371

Schiemann, O., and Prisner, T. F. (2007). Long-range Distance Determinations in Biomacromolecules by EPR Spectroscopy. *Quart. Rev. Biophys.* 40, 1–53. doi:10.1017/s003358350700460x

Schleicher, E., and Weber, S. (2012). Radicals in Flavoproteins. *Top. Curr. Chem.* 321, 41–65. doi:10.1007/128_2011_301

Schnegg, A. (2017). Very-high-frequency EPR. *eMagRes* 6, 115–132. doi:10.1002/9780470034590.emrstm1526

Sorigué, D., Légeret, B., Cuiné, S., Blangy, S., Moulin, S., Billon, E., et al. (2017). An Algal Photoenzyme Converts Fatty Acids to Hydrocarbons. *Science* 357, 903–907.

Stehlik, D., Bock, C. H., and Petersen, J. (1989). Anisotropic Electron Spin Polarization of Correlated Spin Pairs in Photosynthetic Reaction Centers. *J. Phys. Chem.* 93, 1612–1619. doi:10.1021/j100341a084

Stoll, S. (2017). Pulse EPR. *eMagRes* 6, 23–38. doi:10.1002/9780470034590.emrstm1510

Tan, J., Thurnauer, M. C., and Norris, J. R. (1994). Electron Spin Echo Envelope Modulation Due to Exchange and Dipolar Interactions in a Spin-Correlated Radical Pair. *Chem. Phys. Lett.* 219, 283–290. doi:10.1016/0009-2614(94)87059-4

Tang, J., Thurnauer, M. C., Kubo, A., Hara, H., and Kawamori, A. (1997). Anomalous Pulse-Angle and Phase Dependence of Hahn's Electron Spin Echo and Multiple-Quantum Echoes in a Photoinduced Spin-Correlated Radical Pair. *J. Chem. Phys.* 106, 7471–7478. doi:10.1063/1.473752

Tang, J., Thurnauer, M. C., and Norris, J. R. (1995). Abnormal Electron Spin Echo and Multiple-Quantum Coherence in a Spin-Correlated Radical Pair System. *Appl. Magn. Reson.* 9, 23–31. doi:10.1007/bf03162343

Timmel, C. R., Fursman, C. E., Hoff, A. J., and Hore, P. J. (1998). Spin-correlated Radical Pairs: Microwave Pulse Effects on Lifetimes, Electron Spin Echo

Envelope Modulations, and Optimum Conditions for Detection by Electron Spin Echo Spectroscopy. *Chem. Phys.* 226, 271–283. doi:10.1016/s0301-0104(97)00283-8

van Doorslaer, S. (2017). Hyperfine Spectroscopy: ESEEM. *eMagRes* 6, 51–70. doi:10.1002/9780470034590.emrstm1517

Weber, S. (2017). Transient EPR. *eMagRes* 6, 255–270. doi:10.1002/9780470034590.emrstm1509

Weigend, F., and Ahlrichs, R. (2005). Balanced Basis Sets of Split Valence, Triple Zeta Valence and Quadruple Zeta Valence Quality for H to Rn: Design and Assessment of Accuracy. *Phys. Chem. Chem. Phys.* 7, 3297–3305. doi:10.1039/b508541a

Weil, J. A., Bolton, J. R., and Wertz, J. E. (1994). *Electron Paramagnetic Resonance. Elementary Theory and Practical Applications*. New York, NY: John Wiley & Sons, Inc.

Weissman, S. I. (1982). Recent Developments in Electron Paramagnetic Resonance: Transient Methods. *Annu. Rev. Phys. Chem.* 33, 301–318. doi:10.1146/annurev.pc.33.100182.001505

Weng, Y., Song, C., Chiang, C.-W., and Lei, A. (2020). Single Electron Transfer-Based Peptide/protein Bioconjugations Driven by Biocompatible Energy Input. *Commun. Chem.* 3, 171. doi:10.1038/s42004-020-00413-x

Xu, J., Jarocha, L. E., Zollitsch, T., Konowalczyk, M., Henbest, K. B., Richert, S., et al. (2021). Magnetic Sensitivity of Cryptochrome 4 from a Migratory Songbird. *Nature* 594, 535–540. doi:10.1038/s41586-021-03618-9

Yoshii, T., Hara, H., Kawamori, A., Akabori, K., Iwaki, M., and Itoh, S. (1999). ESEEM Study of the Location of Spin-Polarized Chlorophyll-Quinone Radical Pair in Membrane-Oriented Spinach Photosystems I and II Complexes. *Appl. Magn. Reson.* 16, 565–580. doi:10.1007/bf03161952

Zech, S. G., Kurreck, J., Eckert, H.-J., Renger, G., Lubitz, W., and Bittl, R. (1997). Pulsed EPR Measurement of the Distance between $P_{680}^{+\bullet}$ and $Q_A^{-\bullet}$ in Photosystem II. *FEBS Lett.* 414, 454–456.

Zech, S. G., Kurreck, J., Renger, G., Lubitz, W., and Bittl, R. (1999). Determination of the Distance between Yox Z and Q− A in Photosystem II by Pulsed EPR Spectroscopy on Light-Induced Radical Pairs. *FEBS Lett.* 442, 79–82. doi:10.1016/s0014-5793(98)01628-7

Zech, S. G., Lubitz, W., and Bittl, R. (1996). Pulsed EPR Experiments on Radical Pairs in Photosynthesis: Comparison of the Donor-Acceptor Distances in Photosystem I and Bacterial Reaction Centers. *Berichte Bunsenges. für Phys. Chem.* 100, 2041–2044. doi:10.1002/bbpc.19961001220

Zollitsch, T. M., Jarocha, L. E., Bialas, C., Henbest, K. B., Kodali, G., Dutton, P. L., et al. (2018). Magnetically Sensitive Radical Photochemistry of Non-natural Flavoproteins. *J. Am. Chem. Soc.* 140, 8705–8713. doi:10.1021/jacs.8b03104

Conflict of Interest: The authors declare that the research was conducted in the absence of any commercial or financial relationships that could be construed as a potential conflict of interest.

Publisher's Note: All claims expressed in this article are solely those of the authors and do not necessarily represent those of their affiliated organizations, or those of the publisher, the editors, and the reviewers. Any product that may be evaluated in this article, or claim that may be made by its manufacturer, is not guaranteed or endorsed by the publisher.

frontiers | Frontiers in Molecular Biosciences

MINI REVIEW
published: 27 June 2022
doi: 10.3389/fmolb.2022.886417

A Review of Methodologies for the Detection, Quantitation, and Localization of Free Cysteine in Recombinant Proteins: A Focus on Therapeutic Monoclonal Antibodies

Clive Metcalfe *

Division of Biotherapeutics, National Institute for Biological Standards and Control, Potters Bar, United Kingtom

Free-cysteine residues in recombinant biotherapeutics such as monoclonal antibodies can arise from incorrect cellular processing of disulfide bonds during synthesis or by reduction of disulfide bonds during the harvest and purification stage of manufacture. Free cysteines can affect potency, induce aggregation, and decrease the stability of therapeutic proteins, and the levels and positions of free cysteines in proteins are closely monitored by both manufacturers and regulators to ensure safety and efficacy. This review summarizes the latest methodologies for the detection and quantification of free cysteines.

Keywords: therapeutic monoclonal antibodies, disulfide bond, free cysteine, quantitative mass spectrometry, and post-translation modification

OPEN ACCESS

Edited by:
Milena Quaglia,
National Measurement Laboratory at LGC, United Kingdom

Reviewed by:
John Schiel,
National Institute of Standards and Technology (NIST), United States

***Correspondence:**
Clive Metcalfe
Clive.Metcalfe@NIBSC.org

Specialty section:
This article was submitted to Structural Biology, a section of the journal Frontiers in Molecular Biosciences

Received: *28 February 2022*
Accepted: *17 May 2022*
Published: *27 June 2022*

Citation:
Metcalfe C (2022) A Review of Methodologies for the Detection, Quantitation, and Localization of Free Cysteine in Recombinant Proteins: A Focus on Therapeutic Monoclonal Antibodies. Front. Mol. Biosci. 9:886417. doi: 10.3389/fmolb.2022.886417

INTRODUCTION

Cysteine residues (Cys) in proteins are the most conserved residues throughout the entire proteome. They are redox-active, meaning that they can be oxidized or reduced, and this imparts several distinct functions such as active site catalytic functions in enzymes or forming disulfide bonds (Wong and Hogg, 2010). Disulfide bonds are the covalent bonds formed between the oxidized sulfur atoms of Cys residues and provide mechanical stabilization of protein tertiary and quaternary structures. This is particularly true for proteins that reside extracellularly where disulfide bonds help protect them from the harsh pH-variable, protease-rich environment (Pace et al., 1988).

The recombinant DNA technology has facilitated the bulk production of biotherapeutic proteins. In particular, immunoglobulins (Ig) have been utilized in the form of monoclonal antibodies (Carrara et al., 2021) (mAbs) to treat many inflammatory diseases and cancers. Immunoglobulin gamma subtype 1 (IgG1) is the most common mAb scaffold in antibody therapeutics (Shepard et al., 2017) and consists of two light chains (composed of two Ig domains each) and two heavy chains (formed from four Ig domains each). **Figure 1** shows how these chains are arranged to form the distinctive Y-Shape of IgG1 with each of the Ig domains stabilized by a buried intrachain disulfide bond, with the quaternary structure stabilized by four interchain disulfide bonds, giving 16 in total (Janeway et al., 2001).

Although the disulfide bonding patterns of IgG1 are well conserved and there are relatively few noncanonical Cys found, even in the variable region, free-Cys have been detected in Ig extracted from sera and recombinantly produced mAbs. The majority of detected free-Cys arises from incomplete processing within the host cell during manufacture where high conditions of cellular stress are encountered or through extracellular reduction by intercellular host proteins such as thioredoxin in

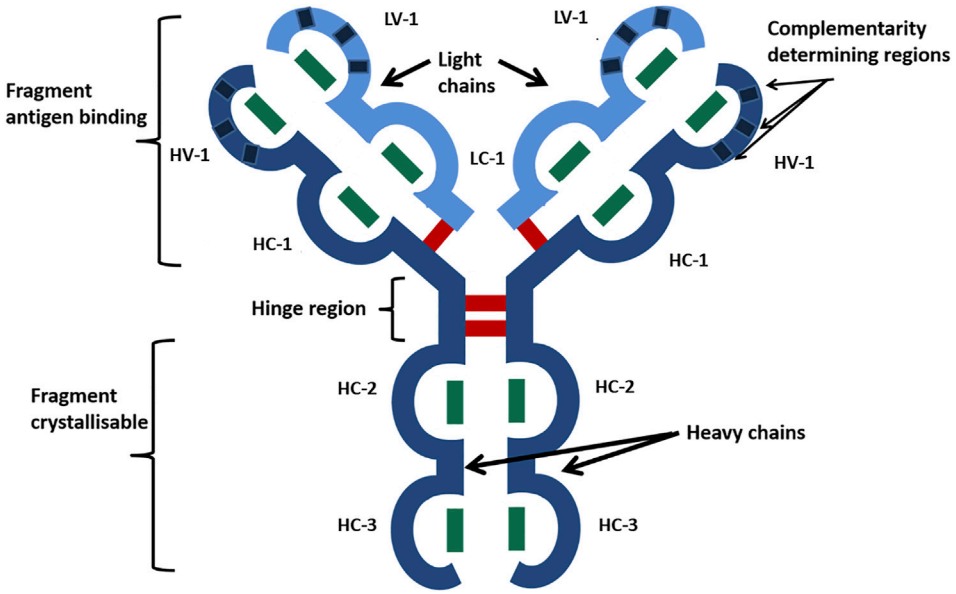

FIGURE 1 | Schematic of the IgG1 mAb characteristic Y-shaped structure. Heavy chains are shown in dark blue, and light chains in are shown light blue. Ig-like domains are represented as bulges in the linear protein sequence and are named HV, heavy variable; HC, heavy constant; LV, light variable; and LC, light constant. Disulfide bonds are represented by bars, with green being disulfide bonds buried within Ig domains and red being exposed interchain disulfide bonds. Reproduced with permission from Gurjar et al., 2019.

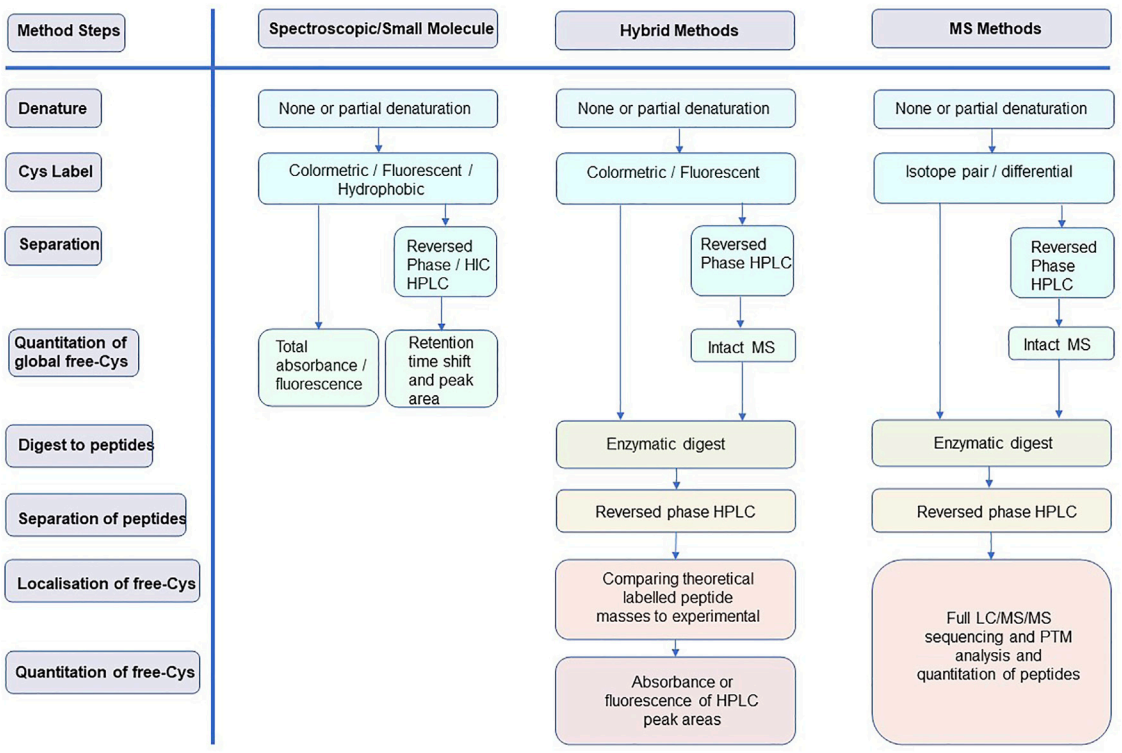

FIGURE 2 | Typical workflows for the three method classes discussed in this review highlighting how each of the method steps is addressed.

the harvest and purification of mAbs. Free-Cys arising from disulfide bond reduction in mAbs is undesirable due to the negative effects this has on affinity (Harris, 2005), functions (Gurjar et al., 2019), aggregation (Trivedi et al., 2009; Buchanan et al., 2013; Chung et al., 2017), and stability (Lacy et al., 2008); manufacturers go to great lengths to minimize the amount of free-Cys in therapeutic mAb preparations (Trexler-Schmidt et al., 2010). Although as yet there are no guidelines from regulators on acceptable levels, manufacturers justify the levels on a safety and efficacy basis for each product. Furthermore, the development of structurally diverse next-generation therapeutic antibody platforms and antibody-drug conjugates exogenous cysteines are often added to stabilize structures (Sawant et al., 2020) or to conjugate payloads (You et al., 2021). The methods discussed herein can easily be adapted to quantify the level of free-Cys in these systems.

The purpose of this study is to review the relevant methods for identifying and quantifying free-Cys in proteins, with a focus on mAbs. Pros and cons are discussed to provide insight into methodologies and inform readers so that they are able to select and improve upon their application. The focus is on methodologies developed over the last 15 years and is presented in three sections of increasing technical complexity: 1) spectroscopic methods, 2) hybrid spectroscopic-mass spectrometry methods, and 3) wholly mass spectrometry-based methods. Typical workflows for each of these method classes are represented in **Figure 2**.

SPECTROSCOPIC METHODS

The first, reliable spectroscopic method for the determination of free-Cys in proteins was developed by Ellman (Ellman, 1959). Free-Cys in a protein are reacted with 5,5-dithio-bis(2-nitrobenzoic acid) (DTNB) forming stable yellow-colored 2-nitro-5-thiobenzoic acid (TNB), which can be quantified by measuring the absorbance at 412 nm and applying a molar extinction coefficient of 13,600 M^{-1} cm^{-1}; however, with a limit of detection of around 3 μM free-Cys, the method is not sensitive enough for the detection of the low levels encountered in mAbs. Wright et al. (Wright and Viola, 1998) used a systematic approach to greatly increase the sensitivity of DNTB down to 0.3 μM using carefully controlled conditions such as dialysis, an extended range of standards, and careful control of protein to reagent ratios with accurate quantitation of protein concentration. Partial denaturing conditions and control of reaction times can be used to identify surface accessible versus buried Cys. They also utilized the fluorescent reagent monobromobimane (mBBr), which reacts with free-Cys to form fluorescent adducts which emit at 360 nm when excited at 280 nm. Free-Cys are routinely detectable down to 1 μM, and concentrations as low as 10 nM can be achieved using high-performance liquid chromatography (HPLC) separation of the labeled proteins with the Cys adducts detected using a spectroscopic detector (Fahey et al., 1981). ThioGlo reagents are naphthopyranones derivatized with maleimide which react rapidly with accessible Cys and produce a highly fluorescent product (Langmuir et al., 1995) with sensitivity down to 50 fmol and much increased reproducibility with HPLC methods (Ercal et al., 2001).

An interesting take on colorimetric quantification of thiols is the papain amplification assay (Singh et al., 1993; Singh et al., 1995), in which an inactivated mixed disulfide form of papain is reacted with a thiol to generate a stoichiometric amount of papain. This is assayed using an N-benzoyl-L-arginine-p-nitroaniline substrate that releases the chromogenic substrate p-nitroaniline. As this is an amplification assay, very high levels of sensitivity approaching those of fluorescence can be reached.

Although none of the aforementioned methods have been specifically applied to free-Cys in mAbs, there is no reason why they could not be adapted to perform quick, reliable quantitation of therapeutic mAbs. However, in 2002, Zhang et al. undertook a detailed study on quantifying free-Cys in mAbs using N-(1-pyrenyl) maleimide, which fluoresces at 380 nm when covalently linked to a Cys (Zhang and Czupryn, 2002). To quantify, a standard curve of NPM-derivatized N-acetyl-Cys was used and free-Cys levels of 0.02 and 0.1 mol/mol of protein under native and denaturing conditions, respectively, were detected.

An interesting development of maleimide labeling has been recently employed, where free-Cys in mAbs are labeled with N-tert-butylmaleimide (NtBM) (Welch et al., 2018). When unlabeled and NtBM-labeled mAb are analyzed on C4 RP-HPLC, there is a retention time shift associated with NtBM-labeled mAb, allowing resolution of the two peaks and quantitation of free-Cys. A similar method utilizes N-cyclo-hexylmaleimide as the free thiol label and hydrophobic interaction chromatography for separation (Wei et al., 2019).

HYBRID SPECTROSCOPIC/MASS SPECTROMETRY METHODS

Combining mass spectrometry with spectroscopic quantitation of free-Cys, Chumsae et al. (2009) reported a combined fluorescent label and mass spectrometry approach that not only identifies the number of free-Cys but also simultaneously localizes them. Five recombinant IgG1 mAbs were first treated with 5-iodoacetamidofluorescein (5-IAF) under partially denaturing conditions of 4M guanidine hydrochloride to expose all free sulfhydryl groups; a 10:1 5-IAF:mAb ratio ensured efficient alkylation and 'fixed' the redox state of free-Cys. Following this, remaining disulfide-bonded Cys were differentiated from the nonbonded Cys by reacting them with IAA after full denaturing and reduction. Initial analysis by matrix-associated laser desorption/ionization time of flight mass spectrometry (MALDI-Tof MS) revealed the quantified number of free-Cys as each one alkylated with 5-IAF gave a mass shift of 387.4 Da. Then, to determine *where* the free-Cys resided, mAbs were digested with trypsin and tryptic peptides separated by RP-HPLC using fluorescence detection at 520 nm specific for 5-IAF-modified peptides. These peaks were collected and the sequences were determined by MALDI-Tof MS, allowing the determination of the positions and domain localization of the free cysteines.

Huh et al. (2013) used a similar approach but with a fluorescent Alexa Fluor C-5-coupled maleimide reagent (AF594) as the probe for free-Cys in several recombinant IgG1 and IgG2 mAbs. Under partial denaturing conditions (7M guanidine HCl), the intact antibodies showed similar levels of free-Cys using total AF594 fluorescence and RP-HPLC separation to that of DNTB; mAb constant domains contain 1–2.7% free-Cys for IgG1 and 1–2.8% for IgG2. To identify the free-Cys-containing peptides, the mAbs were Lys-C-digested and separated on RP-HPLC, and the experimental masses of the peptides plus labels compared to theoretical masses. Comparison of the total fluorescence at 594 nm of the peptide peaks to an AF594 standard curve was used to quantitate the levels of free-Cys per peptide. They then applied these methods to show that mechanical agitation of the mAbs results in breakage of disulfide bonds and covalent aggregation via the liberated Cys.

WHOLLY MASS SPECTROMETRY METHODS

Coupling stable isotope pairs to differentially alkylate free-Cys to high sensitivity, high-resolution LC-MS/MS provides the most comprehensive analysis of the redox and disulfide-bonded state of Cys in proteins/mAbs. Xiang et al. used ^{12}C-iodoacetic acid (^{12}C-IAA) and ^{13}C-iodoacetic acid (^{13}C-IAA) to differentially label five mAbs and quantify the levels and location of free-Cys in the mAb sequence. The 2 Da mass shift between the labels meant that the authors could identify, and distinguish between, the free Cys originally present in the mAbs and the free Cys liberated from denaturation and reduction of the mAbs. Liquid chromatography–mass spectrometry (LC-MS) was performed after multi-enzyme digest (trypsin, Lys-C, chymotrypsin, Asp-N, or Glu-C), and MS peaks for each peptide were identified from calculated masses of the peptide sequence plus any Cys modification. They calculated peptide isotope peak areas from MS^1 spectra for both the ^{12}C-IAA and ^{13}C-IAA peptide adducts to get relative percentages of each form. Spiking experiments showed they could accurately quantify down to 0.5% free-Cys for each peptide, and over the five mAbs they studied, they found levels of free-Cys ranging from 1.5 to 5.6%, with the heavy chain CH3 domain having the highest level of free-Cys. The same group went on to further utilize this method in determining the stability of each disulfide bond in IgG1 mAbs (Liu et al., 2010). It should be noted that the main pitfall of this method is that it is limited to the LC-MS analysis and does not make use of modern LC-MS/MS peptide sequencing and modification localization, therefore relying on time-consuming manual matching of LC-MS peaks with theoretical predicted peptide masses.

A similar method that did use a full nano-LC-MS/MS analysis used ^{18}O$^-$-labeled iodoacetamide (^{18}O-IAA), whereby differential labeling was carried out by alkylating free-Cys with normal IAA, denaturing, reducing, and alkylating with ^{18}O-IAA, trypsin digestion, and LC-MS/MS analysis (Wang and Kaltashov, 2012; Wang and Kaltashov, 2015). The percentage free-Cys was calculated using the peak area of the extracted ion chromatogram for a given ^{18}O-IAA-labeled peptide from the total ion chromatogram and quoted as a percentage of the total area of IAA + ^{18}O-IAA-extracted ion chromatograms. Recombinant human transferrin was used as a model protein, but this could easily be applied to mAbs or other therapeutic proteins.

In another example reported by Chiu (Chiu, 2019), a stable isotope pair of 2-iodo-N-phenylacetamide (^{12}C-IPA) and its carbon-13 derivative (^{13}C-IPA) was used. This pair has a 6 Da mass difference, and the hydrophobic nature of the alkylating agent allows it to penetrate the hydrophobic core of protein domains without the need for partial denaturation, as demonstrated by quantitation of disulfide bond redox states in the platelet integrin αIIb βIII (Chiu, 2019; Pijning et al., 2021) and Influenza A Hemagglutinin (Florido et al., 2021). Differential alkylation, data analysis, and determination of % free-Cys were performed as in the aforementioned method.

In addition, stable isotopes of iodoacetamide Cys alkylating agents here are also stable isotopes of maleimide-derived Cys alkylating agents. N-Ethylmaleimide (d_0-NEM) and d^5-N-ethylmaleimide (d_5-NEM) can be used differentially to alkylate cysteines within a protein with the d_5-NEM producing a 5 Da mass shift compared to d_0-NEM. An early example of this was the quantification of thioredoxin-catalyzed disulfide bond reduction in the cell surface receptor CD44 (Kellett-Clarke et al., 2015). This maleimide chemistry was also used by Robotham et al., who devised a complete strategy for the quantitation of free-Cys in mAbs at both the intact mAb level and the peptide level (Robotham and Kelly, 2019). They looked at three commercially available mAbs and used B-lactoglobulin A as a control as it is known to have a free-Cys. These proteins were reacted with maleimide-PEG$_2$-Biotin (MPB), which adds a mass of 525 Da per labeled Cys, and the intact labeled mAbs were analyzed by LC-MS. In spiking experiments, the authors could quantify mAbs containing a free-Cys down to less than 2% (~0.02 mol SH per mol protein) of the total mAb population. Furthermore, reduction of the labeled mAbs with TCEP allowed the independent analysis of the heavy and light chains; thus, the percentage of MPB labeling on each of the heavy and light chains could be ascertained. All their estimations of free-Cys levels agreed well with spectroscopic methods. They went on to demonstrate site-specific quantitation of free-Cys in different redox states by differentially labeling using the d_0-NEM/d_5-NEM isotope pair. mAbs partially reduced by 6M guanidine hydrochloride were labeled at pH 5.5 with d_0-NEM, after which the mAbs were fully denatured and reduced prior to further labeling with d_5-NEM. The mAbs were deglycosylated with PNGase, trypsin-digested, and subjected to LC-MS/MS analysis. Of the 17 cysteine residues in SigmaMAb, 16 were identified and the percentage of free-Cys was calculated by comparing the area of d_0-NEM-labeled peptide to the total area of d_0-NEM + d_5-NEM-labeled peptides. Again, spiking experiments showed that <2% free-Cys per peptide could be easily detected.

More recently, we developed a differential alkylation strategy to investigate mAbs that does not require stable isotope pairs (Gurjar et al., 2019). Instead, IAA is used to initially alkylate native free-Cys, and then NEM is subsequently used to alkylate

free-Cys liberated upon denaturation and reduction. Additionally, a "standard" is prepared—in this case, an mAb fully denatured, reduced, and 100% alkylated with IAA. A label-free LC-MS/MS analysis is performed to sequence the peptides and localize the alkylated Cys; then, extracted peak areas of IAA-labelled Cys peptides in the sample runs are compared to extracted peak areas of the same IAA-labeled Cys peptide in the 100% standard (control). Non-Cys-containing peptides are used to normalize the intensities of the peptides between the different LC-MS/MS runs. The method was applied to five therapeutic mAbs, allowing quantitation of the redox state and amount of free-Cys after various treatments, with sensitivity down to 2%. This has since been successfully applied to determine free-Cys levels in therapeutic recombinant coagulation factor VIII products (Arsiccio et al., 2022). A recent development of this method forgoes the use of a fully NEM-alkylated mAb standard and directly quantified NEM-labeled free-Cys with IAA-labeled Cys derived from disulfide bonds (Li et al., 2021). However, it should be noted that the ionization properties of NEM- and IAA-labeled peptides will not be comparable and may potentially lead to inaccurate quantitation which should be addressed in detailed method validation.

DISCUSSION

Since the 1959 study by Ellman (Ellman, 1959), the sensitivity and limits of free-Cys quantification in proteins have steadily increased as technologies have evolved. Pure spectroscopic methods permit the quantitation of free-Cys within a protein/mAb but do not inform on where the free-Cys resides. A hybrid approach combining spectroscopic free-Cys detection with mass spectrometry can provide partial localization information but no detailed information. This is because it only utilizes MS to provide an experimental peptide mass that is then compared to the theoretical mass of the peptide in question plus any additional probe mass—no peptide sequencing occurs. As such, it requires a lot of manual annotation and an offline data analysis.

The evolution of MS/MS peptide sequencing when coupled to the nano-ultra-HPLC separation technology allows for the fast and efficient sequencing of peptides along with identification and quantitation of any post-translational modification of amino acids either during synthesis or with exogenously added chemical probes (Prus et al., 2019). Furthermore, the use of stable isotopes of the same thiol-reactive probe allows for the quantitation of free-Cys levels in a single mass spectrometry run, alleviating the need for any standard curves to be generated and therefore any commutability issues that may occur between the behavior of the standards and the samples to be analyzed. Isotope pairs of Cys-reactive probes offer a means of identifying which label has alkylated the Cys on a given peptide based on a mass shift between the heavy and light probes; however, they possess the same physicochemical characteristics showing no difference in specificity or reactivity, nor do they introduce different ionization characteristics or retention time shifts into the LC-MS/MS analysis. Despite this, the stable isotope technology has mainly evolved in the redox-labile allosteric disulfide bond field where it is utilized in determining the relative reactivity of multiple disulfide bonds within a protein as well as the percentage of reduction in each disulfide bond, either in the native state or after treatment (Cook and Hogg, 2013). Strangely, given its ease of use and sensitivity, its uptake in quantifying free-Cys in therapeutic proteins such as mAbs has been slow and sparse.

The differing sensitivity and complexity of the methods mean that varying amounts of protein are needed for each analysis. This ranges from low mg to high µg for spectroscopic methods, especially if coupled with HPLC, to low µg and below for the LC-MS/MS methods. Both methods lend themselves to analysis at different stages of recombinant mAb development and manufacture. For example, if the desire is to monitor the overall level of free-Cys in an mAb product at different manufacturing stages, online spectroscopic methods will provide a good inline scalable solution. However, at the research and development stage, where many clones are being assessed for their stability and the material is at a premium, a full LC-MS/MS analysis might be beneficial to pinpoint the areas of the mAb where the free-Cys is occurring.

AUTHOR CONTRIBUTIONS

CM researched and wrote the manuscript.

FUNDING

CM is partially funded by the NIHR Policy Research Programme (NIBSC Regulatory Science Research Unit). The views expressed in the publication are those of the author(s) and not necessarily those of the NHS, the NIHR, the Department of Health, 'arms' length bodies, or other government departments.

ACKNOWLEDGMENTS

The author acknowledges Carmen Coxon for the critical review of the manuscript.

REFERENCES

Arsiccio, A., Metcalfe, C., Pisano, R., Raut, S., and Coxon, C. (2022). A Proximity-Based In Silico Approach to Identify Redox-Labile Disulfide Bonds: The Example of FVIII. *PLoS One* 17, e0262409. doi:10.1371/journal.pone.0262409

Buchanan, A., Clementel, V., Woods, R., Harn, N., Bowen, M. A., Mo, W., et al. (2013). Engineering a Therapeutic IgG Molecule to Address Cysteinylation, Aggregation and Enhance Thermal Stability and Expression. *MAbs* 5, 255–262. doi:10.4161/mabs.23392

Carrara, S. C., Ulitzka, M., Grzeschik, J., Kornmann, H., Hock, B., and Kolmar, H. (2021). From Cell Line Development to the Formulated Drug Product: The Art

of Manufacturing Therapeutic Monoclonal Antibodies. *Int. J. Pharm.* 594, 120164. doi:10.1016/j.ijpharm.2020.120164

Chiu, J. (2019). Quantification of the Redox State of Protein Disulphide Bonds. *Methods Mol. Biol.* 1967, 45–63. doi:10.1007/978-1-4939-9187-7_4

Chumsae, C., Gaza-Bulseco, G., and Liu, H. (2009). Identification and Localization of Unpaired Cysteine Residues in Monoclonal Antibodies by Fluorescence Labeling and Mass Spectrometry. *Anal. Chem.* 81, 6449–6457. doi:10.1021/ac900815z

Chung, W. K., Russell, B., Yang, Y., Handlogten, M., Hudak, S., Cao, M., et al. (2017). Effects of Antibody Disulfide Bond Reduction on Purification Process Performance and Final Drug Substance Stability. *Biotechnol. Bioeng.* 114, 1264–1274. doi:10.1002/bit.26265

Cook, K. M., and Hogg, P. J. (2013). Post-translational Control of Protein Function by Disulfide Bond Cleavage. *Antioxidants Redox Signal.* 18, 1987–2015. doi:10.1089/ars.2012.4807

Ellman, G. L. (1959). Tissue Sulfhydryl Groups. *Archives Biochem. Biophysics* 82, 70–77. doi:10.1016/0003-9861(59)90090-6

Ercal, N., Yang, P., and Aykin, N. (2001). Determination of Biological Thiols by High-Performance Liquid Chromatography Following Derivatization by ThioGlo Maleimide Reagents. *J. Chromatogr. B Biomed. Sci. Appl.* 753, 287–292. doi:10.1016/s0378-4347(00)00560-0

Fahey, R. C., Newton, G. L., Dorian, R., and Kosower, E. M. (1981). Analysis of Biological Thiols: Quantitative Determination of Thiols at the Picomole Level Based upon Derivatization with Monobromobimanes and Separation by Cation-Exchange Chromatography. *Anal. Biochem.* 111, 357–365. doi:10.1016/0003-2697(81)90573-x

Flórido, M., Chiu, J., and Hogg, P. J. (2021). Influenza A Virus Hemagglutinin Is Produced in Different Disulfide-Bonded States. *Antioxidants Redox Signal.* 35, 1081–1092. doi:10.1089/ars.2021.0033

Gurjar, S. A., Wheeler, J. X., Wadhwa, M., Thorpe, R., Kimber, I., Derrick, J. P., et al. (2019). The Impact of Thioredoxin Reduction of Allosteric Disulfide Bonds on the Therapeutic Potential of Monoclonal Antibodies. *J. Biol. Chem.* 294, 19616–19634. doi:10.1074/jbc.ra119.010637

Harris, R. J. (2005). Heterogeneity of Recombinant Antibodies: Linking Structure to Function. in *State of the Art Analytical Methods for the Characterization of Biological Products and Assessment of Comparability*. Basel, Karger: Dev BioI (Basel). Editors A. R. Mire-Sluis, 22, 117–127.

Huh, J. H., White, A. J., Brych, S. R., Franey, H., and Matsumura, M. (2013). The Identification of Free Cysteine Residues within Antibodies a Potential Role for Free Cysteine Residues in Covalent Aggregation Because of Agitation Stress. *J. Pharm. Sci.* 102, 1701–1711. doi:10.1002/jps.23505

Janeway, C. A., Jr, Travers, P., Walport, M., and Shlomchik, M. J. (2001)The Structure of a Typical Antibody Molecule. *Immunobiology: The Immune System in Health and Disease*. 5th edition. New York: Garland Science

Kellett-Clarke, H., Stegmann, M., Barclay, A. N., and Metcalfe, C. (2015). CD44 Binding to Hyaluronic Acid Is Redox Regulated by a Labile Disulfide Bond in the Hyaluronic Acid Binding Site. *PLoS One* 10, e0138137. doi:10.1371/journal.pone.0138137

Lacy, E. R., Baker, M., and Brigham-Burke, M. (2008). Free Sulfhydryl Measurement as an Indicator of Antibody Stability. *Anal. Biochem.* 382, 66–68. doi:10.1016/j.ab.2008.07.016

Langmuir, M. E., Yang, J.-R., Moussa, A. M., Laura, R., and Lecompte, K. A. (1995). New Naphthopyranone Based Fluorescent Thiol Probes. *Tetrahedron Lett.* 36, 3989–3992. doi:10.1016/0040-4039(95)00695-9

Li, X., Xiao, L., Kochert, B., Donnelly, D. P., Gao, X., and Richardson, D. (2021). Extended Characterization of Unpaired Cysteines in an IgG1 Monoclonal Antibody by LC-MS Analysis. *Anal. Biochem.* 622, 114172. doi:10.1016/j.ab.2021.114172

Liu, H., Chumsae, C., Gaza-Bulseco, G., and Goedken, E. R. (2010). Domain-level Stability of an Antibody Monitored by Reduction, Differential Alkylation, and Mass Spectrometry Analysis. *Anal. Biochem.* 400, 244–250. doi:10.1016/j.ab.2010.02.004

Pace, C. N., Grimsley, G. R., Thomson, J. A., and Barnett, B. J. (1988). Conformational Stability and Activity of Ribonuclease T1 with Zero, One, and Two Intact Disulfide Bonds. *J. Biol. Chem.* 263, 11820–11825. doi:10.1016/s0021-9258(18)37859-1

Pijning, A. E., Blyth, M. T., Coote, M. L., Passam, F., Chiu, J., and Hogg, P. J. (2021). An Alternate Covalent Form of Platelet αIIbβ3 Integrin that Resides in Focal Adhesions and Has Altered Function. *Blood* 138, 1359–1372. doi:10.1182/blood.2021012441

Prus, G., Hoegl, A., Weinert, B. T., and Choudhary, C. (2019). Analysis and Interpretation of Protein Post-Translational Modification Site Stoichiometry. *Trends Biochem. Sci.* 44, 943–960. doi:10.1016/j.tibs.2019.06.003

Robotham, A. C., and Kelly, J. F. (2019). Detection and Quantification of Free Sulfhydryls in Monoclonal Antibodies Using Maleimide Labeling and Mass Spectrometry. *MAbs* 11, 757–766. doi:10.1080/19420862.2019.1595307

Sawant, M. S., Streu, C. N., Wu, L., and Tessier, P. M. (2020). Toward Drug-like Multispecific Antibodies by Design. *Int. J. Mol. Sci.* 21, 7496. doi:10.3390/ijms21207496

Shepard, H. M., Phillips, G. L., Thanos, C. D., and Feldmann, M. (2017). Developments in Therapy with Monoclonal Antibodies and Related Proteins. *Clin. Med.* 17, 220–232. doi:10.7861/clinmedicine.17-3-220

Singh, R., Blättler, W. A., and Collinson, A. R. (1995). [20] Assay for Thiols Based on Reactivation of Papain. *Methods Enzymol.* 251, 229–237. doi:10.1016/0076-6879(95)51125-3

Singh, R., Blattler, W. A., and Collinson, A. R. (1993). An Amplified Assay for Thiols Based on Reactivation of Papain. *Anal. Biochem.* 213, 49–56. doi:10.1006/abio.1993.1384

Trexler-Schmidt, M., Sargis, S., Chiu, J., Sze-Khoo, S., Mun, M., Kao, Y. H., et al. (2010). Identification and Prevention of Antibody Disulfide Bond Reduction during Cell Culture Manufacturing. *Biotechnol. Bioeng.* 106, 452–461. doi:10.1002/bit.22699

Trivedi, M., Laurence, J., and Siahaan, T. (2009). The Role of Thiols and Disulfides on Protein Stability. *Curr. Protein Pept. Sci.* 10, 614–625. doi:10.2174/138920309789630534

Wang, S., and Kaltashov, I. A. (2012). A New Strategy of Using O18-Labeled Iodoacetic Acid for Mass Spectrometry-Based Protein Quantitation. *J. Am. Soc. Mass Spectrom.* 23, 1293–1297. doi:10.1007/s13361-012-0396-9

Wang, S., and Kaltashov, I. A. (2015). Identification of Reduction-Susceptible Disulfide Bonds in Transferrin by Differential Alkylation Using O16/O18 Labeled Iodoacetic Acid. *J. Am. Soc. Mass Spectrom.* 26, 800–807. doi:10.1007/s13361-015-1082-5

Wei, B., Han, G., Tang, J., Sandoval, W., and Zhang, Y. T. (2019). Native Hydrophobic Interaction Chromatography Hyphenated to Mass Spectrometry for Characterization of Monoclonal Antibody Minor Variants. *Anal. Chem.* 91, 15360–15364. doi:10.1021/acs.analchem.9b04467

Welch, L., Dong, X., Hewitt, D., Irwin, M., Mccarty, L., Tsai, C., et al. (2018). Facile Quantitation of Free Thiols in a Recombinant Monoclonal Antibody by Reversed-phase High Performance Liquid Chromatography with Hydrophobicity-Tailored Thiol Derivatization. *J. Chromatogr. B* 1092, 158–167. doi:10.1016/j.jchromb.2018.05.039

Wong, J. W. H., and Hogg, P. J. (2010). Analysis of Disulfide Bonds in Protein Structures. *J. Thromb. Haemost.* 8, 2345. doi:10.1111/j.1538-7836.2010.03894.x

Wright, S. K., and Viola, R. E. (1998). Evaluation of Methods for the Quantitation of Cysteines in Proteins. *Anal. Biochem.* 265, 8–14. doi:10.1006/abio.1998.2858

You, J., Zhang, J., Wang, J., and Jin, M. (2021). Cysteine-Based Coupling: Challenges and Solutions. *Bioconjugate Chem.* 32, 1525–1534. doi:10.1021/acs.bioconjchem.1c00213

Zhang, W., and Czupryn, M. J. (2002). Free Sulfhydryl in Recombinant Monoclonal Antibodies. *Biotechnol. Prog.* 18, 509–513. doi:10.1021/bp025511z

Conflict of Interest: The authors declare that the research was conducted in the absence of any commercial or financial relationships that could be construed as a potential conflict of interest.

frontiers | Frontiers in Molecular Biosciences

ORIGINAL RESEARCH
published: 04 July 2022
doi: 10.3389/fmolb.2022.868460

Impact of Formulation Choices on the Freeze-Drying of an Interleukin-6 Reference Material

Paul Matejtschuk[1], Christopher Bird[2], Ernest Ezeajughi[1], Kirsty MacLellan-Gibson[1] and Meenu Wadhwa[2]*

[1]Analytical and Biological Sciences, NIBSC, Medicines and Healthcare Products Regulatory Agency, Potters Bar, United Kingdom, [2]Biotherapeutics, NIBSC, Medicines and Healthcare products Regulatory Agency, Potters Bar, United Kingdom

Formulation is critical to successful delivery of lyophilized biologics. We have compared the impact of buffer choice and the addition of sodium chloride (a formulant often viewed as unfavorable for freeze-drying applications) on the outcome of trial lyophilization of an interleukin-6 reference material. While phosphate buffer was a preferred choice and yielded well-formed cakes associated with fair recovery of biological activity, the resultant residual moisture content was high (2–4% w/w). By inclusion of isotonic levels of NaCl, the freeze-dried appearance and process were not impaired, but the residual moisture delivered was considerably reduced to levels <1% w/w. We postulate that this is due to the presence of a more open-cake structure and support this with evidence from thermal analysis and scanning electron microscopy. This work illustrates the importance of wide ranging empirical investigation of formulation options in order to optimize freeze-drying outcomes for biologics.

Keywords: freeze drying, formulation, interleukin-6, sodium chloride, scanning electron microscopy, differential scanning calorimetry

OPEN ACCESS

Edited by:
Milena Quaglia, National Measurement Laboratory at LGC, United Kingdom

Reviewed by:
John Patrick Gleeson, Merck & Co., Inc., United States
Evangelos Tsotsas, Otto von Guericke University Magdeburg, Germany

****Correspondence:***
Paul Matejtschuk
paul.matejtschuk@nibsc.org

Specialty section:
This article was submitted to Structural Biology, a section of the journal Frontiers in Molecular Biosciences

Received: *02 February 2022*
Accepted: *11 May 2022*
Published: *04 July 2022*

Citation:
Matejtschuk P, Bird C, Ezeajughi E, MacLellan-Gibson K and Wadhwa M (2022) Impact of Formulation Choices on the Freeze-Drying of an Interleukin-6 Reference Material. Front. Mol. Biosci. 9:868460. doi: 10.3389/fmolb.2022.868460

INTRODUCTION

Freeze-drying is widely used to stabilize labile biological medicines and diagnostics; however, formulation can be critical to ensure maximal preservation of activity and stability (Hubbard et al., 2007). Formulation choices also influence the success of the freeze-drying process and can greatly influence the length and hence affordability of freeze-drying processes (Gervasi et al., 2019; Haueser et al., 2020). Many articles have described the selection processes, and general guidelines have been published (Carpenter et al., 1997; Carpenter et al., 2002; Liu and Zhou, 2021). Typically, ionic salts should be avoided as they reduce the shelf temperature at which drying can be successfully undertaken and indeed make operating conditions impractical (Franks and Auffret, 2007). The choice of the stabilizer has also been well-described, with non-reducing disaccharides being the stabilizer of choice. Other components such as amino acids and surfactants may have an important role to play, and buffer selection may influence activity recovery during the freezing stages.

Lyophilization is also applied commonly in the stabilization of reference materials such as those prepared at the NIBSC on behalf of the World Health Organization. Such standards are physical reference materials, with defined assigned bioactivity (Coxon et al., 2019) established after multiple collaborator evaluation, and standardize and assure the validity of measurements made in many areas of clinical diagnosis and medicine. So, it is critical that they remain stable for their entire lifetimes, often well in excess of a decade. For instance, the international standard for interleukin-2

showed highly preserved bioactivity when tested even after 25 years from preparation (Wadhwa et al., 2013).

Originally discovered as a B cell stimulatory factor (BSF-2) based on its ability to stimulate the maturation of B cells into immunoglobulin-secreting cells (Kishimoto and Ishizaka, 1973), human interleukin-6 (IL-6) was isolated and cloned in 1986 (Hirano et al., 1986). Since then, extensive studies have tried to elucidate the structural aspects of IL-6 and its highly complex biology, including its receptors and signaling pathways (e.g., the classical, the trans-signaling and the trans-presentation), given its ability to elicit a diverse array of functions relevant to tissue homeostasis, hematopoiesis, metabolism, and immune regulation (Garbers et al., 2018; Choy et al., 2020). Structurally, IL-6 is a four-helical cytokine of 184 amino acids with two potential N-glycosylation sites and four cysteine residues. The core protein is about 20 kDa, and the glycosylation accounts for the 21-to-26-kDa size of natural IL-6 (Tanaka and Kishimoto, 2014). IL-6 is a pleiotropic cytokine secreted in response to appropriate stimulation during infection, inflammation, or cancer by multiple cell types and exerts both pro- and anti-inflammatory effects, which are of critical importance in regulating B cell and T cell responses and for coordinating the activity of the innate and adaptive immune systems (Tanaka and Kishimoto, 2014). Dysregulation in IL-6 can cause chronic inflammation, autoimmune disorders, and malignancies, and so IL-6 is a key target for clinical intervention with various anti–IL-6/IL-6 receptor therapeutics approved or in development (Garbers et al., 2018; Choy et al., 2020). These include siltuximab, a monoclonal antibody (mAb) targeting IL-6 for use in Castleman's disease and mAbs such as tocilizumab, which is indicated for use in rheumatoid arthritis (RA), juvenile idiopathic arthritis, adult-onset Still's disease, giant cell arteritis, Takayasu arteritis, for cytokine release syndrome (CRS) associated with CAR-T cell therapy, and more recently for COVID-19 treatment by the European Medicines Agency and Sarilumab for RA; both mAbs bind and block the IL-6 receptor subunit of the IL-6 receptor (Garbers et al., 2018; Choy et al., 2020; https://www.ema.europa.eu/en/news/ema-recommends-approval-use-roactemra-adults-severe-covid-19).

The International Standards (IS) from the WHO function in value assigning and for controlling the potency of cytokine therapies, where relevant, in standardizing cytokine assays, which may direct and advise therapeutic interventions and also in other applications. For instance, the IL-6 IS is used for calibrating IL-6 preparations which are in use 1) as critical reagents in cell-based assays for potency testing of mAbs-targeting IL-6 and IL-6 receptors, 2) as cell-culture supplements for growth of antibody-producing hybridomas and *ex vivo* expansion of hemopoietic stem cells, and 3) in calibrating immunoassays for measuring IL-6 levels as a biomarker of inflammation or disease pathology in clinical settings, for example, sepsis, autoimmune, infectious diseases, and in nonclinical and/or clinical/safety testing of immunotherapies (e.g., cytokine-related syndrome associated with CAR-T cells).

The first international standard for interleukin-6 (NIBSC code 89/548) was launched in 1992 (Gaines Das and Poole, 1993) and shown to be a suitable standard for such applications. However, stocks are running low after nearly 30 years of use, and an exercise was undertaken in lyophilizing a replacement material, including revisiting the formulation and freeze-drying cycle design to accommodate process advancements and current best practice. Using human interleukin-6 (IL-6) as an example, we emphasize the importance of thermal analytical methods in predicting successful freeze-drying outcomes to provide efficiencies by avoiding expensive and time-consuming unacceptable freeze-drying runs.

MATERIALS AND METHODS

Formulation Options

IL-6 (Bio-Techne, Minneapolis, United States) was formulated to achieve a 1 μg/ml solution post reconstitution of the ampoule, given that the first WHO IS also contains 1 μg per ampoule, and a majority of IL-6 bioassays for the activity of IL-6 often begin at a starting concentration of 1–2 ng/ml. Trehalose was selected as the disaccharide stabilizer since it was used in the production of an earlier interim standard or for the existing first IS (code 89/548). An array of different buffers were selected based on the use of either sodium acetate or sodium phosphate in the formulation of previous IL-6 standards (e.g., 89/548 or 88/514, which served as the interim standard and contained *E. coli*, expressed IL-6 similar to the intended candidate standard prior to the establishment of the first WHO IS code 89/548). Formulations with and without isotonic NaCl were compared in this evaluation.

Thermal Analysis

Freeze-drying microscopy: analysis was performed using 2-μL aliquots pipetted into a quartz crucible and analyzed using the Lyostat 5 freeze-drying microscope (Biopharma Ltd., Winchester, United Kingdom); with a freeze rate of 10°C/min to −50°C, vacuum was applied and a ramp rate of 5–10°C/min warming was used until the collapse was visible.

Modulated differential scanning calorimetry: (mDSC) (Q2000, TA Instruments, Wilmslow, United Kingdom) High-volume steel pans were filled with samples in duplicate (80 μL) against an empty pan, and the samples were frozen to −90°C and then ramped at 3°C/min to ambient temperature with modulation at 1°C/min.

Freeze-Drying

Trial freeze-drying was performed on a VirTis Genesis 25EL dryer (Biopharma Process Systems, Winchester, United Kingdom), with bespoke 5-ml type I glass ampoules being used and a fill volume of 1 ml. Ampoules (Schott) and halobutyl closures (13 mm diameter igloo) (West Pharma igloo) were obtained from Adelphi Packaging (Haywards Heath, United Kingdom). Filling was performed manually using a Gilson P1000 pipette (Anachem, Luton, United Kingdom), and the samples were dried using a conservative freeze-drying cycle. Freezing was down to −50°C and then primary drying was at −40°C for 22 hours followed by ramping to 25°C and secondary drying for a minimum of 20 h, all at 30 μbar vacuum. Ampoules

TABLE 1 | Descriptors of formulation options SS-879, SS-880, SS-889, and 21/308.

	SS-879		SS-880	SS-889				21/308
Identifier	—	—	—	Red ring	Blue ring	Black stripe	Clear	—
Trehalose	0.6%	0.6%	0.6%	0.6%	0.6%	0.6%	0.6%	0.6%
HSA	0.2%	0.1%	0.1%	0.1%	0.1%	0.1%	0.1%	0.1%
Buffer	50 Mm NaAc pH 5	50 mM NaP pH 7	50 mM Na P pH 7	50 mM Na P pH 7	50 mM Na P pH 7	50 mM Na P pH 7	50 mM Na P pH 7	50 mM Na P pH 7
IL-6	None	None	1 µg/ml	1 µg/ml	1 µg/ml	—	—	1 µg/ml
NaCl	—	—	—	—	0.9% w/v	—	0.9% w/v	0.9% w/v

were backfilled with low-moisture nitrogen and stoppered *in situ* before removal and flame sealing.

Several trial runs were conducted (**Table 1**).

1) Trial run SS-879 included a comparison of two formulations without active material
   - 0.6% trehalose, 0.2% human serum albumin (HSA), and 50 mM sodium acetate pH5,
   - 0.6% trehalose, 0.1% HSA, and 50 mM sodium phosphate pH 7,

Ampoules were subjected to freeze-drying over 2 days, with a temperature of −40°C, 30 µ bar vacuum primary drying, and 25°C secondary drying. Ampoules from both formulations were analyzed by FDM and mDSC.

2) In trial run SS-880, the successful NaP formulation from SS-879 was scaled up and 60 ampoules dried with 1 µg/ml IL-6 was added. A 4-day instead of a 2-day freeze-drying cycle for SS-879 was used with −40°C primary drying and elevated 30°C secondary drying for 20 h.
3) In trial run SS-889, a comparison was made with both excipients only (without IL-6) and with IL-6 containing formulations, with and without the addition of 0.9% NaCl to the formulation:

These were freeze-dried using a 3-day cycle but with an elevated primary drying shelf temperature of −35°C and a vacuum setpoint of 100 µ bar, (70mTorr) with the intention of removing excess water during drying and of getting a lower final residual moisture.

4) Candidate definitive batch 21/308. A definitive fill was performed in the CS100 (Serail, Arguenteil, France) dryer in the CBRM in November 2021 using a 4-day cycle but based around the conditions applied for trial SS-889.

Scanning Electron Microscopy

The samples were prepared in a dry box operating at less than 8% humidity (Deben, Bury St Edmunds, United Kingdom) by breaking the glass vial to release the freeze-dried cake. The cake was then sectioned across the approximate center with a razor blade, and the section was removed from the vial. The section was trimmed to produce a ~5-mm section from the central region, and these were attached to a 12.5-mm SEM stub by Silver Conductive Adhesive 503 (Agar Scientific Stansted, United Kingdom and Electron Microscopy Sciences, Hatfield, PA, United States, respectively), with the "center" side facing upward. Arrows on the stub were used to indicate the top of the cake. When the paint was completely dry, the samples were thinned and leveled with a razor blade, if required, and then sputter-coated with 4 nm gold by using a Leica ACE600 coater (Leica Microsystems, Milton Keynes). The samples were held under vacuum in the sputter coater until they were transferred to the SEM holder. When placed in the holder, the top of the cake was positioned to the posterior of the chamber to allow easy orientation in the microscope. The samples were imaged in a JSM7401F scanning electron microscope (Jeol UK, Welwyn Garden City, United Kingdom) at 5 kV, 1.5–3 µA, with a probe current of 7. The images were acquired by the in-lens secondary electron detector (LEI) at magnifications of ×300, ×850, and ×1,500 as required. For each cake, three positions were imaged at the bottom of the cake, the center of the cake, and the top of the cake.

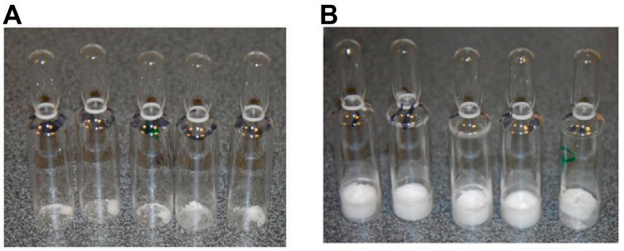

FIGURE 1 | FD trial SS-879 options **(A)** acetate and **(B)** phosphate-physical appearance.

Residual moisture was measured using Karl Fischer coulometric titration on an automated CA-200 Mitsubishi coulometer with a Gilson GX-270 robotic sampler (A1 Envirosciences, Blyth, United Kingdom). Freeze-dried samples were broken up in a pyramid dry bag (Cole Parmer, London, United Kingdom) under low moisture conditions (~10% RH maintained by a continuous flow of dry nitrogen) and then dispensed into HPLC autosampler vials (4-ml screw-capped vials fitted with PTFE membrane pierceable lids, C4015-88 Thermo Scientific, Hemel Hempstead, United Kingdom). The samples were weighed and analyzed in triplicate, and the coulometer calibration was checked with bracketed samples of a water standard (Mitsubishi Aquamicon P, A1 Envirosciences). Container blanks (containing no product) were also run and

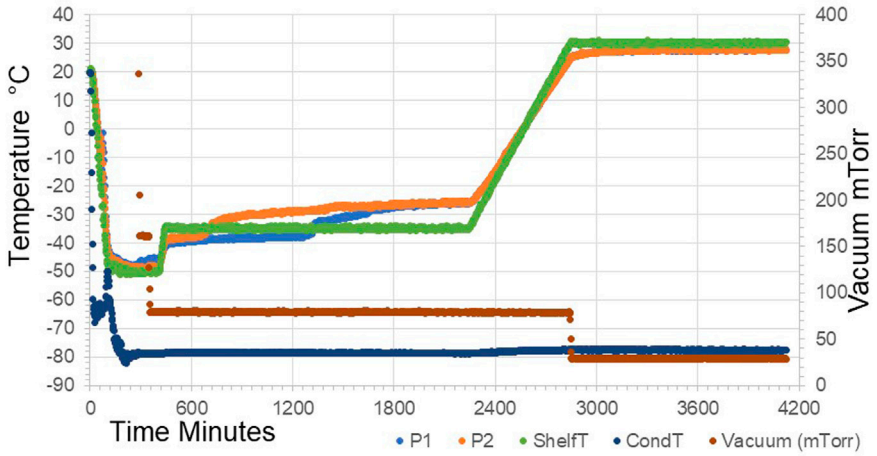

FIGURE 2 | Freeze-drying profile of SS-889 trial with (P1) and without (P2) additional NaCl in formulation.

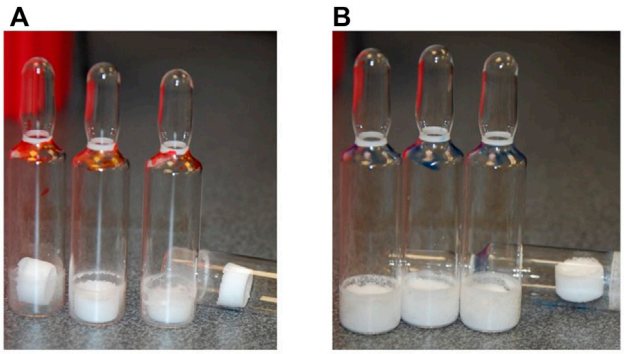

FIGURE 3 | SS-889 FD options **(A)** without NaCl and **(B)** with NaCl (SS-889).

subtracted from the observed moisture content. Moisture on the definitive batch was determined by manual coulometric Karl Fischer titration on the same model coulometer but operated in a nitrogen dry box.

Oxygen Headspace content: Ampoules were backfilled with nitrogen prior to sealing, and so as an indicator of the integrity of the sealed ampoules, measurements of the oxygen headspace content were made non-invasively using infrared frequency–modulated spectroscopy at 760 nm (for oxygen) with the FMS-760 spectrometer (Lighthouse Instruments, Charlottesville VA, United States) against NIST traceable oxygen standards in identical container types.

Bioactivity Assay

The bioactivity of IL-6 preparations was measured using the human embryonic kidney 293 (HEK293)–derived HEK-Blue™ IL-6 reporter gene cell line (Invivogen, Toulouse, France), stably transfected with genes encoding human IL-6R and STAT3 linked to a reporter gene expressing secreted embryonic alkaline phosphatase (SEAP) under the control of the IFN-β minimal promoter. The cell line was cultured, and the bioassay was performed as per the manufacturer's procedure. Briefly, IL-6 was serially diluted (from 2000 pg/ml to 1.95 pg/ml) in assay medium (Dulbecco's modified Eagle medium containing 10% heat-inactivated fetal bovine serum, 2 mM L-glutamine, and penicillin/streptomycin (50U/ml/50 µg/ml) in 96-well tissue culture plates, and 5×10^4 cells were added to individual wells. Following incubation for 20–24 h at 37°C in a humidified CO_2 incubator, SEAP levels were measured by incubating cell supernatants with QUANTI-Blue™ solution (Invivogen, Toulouse, France) as per the manufacturer's instructions for 2 h at 37°C in a humidified CO_2 incubator. The quantity of SEAP secreted into the cell supernatant is proportional to the IL-6 concentration and determined by measuring the absorbance at 620 nm using a microplate reader (Spectramax M5, Molecular Devices UK, Wokingham, United Kingdom). Estimates of potency relative to the bulk unformulated

TABLE 2 | QC batch details for trials and candidate definitive batch 21/308.

Parameter	Samples of SS-889 trial				–
–	IL-6 no NaCl (red)	IL-6 + NaCl (blue)	Excipient–no NaCl (black stripe)	Excipient + NaCl (clear)	Definitive 21/308
Fill weight g (CV, n_)	0.959 (0.85%, 3)	0.967 (2.38%, 3)	0.939 (7.5%, 3)	0.968 (1.65%, 3)	1.0077 g (CV 0.26%, 183)
Dry weight mg (CV, n)	13.6 (1.27%, 3)	21.3 (3.34%, 3)	13.2 (15%, 3)	21.3 (1.6%, 3)	15.99 mg (CV = 11.8%, 5)
Residual moisture- w/w (CV, n)	2.37% (9.1%, 3)	0.31% (23.7%, 3)	4.3% (35.1%, 3)	0.40% (47.5%, 3)	0.27% (CV = 17.8%, 12)
Appearance	Slight lateral pinching	Adherent	Slight lateral pinching	Adherent	Adherent

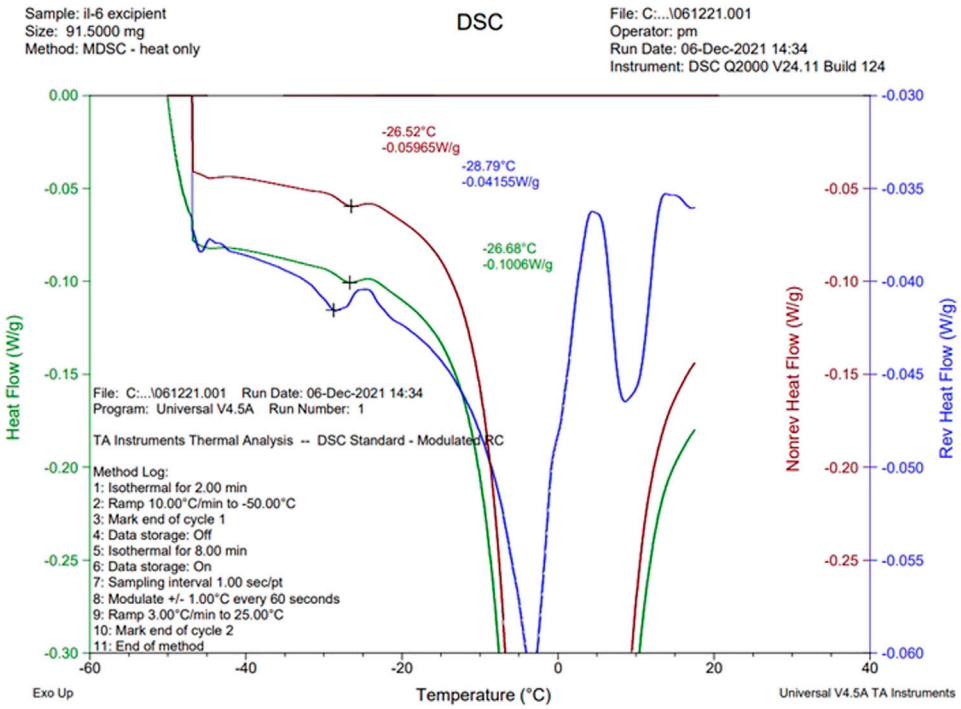

FIGURE 4 | Thermal analysis (mDSC) of sodium phosphate formulation with 0.9% w/v NaCl.

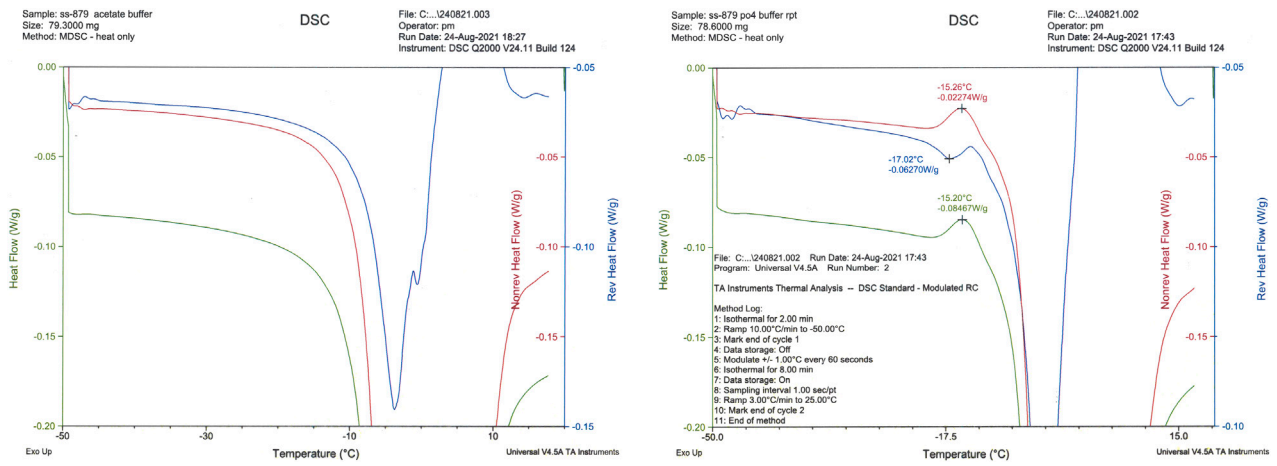

FIGURE 5 | mDSC traces of sodium acetate (LHS) and sodium phosphate (RHS) formulations SS-879.

TABLE 3 | Potency estimates for IL-6 SS-889 trial run relative to unformulated bulk IL-6.

Sample	Estimated potency (n)	Lower 95 (%)limit	Upper 95 (%)limit
Lyophilized (NaP)	72.7% (6)	69.7	75.8
Lyophilized (NaP + 0.9% NaCl)	78.0% (6)	74.8	81.3

(n), denotes number of estimates made.

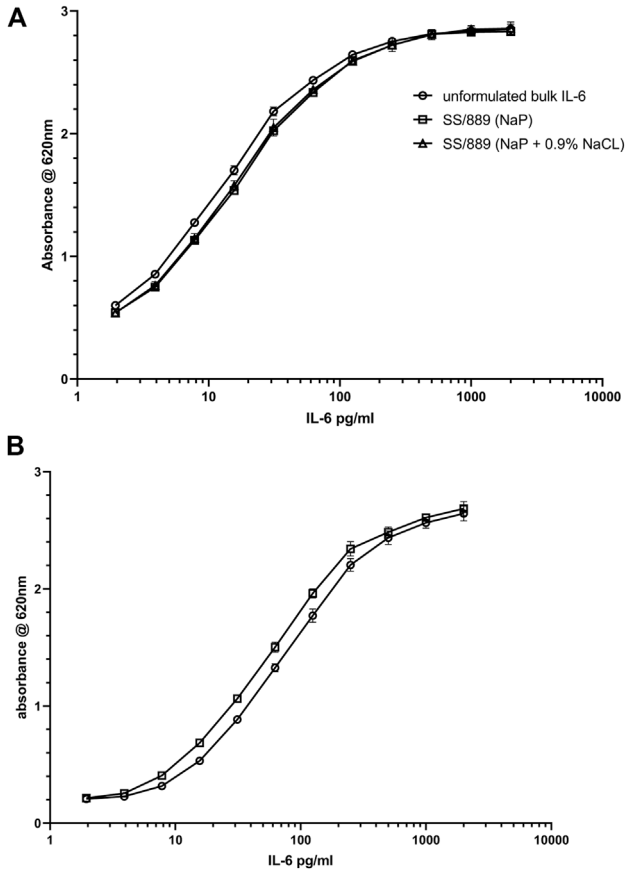

FIGURE 6 | Bioactivity of IL-6 samples **(A)** (IL-6 trial SS-889) in NaP formulation with (open triangle) and without (open square) addition of 0.9% NaCl, compared with IL-6 unformulated bulk material (open circle) in the HEK-Blue™ IL-6 reporter gene assay and **(B)** bioactivity of the IL-6 candidate preparation 21/308 (open square) compared to the international standard IL-6 89/548 (open circle) in the HEK-Blue™ IL-6 reporter gene assay.

IL-6 were calculated using CombiStats v6.0 (www.edqm.eu), with a sigmoid curve model.

RESULTS

Freeze-Drying Appearance

Both acetate- and phosphate-based formulations (SS-879) were compared in the first trial (**Figure 1**) and under the conditions used revealed formation of a good cake for the NaP buffer but a total collapse and powder-like appearance of the lyophilizate with the formulation containing acetate buffer under these quite conservative drying conditions. So, phosphate was subjected to a repeat trial (SS-880) and again performed well. The bioactivity was good, but the residual moisture content was high >2% despite an extended period of secondary drying. An increase in the duration of the freeze-drying cycle to 4 days failed to provide an acceptable moisture content (<1%w/w).

The previous interim standard with *E. coli*–expressed IL-6 (coded 88/514) had been formulated in a base of saline, and hence 0.9 w/w NaCl was added in to the formulation and compared (trial SS-889, **Figure 2**) with the low salt formulation (NaCl-free). Surprisingly, although both gave good freeze-dried cakes, **Figure 3** the moisture of the isotonic NaCl formulation was much lower on the same cycle than the formulation without NaCl, both in excipient-only ampoules and those formulated with active IL-6 (**Table 2**).

A scaled-up candidate definitive batch 21/308 was produced with the isotonic saline formulation and over 5,000 ampoules dried in a Serail CS-100 freeze-dryer (Serail Arguentil, France) with the same cycle. As for SS-889, the isotonic saline formulation resulted in a batch of ampoules with well-formed cakes and low moisture content of 0.27% w/w, with good bioactivity.

Thermal Analysis

The three formulations, acetate-based, phosphate-based, and phosphate-based plus NaCl, were analyzed by thermal analysis. The acetate-based formulation did not show any clear thermal events, and on drying an unacceptable appearance resulted (**Figure1**) Freeze-drying microscopy indicated a collapse temperature approximately −33°C (n = 2) for the phosphate buffer, but collapse was visible even from below −50°C for the acetate formulation.

The NaCl-containing phosphate-buffered excipient and the NaCl-containing definitive product showed a clear event in the mDSC profile at approximately −26°C, indicative of crystallization of NaCl (**Figure 4**). This was absent in the NaCl-free formulation, though an exothermic event did occur around −15°C (**Figure 5**).

Bioactivity data: Evaluation of the bioactivity of the formulations with and without NaCl showed acceptable retention of bioactivity, if anything slightly higher for the formulation with NaCl (78 vs. 73% over six measurements) as shown in **Table 3**. The plots of the dilution curves show that the bioactivity of the two formulated preparations was very similar (**Figure 6A**). The recovery of bioactivity in the candidate definitive batch 21/308 containing NaCl in the formulation was also well-preserved (**Figure 6B**) and was comparable to the existing international standard.

Structural Analysis by SEM

SEM was undertaken on NaCl-omitted and NaCl-containing formulations and also on the candidate definitive batch 21/308 (**Figure 7**). Examination of the freeze-dried cakes of formulations with and without NaCl showed that NaCl-containing formulation (SS-889 clear and 21/308) (Image J) had a more consistent and well-formed cake with a wider open-pore structure than that formulated without NaCl (SS-889 red ring) (image k). At the highest resolution, (images g–i and l–m) fine details indicative of a more crystalline structure were evident in NaCl-containing preparations (**Figure 7**). This is consistent with the NaCl-containing formulated freeze-dried cakes having a more open cake and therefore being able to dry more completely.

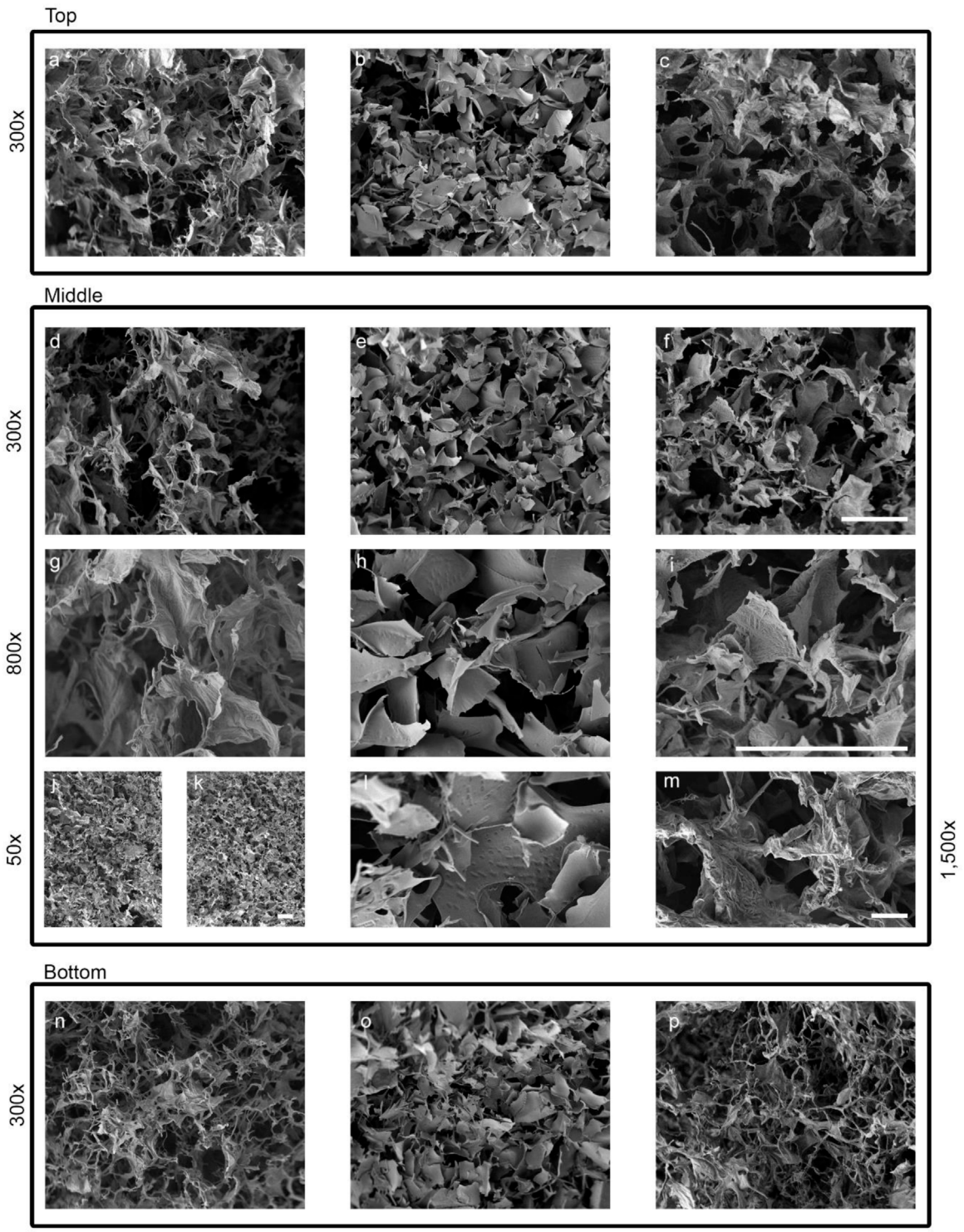

FIGURE 7 | High-resolution SEM images of the NaCl-containing definitive (21/308) and the with NaCl (SS-889 clear) and without NaCl (SS-889 red ring) trial freeze-dried cakes. Images a-f and n-p show top, middle and bottom of the cakes at 300 × magniifcation. Images g-i show a highr magnificiation view at 800× of the middle section of the cakes. Images j to m show lower ×50 (j,k) and higher ×1,500 magnifications [(l,m), respectively] of formulations without NaCl, (j) and (l) (SS-889 red ring), and with NaCl, (k) and (m) (SS-889 clear). Gradation scale = 100 μm in all panels.

DISCUSSION

For lyophilized materials intended as standards, collapsed appearance is generally unacceptable, although this may not necessarily correlate with loss of activity of the material. In general, the advice is to reduce or omit inorganic salts from formulations as they reduce the glass transition temperature value of formulations and result in lower temperature primary drying and hence longer, slower cycles. However, sometimes, the benefits of crystalline excipient can be overlooked. Here, we demonstrated that in terms of the final residual moisture and the cake structure of the freeze-dried mass, NaCl addition provided a crystalline matrix, which resulted in a better pore structure and led to lower residual moisture than a non-NaCl formulation on the same cycle. Most telling is that even though a long and higher temperature secondary drying was used in trial SS-880, the NaCl-free formulation still retained much higher levels of residual moisture, a conclusion supported by the direct comparative study SS-889. Comparative analysis of the two formulations by SEM showed the cake structure with the inclusion of NaCl to be superior, with an open pore structure, and so it is tempting to relate this to the observed poorer structure to the less efficient water sublimation and higher residual moisture content.

This result complements our earlier finding (Duru et al., 2015), which showed that for freeze-dried influenza antigen reference preparations, NaCl crystallization was a critical factor—an increase in the amorphous content using raised levels of sucrose (above 1.4% w/w) resulted in a collapsed freeze-dried appearance. From the mDSC, it was concluded that raising the sucrose content (although usually a desirable stabilizer for freeze drying), resulted in inhibition of the crystallization of the NaCl co-formulant and that this crystallization was critical in producing an acceptable freeze-dried appearance. In the present study also, the presence on mDSC of the eutectic event in the "with NaCl" formulation and its absence in the "without NaCl" sample when analyzed correlated to the crystallization of the NaCl, resulting in improved overall structure of the freeze-dried cake.

Shalaev et al. (1996) described the glass transitions, softening points, devitrification, and melting points for the ternary system water–sucrose–sodium chloride by DSC and showed that NaCl crystallization can be inhibited by amorphous solutes such as sucrose. Goshima et al. (2016) have shown that inclusion of NaCl may improve the stability of freeze-dried model protein albumin. Thakral et al. (2021) have systematically reviewed the interactions between formulation components both in frozen and freeze-dried systems.

In conclusion, from the IL-6 standard perspective, the addition of NaCl to the NaP formulation provided a robust cake with a lower moisture content below 1% w/w, which in agreement with the WHO specifications, is more likely to give a highly stable reference material (WHO, 2006). The difference in formulation did not seem to have any negative influence on the bioactivity as measured by the reporter gene assay. The NaCl-containing formulation was, therefore, selected for scale up for the candidate definitive material 21/308.

More generally, in terms of formulation for freeze-drying, though guided by general principles (Kharaghani et al., 2017), consideration must be given on a case-by-case basis to the influence of individual components on the thermal properties and final freeze-dried appearance of any given formulation. This again underlines the value of thermal analytical methods in predicting successful freeze-drying outcomes and other new analytical techniques are being introduced (Thomik et al., 2022), and their use will help avoid expensive and time-consuming unacceptable freeze-drying runs in the development of lyophilization processes.

DATA AVAILABILITY STATEMENT

The datasets presented in this article are not readily available because none of them are mentioned. Requests to access the datasets should be directed to paul.matejtschuk@nibsc.org.

AUTHOR CONTRIBUTIONS

CB, PM, and MW devised the project and CB KM-G, EE, and PM all contributed to the experimental data. All authors co-wrote and reviewed the manuscript. All the authors declare no conflicts of interest and agree to the publication if accepted.

ACKNOWLEDGMENTS

We thank staff of the Standards Processing Division for producing the definitive scale material.

REFERENCES

Carpenter, J. F., Chang, B. S., Garzon-Rodriguez, W., and Randolph, T. W. (2002). "Rational Design of Stable Lyophilized Protein Formulations: Theory and Practice," in *Rational Design of Stable Protein Formulations*. Pharmaceutical Biotechnology. Editors J. F. Carpenter and M. C. Manning (Boston, MA: Springer), 13, 109–133. doi:10.1007/978-1-4615-0557-0_5

Carpenter, J. F., Pikal, M. J., Chang, B. S., and Randolph, T. W. (1997). Rational Design of Stable Lyophilized Protein Formulations: Some Practical Advice. *Pharm. Res.* 14 (8), 969–975. doi:10.1023/a:1012180707283

Choy, E. H., De Benedetti, F., Takeuchi, T., Hashizume, M., John, M. R., and Kishimoto, T. (2020). Translating IL-6 Biology into Effective Treatments. *Nat. Rev. Rheumatol.* 16, 335–345. doi:10.1038/s41584-020-0419-z

Coxon, C.H., Longstaff, C., and Burns, C. (2019). Applying the science of measurement to biology:Why bother? *PLoS Biol.* 17(6), e3000338. doi:10.1371/journal.pbio.3000338

Duru, C., Swann, C., Dunleavy, U., Mulloy, B., and Matejtschuk, P. (2015). The Importance of Formulation in the Successful Lyophilization of Influenza Reference Materials. *Biologicals* 43 (2), 110–116. doi:10.1016/j.biologicals.2014.12.001

Franks, F., and Auffret, A. (2007). *Freeze-drying of Pharmaceuticals and Biopharmaceuticals*. Cambridge, UK: RSC Press.

Gaines Das, R. E., and Poole, S. (1993). The International Standard for Interleukin-6. Evaluation in an International Collaborative Study. *J. Immunol. Methods* 160 (2), 147–153. doi:10.1016/0022-1759(93)90172-4

Garbers, C., Heink, S., Korn, T., and Rose-John, S. (2018). Interleukin-6: Designing Specific Therapeutics for a Complex Cytokine. *Nat. Rev. Drug Discov.* 17, 395–412. doi:10.1038/nrd.2018.45

Gervasi, V., Cullen, S., McCoy, T., Crean, A., and Vucen, S. (2019). Application of a Mixture DOE for the Prediction of Formulation Critical Temperatures during Lyophilisation Process Optimisation. *Int. J. Pharm.* 572, 118807. doi:10.1016/j.ijpharm.2019.118807

Goshima, H., Forney-Stevens, K. M., Liu, M., Qian, K. K., Tyagi, M., Cicerone, M. T., et al. (2016). Addition of Monovalent Electrolytes to Improve Storage Stability of Freeze-Dried Protein Formulations. *J. Pharm. Sci.* 105 (2), 530–541. doi:10.1016/j.xphs.2015.10.004

Haeuser, C., Goldbach, P., Huwyler, J., Friess, W., and Allmendinger, A. (2020). Excipients for Room Temperature Stable Freeze-Dried Monoclonal Antibody Formulations. *J. Pharm. Sci.* 109 (1), 807–817. Epub 2019 Oct 14.PMID: 31622600. doi:10.1016/j.xphs.2019.10.016

Hirano, T., Yasukawa, K., Harada, H., Taga, T., Watanabe, Y., Matsuda, T., et al. (1986). Complementary DNA for a Novel Human Interleukin (BSF-2) that Induces B Lymphocytes to Produce Immunoglobulin. *Nature* 324, 73–76. doi:10.1038/324073a0

Hubbard, A., Bevan, S., and Matejtschuk, P. (2007). Impact of Residual Moisture and Formulation on Factor VIII and Factor V Recovery in Lyophilized Plasma Reference Materials. *Anal. Bioanal. Chem.* 387 (7), 2503–2507. doi:10.1007/s00216-006-0855-x

Kharaghani, A., Tsotsas, E., Wolf, C., Beutler, T., Guttzeit, M., and Oetjen, G.-W. (2017). "Freeze-Drying," in *Ullmann's Encyclopedia of Industrial Chemistry* (Weinheim, Germany), 1–47. doi:10.1002/14356007.h12_h01.pub2

Kishimoto, T., and Ishizaka, K. (1973). Regulation of Antibody Response *In Vitro*. VII. Enhancing Soluble Factors for IgG and IgE Antibody Response. *J. Immunol.* 111, 1194–1205.

Liu, B., and Zhou, X. (2021). Freeze-drying of proteins. In: Cryopreservation and Freeze-Drying Protocols. Editors W. F. Wolkers and H. Oldenhof (New York, NY: Humana), 2180. doi:10.1007/978-1-0716-0783-1_37

Shalaev, E. Y., Franks, F., and Echlin, P. (1996). Crystalline and Amorphous Phases in the Ternary System Water–Sucrose–Sodium Chloride. *J. Phys. Chem.* 100 (4), 1144–1152. doi:10.1021/jp951052r

Tanaka, T., and Kishimoto, T. (2014). The Biology and Medical Implications of Interleukin-6. *Cancer Immunol. Res.* 2, 288–294. doi:10.1158/2326-6066.CIR-14-0022

Thakral, S., Sonje, J., Munjal, B., and Suryanarayanan, R. (2021). Stabilizers and Their Interaction with Formulation Components in Frozen and Freeze-Dried Protein Formulations. *Adv. Drug Deliv. Rev.* 173, 1–19. doi:10.1016/j.addr.2021.03.003

Thomik, M., Gruber, S., Foerst, P., Tsotsas, E., and Vorhauer-Huget, N. (2022). Determination of 3D Pore Network Structure of Freeze-Dried Maltodextrin. *Dry. Technol.* 40, 748–766. doi:10.1080/07373937.2021.1966030

Wadhwa, M., Bird, C., Heath, A. B., Dilger, P., and Thorpe, R. (2013). The 2nd International Standard for Interleukin-2 (IL-2) Report of a Collaborative Study. *J. Immunol. Methods* 397 (1-2), 1–7. doi:10.1016/j.jim.2013.07.012

WHO (2006). *Recommendations for the Preparation, Characterization and Establishment of International and Other Biological Reference Standards (Revised 2004)* WHO Technical Report Series *No 932*, 75–131. Geneva, Switzerland: WHO.

Conflict of Interest: The authors declare that the research was conducted in the absence of any commercial or financial relationships that could be construed as a potential conflict of interest.

Publisher's Note: All claims expressed in this article are solely those of the authors and do not necessarily represent those of their affiliated organizations, or those of the publisher, the editors, and the reviewers. Any product that may be evaluated in this article, or claim that may be made by its manufacturer, is not guaranteed or endorsed by the publisher.

frontiers | Frontiers in Molecular Biosciences

ORIGINAL RESEARCH
published: 07 July 2022
doi: 10.3389/fmolb.2022.866843

Impact of Bioconjugation on Structure and Function of Antibodies for Use in Immunoassay by Hydrogen-Deuterium Exchange Mass Spectrometry

Luise Luckau[1], Kate Groves[1], Chris Blencowe[2], Sam Scrimshaw[2], Alastair Dent[2] and Milena Quaglia[1]*

[1]National Measurement Laboratory at LGC, Teddington, United Kingdom, [2]Fleet Bioprocessing Ltd., Hartley Wintney, United Kingdom

OPEN ACCESS

Edited by:
James A. Garnett,
King's College London,
United Kingdom

Reviewed by:
Robert Kelley,
Genentech, Inc., United States
Frank Sobott,
University of Leeds, United Kingdom

***Correspondence:**
Luise Luckau
luise.luckau@lgcgroup.com

Specialty section:
This article was submitted to Structural Biology, a section of the journal Frontiers in Molecular Biosciences

Received: 31 January 2022
Accepted: 15 June 2022
Published: 07 July 2022

Citation:
Luckau L, Groves K, Blencowe C, Scrimshaw S, Dent A and Quaglia M (2022) Impact of Bioconjugation on Structure and Function of Antibodies for Use in Immunoassay by Hydrogen-Deuterium Exchange Mass Spectrometry. Front. Mol. Biosci. 9:866843. doi: 10.3389/fmolb.2022.866843

Monoclonal antibodies (mAbs) are widely used as analytical components in immunoassays to detect target molecules in applications such as clinical diagnostics, food analysis and drug discovery. Functional groups are often conjugated to lysine or cysteine residues to aid immobilization of mAbs or to enable their detection in an antibody antigen complex. Good assay performance depends on the affinity and specificity of the mAbs for the antigen. The conjugation reaction however can cause higher order structural (HOS) changes and ultimately affect the assay performance. In this study, four differently conjugated mAbs were selected as model systems and characterized by mass spectrometry. Particularly, intact protein analysis by liquid-chromatography mass-spectrometry (LC-MS) was performed to determine the amount and distribution of conjugation. Hydrogen deuterium exchange mass spectrometry (HDX-MS) experiments were carried out for the structural characterization of the conjugated mAbs. Immunoassay experiments were performed to monitor the effects of conjugation on the binding properties of the antibodies selected. Good agreement between the mass spectrometry and binding experiment results was found. Particularly, it was noted that the overall structural flexibility of the antibodies increases upon cysteine conjugation and decreases for lysine conjugation. The conjugation of mAbs with bulky functional groups tends to decrease the deuterium uptake kinetics due to induced steric effects. Overall, this study shows correlations between conjugation, structure and function of immunoassay antibodies and the benefits of mass spectrometry to improve understanding of the conjugation reaction and provide insights that can predict immunoassay performance.

Keywords: hydrogen-deuterium exchange mass spectrometry, antibody conjugate, immunoassay, lysine conjugation, cysteine conjugation, structure-function analysis

INTRODUCTION

Immunoassays are bioanalytical methods that use the specificity of an antibody to detect and quantify target molecules in complex matrices. They are known for their high sensitivity and specificity and are widely used in clinical diagnostics, drug discovery, food and environmental testing (Xiao and Lin 2015; Di Nardo et al., 2021). Various immunoassay designs are in use including competitive and immunometric ("sandwich") formats. The format selected depends on the analyte, the available reagents and the dynamic range required for the particular assay (Cox et al., 2019). Sandwich assays have been reported to be more sensitive and robust and are therefore most commonly used (Cox et al., 2019). In sandwich assays, antigen-capture antibodies are often biotin-conjugated to enable immobilization onto streptavidin-coated assay surfaces. The detection of the antibody-antigen (Ab-Ag) complex is achieved by a second antigen-specific antibody, which is typically conjugated with reporter molecules such as fluorophores or enzymes that, in the presence of an Ab-Ag complex, generate a measurable response. Method development and validation is essential to provide a good and reliable assay performance in terms of sensitivity and specificity. As part of this, the characterization of the conjugated mAb has an important role, as for example the amount and location of conjugation can have an impact on structure and function of the mAb and consequently its binding affinity to the antigen of interest. To the best of our knowledge, the steric effects of conjugation on antibody binding and any changes in the antibody higher order structure (HOS) due to conjugation have yet to be investigated. Mass spectrometry is a powerful tool for characterization of mAb conjugates as it can provide both detailed information on the level of conjugation and any mAb structural changes induced by the conjugation (Huang and Chen, 2016; Leurs et al., 2017; Zhu et al., 2020). Particularly, top-down high-resolution intact protein analysis by liquid chromatography - mass spectrometry (LC-MS) can provide information on the amount and distribution of conjugation between heavy chain (HC) and light chain (LC) subunits (Wakankar et al., 2011; Zhu et al., 2020). Hydrogen-deuterium exchange mass spectrometry (HDX-MS) is a powerful technique for the structural characterization of large proteins such as mAbs in solution and for definition of any locally induced structural changes (such as those caused by conjugation) (Konermann et al., 2014; Zhang et al., 2014; Groves et al., 2020). HDX-MS has shown great potential in characterizing protein-protein interactions, providing useful information on the antigen binding site of mAbs (paratope mapping) and the binding sites on the antigen (epitope mapping) (Puchades et al., 2019; Sun et al., 2021; Zhu et al., 2021). During HDX-MS experiments, structural changes or protein-protein interactions result in variations in the exposure of the amide protein backbone towards surrounding solvent when incubated in deuterated water, affecting the ability of the amide protons to exchange with deuterions in the solvent. In a typical bottom-up HDX-MS workflow, changes in HDX rates of proteins or protein complexes are monitored at different incubation times. After incubation, the reaction is quenched at low pH and the proteins of interest are proteolytically digested using acid tolerant proteases, most typically pepsin. In order to obtain valuable insights into structural differences at the residue level, in particular to define protein-protein interaction sites, a high level of protein coverage and sequence overlapping proteolytic peptides (redundancy) is required. Due to the increased complexity of peptide mixtures when analyzing mAbs (~ 148 kDa) and Ab-Ag complexes (>148 kDa), peptide identification and data analysis can become more challenging due to co-eluting peptides and interferences. To overcome this, ion mobility spectrometry (IMS) can be used as an orthogonal dimension of peptide separation to the reverse phase separation generally used for HDX-MS workflows, by also separating peptides according to their size and charge as gas phase ions. Additionally, it has been shown that peptide identification of more complex biological samples can be significantly increased when the data independent acquisition (DIA) approach, MS^E, is combined with IMS ($HDMS^E$) and furthermore, when optimized precursor collision energies are applied ($UDMS^E$) (Cryar et al., 2017).

In this study, intact protein analysis by LC-MS and HDX-IM-MS with the $UDMS^E$ approach were applied to characterize conjugated antibodies. A panel of commercially available mAbs (Humira (Adalimumab), Opdivo (Nivolumab), Xolair (Omalizumab) and Herceptin (Trastuzumab)) were selected to undergo conjugation with biotin and fluorescein at lysine (Lys or K) or cysteine (Cys or C) residues using different linker reagents and chemistries. The selection of the most appropriate combination "conjugation:antibody:antigen" for MS analysis was performed by immunoassay. Four conjugates were selected: fluorescein-isothiocyanate (FITC) conjugated Adalimumab at Lys residues (Adalimumab-Lys), biotinylated Nivolumab *via* an N-hydroxy succinimide (NHS) activated ester reacting at Lys residues (Nivolumab-Lys), fluorescein labelled Omalizumab using fluorescein-5-malimide at Cys residues (Omalizumab-Cys) and biotinylated Trastuzumab at Cys residues using a dibromomaleimide (DBM) linker (Trastuzumab-Cys). These conjugates will be referred in this paper as Adalimumab-Lys, Nivolumab-Lys, Omalizumab-Cys and Trastuzumab-Cys respectively indicating the type of mAb and the conjugation at Cys or Lys residues. For the structural characterization of the changes induced upon conjugation of the Omalizumab antibody and Trastuzumab antibody, native and conjugated forms were directly compared by HDX-MS. For the Adalimumab-Lys and Nivolumab-Lys, a more complex experimental design was applied to simultaneously define structural differences between native and conjugated mAbs at the antigen binding site (paratope), which consists of a set of three complementarity-determining regions (CDR) in both the heavy (HC) and light chain (LC), respectively defined as CDR-H1, -H2, -H3, CDR-L1, -L2, -L3. For this purpose, the native mAbs were analyzed and compared to the native and conjugated mAb in complex with their respective antigens: tumor-necrosis factor α (TNFα) for Adalimumab and the programmed cell death protein 1 (PD-1) for Nivolumab.

MATERIALS AND METHODS

Materials

Chemicals such as urea, dithiothreitol (DTT), HABA/Avidin reagent and deuterium oxide were purchased from Sigma-Aldrich (Gillingham, United Kingdom). Potassium phosphate (monobasic, dibasic), formic acid, tris(2-carboxy-ethyl) phosphine (TCEP), biotin-XX SE, biotin-PEG_2-malimide and FITC were purchased from Fisher Scientific (Loughborough, United Kingdom). Fluorescein-5-maleimide was purchased from TCI (Tokyo, Japan). Trastuzumab, Adalimumab, Nivolumab and Omalizumab were purchased from Medizone (Oberhaching, Germany). All native and conjugated mAbs were provided as solutions in 100 mM potassium phosphate buffer pH 7.5 by Fleet Bioprocessing: 34 μM of Omalizumab, 34 μM Adalimumab, 34 μM Nivolumab, 16 μM of Trastuzumab, 20 μM Adalimumab-Lys, 20 μM Nivolumab-Lys, 20 μM Omalizumab-Cys and 15 μM Trastuzumab-Cys. The recombinant human proteins TNFα (Fisher Scientific, Loughborough, United Kingdom) and PD-1 (Sino Biological, Frankfurt, Germany) were solubilized at 1 g/L (57.5 μM) in water. A tetrapeptide (PPPI) was synthesized and purchased from Thermo Fisher Scientific (Loughborough, United Kingdom). The peptide standard glu-1-fibrinopeptide B was purchased from Sigma-Aldrich (Gillingham, United Kingdom). Optigrade HPLC Special Grade acetonitrile and ultra-pure water (18 MΩ cm^{-1}) were used. 96 well polystyrene microtitre plates were purchased from Greiner Bio-One (Stonehouse, United Kingdom). Sure Blue Reserve TMB substrate solution was purchased from Insight Biotechnology (Wembley, United Kingdom). Gyrolab XP, Bioaffy CD1000 and Rexxip buffers were purchased from Gyros Protein Technologies AB (Uppsala, Sweden). Anti-Fc, anti-nivolumab, anti-trastuzumab, anti-omalizumab and anti-adalimumab were purchased from Bio Rad (Watford, United Kingdom).

Conjugation of Biotin and Fluorescein Labels

The preparation of mAb conjugates was carried out using well-established literature methods and is described in supporting information S1-1. Trastuzumab-Cys was conjugated by mild TCEP reduction and reaction with dibromomaleimide-biotin; the aim was to conjugate a single biotin across one reduced inter-chain disulfide residue. Omalizumab-Cys was conjugated by forcing conditions using TCEP reduction and reaction with fluorescein-maleimide aiming for conjugation to all reduced inter-chain disulfide residues. Adalimumab-Lys and Nivolumab-Lys were conjugated with FITC and biotin-XX-NHS respectively, both aiming for high incorporations of label.

Intact Protein Analysis by LC-MS

For the intact protein analysis of native and conjugated mAbs, the mAb stock solutions were diluted to a 6 μM mAb concentration in 100 mM Tris (pH 7.4). Deglycosylation of the samples was performed by adding 2 μL peptide:N-glycosidase (PNGase F, 10 ku/mL, Promega, Southampton, United Kingdom) to 18 μL of 6 μM mAb, followed by incubation at 37°C for 24 h. The completion of the deglycosylation of native mAbs was confirmed by LC-MS and deconvoluted masses of glycosylated and deglycosylated mAbs are provided in supporting information S1-2. For the middle-down LC-MS analysis of native and conjugated mAbs, 10 μL DTT (50 mM) was added to 10 μL of the deglycosylated mAb sample and incubated at room temperature for 30 min to separate the HC and LC. For the LC-MS analysis, the deglycosylated and deglycosylated plus reduced mAb samples were diluted to a mAb concentration of 3 μM and 5% acetonitrile.

10.5 pmol of sample was injected onto a MAbPac Reversed Phase HPLC Column (2.1 × 100 mm, 4 μm, Thermo Fisher Scientific) in a Vanquish UHPLC system (Thermo Fischer Scientific, Bremen, Germany). Chromatographic separation was achieved using a linear gradient starting from 85% A/15% B to 70% A/30% B over 1 min to 60% A/40% B over 13 min at a flow rate of 250 μL/min and 65°C column temperature. Mobile phases were aqueous, 0.5% formic acid (A), and acetonitrile, 0.5% formic acid (B).

MS experiments were performed using a Q-Exactive Plus Orbitrap instrument with a HESI-II probe source (Thermo Fisher Scientific, Bremen, Germany) in positive nanoelectrospray ionization (nESI) mode using a 320°C source temperature, 3.5 kV capillary voltage, 100 S-lens RF, 25 a. u. sheath gas, 5 a.u. aux gas, 100 eV in-source CID, 200 ms maximum injection time, $3E^6$ AGC target value and 10 microscans. Data were acquired in 35 K resolution mode over a range of 1,000–5,000 m/z (high mass range (HMR) mode). Protein deconvolution was performed using BioPharma finder v 2.0 software (Thermo Fisher Scientific, Waltham, MA) using the ReSpect algorithm. Deconvolution was performed in the 10–180 kDa range, considering 4–60 charge states, a range of 4–10 minimum charge states and a target mass of 147 kDa.

Sample Preparation for Hydrogen Deuterium Exchange Experiments

Antibodies and proteins were stored separately at 4°C until analysis. All native and conjugated antibodies were diluted to a final protein concentration of 10 μM with 50 mM potassium phosphate buffer, pH 7.4. For the direct comparison between native and conjugated mAbs, two sets of samples were prepared: Omalizumab *vs.* Omalizumab-Cys and Trastuzumab *vs.* Trastuzumab-Cys. The more complex HDX-MS experiment for the structural characterization of Adalimumab-Lys and Nivolumab-Lys included four samples, the native mAb (Adalimumab or Nivolumab), the free antigen (TNFα or PD-1), the native mAb in complex with antigen (Adalimumab:TNFα, ratio 1:1 and Nivolumab:PD-1, ratio 1:2) and the conjugated mAb in complex with antigen (Adalimumab-Lys:TNFα, ratio 1:1 and Nivolumab-Lys:PD-1, ratio 1:2). The peptide PPPI as internal standard was added to each sample at 10 μM.

HDX–Ion Mobility Mass Spectrometry

Sample handling and mixing steps were performed using a first-generation LEAP PAL system set (LEAP Technologies, Morrisville, NC). 15 µL sample was diluted 10-fold either in 50 mM potassium phosphate buffer, pH 7.4 for the generation of peptide maps or in 50 mM potassium phosphate buffer (pH 7.0) prepared in D_2O for exchange experiments. The HDX time course for each HDX-MS data set is summarized in supporting information S2. Each exchange time point was run in triplicate and quenched by a 2-fold dilution with 50 µL of 1 M TCEP, 8 M Urea in 100 mM potassium phosphate buffer (pH 2.5) at 4°C for 10 min. 95 µL of quenched sample was injected onto a refrigerated nano-ACQUITY UPLC system with HDX technology (Waters, Milford, MA) for on-line pepsin digestion and chromatographic separation. Protein digestion was performed on an Enzymate BEH pepsin column (300 Å, 5 µm, 2.1 × 30 mm, Waters, Milford, MA) at a flow rate of 70 µL/min (0.5% v/v formic acid) and a pressure of 4,800 psi. The digestion pressure was held by using a PEEK restrictor placed after the trap column. Digestion temperature was maintained at 15°C for Adalimumab, Trastuzumab, Nivolumab and at 20°C for Omalizumab. After digestion, the proteolytic peptides were trapped and desalted for 3.8 min using an ACE C18 guard cartridge (5 µm, 2.1 mm) and chromatographically separated on an ACE Excel 2 Super C18 column (2 µm, 2.1 × 100 mm, Hichrom, Reading, United Kingdom) at a flow rate of 100 µL/min using a 7 min linear gradient from 8% B to 35% B. Mobile phases were aqueous, 0.1% v/v formic acid (A) and acetonitrile, 0.1% v/v formic acid (B).

ESI-IM-MS experiments were performed on a Synapt G2Si Q-TOF-MS instrument (Waters, Milford, MA) in positive nanoelectrospray ionization mode, sensitivity mode, 100°C source temperature, 3 kV capillary voltage, 80 V cone voltage, 80 V source offset and 250°C desolvation temperature.

For the peptide map generation, the instrument was operated in the $UDMS^E$ mode, which is MS^E with applied ion mobility and optimized collision energies based on measured ion arrival times. Optimized collision energies were from Distler and co-workers (Distler et al., 2014). Deuterium exchange experiments were acquired in IM-MS mode. Data acquisition in both modes $UDMS^E$ and IM-MS was carried out over a range of 50–2000 m/z, a scan time of 0.2 s using the same ion mobility settings as follows: 650 m/s wave velocity, 40 V wave amplitude, 190 m/s transfer velocity, 4 V transfer wave amplitude, 450 µsec mobility trapping release time and a wave velocity ramp of 800–500 m/sec. Data was lock mass corrected against *m/z* 785.8426 of glu-1-fibrinopeptide B (100 fmol solution in 50% methanol, 0.1% formic acid), applied post acquisition.

To generate peptide lists, $UDMS^E$ data was analyzed with the ProteinLynx Global Server (PLGS) software v3.0.3 (Waters, Milford, MA) against protein sequences of interest. PLGS outputs were imported to DynamX v3.0 (Waters, Milford, MA) to generate peptide maps and analyze HDX-MS data. The 3σ approach was applied as statistical test for significance. Full details of PLGS and DynamX processing conditions and protein amino acid sequences used for database search are listed in the supporting information S1-3 and S1-4. To allow access to the HDX data of this study, the HDX data summary table and the HDX data table are included in the supporting information S2 and S3 respectively as per consensus guidelines (Masson et al., 2019).

Determination of Labelling of mAb by Colorimetry

Fluorescein incorporations were determined by UV-vis spectrophotometry using an 495 nm extinction coefficient of 150.5 $(mg/ml)^{-1}$ cm^{-1} and 280:495 Rz of 0.34. Biotin incorporations were determined by HABA/Avidin colorimetric assay following the instructions provided by the reagent supplier, using a 500 nm extinction coefficient of 34,000 M^{-1} cm^{-1}.

Anti-Fc and Antigen Binding Affinity Assay

A description of the different immunoassay formats is provided in the supporting information S1-5. A total of seven different assay formats (Fc binding, complex binding, competitive, immunometric, bridging, Fc capture and streptavidin capture) were used to characterize the conjugate performance relative to each other and the unconjugated mAbs.

RESULTS AND DISCUSSION

Characterization of Conjugated mAbs by LC-MS

Intact protein analysis of mAbs was carried out to elucidate the extent of conjugation, its location (for example heavy chain (HC) *vs* light chain (LC)) and the sample heterogeneity. The results are summarized in **Table 1**. The deconvoluted mass spectra and the conjugated mAb amount are shown in supporting information S1-6. In this study both mAbs, Omalizumab and Trastuzumab, belong to the immunoglobulin G subtype 1 class (IgG1), typically containing 12 intra-chain and 4 inter-chain disulfide bridges. In particular, inter-chain disulfide bridges are the target for conjugation as they are more prone to reduction and more accessible to conjugation (Adumeau et al., 2016). An advantage of conjugating at the inter-chain disulfide bridges is that it expected to have lower impact on antigen binding due to its distance from the mAb binding site.

For the Omalizumab antibody, conjugation was achieved by using a commercially available linker fluorescein-5-maleimide. By LC-MS intact protein analysis, no residual intact antibody was detected, and the free HC and LC were observed to contain three and one conjugate molecules respectively (**Table 1**, supporting information S1-6: **Figure 1**). This indicated that all eight sulfhydryl groups of the four inter-chain disulfide bonds were conjugated as anticipated and that the structure of Omalizumab-Cys was mainly stabilized through non-covalent interactions between the mAb chains.

The Trastuzumab was initially conjugated with biotin by using a bifunctional dibromomaleimide (DBM) derived biotin reagent, which was made according to the method of Baker and coworker (Schumacher et al., 2014), and similar reaction conditions as used for Omalizumab-Cys. In this approach, the inter-chain disulfide

TABLE 1 | Amount of mAb conjugation by intact LC-MS protein analysis and colorimetry.

mAb Conjugates	Conjugation Amount per Intact mAb by LC-MS		Conjugation Amount per Intact mAb by Colorimetry
	total	most abundant	total
Omalizumab-Cys	n.a	n.a	5.9[a]
Trastuzumab-Cys	0–3	0	0.9[b]
Adalimumab-Lys	2–6	2–4	5.2[a]
Nivolumab-Lys	28–42	35–36	16.1[b]

UV-vis spectroscopy[a] and by HABA/Avidin colorimetric assay[b].

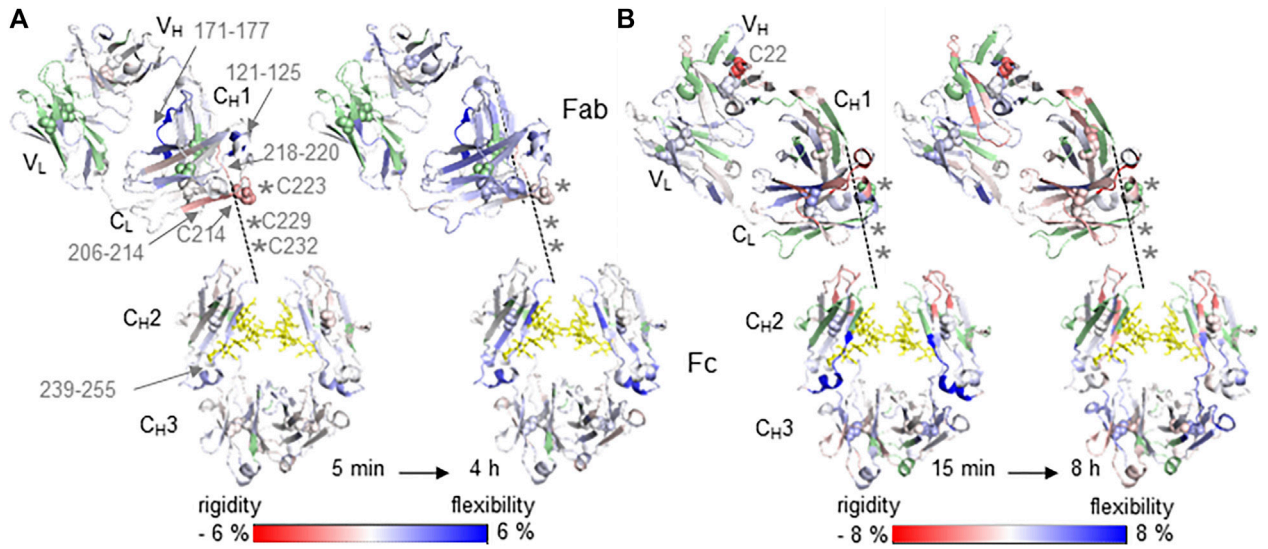

FIGURE 1 | Relative differences in HDX-MS between native (reference state) and cysteine conjugated mAb samples Trastuzumab with DBM-biotin **(A)** and Omalizumab with fluorecein-5-maleimide **(B)** are illustrated on the crystal structure of the generic IgG1 Fc domain (PDB: 5vgp) and the specific Fab domains PDB: 6 mh2 **(A)** and PDB: 2xa8 **(B)**. Increased (blue) and decreased (red) HDX-MS rates as relative changes from the native mAbs are indicated by the color bar and are shown between the lowest and highest time points, from 5 min to 4 h **(A)** and 15 min to 8 h **(B)**. Light chain (LC) domains located in Fab are V_L and C_L. Heavy chain (HC) domains are V_H and C_H1 of Fab and C_H2/C_H3 of Fc. The hinge region with inter-chain disulfide bonds is unresolved in crystal 3D structures and is sketched by the dashed line connecting the C_H1 and C_H2 of HC. Missing cysteine residues of the HC in the hinge region are indicated as asterisks. Missing sequence information for deuterium uptake kinetics are highlighted in green. Glycans are indicated as yellow sticks and cysteine residues forming disulfide bonds as spheres.

bonds are "maintained" by cross-linking cysteine bridges via double substitution of the DBM moiety (Badescu et al., 2014). Intact protein analysis of the reduced Trastuzumab conjugate by LC-MS showed that the main mAb populations are the intact antibody and the HC-HC-LC. Only traces of free LC and HC were observed (supporting information S1-6: **Figure 2A**) indicating that the antibody chains of Trastuzumab-Cys are irreversible cross-linked through the DBM linker. 46% of the intact and HC-HC-LC Trastuzumab-Cys population was unconjugated due to low incorporation efficiency of the biotin-DBM reagent. However, 54% of the intact and HC-HC-LC population was conjugated containing 1-3 biotin molecules/antibody with a relative abundancy of 36.7%, 15.1 and 2.3% respectively (supporting information S1-6: **Figure 2** and **Tables 1**, **2**). Because mAb chains as LC and HC are mainly cross-linked using the DBM linker, the conjugation distribution between HC and LC is not clearly determinable. However, the main presence of conjugated intact and HC-HC-LC populations proves that inter-chain disulfide bonds are the target of the conjugation approach.

As previously described the Adalimumab and Nivolumab antibodies were conjugated at the Lys residues using commercially available FITC (fluorescein-isothiocyanate) and biotin-NHS reagents. Because of the high abundance of Lys residues (86 residues in Adalimumab and 78 residues in Nivolumab) and the statistical nature of Lys-based conjugations, the results from LC-MS (**Table 1**) showed the presence of a highly heterogeneous mixture of conjugated antibody with varying degrees of conjugation occurring at different residues, in agreement with previous studies (Wang et al., 2005; Kim et al., 2014; Goldmacher et al., 2015; Sang et al., 2017). Luo and colleagues previously characterized a Lys antibody drug conjugate observing a drug to antibody ratio ranging from 0–8. In this study, 76 Lys residues were conjugated at different degrees, representing 83% of all putative Lys residues (Luo et al., 2016). For the Nivolumab-Lys, a mixture of species

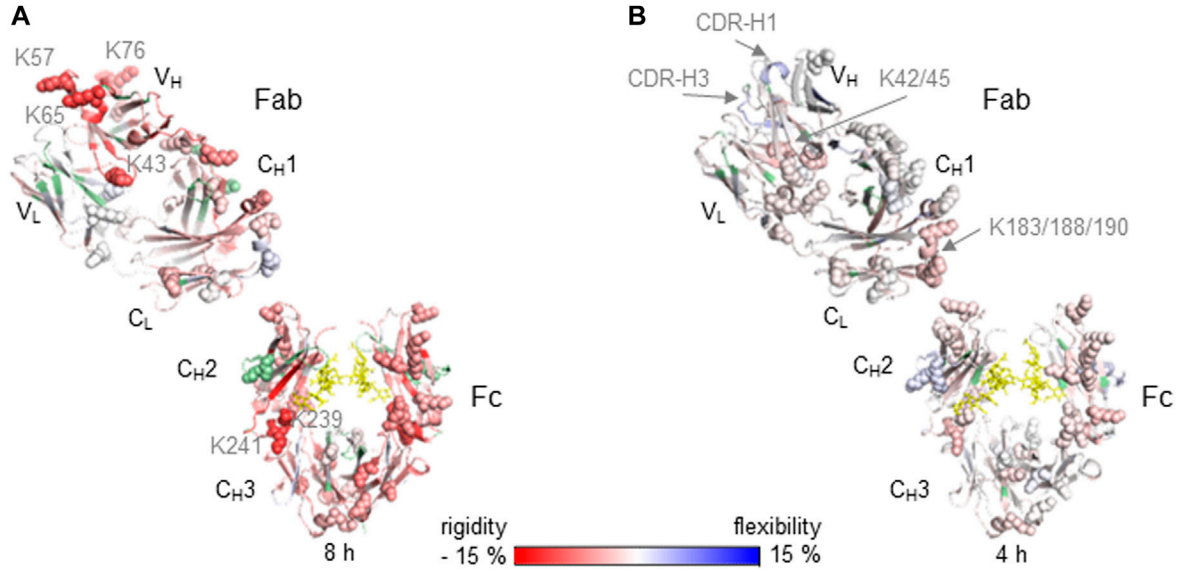

FIGURE 2 | Relative differences in HDX-MS between native (reference state) and lysine conjugated mAb samples are illustrated on the crystal structure for Nivolumab of the generic IgG4 Fc domain (PDB: 4c54) and the Nivolumab specific Fab domain PDB: 5ggq **(A)** and for Adalimumab on the IgG1 Fc domain (PDB: 5vgp) and Adalimumab specific Fab PDB: 3wd5 **(B)**. Increased (blue) and decreased (red) HDX-MS rates as relative changes from the native mAbs are indicated by the color bar and are shown for the highest incubation time 8 h **(A)** and 4 h **(B)**. Light chain (LC) domains located in Fab are V_L and C_L. Heavy chain (HC) domains are V_H and C_H1 of Fab and C_H2/C_H3 of Fc. Missing sequence information for deuterium uptake kinetics are highlighted in green. Glycans are indicated as yellow sticks and lysine residues as spheres.

TABLE 2 | Relative performance of conjugated mAbs against the native mAbs as measured by different immunoassay formats.

mAb Conjugate	Fc Recognition (%)	Antigen Recognition (%)
Adalimumab-Lys	98.3 (80.4–120.1)[a]	91.0 (74.4–111.2)[b]
Nivolumab-Lys	61.1 (50.0–74.7)[a]	132.5 (108.4–161.9)[c]
Omalizumab-Cys	91.8 (75.1–112.2)[a]	65.7 (53.7–80.3)[b]
Trastuzumab-Cys	67.0 (54.8–81.9)[d]	100.0 (81.8–122.2)[e]

Rel. binding to native mAb: Fc binding[a], complex binding[b], competitive[c], Rel. binding to highest signal of a conjugated mAb panel: Fc capture[d], streptavidin capture[e].

with 28–42 conjugated residues was observed, which implies that potentially all Lys residues might be conjugated to different degrees. The most abundant conjugated forms of Nivolumab-Lys showed 35–36 biotin molecules. Intact LC-MS analysis of the Adalimumab-Lys conjugate showed the presence of a mixture of conjugates containing 2-6 FITC molecules per antibody with the most abundant form containing 2-4 incorporated FITC molecules. This result was in good agreement with the fluorescein incorporation as determined by UV-vis colorimetry. In contrast, the biotin incorporation for Nivolumab determined by HABA/Avidin colorimetric assay was grossly under-estimated, possibly due to a limitation of the assay due to steric effects, which is likely to be a universal limitation of this colorimetric assay. Unexpectedly, it was shown after reduction and LC-MS analysis of Adalimumab-Lys the only indication of fluorescein conjugation was present on the LC.

HDX-MS Characterization of Cysteine Conjugated Antibodies

The influence of conjugation at Cys residues on the structure of mAbs was determined by HDX-MS experiments as a direct comparison of differential HDX rates between native and conjugated mAbs of both Trastuzumab and Omalizumab (**Figure 1**). The coverage of the peptide maps at the hinge regions of both antibodies was poor because of the challenges in proteolytic digestion as previously reported (Leurs et al., 2017), however decreased deuterium uptake kinetics were observed for both conjugates Trastuzumab-Cys and Omalizumab-Cys in regions which are in close proximity to the hinge region, when compared with the native forms of the antibodies, Trastuzumab and Omalizumab respectively (**Figures 1A,B**). This is likely due to the decreased solvent accessibility induced by the conjugation. In contrast, deuterium uptake kinetics are increased in all those mAb regions, which are more distant from conjugation sites, indicating a long-range loss of structure and increase of flexibility induced by the conjugation process including both the reduction and conjugation steps. Particularly, the Trastuzumab-Cys (**Figure 1A**) showed significantly decreased deuterium uptake kinetics in the C_L domain (sequence 206–214) containing Cys214, which interacts with Cys223 of the C_H1 domain showing decreased deuterium uptake kinetics for adjacent residues 218–220. Increased deuterium uptake kinetics were observed in the regions C_L (121–125), C_H1 (171–177) and C_H2 (239–255) located distant from the hinge region, consistent with the extension of the typical disulfide bond

distance via the incorporated succinimide ring during conjugation, which results in opening up the surrounding protein structure.

The effect of decreased deuterium uptake kinetics in close proximity to conjugation sites was more significant for the Omalizumab-Cys conjugate (**Figure 1B**) as all four inter-chain disulfide bonds were involved in conjugation, meaning 8 biotin molecules were incorporated in the mAb molecule revealed by LC-MS analysis (**Table 1**). Furthermore, for the Cys22 in the V_H region, decreased deuterium uptake kinetics were observed indicating that this Cys residue maybe more prone to conjugation due to higher steric accessibility. The disulfide bond comprising Cys22 in native Omalizumab might be in the free thiol form as has been shown previously (Harris 2005).

Overall, the conjugation of Omalizumab *via* the classical maleimide linker fluorescein-5-maleimide caused reduction of the disulfide bonds and an increased molecular distance between cysteine residues with a consequent loss of structure and increased flexibility.

HDX-MS Characterization of Lysine Conjugated Antibodies

The impact of conjugated Lys residues on the mAb structure was determined by HDX-MS as a comparison of differential deuterium uptake kinetics between the native and conjugated Nivolumab and Adalimumab mAbs in the presence and absence of the antigens PD-1 (Nivolumab) and TNFα (Adalimumab) (**Figure 2**). The Nivolumab-Lys conjugate showed high conjugation at Lys residues with a total label distribution of 28–42 biotin molecules per mAb by intact protein analysis (**Table 1**). Because of the expected high heterogeneity of conjugated Nivolumab-Lys, it is possible to assume that most of the Lys residues are conjugated to different extents depending on the location of Lys residues within the antibody and accessibility to the conjugation reagents. HDX-MS experiments show that the deuterium uptake kinetics are significantly decreased in the whole Nivolumab-Lys (**Figure 2A**). It is possible to observe that the Lys residues in the V_H region as K43, K57, K65 and K76 show significant decreased deuterium uptake kinetics. Those are in proximity to the CDR regions of HC and the results suggest that conjugation may have an impact on the binding of the antigen for the Optivo-Lys. It has been in fact already reported, that the CDR regions of the HC are predominantly involved in the antigen binding (Lee et al., 2016; Zhang et al., 2020).

The higher order structure of Adalimumab-Lys conjugate with only two FITC molecules on the LC was much less impacted by the conjugation, most likely due to the lower level of conjugation as was observed from the intact mass spectrometry analysis (**Figure 2B**). In particular, the LC in the F_{ab} region (V_L, C_L) shows slightly decreased deuterium uptake kinetics in peptides which contain Lys residues as K42/45 in the N-terminus and K183/188/190 in the C-terminus. Because of the proximity of these Lys residues to each other, it was difficult to determine the site of conjugation without any further experimentation, which was outside the scope of this work. No significant structural differences were observed for the HC of the F_{ab} region (V_H, C_H1) when comparing the native and conjugated antibody. However, for CDR-H1 and -H3 increased deuterium uptake kinetics were observed suggesting a loss of structure that may also have an impact on the binding properties of the antibody. The structural differences in the C_H2 of the Fc domain are similar, albeit on a lesser scale, to the Nivolumab-Lys conjugate indicating that the conjugation has an indirect impact on the mAb structure. According to intact protein MS experiments, the Fc domain was not conjugated.

For the Lys conjugates a correlation between the amount of conjugation and the higher order structural differences observed was clearly demonstrated by HDX-MS experiments (**Figure 2**). Particularly, an increase in conjugation at Lys residues resulted in a decreased deuterium uptake kinetics across the whole protein structure.

Characterization of Conjugated mAb Candidates by Different Immunoassay Formats

A panel of mAb conjugates generated were analyzed by different immunoassay formats in order to check differences in the binding properties of the conjugated mAb *vs* the native counterpart. Particularly, seven different assays (Fc binding, complex binding, competitive, immunometric, bridging, Fc capture and streptavidin capture) were initially developed for each pair (conjugated and unconjugated) to discern differences in the binding pattern and provide preliminary information about which part of the mAb, Fab or Fc, has been modified. The different assay formats are explained and summarized in the supporting information S1-4. As previously mentioned, the commercially available antibodies Adalimumab, Nivolumab, Omalizumab and Trastuzumab were conjugated with biotin or FITC using a variety of linkers, chemistries and ratios. The performance of these mAb conjugates regarding modification of the Fc or Fab region was evaluated through comparison of specific assay responses between conjugated and native antibody. The results of the relative Fc binding and antigen (complex) binding of the four selected conjugates Adalimumab-Lys, Nivolumab-Lys, Omalizumab-Cys and Trastuzumab-Cys are listed in **Table 2**.

The range of recognition values is based on a typical immunoassay CV of ±10%. As recognition values are calculated from two assay results (conjugated, unconjugated), each with CV of 10%, the potential error around the recognition value was calculated as follows: recognition value x 0.818 (0.9/1.1) to recognition value x 1.222 (1.1/0.9).

For the determination of relative Fc recognition of Adalimumab-Lys, Nivolumab-Lys and Omalizumab-Cys, an anti-Fc antibody was used to estimate the differences in the Fc binding between native and conjugated mAb. Similarly, a specific anti-complex mAb for Adalimumab-Lys and Omalizumab-Cys, which detects only the Ab-Ag complex and not Ab or Ag alone, was applied to analyze the relative antigen recognition between native and conjugated mAb. In contrast, the antigen recognition of Nivolumab-Lys was determined by using a competitive assay,

where the conjugate binds the immobilized antigen and displacement occurs by varying free antigen concentrations. With increasing concentrations of free antigen, the conjugate is displaced from the immobilized antigen resulting in a signal decrease. Nivolumab conjugates were then ranked by calculating the free antigen concentration required to produce 50% reduction in the signal. In the case of the Trastuzumab-Cys conjugate, the biotin label is used in the streptavidin capture assay to validate the Fc binding and antigen affinity and thus the signals relate to the Trastuzumab conjugate with the least modification of the variable region (100%) out of a mAb conjugate panel.

The relative Fc binding for Adalimumab-Lys is largely unchanged compared to the native mAb showing that the conjugation does not have a significant impact on the Fc domain, whereas the relative antigen recognition is slightly reduced to 91% indicating conjugation might be more present in the Fab region of the mAb. The results for Nivolumab-Lys show a great contrast in the sense that the Fc binding is reduced to 61.1%, whereas the sensitivity in a competitive assay format is actually increased to 132.5% compared to the native mAb. As the Fc binding is significantly reduced due to the conjugation, it is assumed that the conjugation has predominantly modified the Fc region. However, results from the competitive assay indicate some modification of the binding site. Whilst this would typically be expected to reduce the utility of the conjugate, because of the competitive format used, slight changes to antigen recognition appear to have increased the ease with which displacement by free antigen occurs, increasing the sensitivity of the end assay and indicating a change in the Ab-Ag interaction. Trastuzumab-Cys shows the best antigen affinity within a conjugated mAb panel, whereas the Fc binding assay result is significantly reduced to 67% implying that the conjugation has modified mainly the Fc region. Omalizumab-Cys shows a significant reduction in antigen recognition. Whilst there is a detectable reduction in Fc recognition, this is relatively small compared to the change in antigen recognition. Taken together, these results suggest that both Fab and Fc regions of Omalizumab-Cys have been modified, with the Fab modification being most significant in potential assay performance terms.

DISCUSSION

Monoclonal antibodies are used as analytical tools in immunoassays to immobilize or detect antigens or molecules of interest. In order to do this, conjugation is carried out through a chemical reaction. However, the effects of conjugation regarding amount and location on the structure and functionality of the mAb which ultimately may affect immunoassay performance, are often undetermined. In this study, the conjugation reaction efficiency was studied by intact MS analysis and the impact of conjugation at either Lys or Cys residues on the mAb higher order structure and its binding properties was assessed by HDX-MS and immunoassay respectively. The results of the mass spectrometric characterization of different mAb conjugates correlate very well with the mAb function and binding affinity.

The cysteine conjugation occurs in a specific manner as the inter-chain disulfide bonds are typically targeted. For the Trastuzumab conjugate, the Cys residues of a disulfide bond are dithiosuccinimide-bridged maintaining the disulfide bonding, but with an extension of the typical distance. When using a classical maleimide linker such as fluorescein-5-maleimide for the cysteine conjugation of Omalizumab, the rebuilding of disulfide bridges is not possible. In both cases, the overall mAb structure for Trastuzumab and Omalizumab conjugates show predominantly increased deuterium uptake kinetics due to extended bond distances (Trastuzumab) or reduced disulfide bonds (Omalizumab) resulting in more flexibility in structure. In contrast, protein regions in close proximity to the hinge region and inter-chain disulfide bonds show decreased deuterium uptake kinetics due to the conjugation with bulky groups, which reduces solvent accessibility. The intact protein analysis results correlate well with the HDX-MS results where an increased amount of conjugation per mAb was also associated with a relative decrease in deuterium uptake kinetics. In this regard, the most accessible inter-chain disulfide of Trastuzumab-Cys modified using the chemistry employed is Cys214 of the C_L domain and Cys223 of the C_H1 domain implying no significant structural changes at the antigen binding site. This also correlates well with the immunoassay results that the selected Trastuzumab-Cys mAb shows the best antigen affinity within a conjugated mAb panel. For the Omalizumab-Cys candidate, results of intact protein analysis and HDX-MS reveal that all eight sulfhydryl groups of inter-chain disulfide bonds are conjugated and thus the mAb structure relies only on non-covalent interactions between heavy and light chain causing major structural changes with loss of recognition properties shown by immunoassay experiment results for both the Fab and Fc regions.

As expected, compared to the cysteine conjugation, the conjugation at lysine residues generated more heterogenous mixtures of different conjugated mAb variants (Nivolumab and Adalimumab). Conjugation with biotin and FITC was chemically performed without reduction and therefore the disulfide bridges were maintained. The HDX-MS data showed decreased deuterium uptake kinetics of the conjugated mAbs *vs* the native form, with the relative level of conjugation correlating well with the relative decrease of deuterium uptake kinetics. Particularly, the Nivolumab-Lys is highly conjugated (28–42 biotin molecules per mAb) and the significantly decreased deuterium uptake indicates a potential change of higher order structure that could have a negatively impact on the antigen recognition. This was also confirmed by the immunoassay experiment results. In contrast, conjugation of the Adalimumab mAb had less effects on the deuterium uptake kinetics and binding properties of the antibody as was shown by both HDX-MS and immunoassay experiments. This possibly due to the 2-6 FITC conjugation mostly occurring on the LC as was shown by intact protein MS analysis. Consistent with the immunoassay results which indicate that the conjugation is more present in the Fab region and the Fc part is not significantly impacted.

Overall, this study shows that conjugation can have an impact on the performance of the antibodies used for immunoassay engineering and that mass spectrometry experiments can aid an

improved understanding and optimization of the conjugation reaction. This will ultimately aid to better performance. Furthermore, a thorough characterization of the conjugation reaction will ensure continuity in performance over time and across different batches.

DATA AVAILABILITY STATEMENT

The datasets presented in this study can be found in online repositories. The names of the repository/repositories and accession number(s) can be found in the article/ **Supplementary Material**.

AUTHOR CONTRIBUTIONS

LL and KG performed antibody characterization by LC-MS. CB prepared antibody conjugates and performed colorimetry measurements. SS performed immunoassay analysis. MQ and AD contributed to conception and design of the study. All authors contributed to manuscript revision, read and approved the submitted version.

FUNDING

The work described in this paper was funded (in part) by the United Kingdom government Department for Business, Energy and Industrial Strategy (BEIS); and the Innovate United Kingdom Strategic Priorities Fund (Grant number 105569).

SUPPLEMENTARY MATERIAL

The Supplementary Material for this article can be found online at: https://www.frontiersin.org/articles/10.3389/fmolb.2022.866843/full#supplementary-material

REFERENCES

Adumeau, P., Sharma, S. K., Brent, C., and Zeglis, B. M. (2016). Site-Specifically Labeled Immunoconjugates for Molecular Imaging-Part 1: Cysteine Residues and Glycans. *Mol. Imaging Biol.* 18, 1–17. doi:10.1007/s11307-015-0919-4

Aydin, S. (2015). A Short History, Principles, and Types of ELISA, and Our Laboratory Experience with Peptide/protein Analyses Using ELISA. *Peptides* 72, 4–15. doi:10.1016/j.peptides.2015.04.012

Badescu, G., Bryant, P., Bird, M., Henseleit, K., Swierkosz, J., Parekh, V., et al. (2014). Bridging Disulfides for Stable and Defined Antibody Drug Conjugates. *Bioconjugate Chem.* 25, 1124–1136. doi:10.1021/bc500148x

Cox, K. L., Devanarayan, V., Kriauciunas, A., Manetta, J., Montrose, C., and Sittampalam, S. (2019). "Immunoassay Methods," in *Assay Guidance Manual [Internet]*. S. Markossian, A. Grossman, K. Brimacombe, et al. (Bethesda, MD: Eli Lilly & Company and the National Center for Advancing Translational Sciences).

Cryar, A., Groves, K., and Quaglia, M. (2017). Online Hydrogen-Deuterium Exchange Traveling Wave Ion Mobility Mass Spectrometry (HDX-IM-MS): a Systematic Evaluation. *J. Am. Soc. Mass Spectrom.* 28, 1192–1202. doi:10.1007/s13361-017-1633-z

Di Nardo, F., Chiarello, M., Cavalera, S., Baggiani, C., and Anfossi, L. (2021). Ten Years of Lateral Flow Immunoassay Technique Applications: Trends, Challenges and Future Perspectives. *Sensors* 21 (15), 5185. doi:10.3390/s21155185

Distler, U., Kuharev, J., Navarro, P., Levin, Y., Schild, H., and Tenzer, S. (2014). Drift Time-specific Collision Energies Enable Deep-Coverage Data-independent Acquisition Proteomics. *Nat. Methods* 11, 167–170. doi:10.1038/nmeth.2767

Goldmacher, V. S., Amphlett, G., Wang, L., and Lazar, A. C. (2015). Statistics of the Distribution of the Abundance of Molecules with Various Drug Loads in Maytansinoid Antibody-Drug Conjugates. *Mol. Pharm.* 12, 1738–1744. doi:10.1021/mp5007536

Groves, K., Cryar, A., Cowen, S., Ashcroft, A. E., and Quaglia, M. (2020). Mass Spectrometry Characterization of Higher Order Structural Changes Associated with the Fc-Glycan Structure of the NISTmAb Reference Material, RM 8761. *J. Am. Soc. Mass Spectrom.* 31, 553–564. doi:10.1021/jasms.9b00022

Harris, J. P. (2005). Heterogeneity of Recombinant Antibodies: Linking Structure to Function. *Dev. Biol.* 122, 117–127.

Huang, R. Y.-C., and Chen, G. (2016). Characterization of Antibody-Drug Conjugates by Mass Spectrometry: Advances and Future Trends. *Drug Discov. Today* 21, 850–855. doi:10.1016/j.drudis.2016.04.004

Kim, M. T., Chen, Y., Marhoul, J., and Jacobson, F. (2014). Statistical Modeling of the Drug Load Distribution on Trastuzumab Emtansine (Kadcyla), a Lysine-Linked Antibody Drug Conjugate. *Bioconjugate Chem.* 25, 1223–1232. doi:10.1021/bc5000109

Konermann, L., Vahidi, S., and Sowole, M. A. (2014). Mass Spectrometry Methods for Studying Structure and Dynamics of Biological Macromolecules. *Anal. Chem.* 86, 213–232. doi:10.1021/ac4039306

Lee, J. Y., Lee, H. T., Shin, W., Chae, J., Choi, J., Kim, S. H., et al. (2016). Structural Basis of Checkpoint Blockade by Monoclonal Antibodies in Cancer Immunotherapy. *Nat. Commun.* 7, 13354. doi:10.1038/ncomms13354

Leurs, U., Beck, H., Bonnington, L., Lindner, I., Pol, E., and Rand, K. (2017). Mapping the Interactions of Selective Biochemical Probes of Antibody Conformation by Hydrogen-Deuterium Exchange Mass Spectrometry. *Chembiochem* 18, 1016–1021. doi:10.1002/cbic.201600670

Luo, Q., Chung, H. H., Borths, C., Janson, M., Wen, J., Joubert, M. K., et al. (2016). Structural Characterization of a Monoclonal Antibody-Maytansinoid Immunoconjugate. *Anal. Chem.* 88, 695–702. doi:10.1021/acs.analchem.5b03709

Masson, G. R., Burke, J. E., Ahn, N. G., Anand, G. S., Borchers, C., Brier, S., et al. (2019). Recommendations for Performing, Interpreting and Reporting Hydrogen Deuterium Exchange Mass Spectrometry (HDX-MS) Experiments. *Nat. Methods* 16, 595–602. doi:10.1038/s41592-019-0459-y

Puchades, C., Kűkrer, B., Diefenbach, O., Sneekes-Vriese, E., Juraszek, J., Koudstaal, W., et al. (2019). Epitope Mapping of Diverse Influenza Hemagglutinin Drug Candidates Using HDX-MS. *Sci. Rep.* 9, 4735. doi:10.1038/s41598-019-41179-0

Sang, H., Lu, G., Liu, Y., Hu, Q., Xing, W., Cui, D., et al. (2017). Conjugation Site Analysis of Antibody-Drug-Conjugates (ADCs) by Signature Ion Fingerprinting and Normalized Area Quantitation Approach Using Nano-Liquid Chromatography Coupled to High Resolution Mass Spectrometry. *Anal. Chim. Acta* 955, 67–78. doi:10.1016/j.aca.2016.11.073

Schumacher, F. F., Nunes, J. P. M., Maruani, A., Chudasama, V., Smith, M. E. B., Chester, K. A., et al. (2014). Next Generation Maleimides Enable the Controlled Assembly of Antibody-Drug Conjugates via Native Disulfide Bond Bridging. *Org. Biomol. Chem.* 12, 7261–7269. doi:10.1039/c4ob01550a

Sun, H., Ma, L., Wang, L., Xiao, P., Li, H., Zhou, M., et al. (2021). Research Advances in Hydrogen-Deuterium Exchange Mass Spectrometry for Protein Epitope Mapping. *Anal. Bioanal. Chem.* 413, 2345–2359. doi:10.1007/s00216-020-03091-9

Wakankar, A., Chen, Y., Gokarn, Y., and Jacobson, F. S. (2011). Analytical Methods for Physicochemical Characterization of Antibody Drug Conjugates. *MAbs* 3, 161–172. doi:10.4161/mabs.3.2.14960

Wang, L., Amphlett, G., Blättler, W. A., Lambert, J. M., and Zhang, W. (2005). Structural Characterization of the Maytansinoid-Monoclonal Antibody Immunoconjugate, huN901-DM1, by Mass Spectrometry. *Protein Sci.* 14, 2436–2446. doi:10.1110/ps.051478705

Xiao, Q., and Lin, J.-M. (2015). Advances and Applications of Chemiluminescence Immunoassay in Clinical Diagnosis and Foods Safety. *Chin. J. Anal. Chem.* 43 (6), 929–938. doi:10.1016/S1872-2040(15)60831-3

Zhang, A., Hu, P., MacGregor, P., Xue, Y., Fan, H., Suchecki, P., et al. (2014). Understanding the Conformational Impact of Chemical Modifications on Monoclonal Antibodies with Diverse Sequence Variation Using Hydrogen/deuterium Exchange Mass Spectrometry and Structural Modeling. *Anal. Chem.* 86, 3468–3475. doi:10.1021/ac404130a

Zhang, M. M., Huang, R. Y.-C., Beno, B. R., Deyanova, E. G., Li, J., Chen, G., et al. (2020). Epitope and Paratope Mapping of PD-1/Nivolumab by Mass Spectrometry-Based Hydrogen-Deuterium Exchange, Cross-Linking, and Molecular Docking. *Anal. Chem.* 92, 9086–9094. doi:10.1021/acs.analchem.0c01291

Zhu, S., Liuni, P., Chen, T., Houy, C., Wilson, D., and James, A. (2021). Epitope Screening Using Hydrogen/Deuterium Exchange Mass Spectrometry (HDX-MS): An Optimized Workflow for Accelerated Evaluation of Lead Monoclonal Antibodies. *Biotechnol. J.* 17, e2100358. doi:10.1002/biot.202100358

Zhu, X., Huo, S., Xue, C., An, B., and Qu, J. (2020). Current LC-MS-based Strategies for Characterization and Quantification of Antibody-Drug Conjugates. *J. Pharm. Analysis* 10, 209–220. doi:10.1016/j.jpha.2020.05.008

Conflict of Interest: CB, SS, and AD were employed by the Company Fleet Bioprocessing Ltd.

The remaining authors declare that the research was conducted in the absence of any commercial or financial relationships that could be construed as a potential conflict of interest.

Publisher's Note: All claims expressed in this article are solely those of the authors and do not necessarily represent those of their affiliated organizations, or those of the publisher, the editors and the reviewers. Any product that may be evaluated in this article, or claim that may be made by its manufacturer, is not guaranteed or endorsed by the publisher.

frontiers | Frontiers in Molecular Biosciences

REVIEW
published: 22 July 2022
doi: 10.3389/fmolb.2022.908285

Redesigning Enzymes for Biocatalysis: Exploiting Structural Understanding for Improved Selectivity

*Yaoyu Ding, Gustavo Perez-Ortiz, Jessica Peate and Sarah M. Barry**

Department of Chemistry, Faculty of Natural, Mathematical and Engineering Sciences, King's College London, London, United Kingdom

The discovery of new enzymes, alongside the push to make chemical processes more sustainable, has resulted in increased industrial interest in the use of biocatalytic processes to produce high-value and chiral precursor chemicals. Huge strides in protein engineering methodology and *in silico* tools have facilitated significant progress in the discovery and production of enzymes for biocatalytic processes. However, there are significant gaps in our knowledge of the relationship between enzyme structure and function. This has demonstrated the need for improved computational methods to model mechanisms and understand structure dynamics. Here, we explore efforts to rationally modify enzymes toward changing aspects of their catalyzed chemistry. We highlight examples of enzymes where links between enzyme function and structure have been made, thus enabling rational changes to the enzyme structure to give predictable chemical outcomes. We look at future directions the field could take and the technologies that will enable it.

Keywords: biocatalysis, enzymes, protein engineering, structural biology, regioselectivity, stereoselectivity, rational design

OPEN ACCESS

Edited by:
Alex Jones,
National Physical Laboratory, United Kingdom

Reviewed by:
Xiang Sheng,
Tianjin Institute of Industrial Biotechnology (CAS), China
Lujia Zhang,
East China Normal University, China

****Correspondence:***
Sarah M. Barry
sarah.barry@kcl.ac.uk

Specialty section:
This article was submitted to Structural Biology, a section of the journal Frontiers in Molecular Biosciences

Received: *30 March 2022*
Accepted: *08 June 2022*
Published: *22 July 2022*

Citation:
Ding Y, Perez-Ortiz G, Peate J and Barry SM (2022) Redesigning Enzymes for Biocatalysis: Exploiting Structural Understanding for Improved Selectivity. Front. Mol. Biosci. 9:908285. doi: 10.3389/fmolb.2022.908285

1 INTRODUCTION

Enzymes are of interest in chemical synthesis as they catalyze a wide array of chemical transformations (e.g., C–H bond activation, cyclization, and stereospecific reduction) which are extremely challenging, using even modern small-molecule catalysis. Furthermore, enzymes carry out these reactions often with unrivaled chemo-, regio-, and stereoselectivity and under mild conditions. The drive to make synthesis more sustainable has led to a rapid expansion in the use of enzymes in industry and is facilitated by improved availability of reliable off-the-shelf biocatalysts and screening methodologies (Hughes and Lewis, 2018). Several factors have influenced the availability of biocatalysts. The vast increase in sequence data has allowed genome mining for enzymes with specific domains which give rise to known functionalities, e.g., alcohol dehydrogenases, cytochrome P450s, etc. Improvements in cloning technology and construct optimization, as well as an array of expression strains and solubility tags, have given protein scientists an impressive toolbox to optimize the production of previously incalcitrant proteins. Additionally, cofactor recycling systems have made biocatalytic reactions that were unviable due to expensive enzyme cofactors, e.g., S-adenosylmethionine and NADPH consumed in reactions, now more economical. However, going forward, to expand biocatalysis for sustainable chemical synthesis, methods and understanding are needed to harness enzymes with desired functionality to replace and complement existing synthetic strategies. This can be accomplished through a combination of

enzyme discovery and protein engineering. In fact, future developments in protein engineering are likely to have the most profound impact on industrial biocatalysis (Bell et al., 2021).

Engineering enzymes can be carried out via rational design, e.g., targeting specific domains, conserved motifs, creating fusion proteins, or via non-rational methods such as directed evolution (Arnold, 2018) (Yang et al., 2019) (Ali et al., 2020) (Lovelock et al., 2022). Directed evolution strategies have already been successfully applied to the industrial production of high-value molecules, for example, the use of a transaminase to produce sitagliptin by Merck and Codexis (Savile et al., 2010). Transaminases are pyridoxyl phosphate-dependent enzymes that utilize an aldehyde or ketone, and an amine to catalyze the chemical equivalent of a stereospecific reductive amination. This is an increasingly important method to make chiral amines in industrial biocatalysis (Kelly et al., 2020). To introduce a key chiral amine in sitagliptin the transaminase was subjected to directed evolution. The resulting engineered enzyme contains five mutations around the active site to accommodate the large trifluorophenyl group on pro-sitagliptin (Savile et al., 2010).

However, directed evolution strategies, while extremely powerful, require high throughput methods to screen thousands of mutants and usually an operationally simple colorimetric assay, to select positive hits (Wang et al., 2021). These assays can be difficult to optimize and are usually designed to detect only the desired outcome. This could miss unpredicted, but useful changes in catalyzed chemistry (Hubert and Barry, 2016). Semi-rational design requires an enzyme structure or homology model, enabling the identification of key enzyme residues or motifs, and employs various strategies such as site saturation mutagenesis, Combinatorial Active-Site Saturation Test (CAST), and Iterative Saturation Mutagenesis (ISM) (Wang et al., 2017). These strategies can also generate hundreds of mutants and screening is a common bottleneck. Rational engineering generally involves targeting a limited number of residues in a binding pocket, consensus sequence, or motif. Thus, it produces fewer mutants that can be screened using low-medium throughput methods such as High performance liquid chromatography (HPLC). Chromatographic screening methods gather more information, such as unexpected products and the regio and stereoselectivity of the reaction, which is of vital importance in synthesis. But, while high throughput HPLC methodology has improved, it is comparatively expensive. However, rational mutation relies on significant knowledge of the structure and mechanism of the enzyme.

Here, we discuss rational or semi-rational protein engineering approaches to alter aspects of enzyme chemistry with a focus on improving stereo- and/or regioselectivity. We briefly discuss expanding substrate tolerance. These approaches help to provide insight into enzyme structure-activity relationships and highlight gaps in our understanding. The following is not intended to be an exhaustive review. We focus on approaches which are guided by, or can be explained through, structural and mechanistic understanding of the enzyme. We have also selected examples to illustrate each approach, focusing on enzymes already used in industrial contexts or transformations of particular interest in organic synthesis (Winkler et al., 2021) (Marshall et al., 2021).

2 RATIONAL MUTAGENESIS

Stereoselective and regioselective reactions are vital for the successful chemical synthesis of complex molecules. However, many stereoselective reactions are catalyzed by heavy metal-containing small-molecule catalysts which can be toxic. The benefit of small-molecule catalysts is that they can be designed to produce one or the other enantiomer selectively.

Enzymes can carry out transformations under mild conditions avoiding the need for heavy metals and solvents, and thus offer a path to more sustainable chemistry. Most enzymes also afford a single stereo or regioisomer. Should this not be the desired isomer of a given chemical target, a complementary enzyme may need to be identified. In other cases, enzymes produce mixtures of products which then require time-consuming separation. Both problems could be solved by a bioinformatics approach, i.e., searching genetics databases for similar enzymes, followed by extensive production and screening of candidate enzymes. This is time-consuming and success is not guaranteed. For many enzyme families, predicting the substrate and chemistry based on sequence or homology model alone is still difficult. For this reason, many efforts have been made to develop selective biocatalysts via rational protein engineering.

Rational mutagenesis can involve strategies of differing complexity. Sequence alignment and sufficient knowledge of conserved motifs can often provide sufficient guidance. However, for enzymes that undergo substantial conformational change on substrate binding, crystal structure data, homology modelling, and substrate docking studies may be required to produce a more detailed picture. Detailed information about the enzyme mechanism could also be necessary. Here we discuss several rational engineering strategies to alter enzyme reaction outcomes. They include, mutating residues directly involved in substrate binding interactions to alter substrate orientation, change steric crowding in the active site to promote altered regio- and stereoselectivity and improved enzyme promiscuity, and also mutating residues directly involved in catalysis.

2.1 Analysis of Protein Sequence and Structure to Aid Protein Engineering

Structurally characterized enzymes, especially with substrate and/or cofactors bound, offer the best opportunities for rational design. However, identifying where mutations should be introduced, is enzyme or enzyme family dependent, as the structural drivers of stereo and regioselectivity will differ. Furthermore, many enzymes cannot be structurally characterized in the presence of substrate because the enzyme turns over the substrate and appropriate inert substrate analogs may not be available. Key information about substrate orientation, active site interactions, and conformational change resulting from ligand binding will

thus be missing. Thus, computationally docking substrates into crystal structures or even homology models can be a powerful tool enabling rational protein engineering. For example, the plant cytochrome P450 (CYP72A63) oxidizes the terpene 11-oxo-β-amyrin producing a mixture of oxidized products. The reaction occurs at a single carbon and the enzyme sequentially oxidizes the carbon in a series of two-electron oxidations from C-H to alcohol, aldehyde, and finally a carboxylic acid (Sun et al., 2020). Cytochrome P450s are heme-dependent enzymes that utilize molecular oxygen to facilitate a wide variety of oxidative transformations on a vast array of substrates (Greule et al., 2018). Despite functional and primary sequence diversity, their tertiary structures are highly conserved and contain several key motifs which significantly influence catalysis (Poulos, 2014). Docking studies of CYP72A63 revealed just three residues responsible for chemo- and regio-selectivity (Sun et al., 2020). It appeared that the methyl group of T338, in a conserved motif located in the I-helix above the heme, reduced the enzyme's affinity for the partially oxidized intermediates (alcohol and aldehyde). This resulted in intermediate release and prevented further oxidation to the acid. The T338S mutant decreased hydrophobicity in the active site resulting in retention of the intermediate and thus production of the carboxylic acid, glycyrrhetinic acid. Furthermore, a single mutation L398I rotated 11-oxo-β-amyrin and relocated C-29 close to the heme-Fe center (Sun et al., 2020). Cytochrome P450s are of growing interest as biocatalysts due to their potential as C-H bond activation catalysts as illustrated in the example above (Zhang et al., 2019). The ability to activate inert C-H bonds selectively, even on complex substrates, is considered a holy grail of synthetic chemistry and an important green chemistry target (Arndtsen et al., 1995) (Dalton et al., 2021). There are however still significant gaps in our understanding of the relationship between P450 structure and function.

Identifying conserved residues or motifs in an enzyme is also enabled by easy access to the large bank of sequence data and bioinformatic tools. This information is vital for "preengineering". For example, in an imine reductase G-36 (IRED), N121 and S260 were identified from the docking model as targets to enable expansion of the binding cavity. Additional target residues were identified from a sequence alignment of 70 IREDs. Thus, just seven variants were screened and the catalytic efficiency was improved ten times with a near-perfect stereoselectivity (R, 99% enantiomeric excess (ee)) (Zhang et al., 2022). Equally, in the transaminase from *Vibrio fluvialis* (ATA-Vfl), a single amino acid mutation, L56V, improved selectivity increasing diastereomeric excess (de) from 14 to 89% compared to WT (Skalden et al., 2015). First, the residue Leu56 was identified from the docking model. The distribution of residues at this position in amine transaminases (ATAs) was analyzed using the 3DM database, a powerful tool for multiple sequence alignment (Kuipers et al., 2010). Only six amino acids were selected to develop a small mutant library (Skalden et al., 2015). Furthermore, even without a docking model, sequence alignments identify key function determining residues. Sclareol synthase from *Salvia sclarea* (SsSS), a class I terpene synthase, catalyzes hydroxyl group insertion. Three key sites (N431, S433, and T436) were selected from sequence alignment with other family members. Mutating these sites changed the water molecule nucleophile position in the active site, allowing it to attack the double bond from differing directions, selectively producing different stereoisomers (Jia et al., 2018).

2.2 Mutating Residues Involved in Direct Enzyme–Substrate Interactions

Through inspection of the enzyme–substrate complex or substrate docking model, amino acids which interact directly with a substrate can be identified. Mutating these residues can eliminate or reduce affinity for a substrate by removing hydrogen bonds, electrostatic or hydrophobic interactions. However, if done carefully this approach can succeed in shifting the orientation of the substrate in the active site, thus altering the direction of reaction (e.g., hydride addition) or on which atom the reaction occurs, giving different stereoselectivity or regioselectivity respectively. For example, after examining the crystal structure of the imine reductase (IRED) AolRED, an N241A mutant was created to interrupt the interaction between the imine nitrogen atom and Asn241, moving the imine toward NADPH, thus changing the enantioselectivity (Aleku et al., 2016) (**Figure 1A**). In the flavin-dependent enzyme, YqjM, from the OYE family, two histidines act as hydrogen bond donors for the carbonyl oxygen of the α, β-unsaturated ester. Disrupting this interaction by mutating His167 to Ala, allowed the substrate to rotate and switched the stereochemistry of the product (Rüthlein et al., 2015) (**Figure 1B**).

Conversely, introducing hydrogen bonds through single amino acid mutagenesis can fine-tune substrate-binding positions as exemplified by the epoxide hydrolase VrEH2 (**Figure 1C**). Asn was introduced at position 263, moving the β carbon away from the catalytic Asp101, thus improving regioselectivity to 99% (Li F.-L. et al., 2018). A final example is PntE, which catalyzes Baeyer-Villiger oxidation in the biosynthesis of pentalenolactone D (**Figure 1D**). The flavin-dependent Baeyer-Villiger monooxygenases catalyze Baeyer-Villiger oxidations by using molecular oxygen to create a reactive peroxide species. This transformation, ketone to ester, is common in synthetic chemistry. The analogous chemical reaction uses organic peracids, e.g., mCBPA (meta chloroperbenzoic acid) which can be explosive. The oxygen atom is inserted adjacent to the carbonyl group via nucleophilic attack by the peroxide on the carbonyl, followed by rearrangement via a Criegee intermediate to afford the ester or lactone product (Liu et al., 2020). When a single mutation, L185S, was introduced into PntE a complete change in the regioselectivity of the reaction was observed. It was proposed that the serine side chain forms a hydrogen bond with the FAD (flavin adenine dinucleotide)-binding motif, altering the Criegee intermediate conformation, and switching the carbon that migrates (Chen et al., 2016) (**Figure 1D**).

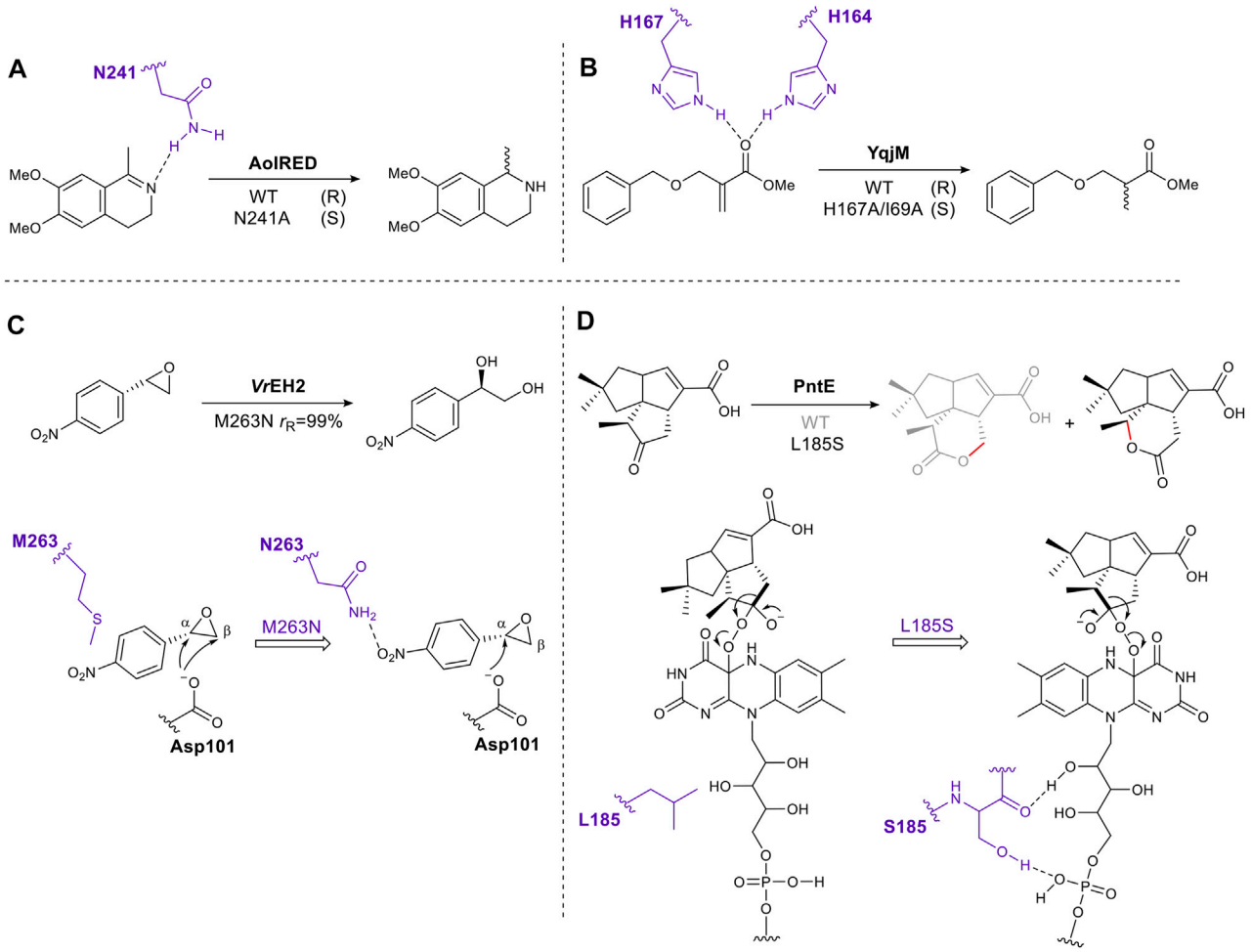

FIGURE 1 | Schematic representation of rationally engineered residues directly involved in substrate binding tune reaction selectivity. **(A)**. Mutation to remove a hydrogen bond, altering the stereoselectivity of an imine reductase. **(B)**. Mutation of an active site histidine residue to remove a substrate hydrogen bond alters stereoselectivity of the ene-reductase, YqjM. **(C)**. Introduction of an enzyme-substrate interaction to alter regioselectivity (r_R, ratio of regioisomers produced as a result of attack at α and β positions, producing R stereochemistry in each case). **(D)**. Mutation introducing enzyme-cofactor interactions changes regioselectivity of a Baeyer-Villiger oxygenase, PntE. Key residues are shown in purple.

2.3 Rational Mutagenesis to Substrate Binding Pockets to Alter Regio- and Stereoselectivity

Many enzyme families have highly defined, hydrophobic substrate binding sites that lend themselves to rational mutagenesis, both to increase substrate tolerance and change the selectivity of the enzyme. Bulky hydrophobic residues that line an enzyme active site are attractive targets for rational enzyme engineering. Modification of these residues can markedly reshape the substrate-binding pocket, usually creating more space and altering the hydrophobicity. Just enlarging the pocket can give rise to multiple substrate binding orientations which can lead to a loss of selectivity and multiple regio or stereoisomers. Thus, a balance is required between increased space to allow for more promiscuous substrate tolerance and ensuring the binding of specific orientations to maintain selectivity.

This approach is exemplified in biocatalyzed stereoselective reduction reactions. Alcohol dehydrogenases and ene-reductases, catalyze the asymmetric reduction of carbonyl groups and activated carbon-carbon double bonds, respectively (Toogood and Scrutton, 2014) (Koesoema et al., 2020). These enzyme families have been studied extensively and are used in industrial biocatalysis (de Gonzalo and Paul, 2021) (Toogood and Scrutton, 2018). The mechanism involves the formation of an sp^3 center from a prochiral sp^2 carbon, creating a new stereocenter (**Figure 2A**). The enzyme binding pocket contains two sites that selectively bind the groups on either side of the carbonyl carbon in a *pro*-S or *pro*-R orientation, thus ensuring stereoselectivity. The typical approach for the rational redesign of these sites is to replace one or two large residues

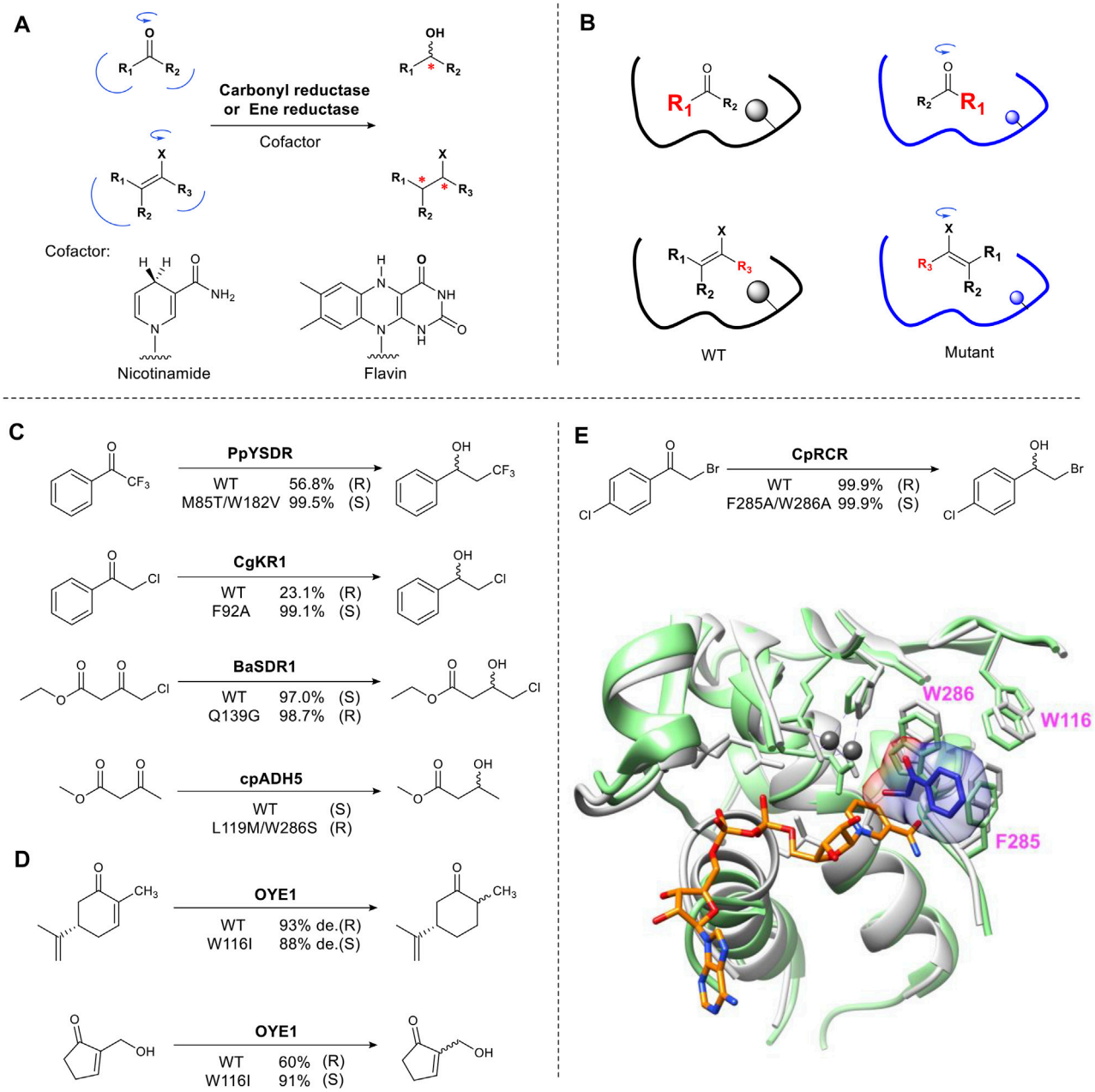

FIGURE 2 | Reshaping the substrate-binding pocket flips substrate binding. **(A)** Carbonyl and ene-reduction are catalyzed by carbonyl reductase and ene reductase in the presence of cofactor. X = electron-withdrawing group. **(B)** Schematic representation of reversing stereoselectivity of enzymatic reduction using mutagenesis. **(C)** Examples of inverted stereoselectivity introduced by site-directed mutation in carbonyl reductases. **(D)** Examples of inverted stereoselectivity introduced by site-directed mutation in ene reductases. **(E)** Overlay of CpRCR crystal structure. Wild type CpRCR bound to NAD^+ (orange) shown in grey (PDB: 3WLE) and H49A CpRCR bound to substrate hydroxyl phenylethanone (blue) shown in light green (PDB: 3WNQ). Zinc ions shown in dark grey (Wang et al., 2014). Bulky W286 and F285 in small binding pocket means only a small hydroxyl group can be accommodated.

(Phe, Trp) located in the small binding pocket and mutate them to a smaller residue (Ala, Gly) resulting in "flipped" substrate binding e.g. from *pro*-R to *pro*-S or vice versa (**Figure 2B**). In practice this results in the hydride approaching the substrate from the opposite face (*Re* or *Si*) of the plane of the carbonyl, thus changing the enantiomer formed. Several alcohol dehydrogenases (ADHs) have been engineered to change their stereoselectivity including PpYSDR (Li et al., 2016), CgKR1 (Qin et al., 2016), CpRCR (Wang et al., 2014) (Nie et al., 2018), BaSDR1 (Li et al., 2021) and cpADH5 (Ensari et al., 2017) which catalyze asymmetric reduction of various α-halogen-substituted acetophenones and β-ketoesters (**Figures**

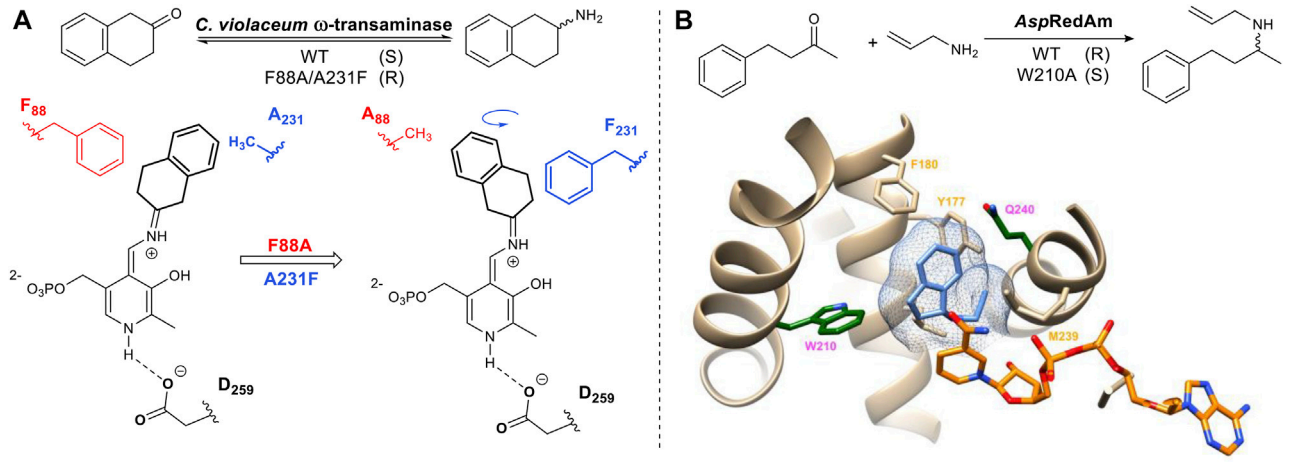

FIGURE 3 | (A) Example of stereo-complementary transamination reaction and schematic representation of its reversed conformation, induced by mutation. The intermediate is formed via imine (Schiff base) formation of the ketone with the pyridoxyl phosphate cofactor. Stereoselective protonation of the Schiff base leads to a chiral amine product. The amine donor in this reaction is alanine. **(B)** An example of AspRedAm-catalyzed reductive amination. AspRedAm crystal structure (PDB: 5G6S) (Aleku et al., 2017), NADP(H) shown in orange and product rasagiline shown in light blue. Mutation of Q240 and W210 (dark green) can enhance and reverse stereoselectivity.

2C,E). Optimization of the reversed enantioselectivity can be achieved by further enlarging the binding pocket (Qin et al., 2018).

The well characterized flavin-dependent ene-reductase biocatalyst, old yellow enzyme family (OYE), catalyzes the reduction of α, β-unsaturated ketones. Mutating the hotspot Trp116 results in reversed stereoselectivity of OYE1. This was first reported using (S)-carvone as a substrate (Padhi et al., 2009) (**Figure 2D**). OYE1 can also accept numerous Baylis-Hillman adducts to afford complementary chiral β-hydroxy carbonyl compounds (**Figure 2D**) (Walton et al., 2011). Mutating Trp116 to a small residue such as Ala, flipped substrate binding, reversing the stereoselectivity. Introducing a large residue (Phe) did not affect stereoselectivity (Pompeu et al., 2013). For the reduction of Baylis-Hillman adducts, W116I not only provides more space for the substrate but also for a water molecule, which stabilizes the alcohol group of substrates through hydrogen bonding (Pompeu et al., 2012).

The above mentioned strategy has also been applied to the pyridoxyl phosphate-dependent transaminases. Humble *et al* utilized homology models of a transaminase from *Chromobacterium violaceum* allowing the rational design of the aldehyde/pyridoxal phosphate binding site to successfully switch the stereoselectivity of the reaction (**Figure 3A**) (Humble et al., 2012). Imine reductases (IRED) catalyze the same overall reaction to transaminases but differ in their mechanism of action. Imine reductases are NAD(P)H-dependent enzymes that catalyze the stereoselective addition of hydride to an imine (**Figure 3B**). For the imine reductase *Asp*RedAM, mutating key substrate interacting residues identified from the crystal structure e.g. W210 resulted in a complete switch in stereochemical outcome. Trp and Gln are located on either side of the chiral amine substrate. Mutants W210A and Q240A not only switched the stereochemistry of the product but also improved the stereoselectivity from 30% ee to greater than 90% ee (Aleku et al., 2017) (Aleku et al., 2018).

As described in **Section 2.2** flavin-dependent Baeyer-Villiger monooxygenases catalyze the transformation, ketone to ester or lactone (Liu et al., 2020). The regioselectivity of chemical Baeyer Villiger oxidations can be predicted based on the migratory ability of the carbons alpha to the carbonyl carbon. This is determined by the capacity of the carbon to stabilize the partial positive charge which develops in the transition state via the inductive effect. Thus tertiary carbons migrate in favor of primary carbons (Li G. et al., 2018). However, enzymatic reactions can result in unexpected Baeyer Villiger products due to the influence of the binding site on the transition state, favoring an alternative rearrangement of the Criegee intermediate (**Figure 4A**). Changing the steric bulk and hydrophobicity of residues in the binding pocket can thus result in the inversion of regioselectivity. For example, cyclohexanone monooxygenase from *Arthrobacter* sp. (CHMOArthro) catalyzes the oxidation of *trans* dihydrocarvone to a lactone (**Figure 4B**). The regioselectivity was reversed by the substitution of three phenylalanine residues with alanine, resulting in a change in substrate binding in the enlarged pocket (**Figure 4B**) (Balke et al., 2016). The same strategy was used for trimethylcyclopentenylacetyl-CoA monooxygenase (OTEMO) (Balke et al., 2017) and $CHMO_{Phi1}$ (Messiha et al., 2018) (**Figure 4B**). Surprisingly, a single phenylalanine residue determines selectivity among CHMOs. Mutagenesis of this conserved phenylalanine close to the binding pocket in CHMOs predictably changes the regioselectivity of lactone formation (Hu et al., 2020).

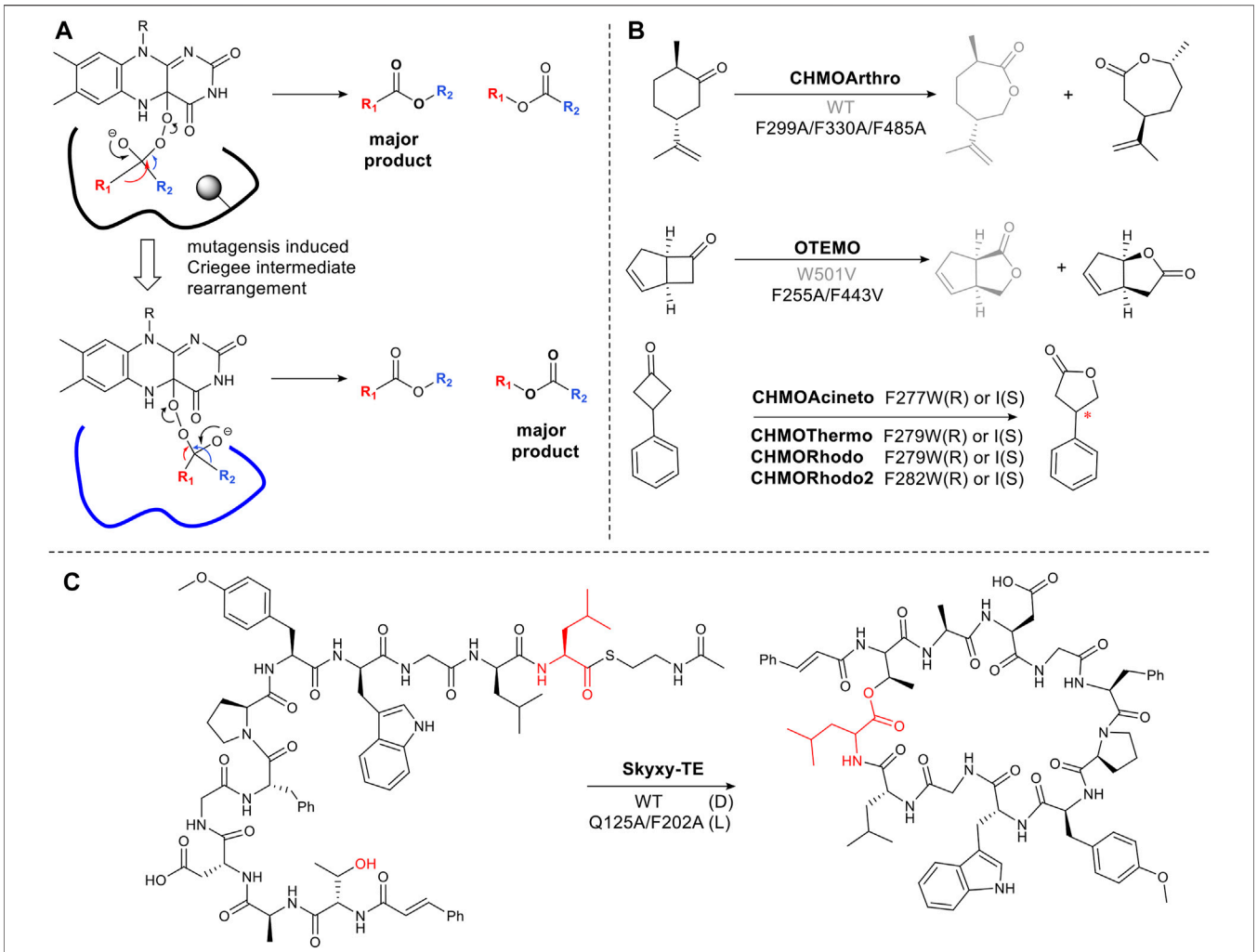

FIGURE 4 | Steric hinderance control reaction selectivity. **(A)** Origin of selectivity in Baeyer Villiger reactions showing how a sterically bulky residue (shown in circle shadow) in the active site affects the orientation of the Criegee intermediate. **(B)** Examples of Baeyer-Villiger reaction catalyzed by BVMOs, **(C)** Bifunctional thioesterase (Skyxy-TE) catalyzing epimerization and cyclization of linear Skyllamycin analog, the wild type containing large residues Q125 and F202, only accepted the epimerized linear peptides.

The approach of targeting large hydrophobic residues and mutating them to reduce the steric bulk and hydrophobicity in an active site, can hold for a variety of enzymes even on large complex molecules. Skyxy-TE, a single thioesterase domain from a multi-modular, non-ribosomal peptide synthetase megaenzyme, catalyzes epimerization and cyclization of a linear peptide (**Figure 4C**). The epimerization is a highly unusual reaction for thioesterases which typically catalyzes either macrocyclization or hydrolysis. However, the small space around a conserved serine residue which covalently binds the linear peptide as an ester, constrains the intermediate in a *pro-R* configuration. Expanding the space, via mutation to Ala, allowed L-configuration (Yu et al., 2021) (**Figure 4C**).

The cytochrome P450s TxtE and 5NTSlav can perform direct regioselective nitration of L-tryptophan producing 4-nitro-L-tryptophan and 5-nitro-L-tryptophan respectively, using oxygen and nitric oxide as co-substrates (Barry et al., 2012) (Dodani et al., 2014). Nitration is a highly unusual reaction for a cytochrome P450, which typically carries out monooxygenation reactions e.g. hydroxylation, epoxidation as described in **Section 2.1**. The complementary regioselectivity of the reactions of TxtE and 5NTSlav is also intriguing. Dodani *et al.* identified that in TxtE His176 is involved in a direct edge-to-face interaction with the substrate, L-tryptophan. A single mutation of this residue in the flexible F/G loop of TxtE simultaneously controls loop dynamics and completely shifts the enzyme's regioselectivity from the C4 to the C5 position of L-tryptophan. The resulting mutants TxtE-H176F; TxtE-H176Y and TxtE-H176W (this is the residue found in 5NTSlav) had also an increased affinity for L-tryptophan (Dodani et al., 2014). The larger side chains

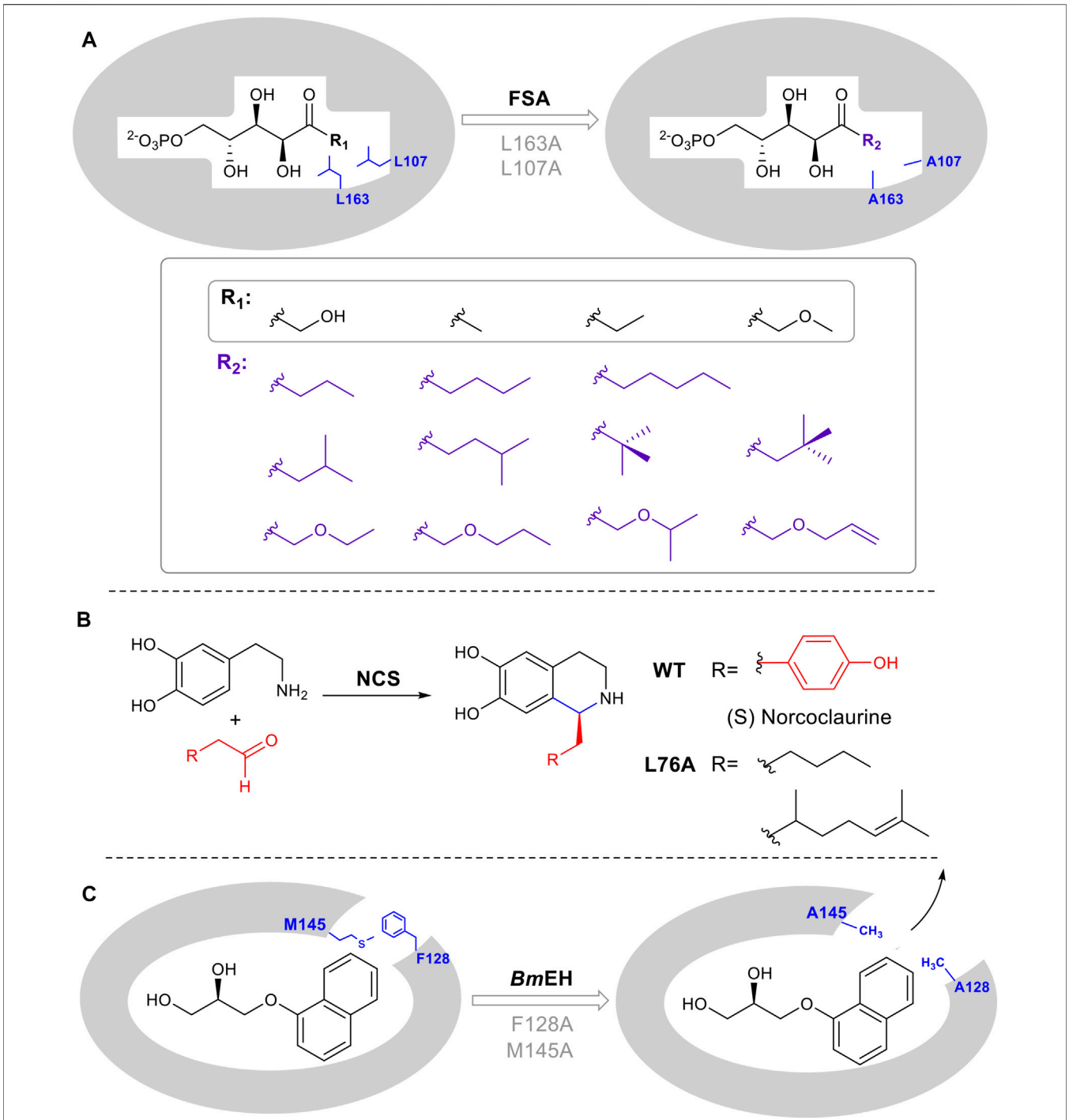

FIGURE 5 | Enlarging active site augments substrate promiscuity. **(A)** D-fructose-6-phosphate aldolase (FSA) accommodates D-Fructose 6-Phosphate in the active site. Mutation of L107 and L163 to Ala, increases the pocket volume. **(B)** Norcoclaurine synthase catalyzes a Pictet-Spengler cyclization. L76A point mutation guided by mechanistic and computational studies, leads to improved substrate promiscuity. **(C)** Epoxide hydrolase BmEH M145 and F128 block the substrate tunnel. Mutation increases the size and improves the rate of product release.

of these amino acids lead to a more tightly packed active site with different interactions with water molecules that shift the position of the substrate toward the heme, placing C-5 closer to the nitrogen of the proposed ferric-peroxynitrite catalytic intermediate (Barry et al., 2012) (Dodani et al., 2014) (Louka et al., 2020). Interestingly, the structure of TxtE

does not significantly differ from that of conventional hydroxylating P450s and it is unclear why it carries out nitration and not hydroxylation. In fact, despite many decades of study it is not possible based on sequence or tertiary structure to predict what chemistry a particular P450 will catalyze.

2.4 Rational Mutagenesis to Expand Substrate Tolerance

While enzymes are attractive as catalysts due to their inherent stereo and regioselectivity, this often comes hand in hand with limited substrate tolerance which constrains potential biocatalytic application. There are several commonly used strategies to rationally expand and introduce promiscuity including enlarging the substrate-binding pocket, tuning the properties of a substrate tunnel or any conformationally flexible loops involved in substrate binding. Positions for mutagenesis can be identified using a crystal structure or homology model, followed by site-directed mutagenesis. For example, aldolases that catalyze the reversible, synthetically important condensation of aldehydes and ketones, are often limited by restricted recognition of donor components. Mutants L107A and L163A were designed in D-fructose-6-phosphate aldolase (FSA) from *Escherichia coli,* to accept a series of substrates containing various aliphatic side chains (Güclü et al., 2016) (**Figure 5A**). Additionally, in the computationally designed aldolase RA95.5-8F, a single amino acid mutation F112L makes the enzyme active toward large bulky cyclopentanone (MacDonald et al., 2020). In the epoxide hydrolase from *Bacillus megaterium* (*Bm*EH), mutagenesis on two predicted hotspots M145 and F128 enhanced enzyme activities of 6- to 430- fold toward various bulky substrates (Kong and Ma, 2014). A similar structure/computational guided approach was taken for norcoclaurine synthase (NCS). NCS is a plant alkaloid biosynthetic enzyme that catalyzes a stereoselective Pictet-Spingler condensation to produce pharmaceutically important tetrahydroisoquinolines (**Figure 5B**) (Lichman et al., 2015). A combination of structural and computational studies helped to elucidate the conformation of substrates in the NCS active site. A single leucine residue in the active site was identified as interacting with the substrate aldehyde R group. Once mutated, the change in the binding pocket made it possible to diversify the aldehydes tolerated by the enzyme (Lichman et al., 2015).

In several enzyme families, the substrate must pass through a tunnel connecting the buried active site with the enzyme surface. The tunnel is thus substrate selective and altering its properties can result in a broadening of substrates used by the enzyme, thus increasing promiscuity. *Bm*EH an epoxide hydrolase, showed poor activity toward bulky α-naphthyl glycidyl. The introduction of M145A or F128A expanded the tunnel, enabling product release. The activity was increased 42 and 25 times respectively (**Figure 5C**) (Kong and Yuan, 2014).

2.5 Mutating Residues Directly Involved in Catalysis

Amino acids directly involved in catalysis are usually not the first choice for mutation when attempting to alter stereo- or regioselectivity, as it tends to result in loss of activity or negative changes in kinetic parameters. However, there are several examples where this approach has been successful. Bacterial tryptophan C6-prenyltransferases (6-DMATS) catalyze selective alkylation at C6 of the tryptophan indole ring. The reaction occurs via Friedel-Crafts alkylation using dimethylallyl diphosphate as the prenyl donor (**Figure 6A**). A double mutant V259Q/H329Y changed the catalytic base from His329, adjacent to carbon 6 to Gln259. This changed the regioselectivity of deprotonation via a structured water molecule, redirecting the prenylation to carbon 5. This approach was informed by structural elucidation and comparison of 6-DMATS and the complementary C5-prenyltranserase, 5-DMATS, allowing structure-guided engineering. The authors also note the challenges in this work in which several mutants lose selectivity and produce multiple regioisomers (Ostertag et al., 2021).

The cytochrome P450, P450cin, catalyzes an enantiospecific hydroxylation of monoterpene, 1,8-cineole, to produce (1R)-6-hydroxycineole (**Figure 6B**). P450cin contains a deviation from a P450 key motif (Stok et al., 2019). The I -Helix of P450s lies above the heme cofactor and contains the consensus sequence (AGXD/ET) which introduces a kink in the helix (Poulos, 2014). The threonine plays a vital role in the catalytic cycle, enabling the protonation of key intermediates in the reduction of oxygen to form the active oxidizing species (Nagano and Poulos, 2005). The residue in this position in P450cin is asparagine instead of threonine. When N242 is mutated to the consensus residue, threonine, the orientation of the substrate in the active site is changed, exposing a different C-H bond to hydrogen abstraction. The result is a dramatic alteration in regio and stereoselectivity (**Figure 6B**).

Alteration of catalytic residues can also confer new reactivity on enzymes, as exemplified by a redesigned pyruvate decarboxylase, *Zm*PDC which catalyzes asymmetric carbon-carbon bond formation (Meyer et al., 2011). Wild type *Zm*PDC uses Glu473 as a proton donor to enable the formation of a carbanion intermediate in the decarboxylation catalytic cycle releasing acetaldehyde. Replacing Glu473 with Gln, as well as providing benzaldehyde as an acceptor, enables the synthesis of phenylacetylcarbinol, thereby constructing a new C-C bond and a stereocenter (Meyer et al., 2011). Intriguingly, further study on Glu473 enabled precise control of its stereoselectivity by replacing it with larger or smaller residues (Wechsler et al., 2015).

3 STRUCTURE-GUIDED SEMI-RATIONAL ENGINEERING

The examples above show that adjusting steric constraints in the binding pocket and changing key residues involved in catalysis or

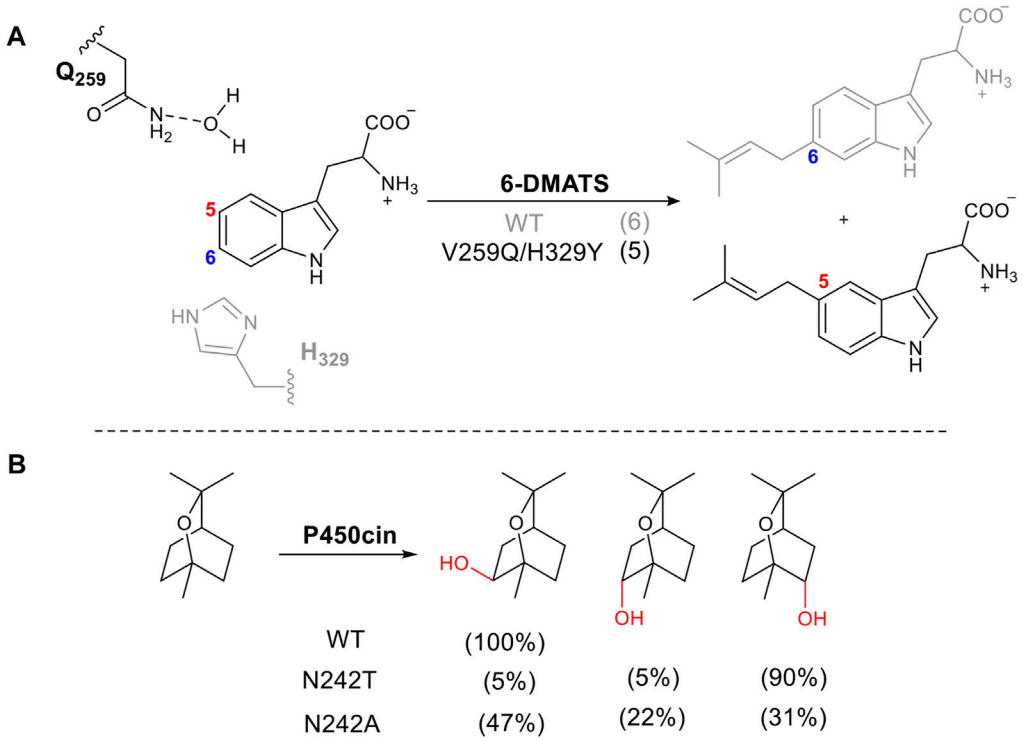

FIGURE 6 | Tuning regioselectivity through altering catalytic residue. **(A)** 6-MATS catalyzes prenylation of tryptophan, natural selectivity shown in grey. **(B)** Effect of mutation of I-helix on P450cin hydroxylation.

substrate binding, are powerful strategies to alter reaction outcomes. However, interactions between the substrate and the enzyme are often challenging to predict, and the steric modification strategy is substrate-dependent. For example, with carbonyl reductases, this strategy still limits substrates to an aromatic ring and a short-carbon chain on either side of the carbonyl carbon (Li et al., 2021). Structure-guided semi-rational engineering, through mechanistic understanding and computational modeling or more extensive screening of mutants, to identify key residues, are valuable additional strategies (Wang, Li and Reetz, 2017).

3.1 Computational Modelling

Computational tools are increasingly important in protein engineering. Free and easy-to-use software now exists to enable researchers to carry out bioinformatic analysis, create homology models and dock substrates into active sites. The power of these tools is apparent in the examples given above. However, these strategies do not account for protein dynamics affecting substrate binding/release or other aspects of the catalytic cycle. More powerful computational modeling such as Quantum Mechanics/Molecular Mechanics (QM/MM) methods, molecular dynamics (MD), quantum chemical (QC), and empirical valence bond (EVB) calculations are required to create a more nuanced understanding of the relationships between protein structure and function (Derat and Kamerlin, 2022). These techniques are widely used to enable the interpretation of experimental data to understand enzymatic mechanisms and rationalize the enzyme selectivity in several of the enzyme families discussed in this review including ene-reductases (Lonsdale and Reetz, 2015), diels-alderase (Byrne et al., 2016), BVMOs regioselectivity (Li G. et al., 2018) (Dong et al., 2022) and ketoreductase stereoselectivity (Serapian and Van Der Kamp, 2019).

A key attraction of computational methodology is the ability to carry out mutagenesis *in silico* and, thus, rationally redesign the enzyme, "preengineer", prior to experiments. This can reduce experimental effort and generates key insights into the relationship between structure and mechanism. Empirical valence bond (EVB) calculates the reaction activation energy. This can be used to predict the effect on the catalysis of particular mutations. This approach allows the computational optimization of enzyme catalysis of a given reaction rather than predicting changes in selectivity (Mondal et al., 2020). Using, for example, Rossetta, enzyme specificity and substrate tolerance can be altered, by focusing on key areas of the active stite, introducing geometric constraints on areas that need to remain unchanged and analyzing the dynamic conformations to predict the outcome (Wijma et al., 2015). A recent example is AspB, an aspartase from *Bacillus sp*. YM55-1 that catalyzes the reversible deamination of aspartate. Wild-type AspB is highly substrate selective. A mutant of AspB, which demonstrated activity as a β-amino acid lyase, was only detected after cluster screening of

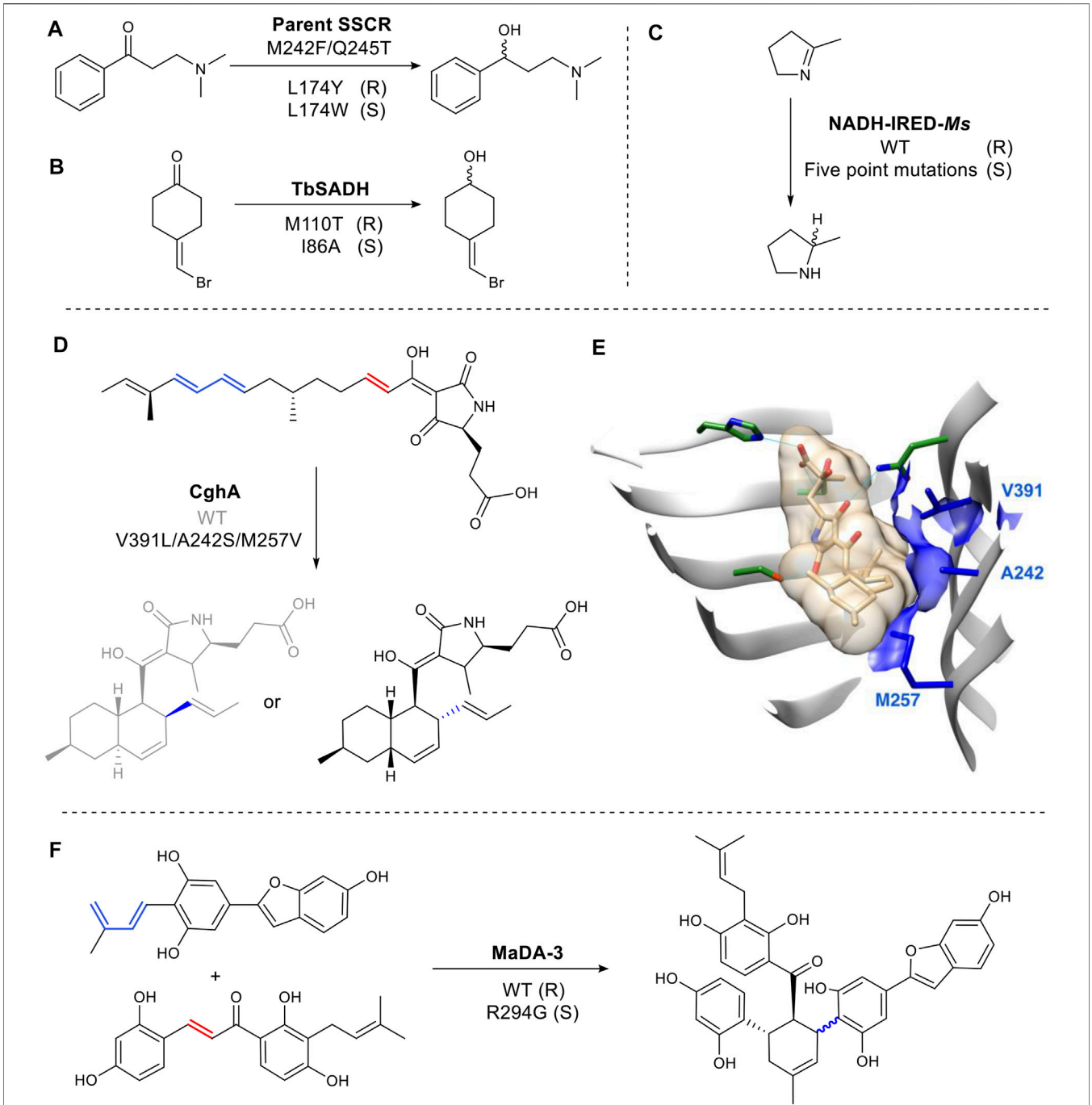

FIGURE 7 | Examples of structure-guided engineering for altered steroselectivity. **(A)** Reductase SSCR reduces ketones to alcohols stereoselectively. **(B)** TbSADH is an alcohol dehydrogenase. **(C)** A multiple mutant of the imine reductase gives complementary stereochemistry to the WT. **(D)** Diels Alderase CghA WT and mutant produce different stereoisomers. **(E)** Crystal structure of CghA in complex with Diels–Alder adduct. Substrate binding residues involved in electrostatic interactions are shown in dark green. Hydrophobic interactions with the diene and dienophile and V391, A242, and M257 are indicated in blue. (PDB: 6KBC for the Cgh-1 complex structure, PDB: 6KAW for the apo CghA structure) (Sato et al., 2021). **(F)** Diels Alderase MaDA-3 WT and mutant produce different stereoisomers.

300,000 clones (Vogel et al., 2014). Recently, understanding of the enzymatic mechanism and structure of AspB was exploited to rationally engineer promiscuous variants for hydroamination. Engineering was carried out *in silico* using Rosetta Enzyme Design. This programme allows the selective redesign of particular parts of a binding pocket leaving key enzyme-substrate interactions untouched (Li R. et al., 2018). For example, four residues (Thr187, Met321, Lys324, and Asn326) which line the original aspartate, α carboxylate, binding site were replaced with hydrophobic residues to facilitate binding of

the new α,β-unsaturated carbonyl electrophiles (Li et al.). Depending upon the penalty score of the constraints and structural inspection, just a few variants were identified and experimentally tested. Engineered AspB catalyzed hydroamination of various substituted acrylates (34 designs were screened for crotonic acid, 5 designs for (E)-2-pentenoic acid, 6 designs for fumaric acid monoamide and 30 designs for (E)-cinnamic acid). Moreover, the amine binding pocket of AspB was also engineered using the same strategy. A series of β-amino acids were thus synthesized with high regio- and enantioselectivity and on industrially relevant scales (Cui et al., 2021). These examples show how computational modelling can dramatically reduce experimental efforts.

Flexible loops around the active site play an important role in enzyme function but are often poorly defined in crystal structures. Molecular Dynamics (MD) simulations can identify key residues to influence substrate promiscuity. In the alcohol dehydrogenase, TbSADH, two rigid residues located on the loop near the binding pocket were identified from the analysis of the Root Mean Square Fluctuations (RMSFs) (Liu et al., 2019). Saturation mutagenesis of these residues was carried out to increase loop fluctuation. This generated a variant which could catalyze the reduction of a series of bulky ketones that are not accepted by the wild-type enzyme (Liu et al., 2019). Similarly, proline residues can provide structural rigidity and thus often play important roles in controlling protein structural dynamics. Mutating proline and its flanking residues located in loop regions near the active site can increase flexibility, thus indirectly adjusting the size of the binding pocket. For example, the TbSADH mutant P84S can accommodate non-natural bulky diaryl ketones, and mutant P84S/I86A carried out the reaction with a near-perfect conversion and stereoselectivity (Qu et al., 2021). In the case of phenylacetone monooxygenase (PAMO), the substitution of two conserved proline residues near the active site, increases the activity toward a series of 2-substituted cyclohexanones, which are not accepted by the wild-type PAMOs (Reetz and Wu, 2009) (Wu et al., 2010).

3.2 Structure Guided Semi-Rational Mutagenesis

Instead of subjecting one or two aminos acids to site-directed mutagenesis to alter selectivity, it is often necessary to investigate an entire loop or structural motif to identify the key residue or residues. This approach can generate many mutants but it is useful when there is no other obvious method to predict important residues or interactions. Common strategies include alanine scanning (mutating each residue to alanine to identify an effect) or saturation mutagenesis (mutating individual residues to all 20 proteinogenic amino acids to determine the most advantageous) (Wang et al., 2017). This methodology has been applied across diverse enzyme families catalyzing a variety of chemistries.

In the active site of the carbonyl reductase (SSCR) from *Sporobolomyces salmonicolor* AKU4429 (**Figure 7A**), a Tyr174 introduces a hydrogen bond between the tyrosine hydroxyl group and the substrate carbonyl oxygen resulting in the stabilization of *pro*-R conformation. While the mutant, Trp174, gave rise to the opposite orientation (Zhang et al., 2015) (**Figure 7A**). Reduction of 4-(bromomethylidene) cyclohexanone is catalyzed by wild-type TbSADH with a poor enantioselectivity (66% ee), as its highly symmetric structure can bind either a *pro*-R or *pro*-S conformation (**Figure 7B**). Mutating M110 to threonine increased R selectivity to 97% e.e. while mutation at I86 enhanced S selectivity to 98% ee. (Agudo et al., 2013). It was proposed that the side chain of Thr110 is responsible for the formation of a *pro*-R conformation by forming a hydrogen bond with a bromine identified through molecular dynamics simulations (Maria-Solano et al., 2017) (**Figure 7B**). The hydrogen bonding of the halogen atom and XH/π interaction have been shown on a molecular level to play a critical role in determining the stereoselectivity (Chen et al., 2018).

While rare, changes to the binding site of a cofactor can also be used change selectivity. For example, in the imine reductase NADH-IRED-Ms (**Figure 7C**), five amino acid mutations (positions 241- 245) change the orientation of NADH cofactor binding. The resulting switch in hydride attack, gives an inversion of product stereochemistry compared to wild type (Stockinger et al., 2021).

Over the last several years there has been interest in the discovery and characterization of Diels Alderases (DAs) (Minami and Oikawa, 2016), as well as the design of artificial enzymes for Diels–Alder reactions (Ghattas et al., 2021). A biocatalysed Diels Alder reaction is of significant interest as the chemical transformation often requires high pressures or temperatures and long reaction times (Yang and Gao, 2018). However, stereochemical control (endo/exo) of the enzymatic reaction is vital to make any future biocatalytic process viable. CghA catalyzes an intramolecular Diels–Alder reaction to form octalin natural products (Sato et al., 2021). The stereoselectivity was successfully converted from endo to unfavored exo-selectivity by reshaping the active site with three mutations to organize an exo transition state for the diene and the dienophile (Sato et al., 2021) (**Figures 7D,E**). *Morus alba* Diels-Alderase (MaDA) catalyzes an intermolecular Diels–Alder reaction. Interestingly, MaDA-3 has natural exo-selectivity. The transition state is stabilized through a cation-π interaction between a key R294 residue and the dihydroxylphenyl ring of the dienophile. Replacement of the residue afforded some endo product (Gao et al., 2021) (**Figure 7F**).

Glycosylation is a common, vital, late-stage functionalization reaction in natural product biosynthesis (Kren and Martinkova, 2012) (Liao et al., 2018). Selective chemical glycosylation of complex molecules is challenging, often requiring tedious protection and deprotection steps. Thus a selective enzymatic route is desirable. Wild type glycosyltransferases (GTs) catalyze glycosidic bond formation, which suffers from poor regioselectivity due to its large binding pocket, and thus multiple substrate-binding modes or conformations (Nidetzky et al., 2018). Longer distances between substrate and enzyme make it difficult to determine in a rational way which sites affect the substrate binding position. To narrow this down without alanine scanning the whole site or using full saturation mutagenesis of each site, an approach known as "small but smart" was used. This less intensive method mutates the target

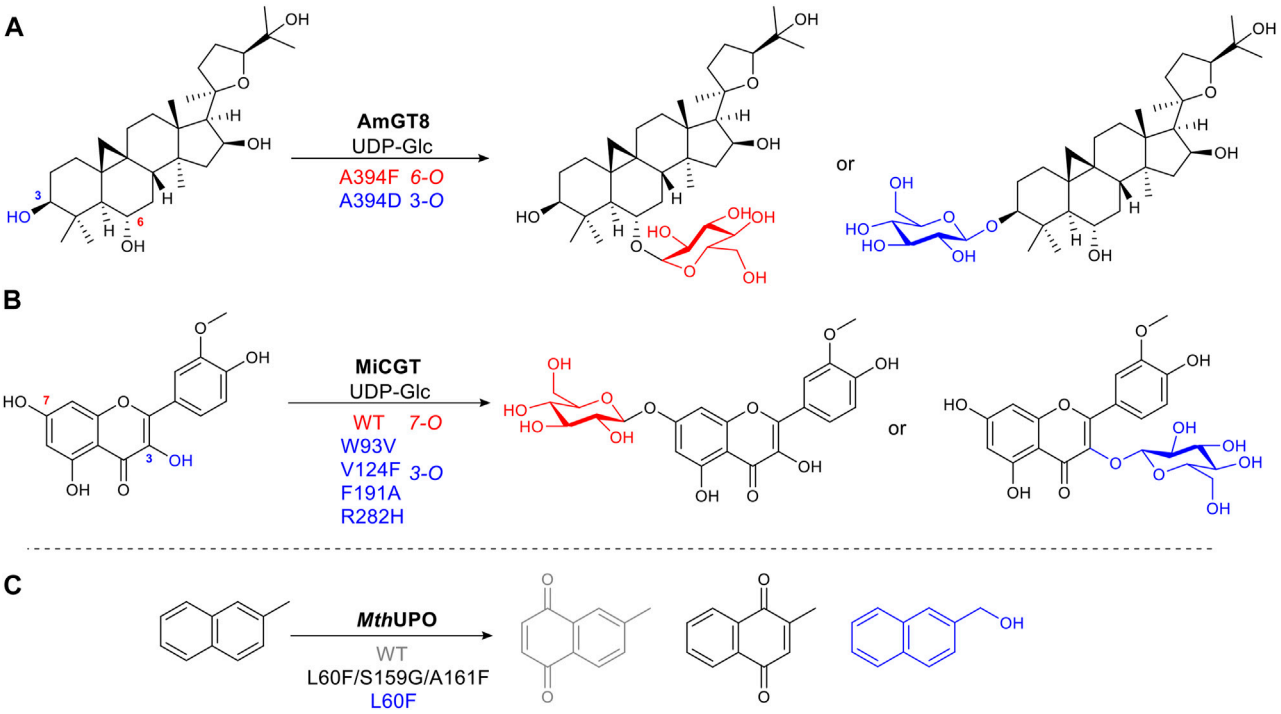

FIGURE 8 | Examples of structure-guided protein engineering to alter regioselectivity. **(A)** Glycosyltransferase AmGT8 catalyzing triterpene 3-/6-O-glycosylation, a conserved residue at position 394 is important for regioselectivity. **(B)** 3-/7-O-Glycosylation of a flavonoid catalyzed by wild-type glycosyltransferase MiCGT and a VFAH mutant. **(C)** Heme-containing peroxygenase *Mth*UPO catalyzing aromatic oxidation. Mutations alter substrate binding position to afford diverse products.

residue to a representative of each class of amino acids, e.g. positively charged, negatively charged, polar uncharged etc., to identify which group makes the greatest impact, thus significantly reducing experimental effort. AmGT8 catalyzes glycosylation of triterpenes (**Figure 8A**). Activity assays using a selection of substrate derivatives were performed, followed by the comparison of different docking models of the substrate with desired regioselectivity. From the activity study of various size triterpenes, three AmGT8 docking models with different regioselectivities were established, and active site amino acids were divided into four groups. After screening a small set of mutants, the conserved residue, A394, was identified as crucial for regioselectivity (Zhang et al., 2021).

Alanine scanning the active site was utilised to change the selectivity of MiCGT, which catalyzes glycosylation of flavonoids. After iterative saturation mutagenesis, a mutant containing four amino acid changes, that shifted the regioselectivity from 7-O to 3-O, was identified (Wen et al., 2021) (**Figure 8B**).

The peroxygenase *Mth*UPO catalyzes the oxidation of 2-methylnaphthalene. Fine-tuning substrate position relative to the active oxygen species formed on the heme iron center, accomplished diverse chemo- and regioselective oxidation reactions. For mutant L60F, introducing a bulky phenylalanine allowed only the methyl group to get close enough to the catalytic center to be oxidized. Additional mutations, L60F/S159G/A161F, increased hydrophobicity, pushing the naphthyl aromatic ring moiety toward the heme-iron center, to afford a different quinone product (Knorrscheidt et al., 2021) (**Figure 8C**).

4 FUTURE CHALLENGES AND OUTLOOK

There is little doubt that biocatalysis will feature heavily in the future of synthesis whether it is bulk chemicals or complex molecules. Small precursor chemicals are frequently derived from fossil fuels and are thus unsustainable. Equally, there is a need for optically pure precursors and enzymes are well suited to their production. Complex, high-value molecules, represent excellent targets for biocatalysis, especially as the initial high cost of biocatalyst development may be more justifiable. A recent application of biocatalysis to the synthesis of the COVID-19 drug by Merck shows that there is already a recognition of the power of biocatalysis and a clear push from industry toward increased use (McIntosh et al., 2021).

Great strides have been made in both the understanding and engineering of enzymes and this is an exciting time in the field. This has been facilitated by several factors. Advances in molecular biology mean that processes such as cloning and mutagenesis are facile and can even be automated. Structural information from X-ray crystallography, NMR and now EM is vital for enzyme engineering, as demonstrated above. Developments in these techniques and data processing has speeded up the process of structure elucidation. Excitingly, AlphaFold now offers the opportunity to predict structures of structurally uncharacterized or indeed un-crystallizable enzymes (Jumper et al., 2021) (Varadi et al., 2022). Improved computational methods are providing greater insight into catalytic mechanisms and molecular dynamics. Developments in

cofactor recycling and improving enzyme stability mean that enzymes previously thought of as too complex or those requiring expensive cofactors are now viable targets for use as biocatalysts (Mordhorst and Andexer, 2020).

Such progress has meant that the ambition of the field has also grown. The goal for many in the field is to redesign enzymes to carry out new reactions, particularly those chemistries not currently found in biology, so-called "new to nature" transformations. Some of the best examples of new to nature reactions have come via directed evolution as pioneered by Frances Arnold (Chen and Arnold, 1993). A classic example from the Arnold lab evolved $P450_{BM3}$ to carry out cyclopropanation using a carbene generated *in situ* (Coelho et al., 2013). While cyclopropanation reactions are not new to nature, they are new to P450s. In addition, the chemistry, using a diazoacetate to generate the Fe-bound carbene, does not have a known analog in biological chemistry (Liu and Arnold, 2021). This result has been built on in recent examples, including engineered cytochrome P450 catalyzed atom transfer radical cyclization (ATRC), where a new C-C bond and a new C-Halogen bond are formed (Zhou et al., 2021). In a further recent development from the Arnold lab, they report the P450 catalyzed enantioselective ring expansion of aziridines to azetidines (Miller et al., 2022). Other methods to enable new to nature reactions (Leveson-Gower et al., 2019) include utilizing expanded genetic code via amber codon technology and tuning active site electronics (Ortmayer et al., 2020) as well as using Rosetta to design enzymes to carry out new to nature chemistry (Crawshaw et al., 2021).

The integration of chemocatalysis and enzymes has also been pursued as a way of combining the advantages of chemical and enzymatic catalysis. The goal is to utilize proteins or enzymes as scaffolds to house small-molecule catalysts (Schwizer et al., 2018). The catalysts themselves are usually organometallic and carry out the chemistry that is rare or not found in nature. They effectively act as an unnatural cofactor, coordinated to a native or engineered protein scaffold. This delivers all the advantages of enzyme catalysis, e.g., hydrophobic environment, increase in the effective concentration of reactants and most importantly, stereo and regioselectivity, which are key challenges in organic synthesis (Schwizer et al., 2018). Scaffolds are chosen to be accessible to a broad range of substrates.

Despite this progress, significant challenges remain. Protein engineering either rationally or via directed evolution is time-consuming. Efficient screening of mutants usually requires operationally simple, robust spectrophotometric assays, that can be read on plate reader or similar. Creating such assays is in turn time consuming and in some cases may not be possible. Equally, screening for one output may miss other potentially useful data, e.g., changes in chemistry or selectivity. Detection of serendipitous outcomes requires more powerful analytics. High-throughput LCMS would provide more information, i.e, all reaction products including stereo- and regioisomers but it is more operationally complex and expensive. Additionally, major improvements in the analysis of high throughput LCMS data, which is orders of magnitude more complex than that from a colorimetric assay, are required.

As seen in examples throughout this review "preegineering" *in silico* is increasingly important. Improved methods for *in silico* screening, such as deep mutational analysis (Dunham and Beltrao, 2021), will reduce experimental effort and increase the rate of progress. The logical progression of these strategies is *in silico* enzyme design facilitated by, for example, Rosetta. This tool has already been applied by several groups (Crawshaw et al., 2021) (Basanta et al., 2020) (Richter et al., 2011). Both approaches will also generate greater insight into the factors affecting substrate binding and catalytic mechanism which in turn will lead to more predictability. (Bunzel et al., 2021) (Jindal et al., 2019).

Thus, there are many exciting routes from which new biocatalysts will emerge. What is clear, is a greater understanding of the relationship between protein structure and enzyme function is needed. While crystallographic data is crucial for our understanding of enzymes, they offer us a static picture of an enzyme in one state. Insight into protein dynamics during catalysis will enable a greater understanding of the roles of residues in the active site and beyond, including their cooperativity. The importance of flexible regions in enzyme catalysis, often poorly defined in crystal structures, has been poorly explored. Computational methodology will enable a greater understanding of the role of flexible regions and protein dynamics in catalysis. Thus new computational tools and their democratization will, alongside the ongoing protein engineering revolution, lead to the second great revolution in enzyme engineering and is already proving exciting (Büchler et al., 2022) (Crawshaw et al., 2021). This combination will provide a much-needed pool of sustainable catalysts and hopefully a new era in chemical synthesis.

AUTHOR CONTRIBUTIONS

YD, GP-O, JP, and SMB researched and wrote the article, designed and created the figures.

FUNDING

Research on enzymology in the Barry lab was supported by grants from the RSC (E21-2982458970) and BBSRC (BB/P019811/1). JP is funded by a PhD scholarship from KCL.

REFERENCES

Agudo, R., Roiban, G.-D., and Reetz, M. T. (2013). Induced Axial Chirality in Biocatalytic Asymmetric Ketone Reduction. *J. Am. Chem. Soc.* 135 (5), 1665–1668. doi:10.1021/ja3092517

Aleku, G. A., France, S. P., Man, H., Mangas-Sanchez, J., Montgomery, S. L., Sharma, M., et al. (2017). A Reductive Aminase from Aspergillus oryzae. *Nat. Chem.* 9 (10), 961–969. doi:10.1038/nchem.2782

Aleku, G. A., Man, H., France, S. P., Leipold, F., Hussain, S., Toca-Gonzalez, L., et al. (2016). Stereoselectivity and Structural Characterization of an Imine Reductase (IRED) from Amycolatopsis Orientalis. *ACS Catal.* 6 (6), 3880–3889. doi:10.1021/acscatal.6b00782

Aleku, G. A., Mangas-Sanchez, J., Citoler, J., France, S. P., Montgomery, S. L., Heath, R. S., et al. (2018). Kinetic Resolution and Deracemization of Racemic Amines Using a Reductive Aminase. *ChemCatChem* 10 (3), 515–519. doi:10.1002/cctc.201701484

Ali, M., Ishqi, H. M., and Husain, Q. (2020). Enzyme Engineering: Reshaping the Biocatalytic Functions. *Biotechnol. Bioeng.* 117 (6), 1877–1894. doi:10.1002/bit.27329

Arndtsen, B. A., Bergman, R. G., Mobley, T. A., and Peterson, T. H. (1995). Selective Intermolecular Carbon-Hydrogen Bond Activation by Synthetic Metal Complexes in Homogeneous Solution. *Acc. Chem. Res.* 28 (3), 154–162. doi:10.1021/ar00051a009

Arnold, F. H. (2018). Directed Evolution: Bringing New Chemistry to Life. *Angew. Chem. Int. Ed.* 57 (16), 4143–4148. doi:10.1002/anie.201708408

Balke, K., Bäumgen, M., and Bornscheuer, U. T. (2017). Controlling the Regioselectivity of Baeyer-Villiger Monooxygenases by Mutation of Active-Site Residues. *ChemBioChem* 18 (16), 1627–1638. doi:10.1002/cbic.201700223

Balke, K., Schmidt, S., Genz, M., and Bornscheuer, U. T. (2016). Switching the Regioselectivity of a Cyclohexanone Monooxygenase toward (+)-Trans-Dihydrocarvone by Rational Protein Design. *ACS Chem. Biol.* 11 (1), 38–43. doi:10.1021/acschembio.5b00723

Barry, S. M., Kers, J. A., Johnson, E. G., Song, L., Aston, P. R., Patel, B., et al. (2012). Cytochrome P450-Catalyzed L-Tryptophan Nitration in Thaxtomin Phytotoxin Biosynthesis. *Nat. Chem. Biol.* 8 (10), 814–816. doi:10.1038/nchembio.1048

Basanta, B., Bick, M. J., Bera, A. K., Norn, C., Chow, C. M., Carter, L. P., et al. (2020). An Enumerative Algorithm for De Novo Design of Proteins with Diverse Pocket Structures. *Proc. Natl. Acad. Sci. U.S.A.* 117 (36), 22135–22145. doi:10.1073/pnas.2005412117

Bell, E. L., Finnigan, W., France, S. P., Green, A. P., Hayes, M. A., Hepworth, L. J., et al. (2021). Biocatalysis. *Nat. Rev. Methods Prim.* 1 (1), 46. doi:10.1038/s43586-021-00044-z

Büchler, J., Malca, S. H., Patsch, D., Voss, M., Turner, N. J., Bornscheuer, U. T., et al. (2022). Algorithm-aided Engineering of Aliphatic Halogenase WelO5* for the Asymmetric Late-Stage Functionalization of Soraphens. *Nat. Commun.* 13 (1), 1–11. doi:10.1038/s41467-022-27999-1

Bunzel, H. A., Anderson, J. L. R., Hilvert, D., Arcus, V. L., van der Kamp, M. W., and Mulholland, A. J. (2021). Evolution of Dynamical Networks Enhances Catalysis in a Designer Enzyme. *Nat. Chem.* 13 (10), 1017–1022. doi:10.1038/s41557-021-00763-6

Byrne, M. J., Lees, N. R., Han, L.-C., van der Kamp, M. W., Mulholland, A. J., Stach, J. E. M., et al. (2016). The Catalytic Mechanism of a Natural Diels-Alderase Revealed in Molecular Detail. *J. Am. Chem. Soc.* 138 (19), 6095–6098. doi:10.1021/jacs.6b00232

Chen, K., and Arnold, F. H. (1993). Tuning the Activity of an Enzyme for Unusual Environments: Sequential Random Mutagenesis of Subtilisin E for Catalysis in Dimethylformamide. *Proc. Natl. Acad. Sci. U.S.A.* 90 (12), 5618–5622. doi:10.1073/pnas.90.12.5618

Chen, K., Wu, S., Zhu, L., Zhang, C., Xiang, W., Deng, Z., et al. (2016). Substitution of a Single Amino Acid Reverses the Regiospecificity of the Baeyer-Villiger Monooxygenase PntE in the Biosynthesis of the Antibiotic Pentalenolactone. *Biochemistry* 55 (48), 6696–6704. doi:10.1021/acs.biochem.6b01040

Chen, X., Zhang, H., Feng, J., Wu, Q., and Zhu, D. (2018). Molecular Basis for the High Activity and Enantioselectivity of the Carbonyl Reductase from Sporobolomyces Salmonicolor toward α-Haloacetophenones. *ACS Catal.* 8 (4), 3525–3531. doi:10.1021/acscatal.8b00591

Coelho, P. S., Brustad, E. M., Kannan, A., and Arnold, F. H. (2013). Olefin Cyclopropanation via Carbene Transfer Catalyzed by Engineered Cytochrome P450 Enzymes. *Science* 339 (6117), 307–310. doi:10.1126/science.1231434

Crawshaw, R., Crossley, A. E., Johannissen, L., Burke, A. J., Hay, S., Levy, C., et al. (2021). Engineering an Efficient and Enantioselective Enzyme for the Morita-Baylis-Hillman Reaction. *Nat. Chem.* 14, 313–320. doi:10.1038/s41557-021-00833-9

Cui, Y., Wang, Y., Tian, W., Bu, Y., Li, T., Cui, X., et al. (2021). Development of a Versatile and Efficient C-N Lyase Platform for Asymmetric Hydroamination via Computational Enzyme Redesign. *Nat. Catal.* 4 (5), 364–373. doi:10.1038/s41929-021-00604-2

Dalton, T., Faber, T., and Glorius, F. (2021). C-H Activation: Toward Sustainability and Applications. *ACS Cent. Sci.* 7 (2), 245–261. doi:10.1021/acscentsci.0c01413

de Gonzalo, G., and Paul, C. E. (2021). Recent Trends in Synthetic Enzymatic Cascades Promoted by Alcohol Dehydrogenases. *Curr. Opin. Green Sustain. Chem.* 32, 100548. doi:10.1016/j.cogsc.2021.100548

Derat, E., and Kamerlin, S. C. L. (2022). Computational Advances in Protein Engineering and Enzyme Design. *J. Phys. Chem. B* 126 (13), 2449–2451. doi:10.1021/acs.jpcb.2c01198

Dodani, S. C., Cahn, J. K. B., Heinisch, T., Brinkmann-Chen, S., McIntosh, J. A., and Arnold, F. H. (2014). Structural, Functional, and Spectroscopic Characterization of the Substrate Scope of the Novel Nitrating Cytochrome P450 TxtE. *ChemBioChem* 15 (15), 2259–2267. doi:10.1002/cbic.201402241

Dong, Y., Li, T., Zhang, S., Sanchis, J., Yin, H., Ren, J., et al. (2022). Biocatalytic Baeyer-Villiger Reactions: Uncovering the Source of Regioselectivity at Each Evolutionary Stage of a Mutant with Scrutiny of Fleeting Chiral Intermediates. *ACS Catal.* 12 (6), 3669–3680. doi:10.1021/acscatal.2c00415

Dunham, A. S., and Beltrao, P. (2021). Exploring Amino Acid Functions in a Deep Mutational Landscape. *Mol. Syst. Biol.* 17 (7), 1–14. doi:10.15252/msb.202110305

Ensari, Y., Dhoke, G. V., Davari, M. D., Bocola, M., Ruff, A. J., and Schwaneberg, U. (2017). Inversion of cpADH5 Enantiopreference and Altered Chain Length Specificity for Methyl 3-Hydroxyalkanoates. *Chem. Eur. J.* 23 (51), 12636–12645. doi:10.1002/chem.201702581

Gao, L., Zou, Y., Liu, X., Yang, J., Du, X., Wang, J., et al. (2021). Enzymatic Control of Endo- and Exo-Stereoselective Diels-Alder Reactions with Broad Substrate Scope. *Nat. Catal.* 4, 1059–1069. doi:10.1038/s41929-021-00717-8

Ghattas, W., Mahy, J. P., Réglier, M., and Simaan, A. J. (2021). Artificial Enzymes for Diels-Alder Reactions. *ChemBioChem* 22, 443–459. doi:10.1002/cbic.202000316

Greule, A., Stok, J. E., De Voss, J. J., and Cryle, M. J. (2018). Unrivalled Diversity: the Many Roles and Reactions of Bacterial Cytochromes P450 in Secondary Metabolism. *Nat. Prod. Rep.* 35 (8), 757–791. doi:10.1039/c7np00063d

Güclü, D., Szekrenyi, A., Garrabou, X., Kickstein, M., Junker, S., Clapés, P., et al. (2016). Minimalist Protein Engineering of an Aldolase Provokes Unprecedented Substrate Promiscuity. *ACS Catal.* 6 (3), 1848–1852. doi:10.1021/acscatal.5b02805

Hu, Y., Xu, W., Hui, C., Xu, J., Huang, M., Lin, X., et al. (2020). The Mutagenesis of a Single Site for Enhancing or Reversing the Enantio- or Regiopreference of Cyclohexanone Monooxygenases. *Chem. Commun.* 56 (65), 9356–9359. doi:10.1039/d0cc03721d

Hubert, C. B., and Barry, S. M. (2016). New Chemistry from Natural Product Biosynthesis. *Biochem. Soc. Trans.* 44 (3), 738–744. doi:10.1042/BST20160063

Hughes, G., and Lewis, J. C. (2018). Introduction: Biocatalysis in Industry. *Chem. Rev.* 118 (1), 1–3. doi:10.1021/acs.chemrev.7b00741

Humble, M. S., Cassimjee, K. E., Abedi, V., Federsel, H.-J., and Berglund, P. (2012). Key Amino Acid Residues for Reversed or Improved Enantiospecificity of an ω-Transaminase. *ChemCatChem* 4 (8), 1167–1172. doi:10.1002/cctc.201100487

Jia, M., O'Brien, T. E., Zhang, Y., Siegel, J. B., Tantillo, D. J., and Peters, R. J. (2018). Changing Face: A Key Residue for the Addition of Water by Sclareol Synthase. *ACS Catal.* 8 (4), 3133–3137. doi:10.1021/acscatal.8b00121

Jindal, G., Slanska, K., Kolev, V., Damborsky, J., Prokop, Z., and Warshel, A. (2019). Exploring the Challenges of Computational Enzyme Design by Rebuilding the Active Site of a Dehalogenase. *Proc. Natl. Acad. Sci. U.S.A.* 116 (2), 389–394. doi:10.1073/pnas.1804979115

Jumper, J., Evans, R., Pritzel, A., Green, T., Figurnov, M., Ronneberger, O., et al. (2021). Highly Accurate Protein Structure Prediction with AlphaFold. *Nature* 596 (7873), 583–589. doi:10.1038/s41586-021-03819-2

Kelly, S. A., Mix, S., Moody, T. S., and Gilmore, B. F. (2020). Transaminases for Industrial Biocatalysis: Novel Enzyme Discovery. *Appl. Microbiol. Biotechnol.* 104 (11), 4781–4794. doi:10.1007/s00253-020-10585-0

Knorrscheidt, A., Soler, J., Hünecke, N., Püllmann, P., Garcia-Borràs, M., and Weissenborn, M. J. (2021). Accessing Chemo- and Regioselective Benzylic and Aromatic Oxidations by Protein Engineering of an Unspecific Peroxygenase. *ACS Catal.* 11 (12), 7327–7338. doi:10.1021/acscatal.1c00847

Koesoema, A. A., Standley, D. M., Senda, T., and Matsuda, T. (2020). Impact and Relevance of Alcohol Dehydrogenase Enantioselectivities on Biotechnological Applications. *Appl. Microbiol. Biotechnol.* 104 (7), 2897–2909. doi:10.1007/s00253-020-10440-2

Kong, X.-D., Ma, Q., Zhou, J., Zeng, B.-B., and Xu, J.-H. (2014). A Smart Library of Epoxide Hydrolase Variants and the Top Hits for Synthesis of (S)-β-Blocker Precursors. *Angew. Chem. Int. Ed.* 53 (26), 6641–6644. doi:10.1002/anie.201402653

Kong, X.-D., Yuan, S., Li, L., Chen, S., Xu, J.-H., and Zhou, J. (2014). Engineering of an Epoxide Hydrolase for Efficient Bioresolution of Bulky Pharmaco Substrates. *Proc. Natl. Acad. Sci. U.S.A.* 111 (44), 15717–15722. doi:10.1073/pnas.1404915111

Kren, V., and Martinkova, L. (2012). Glycosides in Medicine: "The Role of Glycosidic Residue in Biological Activity. *Curr. Med. Chem.* 8 (11), 1303–1328. doi:10.2174/0929867013372193

Kuipers, R. K., Joosten, H.-J., van Berkel, W. J. H., Leferink, N. G. H., Rooijen, E., Ittmann, E., et al. (2010). 3DM: Systematic Analysis of Heterogeneous Superfamily Data to Discover Protein Functionalities. *Proteins* 78 (9), NA. doi:10.1002/prot.22725

Leveson-Gower, R. B., Mayer, C., and Roelfes, G. (2019). The Importance of Catalytic Promiscuity for Enzyme Design and Evolution. *Nat. Rev. Chem.* 3 (12), 687–705. doi:10.1038/s41570-019-0143-x

Li, A., Wang, T., Tian, Q., Yang, X., Yin, D., Qin, Y., et al. (2021). Single-Point Mutant Inverts the Stereoselectivity of a Carbonyl Reductase toward β-Ketoesters with Enhanced Activity. *Chem. Eur. J.* 27 (20), 6283–6294. doi:10.1002/chem.202005195

Li, A., Ye, L., Yang, X., Yang, C., Gu, J., and Yu, H. (2016). Structure-guided Stereoselectivity Inversion of a Short-Chain Dehydrogenase/reductase toward Halogenated Acetophenones. *Chem. Commun.* 52 (37), 6284–6287. doi:10.1039/c6cc00051g

Li, F.-L., Kong, X.-D., Chen, Q., Zheng, Y.-C., Xu, Q., Chen, F.-F., et al. (2018). Regioselectivity Engineering of Epoxide Hydrolase: Near-Perfect Enantioconvergence through a Single Site Mutation. *ACS Catal.* 8 (9), 8314–8317. doi:10.1021/acscatal.8b02622

Li, G., Garcia-Borràs, M., Fürst, M. J. L. J., Ilie, A., Fraaije, M. W., Houk, K. N., et al. (2018). Overriding Traditional Electronic Effects in Biocatalytic Baeyer-Villiger Reactions by Directed Evolution. *J. Am. Chem. Soc.* 140 (33), 10464–10472. doi:10.1021/jacs.8b04742

Li, R., Wijma, H. J., Song, L., Cui, Y., Otzen, M., Tian, Y. e., et al. (2018). Computational Redesign of Enzymes for Regio- and Enantioselective Hydroamination. *Nat. Chem. Biol.* 14 (7), 664–670. doi:10.1038/s41589-018-0053-0

Liao, H., Ma, J., Yao, H., and Liu, X.-W. (2018). Recent Progress of C-Glycosylation Methods in the Total Synthesis of Natural Products and Pharmaceuticals. *Org. Biomol. Chem.* 16 (11), 1791–1806. doi:10.1039/c8ob00032h

Lichman, B. R., Gershater, M. C., Lamming, E. D., Pesnot, T., Sula, A., Keep, N. H., et al. (2015). 'Dopamine-first' Mechanism Enables the Rational Engineering of the Norcoclaurine Synthase Aldehyde Activity Profile. *FEBS J.* 282 (6), 1137–1151. doi:10.1111/febs.13208

Liu, B., Qu, G., Li, J. K., Fan, W., Ma, J. A., Xu, Y., et al. (2019). Conformational Dynamics-Guided Loop Engineering of an Alcohol Dehydrogenase: Capture, Turnover and Enantioselective Transformation of Difficult-to-Reduce Ketones. *Adv. Synth. Catal.* 361 (13), 3182–3190. doi:10.1002/adsc.201900249

Liu, C., Wen, K. G., Zeng, X. P., and Peng, Y. Y. (2020). Advances in Chemocatalytic Asymmetric Baeyer-Villiger Oxidations. *Adv. Synth. Catal.* 362 (5), 1015–1031. doi:10.1002/adsc.201901178

Liu, Z., and Arnold, F. H. (2021). New-to-nature Chemistry from Old Protein Machinery: Carbene and Nitrene Transferases. *Curr. Opin. Biotechnol.* 69, 43–51. doi:10.1016/j.copbio.2020.12.005

Lonsdale, R., and Reetz, M. T. (2015). Reduction of α,β-Unsaturated Ketones by Old Yellow Enzymes: Mechanistic Insights from Quantum Mechanics/Molecular Mechanics Calculations. *J. Am. Chem. Soc.* 137 (46), 14733–14742. doi:10.1021/jacs.5b08687

Louka, S., Barry, S. M., Heyes, D. J., Mubarak, M. Q. E., Ali, H. S., Alkhalaf, L. M., et al. (2020). Catalytic Mechanism of Aromatic Nitration by Cytochrome P450 TxtE: Involvement of a Ferric-Peroxynitrite Intermediate. *J. Am. Chem. Soc.* 142 (37), 15764–15779. doi:10.1021/jacs.0c05070

Lovelock, S. L., Crawshaw, R., Basler, S., Levy, C., Baker, D., Hilvert, D., et al. (2022). The Road to Fully Programmable Protein Catalysis. *Nature* 606, 49–58. doi:10.1038/s41586-022-04456-z

MacDonald, D. S., Garrabou, X., Klaus, C., Verez, R., Mori, T., and Hilvert, D. (2020). Engineered Artificial Carboligases Facilitate Regioselective Preparation of Enantioenriched Aldol Adducts. *J. Am. Chem. Soc.* 142 (23), 10250–10254. doi:10.1021/jacs.0c02351

Maria-Solano, M. A., Romero-Rivera, A., and Osuna, S. (2017). Exploring the Reversal of Enantioselectivity on a Zinc-dependent Alcohol Dehydrogenase. *Org. Biomol. Chem.* 15 (19), 4122–4129. doi:10.1039/c7ob00482f

Marshall, J. R., Mangas-Sanchez, J., and Turner, N. J. (2021). Expanding the Synthetic Scope of Biocatalysis by Enzyme Discovery and Protein Engineering. *Tetrahedron* 82, 131926. doi:10.1016/j.tet.2021.131926

McIntosh, J. A., Benkovics, T., Silverman, S. M., Huffman, M. A., Kong, J., Maligres, P. E., et al. (2021). Engineered Ribosyl-1-Kinase Enables Concise Synthesis of Molnupiravir, an Antiviral for COVID-19. *ACS Cent. Sci.* 7 (12), 1980–1985. doi:10.1021/acscentsci.1c00608

Messiha, H. L., Ahmed, S. T., Karuppiah, V., Suardíaz, R., Ascue Avalos, G. A., Fey, N., et al. (2018). Biocatalytic Routes to Lactone Monomers for Polymer Production. *Biochemistry* 57 (13), 1997–2008. doi:10.1021/acs.biochem.8b00169

Meyer, D., Walter, L., Kolter, G., Pohl, M., Müller, M., and Tittmann, K. (2011). Conversion of Pyruvate Decarboxylase into an Enantioselective Carboligase with Biosynthetic Potential. *J. Am. Chem. Soc.* 133 (10), 3609–3616. doi:10.1021/ja110236w

Miller, D. C., Lal, R. G., Marchetti, L. A., and Arnold, F. H. (2022). Biocatalytic One-Carbon Ring Expansion of Aziridines to Azetidines via a Highly Enantioselective [1,2]-Stevens Rearrangement. *J. Am. Chem. Soc.* 144 (11), 4739–4745. doi:10.1021/jacs.2c00251

Minami, A., and Oikawa, H. (2016). Recent Advances of Diels-Alderases Involved in Natural Product Biosynthesis. *J. Antibiot.* 69 (7), 500–506. doi:10.1038/ja.2016.67

Mondal, D., Kolev, V., and Warshel, A. (2020). Combinatorial Approach for Exploring Conformational Space and Activation Barriers in Computer-Aided Enzyme Design. *ACS Catal.* 10 (11), 6002–6012. doi:10.1021/acscatal.0c01206

Mordhorst, S., and Andexer, J. N. (2020). Round, Round We Go - Strategies for Enzymatic Cofactor Regeneration. *Nat. Prod. Rep.* 37 (10), 1316–1333. doi:10.1039/d0np00004c

Nagano, S., and Poulos, T. L. (2005). Crystallographic Study on the Dioxygen Complex of Wild-type and Mutant Cytochrome P450cam. *J. Biol. Chem.* 280 (36), 31659–31663. doi:10.1074/jbc.M505261200

Nidetzky, B., Gutmann, A., and Zhong, C. (2018). Leloir Glycosyltransferases as Biocatalysts for Chemical Production. *ACS Catal.* 8 (7), 6283–6300. doi:10.1021/acscatal.8b00710

Nie, Y., Wang, S., Xu, Y., Luo, S., Zhao, Y.-L., Xiao, R., et al. (2018). Enzyme Engineering Based on X-Ray Structures and Kinetic Profiling of Substrate Libraries: Alcohol Dehydrogenases for Stereospecific Synthesis of a Broad Range of Chiral Alcohols. *ACS Catal.* 8 (6), 5145–5152. doi:10.1021/acscatal.8b00364

Ortmayer, M., Fisher, K., Basran, J., Wolde-Michael, E. M., Heyes, D. J., Levy, C., et al. (2020). Rewiring the "Push-Pull" Catalytic Machinery of a Heme Enzyme Using an Expanded Genetic Code. *ACS Catal.* 10 (4), 2735–2746. doi:10.1021/acscatal.9b05129

Ostertag, E., Zheng, L., Broger, K., Stehle, T., Li, S.-M., and Zocher, G. (2021). Reprogramming Substrate and Catalytic Promiscuity of Tryptophan PrenyltransferasesJournal of Molecular Biology. *J. Mol. Biol.* 433 (2), 166726. doi:10.1016/j.jmb.2020.11.025

Padhi, S. K., Bougioukou, D. J., and Stewart, J. D. (2009). Site-saturation Mutagenesis of Tryptophan 116 of Saccharomyces Pastorianus Old Yellow Enzyme Uncovers Stereocomplementary Variants. *J. Am. Chem. Soc.* 131 (9), 3271–3280. doi:10.1021/ja8081389

Pompeu, Y. A., Sullivan, B., and Stewart, J. D. (2013). X-ray Crystallography Reveals How Subtle Changes Control the Orientation of Substrate Binding in an Alkene Reductase. *ACS Catal.* 3 (10), 2376–2390. doi:10.1021/cs400622e

Pompeu, Y. A., Sullivan, B., Walton, A. Z., and Stewart, J. D. (2012). Structural and Catalytic Characterization of Pichia Stipitis OYE 2.6, a Useful Biocatalyst for Asymmetric Alkene Reductions. *Adv. Synth. Catal.* 354 (10), 1949–1960. doi:10.1002/adsc.201200213

Poulos, T. L. (2014). Heme Enzyme Structure and Function. *Chem. Rev.* 114 (7), 3919–3962. doi:10.1021/cr400415k

Qin, F., Qin, B., Mori, T., Wang, Y., Meng, L., Zhang, X., et al. (2016). Engineering of Candida Glabrata Ketoreductase 1 for Asymmetric Reduction of α-Halo Ketones. *ACS Catal.* 6 (9), 6135–6140. doi:10.1021/acscatal.6b01552

Qin, F., Qin, B., Zhang, W., Liu, Y., Su, X., Zhu, T., et al. (2018). Discovery of a Switch between Prelog and Anti-prelog Reduction toward Halogen-Substituted Acetophenones in Short-Chain Dehydrogenase/Reductases. *ACS Catal.* 8 (7), 6012–6020. doi:10.1021/acscatal.8b00807

Qu, G., Bi, Y., Liu, B., Li, J., Han, X., Liu, W., et al. (2021). Unlocking the Stereoselectivity and Substrate Acceptance of Enzymes: Proline-Induced Loop Engineering Test. *Angew. Chem.* 134. doi:10.1002/ange.202110793

Reetz, M. T., and Wu, S. (2009). Laboratory Evolution of Robust and Enantioselective Baeyer–Villiger Monooxygenases for Asymmetric Catalysis. *J. Am. Chem. Soc.* 131 (42), 15424–15432. doi:10.1021/ja906212k

Richter, F., Leaver-Fay, A., Khare, S. D., Bjelic, S., and Baker, D. (2011). De Novo enzyme Design Using Rosetta3. *PLoS ONE* 6 (5), e19230–12. doi:10.1371/journal.pone.0019230

Rüthlein, E., Classen, T., Dobnikar, L., Schölzel, M., and Pietruszka, J. (2015). Finding the Selectivity Switch - A Rational Approach toward Stereocomplementary Variants of the Ene Reductase YqjM. *Adv. Synth. Catal.* 357 (8), 1775–1786. doi:10.1002/adsc.201500149

Sato, M., Kishimoto, S., Yokoyama, M., Jamieson, C. S., Narita, K., Maeda, N., et al. (2021). Catalytic Mechanism and Endo-To-Exo Selectivity Reversion of an Octalin-Forming Natural Diels-Alderase. *Nat. Catal.* 4 (3), 223–232. doi:10.1038/s41929-021-00577-2

Savile, C. K., Janey, J. M., Mundorff, E. C., Moore, J. C., Tam, S., Jarvis, W. R., et al. (2010). Biocatalytic Asymmetric Synthesis of Chiral Amines from Ketones Applied to Sitagliptin Manufacture', *Science. Am. Assoc. Adv. Sci.* 329 (5989), 305–309. doi:10.1126/science.1188934

Schwizer, F., Okamoto, Y., Heinisch, T., Gu, Y., Pellizzoni, M. M., Lebrun, V., et al. (2018). Artificial Metalloenzymes: Reaction Scope and Optimization Strategies. *Chem. Rev.* 118 (1), 142–231. doi:10.1021/acs.chemrev.7b00014

Serapian, S. A., and Van Der Kamp, M. W. (2019). Unpicking the Cause of Stereoselectivity in Actinorhodin Ketoreductase Variants with Atomistic Simulations. *ACS Catal.* 9 (3), 2381–2394. doi:10.1021/acscatal.8b04846

Skalden, L., Peters, C., Dickerhoff, J., Nobili, A., Joosten, H.-J., Weisz, K., et al. (2015). Two Subtle Amino Acid Changes in a Transaminase Substantially Enhance or Invert Enantiopreference in Cascade Syntheses. *ChemBioChem* 16 (7), 1041–1045. doi:10.1002/cbic.201500074

Stockinger, P., Borlinghaus, N., Sharma, M., Aberle, B., Grogan, G., Pleiss, J., et al. (2021). Inverting the Stereoselectivity of an NADH-Dependent Imine-Reductase Variant. *ChemCatChem* 13, 5210–5215. doi:10.1002/cctc.202101057

Stok, J. E., Giang, P. D., Wong, S. H., and De Voss, J. J. (2019). Exploring the Substrate Specificity of Cytochrome P450cin. *Archives Biochem. Biophysics* 672 (July), 108060. doi:10.1016/j.abb.2019.07.025

Sun, W., Xue, H., Liu, H., Lv, B., Yu, Y., Wang, Y., et al. (2020). Controlling Chemo- and Regioselectivity of a Plant P450 in Yeast Cell toward Rare Licorice Triterpenoid Biosynthesis. *ACS Catal.* 10 (7), 4253–4260. doi:10.1021/acscatal.0c00128

Toogood, H. S., and Scrutton, N. S. (2018). Discovery, Characterization, Engineering, and Applications of Ene-Reductases for Industrial Biocatalysis. *ACS Catal.* 8 (4), 3532–3549. doi:10.1021/acscatal.8b00624

Toogood, H. S., and Scrutton, N. S. (2014). New Developments in 'ene'-Reductase Catalysed Biological Hydrogenations. *Curr. Opin. Chem. Biol.* 19 (1), 107–115. doi:10.1016/j.cbpa.2014.01.019

Varadi, M., Anyango, S., Deshpande, M., Nair, S., Natassia, C., Yordanova, G., et al. (2022). AlphaFold Protein Structure Database: Massively Expanding the Structural Coverage of Protein-Sequence Space with High-Accuracy Models. *Nucleic Acids Res.* 50 (D1), D439–D444. doi:10.1093/nar/gkab1061

Vogel, A., Schmiedel, R., Hofmann, U., Gruber, K., and Zangger, K. (2014). Converting Aspartase into a β-Amino Acid Lyase by Cluster Screening. *ChemCatChem* 6 (4), 965–968. doi:10.1002/cctc.201300986

Walton, A. Z., Conerly, W. C., Pompeu, Y., Sullivan, B., and Stewart, J. D. (2011). Biocatalytic Reductions of Baylis-Hillman Adducts. *ACS Catal.* 1 (9), 989–993. doi:10.1021/cs200223f

Wang, J.-b., Li, G., and Reetz, M. T. (2017). Enzymatic Site-Selectivity Enabled by Structure-Guided Directed Evolution. *Chem. Commun.* 53 (28), 3916–3928. doi:10.1039/c7cc00368d

Wang, S., Nie, Y., Xu, Y., Zhang, R., Ko, T.-P., Huang, C.-H., et al. (2014). Unconserved Substrate-Binding Sites Direct the Stereoselectivity of Medium-Chain Alcohol Dehydrogenase. *Chem. Commun.* 50 (58), 7770–7772. doi:10.1039/c4cc01752h

Wang, Y., Xue, P., Cao, M., Yu, T., Lane, S. T., and Zhao, H. (2021). Directed Evolution: Methodologies and Applications. *Chem. Rev.* 121 (20), 12384–12444. doi:10.1021/acs.chemrev.1c00260

Wechsler, C., Meyer, D., Loschonsky, S., Funk, L.-M., Neumann, P., Ficner, R., et al. (2015). Tuning and Switching Enantioselectivity of Asymmetric Carboligation in an Enzyme through Mutational Analysis of a Single Hot Spot. *ChemBioChem* 16 (18), 2580–2584. doi:10.1002/cbic.201500529

Wen, Z., Zhang, Z.-M., Zhong, L., Fan, J., Li, M., Ma, Y., et al. (2021). Directed Evolution of a Plant Glycosyltransferase for Chemo- and Regioselective Glycosylation of Pharmaceutically Significant Flavonoids. *ACS Catal.* 11, 14781–14790. doi:10.1021/acscatal.1c04191

Wijma, H. J., Floor, R. J., Bjelic, S., Marrink, S. J., Baker, D., and Janssen, D. B. (2015). Enantioselective Enzymes by Computational Design and In Silico Screening. *Angew. Chem.* 127 (12), 3797–3801. doi:10.1002/ange.201411415

Winkler, C. K., Schrittwieser, J. H., and Kroutil, W. (2021). Power of Biocatalysis for Organic Synthesis. *ACS Cent. Sci.* 7 (1), 55–71. doi:10.1021/acscentsci.0c01496

Wu, S., Acevedo, J. P., and Reetz, M. T. (2010). Induced Allostery in the Directed Evolution of an Enantioselective Baeyer-Villiger Monooxygenase. *Proc. Natl. Acad. Sci. U.S.A.* 107 (7), 2775–2780. doi:10.1073/pnas.0911656107

Yang, B., and Gao, S. (2018). Recent Advances in the Application of Diels-Alder Reactions Involving O-Quinodimethanes, Aza-O-Quinone Methides and O-Quinone Methides in Natural Product Total Synthesis. *Chem. Soc. Rev.* 47 (21), 7926–7953. doi:10.1039/c8cs00274f

Yang, K. K., Wu, Z., and Arnold, F. H. (2019). Machine-learning-guided Directed Evolution for Protein Engineering. *Nat. Methods* 16 (8), 687–694. doi:10.1038/s41592-019-0496-6

Yu, J., Song, J., Chi, C., Liu, T., Geng, T., Cai, Z., et al. (2021). Functional Characterization and Crystal Structure of the Bifunctional Thioesterase Catalyzing Epimerization and Cyclization in Skyllamycin Biosynthesis. *ACS Catal.* 11 (18), 11733–11741. doi:10.1021/acscatal.1c03064

Zhang, D., Chen, X., Chi, J., Feng, J., Wu, Q., and Zhu, D. (2015). Semi-Rational Engineering a Carbonyl Reductase for the Enantioselective Reduction of β-Amino Ketones. *ACS Catal.* 5 (4), 2452–2457. doi:10.1021/acscatal.5b00226

Zhang, J., Liao, D., Chen, R., Zhu, F., Ma, Y., Gao, L., et al. (2022). Tuning an Imine Reductase for the Asymmetric Synthesis of Azacycloalkylamines by Concise Structure-Guided Engineering. *Angew. Chem. Int. Ed.* 61, 300457. doi:10.1002/anie.202201908

Zhang, M., Yi, Y., Gao, B. H., Su, H. F., Bao, Y. O., Shi, X. M., et al. (2021). Functional Characterization and Protein Engineering of a Triterpene 3-/6-/2′-O -Glycosyltransferase Reveal a Conserved Residue Critical for the Regiospecificity. *Angew. Chem.* 134, 230026. doi:10.1002/ange.202113587

Zhang, R. K., Huang, X., and Arnold, F. H. (2019). Selective C H Bond Functionalization with Engineered Heme Proteins: New Tools to Generate Complexity. *Curr. Opin. Chem. Biol.* 49, 67–75. doi:10.1016/j.cbpa.2018.10.004

Zhou, Q., Chin, M., Fu, Y., Liu, P., and Yang, Y. (2021). Stereodivergent Atom-Transfer Radical Cyclization by Engineered Cytochromes P450. *Science* 374 (6575), 1612–1616. doi:10.1126/science.abk1603

Conflict of Interest: The authors declare that the research was conducted in the absence of any commercial or financial relationships that could be construed as a potential conflict of interest.

Publisher's Note: All claims expressed in this article are solely those of the authors and do not necessarily represent those of their affiliated organizations, or those of the publisher, the editors, and the reviewers. Any product that may be evaluated in this article, or claim that may be made by its manufacturer, is not guaranteed or endorsed by the publisher.

frontiers | Frontiers in Molecular Biosciences

TYPE Perspective
PUBLISHED 25 November 2022
DOI 10.3389/fmolb.2022.975054

OPEN ACCESS

EDITED BY
Milena Quaglia,
National Measurement Laboratory at LGC, United Kingdom

REVIEWED BY
Enoch Y. Park,
Shizuoka University, Japan

*CORRESPONDENCE
Eli Keshavarz-Moore,
e.keshavarz-moore@ucl.ac.uk
Emiliana De Santis,
emiliana.de.santis@npl.co.uk

†These authors have contributed equally to this work and share first authorship

SPECIALTY SECTION
This article was submitted to Structural Biology,
a section of the journal
Frontiers in Molecular Biosciences

RECEIVED 21 June 2022
ACCEPTED 15 November 2022
PUBLISHED 25 November 2022

CITATION
De Sá Magalhães S, De Santis E, Hussein-Gore S, Colomb-Delsuc M and Keshavarz-Moore E (2022), Quality assessment of virus-like particle: A new transmission electron microscopy approach.
Front. Mol. Biosci. 9:975054.
doi: 10.3389/fmolb.2022.975054

Quality assessment of virus-like particle: A new transmission electron microscopy approach

Salomé De Sá Magalhães[1†], Emiliana De Santis[2*†], Saba Hussein-Gore[3†], Mathieu Colomb-Delsuc[3] and Eli Keshavarz-Moore[1*]

[1]Department of Biochemical Engineering, University College London, UCL, London, United Kingdom, [2]National Physical Laboratory, NPL, Teddington, United Kingdom, [3]Vironova AB, Stockholm, Sweden

Transmission electron microscopy (TEM) is a gold standard analytical method for nanoparticle characterization and is playing a valuable role in virus-like particle (VLP) characterization extending to other biological entities such as viral vectors. A dedicated TEM facility is a challenge to both small and medium-sized enterprises (SMEs) and companies operating in low-and-middle income countries (LMICs) due to high start-up and running costs. A low-voltage TEM solution with assisted image acquisition and analysis such as the MiniTEM system, coupled with Vironova Imaging and Analysis Software (VIAS) could provide an affordable and practical alternative. The MiniTEM system has a small footprint and software that enables semi-automated data collection and image analysis workflows using built-in deep learning methods (convolutional neural networks) for automation in analysis, increasing speed of information processing and enabling scaling to larger datasets. In this perspective we outline the potential and challenges in the use of TEM as mainstream analytical tool in manufacturing settings. We highlight the rationale and preliminary findings from our proof-of-concept study aiming to develop a method to assess critical quality attributes (CQAs) of VLPs and facilitate adoption of TEM in manufacturing settings. In our study we explored all the steps, from sample preparation to data collection and analysis using synthetic VLPs as model systems. The applicability of the method in product development was verified at pilot-scale during the technology transfer of dengue VLPs development from a university setting to an LMIC- based vaccine manufacturing company, demonstrating the applicability of this analytical technique to VLP vaccine characterization.

KEYWORDS

TEM, vaccines, VLP, LMIC, SMEs, CQA, CNN

Introduction

Virus like particles (VLPs) are made of multiple copies of the same or different peptidic building blocks (monomers) which self-assemble into higher order nanostructures that mimic the morphology and size of viruses but lack the genetic material and therefore are non-infectious (Comas-Garcia et al., 2020). The size of VLPs typically ranges from 20 nm to 200 nm and can be manufactured both recombinantly and synthetically. Despite the challenges in the scale up of VLPs manufacturing, as well as in the characterization of their complex assemblies, these particles have become powerful tools in vaccinology and biomedical research (Qian et al., 2020). For example, VLPs find application as delivery vehicles (DNA encapsulation); antigen presentation (adjuvant) and as vaccine platform (e.g., GARDASIL®, against human papilloma virus, Engerix B®, against hepatitis B virus, Epaxal®, against hepatitis A virus) (Tariq et al., 2022).

Recombinant VLPs can be produced in a variety of systems, from bacteria to mammalian cells, allowing flexibility in the choice of expression platforms (Fuenmayor et al., 2017). Synthetic VLPs are produced *via* chemical synthesis and can be inspired by nature (Castelletto et al., 2016), mimicking existing bioactive sequences, or be designed *de novo* (Noble et al., 2016; De Santis et al., 2017; Kepiro et al., 2020). They offer high control over their sequence, structure and assembly, as intra- and intermolecular interactions are engineered by design. This is advantageous and makes them ideal candidates in the development of model systems and reference materials (Briones et al., 2022) to benchmark critical quality attributes (CQAs) of VLP-based vaccines and drugs, during development and manufacturing. Additionally, VLPs can be engineered to display multiple biological activities, concomitantly (Castelletto et al., 2016), and can span sizes from 10 nm to few microns (Noble et al., 2016).

Analytics for quality attribute assessment

In vaccine production, bioactivity, potency, and stability of VLPs are crucial to ensure an active and safe outcome. Due to the structural complexity of VLPs, bioactivity depends not only on the properties of the building blocks (monomers), but crucially, also on their correct assembly and overall VLP morphology, which must be ensured throughout the development and manufacturing cycles. In essence, the bioactivity for VLPs is more than the sum of its parts. Correct morphology (shape) and size are CQA to ensure functional VLPs and specific measurands (i.e., the quantity to be measured) must be selected to describe these.

The structural complexity of VLPs, alongside the lack of clear acceptance criteria for the VLPs CQAs, makes manufacturing and characterization of VLPs challenging. Suitable analytical tools, methods and standards must be available for their assessment. A broad variety of analytical tools are available for biochemical, biophysical, functionality and stability characterization (Kumar et al., 2020; Nooraei et al., 2021). The assessment of CQA of VLP monomers (e.g., chemical identity and purity) can be informed by techniques and methods employed in the quality control of small molecules and biologics, which are already well-embedded in manufacturing settings. However, CQA associated with the final nanostructures (e.g., morphology, size, polydispersity) are harder to evaluate for biological nanoparticles, such as VLPs and viral vectors, where most of the analytical tools, methods, and standards to assess CQA of nanoparticles are typically optimized for inorganic nanoparticles and/or are not embedded in manufacturing settings. Whilst several techniques can provide information on size and polydispersity of VLPs, these can fail to provide information on their morphology, structural integrity, and any variations to these, which are often at the nanoscale and beyond the detection limit of most techniques commonly employed in manufacturing settings.

Amongst the techniques available, transmission electron microscopy (TEM), provides high resolution information at the nanoscale, playing a key role in defining quality control criteria during process development and manufacturing (De Santis and Ryadnov, 2021). Concomitant information on size, polydispersity, morphology, and structural integrity, can be obtained by TEM at nanoscale resolution, thus making the technique an invaluable tool for the characterization of viral and VLP-based vaccines. However, the use of TEM as routine analytical tool in manufacturing settings is hampered by several factors, including: 1) complexity of sample preparation, typically employing radioactive stains, 2) need for specialist facilities and highly trained staff leading to high costs 3) lack of validated methods and reliable reference materials for biological nanoparticles, such as VLPs. These barriers are even harder roadblocks for SME operators and manufacturers operating in low and middle-income countries (LMIC). In LMICs the frequent outbreaks of infectious diseases, coupled with limited resources (Plotkin et al., 2017; Kis et al., 2019; Khan et al., 2021), hamper vaccine development. Bringing in a user-friendly, accurate and precise method for nanoparticle characterization can significantly improve labor and cost efficiency for VLP vaccine development.

Low voltage TEM systems, such as the MiniTEM (Vironova AB), could help address some of these limitations, thus enabling the use of TEM as routine analytical tool in vaccine development. The reduced installation and maintenance costs of low-voltage TEM, due to the small footprint and ease of use, makes it compatible with any room or laboratory settings and easy to integrate within existing analytical pipelines. The MiniTEM system's resolution of 1 nm allows nanoparticles in the size-range of 10 nm–500 nm to be observed, thus enabling the analysis and characterization of therapeutic nanoparticle

delivery systems used in vaccines, gene therapy and drug delivery. The MiniTEM system is operated *via* a user-friendly software with automated features, VIAS, used to control the microscope, visualize and image samples as well as analyze data for users with little previous knowledge including automated microscope alignment and autofocus features. The software encompasses pattern recognition, AI and machine learning capabilities that enable it to perform advanced particle characterization, classification and measurements. VIAS uses a networked SQL server for optimal performance for data sharing and handling large data sets and storage capabilities.

The MiniTEM system is therefore tailored for non-experts in TEM to rapidly obtain meaningful particle characterization data that complements existing routine analytics in process development, thereby reducing the dependence on expert microscopists and subjective analysis, lifting some of the obstacles that have held back the routine use of TEM analysis in vaccine development settings (Verleysen et al., 2019).

Availability of additional information and more applicable analytical tools and methods for the biophysical characterization of VLPs would positively affect the rate and speed of approval of this class of vaccines in commercial applications and allow the industry to comply with the strict and increasing regulatory demands (Plotkin et al., 2017). To facilitate the uptake of TEM in process development and manufacturing settings, we generated a conceptual framework of the challenges for effective implementation of specific CQA analysis of VLPs using the MiniTEM system. Firstly, the development of a TEM analytical pipeline for VLPs, from sample preparation to data collection and analysis, was optimized to minimize the use of specialist infrastructure and training. Secondly, a proof of concept demonstrating the applicability of the method and analysis workflow to a vaccine product under development was conducted. The MiniTEM system (MiniTEM electron microscope + VIAS software) is currently being designed and developed to meet the requirements of quality control (QC) environments where the setup provides a cohesive solution for safety in data handling and traceability, hence making it a system of choice to be used in a quality-controlled environment and workflow. The VIAS software as such could be used with other TEM systems, but further developments to ensure a QC through the whole workflow would be required to ensure the data and metadata traceability and integrity conservation throughout the system transfers that such a workflow would involve.

The study design and method development focused on measurands that provided quantitative information that describe CQA of VLPs. Specifically, we developed a TEM method for the morphological (roundness and aspect ratio) and size (Feret diameter and area) characterization. The overall study design aimed at assessing the intra-laboratory and inter-laboratory reproducibility for the TEM analysis of selected VLP model systems for further method development.

TEM workflow for the analysis of VLPs

Optimization of specimen preparation using non-radioactive stains

Preparation of efficient embedding and even specimen spreading on the grid support is a prerequisite for an unbiased TEM assessment and imaging (Figure 1A) (Hauser et al., 2020). The stain helps to maintain the specimen integrity while ensuring a good contrast (Figure 1B) for biological samples. Indeed, the image formation in TEM results from the formation of a magnified image of the transmitted electrons from an electron beam passing through a specimen (Figure 1C). A few microliters of sample are deposited onto a TEM grid. Due to the inherently low contrast of biological samples under the electron beam, heavy metals are typically used to increase sample contrast by staining either the sample (positive staining) or the background (negative staining) (Brenner and Horne, 1959; Unwin, 1974). The contrast originates in part from the electron density of the specimen, heavy metals provide a good contrasting agent, with uranyl acetate (UA) being the most widely used stain for imaging biological samples. However, the inherent radioactivity of uranyl acetate and the consequent need for licensed facilities and specialist training, for handling and disposal limits the technological transfer of these methods to manufacturing settings. In this context, alternative solutions, such as employing non-radioactive staining reagents are important to address and promote adoption of TEM in SMEs and LMICs and has the potential to significantly accelerate routes to market for VLP-based vaccines. Significant efforts are ongoing to develop effective, safe, and stable non-radioactive stains and a range of commercially available non-radioactive stains are today available with different pH, metal content or concentrations depending on the analytical needs and specimen properties. However, a limited number of protocols optimised for the TEM analysis of VLPs particles using non-radioactive stains are available, hence limiting their widespread use for this application.

Additionally, vaccines developed during manufacturing often have a complex formulation to ensure stability of the VLPs and these may hamper the preparation of TEM specimens, causing for example stain precipitation and variable staining across the grid. It is therefore essential to take the potentially complex composition in mind when developing protocols for sample preparation. To address this complexity, we have employed Dengue VLPs (See Supplementary information). Evaluating these particles using TEM is an increasing part of defining QC criteria during development and ultimately manufacturing. The quality assessment of these particles is a critical step for quick decision making, saving time, and consequently, costs. We have explored the use of Nano-W™ and NanoVan™ in the

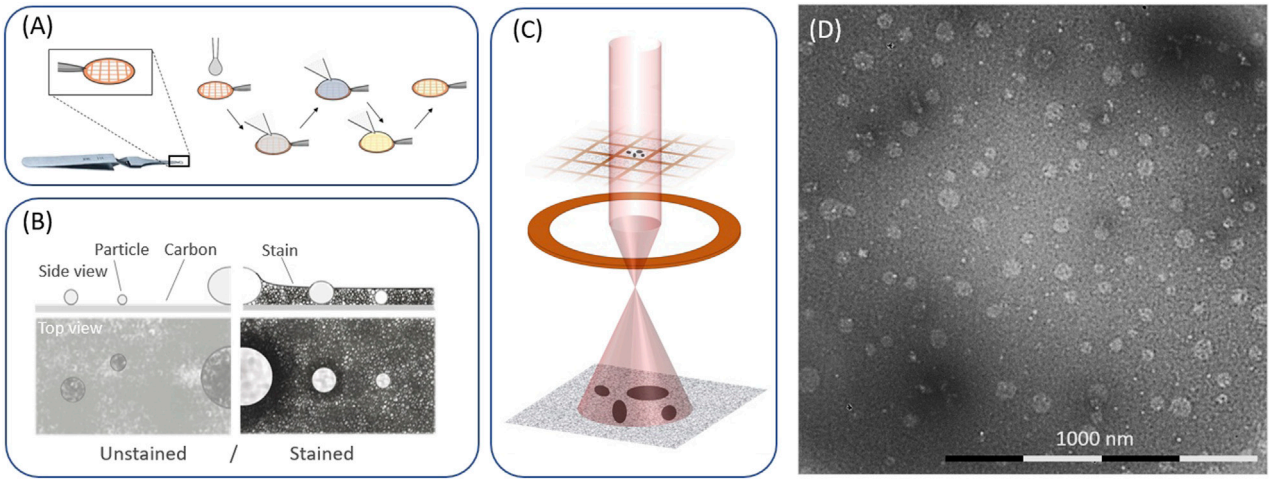

FIGURE 1
TEM workflow. **(A)** Depiction of an EM grid, used as support, and representative steps of a specimen preparation with specimen deposition (1), washing (2, 3), staining (4) and drying (5). **(B)** Schematic representations of an unstained and stain specimen. **(C)** image formation in an electron microscope. **(D)** representative image of a VLP prepared and imaged by negative stain TEM.

preparation of VLP specimens for TEM analysis and demonstrated the equivalence to uranyl acetate. Specimen preparation protocols were developed to optimize stain thickness, sample, and stain interaction (e.g., sample status and aggregation due to precipitation) and grid quality were evaluated enabling to fine tune the sample/grid preparation process. Through this optimized protocol we have reached equivalence of staining using radioactive (uranyl acetate) and non-radioactive stains (Nano-W™) providing greater flexibility for VLP sample preparation (See Supplementary information).

The availability of well-established sample preparation protocols is equally crucial. The nature of the specimen preparation, which requires several steps (e.g., sample deposition, blotting, and stain) and iterations, often suffers from poor reproducibility which can affect the accuracy of the analysis. The experience of the operator also plays a critical role in determining the final quality of the specimens. As a result, sample preparation is widely recognized as the bottleneck of TEM analysis and several efforts are ongoing to develop methods for semi-automated sample preparation to minimize manual handling of the samples, thus increasing safety, throughput and reducing variability (Benmeradi et al., 2015; Monninger et al., 2016; Strader et al., 2018).

Optimization of data collection (MiniTEM) and data analysis using artificial intelligence and neural network

Establishing a data collection scheme for a prepared TEM grid is key to ensure that the data is of suitable quality and statistically representative of the sample. TEM currently offers structural information at very high resolution, often at the expense of the total number of particles that can be investigated. It is therefore essential to devise a data collection schemes that can balance the need to obtain a data set which is representative of the bulk of the samples, without losing the high-resolution information that can accurately describe the measurands of interest. In practice, this is often a compromise between the resolution and the field of view (FOV) to obtain statistically significant information. Figure 1D specific guidance is available to support the users in selecting the most appropriate data collection scheme with respect to the resolution, field of view and number of representative particles (International Organization for Standardization, 2020). The size of the particles under investigation dictates the most appropriate data collection scheme.

Synthetic VLPs, are ideal model systems for method development, due to the rationally engineered interactions which offer high control over their self-assembly and morphology (De Santis and Ryadnov, 2015). Synthetic VLPs also represent ideal candidate reference materials for applications in vaccine development and gene delivery (Briones et al., 2022). Whilst development of VLPs was out of the scope of this study, a specific system was employed as a test model in this proof of concept to support the method development, focusing on key morphological parameters. In our proof of concept, we optimized the data collection scheme, e.g., resolution (0.7 nm/px) and field of view (1,500 nm × 1,500 nm) to obtain information on the key measurands that described the size (Feret diameter and area) and shape (roundness and aspect ratio) for synthetic VLPs. To enable technical transfer of the method beyond its original application,

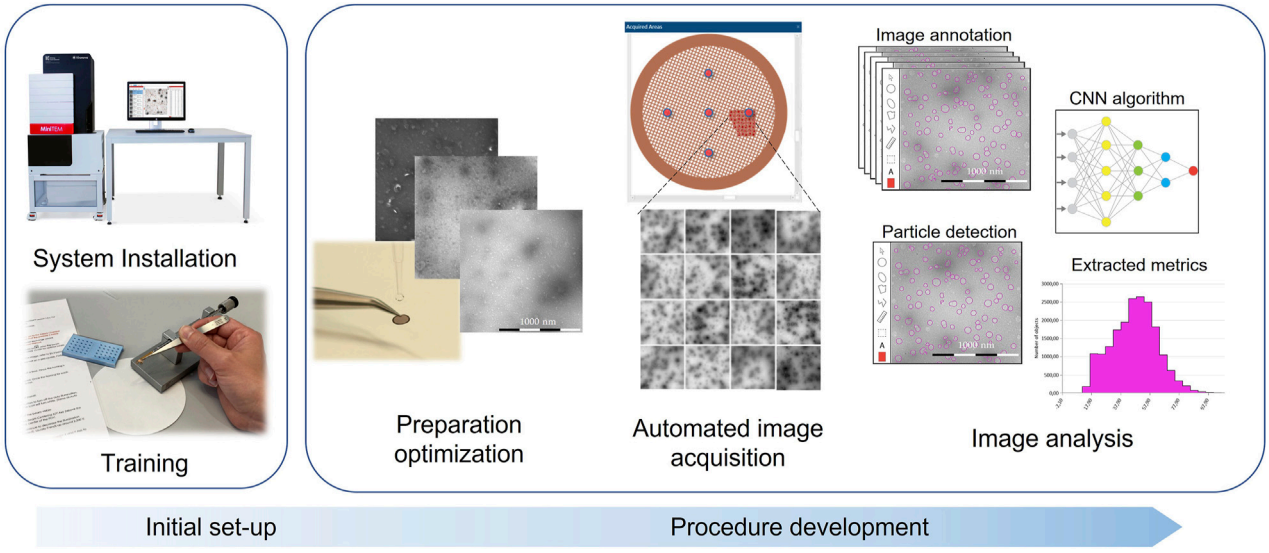

FIGURE 2
Development process for implementation of TEM workflow. After an initial set-up consisting of the system installation and personnel training, the preparation method is optimized by testing different stains, supports and preparation conditions. The prepared specimens are then imaged using an automated data acquisition to screen several grid areas and ensure a good representativity of the sample. Finally, the acquired images are fed into the CNN algorithm, trained *via* manual image annotation prior to the automated analysis, the resulting detection can be visually evaluated, and the data used for specimen evaluation. This whole process can be implemented into a validation framework.

we selected VLPs with a size of around 20 nm, which is comparable to that of some of the viral vectors (such as AAV) typically employed in vaccines development or as gene delivery vectors.

Automated or semi-automated data collection is particularly crucial to minimise/remove bias from the operator during data collection. We employed VIAS software for automated data collection to image a minimum of 3 independent areas well-spaced across the TEM grid to obtain a statistically relevant amount of detected VLPs particles (See Supplementary Information).

Data analysis is employed to derive the numerical values of the selected key measurands. Several approaches are available for data analysis of TEM images, such as ImageJ (Schindelin et al., 2012; Schneider et al., 2012). Although well established, these data analysis methods can suffer from operator bias, are often time consuming and require significant user-input and specialist skills, which limit the uptake of TEM as mainstream analytics in fast-paced manufacturing settings.

Significant efforts over the past few years have been dedicated to the development of artificial intelligence (AI) approaches for the analysis of TEM images, hence speeding-up processes by reducing operator input and improving the objectivity, precision, reliability, and robustness of the obtained data by removing user bias. Those advantages make these approaches good candidates to be implemented in a quality-controlled framework. Recent developments and implementation of analytical workflows using Convolutional Neural Networks (CNN) applied to image analysis of biological specimen appear promising. In this approach, the network is fed with a manually annotated set of data, considered as the raw data, and used to train the CNN model to develop and tune algorithms able to independently perform image segmentation, particle detection and classification on a new set of images. Using this approach with the VIAS software CNN training module, synthetic VLP particles were manually annotated to inform and train the model to enable discrimination between VLP particles, background, and debris. After screening the specimen for determining areas suitable for imaging and subsequently choosing the most appropriate field of view, a set of references images was acquired and annotated to be used as ground truth for the generation and training of the CNN model, prior to testing on a validation data set.

The model was subsequently applied to new TEM images and the automated particle detection performance examined and assessed. The data collection and the analysis workflows generated from these samples were used for the development of different CNN models, to enable automated VLP particle detection and measurement of quality attributes, such as diameter and roundness. The analysis using the CNN model was significantly faster and required no manual input, allowing for a shorter turnaround with less user-variability.

In this study, the CNN models successfully detected VLPs representing diverse morphologies under varied staining thicknesses. Moreover, to demonstrate the applicability of the

method and analysis workflow, the models were successfully applied to Dengue VLP vaccine candidates, providing a flexible and tunable model for future studies and analyses (Figure 2). This has been a successful first step proof of concept for using MiniTEM. Further and future work will focus on assessing other critical quality attributes, such as sample purity, different morphologies and sizes (See Supplementary Information).

The images were analyzed using the MiniTEM proprietary software VIAS, where equivalence of staining using radioactive and non-radioactive stains with adapted/optimized protocols was demonstrated. For both cases, attributes such as size and roundness showed acceptable/good correlation (data not shown). Through image data collected during the study, a dedicated CNN (ref) model was created by Vironova to enable automated VLP particle detection and measurement of quality attributes that include particle count, diameter, and roundness. The CNN model is part of a simple workflow that requires minimal training to operate and has the potential to accelerate decision-making processing during VLP vaccine development (Figure 2). The use of AI and CNN in vaccine development is showing potential on particles such as analysis of extracellular vesicles, exosomes, lentiviral vectors, and other enveloped, pleomorphic particles that are traditionally more difficult for image analysis classification in part due to their variable size and shape.

Final remarks

In this perspective we have provided an overview of the limiting factors in the application of TEM in development and manufacturing settings, highlighting key challenges within a typical TEM workflow. Our proof-of-concept study aims at providing solutions to enable a wider uptake of TEM, with emphasis on facilitations for LMIC countries, where a TEM analytical workflow was created towards the development of an optimized method for the assessment of CQAs of VLPs with defined acceptance criteria. The applicability of the method and analysis workflow to a Dengue VLP vaccine product under development by PT Bio Farma and UCL, was demonstrated, providing technical solutions for vaccine development by LMICs to tackle endemic diseases.

An emphasis on simplification and timesaving was a central point in the *in-situ* applicability of an alternative user-friendly visual technology to standard TEM. This also follows the trend of using AI and machine learning to alleviate and simplify processes by allowing smart automation and introducing non-subjectivity, an increasing requirement from regulatory authorities.

By addressing the obstacle steps of the workflow, from sample preparation to data collection and analysis we strove to enable an easy technical transfer into process development and manufacturing settings and uptake by non-expert microscopists.

Having demonstrated that the MiniTEM is a suitable tool for quality control in vaccine development, further studies will aim at providing detailed analysis of a range of VLPs and related self-assembles systems to support the applicability of MiniTEM and its software to an industrial setting.

This study is closely aligned with the aims of organizations and initiatives established in the UK to support medicine manufacture such as the UK Medicines Manufacturing Industry Partnership (MMIP), the vaccine manufacturing innovation center (VMIC), the Medicines Manufacturing Innovation Centre (MMIC), and academic/industry centers such as Vax Hub which promote efforts to accelerate time to market technology of advanced therapies for manufacturing and regulatory environments.

Data availability statement

The datasets generated for this study are available on request to the corresponding authors.

Author contributions

SdSM, EdS, and SH-G, conceptualization, writing—original draft preparation, review and editing as well as conducting the experiments. MC-D drafted the initial manuscript. EK-M drafted the initial manuscript, review, and editing. All authors provided editorial feedback, revisions and approved the manuscript.

Acknowledgments

We would like to thank PT Bio Farma (Indonesia), Dr. Neni Nurainy and Dr. Acep Riza, for providing us with dengue VLP samples. We would like to thank Dr. Adam Dickinson for providing instrument training to the academic partner, enabling non-experts in electron microscopy to operate the MiniTEM system confidently and autonomously to rapidly obtain particle characterization data. The authors gratefully acknowledge the Engineering and Physical Sciences Research Council (EPSRC), Future Vaccine Research Manufacturing Hub (Vax-Hub, EP/R013756/1) for funding.

Conflict of interest

SH-G and MC-D were employed by the company Vironova AB. Vironova AB provides electron microscopy-based imaging and analysis services, as well as TEM hardware and image analysis software for this purpose.

The remaining authors declare that the research was conducted in the absence of any commercial or financial

relationships that could be construed as a potential conflict of interest.

Publisher's note

All claims expressed in this article are solely those of the authors and do not necessarily represent those of their affiliated organizations, or those of the publisher, the editors and the reviewers. Any product that may be evaluated in this article, or claim that may be made by its manufacturer, is not guaranteed or endorsed by the publisher.

Supplementary material

The Supplementary Material for this article can be found online at: https://www.frontiersin.org/articles/10.3389/fmolb.2022.975054/full#supplementary-material

References

Benmeradi, N., Payre, B., and Goodman, S. L. (2015). Easier and safer biological staining: High contrast UranyLess staining of TEM grids using mPrep/g capsules. *Microsc. Microanal.* 21, 721–722. doi:10.1017/s1431927615004407

Brenner, S., and Horne, R. W. (1959). A negative staining method for high resolution electron microscopy of viruses. *Biochim. Biophys. Acta* 34, 103–110. doi:10.1016/0006-3002(59)90237-9

Briones, A., Martos, G., Bedu, M., Choteau, T., Josephs, R. D., Robert, I., et al. (2022). An SI-traceable reference material for virus-like particles. *Iscience* 25, 104294. doi:10.1016/j.isci.2022.104294

Castelletto, V., De Santis, E., Alkassem, H., Lamarre, B., Noble, J. E., Ray, S., et al. (2016). Structurally plastic peptide capsules for synthetic antimicrobial viruses. *Chem. Sci.* 7, 1707–1711. doi:10.1039/c5sc03260a

Comas-Garcia, M., Colunga-Saucedo, M., Rosales-Mendoza, S., and Comas-Garcia, M. (2020). The role of virus-like particles in medical biotechnology. *Mol. Pharm.* 17, 4407–4420. doi:10.1021/acs.molpharmaceut.0c00828

De Santis, E., Alkassem, H., Lamarre, B., Faruqui, N., Bella, A., Noble, J. E., et al. (2017). Antimicrobial peptide capsids of de novo design. *Nat. Commun.* 8, 2263. doi:10.1038/s41467-017-02475-3

De Santis, E., and Ryadnov, M. G. (2021). Imaging and 3D reconstruction of de novo peptide capsids. *Methods Mol. Biol.* 2208, 149–165. doi:10.1007/978-1-0716-0928-6_10

De Santis, E., and Ryadnov, M. G. (2015). Peptide self-assembly for nanomaterials: The old new kid on the block. *Chem. Soc. Rev.* 44, 8288–8300. doi:10.1039/c5cs00470e

Fuenmayor, J., Gòdia, F., and Cervera, L. (2017). Production of virus-like particles for vaccines. *N. Biotechnol.* 39, 174–180. doi:10.1016/j.nbt.2017.07.010

Hauser, J., Kylberg, G., Colomb-Delsuc, M., Stemme, G., Sintorn, I. M., and Roxhed, N. (2020). A microfluidic device for TEM sample preparation. *Lab. Chip* 20, 4186–4193. doi:10.1039/d0lc00724b

International Organization for Standardization (2020). Nanotechnologies — measurements of particle size and shape distributions by transmission electron microscopy (ISO 21363:2020). Available at: https://www.iso.org/standard/70762.html.

Kepiro, I. E., Marzuoli, I., Hammond, K., Ba, X., Lewis, H., Shaw, M., et al. (2020). Engineering chirally blind protein pseudocapsids into antibacterial persisters. *ACS Nano* 14, 1609–1622. doi:10.1021/acsnano.9b06814

Khan, M. I., Ikram, A., and Hamza, H. B. (2021). Vaccine manufacturing capacity in low-and middle-income countries. *Bull. World Health Organ.* 99, 479–479A. doi:10.2471/BLT.20.273375

Kis, Z., Shattock, R., Shah, N., and Kontoravdi, C. (2019). Emerging technologies for low-cost, rapid vaccine manufacture. *Biotechnol. J.* 14, e1800376. doi:10.1002/biot.201800376

Kumar, R., Banerjee, M., and Rathore, A. S. (2020). Virus-like particles as therapeutic moieties of the future. *Biopharm. Intenational* 21, 21–28.

Monninger, M. K., Nguessan, C. A., Blancett, C. D., Kuehl, K. A., Rossi, C. A., Olschner, S. P., et al. (2016). Preparation of viral samples within biocontainment for ultrastructural analysis: Utilization of an innovative processing capsule for negative staining. *J. Virol. Methods* 238, 70–76. doi:10.1016/j.jviromet.2016.10.005

Noble, J. E., De Santis, E., Ravi, J., Lamarre, B., Castelletto, V., Mantell, J., et al. (2016). A de Novo virus-like topology for synthetic virions. *J. Am. Chem. Soc.* 138, 12202–12210. doi:10.1021/jacs.6b05751

Nooraei, S., Bahrulolum, H., Hoseini, Z. S., Katalani, C., Hajizade, A., Easton, A. J., et al. (2021). Virus-like particles: Preparation, immunogenicity and their roles as nanovaccines and drug nanocarriers. *J. Nanobiotechnology* 19, 59–27. doi:10.1186/s12951-021-00806-7

Plotkin, S., Robinson, J. M., Cunningham, G., Iqbal, R., and Larsen, S. (2017). The complexity and cost of vaccine manufacturing – an overview. *Vaccine* 35, 4064–4071. doi:10.1016/j.vaccine.2017.06.003

Qian, C., Liu, X., Xu, Q., Wang, Z., Chen, J., Li, T., et al. (2020). Recent progress on the versatility of virus-like particles. *Vaccines* 8, 139. doi:10.3390/vaccines8010139

Schindelin, J., Arganda-Carreras, I., Frise, E., Kaynig, V., Longair, M., Pietzsch, T., et al. (2012). Fiji: An open-source platform for biological-image analysis. *Nat. Methods* 9, 676–682. doi:10.1038/nmeth.2019

Schneider, C. A., Rasband, W. S., and Eliceiri, K. W. (2012). NIH image to ImageJ: 25 years of image analysis. *Nat. Methods* 9, 671–675. doi:10.1038/nmeth.2089

Strader, T. E., Stewart, N. R., August, B. K., and Goodman, S. L. (2018). A versatile all-in-one automated processor for electron microscopy. *Microsc. Microanal.* 24, 1122–1123. doi:10.1017/s1431927618006098

Tariq, H., Batool, S., Asif, S., Ali, M., and Abbasi, B. H. (2022). Virus-like particles: Revolutionary platforms for developing vaccines against emerging infectious diseases. *Front. Microbiol.* 12, 790121. doi:10.3389/fmicb.2021.790121

Unwin, P. N. T. (1974). A new electron microscope imaging method for enhancing detail in thin biological specimens. *Z. fur Naturforsch. - Sect. A J. Phys. Sci.* 29, 158–163. doi:10.1515/zna-1974-0118

Verleysen, E., Wagner, T., Lipinski, H., Kägi, R., Koeber, R., Boix-sanfeliu, A., et al. (2019). Evaluation of a TEM based approach for size measurement of particulate (Nano)materials. *Materials* 12 (14), 2274. doi:10.3390/ma12142274

Frontiers in
Molecular Biosciences

Explores biological processes in living organisms on a molecular scale

Focuses on the molecular mechanisms underpinning and regulating biological processes in organisms across all branches of life.

Discover the latest Research Topics

See more →

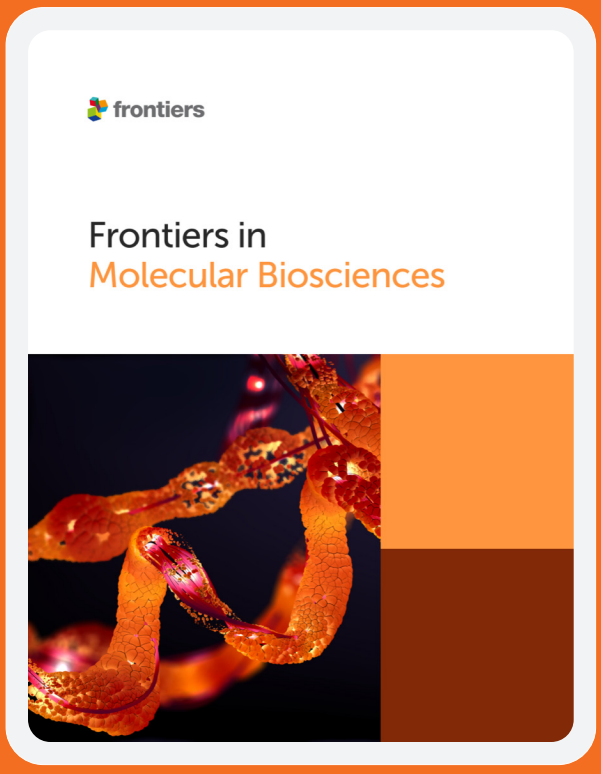

Frontiers

Avenue du Tribunal-Fédéral 34
1005 Lausanne, Switzerland
frontiersin.org

Contact us

+41 (0)21 510 17 00
frontiersin.org/about/contact